DEVELOPMENT OF LIGHTWEIGHT STRUCTURAL HEALTH MONITORING SYSTEMS FOR AEROSPACE APPLICATIONS

PhD Thesis

February 2013

Matthew Pearson (MEng)

Cardiff School of Engineering

Cardiff University

Cardiff

UK

Declaration

This work has not previously been accepted in substance for any degree and is not currently submitted in candidature for any degree.

Signed……..... (candidate) Date……

Statement 1

This thesis is being submitted in partial fulfilment of the requirements for the degree of PhD

Signed……..... (candidate) Date……

Statement 2

This thesis is the result of my own independent work/investigation, except where otherwise stated. Other sources are acknowledged by explicit references.

Signed……..... (candidate) Date……

Statement 3

I hereby give consent for my thesis, if accepted, to be available for photocopying and for inter-library loan, and for the title and summary to be made available to outside organisations.

Signed……..... (candidate) Date……

Statement 4: PREVIOUSLY APPROVED BAR ON ACCESS

I hereby give consent for my thesis, if accepted, to be available for photocopying and for inter-library loans **after expiry of a bar on access previously approved by the Graduate Development Committee.**

Signed……..... (candidate) Date……

Prifysgol Caerdydd **SUMMARY OF THESIS** **Cardiff University**

Candidate's Surname: Pearson **Institute at which study pursued:**

Candidate's Forenames: Matthew Robert Cardiff University

Candidate for Degree of: PhD

Full Title of Thesis: Development of Lightweight Structural Health Monitoring Systems for Aerospace Applications

Summary:

This thesis investigates the development of structural health monitoring systems (SHM) for aerospace applications. The work focuses on each aspect of a SHM system covering novel transducer technologies and damage detection techniques to detect and locate damage in metallic and composite structures. Secondly the potential of energy harvesting and power management methodologies to provide a stable power source is assessed. Finally culminating in the realisation of smart SHM structures.

1. Transducer Technology

A thorough experimental study of low profile, low weight novel transducers not normally used for acoustic emission (AE) and acousto-ultrasonics (AU) damage detection was conducted. This included assessment of their performance when exposed to aircraft environments and feasibility of embedding these transducers in composites specimens in order to realise smart structures.

2. Damage Detection

An extensive experimental programme into damage detection utilising AE and AU were conducted in both composites and metallic structures. These techniques were used to assess different damage mechanism within these materials. The same transducers were used for novel AE location techniques coupled with AU similarity assessment to successfully detect and locate damage in a variety of structures.

3. Energy Harvesting and Power Management

Experimental investigations and numerical simulations were undertaken to assess the power generation levels of piezoelectric and thermoelectric generators for typical vibration and temperature differentials which exist in the aerospace environment. Furthermore a power management system was assessed to demonstrate the ability of the system to take the varying nature of the input power and condition it to a stable power source for a system.

4. Smart Structures

The research conducted is brought together into a smart carbon fibre wing showcasing the novel embedded transducers for AE and AU damage detection and location, as well as vibration energy harvesting. A study into impact damage detection using the techniques showed the successful detection and location of damage. Also the feasibility of the embedded transducers for power generation was assessed.

Key words: Structural health monitoring, damage detection, energy harvesting, power management,

Acknowledgements

I would like to take this opportunity to express a great debt of gratitude to my academic supervisors Prof. Karen Holford, Dr Carol Featherston and Dr. Rhys Pullin for their guidance, immense support and patience throughout my work. I would also thank Dr. Mark Eaton for his advice, help and endless answering of questions. My thanks also to the technical staff at Cardiff School of Engineering especially Steve Mead, Paul Farrugia, Denley Slade, Richard Rogers and Harry Lane for their help, support and technical advice throughout my experimental investigations.

I am also grateful to Tim Bradshaw of Mistras and Christophe Paget of Airbus for the technical feedback and advice

Finally thanks to my parents, sister and the rest of my family as well as girlfriend, Mayada for supporting me though out the years and to my friends who have often reminded to keep smiling and to have fun.

Glossary

Terms relating to AE (ASTM 1982)

Hit - indication that a given AE channel has detected and processed an acoustic emission transient.

Event –A group of AE hits that was received from a single source.

Source - A mechanical mechanism that produces AE signals.

Terms relating to the detection of the signal:

Acoustic emission signal - The electrical signal obtained through the detection of acoustic emission.

Couplant - Substance providing an acoustic coupling between the propagation medium and the transducer.

Transducer - Device that converts the physical parameters of the wave into an electrical signal.

Terms relating to the processing of the signal:

Threshold - A preset voltage level, which has to be exceeded before an AE signal is detected, and processed. The following terms are made with reference to the threshold (Figure i)

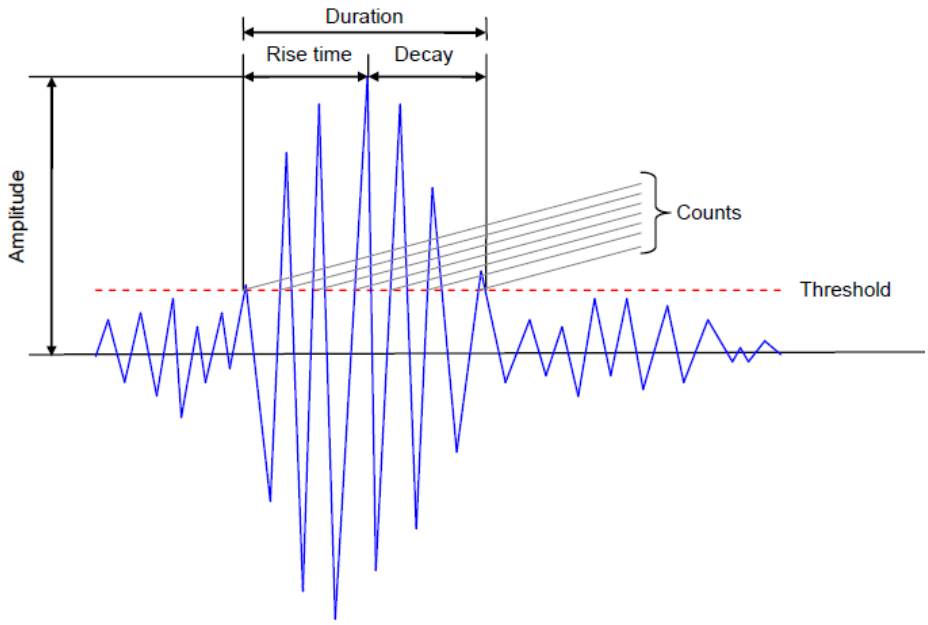

Figure i. AE waveform features

Duration - The interval between the first and last time the threshold was exceeded by the signal.

Peak Amplitude - Maximum signal amplitude within the duration of the signal.

Counts - Number of times the signal amplitude exceeds the threshold.

Rise Time - The interval between the first threshold crossing and the maximum amplitude of the signal.

Initiation Frequency - The average frequency of the waveform from the initial threshold crossing to the peak of the AE waveform.

Energy (Absolute) - The integral of the squared voltage signal divided by the reference resistance (10kOhm) over the duration of the AE waveform packet.

Terms relating to wave propagation:

Dispersion - The phenomenon whereby wave velocity varies with frequency.

Group wave velocity - The perceived velocity at which a packet of energy (or wave packet) travels.

Phase wave velocity - Velocity of individual waves within a packet of energy (or wave packet), each wave may travel at a different velocity (see dispersion). Phase velocity does not have to equal group velocity.

Attenuation - The rate at which signal amplitude is reduces with distance of propagation.

S_0 mode – Symmetrical or extensional fundamental Lamb wave mode that propagates in plate like materials and are sensitive to in-plane damage.

A_0 mode - Asymmetric or flexural fundamental Lamb wave mode that propagates in plate like materials and are sensitive to out of place damage.

Hsu-Nielson (H-N) Source – An artificial source of AE (Hsu and Breckenbridge 1981)

Time of Arrival (TOA) – Conventional AE source location algorithm used to located AE sources in structure. Using the difference in arrival times between transducers and a known wave velocity to estimate the location of an AE event by minimising the error between the measured and calculated different in arrival times.

Delta-T mapping technique – Advanced AE location technique, an area of interest is identified on a structure. Artificial AE source is used at node positions within the interest area

and resulting time of arrival recorded at the transducers. This enables the generation of different in arrival time contour maps for each transducer pairing. These are used to indentify contours when trying to located actual AE events, the maps are overlaid at the intersection of the contours corresponds to an estimate source location.

AIC delta-T mapping technique – Uses the same technique as above but uses the Akiakie Information Criteria (AIC) (Maeda 1985) to determine the onset of an AE wave. The AIC uses the entropy of the signal to determine between when the structures has structure and when it has not i.e. between signal and noise.

Wavestream – Raw AE activity recorded for a set time period irrespective of the threshold used.

Wavelet Transform – Signal processing technique which decomposes a transient signal in order to release a time frequency representation of a wave.

Acousto-ultrasonics – An active monitoring technique which utilises the fundamentals of guided Lamb waves(GLW) to detect damage in structure. An actuation signal is used to generate GLW in a structure by using surface mounted or embedded piezoelectric transducers. The resulting waves are recorded at receivers, where changes in the signal are observed due to scattering and mode conversion due to the presence of damage in the structure.

Cross Correlation – Signal processing technique which can be utilised in AU applications to determine whether damage is present in a structure. Uses the integral of the products of two signals to determine the similarity of the shape of two signals with respect to each other.

Ultrasonic C-scanner – An ultrasonic technique which is used to detect, measure and characterise a range of manufacturing and in-service defects in composites materials.

Thermoelastic stress analysis - The TSA system detects the small temperature changes occurring in a material subject to cyclic transient loading, where the change in temperature observed is directly related to the stress experienced by the material. The system provides a full-field measurement; hence any redistribution of the stress field resulting from damage onset can be detected.

Kernal Density Estimation - This is a statistical analysis of the location data which assess the probability of where a location is most likely to occur based on a statistical analysis of the resulting located events.

Digital Image Correlation - An optical technique that allows for the full field measurement of contour deformation, vibration and strain by tracking the pixels of a black and white speckle pattern applied to the specimen from a baseline image to those under load.

Energy harvesting – The process of scavenging energy from the envrioment using a variety of methods for example piezoelectric and thermoelectric energy harvesting.

Piezoelectric effect – The ability of certain crystals to become electrically polarised when they were subjected to a mechanical strain, the amount of this polarisation is proportional to the mechanical strain.

d_{33} mode – Mode of operation of a piezoelectric material where the applied force and the poling direction are parallel

d_{31} mode - Mode of operation of a piezoelectric material where the applied force and the poling direction are perpendicular

Permittivity – Or the dielectric constant is defined as the dielectric displacement per unit electric field.

Compliance – Is defined as the strain produced per unit stress.

Piezoelectric charge constant – Defined as the electric polarisation per unit mechanical stress applied, or the mechanical strain experience by the material per unit electric field applied.

Piezoelectric voltage constant – Defined as the electric field generated in a material per unit mechanical stress applied to it, or the mechanical strain experience by the material per unit electric displacement applied.

Coupling factor – A measure of the effectiveness with which electrical energy is converted to mechanical energy and vice versa.

Polarisation – The process of making a ceramic piezoelectric in a given direction by applying a strong electric field at a temperature slightly below the Curie point.

Curie point - The temperature at which spontaneous polarisation is lost.

Seebeck effect - Promotes a thermoelectric electromagnetic field across two different semi-conductors when their junctions are placed across a temperature gradient.

Thermoelectric generator (TEG) – Uses the principle of the Seebeck effect to generate a voltage from an applied temperature differential

Power Management - A power management system is therefore required to regulate the dynamic input power from an energy harvesting and provide a stable output power for a load device

Smart structure – A structure which has sensing devices embedded within the structure which are used for SHM techniques.

Nomenclature

Δt	Difference in arrival times between transducer pairs	(s)
C	Wave velocity in the medium	(ms^{-1})
D_s	Distance between transducers	(m)
d_2	Distance from source to first hit transducers	(m)
d_1	Distance from source to seconds hit transducer	(m)
h	Distance between the source and the line connecting transducers	(m)
$\Delta t_{i,obs}$	Difference in observed arrival time between transducers pairs	(s)
$\Delta t_{i,calc}$	Difference in calculated arrival time between transducer pairs	(s)
(X_s,Y_s)	X and Y positions of the source	(m)
(X_1,Y_1)	X and Y location of the first hit transducer	(m)
(X_i, Y_i)	X location and Y location of transducer i	(m)
t	Current sample point	
T	Final sample point	
Var	Variance	(V^2)
x[1;t]	Waveform from first sample to current sample	(V)
x[1;T]	Waveform from current sample to final sample	(V)
C_{xy}	Coherence between two waveforms	
P_{xx}	Power spectrum density of a time series x(t)	($V^2.Hz^{-1}$)
P_{yy}	Power spectrum density of a time series y(t)	($V^2.Hz^{-1}$)
P_{xy}	Power spectrum density the function x(t)*y(t)	($V^2.Hz^{-1}$)
Y	Young's Modulus	(Pa)
v	Poisson's Ratio	
σ_y	Tensile yield strength	(Pa)
σ_{UTS}	Ultimate tensile strength	(Pa)
f	Force	(N)
ρ	Density	($Kg.m^{-3}$)
δ	Mechanical strain	
σ	Mechanical stress	(Pa)
d	Piezoelectric charge constant	($C.N^{-1}$)
E	Electric field	($N.C^{-1}$)
D	Electric displacement/charge density	($C.m^{-2}$)
ε	Permittivity	($F.m^{-1}$)
s	Compliance	($m^2.N^{-1}$)
g	Piezoelectric voltage constant	($V.m.N^{-1}$)
k	Coupling factor	

V	Voltage	(V)
ΔT	Temperature differential	(K)
T_m	Mean temperature	(K)
P_{rms}	RMS Power	(W)
P_{peak}	Peak AC power	(W)
P	Power	(W)

Contents

1 Introduction

This thesis investigates technologies and approaches which will enable the implementation of lightweight structural health monitoring (SHM) systems for aerospace applications. The work focuses on a broad range of research activities that are essential to the realisation of such systems. These include a critical and experimental assessment of suitable transducers, the development of acoustic emission (AE) and acousto-ultrasonics (AU) monitoring techniques for damage detection and location, and the design of energy harvesting and power management solutions.

1.1 SHM

SHM systems allow aerospace structures to be continuously monitored by the use of permanently mounted or embedded transducers utilising non destructive testing (NDT) techniques. Such systems are likened to human nervous systems (Beral and Speckmann 2003) and enable the early detection of the deterioration of a structure, which can be achieved by a variety of techniques (Petitjean et al. 2006).

Scheduled inspections form a significant proportion of when the aircraft is grounded and out of service (Kapoor et al. 2009). These systems allow for maintenance to be carried out when it is required rather than based on operational hours, vastly increasing asset availability and the reduction of direct operating costs. These systems allow inaccessible areas to be monitored in service, this information can be used to dictate maintenance schedules. This results in the optimal use of the aircraft whilst still maintaining reliability and safety, leading to future scenarios where un-scheduled maintenance is completely avoided.

Environmental legislation and increasing fuel costs requires the aerospace industry to develop optimised and efficient structures. Knowing the implementation of these systems at the design stage could reduce conservative safety factors in critical areas. This would allow for the reduction in component weights leading to lighter aircraft, thereby reducing running costs due to improved aircraft performance, lower fuel consumption and emissions and greater maximum range, increasing the existing operational life of the aircraft.

Increased use of composites materials is a further reason for the uptake of these systems. Increasingly prevalent when considering the Airbus' A380 has carbon fibre and glass laminate aluminium reinforced epoxy (GLARE) fuselage sections (Hita-Romero 2006).

Composites materials are susceptible to impact damage and flaws from the manufacturing process. These cause large internal damage which may not be visually detected externally which could dramatically reduce the design strength and component life (Chang and Markmiller 2006). Due to this uncertainty, designs are often conservative leading to heavy components diminishing the inherent strength to weight ratio. Knowing the use of a system at the design stage would remove this uncertainty leading to further optimised composite structures again reducing the weight of the aircraft.

Ageing aircraft are an additional driving factor for SHM systems, these aircraft have been in-service for a number of years and such systems could reduce the life cycle costs by influencing how structures could be maintained in subsequent years to reduce cost, yet still improve safety. This is extremely important when considering monitoring of hot-spot areas which require extensive human labour due to disassembly of components. Although the retrofitting of a system could be high it is thought that impact on the long term benefit of maintenance could easily offset the upfront cost (Chang and Markmiller 2006).

Detection capabilities, self diagnostic capability, durability and inter-changeability (Bockenheimer et al. 2009) are many factors that need to be considered before the implementation on in-service aircraft. For these systems to be lightweight, autonomous wireless transducer nodes with individual power supplies are the only viable option. These nodes require the ability to process information and relay the damage state to a central base station. This thesis investigates the development of key technological areas for the realisation of wireless structural health monitoring systems.

1.2 Aims and Objectives

This thesis approaches the demanding task of developing an autonomous self-powered SHM system in a modular fashion by researching each aspect of a SHM system, with the aim of providing a robust platform for the commercial development of such an SHM system, underpinned by fundamental research. The modules investigated are:

- Transducers
- Damage detection
- Energy harvesting
- Power management
- System integration

The main objectives of this thesis with respect to these core modules are:

- To carry out a thorough investigation into damage detection methodologies using AE and AU approaches for SHM system.
- To further develop the delta-T mapping technique for improved damage location
- To carry out experimental investigations into damage detection and location of different damage mechanisms in both metallic and composite structures
- To assess the requirement of wireless transducer systems and the current generation levels using current energy harvesting techniques directed towards the aircraft environment
- To perform feasibility studies into the use of a single transducers for AE and AU techniques and energy harvesting
- To develop smart structures using embedded transducers
- To assess the current ability of power management systems for thermoelectric and piezoelectric energy harvesters.

1.3 Major Contribution of this work

1.3.1 Novelty Claimed

The novelty claimed in the work is as follows:

- Quantification of the effect of elevated temperature on the response of piezoelectric transducers using a cross correlation methodology
- Development of a wave arrival estimation tool, based on Akaike information criteria (*AIC*) which now provides a considerable improvement in Delta-T mapping, an advanced source location technique. This technique has been used for damage location in metallic and composite specimens and has shown significant improvements over delta T mapping and conventional TOA techniques. This technique has showed on average an improvement of 15mm over conventional techniques
- Robustness testing of the existing Delta-T technique in composite specimens, including location of damage under fatigue loading with validation using a thermal stress analysis.

- Fatigue crack damage location in complex aerospace grade aluminium specimens with comparison between the improve Delta T mapping with the conventional algorithm and time of arrival (TOA) methodologies
- Experimental validation of the improved delta-T mapping technique for location of damage during impact and subsequent fatigue loading.
- Utilisation of Macro fibre composites (MFC) transducers for impact damage detection using AE and AU principles in carbon fibre panels.
- Detection of impact events and damage using embedded MFC transducers in a glass fibre pane, with the same transducer used for AE location using the improved mapping technique and a cross correlation technique for AU damage detection.
- Numerical modelling of estimated power generation levels using a thermoelectric generator for temperature data recorded during several flights.
- Experimental investigation of the power generated from piezoelectric devices for typical aircraft vibrations including optical measurement to generate relationship between the power generated and vibration mode.
- Integration of these SHM techniques to develop a carbon fibre smart wing utilising embedded MFC transducers for improved methods for AE damage location and cross correlation technique for damage detection. Assessment of the viability of using the same transducers for ambient energy harvesting which is an important factor when considering self powered autonomous SHM systems.

1.3.2 Published Outputs

A total of six journal and two conference papers have been published through direct and associated research activities which are either directly related to or associated with this thesis. These include:

Journal Publications

- Pearson, M.R., Eaton, M.J., Featherston, C.A., Holford, K.M. and Pullin, R. (2011). “Impact Damage Detection and Assessment in Composite Panels using Macro Fibre Composites Transducers”. Journal of Physics: Conference Series Vol. 305 Issue 12049 2011.
- Arnold, M., Featherston, C.A., Pearson, M.R., Lees, J and Kural, A. (2012). “Energy Management Systems for Energy Harvesting in Structural Health Monitoring

Applications". Key Engineering Materials: Structural Health Monitoring II Vol. 518 2011

- Pullin, R., Eaton, M.J., Pearson, M.R., Pollard, C., Holford, K.M. (2011). "Assessment of bonded patch bridge repairs using acoustic emission and Acousto-Ultrasonics". Key Engineering Materials: Structural Health Monitoring II Vol. 518 2011
- Pullin, R., Eaton, M.J., Pearson, M.R., Featherston, C.A., Lees, J., Naylon, J., Kural, A., Simpson, D.J and Holford, K.M. (2012b). "On the Development of a Damage Detection System using Macro-fibre Composite Transducers". Journal of Physics: Conference Series Vol. 382 Issue 12049 2012
- Pearson, M.R., Eaton, M.J., Pullin, R., Featherston, C.A. and Holford, K.M. (2012). "Energy Harvesting for Aerospace Structural Health Monitoring Systems". Journal of Physics: Conference Series Vol. 382 Issue 12025 2012
- Pullin, R, Clarke, A., Eaton, M.J, Pearson, M.R. and Holford, K.M. (2012a). "Identification of the Onset of Cracking in Gear Teeth Using Acoustic Emission". Journal of Physics: Conference Series Vol. 382 Issue 12050 2012

Conference Publications

- Eaton, M.J., Pearson, M.R., Holford, K.M., Featherston, C.A., and Pullin, R (2012a). "Detection and Location of Impact Damage using Acoustic Emission" Second International Conference on Advanced Composite Materials and Technologies for Aerospace Applications (ACMTAA-2012), June 11th-13th, Wrexham 2012.
- Eaton, M.J., Pullin, R., Pearson, M.R., Featherston, C.A, and Holford, K.M. (2012c). "Structural Health Monitoring of Composite Structures Using Embedded Transducers". ECCM15 - 15th European Conference on Composite Materials, 24th-28th June, Venice 2012.

1.4 Thesis Overview

The thesis is presented in the form of self-contained chapters, each presenting a literature review and experimental results, discussion and conclusions. A brief summary of the contents is given below:

- Chapter 1 contains an introduction to the thesis including the aims and objectives, an outline of structural health monitoring and the novelty contained within the research

- Chapter 2 describes research and experimental investigation into various different transducers types for SHM applications including operation in harsh environments and novel transducers for dual AE and AU monitoring
- Chapter 3 discusses damage detection in a variety of metallic and composite structure using novel AE location techniques coupled with AU analysis for the detection of damage
- Chapter 4 presents an overview of energy harvesting techniques in particular piezoelectric and thermoelectric harvesters. Also investigation into the power estimation using the two techniques for typical aircraft conditions
- Chapter 5 outlines a review of power management solutions for energy harvesting techniques
- Chapter 6 reports on the integration of the damage detection and vibration energy harvesting techniques for the application of a carbon fibre smart wing with embedded MFC transducer
- Chapter 7 pulls together the overall discussions, conclusions and suggestions for future work
- Chapter 8 lists all the references to work cited throughout the work.

2 Transducers for SHM

2.1 Literature Review

The application of piezoelectric transducer technologies for SHM is well documented see for example Zagrai (2002),Raghaven (2007), Matt (2007), Eaton (2007) and Baxter (2007). These transducers are defined by the active element and fall into four main groups, which includes piezoceramic, piezocomposites, polyvinylidene fluoride (PVDF) and piezoelectric wafer active transducers (PWAS). This literature review will discuss the conventional piezoceramic transducers for AE and AU analysis and then focus on novel transducer types and their application for the desired monitoring techniques for SHM systems. Particular attention will be directed to active fibre composites (AFC), piezoelectric wafer active transducers (PWAS) and Polyvinylidene fluoride (PVDF) transducers. The advantages and disadvantages of these transducers for use in SHM will be assessed and compared with those of commercial AE transducers.

The most common form of piezoceramic material is lead zirconium titanate (PZT), these materials exploit the direct and inverse piezoelectric effects (Raghavan 2007). The piezoelectric effect generates an electrical charge when subjected to a mechanical strain due to the crystalline structure having no centre of symmetry. Applying a stress to the crystal alters the separation between the positive and negative charge sites creating an electrical charge. The inverse piezoelectric effect generates a mechanical strain when subjected to an electrical charge. This enables piezoceramic transducers to act as transducers for AE and actuators for AU techniques. Piezoceramic transducers for SHM detect very small displacements at the surface of the structure due to the propagation of ultrasonic stress waves within the material, this creates a transient voltage trace which is amplified and recorded by an acquisition system. The most common form of piezoceramic AE transducer can be seen in Figure 2-1 and consists of a piezoelectric element with a backing mass, housed in a case and potted with epoxy resin. The resonance of a piezoceramic transducer is defined by the geometry of the crystal itself. If a crystal is excited it will continue to ring and hence requires backing material to damped the response. This leads to a resonant transducer which has a high sensitivity over a narrow frequency band. Resonant transducers can be matched to the most energetic frequency that propagates in a structure which can drastically improve the signal to noise ratio (Baxter 2007). The main disadvantage is that it is harder to discriminate against different frequency plate modes as only a small bandwidth around the resonance is amplified. Plate modes refer to the fundamental modes of

propagation for Lamb waves in plate like structures. If the crystal is excessively dampened, this results in a broadband AE transducers that has a much larger bandwidth (100 to 1000kHz) but are generally less sensitive over this range. However more frequency information is available in the recorded waveforms. Figure 2-2 shows a general transducer configuration for AU consisting of a piezoceramic element bonded to the structure. Due to the brittleness of piezoceramic materials in this form they can be damaged easily. The AE transducer configuration is far more robust, however are often bulkier and heavier than more novel types.

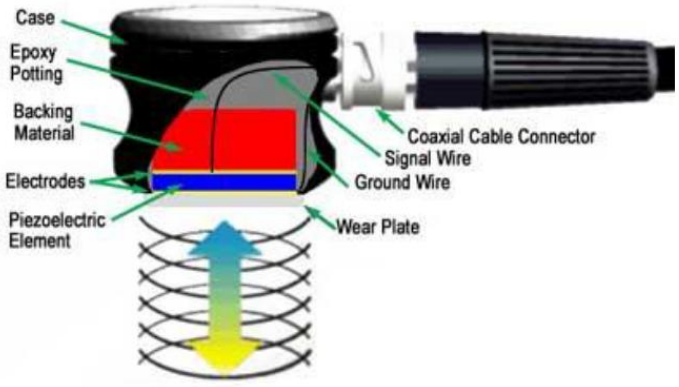

Figure 2-1. Typical construction of an AE transducers (Eaton 2007)

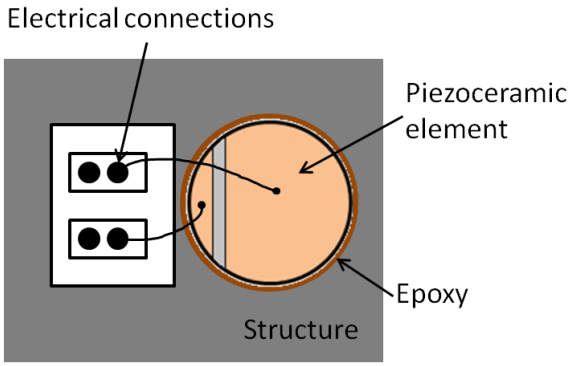

Figure 2-2. Typical transducer configuration for AU applications (Moulin et al. 1997)

Various forms of piezocomposites transducers have been summarised by Williams and Inman (2002) and include 1-3 composites, active fibre composites (AFC) and macro fibre composite (MFC) transducers. 1-3 piezo-composites consist of piezoelectric rods (circular or rectangular in cross section) which are orientated through the thickness of the device. They are manufactured using a soft mould technique where a soft mould copy is

produced from a positive form of the final structure and filled with piezoelectric material and subsequently fired. After firing, the voids in the matrix are filled with a polymer matrix. Electrodes are bonded to either ends of the piezoelectric rods which are then used to polarise the active elements. These devices are typically used for medical ultrasound. AFC transducers consist of circular piezoceramic fibres (hollow or solid) held in a polymer matrix with interdigitated electrodes on the top and bottom surfaces, the fibres in these devices are orientated along the length of the transducer. The circular cross sectional fibres are made from an extrusion process and are expensive to manufacture. MFC transducers were developed at the NASA Langley Research Centre and are manufactured under license through Smart Material Corporation. MFC transducers consist of rectangular piezoceramic fibres that are sliced from a larger monolithic wafer and are cheaper to manufacture then AFCs. The piezoceramic fibres are held in a structural epoxy which inhibits crack growth in the fibre and bonds the transducer together. Interdigitated electrodes are placed on the top and bottom surfaces of the fibre epoxy matrix, which in a sensing application enables the voltage to be transferred from the piezoceramic fibres. Figure 2-3 shows two types of MFC transducer the P1 and the P2, the difference between the two types is the direction that they are poled. The P1 types have alternating polarities of interdigitated electrodes on the top and bottom surfaces, this permits poling of the fibres along their length and can take advantage of the larger in-plane electro-mechanical coupling. While the P2 types have a positive electrode on the top surface and a negative electrode on the bottom surface and this permits poling through the thickness of the fibres and exploit the smaller out of plane electro-mechanical coupling. Although the two types are poled in different orientations, they both actuate in the plane of the device, with the P1 extending and P2 contracting along the length of the device when subjected to a voltage. Therefore in terms of SHM sensing applications the devices will be more sensitive to in-plane ultrasonic stress waves. AFC and MFC transducers were primarily developed for actuation purpose. Actuation applications include vibration suppression in rotor blades and fighter plane fins (by counteracting bending and torsional stresses) and control of vibration in inflatable spacecraft. Their advantages over piezoelectric crystals are that the piezoelectric fibres have much higher strength compared with monolithic wafers of the same material and the fibres are less brittle and have an increased damage tolerance due to their inclusion within a polymer matrix. Due to their low profile they can be easily embedded within composites structures leading to smart structures. Due to their flexibility they can conform to curved surfaces which are a key advantage when considering aerospace structures.

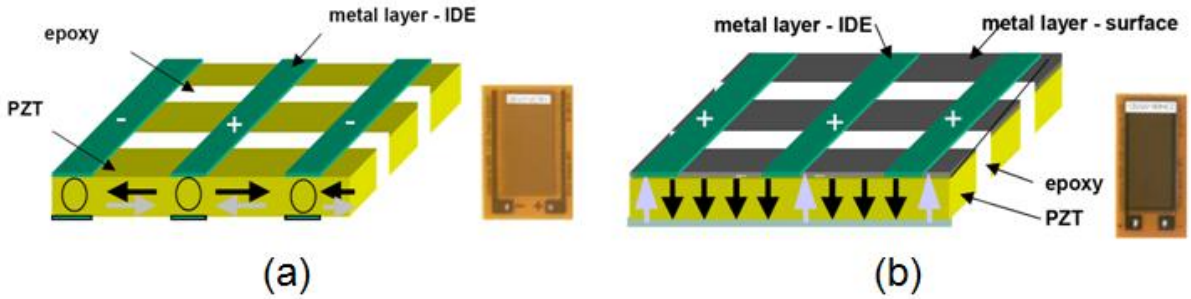

Figure 2-3. Structure of the (a) P1 and (b) P2 type MFCs.

Focussing on the MFC transducers, research into the properties of these devices has mainly been conducted by Virginia Tech and the NASA Langley Research Centre on behalf of manufacturer, Smart Material Corporation. One such study involved characterising the mechanical behaviour of the MFC (Williams et al. 2003a). The research observed a large amount of non-linear behaviour over the entire strain range. This should be accounted for in any structural actuation applications; with this in mind elastic linear hardening and Ramberg-Osgood curve fits (Ramberg and Osgood 1943) can be used to represent or model the behaviour and has shown good agreement with experimental data. Studies have also been conducted on the thermodynamic properties of the MFC, these were investigated and modelled using lamination and finite element analysis (Williams et al. 2003b). Numerically modelled results had good agreement with finite element analysis (FEA) and found that over a temperature range of 0 to 250°C the coefficient of thermal expansion in the fibre direction was constant whilst the coefficient of thermal expansion perpendicular to the fibres varied over the temperature range due to the thermo-elastic properties of the epoxy. The MFC is capable of producing directional in-plane strain in the order of 2000µstrain (Wilkie et al. 2002). Over a life cycle of 75% of the maximum allowable voltage and over 100 million electrical cycles the device only had a 5% loss in the strain. There was also very little loss in the strain over a coupled static and electrical loading of the MFC over 10million electrical cycles. Wright (2005) investigated the use of the MFC for ultrasound transduction which resulted in working frequencies of between 40kHz and 6MHz, with an acoustic impedance that can be adjusted for various different ultrasonic applications.

PVDF is an alternative transducer material suited to structural health monitoring applications. PVDF is a pure thermoplastic fluoropolymer which demonstrates strong piezoelectricity. The use of PVDF or more specifically PVF_2 as an AE transducer for composite materials has been demonstrated (Stiffler and Henneke 1983). PVF_2 consists of 2 fluorine atoms opposite two hydrogen atoms along a carbon backbone of the PVF_2

molecule. Due to the strong electronegativity of fluorine, PVF2, posses a large dipole moment which gives it piezoelectric properties. Processing, which includes polarisation, loading and thermal treatment results in a piezofilm with maximum in-plane sensitivity as well a small amount of out of plane sensitivity. The advantages of these transducers are that they are low profile and mass and can conform to curved surfaces. Their size and shape can be tailored to specific applications and they have high internal damping to flatten the frequency response. Other advantages include cost, ease of fabrication and that they are less brittle than piezoceramics materials.

Although piezo-composite transducers have inherent advantages over conventional AE and AU transducers the suitability for these applications has not been addressed. Several authors have conducted comparison studies. Barbezat et al (2004) investigated the effectiveness of an AFC against that of a commercial AE transducer. The authors manufactured their own AFC's and compared the attenuation and directionality of signals detected. The results for the AFC when the fibres were aligned with the propagation direction were very similar to those obtained with the conventional transducer (DECI SE150-M). However when the propagation direction was perpendicular to the fibre direction the AFC was less sensitive. The AFC showed clear directionality being more sensitive to sources that were parallel with the fibre direction.

Eaton et al (2009) assessed MFC transducers for AE SHM monitoring and further quantified the directional and attenuation response of an M4010-P1 MFC (active area 40x10mm) bonded to an aluminium panel which was 3mm thick. The directional response of the MFC was assessed using H-N sources (Hsu and Breckenbridge 1981) and a cross correlation technique for varying propagation angles. Again highlighting the directional behaviour with greatest sensitivity parallel to the fibre direction. The cross correlation analysis showed a decrease in similarity with varying propagation angle. The sensitivity of these devices were compared with a commercial AE transducer (Mistras Pico) and were found to be less sensitive but with a lower rate of attenuation. This was because the MFC was sensitive to lower frequency components which can propagate further in a structure. Basic AE trend analysis for damage detection was conducted for composite buckling tests and the same trends were observed. The MFC transducer was able to conform to the curvature of the specimen under buckling while the AE transducer was not. Barbezat et al (2007) assessed AFC for AE and AU monitoring of structures, the AFC used in the investigation had dimensions of 40x31x0.3mm with an active area of 20x31mm. A spectrum

analysis of the transducer in response to an H-N source showed peak frequencies in the range 30-50 kHz.

PWAS are low cost, small commercially available piezoceramic wafers which can act as transducers and actuators. They can be either surface mounted or embedded within structures and can operate over a wide frequency band (Zagrai 2002).Lin and Giurgiutiu (2006) investigated the use of PZT and PVDF as the active element in PWAS transducers for monitoring a curved panel. The advantages of the PVDF-PWAS are that it is more flexible than PZT-PWAS and can conform to curved surfaces. The authors developed a model to determine the piezoelectric material properties that affect the performance of the PWAS and to assess the performance of the PVDF-PWAS to that of PZT-PWAS. A linear piezoelectricity model coupled with a charge amplifier model were used to assess the peak to peak voltage output from free vibrations of a cantilever beam, generally the model gave good correlation between the theoretical and experimental results. The PVDF-PWAS had a lower voltage output but greater sensitivity to the higher frequency components when compared with the PZT-PWAS. In a long rod impact investigation the PZT and PVDF-PWAS along with a strain gauge were able to determine tensile and compressive longitudinal waves. The use of PZT and PVDF-PWAS was established for pitch-catch Lamb wave investigation overall the PVDF-PWAS was less sensitive than the PZT-PWAS.

Stiffler and Henneke (1983) investigated a PVF_2 transducer with a dimension of 6.4x6.4mm and 110µm thick with and without a brass backing and compared the performance with that of a unspecified conventional AE transducer. Capillary glass tube tests on an aluminium block found the commercial AE transducer most sensitive followed by the PVF_2 with brass backing and then the PVF_2 transducer. Tensile loading of a GFRP found the PVF_2 had the highest sensitivity suggesting that there is a greater in-plane AE mechanism in composite which favours the in-plane nature of the PVF_2 transducer.

Although AFC, MFC and PVDF transducers have inherent advantages over conventional AE transducer which have already been highlighted when comparing these transducer for application for SHM. The literature suggests that they are less sensitive, directional and have lower working frequencies. However these studies do indicate that these transducers are more sensitive to in-plane acoustic sources which could be an advantage in certain applications.

Despite disadvantages in terms of sensitivity and directionality, there is still a large amount of research conducted into the applications of lightweight flexible sensing elements.

MFC actuators have been used for vibration testing and control of inflated satellite components (Ruggier et al. 2002). Inflated aerospace structures are an alternative to conventional methods in structural design, however there are significant problems due to their light weight, flexibility and high damping coefficients. A system of MFC actuators and transducers could be used to actively control unwanted vibrations.

Sodano et al (2004) evaluated the use of MFC transducers for modal vibration measurement, vibration suppression and impedance based SHM techniques. Vibration modes of an inflatable torus for space applications were measured and controlled using a series of MFC transducers as transducers and actuators, with positive displacement feedback the first out of plane mode was suppressed by 50%. The issues with several actuators and transducers meant vibration modes were sensed in one location and suppressed in another. It was not unreasonable to suggest different vibration characteristics in these locations. This drawback was overcome using a self-sensing circuit, this enables local determination and suppression of frequency modes. This technique was able to suppress the second mode by 90%. Finally an MFC transducer in an impedance-based SHM system was able to measure the same resonant frequencies as achieved with commercial PZT transducers, however the response was affected by the capacitive response. The transducers were able to detect bolt loosening in a composite cantilever beam using a baseline impedance based technique.

More specifically for structural health monitoring applications, Barbezat et al (2007) assessed AFC transducers for AE and AU monitoring of structures. The transducers were used for both AE and AU monitoring of impact damage in a GFRP beam. The AE analysis showed an increase in normalised energy being released with increasing levels of impact damage. The transducers were mounted on the top and bottom face at either ends of the beam, a set of prototype waveforms were calculated for each pulse receive configuration at a baseline condition. After each subsequent impact another set of waveforms were collected. A clustering technique was used to classify each waveform into different clusters. The distance ratio, which describes how well a signal is grouped into a particular cluster, was used to determine damage with increased number of impacts and found increasing distance ratios with increased level of damage.

MFC transducers were used to demonstrate a novel source location technique (Matt and Lanza di Scalea 2007). The technique exploited the inherent directional response of the MFC to a flexural Lamb wave in order to deduce where the source had originated from. The

response of a MFC was modelled and this allowed for longitudinal, transverse and 45° sensitivity factors to be calculated. Arranging the MFC's into rosettes consisting of three MFC's separated by 120°, enabled the calculation of the principal strain angle of the Lamb wave because the response and the sensitivity factor for the each is known. Having at least two rosettes allows for the location of a source in two dimensions.

One of the major attractions of these novel transducers is that they can be embedded into composite structures and could effectively enable smart structures. Paget (2001) investigated the interaction of embedded piezoceramic transducers for use in active health monitoring of composites structures. Results showed that the thickness of the interconnection had no significant influence on the stress state of piezoceramic transducers and using a compliant conductive adhesive reduced the stress concentrations around the edges of the piezoceramic. Paget et al (2000) also assessed the behaviour of an embedded piezoceramic transducer for Lamb wave generation under mechanical loading. A cross ply laminate made from carbon fibre epoxy (HTA/6376C) with the following layup $[0_4/90_4/0_4/90_4/0_2/(PZT)]_s$ was manufactured. This laminate was cured in an autoclave at 180ºC, resulting in a thickness of 4.79mm. The test specimen measured 200 x 30mm. The piezo-element was approximately 10 x 10 x 0.13mm thick and was made from PZ-27[10], material interconnections were made using copper film and bonded to a polyimide layer. Impedance and Lamb Wave analysis was conducted to assess the feasibility of using embedded transducers for damage detection. The impedance analysis showed large working range in static loading with functionality at 1% strain which was higher than the 0.3% strain allowed for typical aircraft designs. The ability of the embedded transducer to generate Lamb waves for an applied fatigue loading was investigated by comparing the FFT after a certain number of cycles to one before testing commenced. Significant changes in the FFT were observed at high stress levels (±170MPa) at around 50000 cycles. Further analysis showed matrix cracks and failures in the transducer element were observed showing that damage can have a significant effect on the performance of the embedded transducer, although debonding of the transducer did not alter Lamb wave generation.

Moulin et al (1997) discussed the effectiveness of generating Lamb waves in composite plate using disk shaped embedded piezoelements. A linear FEM model was implemented to characterise which Lamb wave modes were being generated. The FEM model and a network analyser were used to determine the impedance modulus in terms of the frequency for the transducer in a vacuum. Excellent agreement was observed between the two techniques where five resonant frequencies were determined. The first and fourth

had the highest coupling coefficients. These modes were determined to be radial mode (400kHz) and a thickness mode (1MHz). Embedding the PZT transducer in a 3.85mm composite plate showed a shift in the frequency response of the identified modes due the different acoustical loading conditions. The FEM model was used to determine the wavelength of indentified modes and phase velocity dispersion curves were generated and excellent agreement was observed with the theoretical curves. Using the results from the FEM model a 5mm diameter piezoceramic element was selected for good electromechanical coupling at 400kHz and was embedded in a composite panel. Observed differences between the impedance measured from the embedded FEM model and the experimental results existed but still highlighted resonances at 400, 750 and 1MHz.

Maria de Rosa and Sarasini (2010) assessed the use of PVDF as an AE transducer for in-situ monitoring of glass/epoxy laminates. This study investigated the feasibility of embedded PVDF transducers for AE monitoring of structures. A linear location comparison between PZT disc and the PVDF transducers showed the PZT was most accurate for locating sources, however the results for the PVDF were comparable. An investigation of the mechanical properties of woven glass fibre epoxy laminates found that the embedded transducers had no significant impact on the strength of the material. A simple parametric analysis of the cumulative AE hits from the embedded transducers showed good correlation with damage evolutions and the transducers successfully detected impact damage.

One particular area which has not been discussed so far is the effect of the IDT electrodes on the response of the AFC and MFC transducers. Although these electrodes enable the in-plane poling of the fibres so that they can exploit the stronger longitudinal piezoelectric effect, the geometry of the electrode can have an effect on the recorded signal. Gu and Wang (2009) developed interdigitated electrode PVDF transducers for Lamb wave inspection for structural health monitoring applications. Most designs of IDT consist of a laminate design which can lead to failure of the transducer due to delamination. Careful consideration of the design of the IDT is necessary in order to excite fewest amounts of Lamb wave modes. This is dependent on the material type and thickness and hence dispersion curves can be used to excite non-dispersive Lamb wave modes. Non-dispersive modes for a particular frequency were used to determine the finger spacing between the electrodes. Another important factor is the finger width, however this has less of an effect on the generation of the modes but can affect the amplitude of the received wave and the signal to noise ratio. The most efficient form of an IDT transducer over a narrow band would involve a long length of transducer with many IDT fingers. To overcome the problems with

delamination of the IDT interface, in this study the IDT were imprinted on the PVDF sensing interface using etch back photolithography, this resulted with a 50% ratio of finger width to finger width plus the spacing and a spacing of 4.977mm. This transducer was compared with a PZT transducer and showed comparable results when using continuous wavelet transforms to detect voids in composite specimens.

Bowen et al (2006) used finite element analysis (coupled field analysis) to investigate different geometric features of IDT electrodes, such as the finger width (w), electrode substrate thickness (t) and finger spacing (s). The model was constructed in the plane of the fibre (active element PZT-5A material) and meshed with 2D coupled field elements. The strain generated per unit voltage was used as a metric to quantify the effects of the geometry of the IDT. Results on the electrode width and spacing showed an optimum output when the width to substrate thickness was 0.5 and was independent of electrode spacing, however there is an increase in strain developed for a reduction in finger spacing. At larger electrode widths there was significant dead zone under the electrode where no significant in plane strain was developed. As the substrate thickness was reduced there was an increase in the strain developed, this is due to the electric field being directed into the in-plane direction over a shorter distance reducing this dead zone. Finally investigation into the electrode separation showed that decreasing the separation increased the strain output. Further analysis showed that 80% of the d_{33} response can be achieved if electrode separations must satisfy spacing to thickness ratios of greater than four. Knowing the results of this particular research and the fact that AFC transducer were primarily developed for actuation purpose suggests that these transducer could further be optimised for SHM monitoring applications.

2.2 Experimental Investigations

2.2.1 Macro Fibre Composite Characterisation

2.2.1.1 Introduction

Macro fibre composite transducers are a relative new transducer technology for the application of SHM for aircraft. Therefore a detailed investigation into the suitability of these transducers was undertaken to further understand their use for AE and AU. A series of investigations looking at attenuation, directionality and optimisation was undertaken. The purpose of this was to determine likely transducer spacing and directional behaviour which may affect their suitability for SHM. Furthermore if these types of transducers were found to be unsuitable could there be a MFC configuration that maybe more suitable.

2.2.1.2 Experimental Procedure

An investigation was undertaken to determine whether the geometry of the active area could be optimised for a particular structure thickness. Due to the interdigitated electrodes it was thought that shortening the length of the MFC transducer would not alter the ability of the transducer to function. Therefore several different types of MFC were adhered to two separate 3.18mm thick 2024 aluminium panels. The three types of MFC used were M2807-P1, M2814-P1 and M2814-P2. The four digit number describes the length and width of the active area, this will enable a comparison of the different types and geometry of MFC. For the first investigation the M2807-P1 and M2814-P2 were adhered to a large aluminium panel with dimensions 1.4 x 0.5m and 3.18mm thick. The transducers were coupled to the panel using cyanoacrylate. An attenuation transducer response investigation was performed on the panel. The MFC transducers to be investigated were placed in a linear array aligned with the width of the plate, making sure to leave sufficient distance to the edges of the plate in order to minimise the effect of reflections. Figure 2-4 shows the linear array of the transducers, an H-N source was used to simulate AE, for each distance 10 H-N sources were completed. The distances ranged from 0mm to 1000mm. The 10 collected waveforms from each distance were then extracted and averaged to attain the average peak amplitude. Once completed for a full length 28mm MFC the length was reduced by 7mm using a scalpel and the attenuation procedure was repeated until a final length of 7mm was reached. The two MFCs were clad in a copper coating to reduce noise issues. The H-N source was developed by Hsu and Breckenridge (1981) and is often used to create a broadband artificial AE signal. It involves breaking a 3mm 2H grade 0.5mm diameter pencil lead on a structure using a mechanical pencil. Boczar and Lorenc (2004) investigated the repeatability using a statistical analysis of the generated stress waves created by a H-N source on a transformer tub. The authors concluded for a particular propagating distance H-N sources are repeatable with a 5% margin of error. For example at a distance of 25mm from H-N source to sensor the average amplitude of the recorded signals was 0.48V with a standard deviation of 0.03V and a variance of $1.14 \times 10^{-3} V^2$. In the frequency domain the maximum value of the amplitude spectrum was found to be at 5.46kHz with a standard deviation of 0.8kHz.

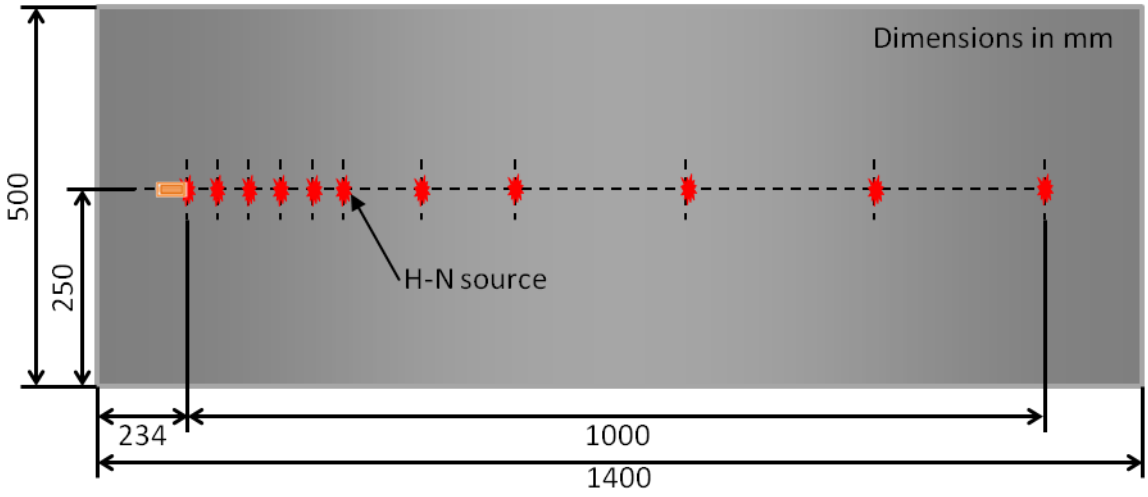

Figure 2-4. Experimental set-up for the attenuation transducer response investigations

The same 2024 aluminium plate was utilised for the directionality transducer response investigations. The investigated transducers were placed in the centre of a 100mm radius semi-circle and H-N sources were used to simulate artificial acoustic emissions. The responses from 10 H-N sources were collected from 0° to 180° at increments of 10°, which can be seen in Figure 2-5 . Again the collected waveforms were extracted and the peak voltage was averaged for the 10 waveforms. The length of the MFC was reduced in increments of 7mm from a full length of 28mm using a scalpel until a final length of 7mm was reached. For each length of MFC the directionality response procedure was repeated. Figure 2-6 and Figure 2-7 show examples of a full size MFC for the M2807-P1 and M2814-P1 respectively. It also shows the final 7mm length MFC which was adhered to the panel and cut down from a length of 28mm. The figures show two separate devices for each type of MFC to show a comparison between the full size and 7mm length MFC transducers. The original and final MFC configurations can be seen for the M2807-P1 and M2814-P1 types respectively. To try and assess how the MFC interacts with propagating wave in the panel, the waveforms recorded from a distance of 200mm were recorded and a wavelet transform was performed using Vallen Wavelet for both the M2807-P1 and M2814-P2. Vallen are an AE system and software manufacturing and have generated software for calculating wavelet transforms. A wavelet transform allows the time-frequency transformation of a signal to be calculated unlike Fourier transforms which only allow for frequency transformations. The short time Fourier transform also allows for a time-frequency transformation, however the wavelet transform enables the scaling of the signal window to achieve good time resolution at higher frequencies and good frequency resolution at lower frequency, unlike the short time Fourier transform which has a fixed time and frequency resolution. The wavelet transform

used in the Vallen wavelet is a Gabor wavelet and is defined by Suzuki et al (1996) and describes this wavelet transform as adequate for AE signals. This type of wavelet transform has been extensively used by Hamstad et al (2002), Jeong (2001), Jiao et al (2004) and Suzuki et al (1996) for AE characterisation and location and therefore it was not deemed necessary to investigate other wavelet transforms

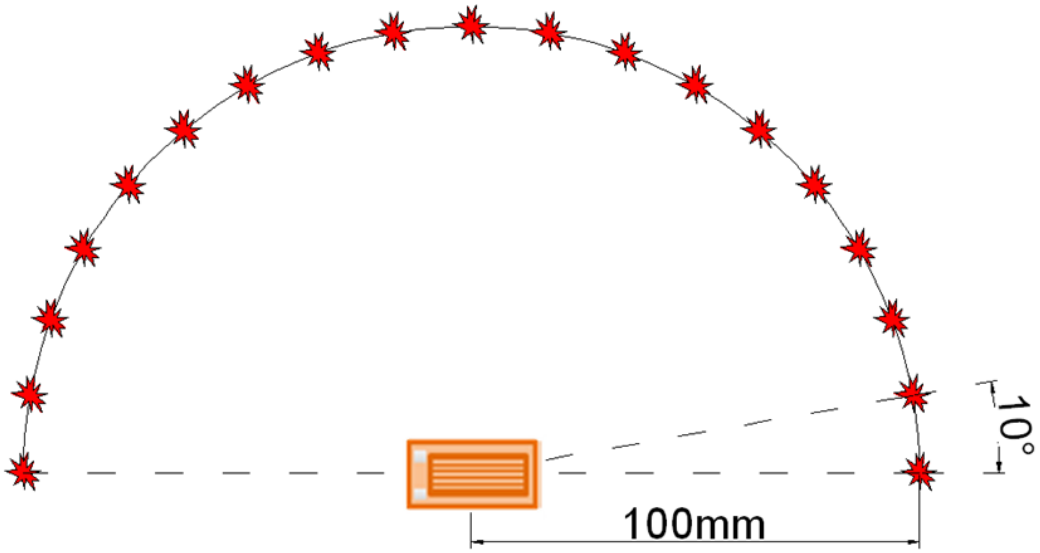

Figure 2-5. Experimental configuration for the directionality transducer response investigations

Figure 2-6. Original M2807-P1 transducer and the final cut down version

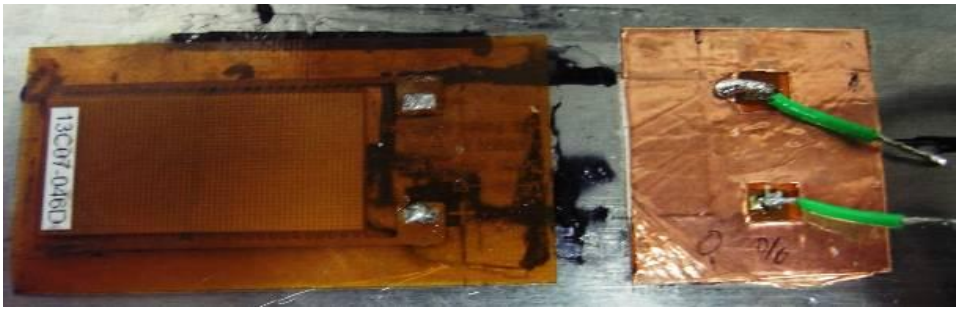

Figure 2-7.M2814-P1 original sized transducer and the final cut down version

A second investigation was conducted using a National Physical Laboratory (NPL) conical transducer which was mounted to a cut-down version of the original panel in order to understand how the waves were propagating in the panel. This type of transducer was employed because it is a broad band point contact transducer. The transducer was developed by NPL as a reference source alternative (Theobald and Thompson 2005) to the H-N source (Hsu and Breckenbridge 1981). The transducer has a broad measurement bandwidth of ±3dB between 50kHz and 1MHz (Theobald and Thompson 2005), this allows for a truer representation of the actual frequencies propagating in a plate, which can be distorted due to resonance effects of normal AE transducers. The transducer also has a 1mm diameter contact tip which means the tip is small compared to the wavelength over the AE frequency range (Yan et al. 2004), this eliminates averaging effects across the sensing interface. Finally on this specimen a M2814-P2 MFC was adhered to the panel and surface and edge H-N sources were collected at a distance of 200mm and 250mm respectively. Again the length of the MFC was reduced using smaller increments and resulted with waveforms collected for the following lengths of 28, 25, 23, 21, 19, 17, 14, 12, 10, 8, 6, 4 and 2mm. Again the wavelet approach was used to understand how the shortened version of the MFC transducers was interacting with the H-N source from two orientations. For a surface H-N source a distance of 200mm was used to match the investigation which included the P1 type MFC.

2.2.1.3 Experimental Results and Discussion

Figure 2-8 shows the results of the attenuation test for the M2814-P1 transducer. The figure shows that as the working area of the transducer is reduced in 7mm length increments the amplitude of the received waveform increases up to an active area of 14x14mm, however the amplitude of the waveform then decreases with a working area of 7x14mm. This effect can only be seen up to 600mm from the source to transducer after this the signal attenuates to the same level of amplitude despite the changes in active area.

The same pattern is evident in the directionality investigations which is shown in Figure 2-9 the figure shows that as the working length of the M2814-P1 transducer is reduced the peak amplitude of received waveforms increases up to an active area of 14x14mm then reducing again for an active area of 7x14mm the maximum difference in amplitude levels is around 0.6V parallel with the fibre direction. It should also be noted that the directionality behaviour mentioned earlier is still apparent even with the changes in working area. The effect is definitely more pronounced in the fibre direction as the difference in amplitude between 40 and 140° is only around 0.2V

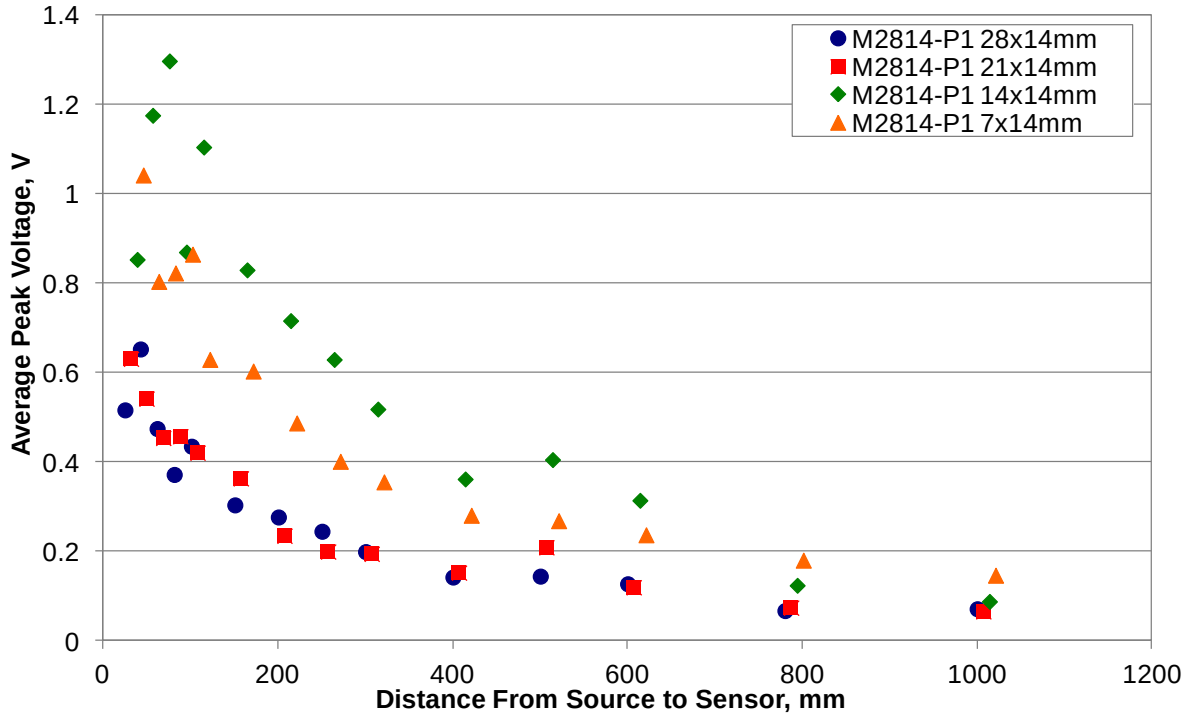

Figure 2-8. MFC response optimisation in terms of attenuation for the M2814-P1

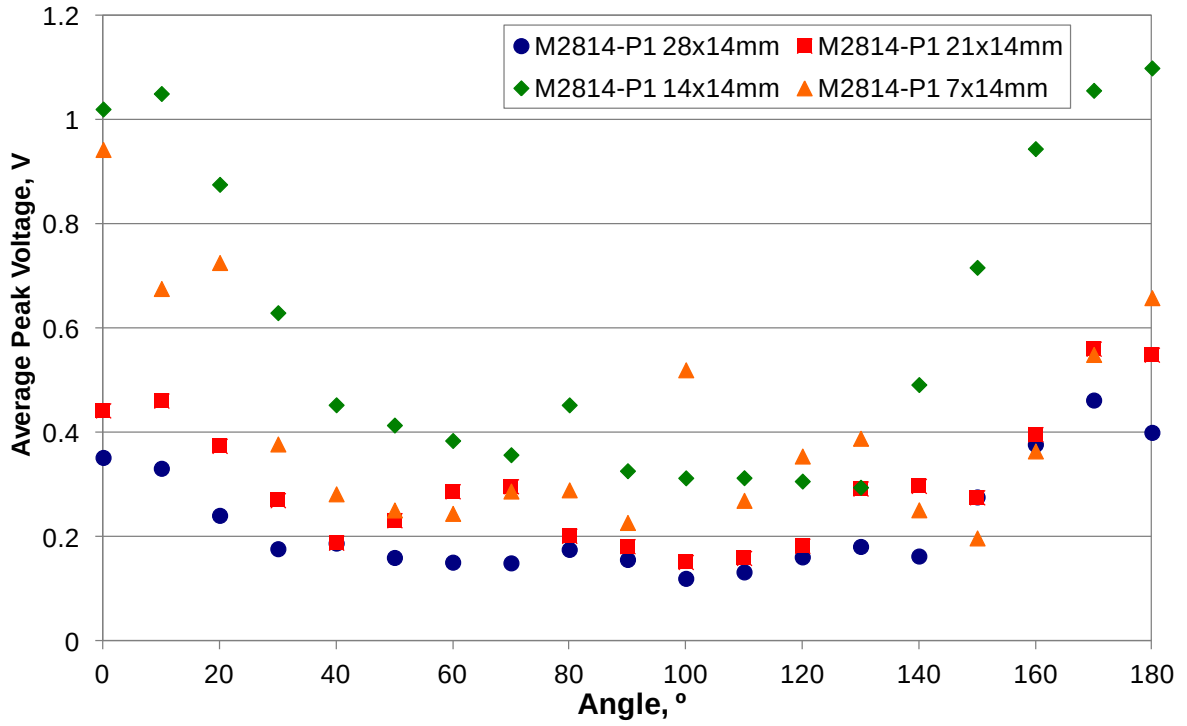

Figure 2-9. MFC response optimisation in terms of directionality for the M2814-P1

Figure 2-10 shows the average peak voltage for different distances from the source to the transducer which form the attenuation investigation for the M2807-P1 MFC. The figure shows the different working areas used in the test and the effect this had on the average peak amplitude received at the transducer. There is an increase in sensed amplitude with a

decrease in the length of the active area. For an active area of 28x7mm and 21x7mm the average amplitude response is very similar. There is an increase in sensitivity between the next two lengths (14x7mm and 7x7mm) from the previous two, however there is little difference between the amplitude response of the 14x7mm and the 7x7mm apart from the initial recorded waveform at 0mm where the 14x7mm has amplitude of 7V compared with 6V of the 7x7mm active area.

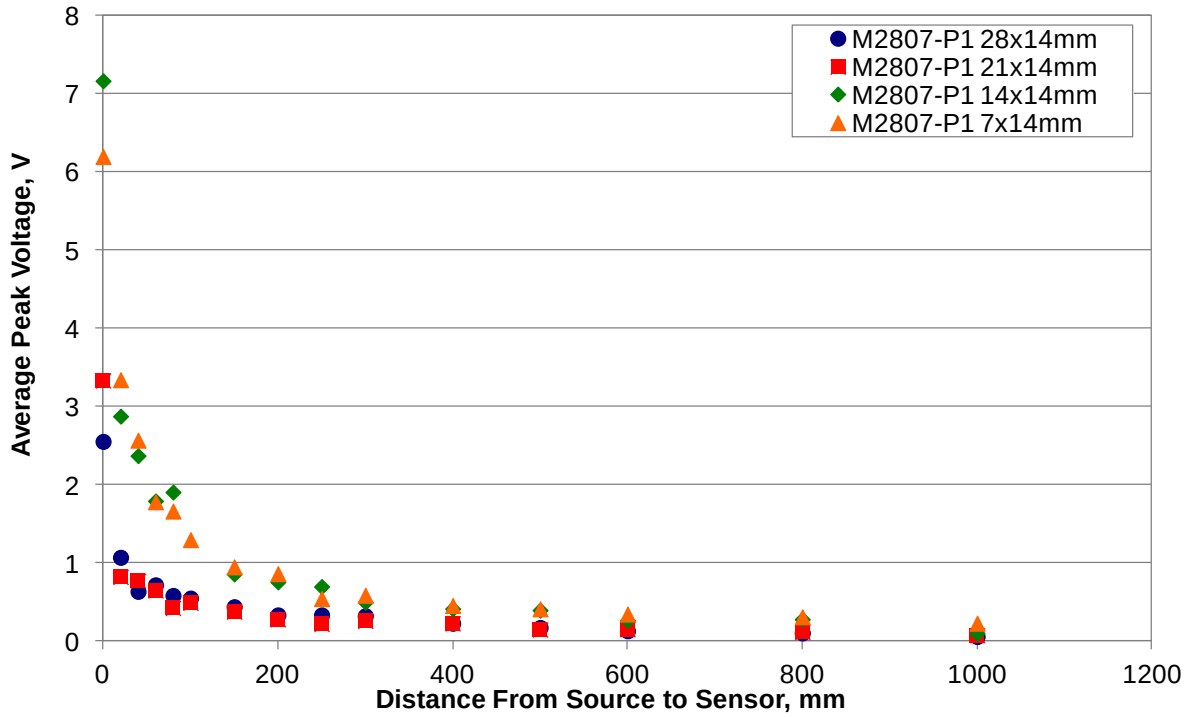

Figure 2-10. MFC response optimisation in terms of attenuation for the M2807-P1

Figure 2-11 shows the changes in average peak power of the received waveforms as the working length of the M2807-P1 transducer is reduced from 28mm to 7mm in increments of 7mm for the directionality investigation. Again the same pattern emerges as previous discussed, however there is no apparent grouping of the 28x7mm and 21x7mm to the 14x7mm and the 7x7mm as outlined in Figure 2-11. As the length of the active area is decreased the peak average amplitude of the sensed waveforms increases up to the length of 14x7mm where the response is a maximum at these points the response then decreases for the 7x7mm. Again the directional behaviour due to the piezoceramic fibres is still apparent. It should also be noted that the width of the active area between the two MFC tested was reduced from 14mm to 7mm which also increased the sensitivity of the MFC transducer showing that the width of the active area also has an effect on the sensitivity of the transducer.

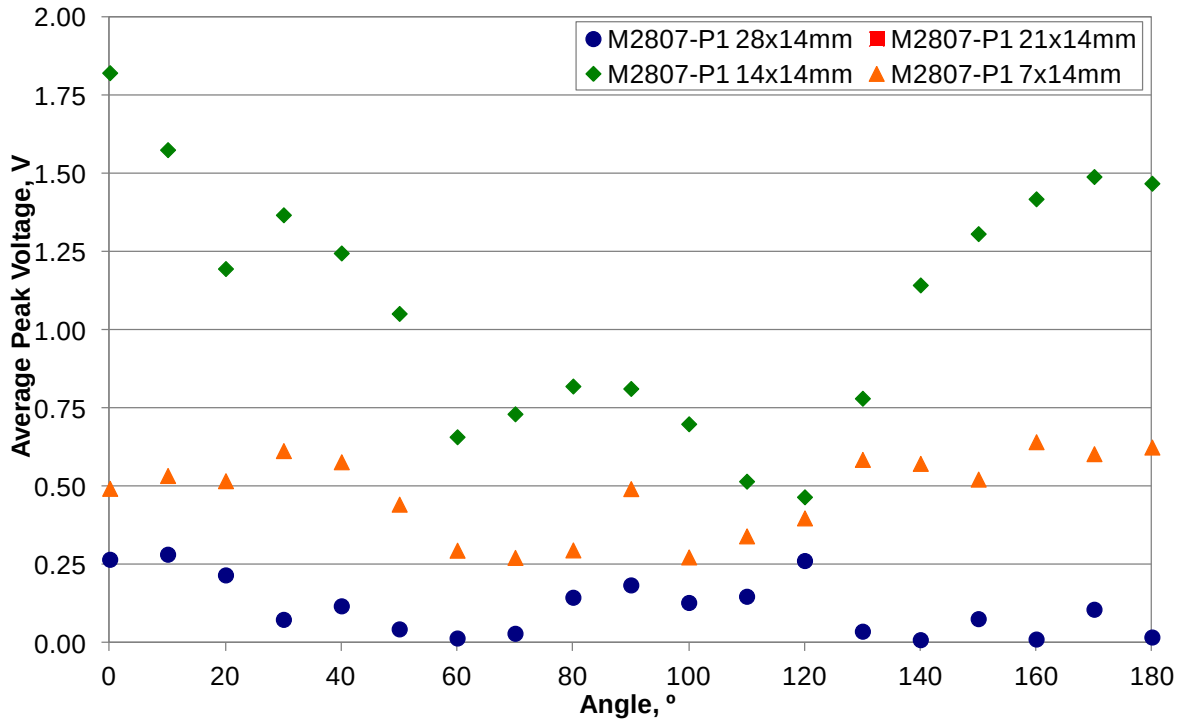

Figure 2-11. MFC response optimisation in terms of directionality for the M2807-P1

From Figure 2-8,Figure 2-9,Figure 2-10 and Figure 2-11 the investigation has shown that the M2807-P1 MFC has a higher sensitivity to that of the M2814-P1 for this particular plate thickness and relates to the active area of the MFC which will affect the frequency response and the relationship with the most energetic frequencies that propagate in the panel. The reasons for the increased amplitude responses as the length of the transducers are reduced are thought to arise due to the relationship between the wavelength of the propagating Lamb wave in the structure and the length of the transducer. As the transducer dimensions are made smaller compared to the wavelength of the propagating wave, the transducer will start to act as a point transducer and can better match the strain present in the structure due to the Lamb wave. This means less strain averaging occurs across the transducer length, which can reduce the transducer output. Further modelling work could be implemented to define this relationship more closely, however this is deemed outside the scope of this thesis. Figure 2-12 and Figure 2-13 show a wavelet transform of a signal received by the conical transducer from an H-N source on the surface at a distance of 200mm from the transducer. Figure 2-12 shows the arrival of the A_o mode at approximately 60µs, a wavelet transform shows the time frequency representation of the recorded signal therefore the figure suggests that most of the energy is contained at approximately 140 to 150µs. A further wavelet transform was calculated for the first 55µs of the same waveform which is shown in Figure 2-13. The approximate arrival time of S_0 mode is at 33µs with most

of the energy being contained at a frequency of 290 kHz and approximately arrives at 40µs. Both of these figures have the dispersion curves overlaid on the wavelet transform. This enables clear identification of the wave modes. The dispersion group velocity curves were calculated for a 3.18mm thick aluminium panel using Vallen Dispersion. Vallen Dispersion is a commercial software packages which produce dispersion curves of Lamb waves propagating in a certain medium. From Figure 2-12 and Figure 2-13 the S_o mode is present between 30 and 55µs and the A_0 mode is present between 57 and 140µs before significant reflection from the boundaries of the panel.

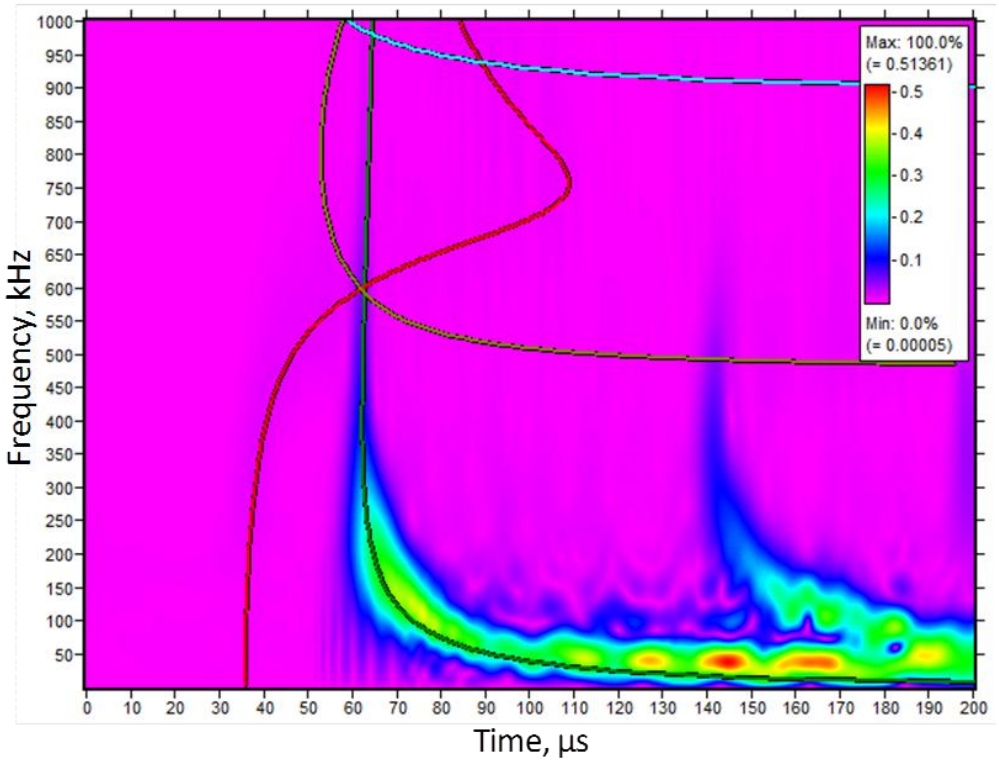

Figure 2-12. Wavelet transform of the signal received by a conical transducer from a 200mm distant surface H-N source

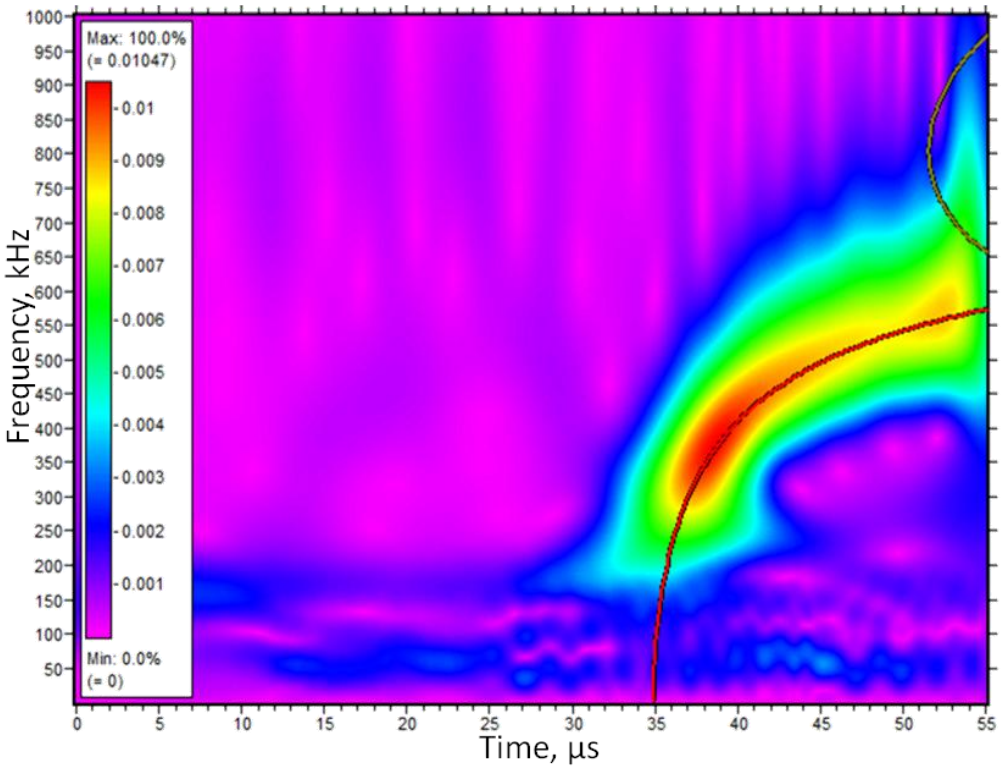

Figure 2-13. Wavelet transform of the signal received by a conical transducer for the first 55µs of the signal from a 200mm distant surface H-N source

Figure 2-16 and Figure 2-17 show the wavelet transforms from signals received by a 28mm and 14mm length M2807-P1 from a surface H-N source on an aluminium panel at a distance of 200mm. Figure 2-16 shows that there is clear evidence of the symmetric and asymmetric wave modes within the same timing windows as for the conical transducer. This suggests that these transducers can still be used as AE transducers as even though the active elements are different. The energy contained within these two wave modes occur at around 40µs and at a frequency of 300 kHz and 85µs and at a frequency of 100 kHz for the S_o and A_o modes respectively. Overall frequency sensitivity of this type of MFC is lower than that of the conical transducer, however this does not promote significant problems with regards to detected AE signals. Figure 2-17 shows the resulting wavelet transform from an H-N source used in the same orientation, distance and MFC as above with a reduced length of 14mm of the active area. Again Figure 2-17 shows that the two wave modes are present within similar timings to that of the conical transducer which suggests the MFC is still functioning even though the length has been reduced by 14mm. when comparing Figure 2-16 and Figure 2-17 it is apparent that there is an overall increase in sensitivity from a maximum wavelet coefficient of 0.65mV to that of 1mV. There is also evidence of a shift in the maximum wavelet coefficients for the two wave modes towards a higher frequency. This

suggests that reducing the length has an effect on the frequency response of the transducer and interaction of the wavelength travelling in the plate to that of the length of the MFC.

Figure 2-14 and Figure 2-15 shows the wavelet transform for signals received by an M2814-P1 MFC with lengths of 28mm and 14mm respectively, from an surface H-N source at a distance of 200mm This type of MFC has an active area which is 28 x 14mm when compared with an active area of 28 x 7mm to the MFC used Figure 2-17. The same principal wave modes are evident and coincide with arrival times observed with the conical transducer. However in the case of the full length and shortened M2814-P1 MFC there is evidence of a much smaller frequency bandwidth when compared with the M2807-P1 MFC. For example comparing Figure 2-16 with Figure 2-14 it can be seen that the M2814-P1 has a much lower frequency bandwidth resulting with S_0 and A_0 frequencies in a the range less than 200kHz. When comparing with the M2807-P1 it can be seen that S_0 frequencies can be observed up to a maximum of 500kHz. This suggests that it would be more difficult to separate the modes on a frequency basis due to the close proximity in terms of frequency of these two wave modes for the M2814-P1. This suggests that the overall area of the active element also has a bearing on the frequency response of the MFC transducer. When comparing Figure 2-14 and Figure 2-15 which show the results for the calculated wavelet transform for an active length of 28mm and 14mm respectively the same frequency shift is observed and a dramatic increase is seen in the maximum wavelet coefficient observed increase from 0.6 to 1.13mV. Figure 2-18 and Figure 2-19 shows the wavelet transform for signals received by an M2814-P2 MFC for active lengths of 28mm and 14mm respectively from an H-N source on the surface of an aluminium panel at a distance of 200mm. The P2 type of MFC is poled through the thickness of the fibre rather than along the length like the P1 type. Even for the same active area for the M2814-P1 the P2 type exhibits the ability to determine the high frequency components of the S_0 mode. Again the same observations are evident when reducing the length of the MFC, where a change in the frequency response occurs. However for the A_0 mode this is less evident due to reflections having an effect on the signal at an earlier stage.

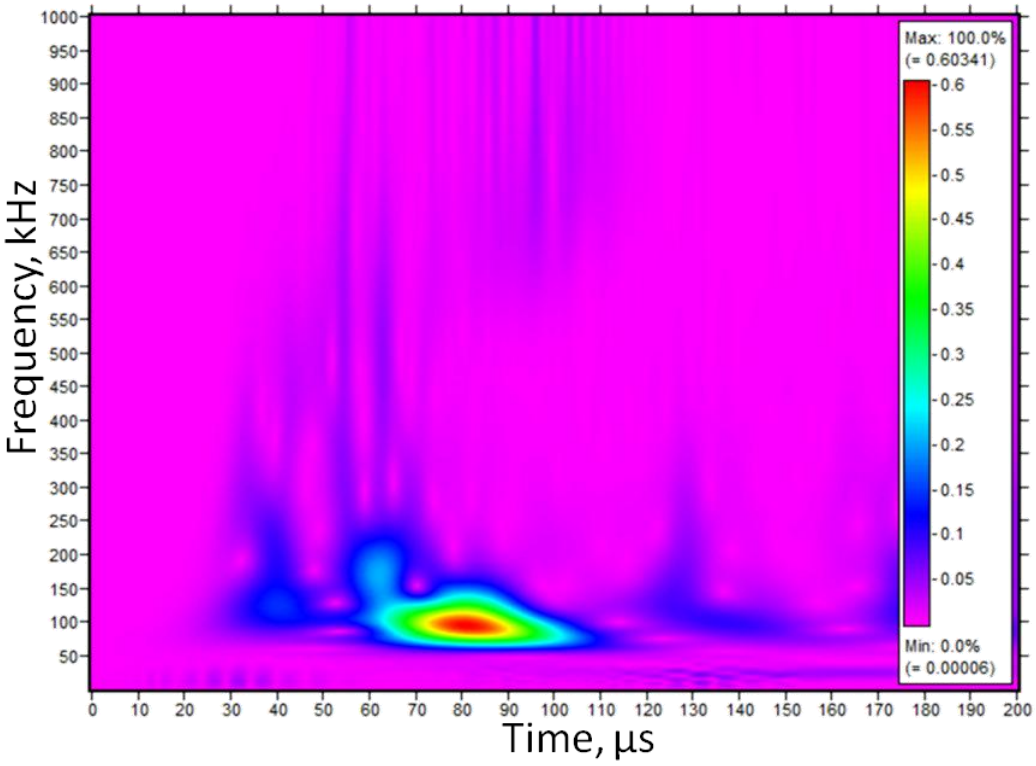

Figure 2-14.Wavelet transform of a signals received by a 28mm M2814-P1 MFC for a surface H-N source at a distance of 200mm

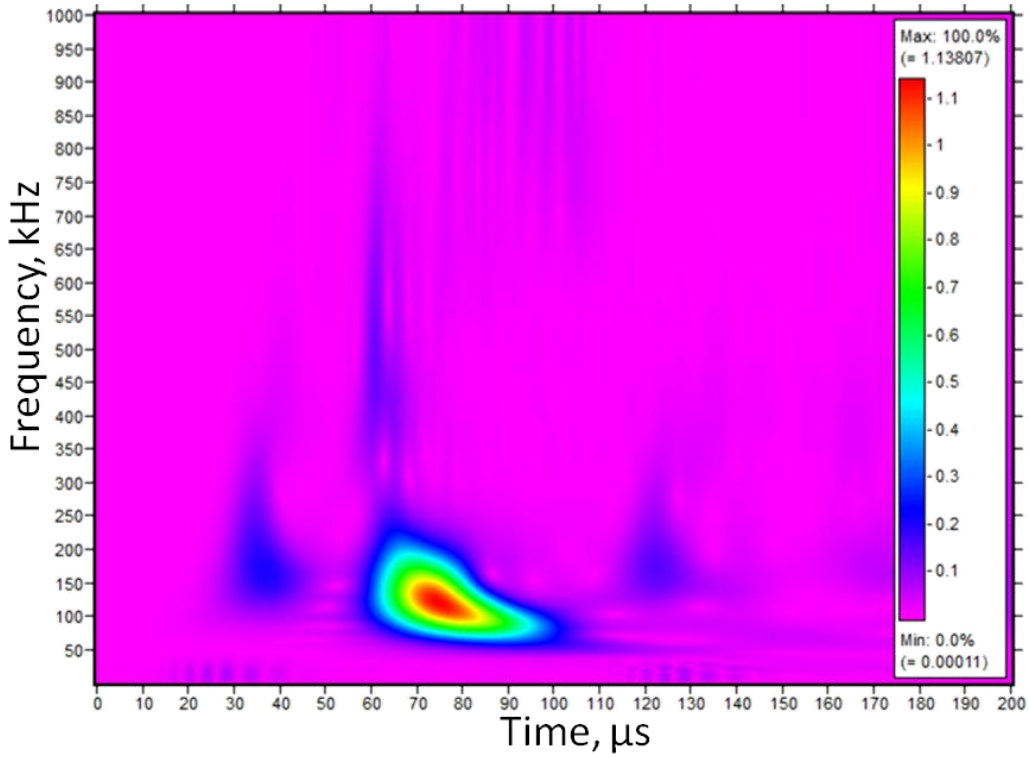

Figure 2-15.Wavelet transform of a signal received by a 14mm M2814-P1 MFC for a surface H-N source at a distance of 200mm

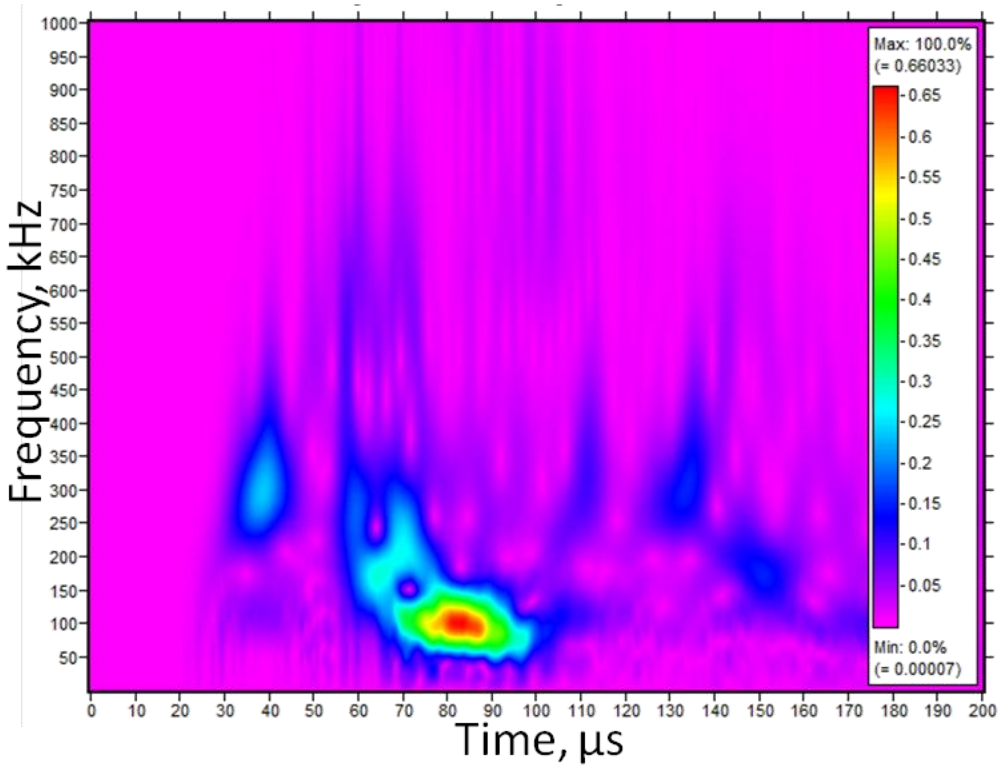

Figure 2-16. Wavelet transform of a signal received by a 28mm M2807-P1 MFC for a surface H-N source at a distance of 200mm

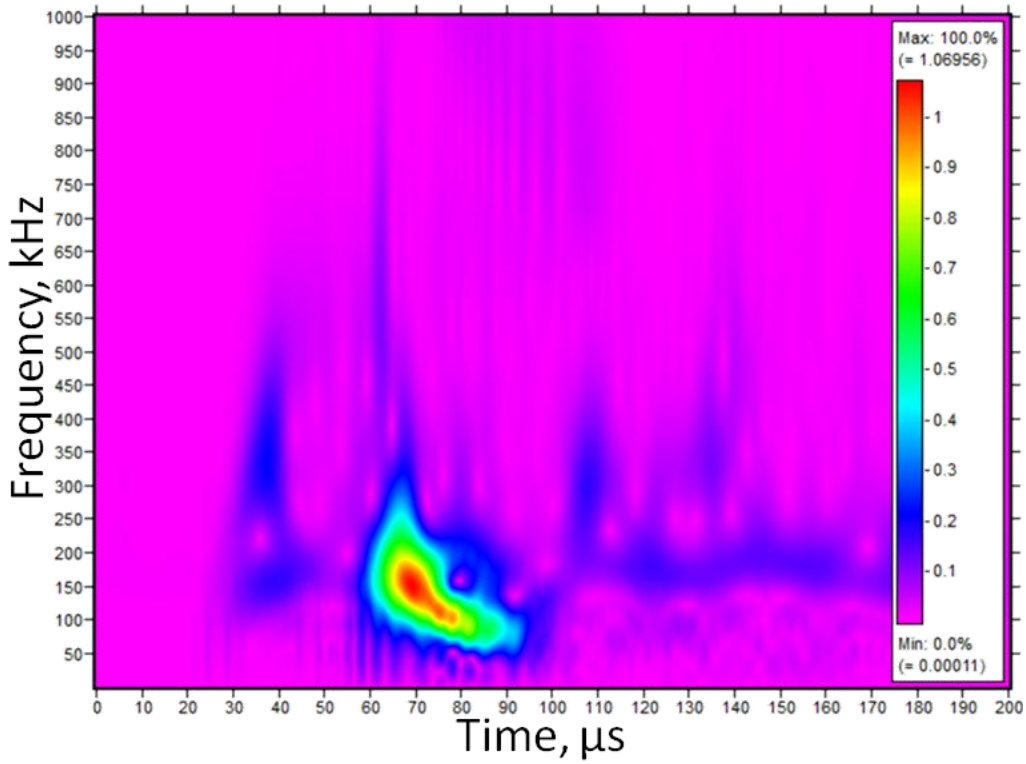

Figure 2-17. Wavelet transform of a signal received by a 14mm M2807-P1 MFC for a surface H-N source at a distance of 200mm

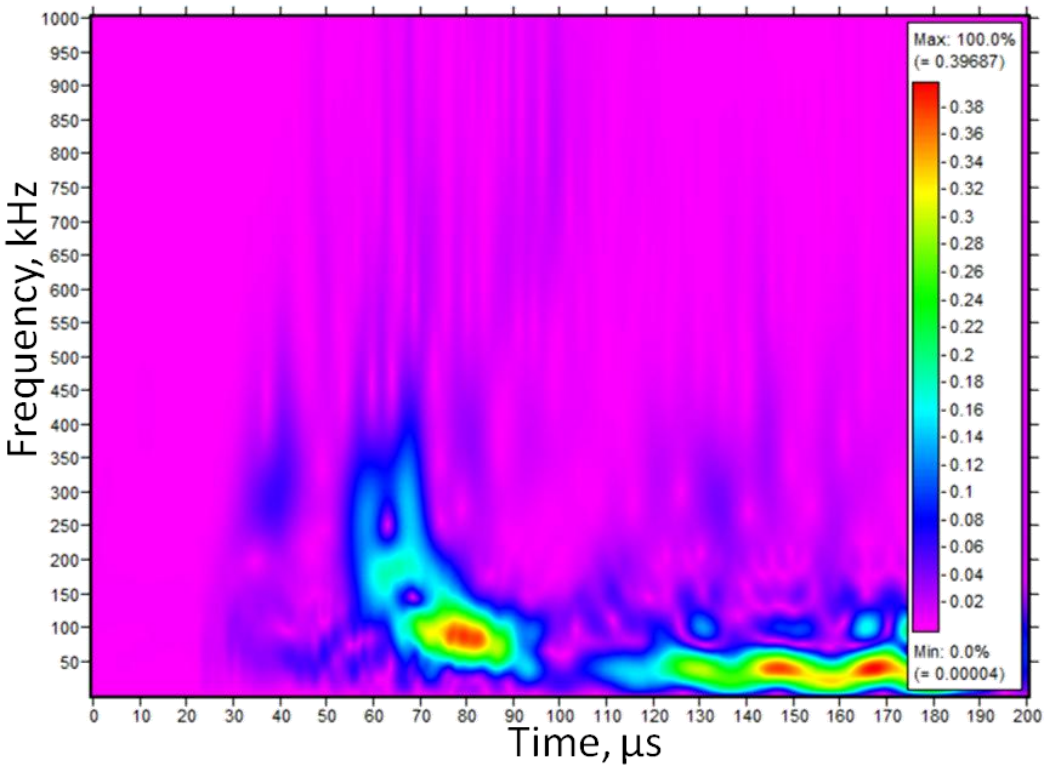

Figure 2-18. Wavelet transform of a signal received by a 28mm M2814-P2 MFC for a surface H-N source at a distance of 200mm

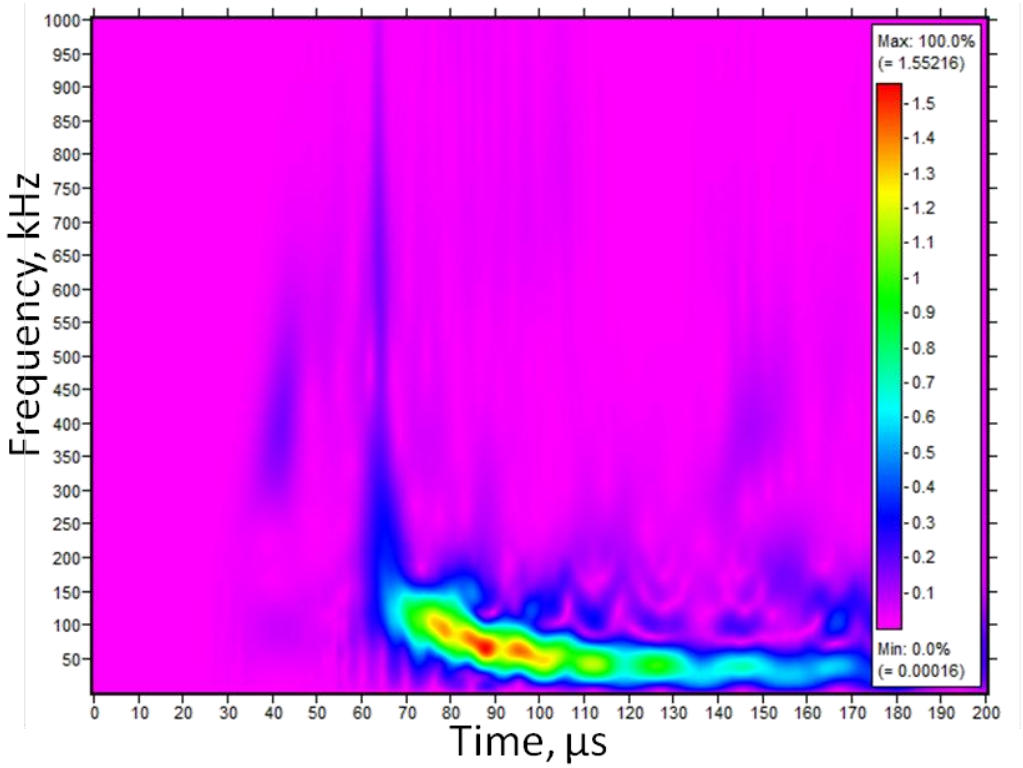

Figure 2-19.Wavelet transform of signal received by a 14mm M2814-P2 MFC from a surface H-N source at a distance of 200mm

Figure 2-20 shows a wavelet transform for a waveform received by the conical transducer from an H-N source on the edge of the aluminium panel at a distance of 200mm from the transducer. Figure 2-20 clearly shows the arrival of the S_o mode at 45µs and the A_o mode at approximately 80µs. Due to orientation of the H-N source being in-plane this creates a much larger S_0 constituent to that of an out of plane H-N source. Figure 2-21, Figure 2-22 and Figure 2-23 show the calculated wavelet transform with the dispersion group velocity curves overlaid. Clearly a strong S_0 mode is evident and very little, if any, A_0 mode is evident from a M2814-P2 MFC with an active length of 28mm and 17mm. Figure 2-23 shows the wavelet transform for active length of 10mm and shows an overall greater sensitivity and A_0 mode is clearly visible. Again the same trend is observed for a reduction in the active length with an increased in sensitivity for certain active lengths. However all of the above figures show both low and higher frequency parts of the S_0 which are only evident when the source is used in-plane to that transducer suggesting an in-plane sensitivity.

A further investigation was conducted to try and establish why the observed changes in the frequency response of the MFC transducers with different lengths occurred. This was achieved by using the M2814-P2 MFC and measuring the maximum wavelet coefficient for a finite timing window around the two wave mode arrival times. During this process the frequency and the arrival time of the maximum value of the wavelet coefficient was recorded.

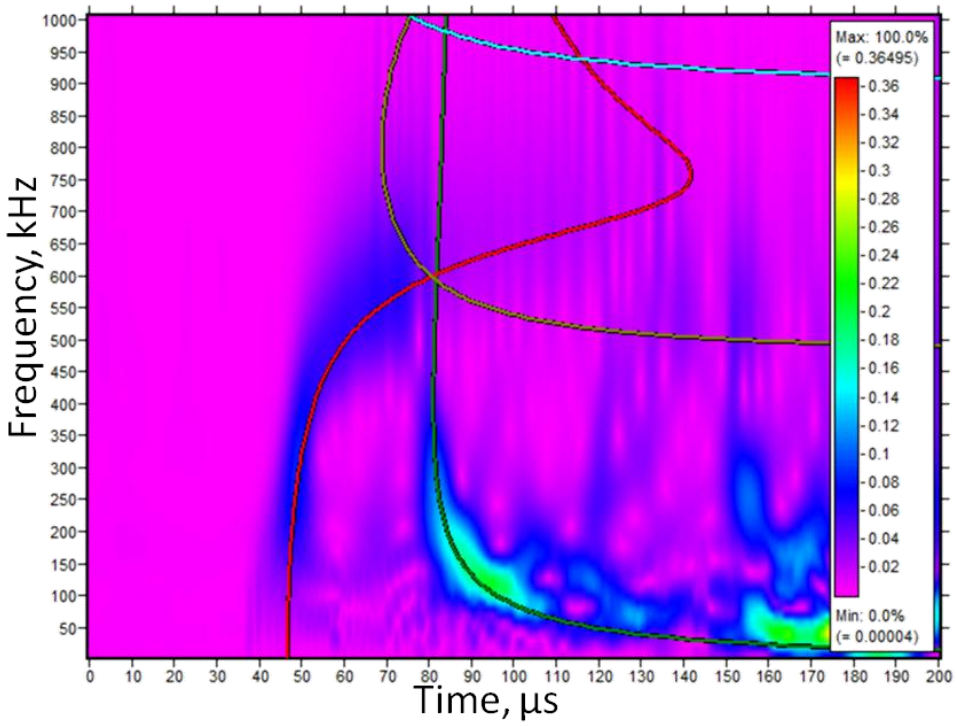

Figure 2-20.Wavelet transform of a signal received by the conical transducer from a 250mm surface H-N source

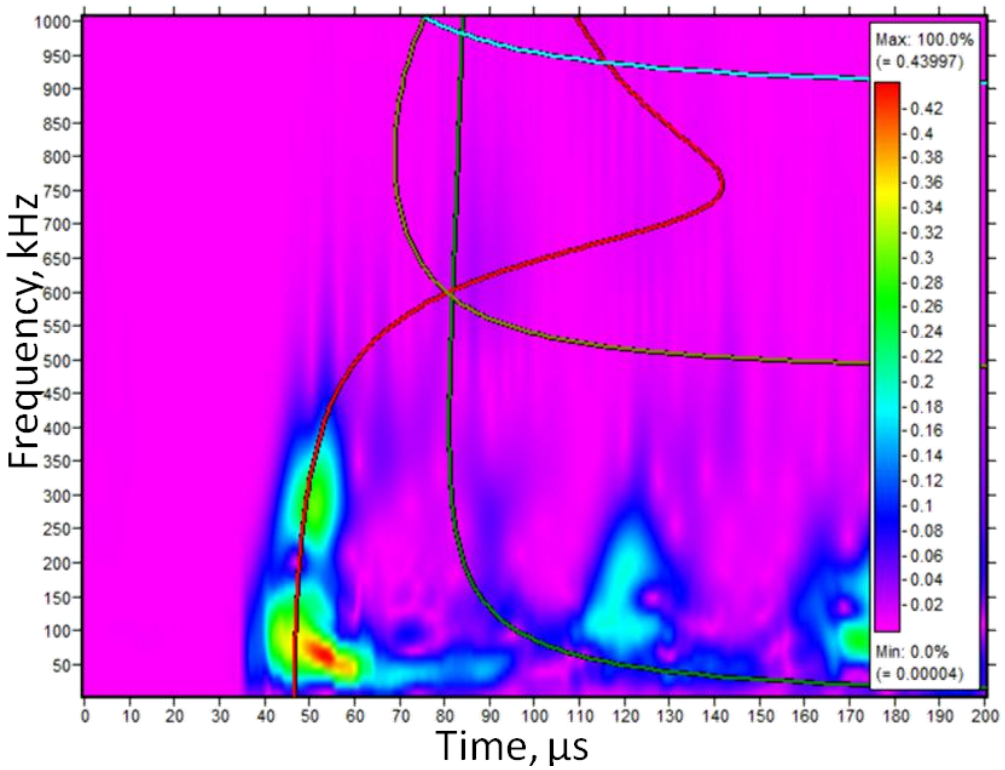

Figure 2-21. Wavelet transform of an in-plane H-N source used at a distance of 250mm recorded at a M2814-P2 with an active length of 28mm

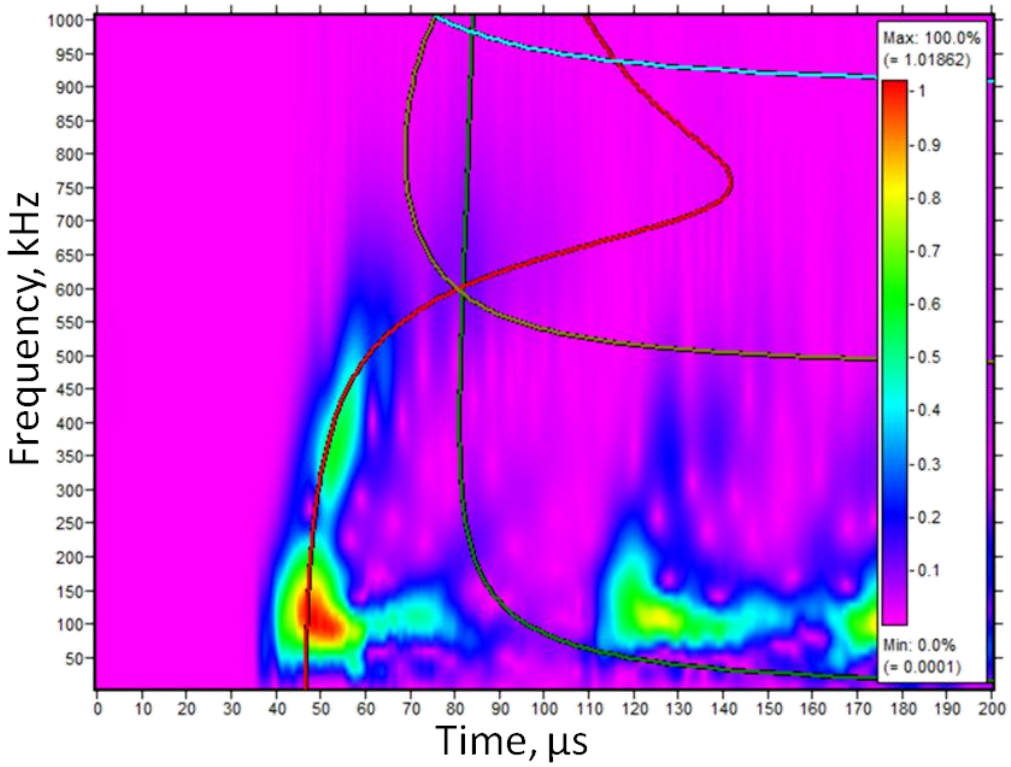

Figure 2-22. Wavelet transform of an in-plane H-N source used at a distance of 250mm recorded at a M2814-P2 with an active length of 17mm

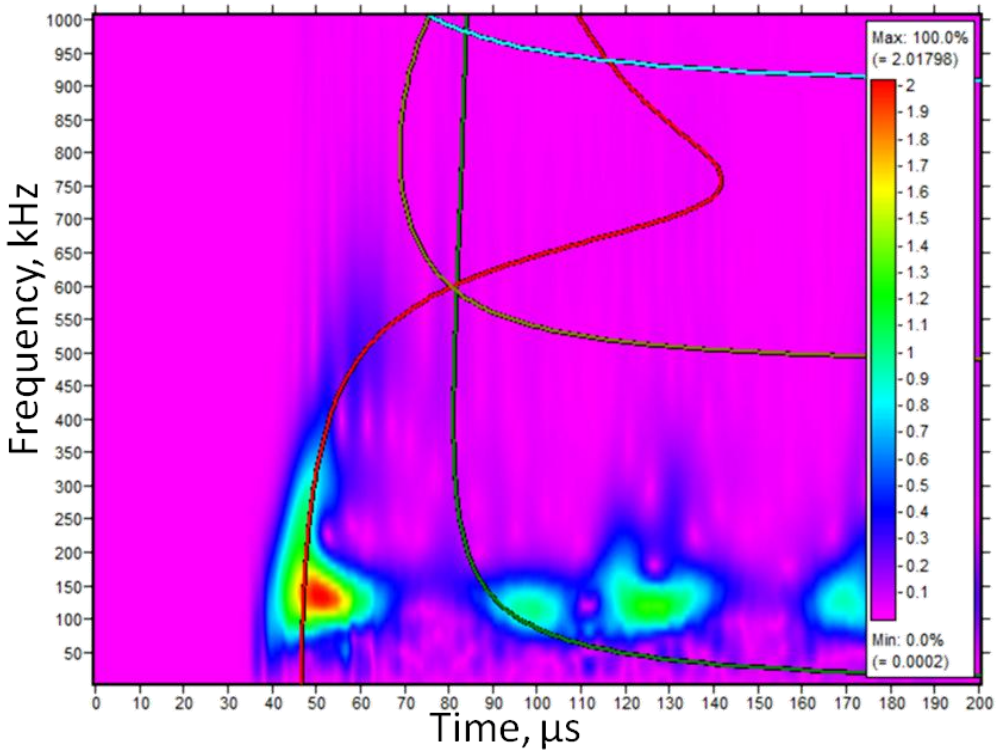

Figure 2-23. Wavelet transform of an in-plane H-N source used at a distance of 250mm recorded at a M2814-P2 with an active length of 10mm

Figure 2-24 shows the maximum wavelet coefficient for the two fundamental wave modes which were calculated by finding the maximum wavelet coefficient for the S_0 timing of 0 to 55µs and an A_0 mode timing of 55 to 100µs. The figure shows that in the case of the S_0 mode the overall sensitivity increases up to approximately 0.3mV at a length of 8mm and then decreases at a slower rate for all subsequent MFC transducer lengths. A similar trend is observed for the maximum wavelet coefficient for the A_0 mode, however the peak sensitivity corresponds to a 17mm length of MFC. This suggests that the MFC can be optimised for any particular thickness of structure that it will be used to monitor. Overall there is an increase in sensitivity of approximately 4.25 and 5.48 for the S_0 and A_0 wave modes respectively. Figure 2-25 shows the frequency which corresponds to the maximum wavelet coefficient for the two timing windows used to determine the two fundamental wave modes. The figure shows that in the case of A_0 mode, the frequency at which the maximum wavelet coefficient occurs is fairly constant and ranges from 70 to 120kHz with an average frequency of 88.5kHz. The figure shows that for the S_0 mode there is a larger fluctuation of the frequency at which the maximum wavelet coefficient occurs; the majority of the frequency in the range between 300 and 400kHz. However there are several measurements which fall outside this range. For an active length of 6mm and 23mm there is a considerable drop in the frequency this is due to

there being much lower frequency content of the S_0 for these two lengths, however the reasons for this are unknown. For a length of 2mm there is a much higher frequency this is attributed to the small length. Averaging the results for the S_0 mode results in a frequency of 342kHz. Figure 2-26 shows the phase velocity curves for a 3.18mm thick aluminium panel for the two fundamental wave modes. This figure determines the wavelength of a particular mode at a particular frequency and has been reported in the literature. As the wave speed is equal to the product of the wavelength and frequency, it is possible to determine the wavelength of the wave corresponding to the maximum wavelet coefficient using average frequency and the phase velocity for that particular frequency for the S_0 and A_0 mode respectively. This calculation gives a wavelength of 15.26mm and 16.73mm for the S_0 and A_0 mode respectively. Figure 2-27 shows the sensitivity of the different lengths of MFC transducer when compared with the ratio of the actual length of the MFC to the calculated wavelength. The figure shows that the maximum wavelet coefficient for the S_0 mode occurs when the MFC length is half the wavelength. For the A_0 mode the maximum wavelet coefficient is observed when the MFC length is equal to the wavelength. This relationship can only be verified for the M2814-P2 MFC as the length of the MFC was altered in 2-3mm but nevertheless suggests that the MFC can be optimised for a particular geometry of the structure. Lamb waves propagated within plate structures in two fundamental modes, the extensional and flexural. The extensional mode is mostly in the plane of the structure and the flexural is mainly out of plane. Within these two modes there will be a particular frequency which will carry the majority of the energy. The frequency of the transducer is defined by the geometry. Therefore there will be a particular geometry of transducer which will increase the transducer output because it matches the most energetic frequency of the structure. However this relationship will only be relevant for a particular geometry as the most energetic frequency will only be valid for a particular plate thickness. If a thicker panel was used for the experiment, higher order modes would be present within the same frequency range and this would complicate this relationship even further. As the Lamb wave propagates in a panel, this causes tiny displacements at the surface and hence strain. Assuming the transducer does not alter the strain field there will be wavelength tuning effects occurring where if the wavelength of the propagating wave is equal to the transducer length a minimum in transducer output occurs due to the strain field averaging out over the wavelength, whereas if the transducer length is half of the propagating wavelength a maximum in output occurs. However this is not the case for A_0 mode for the M2814-P2 MFC, this mostly likely due to the size of the panel and reflections starting to effect the propagating wave at an early stage. Alongside this as the transducer length is reduced it will start to act

as a point contact transducer as the length is smaller compared to the wavelength and hence less strain averaging occurs across the transducer. All these factors give arise to a very complex relationship and further modelling of Lamb wave propagation and transducer to Lamb wave interaction would be required to define definitive relationships to truly optimise these transducers for a particular plate thickness.

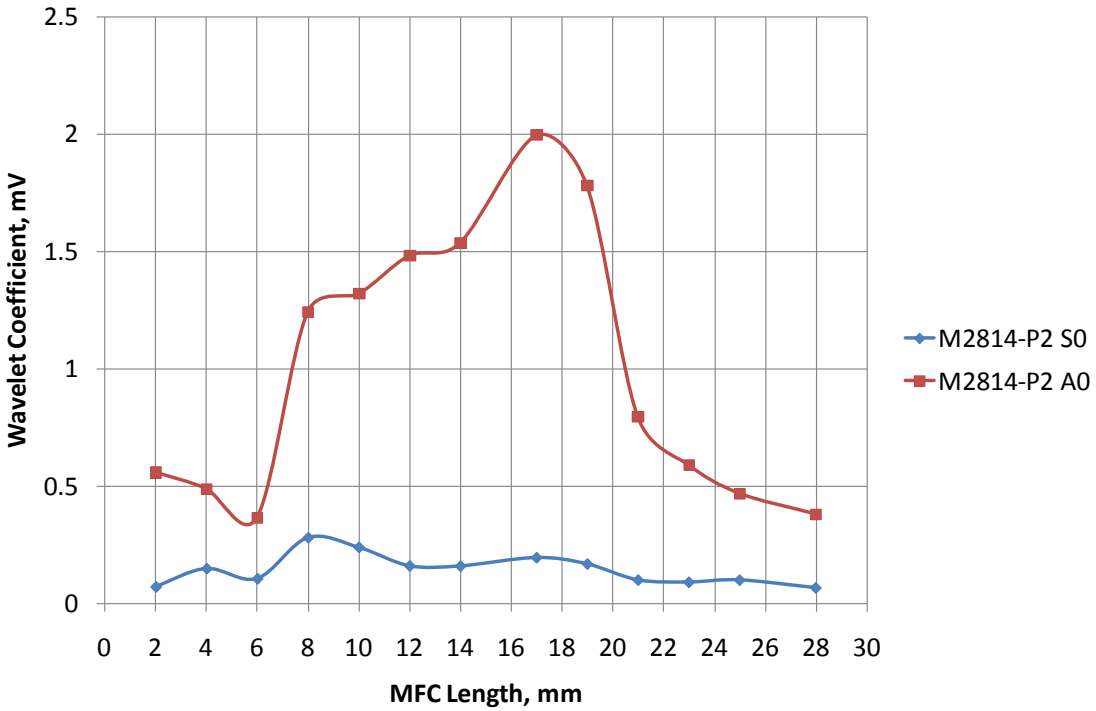

Figure 2-24. Maximum wavelet coefficients for the two wave modes for various length of a M2814-P2 MFC

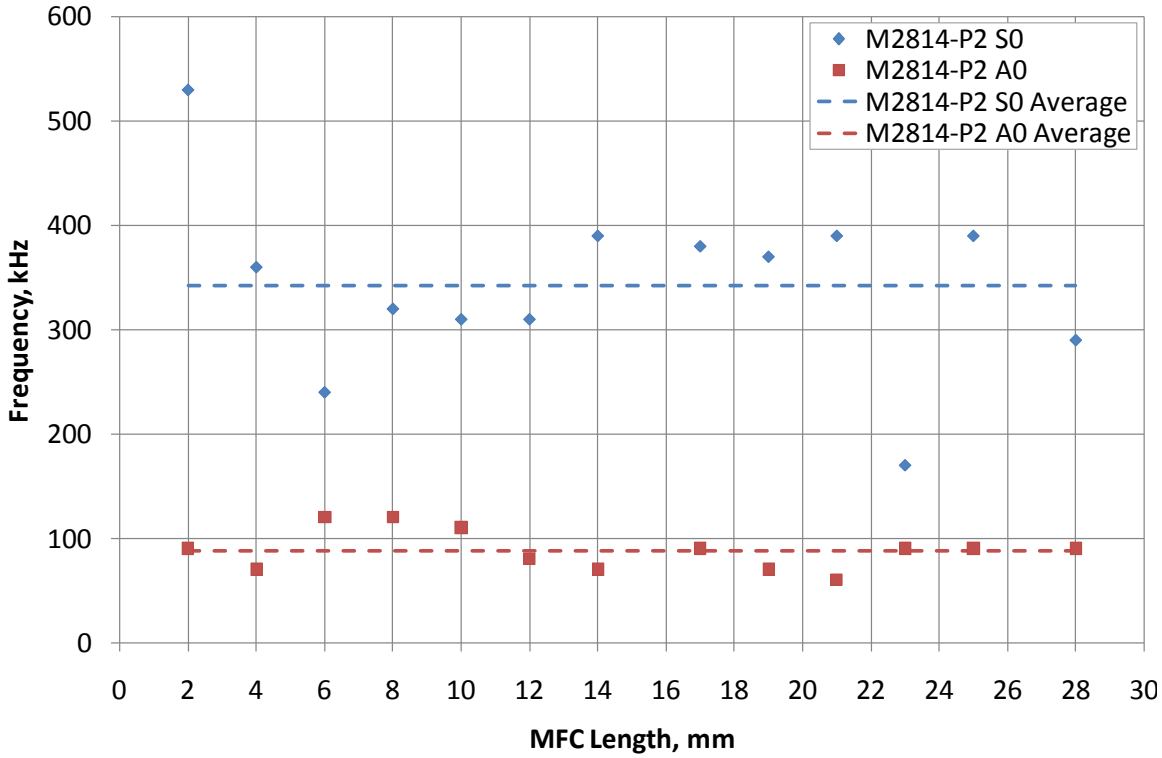

Figure 2-25. Corresponding frequency of the maximum wavelet coefficient for various lengths of M2814-P2 MFC

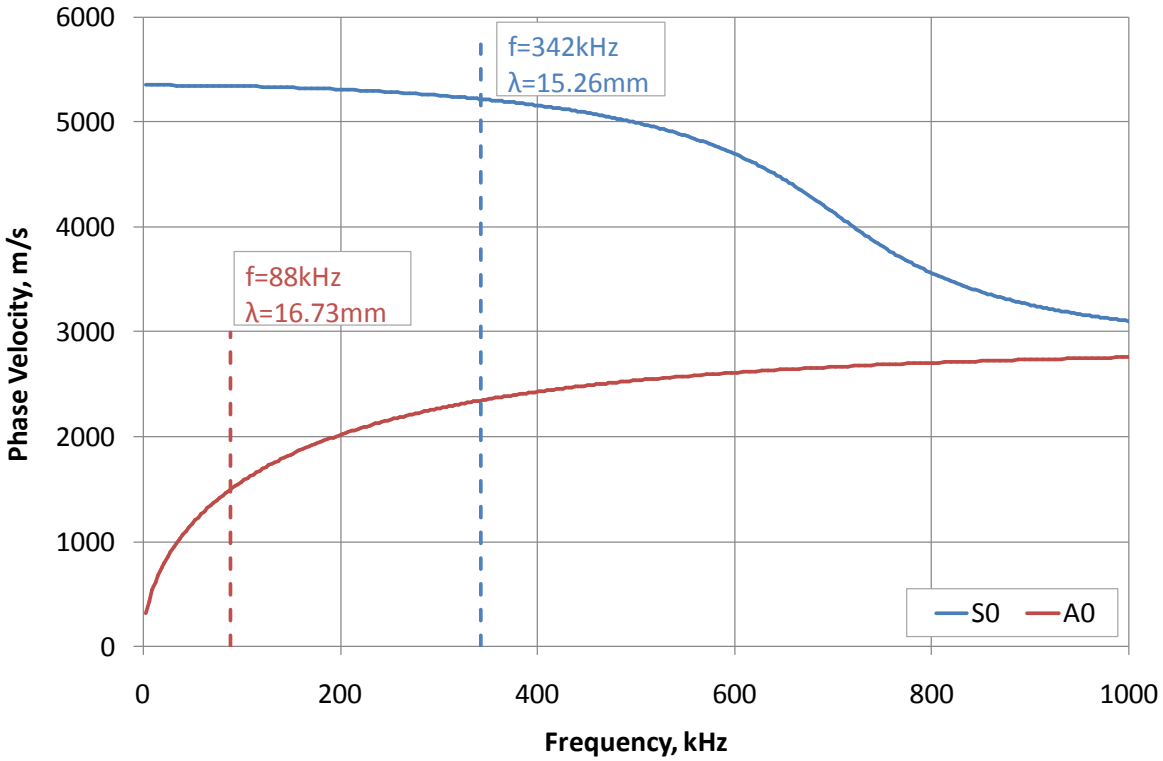

Figure 2-26. Phase velocity curves for a 3.18mm thick aluminium panel

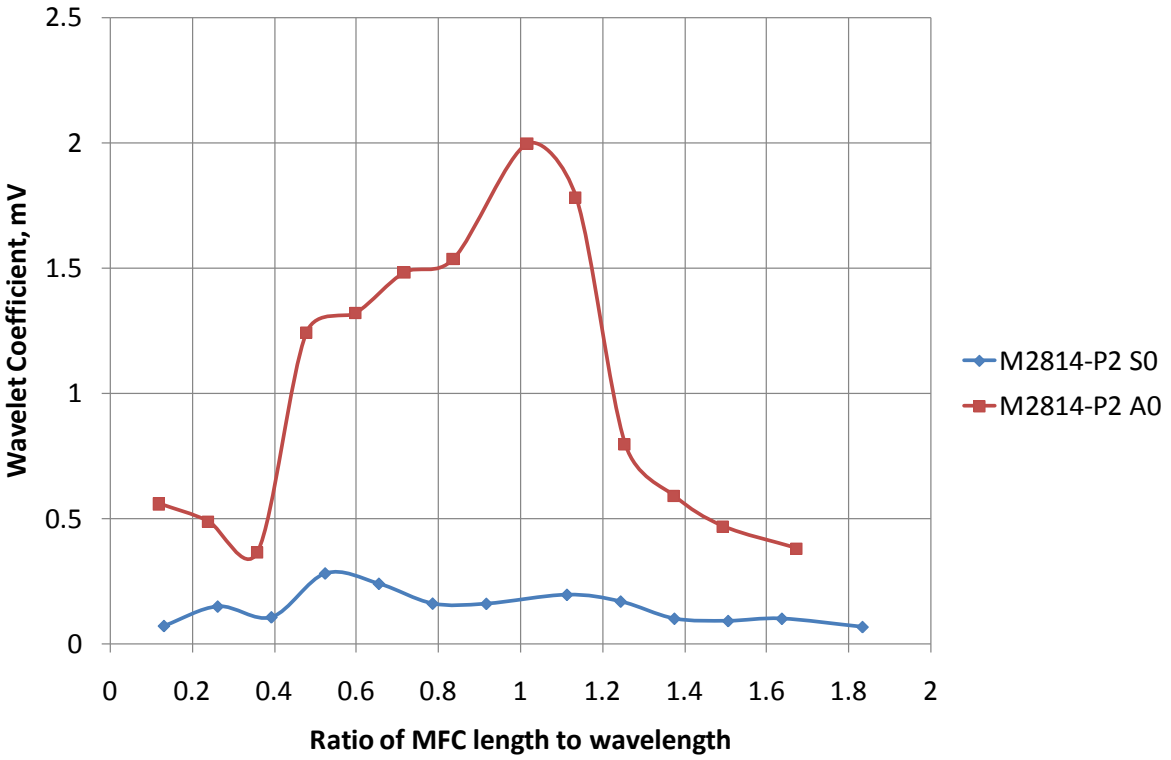

Figure 2-27. Optimum length of the M2814-P2 MFC in terms of the wavelet coefficient

2.2.1.4 Conclusions

The experimental investigation for various different MFC transducers has shown that the sensitivity of the transducer can be increased by decreasing the length. The sensitivity increase was observed both the attenuation and directional investigations. It is also evident the width of the transducer also effects the sensitivity as the smaller active area transducer was considerable more sensitive than the large. Suggesting a relationship between plate thickness, propagation frequency and active area of the MFC. In effect, altering the active length of the transducer affects the frequency response of the transducer and the optimum wavelength which it can detect. For the particular investigation peak sensitivity was observed when the ratio of MFC length to wavelength was 0.5 and 1 for the S_0 and A_0 modes respectively However further work is required to determine definite relationships for different active areas and plate thicknesses..

2.2.2 AE Transducers in Harsh Environments

2.2.2.1 Introduction

Often damage detection methodologies are successfully employed in a laboratory environment to detect damage in structure using both AE and AU techniques. However there is often no consideration of whether these techniques would be effective on real structures

where environmental factors could affect the performance. Such environmental factors include temperature and humidity changes, contact with harsh chemicals and vibrations which are often not present in the laboratory environment. This is extremely important when considering baseline techniques for detecting damage where environmental changes could lead to false alarms due to environmental effects altering the received signal rather than damage. Therefore an investigation was undertaken to assess temperature effects on a commercial AE transducers and the MFCs transducers.

2.2.2.2 Methodology

Three pairs of transducers were chosen for this investigation, two commercially available units Mistras Nano30 and two 150KHz McWade transducers. The final two transducers were M2814-P1 type MFCs which are nominally utilised for strain sensing, guided waves and vibration suppression. In order to reduce other experimental variables such as the couplant, the transducers were mounted dry coupled face to face and secured in place using high temperature adhesive tape. The MFC transducers were mounted in different configurations due to electrical noise issues when mounted dry coupled face to face. The two MFCs were mounted to a small aluminium block and attached in place using high temperature adhesive tape with a layer of high temperature felt wrapped around the transducers to protect them while in the stack configuration. In order to produce an even clamping force on the transducers they were mounted in a stack configuration as seen in Figure 2-28 and a weight was placed on the top of the stack. As can be seen from Figure 2-28 the MFC transducer pair were placed at the bottom followed by the McWade transducers and finally the Nano30 transducers. Figure 2-29 shows the Instron environmental chamber was used to subject the transducers to different hot and cold temperatures.

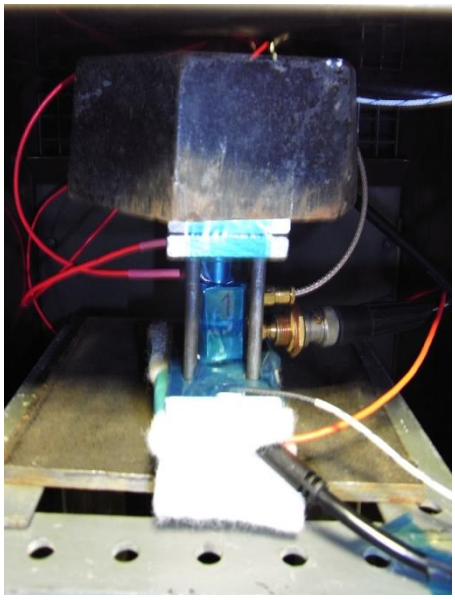

Figure 2-28. Stack configuration for transducer testing in harsh environments

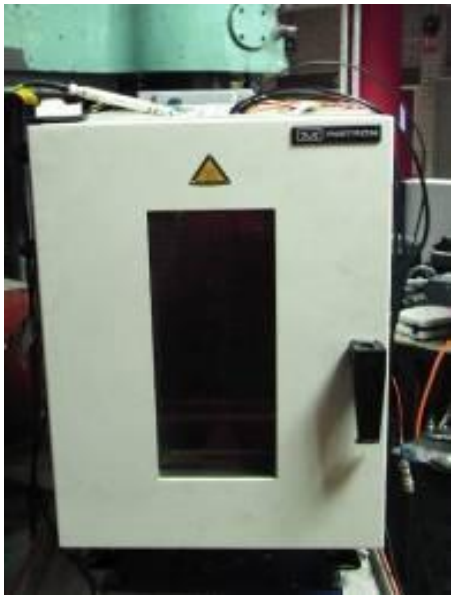

Figure 2-29. Environmental chamber used for the investigation

A small frame was manufactured to place the transducer stack towards the top of the chamber in order that there was a suitable cable length to have all other electrical equipment outside of the chamber. A transducer from the Nano30 and MFC pairs were attached to Mistras 0/2/4 pre-amps with a gain of 40dB and a quoted bandwidth of 20-1200KHz, a McWade transducer was attached to a 150kHz PA0331 pre-amp with a gain of 40dB and a quoted nominal bandwidth of 100-200kHz. Consistent pre-amps were not used in this experiment due to the McWade transducer requiring McWade Pre-amps.

The transducer stack was subjected to two different temperature scenarios that were based on temperature tests from the RTCA DO-160E document (RTCA 2004) for environmental conditions and test procedures for airborne equipment. The harshest tests were chosen to represent the worst case scenario and this resulted in a set of ground survival high and cold temperature tests, these were specified as the worst case temperatures that equipment could be exposed to while the aircraft was on the ground. A baseline chamber temperature of 35°C was used as the start and end conditions for each individual test so that I repeatable state could be achieved within the laboratory environment. The first set of ground survival hot temperature tests are outlined as follows:

- Stabilise the chamber at 35°C then increase the temperature to 85°C and hold for 3 hours then return to 35°C and hold for a further 2hrs

For the ground survival cold temperature tests were outlines as follows:

- Stabilise the chamber at 35°C then decrease the temperature to -65°C and hold for 3 hours then return to 35°C and hold for a further 2hrs

Although the RTCA DO-160E documents only outlines equipment must be functional after being exposed to these temperatures it does not require an assessment of changes in the functionality. Therefore additional tests to quantify the effects of the temperature variations on the performance of the AE transducers were conducted. Therefore one transducer from each pair was used as a transmitter where a 10V square wave at three different frequencies of 100, 300 and 500kHz was used to activate the transducers, the other transducer was used as a receiver to record the response. A square wave was chosen to create a broadband signal to excite several frequencies components much like a typical AE waveform. Three different frequencies were chosen to alter the energy of the main frequency component through the typical AE sensor response range of 10 to 500kHz. A Mistras Wavegen board was used to provide the actuation signal and a Mistras PCI2 system was used to record the response at the receiver transducer with acquisition settings as defined in Table 2-1. A cross correlation technique was used to assess the repeatability of the pulse-receive configuration at each temperature and to detect any changes in the waveform at the specified temperatures from that at the baseline temperature. This resulted in four measurement periods. 50 waveforms were recorded at the initial baseline temperature, another two sets of waveforms was recorded after 30minutes and 3 hours at the specified temperature and finally a final set waveforms were recorded after the chamber had been held at the baseline temperature of 35°C. For the cross correlation analysis the first waveform in at each measurement period was used to correlate to all other signals within that particular data set for each temperature and frequency. To assess any changes in the waveforms the first waveform from each baseline condition was used to correlate to all the other waveforms from each particular data set for each temperature and frequency.

Table 2-1. Acquisitions settings for the temperature investigations

Threshold	50dB
Pre-amp Gain	40dB
Analogue Filter	1kHz - 3MHz
Sample Rate	10MSPS
Pre-trigger length	100µs
Waveform length	7k

2.2.2.3 Experimental Results and Discussion

All figures within this section show the average cross correlation coefficients for signals correlated within a particular data set or to the baseline waveforms over duration of a temperature test. The temperatures at which signals were recorded is highlighted at the top of the figures. Figure 2-30 shows the average cross correlation coefficients for signals recorded for each individual transducer and compared within the data set for an actuation signal of 100kHz for the 85°C temperature test. The figure shows that there is a high level of repeatability between the transmit and receive configuration with majority of cross correlation coefficients being greater than 0.995. The only transducer not to attain the same high level of correlation is the MFC. This was due to the lower sensitivity of this transducers to that of the commercial AE transducer and therefore a higher signal to noise ratio was present in the signals which affects the cross correlation. Therefore further analysis of the ground survival hot temperature tests was required. Figure 2-31, Figure 2-32 and Figure 2-33 show the frequency spectrum for example signals recorded at each specified duration for the 85°C ground survival tests, for a 100, 300 and 500kHz square wave. The figures show the main frequency content of the signal attributed to the transducers response lies in the band between 0 and 100 kHz for this particular sensor arrangement. This shows that the MFC transducers for this arrangement operate at a much lower frequency than the Nano 30 and McWade transducer. This is most probably due to no rigid coupling between the transducers and therefore are less sensitive due to their in plane nature. The two sets of spikes in the data appear at the exact same frequency and same amplitude within a particular temperature test and therefore are attributed to background noise. Therefore a further filtering of the MFC signals was undertaken between the range of 10-100kHz and is shown and referred to in the cross correlation figures as “MFC Filtered”. This frequency band was used unless otherwise stated. The MFC filtered curve in Figure 2-30 shows that after filtering of the signals a much higher level of cross correlation is observed. Knowing that there is high repeatability between the transmit and receive configurations, any drop in correlation observed when comparing the signal recorded to that of the baseline signals are due to the temperature effects only. Figure 2-34 shows the similarity of the signals recorded at each specified interval when compared with the first baseline signal for the 85°C temperature and for a 100 kHz square wave. The figure shows that for all transducers there is a reduction in cross correlation coefficient at 85°C. The Nano 30 transducers show the largest drop in correlation down to approximately 0.54 whereas the filtered MFC signals shows the least fall in correction to 0.75 and the McWade transducer shows a reduction in correlation down to approximately 0.65. Both the MFC and Nano 30 return to a similar level correlation with a

small change in frequency content of the signals due possible damage. However the McWade cross correlation coefficient drops significantly at the end of the test and requires further investigation. Figure 2-35 shows the frequency spectrum for first recorded signals at each specified period and shows a shift in frequency and a reduction in amplitude for the baseline to 85°C however there is a significant change in amplitude with the signals recorded at the end of the test. It was originally hypothesized that it was the attenuation of the frequency content greater than 180kHz which was causing the drop in correlation, however filtering the signal between 10 and 180kHz had no significant improvement in the correlation values. Therefore it is suggested that due to the amplitude reduction and frequency shift is causing a significant reduction in correlation, this may be due to possible damage to the transducers.

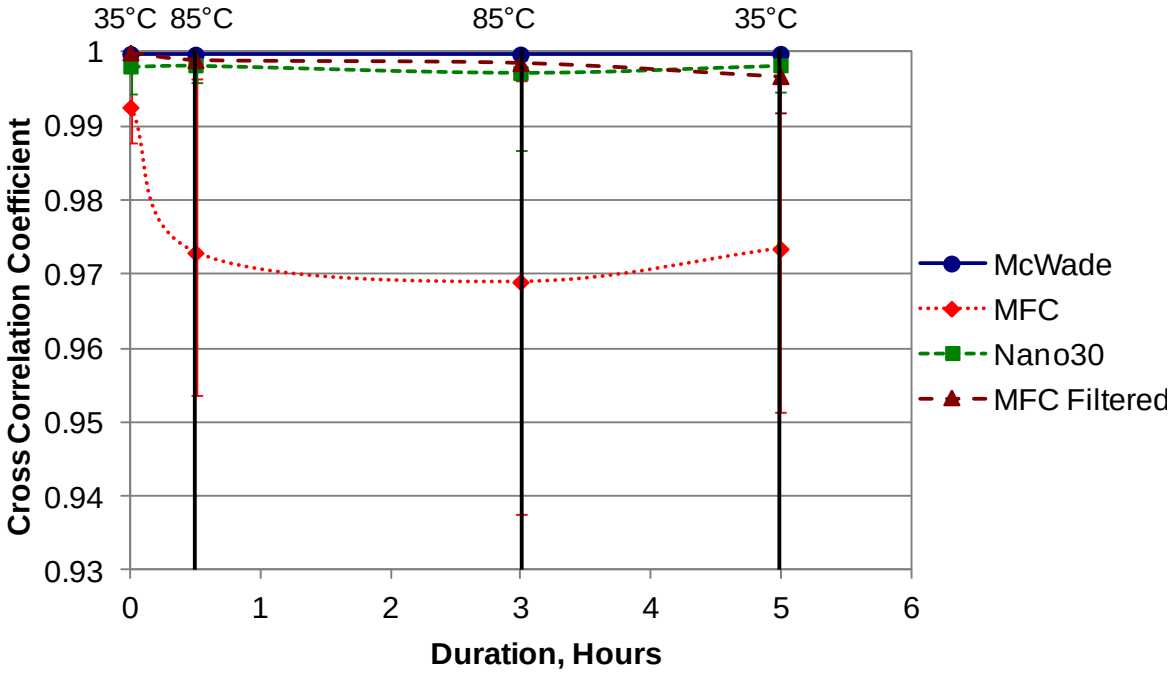

Figure 2-30. Repeatability of the signals from the ground survival 85°C temperature test at 100 kHz

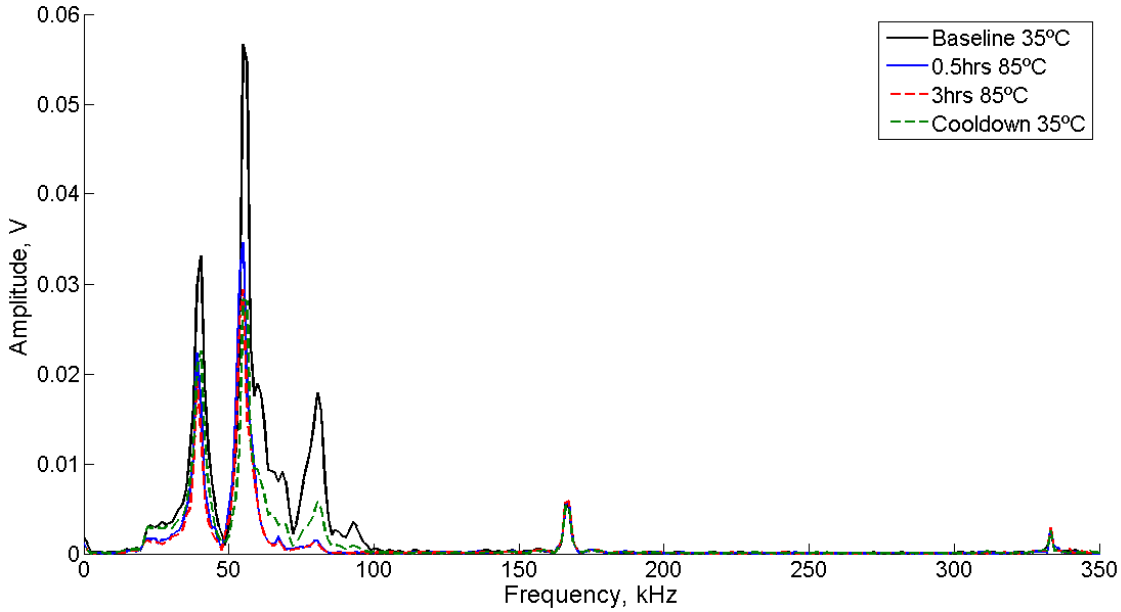

Figure 2-31. Frequency Spectrum for MFC 85°C example signals recorded at each specified time for a 100khz square wave

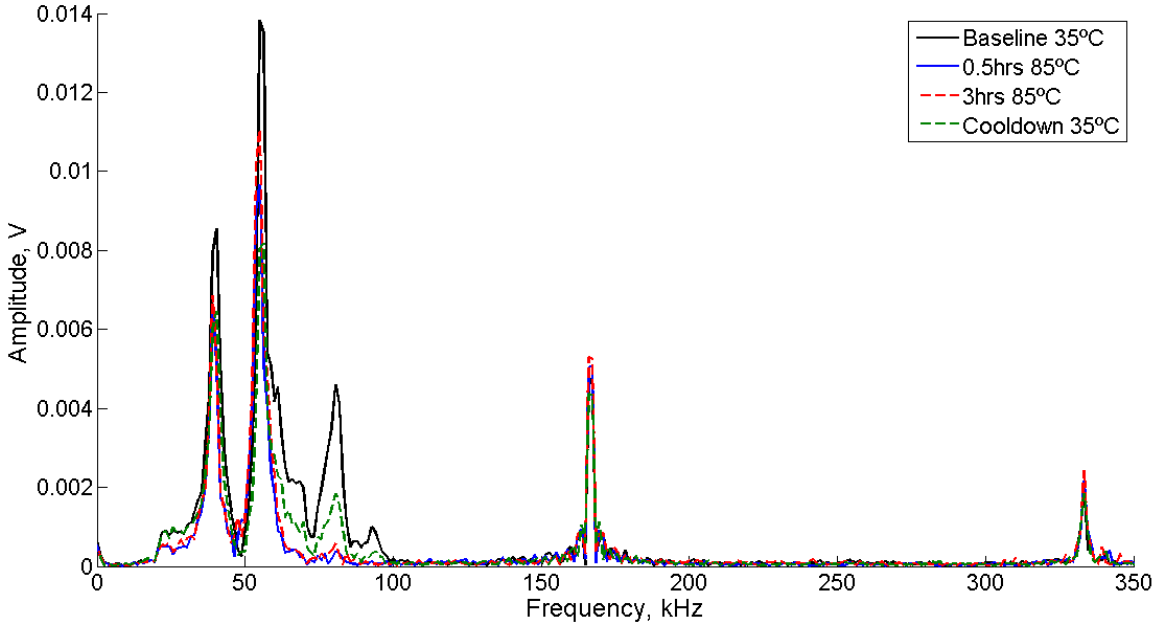

Figure 2-32. Frequency Spectrum for MFC 85°C example signals recorded at each specified time for a 300khz square wave

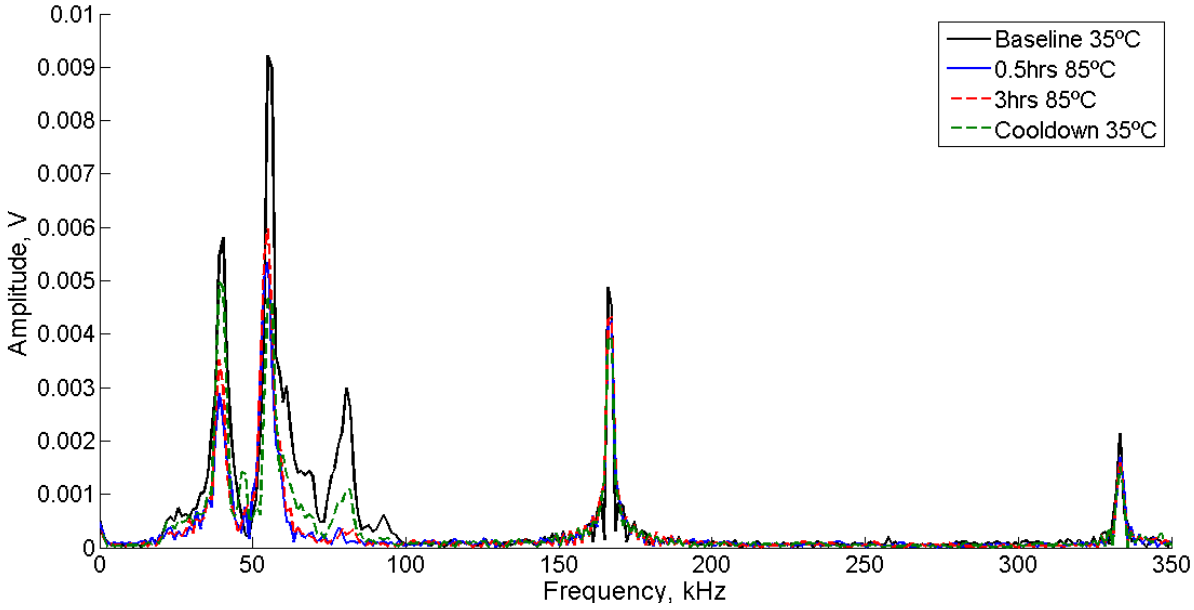

Figure 2-33. Frequency Spectrum for MFC 85°C example signals recorded at each specified time for a 500khz square wave

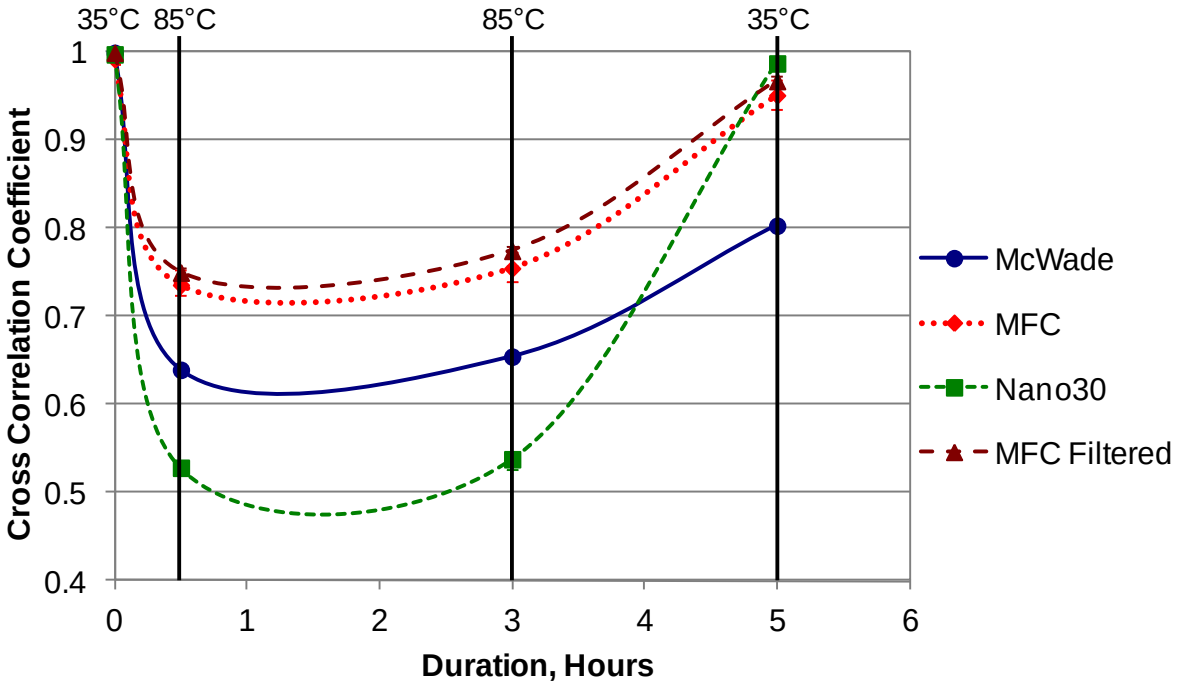

Figure 2-34. Baseline comparison signals from the ground survival 85°C temperature test at 100 kHz

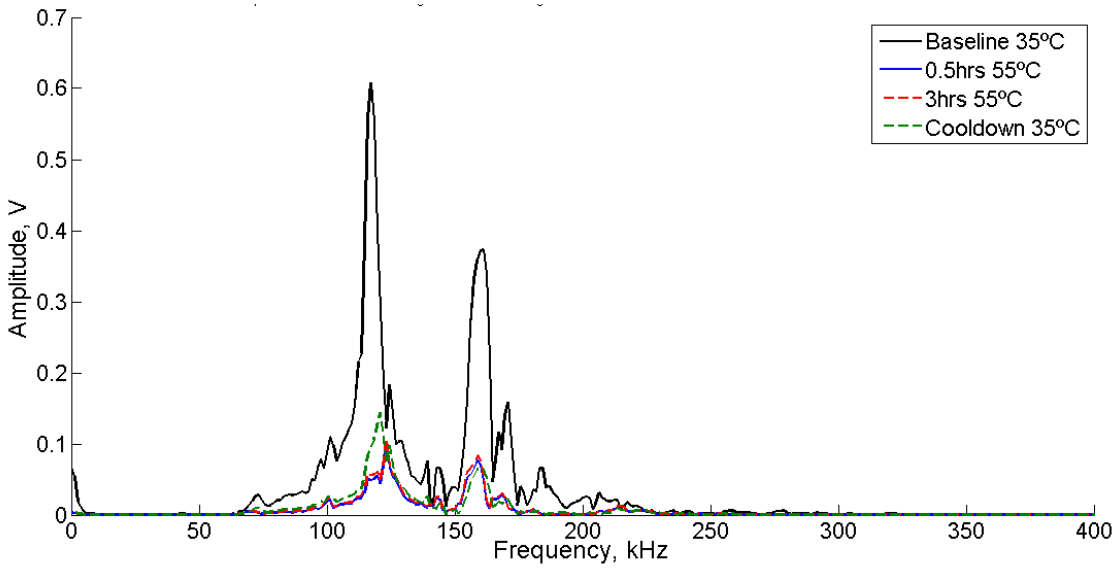

Figure 2-35. Frequency Spectrum for the McWade signals for the 85°C test at 100kHz

Figure 2-36 shows the average cross correlation coefficient for signals correlated within each specified data set for an input square wave of 300kHz for the 85°C investigation, the figure shows a high level of correlation for the McWade and Nano30 transducers again showing repeatability in the data set. However for the MFC transducer there is significant drop in repeatability with an average correlation coefficient of 0.92, this is due to the frequency of the square wave being outside the predominant frequency range of the transducer therefore resulting in inefficient energy transfer and therefore a drop in amplitude and hence a lower signal to noise ratio. After filtering of the signals the MFC signals attain a high repeatability. Figure 2-37 shows the correlation coefficients for all the transducers when the signal recorded at the specified interval are compared with the first baseline waveform, this shows again a reduction in correlation at elevated temperatures. Again the Nano30 shows the largest drop in correlation and filtered MFC signals the lowest drop. The same trend is observed for the McWade 300kHz signal with that of a 100kHz signal and it due to the same reasons as all the measurement for the end of test irrespectively of frequency were taken within same time period.

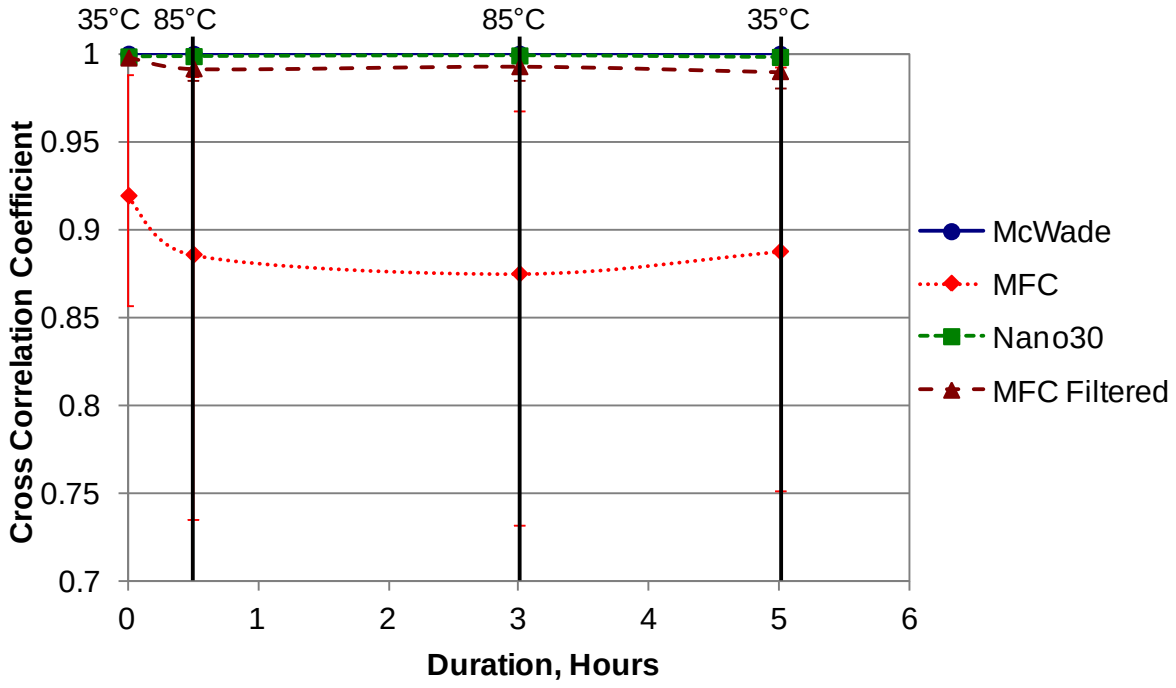

Figure 2-36. Repeatability of the signals from the ground survival 85°C test at 300 kHz

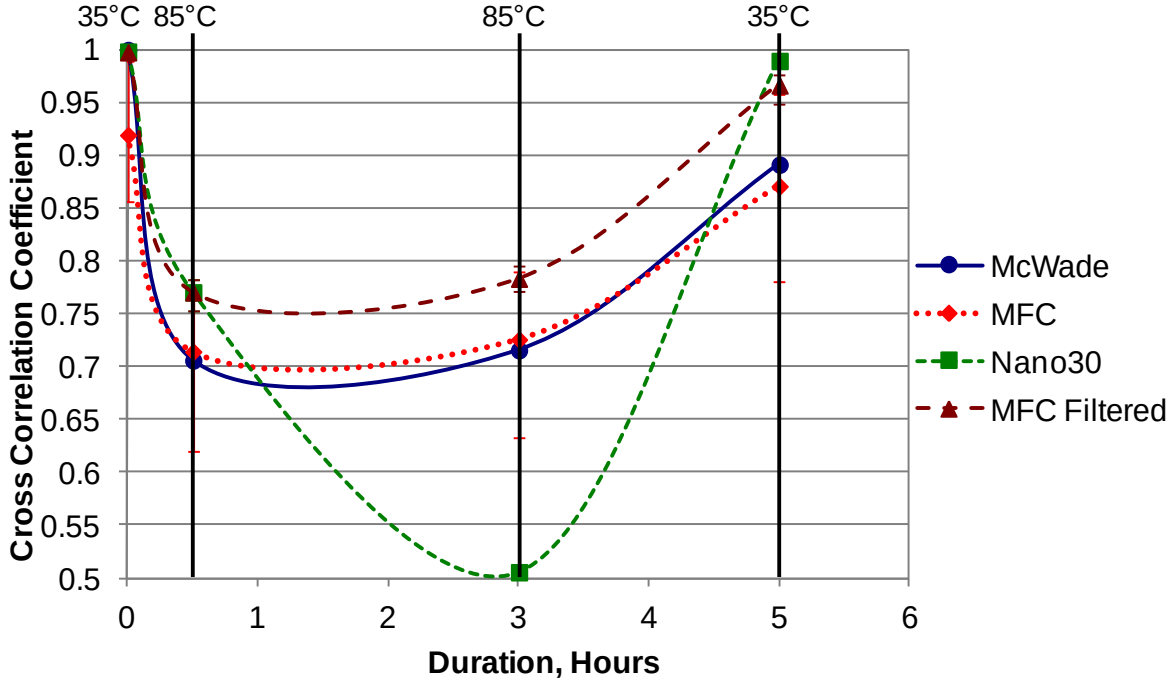

Figure 2-37 . Baseline comparison of signals from the ground survival 85°C test at 300 kHz

Figure 2-38 shows the repeatability of the signal correlated within each data set for the particular measurement interval for all transducer a high level of correlation of approximately 0.99 is observed for a 500kHz square wave for the 85°C investigation. Again after filtering of the MFC signals a much higher level of correlation is observed. Figure 2-39

shows the average correlation coefficient for a 500kHz square wave for the waveforms recorded at each measurement interval when compared with the first baseline waveform again all transducers show a reduction in similarity of the baseline signal at elevated temperatures. Again the same trend occurs in the McWade transducer and for the same possible reasons. The Nano30 returns to the same level of correlation however there is a definite difference in MFC signals at the end of the test when compared with the beginning, however this is still less than 0.05 drop and therefore is not considered significant, however this particular temperature was close to the maximum allowable temperature for the this particular MFC.

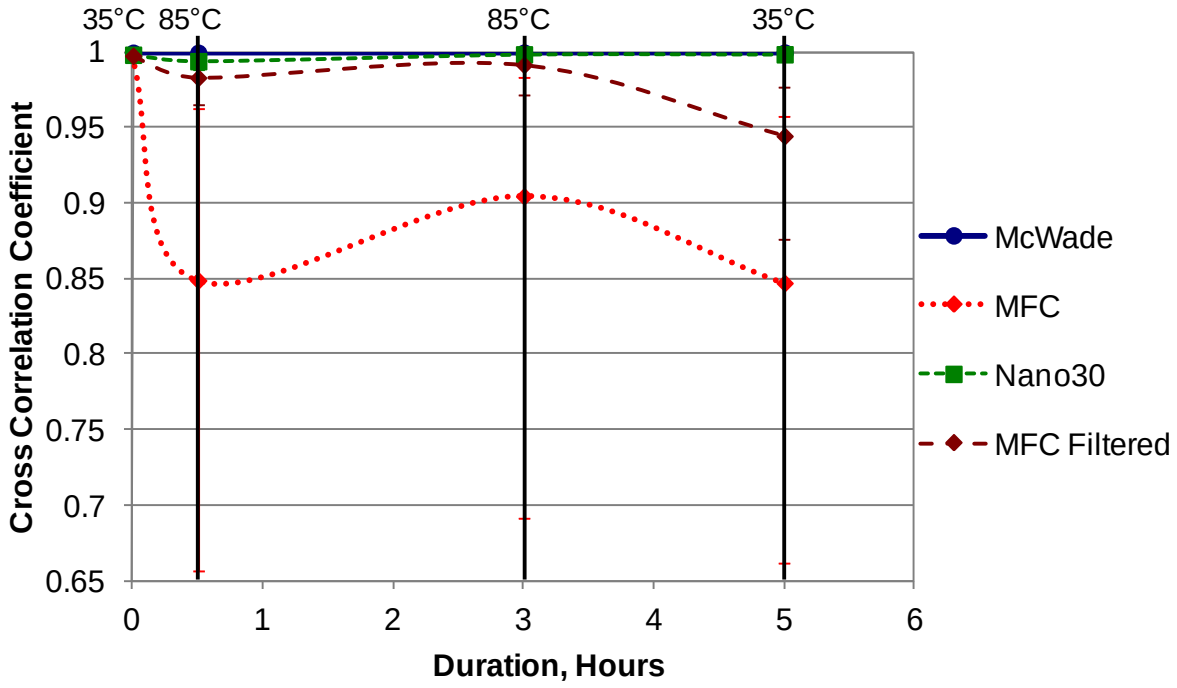

Figure 2-38. Repeatability of the signals from the ground survival 85°C test at 500 kHz

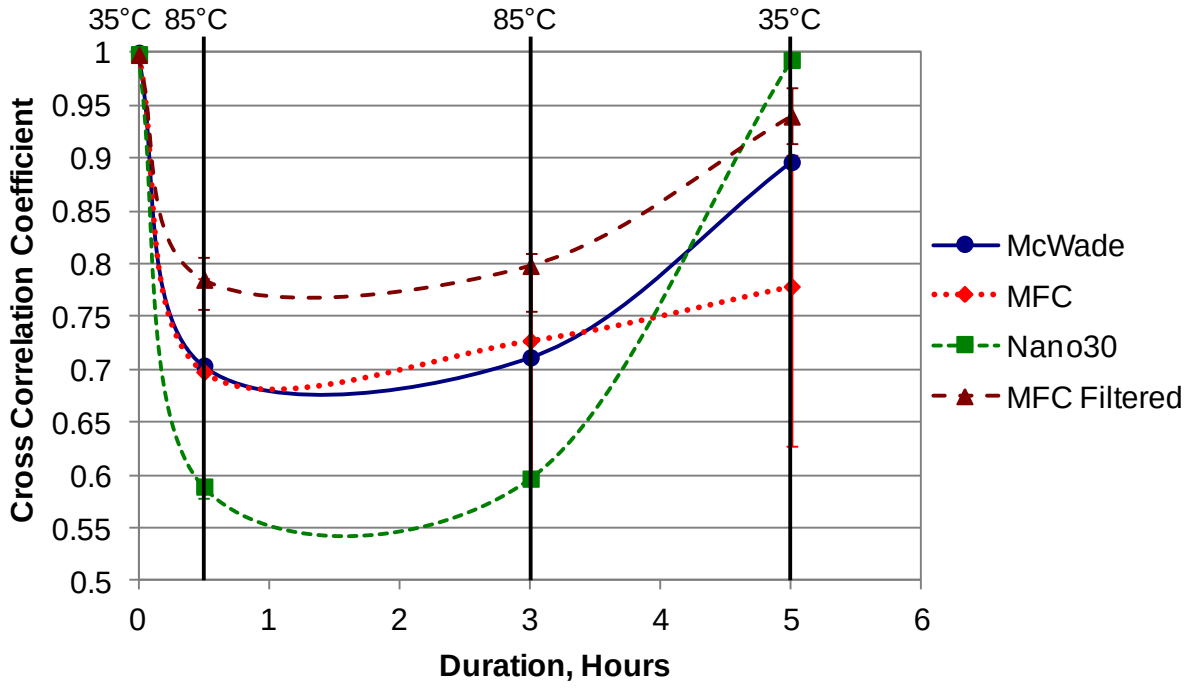

Figure 2-39. Baseline comparison of signals from the ground survival 85°C test at 500 kHz

All resulting figures from this point onwards are for the ground survival cold temperatures -65°C test for 100, 300 and 500kHz square. Figure 2-40 shows the average cross correlation coefficients when compared within that data set for a 100kHz square wave at -65°C, again a high level correlation is observed showing a high repeatability. Again the MFC similarity is lower than the previous transducers and require further filtering. Figure 2-41, Figure 2-42 and Figure 2-43 show the frequency content for each stage in the test for an input square wave of 100, 300 and 500kHz. It is evident from the figures that filtering the signals 10-100kHz is no longer suitable due to the increase frequency bandwidth at sub zeros temperatures. The figures also show the similar noise spikes at the same frequency for each square wave frequency. Therefore the MFC signals were filtered in the range of 10-170kHz. Figure 2-40 shows that the filtered MFC signals now attain a much higher level of repeatability (>0.999). Figure 2-44 shows the average cross correlation coefficients for signal compared with the baseline for each particular duration interval for each specific transducer for a 100khz square wave at -65°C. The figure shows that a reduction in similarity of the signals at sub zero temperatures, however a return to a similar level of correlation at the end of the test at 35°C. At the negative temperatures there is a far greater drop in correlation when compared with the ground survival high temperature tests. It should noted that for all the low temperature tests a higher level of sensitivity is observed at the specified

negative temperature which is most likely due to ice formation between transducer faces acting as a couplant.

Figure 2-45 shows the average cross correlation coefficients for the signals compared within each data set for a 300kHz square wave at -65°C, the figure shows a high level of correlation for the all the transducers (>0.99), again showing high repeatability for the transmit receive configuration. Figure 2-46 shows the average cross correlation coefficients for the signals when compared with baseline for all transducers for a 300kHz square wave at -65°C. The figure shows a reduction in correlation at -65°C to that of 35°C. Importantly all transducers returned to similar levels of correlation at the end of the test, however this is now centred around a correlation of 0.95 suggesting damaging effects.

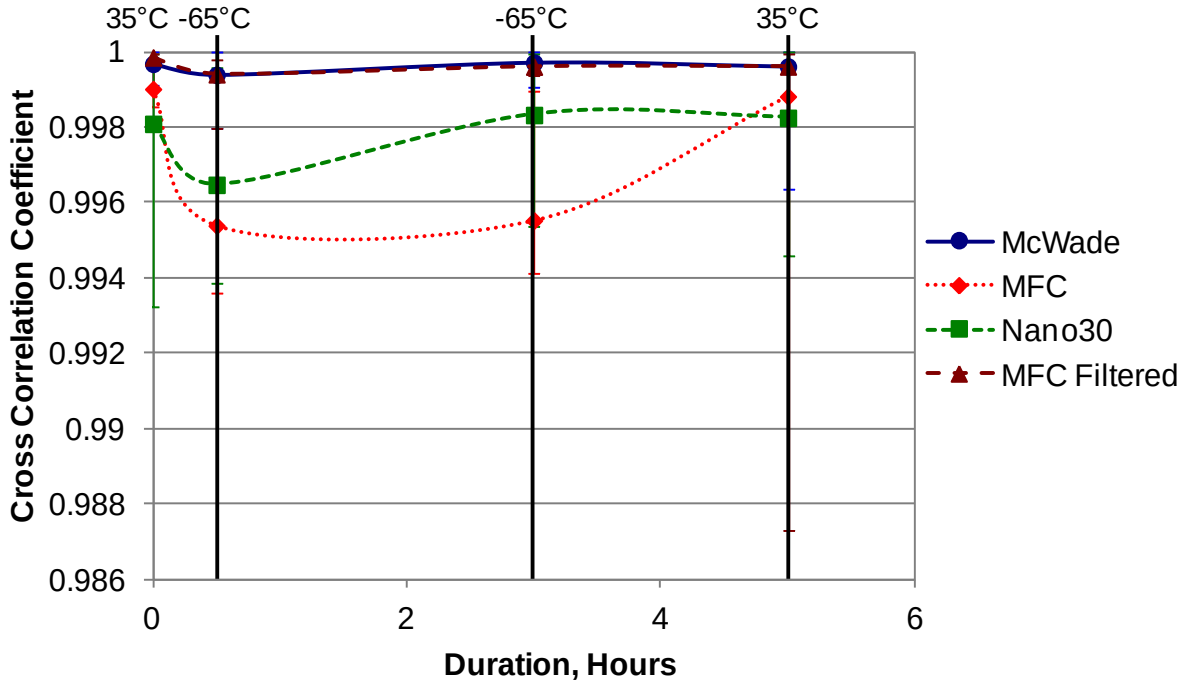

Figure 2-40 Repeatability of the signals from the ground survival -65°C test at 100 kHz

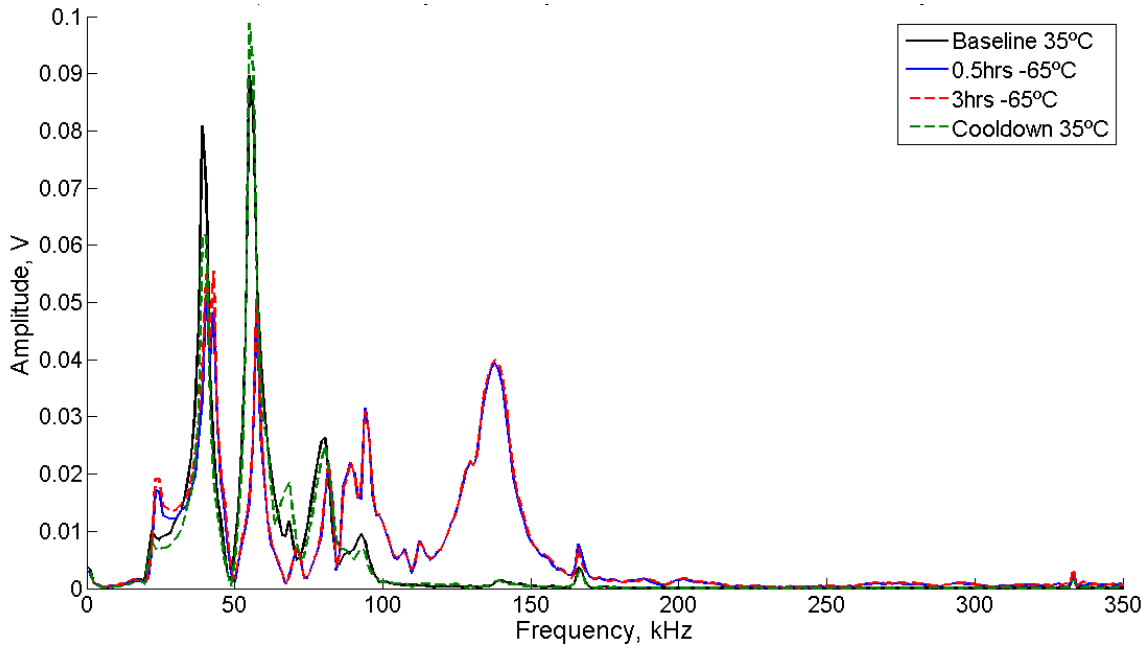

Figure 2-41. Frequency Spectrum for MFC -65°C example signals recorded at each specified time for a 100khz square wave

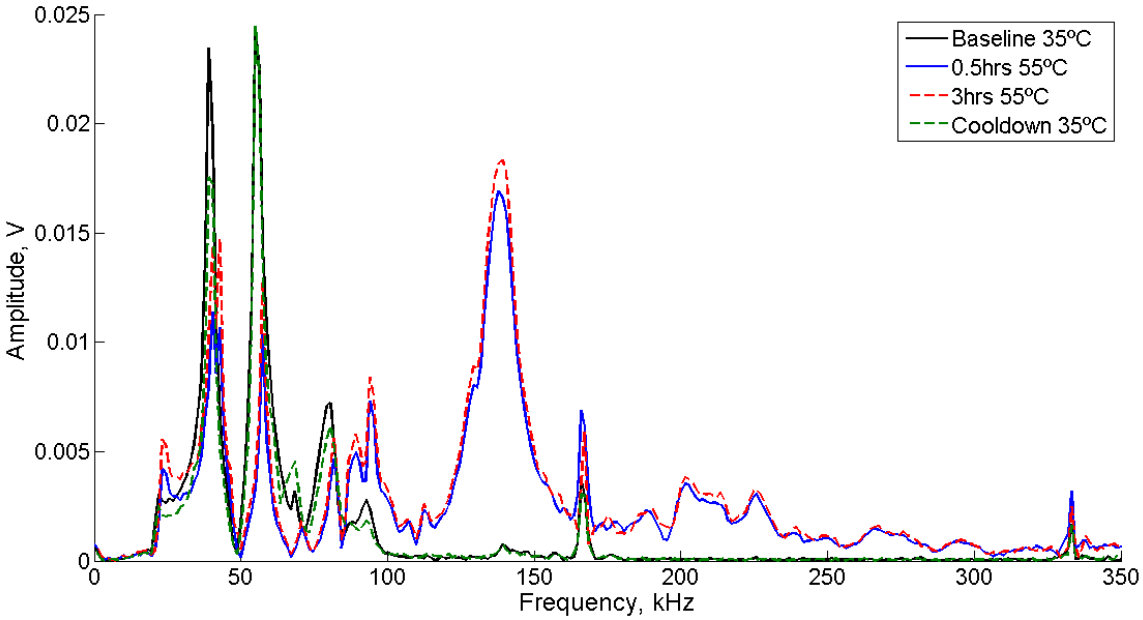

Figure 2-42. Frequency Spectrum for MFC -65°C example signals recorded at each specified time for a 300kHz square wave

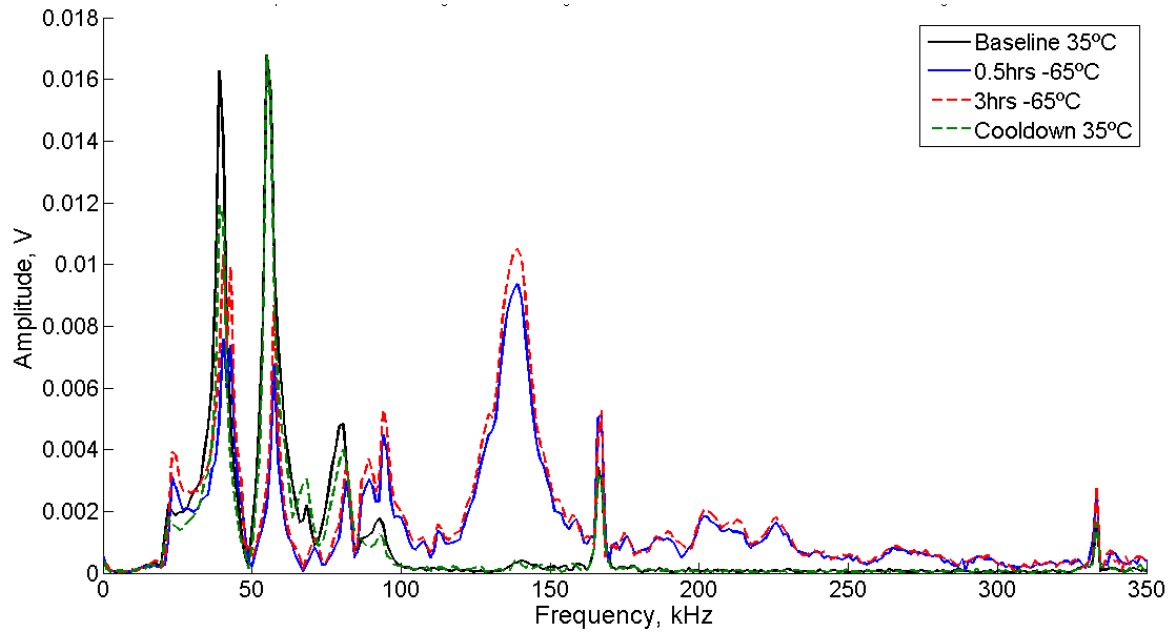

Figure 2-43. Frequency Spectrum for MFC -65°C example signals recorded at each specified time for a 500kHz square wave

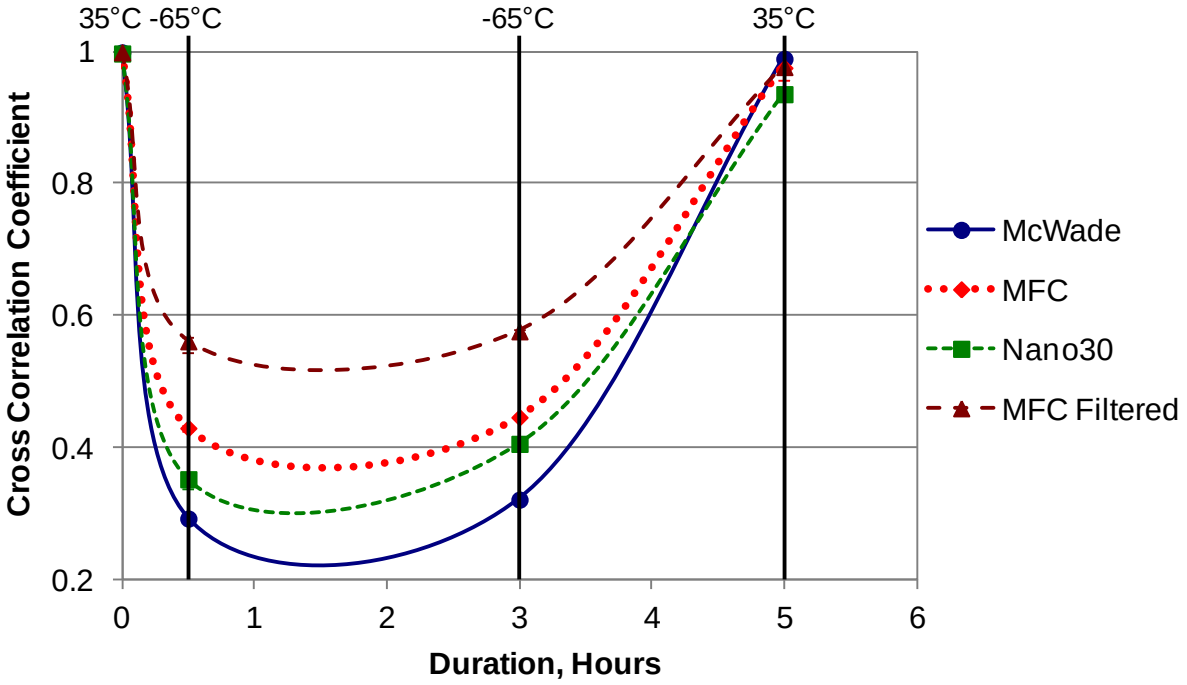

Figure 2-44. Baseline comparison of signals from the ground survival -65°C test at 100 kHz

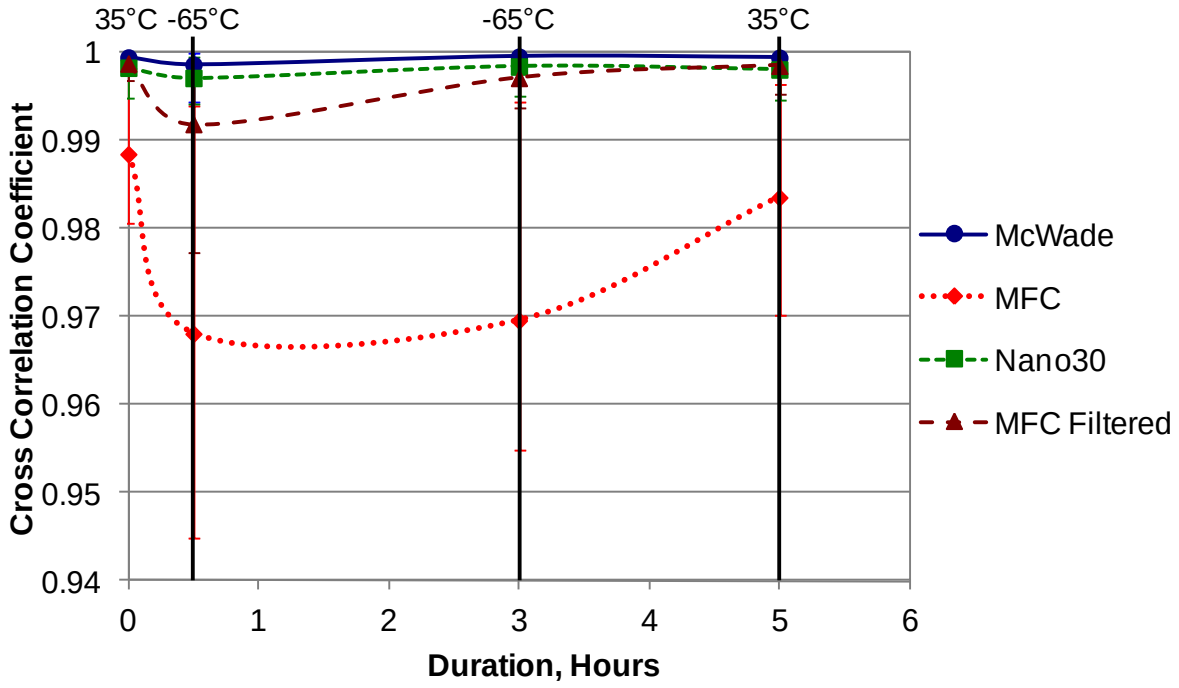

Figure 2-45. Repeatability of the signals from the ground survival -65°C test at 300 kHz

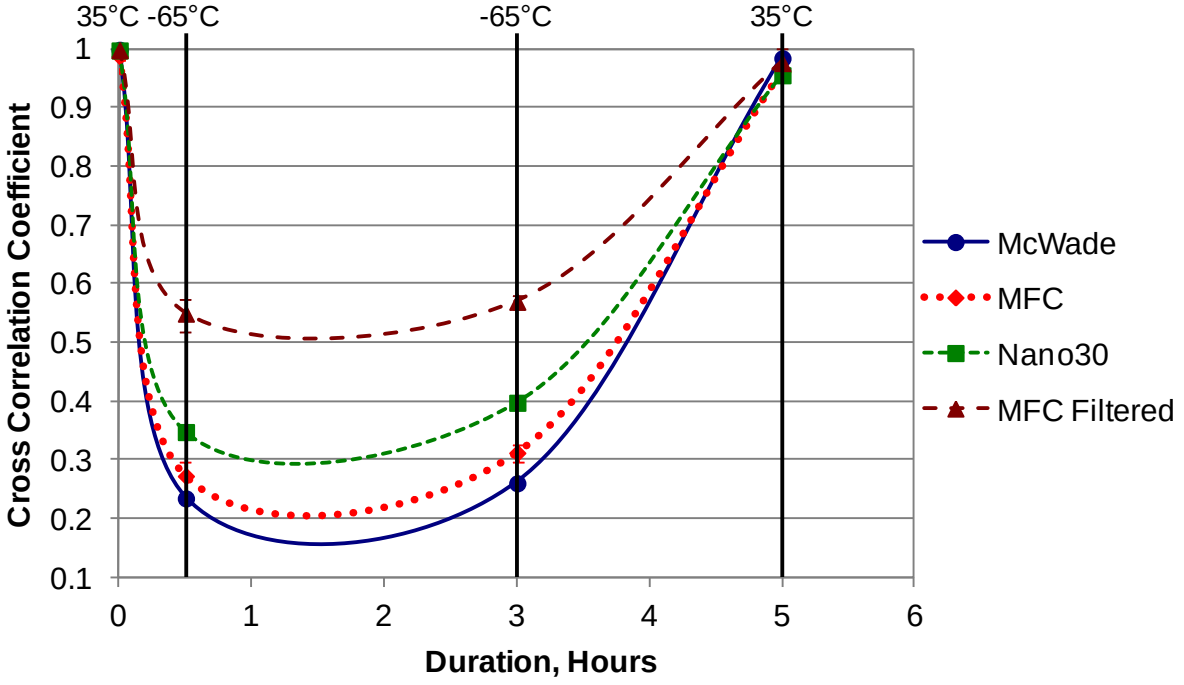

Figure 2-46. Baseline comparison of signals from the ground survival -65°C test at 300 kHz

Figure 2-47 shows the average cross correlation coefficients for signals for all transducer types correlated within a particular data set. A similar trend is seen for the Nano30 and McWade transducers where a high level of correlation is observed (>0.99). However the filtered MFC results shows a significant drop in repeatability within each data

set for all 300 kHz and 500 kHz signals this is due to relatively low amplitude of these signals when actuated with a frequency outside the predominant frequency range of the transducers and it most likely due to damage sustained to the MFC transducer when subjected to a 85°C. Figure 2-48 shows the average cross correlation coefficients for the transducers when the signals are correlated to the baseline at a temperature of -65°C at a frequency of 500kHz. The figure shows a significant reduction in cross correlation drop in correlation for all transducers. For all transducers there is a return to a similar level of correlation suggesting no further damage has occurred.

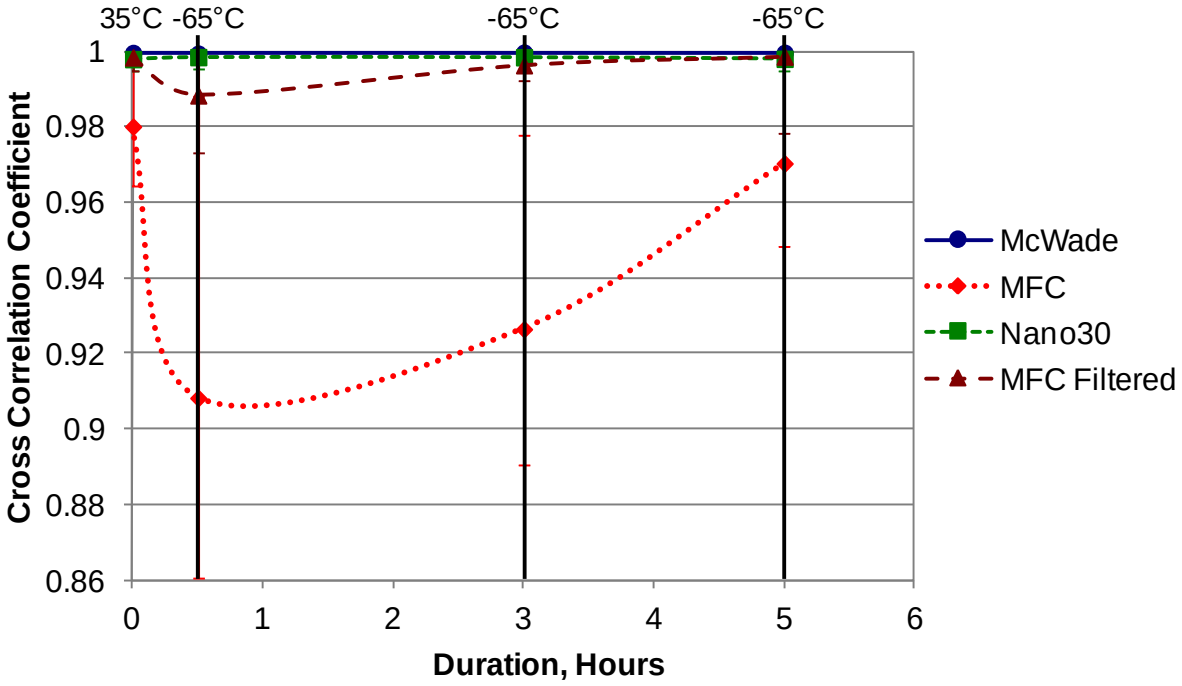

Figure 2-47. Repeatability of the signals from the ground survival -65°C test at 500 kHz

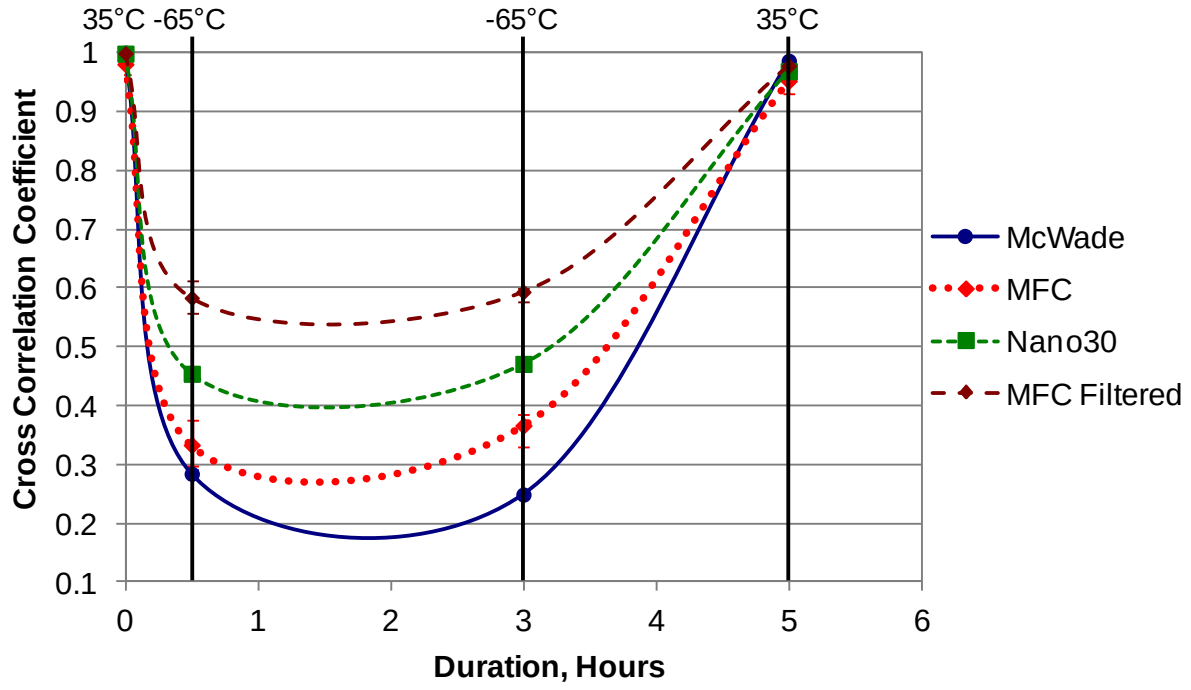

Figure 2-48. Baseline comparison of signals from the ground survival -65°C test at 500 kHz

2.2.2.4 Conclusions

In conclusion, when AE transducers are subjected to temperature changes there is a subtle difference in frequency response of the transducers as the cross correlation technique detects changes in the shape of the waveforms rather than amplitude changes. The most substantial changes in signals are observed at negative temperatures. The Nano30 and McWade transducers seem more sensitive to temperature however this maybe due to these transducer being overall more sensitive than the MFC transducers. The novelty of using MFC transducers as AE transducers at different environmental condition is feasible within the operating limits of this particular transducer. This investigation is important in the context of SHM when considering baseline techniques because subtle changes in the response of a signal due to unknown environmental variations maybe falsely interpreted as damage.

2.2.3 Embedded MFC Transducers in Glass Fibre Panel

2.2.3.1 Introduction

The next generation of all-composite aircraft will require very time consuming and costly inspection and maintenance to ensure their continued safe operation; however, such costs can be reduced through the effective use of a structural health monitoring (SHM) system. This would ideally be done using an autonomous system embedded within a structure that is capable of detecting, locating and characterising damage in complex

structures and often in the presence of high noise levels. This section of the chapter presents the results of a series of experiments in which Macro-Fibre Composite (MFC) transducers were embedded within a glass fibre epoxy composite panel to create a self monitoring “smart structure”. The transducers were used to detect and locate acoustic emission signals within the panel from both artificial sources and real impact events. They were also used to investigate Acousto-Ultrasonic (AU) cross correlation technique for monitoring the impact damage from a baseline state. Therefore this chapter further explores the use of the MFC transducers for dual monitoring in an embedded structure.

2.2.3.2 Experimental Methodology

To investigate the use of MFC transducer for embedded transducers a 550 x 550mm composite panel was manufactured from Amber Composites TES 300 GSM Glass 8-H Satin E644-00 43%Rm satin weave material with a (0,90) layup. The panel consisted of 6 plies of GFRP with four M2814-P2 type MFCs embedded between the third and fourth ply, i.e., at the centre of the thickness of the panel. The MFC piezoelectric fibres of the device were orientated with the 90° fibre direction. The panel was cured at 80°C for a period of 75 minutes, these particular MFC transducers have a maximum working temperature of 130°C which is defined by the epoxy used to bond the piezoelectric fibres rather than the piezoelectric material Curie temperature. Therefore the MFC would not suffer any degradation due to the thermal cycle. The embedded MFC transducers formed a sensing array measuring a 300 x 300mm square around the mid-point of the panel. The experimental set-up for the investigation can be seen in Figure 2-49, the dashed rectangles represent the location of the embedded MFC transducers. The area of interest was determined as this 300x300mm square with a grid spacing of 50mm, this was utilised as the training grid for the AIC delta T mapping technique. The AIC delta T mapping technique is a mapping technique to locate AE events. A brief explanation of the technique is given here but a more detailed explanation can be found in chapter 3. The technique uses an artificial AE source to generate differences in arrival times between transducer pairs and generate contour maps of the difference in arrival time for a particular specimen. These maps are then used to locate actual AE events by identifying the crossing of the contours on the maps. This technique has been implemented with the Akaike information criteria which estimate the arrival time of the signal using a statistical approach. This technique was compared with the conventional time of arrival (TOA) technique which is used in most commercial AE software. The TOA technique again uses the difference in arrival time between transducer pairs, however uses a known wave velocity in the specimen to locate AE events.

Five H-N sources were used at each node position to generate artificial AE and to record the arrival times at the transducers in order to generate the delta T maps used in the technique. Subsequent to the generation of the delta T contour maps, five arbitrary locations were selected and are marked by the crosses and numbers in Figure 2-49, the positions of these points were calculated using the TOA and delta T mapping techniques. 15 impacts were conducted at a single location upon the panel, indicated by the circle in Figure 2-49. During the impact investigations the panel was clamped between two square supporting frames as seen in Figure 2-49, leaving a 400 x 400mm unsupported area indicative of an realistic composite structure. The panel was impacted using a fully instrumented Instron Dynatup 9250HV impact machine. The impactor mass was 5.91kg with a 16mm diameter hemispherical impact tup. The impact energies used and the corresponding drop heights are detailed in Table 2-2. AE monitoring was conducted during each impact event using a Mistras PCI2 system to try and locate the significant amplitude impact events itself. AU monitoring was conducted throughout the investigation, a series of baseline waveforms were recorded when there was no visible damage in the plate and these formed the baseline waveforms. The actuation signal was a 20V peak to peak square wave at a frequency of 300kHz provided by a Agilent 33210A wave generator. A round robin configuration of transmitter and receivers was employed by pulsing a particular transducer and recording on all other transducers then switching transmitter transducer until all transducer had acted as transmitters and receivers. A cross correlation technique was employed measure the similarity of waveforms collected within each data set and then to compare waveform similarity to the of the baseline condition. Wave streaming data was recorded on channel 1 at a sample rate of 5MHz for a period of 5 seconds for the impact events itself.

The MFC transducers were connected to Mistras 0/2/4 pre-amps with a gain setting of 40dB and a bandwidth of 20-1200 kHz. The acquisitions settings for the AE and AU monitoring are detailed in Table 2-3.

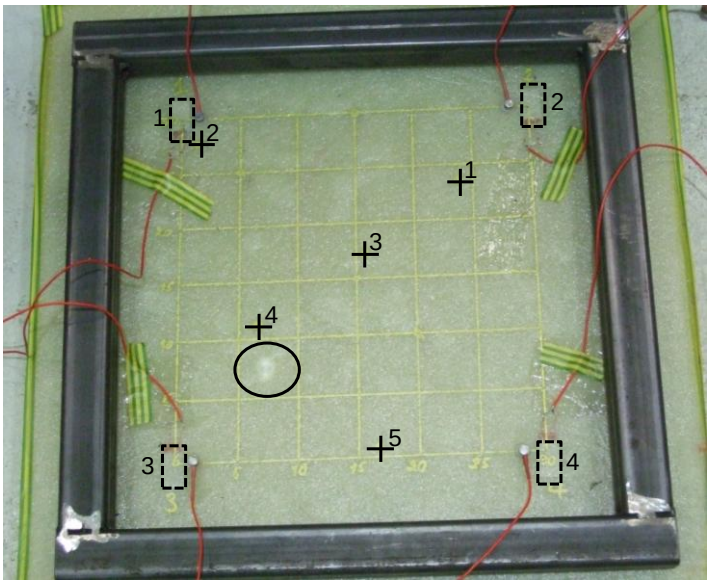

Figure 2-49. Glass fibre panel with embedded MFC transducers

Table 2-2. Details of Impact Events

Impact Number	Impact Energy, J	Drop Height, m	Impact Number	Impact Energy, J	Drop Height, m
1	4	0.069	9	12	0.207
2	4	0.069	10	14	0.241
3	4	0.069	11	18	0.31
4	5	0.086	12	22	0.379
5	6	0.103	13	26	0.448
6	8	0.138	14	30	0.517
7	10	0.172	15	34	0.586
8	10	0.172			

Table 2-3. Acquisition settings for the embedded panel investigation

Threshold	40dB
Pre-amp Gain	40dB
Analogue Filter	20kHz - 2MHz
Sample Rate	5MSPS
Pre-trigger length	400µs
Waveform length	6k

2.2.3.3 Experimental Results and Discussion

Figure 2-50 shows images of the impact location taken after each subsequent impact event. The grids lines represent a square area of 50 x 50mm and give an idea of the scale of the

impact damage in the panel. The images after impact with energies of 4, 4 and 5J respectively show that there is barely any visible damage in the panel after the first three impacts apart from marking of the surface of the specimen. The images taken of the impact site after impacts with energies of 5, 6 and 8J respectively, show for impact 4 that there is a small amount of damage in the panel which subsequently grows slightly for impact 5 and impact 6. It is clear after impact 6 that there is damage present in the panel after six impacts with varying energies at the same location. After impacts 7, 8 and 9 with energies of 10, 10 and 12J the damage area continues to grow slightly. After impacts 10, 11 and 12 with energies of 14, 18 and 22J respectively, there is a clear indication of surface indentation due to the impact tup. The main damage site does not grow significantly, however there is an indication of damage spreading from the impact location which it not clear in any of the previous images. Finally the last three impacts 13, 14 and 15 with energies of 26, 30 and 34J, the figures show there is significant growth in the damage in the final three impacts which corresponds to the large impact energy steps between impacts for any other set of impacts. It can be clearly seen that the damage starts to grow and spread from the impact location. The image for impact 14 and 15 shows cracking of the surface plies as well as growth in the delamination area. Table 2-4 details the approximate damage area for each impact events. This was calculated by importing each individual image into Autodesk AutoCAD, calculating the area of the 50x50mm square and area of the damage from the image, knowing the actual area of the grid square it was possible to estimate the approximate damage area. This was possible because the images were taken perpendicular to the panel. The first confident damage area approximation could be calculated from impact 5 with energy of 6J corresponding to an approximate damage area of 33mm^2, this grew to an area of 50mm^2 for impact 6 and did not propagate for impact 7. For impact 8 through to 10 the damage area grew steadily between approximately 10-20mm^2 after each impact resulting in a delamination area of 104mm^2. For impact 11 the damage area grew to 111mm^2 for impact energy of 11J. For impacts 12 to 13 the delamination grew approximately 20mm^2 for increase in impact energy of 4J. For the final two impacts the damage grew by approximately 30 and 50mm^2 respectively for increases in impact energy of 4J resulting in a final approximate damage area of 223mm^2. The damage area is mainly thought to be made up of a delamination area to begin with, then with an indent area and finally surface cracking of the surface of the specimen.

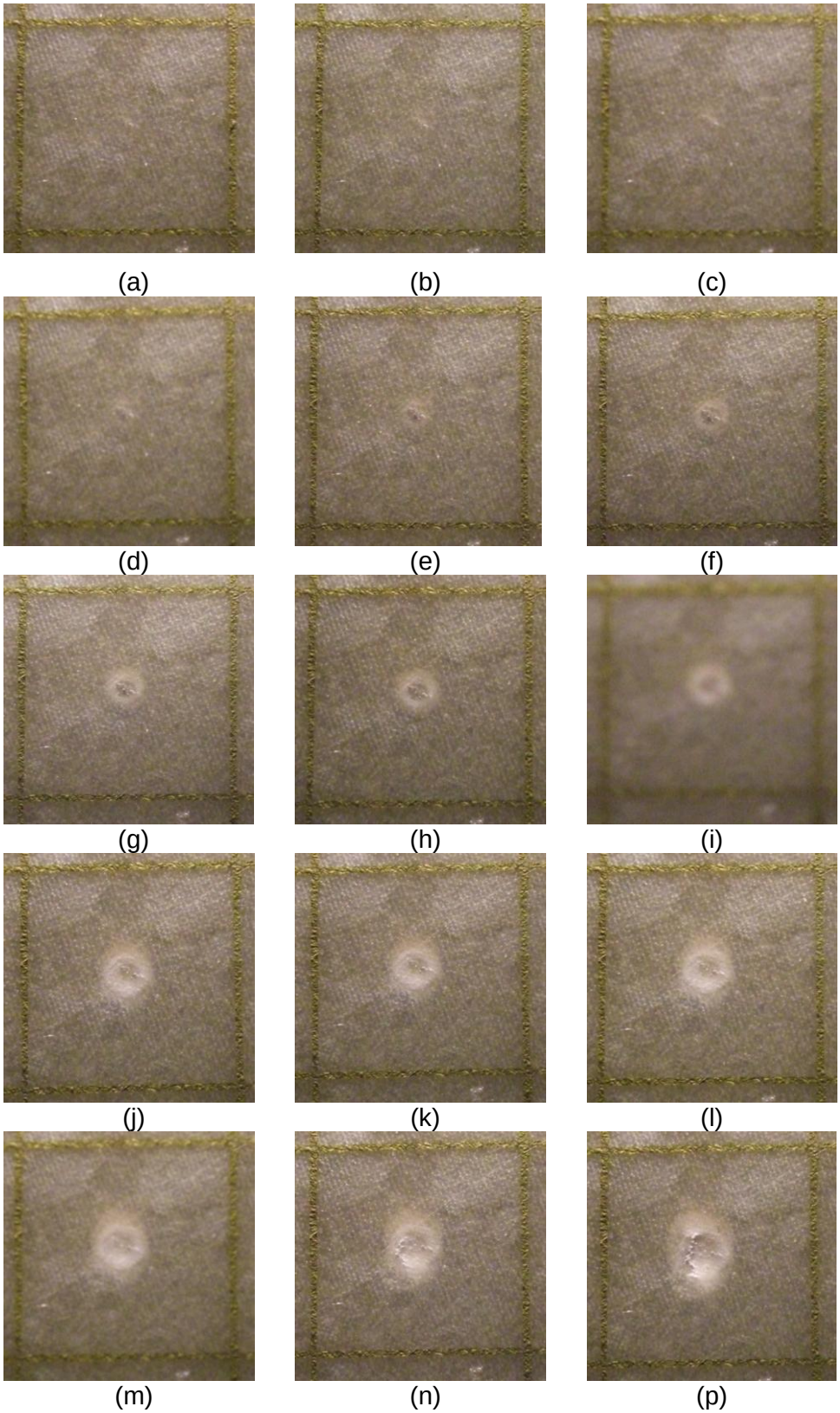

Figure 2-50. Impact Location images for impact energies of (a)-(c) 4J, (d) 5J (e) 6J, (g) 8J, (g)-(h) 10J, (i) 12J, (j) 14J, (k) 18J, (l) 22J, (m) 26J, (n) 30J and (p) 34J.

Table 2-4. Approximate damage area for each impact event

Impact Number	Impact Energy, J	Approximate Damage Area, mm^2
5	6	33
6	8	50
7	10	50
8	10	70
9	12	92
10	14	104
11	18	111
12	22	132
13	26	158
14	30	181
15	34	223

The results of the TOA and AIC delta T mapping techniques to locate each H-N source used at five arbitrary locations can be seen in Figure 2-51. For positions 1 and 3 there is excellent agreement between the actual location and the location calculated by the TOA and AIC delta T mapping techniques. The average Euclidean distance error for each location can be seen in Figure 2-52; the error bars represent the maximum and minimum location distance errors for each individual location. Even though there is close clustering of the locations for location numbers 1 and 3 overall the average error for the TOA for those two points is 4.43mm and 8.46mm respectively. For the same positions the average errors for the AIC delta T mapping are 2.97mm and 2.99mm showing an improvement over the TOA technique of 32% and 65% respectively. Larger deviations exist between the TOA method and AIC delta T mapping technique for locations 4 and 5 where, due to the homogeneous wave speed assumption and location of sources close to the boundary of the transducer array the TOA method starts to break down. For location 4 the average errors for the TOA and AIC delta T mapping technique are 15.70 and 6.65mm respectively, showing a 58% improvement in the AIC delta T location over the TOA method. For location 5 the average errors as shown in Figure 2-52 for the TOA and AIC delta T mapping technique are 15.7 and 6.65mm respectively, again the AIC delta T mapping technique shows an improvement of 87% when compared with the TOA method. The largest errors between the TOA and AIC delta T mapping technique can be seen in Figure 2-53 is for location 2, the TOA method is hindered in this particular position because the actual location is close to the boundary of the transducers array and in close proximity to the transducer and leads to

ambiguous location estimates as small changes in the location in these areas leads to larger errors due to the shape of the contours of constant difference in arrival time which is documented by Rindorf (1981). Although Figure 2-51 does not show the TOA locations on the scale of this particular figure, they were located at an average error of 451.41mm away from the actual position of location 2 as shown in Figure 2-53, comparing this with the average error for the AIC delta T mapping technique shown in Figure 2-52 of 10.84mm the percentage improvement of the AIC delta T mapping to that of the TOA is 98%. It is also important to note that for every single location the AIC delta T mapping technique shows an improvement over the conventional TOA method.

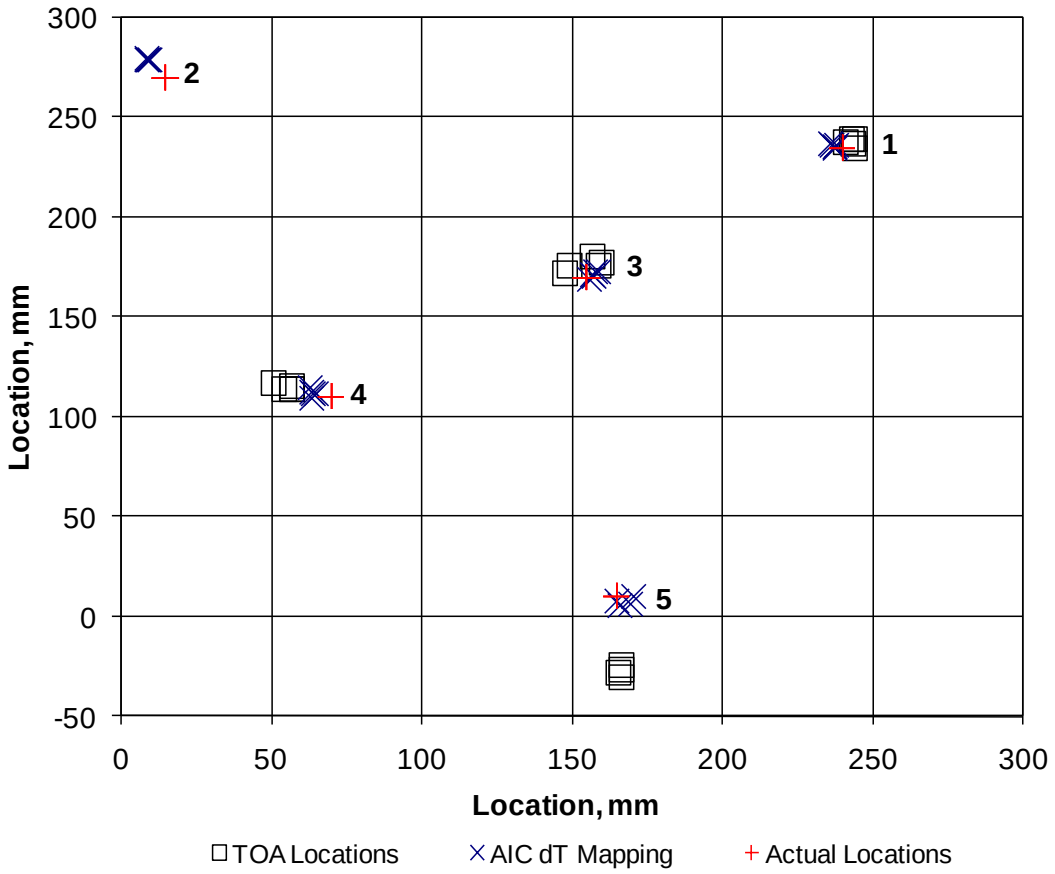

Figure 2-51. AE source locations for the five arbitrary positions

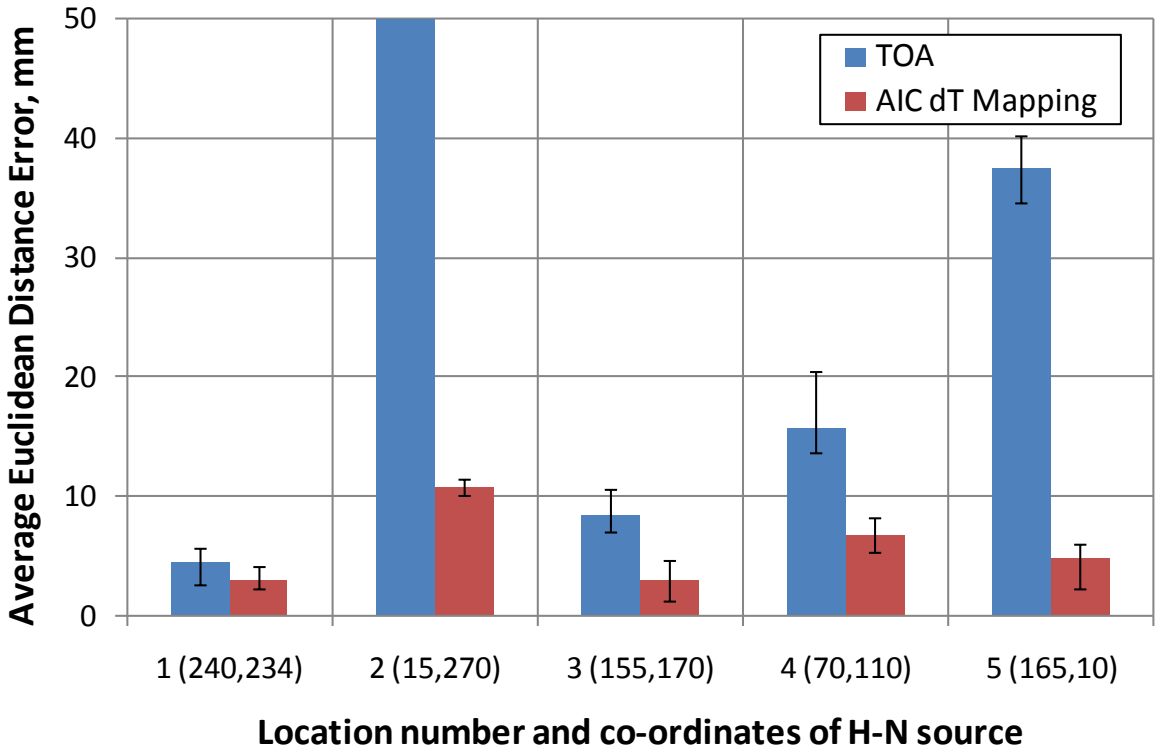

Figure 2-52.Detailed Average Euclidean distance error for each location

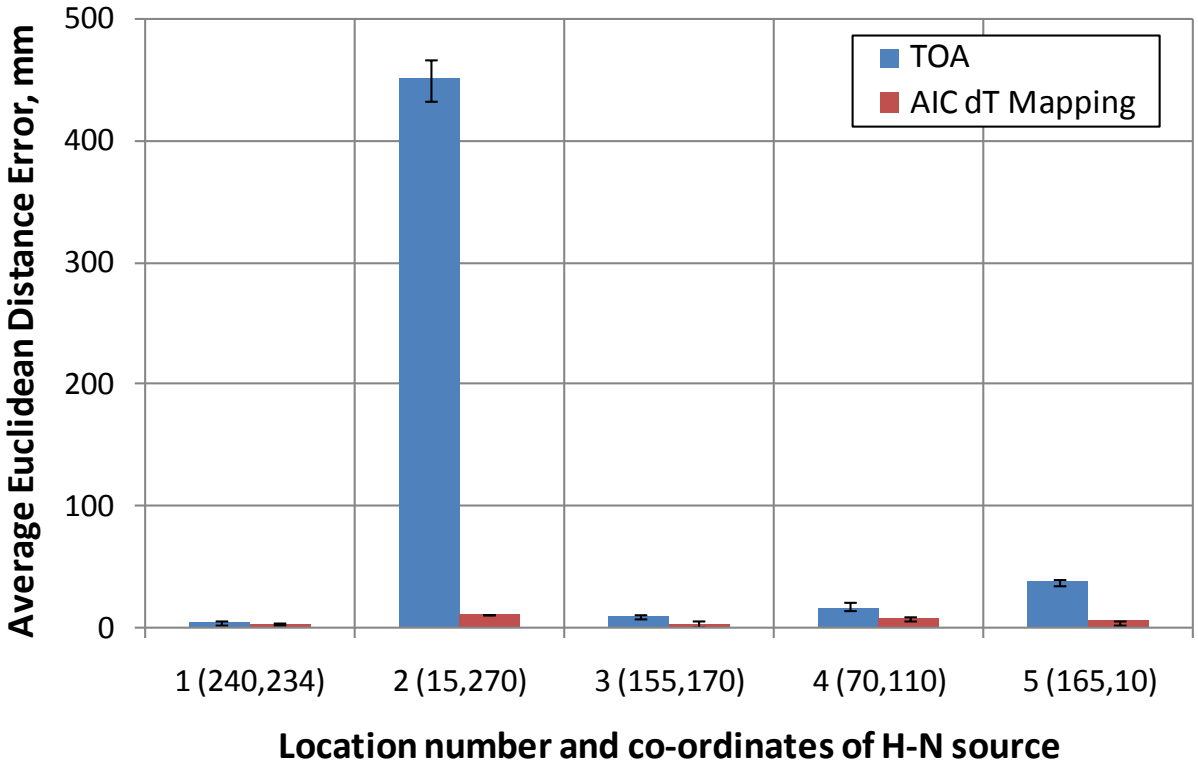

Figure 2-53. Overall average Euclidean distance error for each location

Figure 2-54 shows the locations of the each impact event calculated using the TOA and AIC delta T mapping technique, the figure shows that AIC delta T mapping technique locates the impact events in a closer cluster around the actual impact location when compared with the TOA technique. It should be noted that no significant locations were recorded for impact 1 and 2, however this should not be surprising as Figure 2-50 shows no visible damage. Locations are recorded for both techniques from impact 3 through to impact 15, it should also be noted that a confident approximation of the damage area cannot be drawn until impact 5 as seen in Figure 2-50. This also highlights the ability of AE to detect damage before it is visible. The average Euclidean distance for impacts three through to 15 are shown in Figure 2-55 for both the TOA and AIC delta T mapping technique. The dashed line represent the average distance error for the two techniques resulting in values 8.51mm and 3.46mm from the TOA and AIC delta T mapping respectively. This shows an improvement of around 60% of the AIC delta T mapping over the conventional method. The largest errors for both techniques occur for impact 5 which results in errors of approximately 30mm and 10mm respectively, for the majority of impact events the average error for the AIC delta T mapping technique is less than 5mm this is excellent when considering the active area of the MFC transducer is 28 x 14mm and therefore the location accuracy is noticeable less than the area of transducer. For the AIC technique the largest errors are seen in impact 5 and 15 which correspond to average errors of approximately 10 and 8mm respectively, this corresponds to an average error of 30 and 10mm for the TOA technique. Overall for this particular impact location the location impact events for both the TOA and AIC delta T mapping technique are excellent, however the AIC delta T mapping technique offers a consistent improvement over the TOA method.

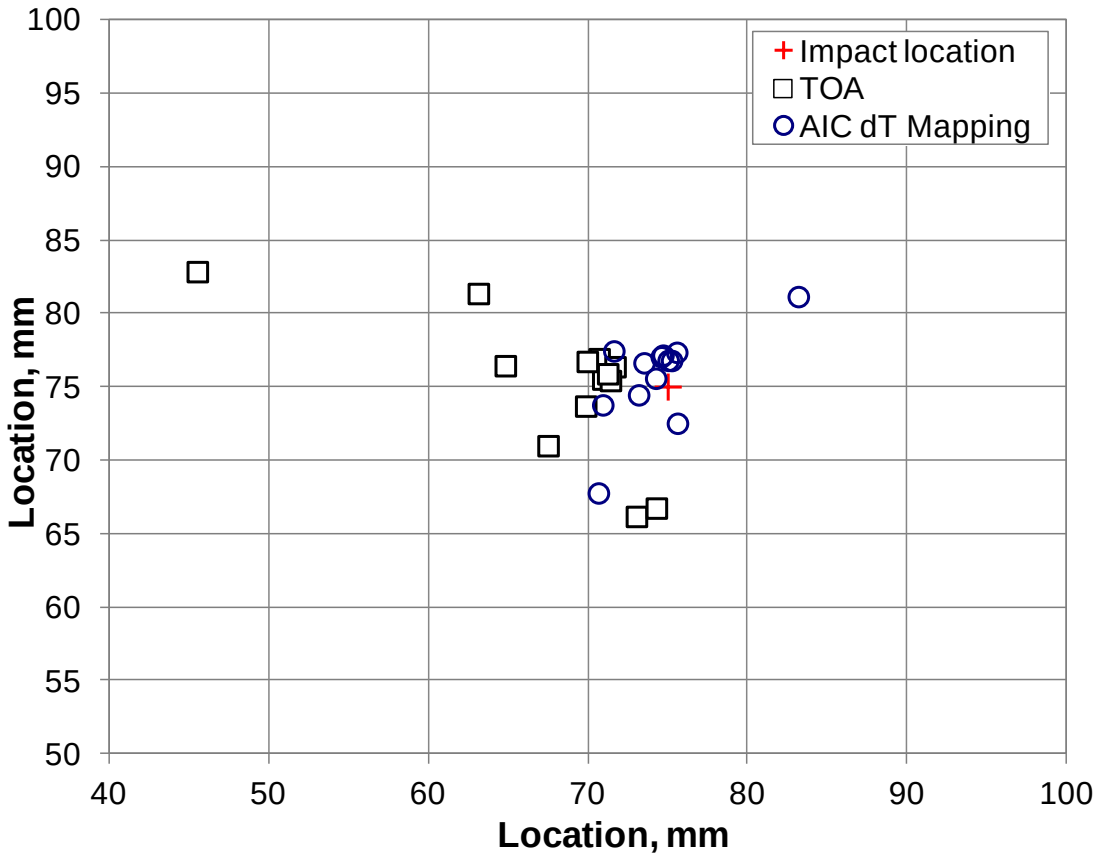

Figure 2-54. Impact locations using TOA and AIC delta T mapping

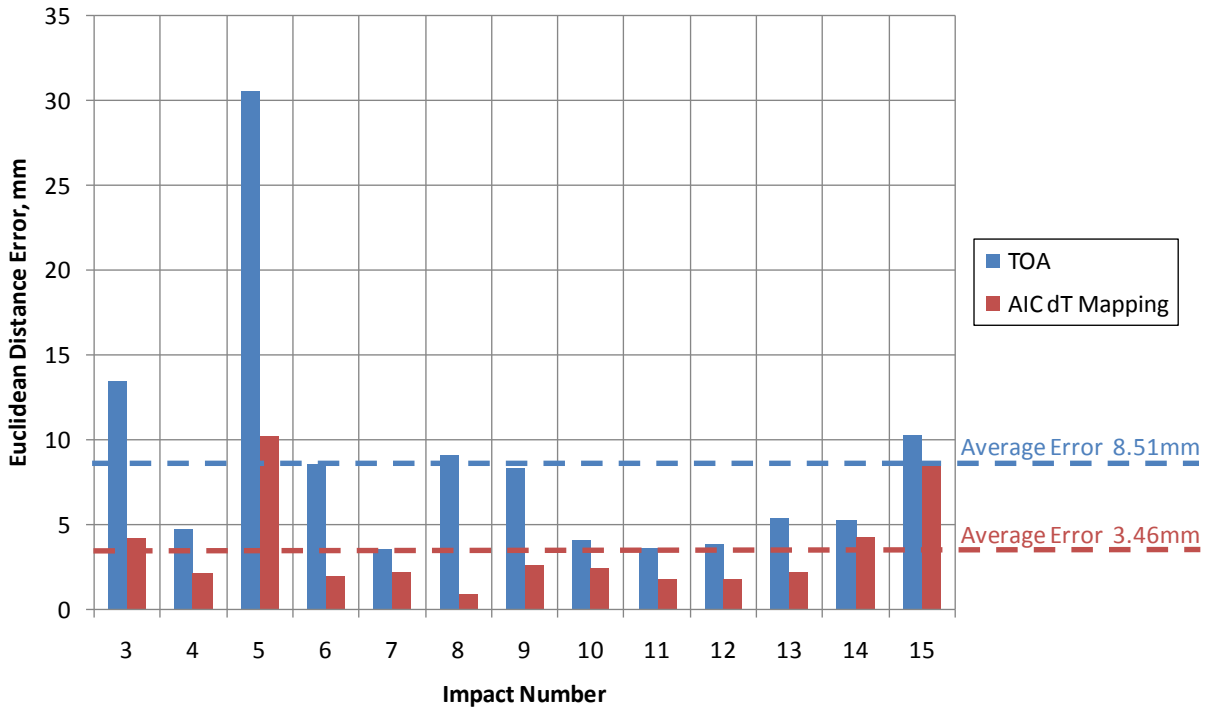

Figure 2-55. Average Euclidean distance error for each individual impact location

During each impact event, wave streaming data was recorded for 5 seconds on channel 1, this records the raw data for time period irrespective of threshold used. Figure 2-56 through Figure 2-59 detail the wave stream data for channel 1 alongside the load trace for the impact load cell for impact number 1, 5, 9 and 15 respectively these impact corresponded to impact energies of 4, 6, 12 and 34J with a corresponding damage area of 0, 33, 92 and 223J. Figure 2-56 shows the wave stream and load trace for impact 1, the figure shows no significant activity in terms of AE from the wave stream data, the corresponding load trace shows a peak load at approximately 800N and duration of around 27000µs. There is no AE activity due to no visible damage in the plate which is further backed by the impact images as seen in Figure 2-50 and no significant AE locations for both the TOA and AIC delta T mapping technique. Another indication of no damage present can be drawn from the load trace, which shows a symmetric smooth curve with no sudden drops in load. Further investigation of the wave stream for impact 5, shown in Figure 2-57, indicates the onset of damage. The approximate delamination area for impact 5 was 33mm^2 detailed in Table 2-4 and is visible in the impact image shown in Figure 2-50. Figure 2-57 shows significantly more AE activity to that of impact 1 and the impact strike itself can be seen at around 2000µs, reflections of the impact strike can be seen until approximately 10000µs, after this period there is a quiet period where no AE activity is observed above the background noise. It is not until approximately 13000µs that AE activity occurs and this corresponds to the discontinuity seen in the load trace which indicates this AE activity is from the damage within the structure. The load trace shows a peak load of 1200N and duration of 25000µs and it can be seen from the figure that the curve itself starts to lose it shape and form which also indicates the presence of damage. The wave stream and load trace for impact 9 give a clear indication of damage which is shown in Figure 2-58, from the figure there is a clear discontinuity in the shape of the load trace at the peak load of 1800N, there is excellent agreement between this discontinuity and an increase in AE activity at that particular time interval further suggesting the packets of AE activity corresponded to activation or growth of the damage area. Further evidence of the damage present can be seen in Figure 2-50 and Table 2-4. Figure 2-59 shows the load trace and wave stream on channel 1 for impact 15, it shows that around the peak load of 2600N there are several discontinuities which correspond to damage in the panel these drops in load are due to the panel giving way under load, there is less symmetry evident in the shape of the load trace further demonstrated damage in the panel. There is a significant amount of AE activity in this time region which corresponds to the observed discontinuity in the load trace, the amplitude is significantly larger than the initial impact strikes which is not the case for the rest of the wave

streaming data. The amplitude of the damage AE activity increases with the observed peak load which can be observed through impact 1 to 15. The duration of the final impact is also much shorter than previous impact events lasting approximately 17000µs. This wave streaming technique clearly shows the onset of damage in the structure.

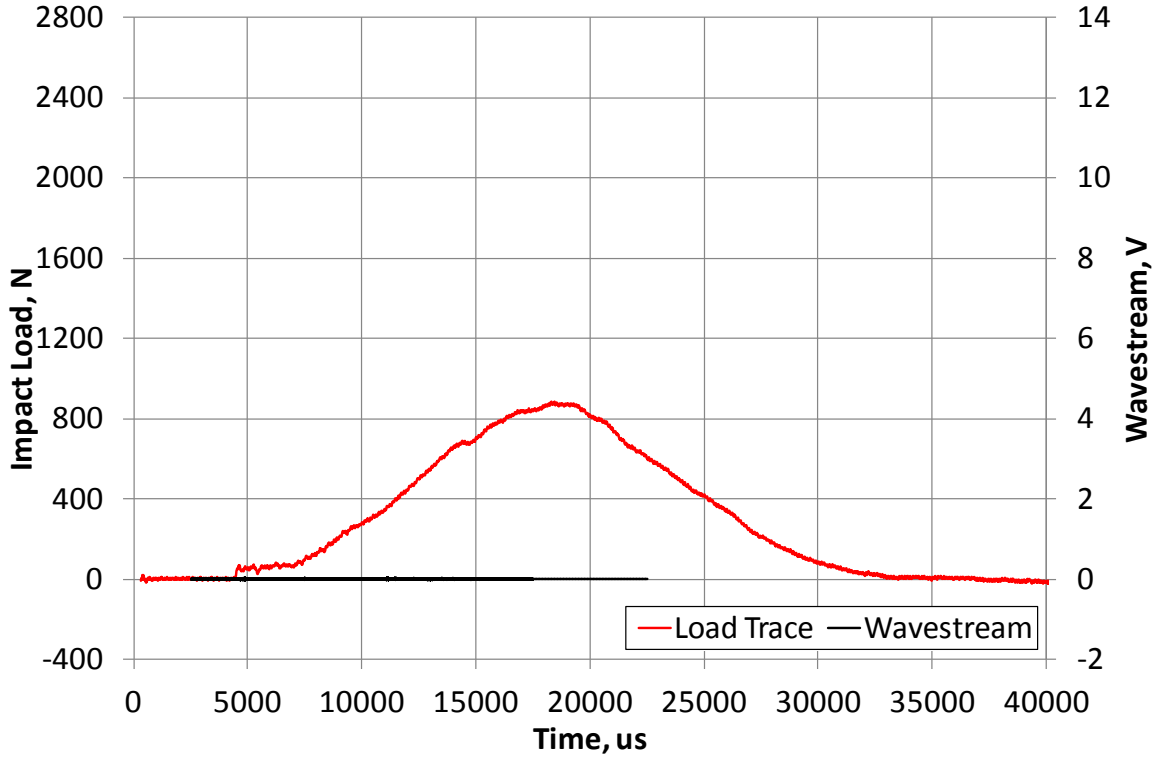

Figure 2-56. Wave stream and resulting impact load cell trace for impact 1

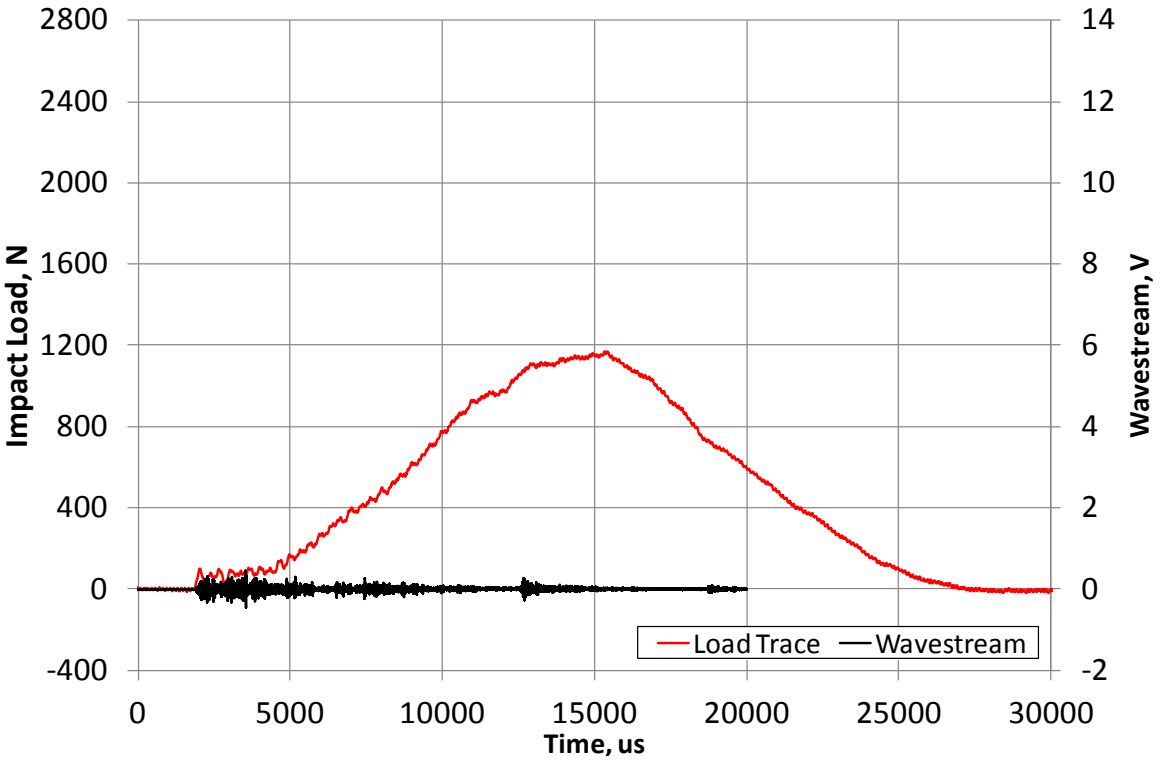

Figure 2-57. Wave stream and resulting impact load cell trace for impact 5

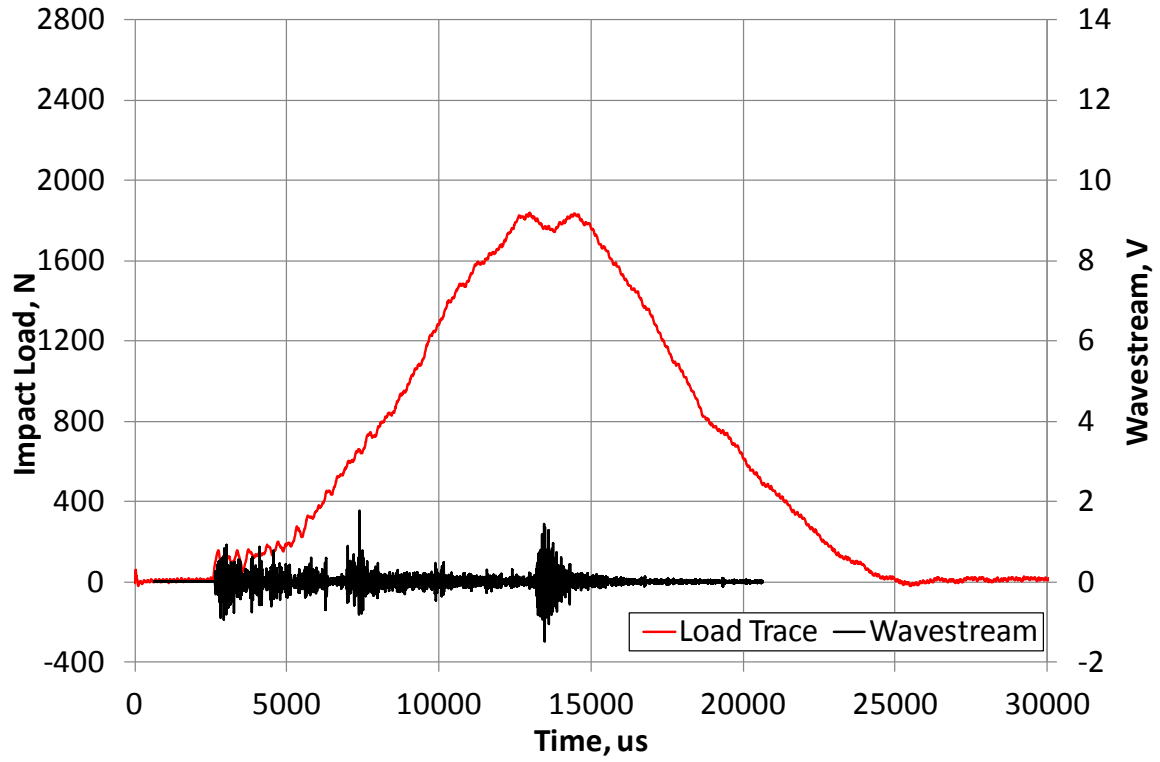

Figure 2-58. Wave stream and resulting impact load cell trace for impact 9

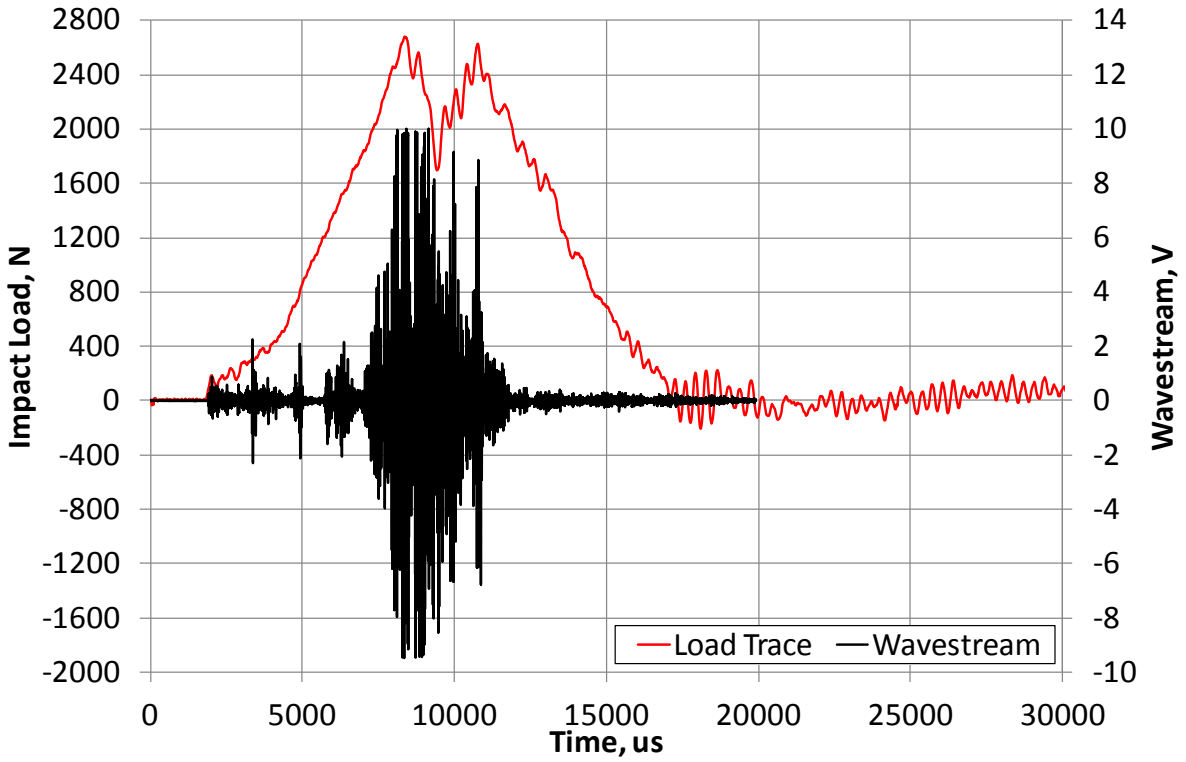

Figure 2-59. Wave stream and resulting impact load cell trace for impact 15

Figure 2-60 shows the propagation paths for each channel as a transmitter for the AU cross correlation analysis. The colour coded arrow corresponds to the individual channels used in the analysis. Figure 2-61 shows the average cross correlation coefficients for 20 waveforms recorded at channel 2, 3 and 4 from an actuation signal of 20Vpp 300kHz square wave at channel 1. Impact 0 refers to the baseline conditions when there was no visible damage in the panel. The coloured squares represent waveforms that were cross correlated in those particular data sets which are referred to as “ccset” and the coloured diamonds represent the waveforms cross correlated to the baseline and referred to as “ccbase”, this nomenclature is continued through the remaining AU analysis. Figure 2-61 shows for the waveform cross correlated within each particular data set a high level of repeatability across all channels, this therefore allows the conclusion that any reduction in correlation when the waveforms are correlated to the baseline waveforms is due to the presence of damage within the panel. The waveforms cross correlated to the baseline state for each individual channel overall show a maximum drop of correlation of 0.008 and although this is outside of the minimum error bars for the waveforms cross correlated within each data set, it is not a significant reduction in correlation and any changes in the environment in a real situation would give larger drops in correlation. The reasons for the small reduction in correlation will be explained later in this chapter. Channel 2 and 4 shows

the greatest sensitivity to the delamination area and confidence in the detection of the damage could be made after impact 7 which corresponds to a delamination area of 50mm^2. Channel 3 shows an overall smaller reduction in correlation even though the propagation path between channel 1 and channel 3 is in closest proximity to the damage which can be seen in Figure 2-60 (a) and this will be discussed shortly. For the waveforms correlated to the baseline state for channel 3 confidence in the separation of the error bars until impact 8 which corresponds to a delamination area of 70mm^2. Figure 2-62 shows a wavelet transform for an example waveform recorded at channel 2, transmitted from channel 1 in the baseline state. The wavelet transform was calculated using Vallen Wavelet, the figure shows that the signal arrives in a time window between 40-80µs, there is a clear reflection which then occurs between 100 to 150µs. These signals were recorded using a threshold triggering and these signals were offset by 50µs for ease of representation. This example wavelet was produced to determine which particular part of the waveform is altered due to the presence of the damage. A wavelet subtraction technique was used to assess which parts of the signal interact with the damage. In order to visualise these changes the cross correlation technique was used to assess the phase difference between the waveforms that give maximum correlation. Once the phase difference was quantified the signals were aligned. This allowed for the changes in the waveforms as part of the correlation process to be visualised. Figure 2-63, Figure 2-64 and Figure 2-65 show the wavelet subtraction of an example waveform after impact 15 from that of the baseline wavelet for signal transmitter on channel 1 and received on channel 2, channel 3 and channel 4 respectively. Figure 2-63 shows the wavelet subtraction of impact 15 from the baseline wavelet for a propagation path from channel 1 to channel 2 and shows the greatest changes of the wavelet in the reflected parts of the waveform around 150µs and 400µs, this suggests the received waveform was altered due to wave scattering and refraction from the damage area. The changes in the reflection are not from changes in the boundary conditions as the supporting frames were kept clamped to the plate throughout the duration of the testing. Since the MFC transducers are most sensitive parallel to the piezoceramic fibre direction coupled with less attenuation due to 0-90 fibre orientation of the composite specimen the greatest received signal amplitude will be observed along propagation path 1 to 3 followed by path 1 to 2 which is still on the glass fibre direction but at the least sensitive due to the propagation path being perpendicular to the piezoceramic fibres, finally path 1 to 4 is the least sensitive due to being less sensitive at 45° to the composite and piezoceramic fibre directions. Figure 2-64 shows the wavelet subtraction for the impact wavelet subtracted from the baseline wavelet for a propagation path from channel 1 to channel 3. Again the greatest changes in coefficient from

baseline to damage state are larger than the above range and show significant changes in the first arrival, first reflection and at reflections at around 480μs this suggests a direct lack of sensitivity to the damage area on a direct path due to the least drop in correlation from Figure 2-61. This is most probably due to the wavelength of the first arrival part of the signal in relation to the damage size. Figure 2-65 shows the wavelet subtraction of the impact 15 wavelet from the baseline wavelet for propagation path from channel 1 to channel 4, this time the greatest changes in the wavelet at around 200 and 550 μs respectively. For this particular propagation direction the alignment of signals in time maybe affecting the wavelet subtraction. Further comparison of the three wavelet subtractions show that there are slight time and frequency shifts for the parts of the wavelet that show the largest change in wavelet transform suggesting that depending on the part of the reflected waveform where these changes occurs different levels of sensitivity to the damage area can occur. This would explain why in Figure 2-61 channel 2 and 4 show the greatest reduction in cross correlation coefficient when compared with channel 3.

Figure 2-66 shows the average cross correlation coefficient for correlation in each data set and to the baseline state respectively for channel 2 as a transmitter and receiving on channel 1, 3 and 4 as can be seen in Figure 2-60 (b). The waveforms recorded and correlated within the data set show a high level of correlation and therefore a high repeatability and therefore any subsequent drop in correlation is due to the presence of damage. Again the greatest confidence of the detection of damage due to clear separation of the errors bars can be made after impact 7, corresponding to a damage area of 50mm^2. Propagation path 2 to 4 shows the least sensitivity to a change in correlation this is due to the damage area being furthest away from the propagation path. Propagation path from channel 2 to 3 is more sensitive to a reduction in correlation however not as great as propagation path from channel 2 to 1, suggesting the waveform is least sensitive to the damage on the direct path and that it is the resulting changes in the reflected parts of the signal which are causing a greater reduction in correlation. Propagation directions 2 to 1 and 2 to 4 are very similar in relation to the damage site, however propagation path 2 to 1 shows a greater reduction in correlation when compared with path 2 to 4. This difference most likely occurs due to the reflection propagation path and orientation to the piezoceramic fibre orientation.

Figure 2-67 shows the average cross correlation coefficients for 20 waveforms recorded and correlated within a particular data set and to the baseline state for transmitting on channel 3 and receiving on propagation paths to channel 1, 2 and 4 respectively as

shown in Figure 2-60 (c). A high level of correlation is observed for all receiver channels and therefore a high repeatability of the transmit and receive configuration is apparent. This allows the deduction that changes in correlation are due to the presence of damage. The waveforms recorded and correlated to the baseline state show an overall reduction in correlation of approximately 0.008. For channel 3 as a transmitter there is much closer agreement of receiving channels than any other propagation direction, this is most likely due to source being most closely situated to the damage. Overall channel 4 shows the greatest reduction in correlation due to the presence of damage followed by similar reduction in correlation coefficients for channel 1 and 2. Again a wavelet subtraction method was used to determine the difference of interaction of the waveforms due to damage as previously described but this time for the transmitter closest to the damage. Figure 2-68, Figure 2-69 and Figure 2-70 shows the wavelet subtraction of example wavelet transform of impact 15 from the baseline wavelet for channel 3 as a transmitter and receiving on channels 1, 2 and 4 respectively. The wavelet subtraction for propagation path from channel 3 to 1 is shown in Figure 2-68 and shows the greatest changes in wavelet for the first reflection and approximately 425µs. In the wavelet subtraction of propagation path from channel 3 to 2 which is shown in Figure 2-69, the greatest change in the signal is observed later in the signal at around 200µs, but even in this propagation path the damage is on the direct path between channel 3 and 2 which again suggests the first arrival of the wave is the least sensitive to the damaged area. Figure 2-70 shows the wavelet subtraction of impact 15 from the baseline wavelet for a propagation path from channel 3 to 4, this figure shows that a higher frequency component of the first arrival and reflection show a change in wavelet subtraction, again the greatest change in the wavelet is observed at 150, 200 and 400µs. This further suggests that specific parts of the reflected wave are more sensitive to damage than propagation paths which are in close proximity to the waveform. Due to the signal attenuation wavelet subtraction from un-damaged to damaged state are not as significant as seen in other propagation paths.

Figure 2-71 shows the average cross correlation coefficients for the 20 waveforms recorded and correlated within each data set and to the baseline state for each impact event for channel 4 as a transmitter. The waveforms correlated in each data set show a high level of correlation at an approximate level of 0.999, this shows high repeatability between the pulse and receive configuration. Reduction in correlation coefficients are observed when the waveforms are compared with the baseline state, overall channel 2 shows the least sensitivity in detecting the damage as it is furthest away from the damage location

confidence of detecting damage at channel 2 outside the error bars of the two methods of correlation cannot be made until impact 10 which corresponds to a delamination area of 104mm^2. Similar levels of reduction of correlation are observed for channel 3 and channel 1. The damage area is not on a direct path of these transducers and therefore further strengthens the argument that it is wave scattering and possible mode conversion which is causing the greatest change in the cross correlation coefficients.

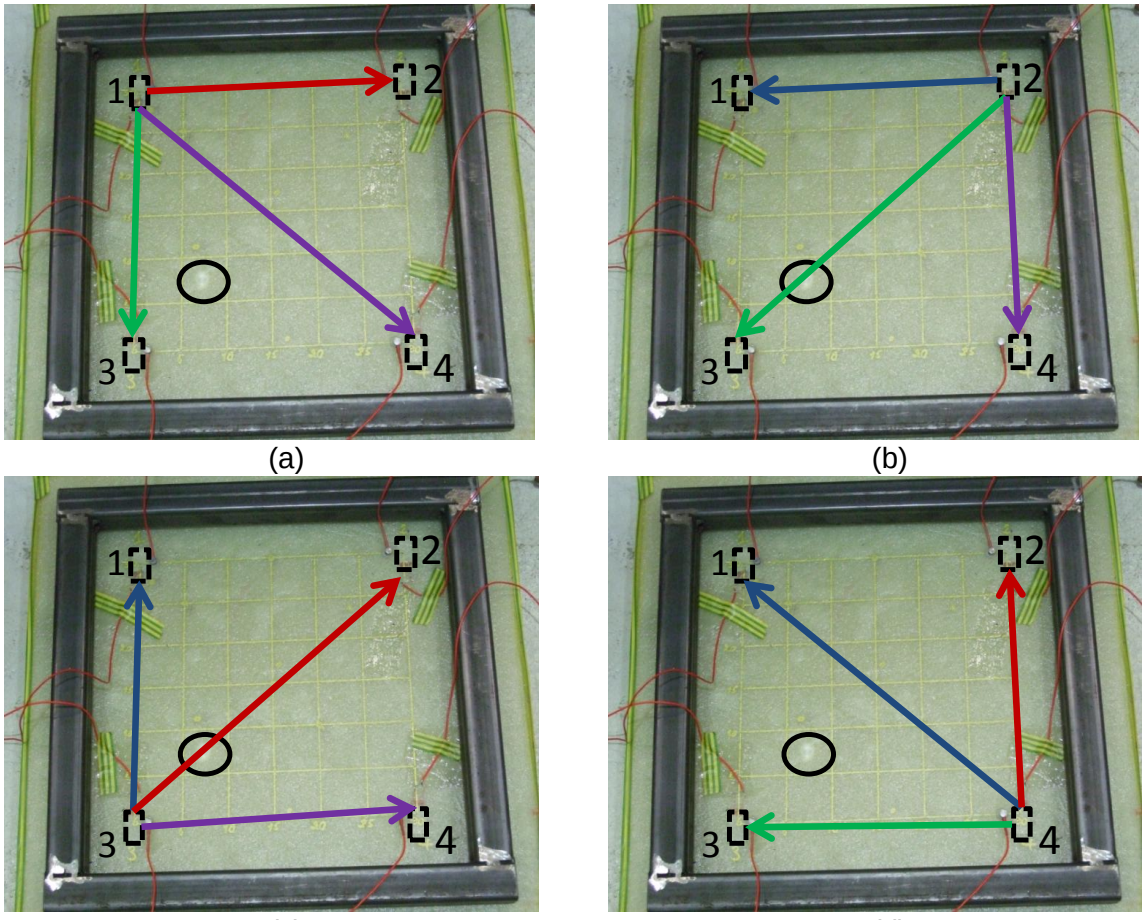

Figure 2-60. Propagation paths for (a) channel 1, (b) channel 2, (c) channel 3, (d) channel 4 as transmitters for the AU analysis

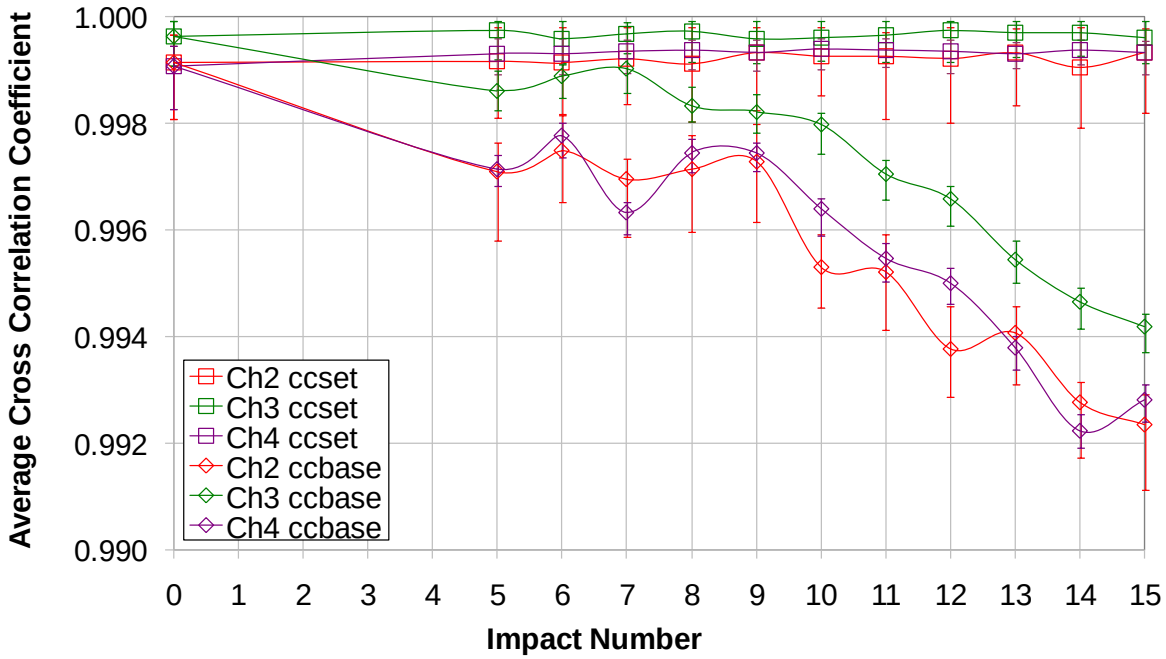

Figure 2-61. Average cross correlation coefficients for each impact for channel 1 as a transmitter

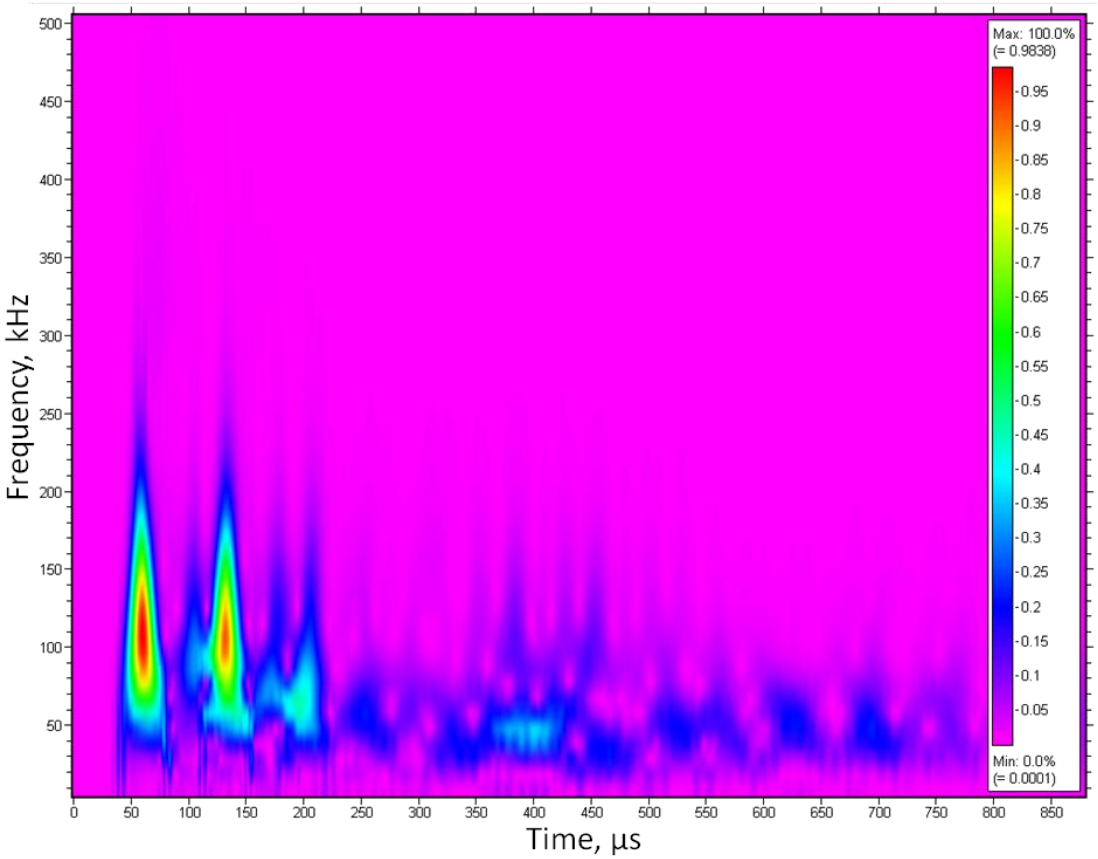

Figure 2-62. Wavelet transform for an example signal for a waveform recording at channel 2 when transmitted from channel 1

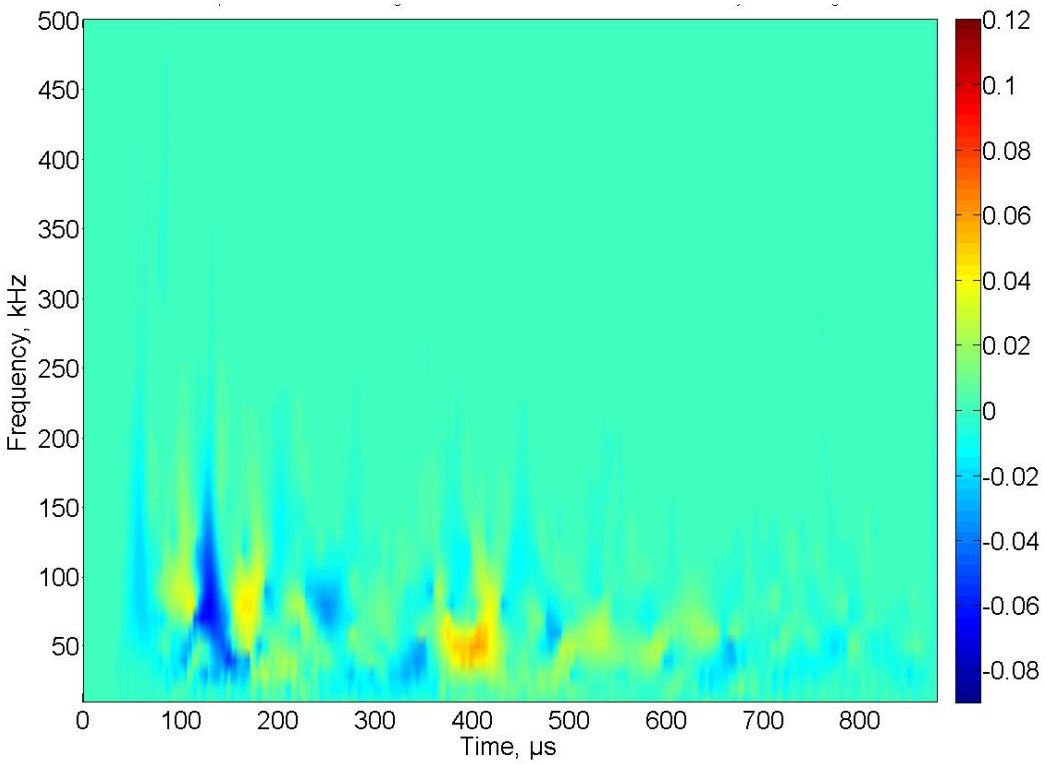

Figure 2-63. Wavelet subtraction of the impact 15 wavelet from the baseline wavelet for signal transmitted at channel 1 and received on channel 2

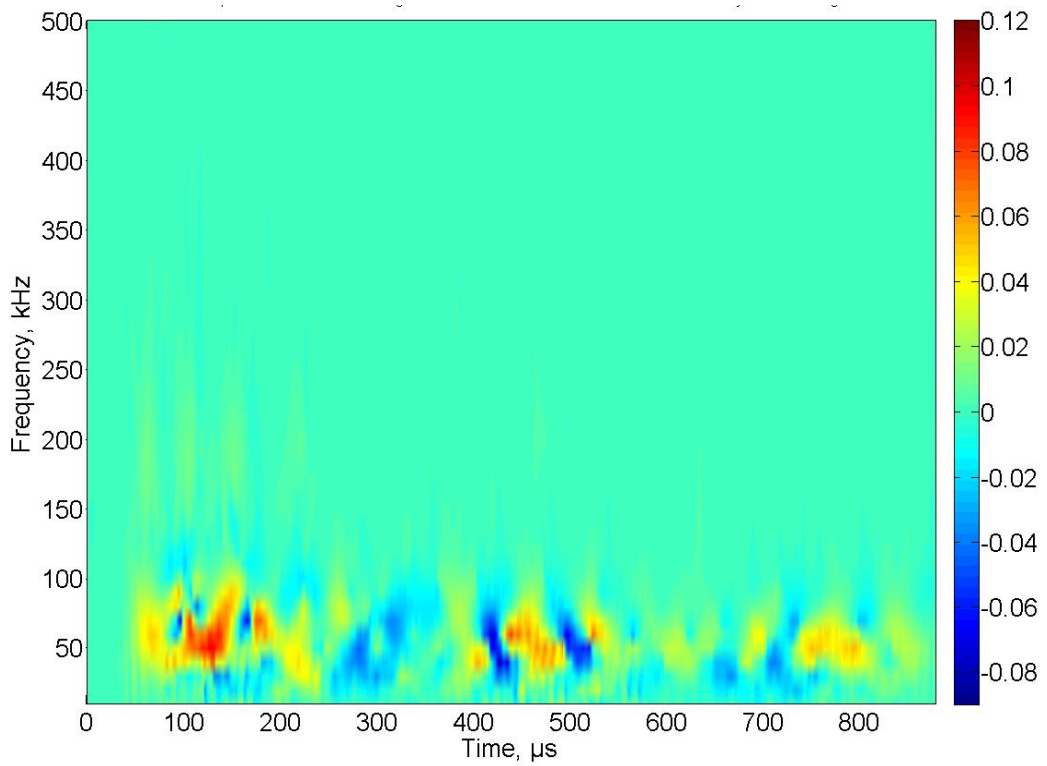

Figure 2-64. Wavelet subtraction of the impact 15 wavelet from the baseline wavelet for signal transmitted at channel 1 and received on channel 3

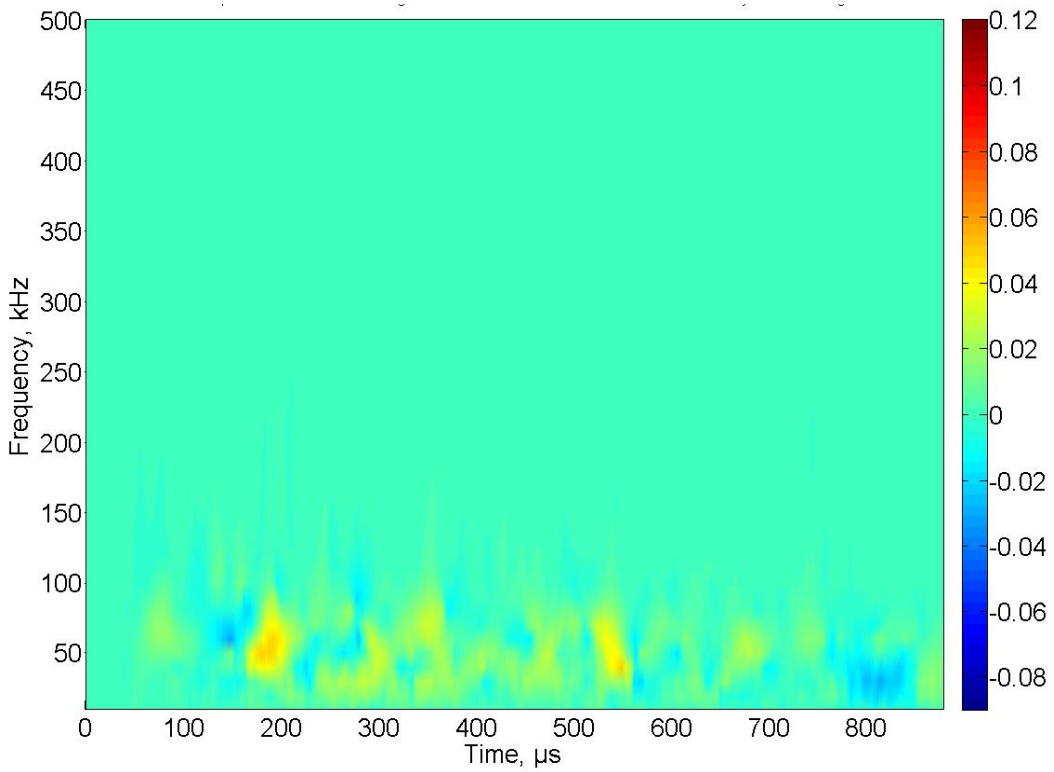

Figure 2-65. Wavelet subtraction of the impact 15 wavelet from the baseline wavelet for signal transmitted at channel 1 and received on channel 4

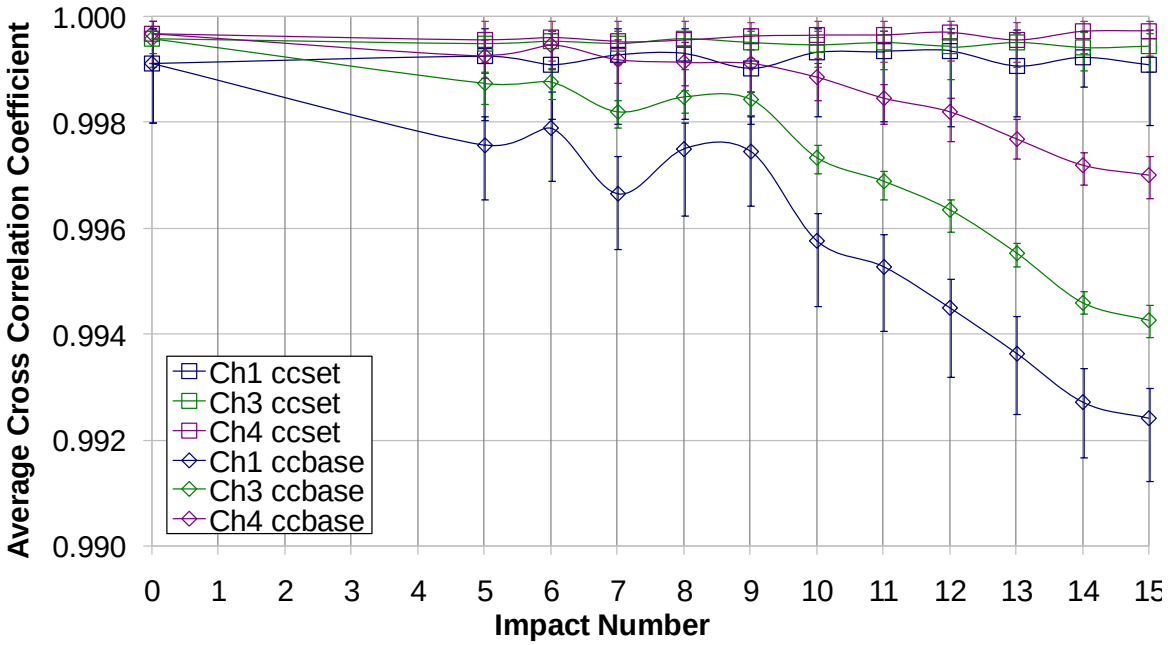

Figure 2-66. Average cross correlation coefficients for each impact for channel 2 as a transmitter

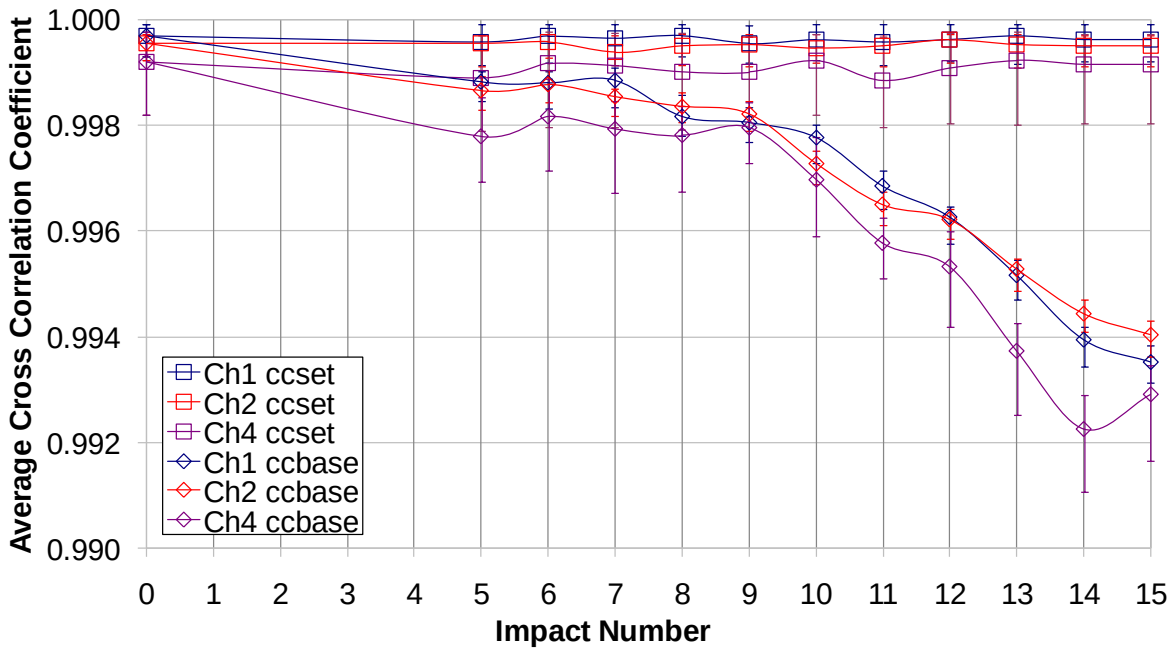

Figure 2-67. Average cross correlation coefficients for each impact for channel 3 as a transmitter

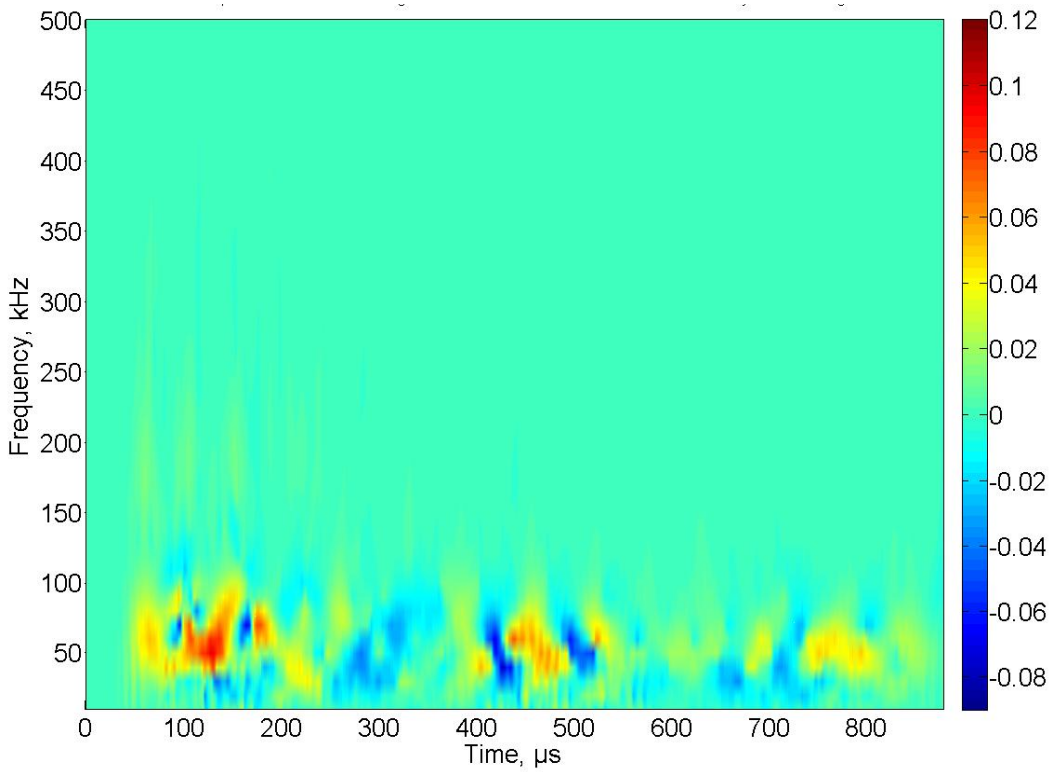

Figure 2-68.Wavelet subtraction of the impact 15 wavelet from the baseline wavelet for signal transmitted at channel 3 and received on channel 1

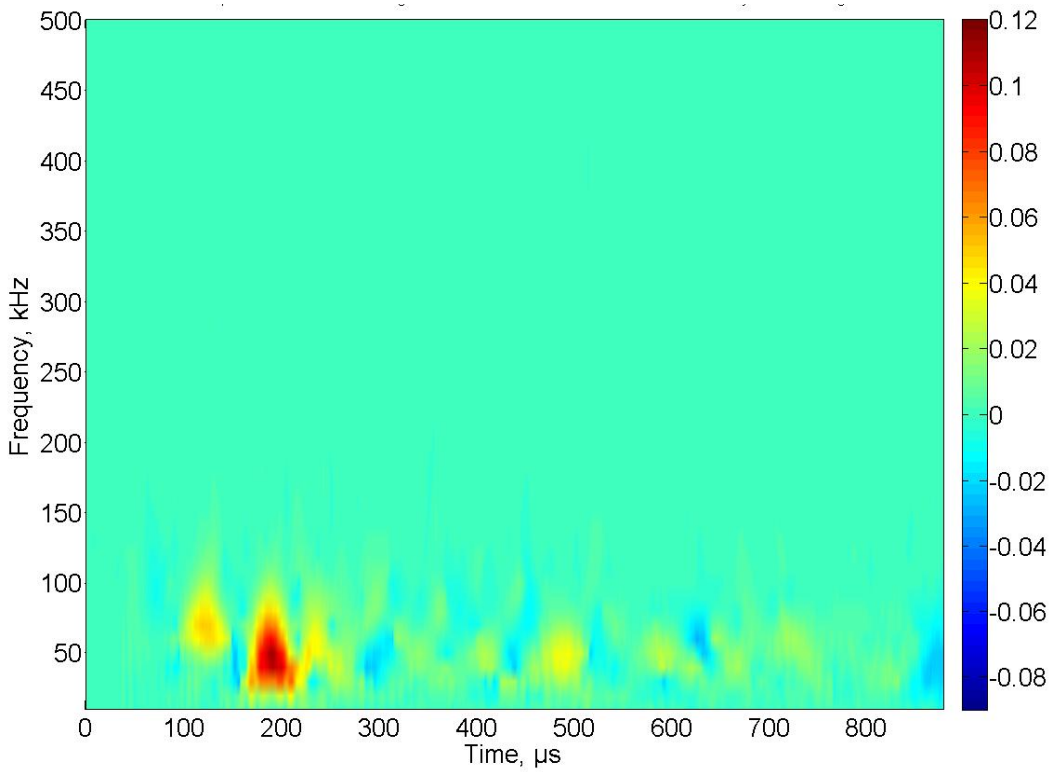

Figure 2-69.Wavelet subtraction of the impact 15 wavelet from the baseline wavelet for signal transmitted at channel 3 and received on channel 2

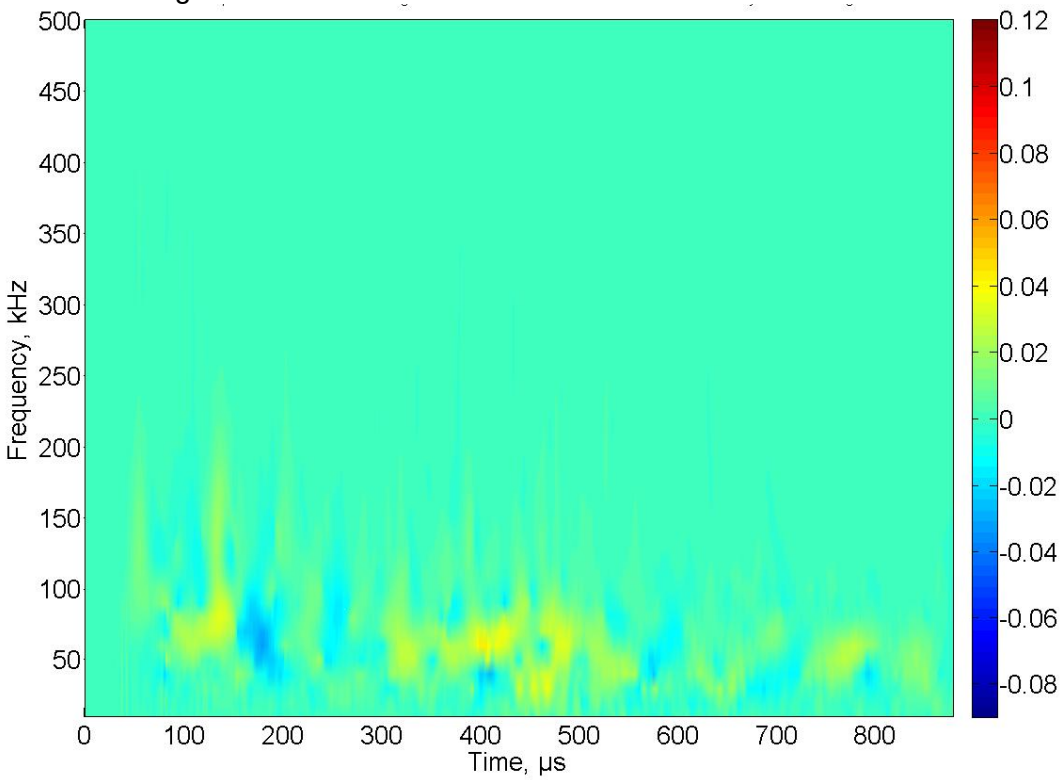

Figure 2-70.Wavelet subtraction of the impact 15 wavelet from the baseline wavelet for signal transmitted at channel 3 and received on channel 4

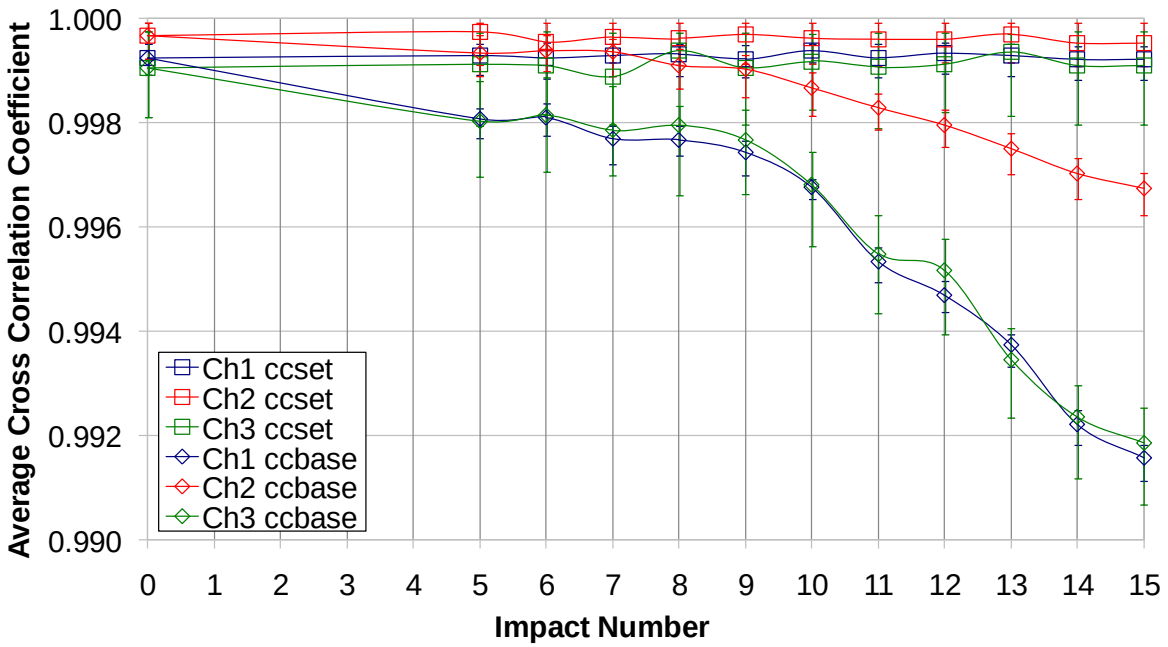

Figure 2-71. Average cross correlation coefficients for each impact for channel 4 as a transmitter

Finally the small changes of correlation due to the presence of damage need to be addressed. A further investigation was conducted using a National Physical Laboratory (NPL) conical transducer, this transducer is broadband so therefore the waveforms it records should represent the waveform that is actually propagating in the plate with little effect due to the frequency response of the transducer. This transducer was used in two configurations; firstly the conical transducer was placed on the panel and an H-N source was used to generate artificial AE at a distance of 300mm. The second configuration used the MFC transducer to pulse a 20Vpp 300kHz square wave which was recorded by the conical transducer at the same distance and glass fibre orientation and perpendicular to the piezoceramic fibre orientation. The wavelet transform corresponding to an H-N source at a distance of 300mm from the conical transducer is shown in Figure 2-72. The figure shows clear indication of the S_0 and A_o modes, the amplitude of the A_0 is far greater than that of the S_0 mode due to the source being out-of-plane. The arrivals of the S_o and S_o reflection correspond to a time of approximately 400 and 465µs and the A_o mode arrives much later due to the slower velocity of this mode, arrival time of this mode is approximately 560µs .Figure 2-73 shows the wavelet transform for a pulse of an MFC transducer and recording of the subsequent wave in the panel using the conical transducer at a distance of 300mm. This figure shows that it is hard to determine the apparent arrival of the A_o mode. However it is clear that the MFC transducer embedded within the centre of the panel is creating a wave

which has the highest sensitivity in the in-plane orientation. Finally consideration of the resulting damage in the plate is necessary, which is most likely to be in the form of delamination, matrix cracking and surface ply splitting. The pulsed MFC propagating wave will interact with the damage area by attenuating the amplitude of the signal, wave scattering from the damage itself and reflecting waves due to the damage. This will create a received wave with probable lower amplitude and further transients contained in the reflected parts of the wave. Later literature study will determine that the A_0 mode is most sensitive to delaminations, therefore with the MFC generating a wave with majority of in-plane orientation and this being least sensitive to delaminations explains why little sensitivity is observed for the cross correlation technique. Also for damage to be detected the wavelength of pulsed wave should ideally be smaller than the size of the damage, this increases the sensitivity of the wave to the damage. It is also likely for a pulsed MFC wave that the wavelength is greater than the damage size, this with the in-plane nature of the wave and out of plane damage mechanism results in little sensitivity to the delamination. Of the other probable damage mechanisms, matrix cracking and ply splitting, the in-plane nature of the pulsed wave is most sensitive to these types of damage, as they are often orientated in the same plane. However these damage types are most probably smaller than the delamination damage and again little sensitivity will be observed due to the wavelength of the pulsed wave being larger than these types of damage. Also the orientation of the damage is also important for example a crack orientated parallel with the propagating wave will so less sensitivity to changes than those orientated perpendicular as this will create more disturbance with the propagating wave. Bearing this in mind it is therefore thought that although there will be several damage mechanisms present at the impact site due to the size of the damage it is thought that the delamination damage that is having the most effect on the propagating wave.

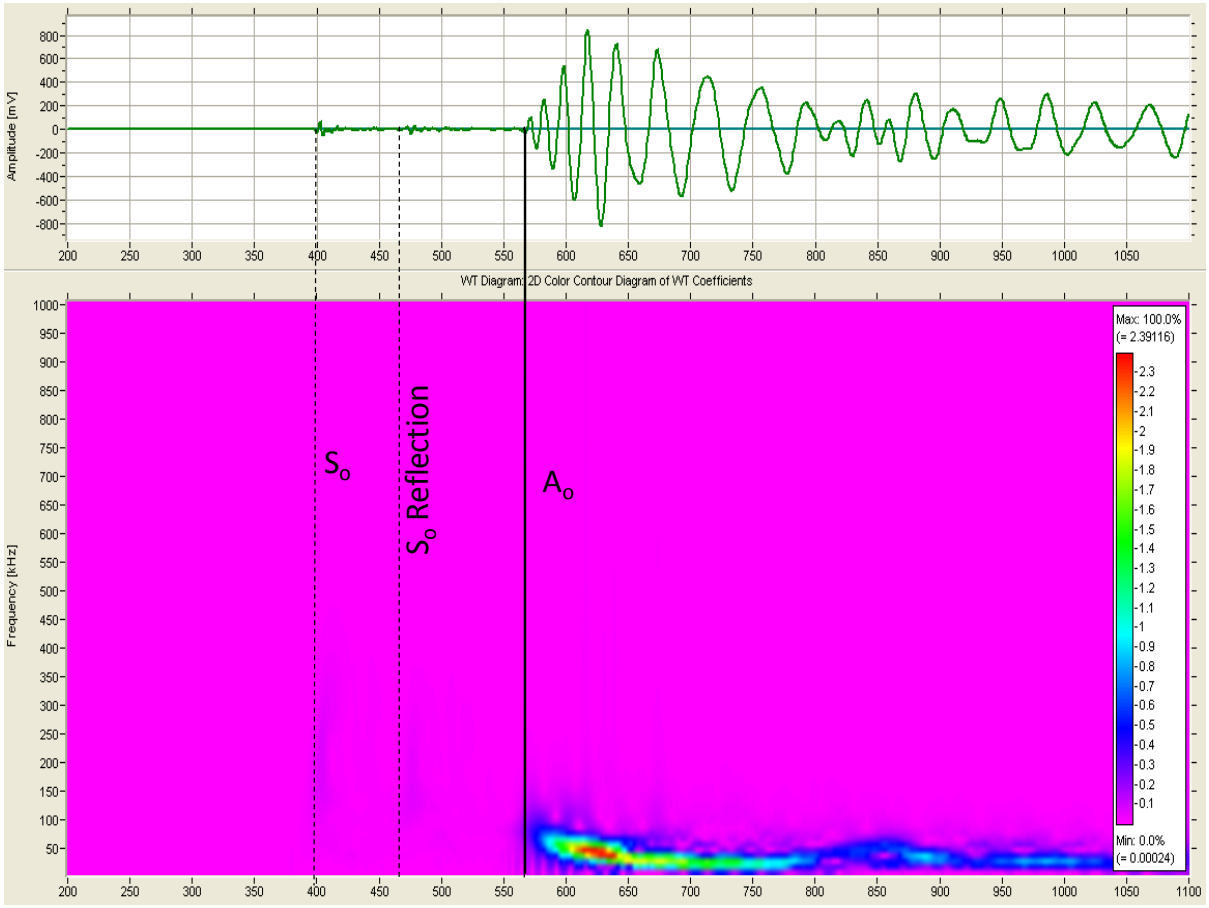

Figure 2-72. Wavelet transform of a H-N source recorded on a NPL conical transducer at a distance of 300mm

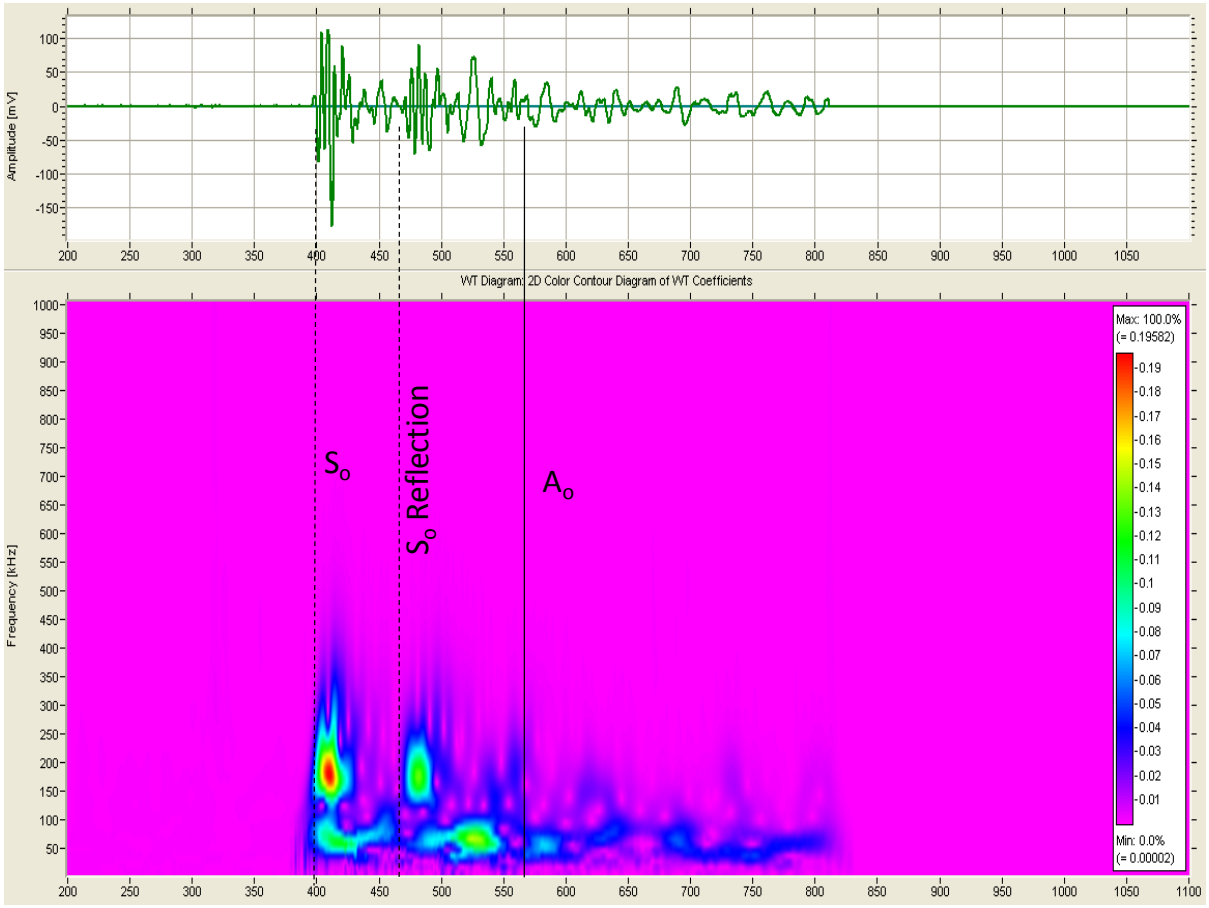

Figure 2-73. Wavelet transform of a resulting waveform from an activated MFC transducer and recorded at the conical transducer at a distance of 300mm

2.2.3.4 Conclusions

In conclusion the MFC transducers were successfully embedded within a glass fibre composite panel and demonstrated the ability to locate and detect impact damage using the AIC delta T mapping and wave streaming techniques. An AU analysis detected damage at an approximate damage size of 50mm^2, however the sensitivity of the technique to delamination was relatively small. Further to this a propagation study was undertaken to assess which parts of the waveform were most sensitive to the delamination and found that certain reflections in the signal were more sensitive to damage due to more interaction with damage due to wave scattering and refraction. Finally it was concluded that the MFC embedded transducers generated a waveform that had the majority of its components in the plane of the plate and is a possible reason for the lack of sensitivity of the waveform due to the delamination damage. This particular investigation showed success of the MFC for both AE and AU monitoring of damage within a structure.

2.3 Conclusions

The main aim of this chapter was to assess the suitability of MFC transducers for structural health monitoring applications. This was achieved by conducting several investigations which included the use of AE transducer in harsh environments, MFC optimisation and damage detection using embedded MFC transducers.

When the MFC transducer was subjected to different temperatures there was a change in the response of the received signals, this was the case for the commercial transducers used in the experiment. This could cause potential problems when using baseline techniques to determine damage in structures and could lead to potential false alarms. It should be noted that this change in signal response for different temperatures was no worse than that observed with commercial transducer, however the working temperature range of the MFC transducer is considerably lower when compared with the commercial AE transducers.

The MFC optimisation results showed that the frequency response of the MFC could be altered with a reduction in the length of the active area, significant increases in sensitivity were achieved. However with an optimised geometry the sensitivity of these transducers is lower than the sensitivity of the commercial transducers. The MFC optimisation work also showed that the MFC is able to determine between the two fundamental modes using wavelet transforms and therefore suggest that even though the sensing element is different they can still function in AE applications.

The low profile nature of these MFC transducers allows them to be embedded within a GFRP panel. Embedded MFC transducers were successfully able to locate impact events and the subsequent damage within the panel using both AE and AU approaches. This shows the novelty of using this type of transducer for dual functionality. It should also be noted that overall frequency bandwidth response of these types of MFC transducer can be considerable lower when compared with commercial transducers. This chapter has shown that the MFC can be used as an AE transducer in order to detect damage in structures for SHM applications. There are certain drawbacks to the use of these transducers but even with these limitations the MFC can still successfully be used as an alternative to conventional transducers, with significant advantages in these types of applications.

3 Damage Detection

3.1 Literature Review

3.1.1 Acoustic Emission

The purpose of the literature review is to identify fundamental research into damage detection methodologies, AE source location and AU techniques for aerospace SHM systems for both aluminium and composites structures.

Much of the fundamental research into AE propagation and location was conducted by Pollock (1986) and Rindorf (1981). Their research alongside other authors has been discussed in detail by Baxter (2007) and Eaton (2007) and therefore only summary of the fundamentals of AE will be given here. AEs are described as the elastic energy that is released when a material is subjected to a deformation. These transient elastic waves propagate through the material which in turns causes tiny deformations at the surface which can be detected using piezoelectric transducers. The general frequency range of AE signals is between 10kHz to 1MHz. AE can be thought as a passive NDT technique as detection of elastic stress waves is due to the structure deformation and not due to an actuation signal of an active technique. AE wave propagation is a complex phenomenon and a brief summary is outline below:

- Initially a wave propagates from a source as a bulk wave. These elastic waves propagate in two forms, longitudinal (pressure) and transverse (shear) and can be seen in Figure 3-1.
- When a surface is introduced this leads to boundary conditions where further wave modes may exist and is describe as a surface wave or Rayleigh wave and can be seen in Figure 3-2.
- If two surfaces are sufficiently close together i.e. in the case of a plate, there are many reflections and mode conversions. These waves couple together into more complex surface waves known as Lamb waves. The two fundamental modes can be seen in Figure 3-3 and are the symmetric or extensional (S_0) mode and the asymmetric or flexural mode (A_0). Higher order wave modes exist however they have lower amplitudes and contain little energy and are often difficult to detect.

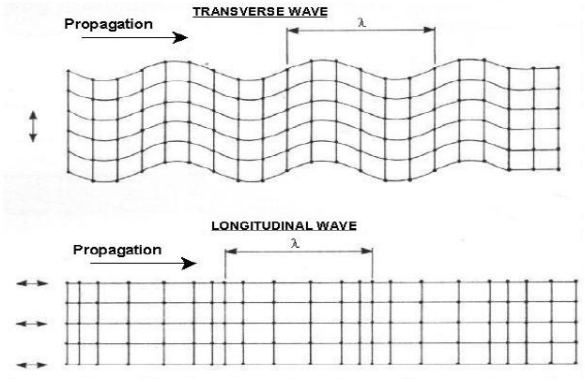

Figure 3-1.Two basic bulk modes in a solid (Rindorf 1981)

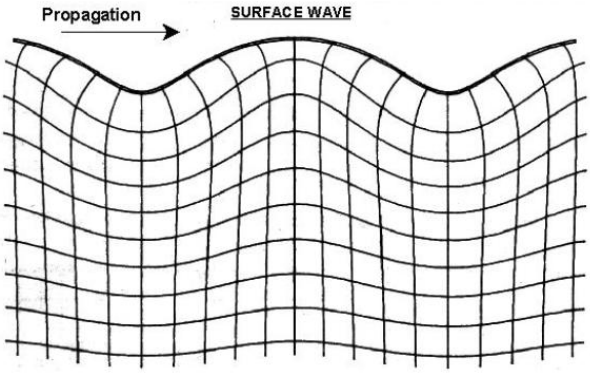

Figure 3-2 Particle motion of a surface Rayleigh wave (Rindorf 1981)

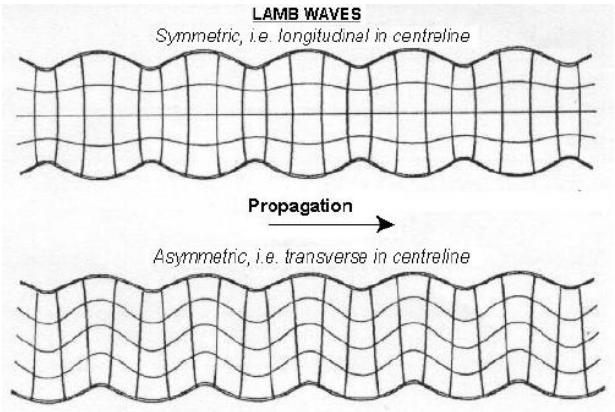

Figure 3-3 Lamb wave modes in a bounded medium such as a plate (Rindorf 1981)

Lamb wave propagation is complex and is dependent on the plate thickness and frequency content. Dispersion behaviour describes the fundamentals of different frequency components of each mode travelling at different wave velocities, which is dependent on the plate thickness. Lamb's homogenous equations are used to produce dispersion curves which describe the wave velocity of each mode as a product of the frequency and plate

thickness. Figure 3-4 shows the dispersion curves for 3.2mm thick aluminium for two fundamental wave modes. The frequency bandwidth for AE applications exits in the range of 20kHz – 500kHz from the figure the S_0 mode travels faster i.e. higher group velocity, however is often lower in amplitude, whilst the A_0 mode travels slower but is larger in amplitude and generally carry the peak amplitude, this is demonstrated further in Figure 3-5. During complex propagation the wave attenuates which describes the loss of energy of the signal as a function of propagation distances. The three main causes of attenuation are geometric spreading, internal friction and dissipation of energy at structural boundaries. Minor causes of attenuation include wave dispersion and scattering. Wave dispersion causes attenuation because a packet of energy will spread out temporally as it propagates due to different frequencies travelling at different velocities. Therefore the energy contained in that packet is spread over an increased temporal area, which means the amplitude of the packet must decrease.

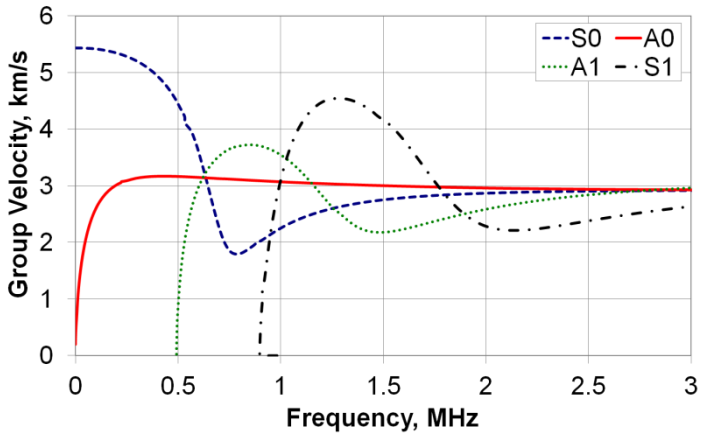

Figure 3-4. Dispersion curves for aluminium (thickness = 3.2mm)

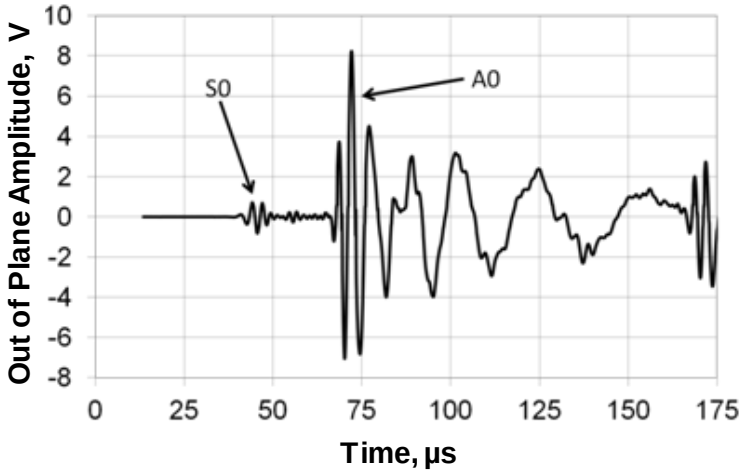

Figure 3-5. Example recorded AE wave with the two fundamental wave modes

One advantage of AE is source location, this is nominal achieved using the time of arrival (TOA) algorithm. Further information can be found in Miller et al (2005) and Rindorf (1981). A summary of the 2D location technique is presented here. The TOA relies on the arrival time of the signal at the transducers as well as a known wave velocity in a material. Figure 3-6 shows an infinite plate with two transducers located D_s apart, the located source lies on a hyperbola between the two transducers

$$\Delta t.C = d_2 - d_1 \tag{3.1}$$

$$h = d_1 sin\theta_{TOA} \tag{3.2}$$

$$h^2 = d_2^2 - (D_s - d_1 cos\theta_{TOA})^2 \tag{3.3}$$

$$d_1^2 sin^2\theta_{TOA} = d_2^2 - (D_s - d_1 cos\theta_{TOA})^2 \tag{3.4}$$

$$d_1^2 = d_2^2 - D_s^2 - 2D_s d_1 cos\theta_{TOA} \tag{3.5}$$

Substituting $d_1 = d_2 + \Delta t.C$ into equation 3.1 gives:

$$d_1 = \frac{1}{2}\frac{{D_s}^2 - \Delta t^2 C^2}{\Delta t.C + D_s cos\theta_{TOA}} \tag{3.6}$$

Where C = group wave velocity in the medium

Δt = difference in arrival time between transducer pairs

d_1 = distance from source to first hit transducer

d_2 = distance from source to second hit transducer

θ_{TOA} = Angle between source and the path between sensor 1 and 2

This however does not locate the event in 2D using two transducers, if a third is added as in Figure 3-7 and the same process is repeated for three pairs of transducers (1-2,1-3 and 2-3), it is possible to locate the source as the intersection of the three hyperbolae. In reality the hyperbolae do not intersect at one location, in practise the resolving of a source location relies on the minimisation of an objective function χ2 in equation (3.7) with respect to a source position in the X and Y (X_s and Y_s).

$$\chi^2 = \sum\left(\Delta t_{i,obs} - \Delta t_{i,calc}\right)^2 \tag{3.7}$$

Where

$$\Delta t_{i,obs} = t_i - t_1 \tag{3.8}$$

and

$$\Delta t_{i,calc} = \left[\sqrt{(X_i - X_s)^2 + (Y_i - Y_s)^2} - \sqrt{(X_1 - X_s)^2 + (Y_1 - Y_s)^2}\right] \times C^{-1} \tag{3.9}$$

The arrival times at the transducers 1 and the ith transducer are t_1 and t_i, C is the wave velocity in a given material, X_s, Y_s, X_1, Y_1, X_i and Y_i are the x and y positions of the source transducer 1 and i respectively. $\Delta t_{i,obs}$ and $\Delta t_{i,calc}$ is the measured difference in arrival time between transducers 1 and i and the calculated difference in arrival time between transducers 1 and i for a given source position S. This results in an iterative process where the errors between the measure and calculated difference in arrival time is minimised resulting in the estimated location of the source.

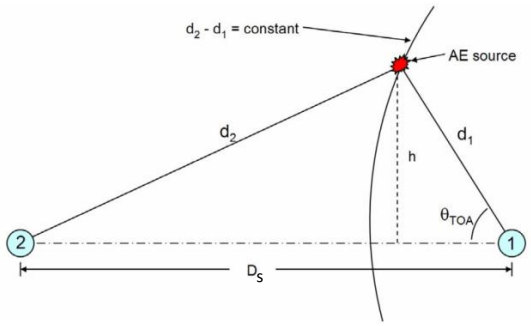

Figure 3-6. 2D source location on an infinite plate (Miller et al. 2005)

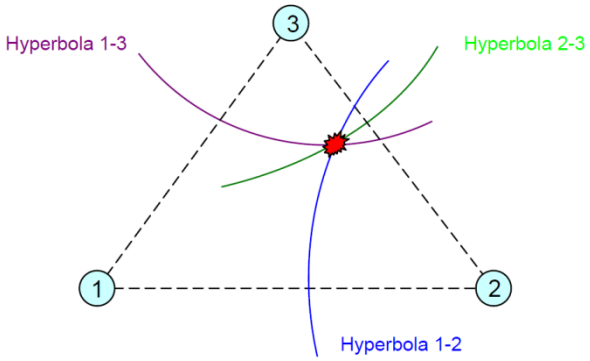

Figure 3-7. Source location using three transducers (Miller et al. 2005)

Initial research assessed the role of AE in damage monitoring of aerospace grade aluminium and assessed the AE source mechanisms released under loading of components.

Much of the AE activity released under tensile loading can be attributed to the fracture of brittle inclusions and sources of AE during plastic deformation are attributed to inclusion fracture and slip (Cousland and Scala 1983). Baram et al (1979) identified several different sources of AE during the plastic deformation under tensile loading and found significant AE rates at strain hardening steps. These were attributed to dislocation propagation which results in acoustic bursts where dislocations break away from pinning points in regions of high stress. 2024 grade aluminium is stated as being the most acoustical active grade due to the smallest average mean free path for moving dislocations. Research into AE released during fatigue crack propagation has been conducted, Baram et al (1981) monitored AE events during tensile loading of 2024 T3 aluminium sheet and recorded the highest amplitude peak every hundred cycles, these events were related to fatigue crack propagation through a phenomenological relationship. These quantities were found to be extremely distributed and required the use of ordered statistics to enable prediction of fatigue life during early stages of the process. Morton et al (1973) found that there was excellent correlation between AE and stress intensity factor, which suggest AE is more closely related to crack tip plastic volume rather than crack extension. The main sources of AE during fatigue loading was attributed to three mechanisms crack, face rubbing, crack propagation and slip and inclusion facture around the heavily deformed region around the crack tip (Scala and Cousland 1983). Scala et al (1985) also investigated the effect of overloads on 2024 aluminium under fatigue loading and found that there was a reduction in AE activity after the overload due to reduction in inclusion fracture, crack propagation is less post overload than compared with pre-overload and a larger damaged zone exist around the crack tip.

The use of wavelet transforms (WT) and modal acoustic emission (MAE) has transformed the use of AE damage detection for structural health monitoring applications. The two techniques have been applied to damage detection and source location in both metallic and composites structures. MAE utilises plate wave theory to determine a more quantitative approach which allows an easier recognition and determination of AE damage signals (Surgeon and Wevers 1999a). The authors showed for various experimental investigations on composites the measured amplitude ratio (MAR) of the first two fundamental Lamb wave modes can be used to determine between in plane and out of plane sources and hence determine between matrix cracking, fibre breakage and delamination. Pullin et al (2005) demonstrated the amplitude ratio technique determining the orientation of AE sources for artificial and fatigue crack sources in aerospace grade steel. By

characterising in-plane and out of plane artificial sources the author was able to determine that the crack data suggested a crack orientated out of plane. Eaton et al (2011) also demonstrated the MAR technique on tensile composite coupons, where AE was successful at detecting the onset of damage and was characterised as matrix cracking using the MAR methodology. This was further validated by x-ray inspection where there was high correlation between the number of significant signals and the number of identified cracks.

Alongside MAE techniques, WTs are a vital tool for processing AE signals with regards to damage detection in structures. WT transform can be thought as a windowed fast Fourier transform (FFT), however a FFT only determines the frequency spectrum of the signals where as a WT enables the frequency content of a signal to be determined as a function of time and can be thought of as a time-frequency transform. The transform results in a series of wavelet coefficients which represent the frequency and time parameters. The WT has been used to determine different damage mechanism in AE signals from a GFRP panel under tensile loading and helped to identify different damage mechanism within a structure (Suzuki et al. 1996). WT is a valuable processing technique for determining dispersion effects in composite materials. Jeong (2001) used the maximum value of a WT coefficient within different frequency bands to determine the group velocity for a particular frequency and hence the dispersion curves from experimental data.

Most practical applications of AE focus on research into the signal processing of AE signals. Automatic classification of acoustic emission data is possible using statistical approaches (Rippengill et al. 2003). The authors demonstrated the automatic classification of different AE source mechanisms through laboratory work on a box girder section of a bridge. A principle component analysis (PCA) was used to perform a dimension reduction by projecting through a linear transformation which meant that the AE features of peak amplitude, rise time, counts and duration were reduced to two principle component scores. This resulted in three clusters of signals. Multidimensional Gaussian distribution function, decision boundaries, kernel density estimates and neural networks were used to automatically classify these clusters. Katerelos et al (2009) used unsupervised pattern recognition and cluster criteria to indentify three classes of damage mechanisms in cross ply composite laminates, these classes were validated using visual observation and were attributed to fibre/matrix interface, matrix cracking and fibre failure. Loutas and Kostopoulos (2009a) also used pattern recognition algorithms, which revealed different damage mechanisms in carbon-carbon woven re-enforced composites. These different classes were observed through time which enabled the evolution of damage to be observed.

This section of the literature study has specifically identified research into acoustic emission damage detection methodologies and signal processing techniques. Significant advances have been made in these areas, however there are some limitations to these techniques. The clustering techniques can identify different groups of signals, however these are often attributed to different damage mechanism through visual observation. MAE is able to determine the orientation of an AE source and WTs can be used to identify different sources of AE. However there is still a lack of ability to determine the exact type of damage real time for a variety of structures.

3.1.2 Acoustic Emission Source Location

Alongside AE damage detection methodologies, another advantage of the AE technique is the ability to locate AE sources. The most common AE source location technique is the TOA method. This technique is used in most commercial AE acquisition systems, however there are certain drawbacks to the technique which can cause errors in the calculation of the source location. One of which is the assumption that the structure is homogenous and the wave modes travel with the same velocity in all propagation directions, this is not the case in composite materials and complex geometry specimens where there is an obstructed path from the source to transducer due to geometric features. Additional causes of error is the determination of the arrival time of the wave, the most conventional technique is the first threshold crossing technique. This states that the arrival time at the transducers is determine when the transducer output first crosses a user defined threshold. Due to signal attenuation, source amplitude and wave dispersion the actual arrival time at the transducers can go undetected causing triggering errors. Another potential problem is due to wave dispersion where a particular phase that triggers the arrival time at the transducer will have a particular frequency and therefore velocity. If this velocity differs from the velocity used in the algorithm errors can occur. For plate like homogenous structures these propagation effects cause only small errors, however when complex structures and composite materials are monitored these propagation effects can cause significant errors in the source location.

Determining accurate arrival time estimation is of paramount importance to minimise potential error in source location calculations. Simple techniques can be used to improve reliability of the first crossing threshold technique, these include lowering the threshold and filtering. Re-processing the recorded data with a reduced threshold has the advantage of not collecting large amounts of data and improves source location accuracy. However careful consideration of the reduced threshold is necessary to avoid early triggering. Filtering

techniques can enhance reliability of arrival time estimation by focussing on particular wave modes or the energy contained within the signal. Narrow band filtering can be advantageous as the wave velocity for a particular frequency can be calculated from dispersion curves. Again careful considering of the frequency at which the signals are filtered is necessary as certain frequency bands may not have sufficient energy in the waveform. More involved arrival time estimation technique exists, Ziola and Gormen (1991) developed a cross correlation technique that modulated the transducer signal using a Gaussian pulse to determine the phase difference of a single frequency in the transducer outputs. This technique gave good results in a 1.5mm thick aluminium panel. Alongside the use of WTs for damage interpretation, they have been extensively used for arrival time determination. Jeong (2001) paved the way for arrival time estimation using WTs by discovering that the peak of the wavelet coefficient within a particular frequency could be used to determine the wave velocity and that particular frequency. Hamstad et al (2002) used the wavelet coefficients around a specific frequency of interest to determine the arrival times at the transducers. This worked well on large plate like structures where edge reflections did not complicate the WT, however this was not the case for smaller specimens and environments which would give rise to low signal to noise ratios. Ding et al (2004) used a 4^{th} level wavelet decomposition and Butterworth filter to manually identify two frequency bands of interest and used a threshold crossing technique to determine the arrival time of the signal at the transducers. Shehadeh et al (2006) assessed several discussed techniques for arrival time estimation for steel pipeline applications. A comparison of a sliding window energy technique, WT and cross correlation, cross correlation, Gabor WT and a threshold crossing were undertaken. The sliding window energy technique was found to give the most reliable results. The technique applied a high pass and low pass filter at a particular frequency of interest for a particular time window, the time window was shifted along the signal. For each time window the ratio of energy for the high pass to low pass filters was calculated and this was used to determine the onset of the signal. All of these presented arrival time estimation techniques have identified a specific frequency of interest or frequency banding. This requires prior knowledge of the structure to be monitored to indentify the most suitable frequencies to aid the arrival time estimation. Furthermore the chosen frequency of interest will be only useful for that particular structure and transducer type. Therefore approaches are required that will determine the arrival time estimation independently of the structure and transducer type.

Techniques that have addressed the above problem have involved the use of statistical processing, Lokajicek and Kilma (2006) used higher order statistics where a sixth

order empirical formula (S_6) was calculated for a moving window of 100 sample points. When the window contained background noise and the start of the waveform a sharp rise was observed in S_6. Therefore the derivative of S_6 and the ratio of the short time to long time average was used to automatically detect the onset of the wave within an accuracy of ±2 sample points. Grosse (2000)developed an automatic arrival time estimation technique based on the Hinkley (1971) criteria where the partial energy is cumulative summed for all samples in the time series, adding a negative trend to the functions enables a global minimum to be observed when the arrival of the signal occurred. However careful choice of the particular variable in the negative trend is required in order to achieve accurate results. The Akaike information criterion (AIC) is an alternative automatic arrival time estimation technique which was developed by Akaike (1974) and Kitagawa (1978). Maeda (1985) developed a modified form of the AIC technique that could be directly applied to a raw transient signal. This form of the AIC technique has extensively been used to determine the arrival of seismic waves and has the following form:

$$AIC(t) = tlog_{10}\big(var(x[1;t])\big) + (T-t-1)log_{10}\big(var(x[t;T])\big) \tag{3.10}$$

The signal is split into two parts, that from time 0 to time “t” and that from time “t” until the end of the signal “T”. Equation (3.10) describes the similarity in entropy between two parts of the signal, for every time “t” throughout the signal duration. When “t” becomes aligned with the onset of the signal, the minimum similarity is observed between the high-entropy uncorrelated noise prior to signal onset and the low-entropy waveform showing marked correlation after signal onset. Hence the minimum of the AIC function corresponds to the signal onset time. A limited time window should be used with the AIC function as several minima will be observed when the whole signal is used. Kurz et al (2005) assessed the effectives of the AIC and the Hinkley criteria specifically for ultrasonic and acoustic emission signals in concrete. The AIC and Hinkley criterion were compared with manual picks. The AIC picker demonstrated better results with a maximum average deviation of 4% to that of 17% of the Hinkley criterion when compared with manual picks. The AIC and Hinkley criterion were compared with the first threshold crossing for locating signals in concrete which resulted with a maximum percentage deviation greater than 5mm of 11% for the AIC when compared with 68% and 73% for the Hinkley criterion and threshold crossing technique. Sedlak et al (2009) developed a two stage AIC process to automatically determine the time window to avoid several minima in the function. A frequency and amplitude sensitive characteristic function (CF) was applied to the signal and the time window was applied to the signal from the start to the maximum of the CF, the AIC picker

was then used to determine a first estimate of the arrival of the signal. A second narrower time window was applied based on the first estimate and the AIC picker was used to determine the actual arrival of the signal. The technique was applied to manganese steel specimens and was able to resolve 93% of arrival times within 1µs.

There have been significant advances in the processing techniques and algorithms used to locate AE sources in a variety of structures and materials. These techniques have used MAE, iterative processes and mapping to accurately detect and locate damage within a structure. The MAE technique was used to determine an AE source location using a single transducer (Surgeon and Wevers 1999b), using the difference in wave velocity of the extensional and flexural wave modes. Calculating the temporal separation of the two wave modes and knowing the individual wave speeds allows the calculation of the radial distance from source to transducer. Pullin et al (2005) demonstrated the single transducer modal analysis location (SSMAL) on a notched aerospace grade steel specimen under four point bending. In comparison the SSMAL located more accurately than the conventional TOA however the standard deviation of the SSMAL was greater. Jaio et al (2004) demonstrated the SSMAL technique, however used WTs around a specific frequency where both the S_0 and A_0 occurred. The modal separation was determined from the WT coefficients and the velocity of the two modes at the specific frequency was determined from dispersion curves. Jingpin et al (2008) utilised modal and frequency analysis on the general triangulation techniques for specific frequency bands and for different frequency bands using WT coefficients to determine the arrival times. Theoretical dispersion curves were calculated and group velocities for the frequencies of interest were determined.

Recent research into addressing the difficulties of source location in anisotropic materials has dealt with the dispersive nature of these materials and the variability of wave velocity with propagation direction. Yamada et al (2000) determined the relationship between wave velocity and propagation angle for a particular frequency of interest. WTs were used to determine the arrival time for the frequency of interest. The arrival time was determined when the WT coefficient reached 20% of the peak value. The first hit transducer determined which quadrant of the specimen the source occurred, within this quadrant the error was minimised between the actual difference in arrival time and a virtual difference in arrival time. This was achieved by moving a virtual point and utilising the relationship between wave speed and propagation angle. This was completed in an iterative process until a certain level of error was determined. The algorithm was used on a variety of different composite lay-ups with a maximum average error of 17mm. A similar approach was demonstrated by Jeong

and Jang (2000) to locate artificial AE events in composites structures. A modified time of arrival (TOA) technique was presented to accurately estimate the position of an AE source in a dispersive media (Lympertos and Dermatas 2007). The technique consisted of three stages, the first minimised the least square error (LSE) of the actual and expected arrival times by using a close-form solution that normalises the distances from the arrival time of a series of events. The second minimised LSE between real and estimated sources transducer distances, this allows for a material constant to be derived which utilises the transducer positions and the normalised distances. Finally a multidimensional scale method is used to locate the estimated source transducer distances and the transducer positions. Effectively using a model the estimated arrival times of a source can be derived the difference between the real and estimated TOA, this presents a formulation of a material constant which then can be used to account for dispersion in the media. The method was only tested using a numerical analysis. Paget et al (2003) developed a closed form triangulation method for locating H-N sources in aeronautical composites structures. The inputs to the technique were the transducers positions and velocities in the transverse and longitudinal directions. The technique assumes an elliptical or a quasi elliptical wave front and determines the source location using a quartic polynomial. The technique was demonstrated on a composites panel and located H-N sources with a maximum error of 1.2mm. Further advances of AE source localisation in anisotropic structures have been realised by Ciampa and Meo (2010). The technique uses a specific triangular transducer layout of six transducers arranged in 3 closely spaced pairs. Enabling a set of six non-linear equations to be developed with six unknown which include x position of source, y position of source, travel time of the master transducer and three group velocities. In addition a continuous wavelet transform is used to determine the difference in arrival time between a specific transducer and the master transducer which is also required to solve the non-linear equations. The solutions to the equations are found by using Newton's method with an unconstrained optimisation which minimises the error of the objective function which represents the six non-linear equations. This technique was able to accurately locate impact events on a composite and sandwich panel with maximum errors of 2 and 3mm respectively with no prior knowledge of the relationship between wave velocity and propagation angle. This technique has been proved to be effective however it does require twice as many transducers in order to deduce source location equations from 14 to six and has a computational time of 2s per event. It also assumes a constant wave velocity in any one propagation direction which may not always be case for complex geometry specimens.

Near field beam forming has been demonstrated for location of AE signals in metallic thin plate structures for the aviation industry (He et al. 2012). The Delay and Sum algorithm was used to determine the source of an AE signal where the time delay between a linear array of transducers is adjusted so that signals associated with a spherical wave front incident from the actual source are aligned in time before they are summed when the focus point is located at the real source. Experimental validation on a steel plate found accurate results within a distance of 300mm from the linear array of transducers, the reasons for this were due to attenuation and dispersion in the specimen.

Statistical approaches have been used to develop probabilistic source location techniques implementing a Bayesian approach (Schumacher et al. 2012). This technique estimates the errors and uncertainties of location algorithms using training data. A simplified predictive model was created which described the estimation of source locations using four parameters (event time, standard deviation of observed arrival times, mean and standard deviation of wave slowness) represented by a probability density function (PDF). The predictive model was used to estimate the location of an additional 22 pencil lead breaks on a concrete beam which reduced the error from ≈40mm of a standard approach to ≈30mm of the Bayesian approach. However the model assumed because of the size of the concrete beam that it behaved homogenously. It also assumes that propagation effects such as attenuation, wave scattering and dispersion are accounted by one predicted parameter model, therefore further improvements to the technique could be made including these as separate parameters.

Techniques for monitoring structures on a global scale using arrays of closely spaced transducers have been developed. This has the advantage of accurately locating sources outside of the array which is not the case using a sparsely distributed array which gives ambiguous results outside of the array. Aljets et al (2010) demonstrated source location on a composite panel using a closely spaced triangular array of three transducers. The technique requires the wave velocity for different propagation directions for the S_0 and A_0 to be developed for a specific frequency of interest. Gabor WT coefficients at the same frequency were used to determine the arrival time and the temporal separation time of the two wave modes using a threshold crossing. Since the A_0 wave velocity does not vary with propagation angle the difference between arrival time of the A_0 mode as well as the first hit transducer is used to determine the propagation angle. The S_0 velocity can be represented numerically using the propagation angle and the minimum and maximum S_0 velocities. Knowing the separation time for each transducer and the S_0 and A_0 velocities it is possible to determine a

distance from each transducer using a single transducer location technique, these distances are then averaged to give the location which can be represented either as polar or Cartesian co-ordinate system. The technique assumes a constant wave speed for a particular propagation direction and was evaluated using H-N sources which give clear wave modes, which might not be the case in a realistic structure. It is also necessary to have a temporal separation of the two wave modes which means the technique cannot locate in close proximity to the array. The errors locating H-N sources in a large composite specimen resulted in a standard deviation of 33mm. Matt and Di Scalea (2007) developed a technique for locating AE sources using MFCs in a rosette arrangement consisting of three transducers separated by 120°. The technique exploits the directionality of the MFC transducer to determine the location of the source by using the flexural mode. Modelling the response of a MFC allowed the calculation of the longitudinal, transverse and 45° sensitivity factors to be calculated. Due to the specific layout of the MFCs it is possible to calculate the principle strain angle of the Lamb wave because the response and the sensitivity factor for the three different MFCs orientated at different angles is known. Having at least two rosettes allows the location of sources in two dimensions. This technique eliminates location errors due to the conventional TOA method in a composite because the wave speed varies with direction of propagation, however the above technique is dependent on the wavelength of the Lamb wave compared to the transducer length in the fibre direction. This could also be used as an advantage and the system could be tuned to specific frequencies possibly allowing for detecting different types of damage. The technique was demonstrated on an aluminium, CFRP and sandwich panel using a H-N sources and showed differing levels of success with the standard deviation of the actual to predicted locations ranging from 0.5 to 200.7.

The final methodology for locating damage within a structure using AE is mapping, several researchers have developed techniques for accurate source location in complex structures. Baxter et al developed the delta T mapping technique which utilises H-N sources at known node positions within a grid placed on a structure to generate maps of the difference in arrival time for each independent transducer pairing. The delta Ts from test data is compared with the training maps which identifies contours of possible locations, overlaying the results from all other transducer pairings enables a crossing point to be determined, a weighted mathematical approach is then used to calculate the co-ordinates of the AE event. Experimental verification of the technique showed improvements over conventional methods on a complex structure and requires no knowledge of transducer positions, wave speed and propagation characteristics. This technique, however does

require more set-up and would not be suitable for monitoring large structures for short duration investigations but chosen areas of interests could be selected. Another disadvantage is the use of a first threshold crossing technique to determine the arrival time of the signal, which can causes errors when triggering occurs from different modes of the signal and trying to locate lower amplitude signals where the actual start of the signal goes undetected. Further robustness testing of the above technique was undertaken through testing on composites specimens (Eaton et al. 2012b). The author conducted an analysis of the effect of the training grid resolution on the accuracy of located artificial H-N sources and found that very little difference in accuracy of location for the delta T mapping technique. A similar technique called the best matched point search method was developed by Scholey et al (Scholey et al. 2009), however in this method the training data was created by using a theoretical approach. The technique involves two stages, point generation and point matching. The first part requires the wave velocity for different propagation angles to be determined. The geometry of the specimen is represented by an array of points and the theoretical arrival time from a point in the array to a transducer is calculated using the relationship for wave speed and propagation angle. The difference in arrival time between transducers pairs is then calculated for every independent transducer pairing. By matching the theoretical and experimental difference in arrival times by minimising the error it is possible to estimate the source location. The technique showed an improvement in location when used to locate 13 H-N sources on a composite specimen with a point array density of 2mm. The technique assumes the wave velocity will be constant for a given propagation direction. Another similar technique was developed by Hensman et al (2010) which used the AIC picker to determine the arrival time of the signal at the transducers, the difference in the technique was the use of Gaussian processes to directly relate the difference in arrival times to Cartesian co-ordinates The technique was trialled on a complex steel specimen with a series of holes machined into the middle section of the specimen. To assess the robustness of the technique the training data for four panels were used in turn to locate signals in the remaining panels. This showed maximum location error of 8mm however the minimum errors occurred when the same panel was used for training and locating artificial AE events. Artificial neural networks (ANN) can be used to locate AE events by the use of training data which is similar to the mapping technique. Generally it is the case that the algorithm is non-transferable to any other object. One way around this is to replace the arrival times in the algorithm by signal arrival time profiles (ATP) (Chlada et al. 2010). The indentified structure is divided into several zones depending on the first arrival at a transducer and localised using the information of which transducer it is nearest. The ATPs are developed using

distances and the arrival time velocity is cancelled out and is independent to scale changes for an isotropic structure. This enables the ANN to be trained on a model and executed on the actual structure. However the ANN struggles when the source distance between all the transducers is similar. The ANN was able to locate H-N sources and damage in a linkage in a landing gear within 9mm for the first two locations, larger errors were apparent on the third location due to source to transducers distances and triggering errors .

3.1.3 Acousto-Ultrasonics

AU is seen as an active SHM technique where using the fundamentals of guided Lamb waves, a structure is excited by an actuation signal at a transmitter the resulting waves are recorded at the receivers, damage is detected by looking for changes in the received waveforms. Raghavan (2007) and Matt (2007) give a good introduction into the fundamentals of guided Lamb waves. This part of the literature review will discuss the application of AU techniques for SHM monitoring. Several authors have investigated the fundamentals of the interaction of Lamb waves with damage in a variety of structures. Often the detected waveforms, even before interaction with damage, are complex as a variety of wave modes will be present in the signal depending on the material and thickness of the structure. Liu et al (2002) modelled single mode excitation of lamb waves using piezoelectric transducer arrays bonded to a composite plate. The model was based on dynamic piezoelectricity theory, discrete layer theory and a multiple integral transform method. Using Fourier transforms mechanical and electric variables can be expressed as two unknown constants and using boundary and continuity conditions results in a final set of governing equations resulting with an analytical frequency domain solution which relies on the determination of the input impedance. However the input impedance relies on the characteristic excitation circuit electronics and the transducer. In order to validate the model an analytical solution based on Mindlin's theory was used for low frequencies for excitation of the fundamental wave modes. The array is arranged with a spacing of half a wavelength of the target mode at the excitation frequency, the technique was simulated on an aluminium plate and using the required wave number of each mode, separation can be conducted. There was good agreement between the two analytical models however it was noted that electromechanical interaction had a large effect on the model. Fromme and Sayir (2002) used the fundamentals of wave scattering to determine damage at a rivet hole. Driving PZTs at a lower frequency than other modes excited only the A_0 mode. A laser vibrometer was used to measure the scattering of the waves at the rivet. Using Mindlin's theory of wave scattering an analytical solution was provided for the scattering at the rivet hole with good

agreement between the two. Introducing a notch at the rivet hole changed the measured scatter field and this was successfully modelled using finite difference methods and results in a significant change in amplitude. Grondel et al (2004) calculated theoretical dispersion curves for a wing box to investigate use of Lamb waves for SHM applications. At the frequency of interest the S_0 and A_0 modes were most susceptible to damage interaction due to the wavelength. Comparing waveforms from healthy to damage states allowed the detection of damage due to attenuation of the two modes. Consideration of Lamb wave propagation in complex structures is necessary when monitoring aerospace structures. Han et al (2006) characterised Lamb waves propagating through a composite plate with a variable thickness. Characterising of Lamb waves is important as it can define location, number and size of transducers at an early stage. Two arrays were used in experimentation, a linear array of five PZT discs in a thin section and a linear array of seven in a thicker part. The group velocity was calculated using the arrival times of the signal at the PZT transducer along with the distance to the PZT transducer in the array. The group velocity of the Lamb waves travelling across the discontinuity was found to be similar to the group velocity in the thinner part. The central frequency of the propagating waves was more affected by the thin region. There were two modes that existed in the thinner part and three modes existing in the thicker section. These fundamental research activities often define the techniques that can be exploited in order to achieve a SHM system.

One particular damage mechanism which aircraft are susceptible to is impact damage, various AU techniques have been developed to locate and assess the severity of the resulting damage within the structure. Tracy and Chang (1996) developed a computer program to indentify impact force and its location in a composite plate. A system model was utilised to indentify the dynamic response of the plate and a response comparator to estimate impact location and force history. Two iterative steps were used to determine the impact load and force history, firstly estimating the impact force-time history by selecting a random impact location. The response comparator performs an optimisation based on least square fitting which generates the impact history, minimising the error between calculated and measured outputs, this enables a figure of merit to be determined. The process continues until the figure of merit is reduced to a minimum. Wang and Chang (2000) developed an active diagnostic technique for detecting and locating impact damage in composite plates. The proposed system utilised a network of piezoceramics as both actuators and transducers. Detecting a scattered wave from damage by using a baseline subtraction method and performing a joint time frequency analysis (spectrogram) it was

possible to determine the arrival time of the scattered wave. The location can be determined from the measured time differences. The damage size can also be estimated by minimising differences between measured arrival and calculated arrival times of scattered waves. Schubert et al (2009) studied the interaction of Lamb Waves in carbon fibre panels with impact damage for the application of AU techniques. Piezoceramic fibres were used to generate fundamental S_0 and A_0 Lamb waves and a scanning vibrometer was used to compare damaged and undamaged panels to determine changes in their fundamental modes. The out of plane parts of the S_0 and A_0 have the greatest interaction with the impact damage, also the interaction of the A_0 mode with the impact damage creates a time delay in that part of the wave when compared to an undamaged panel. Therefore amplitude ratios and the time delay of the A_0 mode could be used to detect impact damage. Markmiller and Chang (2010) developed a transducer location optimisation method to maximise the performance of an impact detection SHM system with the fewest sensing elements. The system was analysed on the probability of detection (POD), this was optimised to give the maximum POD for optimal transducer location. A genetic algorithm was integrated into a SHM system to enable the optimisation process.

Various different signal processing techniques have been developed to locate and assess the severity of damage using AU approaches these include baseline subtraction, time reversal, image fusion, and spectral analysis and will be discussed further. Konstantinidis et al (2007) describes a baseline subtraction and imaging technique based on the Hilbert transform. The signals from a transducer pair are filtered using a Gaussian shaped frequency filter and the Hilbert envelope is calculated. This is compensated for beam spreading, this results with the amplitude of planar reflections being equal and those due to the presence of damage contributing to the Hilbert envelope at a point corresponding to the propagation time to and from the damage. Using the reflection intensity as a function of spatial position allows the damage to be located on the structure. Wanga et al (2003) demonstrated a time reversal technique which uses the principle of waves radiating from a source, which may be reflected, scattered or refracted by an irregularity and received by an array of transducers. Determining the time of flight of the reflected waves and applying a time delay allows the signals to be time reversed. Exciting the transducer with the time reversed signals allows the wave to be focused on the irregularity causing a large amplitude reflection. This particularly study investigated how temporal and spatial focusing of time reversed waves is affected by dispersion and proposed a synthetic time reversal method. The synthetic time reversal method uses an array to send out the delayed excitation signals

producing a stronger diffracted signal at the receiving transducer. A cross correlation technique was developed by Zhao et al (2007) for monitoring complex geometries. A circular array of PZT discs were implemented on a wing panel and a cross correlation analysis was used to detect changes in the received waveforms from a normal to a damaged state. Tracking the magnitude of the change in a signal enabled the monitoring of damage growth. To determine the location of the damage the system assumed the probability of a defect occurring at a particular position based on the severity of signal changes between different transmission paths in the array. Another method of managing the complex received signals is to use various signal processing techniques, using single transmitter multiple receiver (STMR) arrays. STMR arrays have been used to monitor isotropic plates (Rajagipalan et al. 2006). An arrangement of 15 equally spaced transducers on a 150mm diameter circle allowed received signals after the phased addition process to be steered in any direction. When the transmitter is excited a discretely sampled time domain signal is collected at each receiver. When the propagation is non-dispersive the time domain data can be directly transformed in to the spatial domain allowing damage detection using the phase addition algorithms. However to compensate for dispersion an FFT is applied to the time domain signals which results in complex spectra at equally spaced points in the frequency domain. The phased addition works on the assumption that received wave packets from reflections are assumed to have propagated from a certain direction and that the signal received at the other transducer is shifted according to the assumed propagation angle. If the assumed direction is the same as the actual direction then this results in a coherent addition. The locations can then be obtained using an inverse FFT. The SHM application of this method was demonstrated on an aluminium panel. Again a baseline methodology was adopted scanning the plate in a defect free state, then scanning the plate with a defect. The defect free data was used to normalise the damage data as the reflections from the edges are stronger than those emitted from the defect. A circular hole was detected by the system and there was good agreement between actual and predicted locations. Further work has been completed using STMR array for monitoring composite panels (Vishnuvardhan et al. 2009). A circular array of 30 receivers and a single transmitter were used to detect delamination in a composite plate. In order to do this a genetic algorithm was developed to calculate the elastic modulus of the composite by an inversion method carried out on experimental S_0 velocities found for a quadrant of the array. The elastic modulus of the composite was necessary in the use of the phase addition algorithm. This algorithm takes account of the anisotropy in the composite and uses a phased reconstruction which requires dispersion data for the correct propagation direction. The phased addition algorithm effectively images

the composite plate in the near and far field allowing edges and defects to be detected. This is done by splitting the image into polar co-ordinates for a circular array and using calculated time of arrivals of the waves reflected by each pixel it is possible to determine defect locations due to the high amplitudes of the phased added signal at the defect location. A similar technique has been developed using arrays of transducers based on the concept of embedded ultrasonic structural radar (EUSR) (Giurgiutiu 2003). Using linear array of PWAS transducers with a specified spatial distance a wave pattern can be generated from the phased array by superposition of the wave patterns from each element. By exciting the transducers at slightly different times a wave can be focused or steered in any direction, allowing sweeping of the structure much like radar. Damage can then be detected using the pulse-echo method. Further developments of this technique created 2D PWAS phased arrays with 360º scanning using generic beam forming algorithms. This is implemented by delaying the time between pulsing of adjacent transducers in the array. As one transducer acts as the transmitter all other transducers in the array are receivers. This is repeated until all transducers in the areas have transmitted. The 2D EUSR algorithm processes the data set after it has been collected by applying delays to the excitation signal at each transducer in virtual form, changing the direction angle the algorithm steers the beams processing the results in a 2D image. The 2D PWAS array successfully detected damage in an aluminum specimen. Image fusion techniques have been demonstrated for damage detection and location (Michaels and Michaels 2007). Using an array of circular piezoelectric transducers, waveforms are recorded from all pulse receive pairs by using a broadband excitation. The resulting broadband signals are filtered using a digital band pass filters which creates a series of frequency limited signals with different central frequencies. Imaging techniques are then applied to the filter signals creating images for each central frequency, these images are fused for improved damage detection and location. The images are generated by shifting and adding the residual signals according to a time shifting rule. By monitoring the filtered signals over a period of time and assessing the change in these signals damage can be detected. This technique was successfully used to detect damage in an aluminium plate with errors in location from a single image being 30mm and for the fused image being 5.9mm. Spectral analysis is another technique that can enable damage detection in a structure. Kim et al (2007) used surface mounted PZT transducers on the top and bottom surfaces of an object in the same position. Using this set-up it was possible to separate the symmetric and anti-symmetric wave modes by accounting for the phase difference between the upper and lower surfaces. Performing a spectral analysis on signals gathered from an aluminium plate showed that there are different peaks of the symmetric and anti-symmetric modes due to

damage which are different to the excitation frequency. The same methodology was used on a defect free composite plate to obtain the spectral analysis this showed a frequency peak at 280kHz for the symmetric and 250kHz for the anti-symmetric mode. Using the ratio of the spectrum density peak it was shown that the power spectrum ratio of the two peaks differed with increasing size of delamination.

Recent advances in AU techniques have involved the use of several signal processing techniques to create a more robust SHM system with a higher probability of detecting damage. Loutas and Kostopoulos (2009b) developed a SHM method for detecting damage in carbon-carbon woven composites. The AU technique involves exciting a structure at a certain position and reception of the resulting elastic waves by other transducers. Three signal processing techniques were used to analyse the test data. The first was coherence, this compared the coherence of the first waveform when no damage was present with the coherence of waveforms with increasing amounts of damage present. The second technique used a discrete wavelet transform (DWT) to split the signal into a shifted and scaled version of the original waveform. Finally continuous wavelet transformations (CWT) were utilised to assess the differences in the AU waveforms. The coherence, C_{xy}, between two waveforms is defined as in equation 3.11:

$$C_{xy} = \frac{\left|P_{xy}\right|^2}{P_{xx}.P_{yy}} \tag{3.11}$$

Where P_{xx} is the power spectrum density of time series x(t), P_{yy} is the power spectrum density of a time series y(t) and P_{xy} is the power spectrum density of the function x(t)*y(t). The coherence analysis showed an overall decrease in coherence with increasing amount of damage, however increases of coherence were seen in the data and were attributed to matrix cracks closing after unloading. The DWT allowed three wavelets to be split into 10 different energy levels and three of these showed promise for damage monitoring over time. The CWT remained constant throughout testing until the load reached a certain level possibly suggesting it was only capable of detecting final failure mechanisms. Ihn et al (2008) developed a SHM system using several techniques for detecting of cracks and disbonds in both metallic and composites structures. A damage index was utilised which characterised damage at a given location between a pair of transducers in pitch-catch operation. Alongside an imaging based method which used the paths from multiple pitch-catch transducers pairs. Using particular lamb wave modes which are sensitive to different damage types (for example S_0 modes are sensitive to cracks whereas the A_0 modes is

sensitive to delaminations), also using the fact that elastic waves are scattered due to the presence of damage it is possible to create a damage index based on the energy of a scattered wave when compared with a baseline state. Analysis of scattered waves from a damage mechanism can also be used for damage location and size. Using the time delay from baseline and scattered waves and assuming a constant velocity it was possible to create an ellipse with the transducers locations at the foci. Other ellipses need to be generated in order to find the exact location, this was achieved by assuming a location for damage and used a maximising function in order to determine the actual damage location. However this method does not provide enough image resolution due to ellipses not being single lines due to scattered wave packets containing multiple peaks. In addition reflections from boundaries will cause problems when damage is situated close to a boundary, interception of ellipses could occur at locations that do not relate to the actual damage location. Therefore signal processing techniques were used to improve the method to convert raw data to a smooth waveform using a short time Fourier transform and using correlations of the scattered waves.

Most, if not all of these techniques rely on a baseline methodology which determines changes from a healthy state to that of a damaged state. However these techniques require the information of the two states to be recorded within the same environmental conditions which may not always be the case. Changes in the environmental conditions between healthy and damage states may lead to damage being detected when there is no damage present and vice versa. Temperature affects the propagation of Lamb waves in two ways, firstly the thermal expansion or contraction of the material changes the propagating distance, density and thickness of the structure and secondly, changes the ultrasonic velocities which are linked to the elastic moduli. Both of these alter the dispersion curves of the propagating wave (Konstantinidis et al. 2007). There are two main methods for reducing the effects of temperature on a SHM system these are optimal baseline subtraction and the optimal stretch method. The optimal baseline subtraction technique involves storing a database of baseline signals which correspond to different temperatures (Konstantinidis et al. 2007). A signal from damage is compared to every signal in the database and the one with lowest RMS residual error is chosen as the correct baseline signal and baseline subtraction can then be employed. Clarke et al (2009) states that two signals measured at different temperatures will cause a time delay and a phase shift in the frequency domain which is similar to a stretch in frequency content. This difference can be eliminated by stretching or compressing one of signals in the time or frequency domain. Advantages of this type of

method is that a database of baseline signals is not required, however the optimal stretch method requires a simple structure and high mode purity to achieve a compensation for 5°C. In complex structures where mode purity is lower this falls to 0.5°C to 1°C. Therefore often both techniques are used for temperature compensation. Clarke et al (2009) and Croxford et al (2010) successfully used both techniques to successfully locate and detect damage in a shipping container door and an aluminium panel subjected to different temperatures during data collection. Park et al (2009) demonstrated instantaneous baseline detection by collecting a baseline waveform every time it monitors the structure. The system consists of multiple rows of transducers and actuators with the same separation distance on the structure. Comparison of the waveforms collected between each propagation path using a cross correlation technique determined damage within a particular propagation path. This technique was successfully used in a pitch-catch scheme to detect damage within the array and a pulse-echo scheme which detected damage outside of the array. Investigation into temperature compensated baseline methods has been completed (Clarke et al. 2010). This particular method uses an optimal stretch method which takes the frequency step size of the spectrum of the signal at elevated temperature and stretches or compresses it in small steps. At each step the stretched signal is multiplied by a correction factor which is a ratio of the input signal and the stretched input signal.

3.2 Damage Detection Methodologies

3.2.1 AIC delta T Mapping Locations

The delta T Mapping technique was developed by Baxter et al (2007)and has already been discussed in the literature section of this chapter. A summary of the main steps in the algorithm is provided:

- An area of interest is identified on a structure where predicted high stress levels would occur or around complex geometric features. Although the delta T mapping could be utilised to monitor a whole structure this would be very time consuming and therefore should be seen as a technique to improve location around complex features. Several areas of interest could be identified on the structure and this could be realised during or post test to further interrogate areas if several location techniques are used in parallel
- A grid is constructed on the area of interest identified on the structure, the resolution of the grids will affect the accuracy of location, however careful consideration of the resolution when compared with the transducer diameter is necessary as wave theory

states that in principle it is only possible to locate to within 1 transducer diameter of the source. The grid can be orientated differently to the transducers as the grid is used as the reference point and not the transducers. It is not necessary to know the location of the transducers.

- Conduct artificial (H-N) source events at each nodes position within the grid in order to obtain the arrival time at each transducer. Several sources are required in order to remove erroneous data and provide an average result. It has been shown that at least five events at each node are necessary in order to provide reliable data. It is not essential to have data from every node position missing data can be interpolated from surrounding nodes.
- Calculate the difference in arrival time (delta T) maps this is achieved by calculated the delta T for each node position for each transducer pairing. If four transducers are used in the technique this would results in 6 combinations of transducer pairings. Knowing the average delta T for each node position and the Cartesian co-ordinates of that node it is possible to generate a map of delta T for each transducer pairing.
- Calculated the delta T for real data events for each transducer pairing and compare with the delta T maps, this identifies a contour of delta T where possible source location could occur by stacking all the delta T maps a convergence point can be identified. However in reality multiple crossing points would occur therefore a method to determine the number of contours that exist in a given grid square was developed for each combination of ΔT maps. Using this information a weighted mathematical algorithm was developed to estimate the source location. By assessing the number of crossing points a confidence of location can be determined for a particular event.

The technique has been successfully used to determine AE event location in composite and aerospace grade material. However the major disadvantage is that the arrival times of the source at the transducers are determined by a first threshold crossing technique. Erroneous delta T data can be generated due to triggering of different wave modes this can be either due to attenuation or dispersion of the signal which leads to the start of the signal being undetected as it is lower than the threshold level. A solution to this is to utilise the Akiake information criteria (AIC) (Maeda 1985) to determine the exact arrival time of the source events at the transducer for both the training and actual event data. The original delta T mapping programme was re-coded using MATLAB and additional modules which implemented the AIC algorithm were used to determine the actual arrival times, a flow diagram for the improved algorithm overview can be seen in Figure 3-8, alongside a

comparison with the original delta T programme. The figure shows two additional modules which re-calculates the arrival time of waveforms using the AIC picker. The form of the AIC picker used in the MATLAB delta T mapping programme was developed by Maeda (1985) and is the following form:

$$AIC(t) = tlog_{10}\big(var(x[1;t])\big) + (T - t - 1)log_{10}\big(var(x[t;T])\big) \quad (3.11)$$

The signal is split into two parts, that from time 0 to time "t" and that from time "t" until the end of the signal "T". Equation (3.11) describes the similarity in variance between two parts of the signal, for every time "t" throughout the signal duration. When "t" becomes aligned with the onset of the signal, the minimum similarity is observed between the high-variance noise prior to signal onset and the low variance of the waveform showing marked correlation after signal onset. Kurz et al (2005) and Sedlak et al (2009) have successfully applied the technique to arrival time determination of AE waveforms. Mistras AEwin data acquisition and data replay software, which is used on all the Mistras AE acquisitions system, is used to export all the AE waveforms and energy data. The waveforms and energy data are imported into MATLAB, where the original threshold crossing is calculated based on the threshold value. The AIC function is calculated from the start of the waveform up to 500 sample points after the threshold crossing, this is to avoid multiple minimums in the AIC function when the whole waveform is used which has been documented by Kurz et al (2005) and Sedlak et al (2009) . The minimum of the AIC function over this period, therefore determines the actual arrival of the waveform. This is then used as the corrected arrival times as an input to the MATLAB delta T programme, which fellows the steps stated earlier by Baxter et al (2007). Figure 3-9 and Figure 3-10 show arrival time comparisons for the threshold crossing with the AIC techniques for a high amplitude and low amplitude AE waveforms respectively. For the high amplitude source there is a close agreement between the arrival times determined between the two techniques. However for the low amplitude source there is a clear separation between the arrival times determined by the two techniques hence an algorithm using a threshold crossing technique would generate errors as the correct arrival time goes undetected. It should be noted that these examples shows the two extremes of the scale. A further improvement implemented into the MATLAB code, as part of this work was to output the Cartesian co-ordinates of the source, the confidence of the location and the energy contained within the waveform at the first hit transducer within the event group. A comparison of the conventional TOA, delta T mapping and AIC delta T mapping for located AE events in a number of specimens and materials will be presented in the experimental section of this chapter.

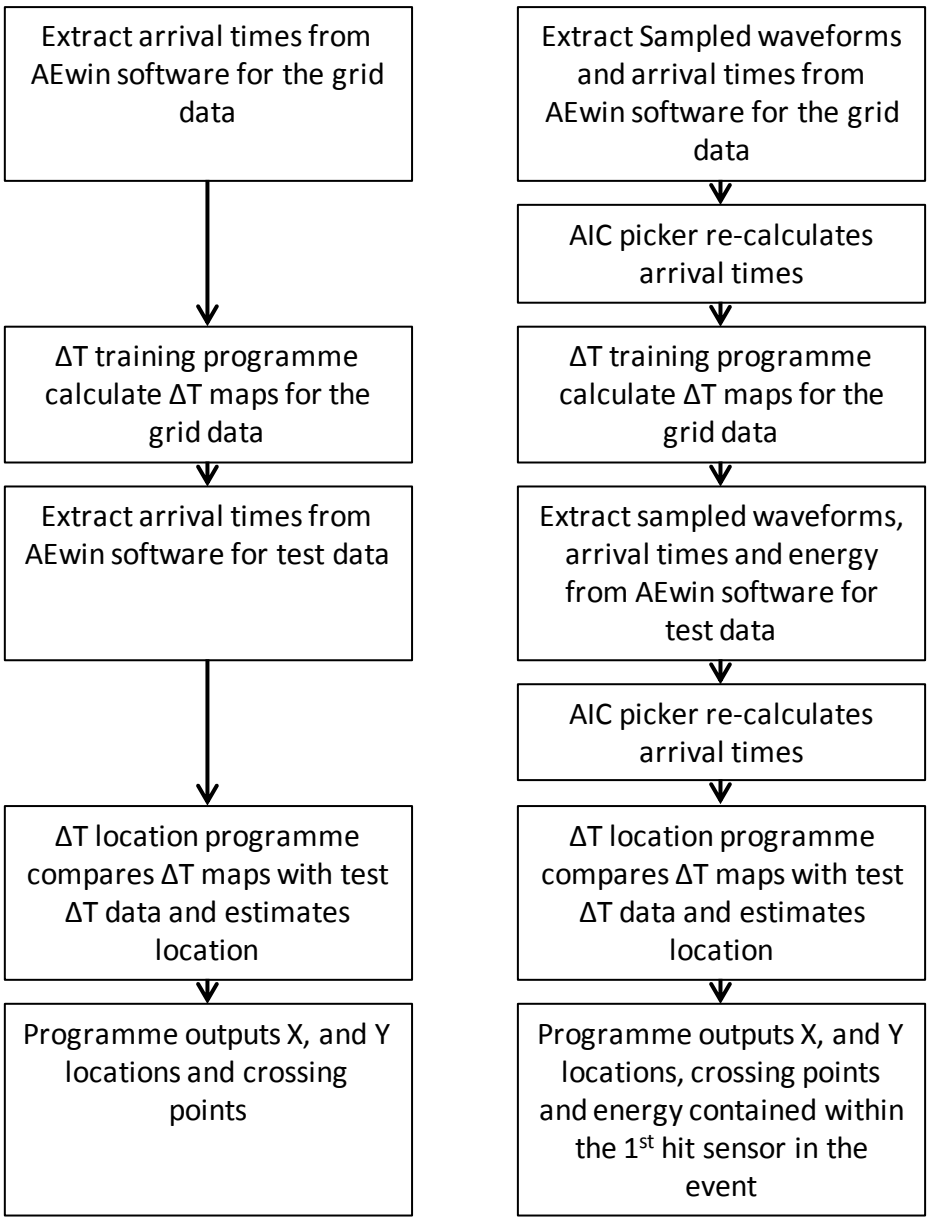

Figure 3-8. Flow diagram representation of the (a) delta T mapping technique and (b) AIC delta T mapping technique

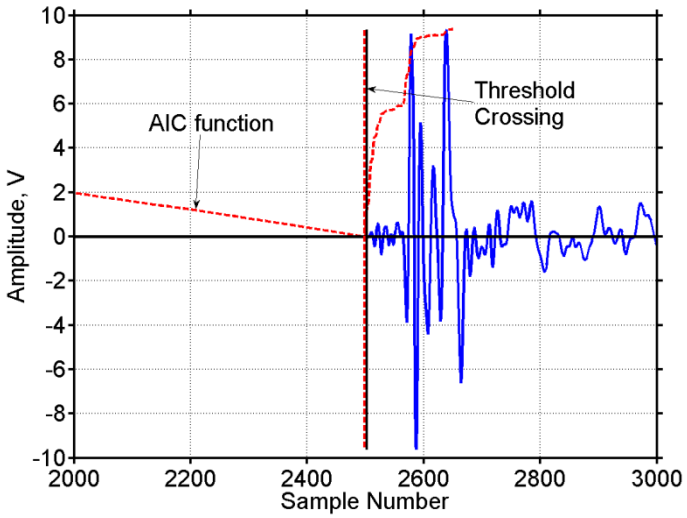

Figure 3-9. Arrival time comparison for a high amplitude AE waveform

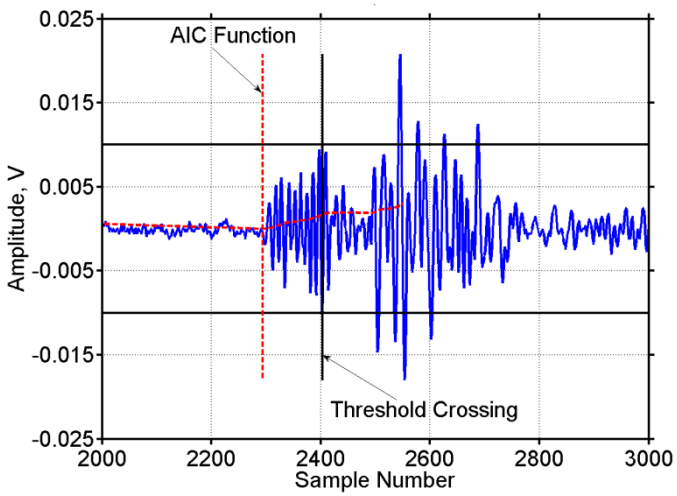

Figure 3-10. Arrival time comparison for a low amplitude AE waveform

3.2.2 Cross Correlation

Cross correlation can be used as a signal processing technique to determine how similar two particular waveforms are to one another. In this work the XCORR function in MATLAB was used to firstly conduct an auto correlation which gave the maximum integral of the product of the waveforms at zero delay and this was then used as a normalisation for the remaining cross correlations. For example two exact waveforms with no delay between them would give a normalised cross correlation coefficient of 1. The cross correlation function alters the phase of one of the signals with respect to the other, the phase shift is altered for each sample and the integral of the cross product of the two waveforms is calculated for each phase shift. The code changes the phase of the waveforms until the maximum integral of the product is realised, these results in a correlation value when the signals are the most

similar, and the code than outputs the normalised maximum integration product of the waveforms at that phase shift. An example of the cross correlation can be seen in Figure 3-11 and Figure 3-12. Figure 3-11 shows two sine waves with different frequencies plotted against sample number these two waveforms were cross correlated against one another and the resulting normalised cross correlation coefficients for autocorrelation (signal 1 correlated with itself)and the cross correlation (signal 1 correlated with signal 2) are shown in Figure 3-12. The figure shows that due to the change in frequency of the sine wave a drop in correlation is observed and a shift in sample number for the peak correlation. This can therefore be used to determine whether changes have occurred in a waveform due to an external factor. This signal processing technique can be utilised in acousto-ultrasonic applications to determine whether damage is present in a structure. The structure to be monitored is instrumented with two or more piezoelectric transducers, one transducer is excited by a chosen waveform and the resulting Lamb waves are recorded at the rest of the transducers. This methodology is implemented when there is no damage presence in the structure in order to collect a series of healthy baseline waveforms. The cross correlation coefficients are computed for a particular data set in order to realise the repeatability of that data by comparing the first waveform to all others in that set. When damage waveforms are recorded the same methodology is used to determine repeatability in the data set Therefore if a high repeatability is seen in both data sets, then when cross correlate healthy to damage waveforms a reduction in cross correlation coefficient is due to the presence of damage in the a structure. This methodology presents a simple technique to determine changes in the waveform due to the presence of damage but it cannot locate and estimate the size of the damage like other guided Lamb wave techniques, where phased arrays or advanced signal processing is utilised. It is thought that this technique will be utilised in addition to AE, where AE will locate sources and AU will confirm the presence of damage. .

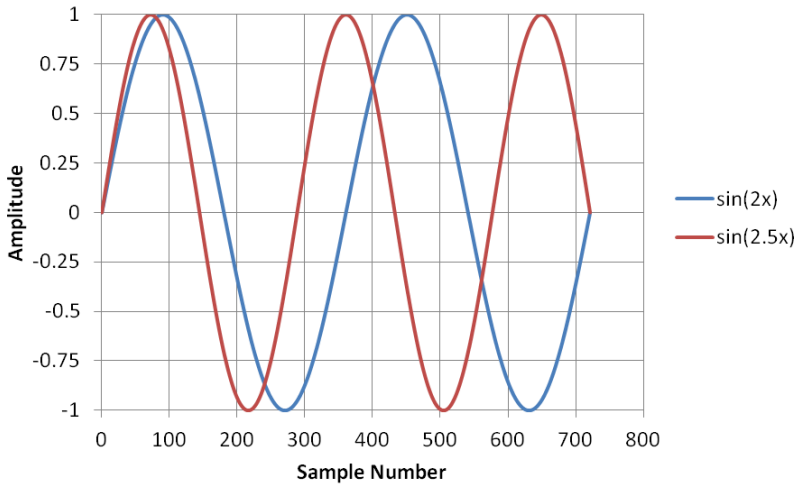

Figure 3-11. Examples of two sine waves used for a cross correlation analysis

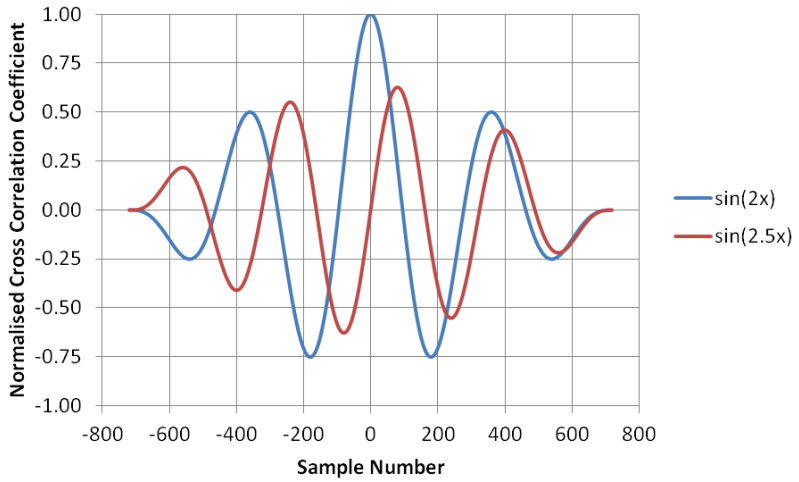

Figure 3-12. Normalised cross correlation coefficients for the two sine waves.

3.3 Experimental Investigations

3.3.1 Damage Introduction into Composite Panels

3.3.1.1 Introduction

An initial investigation was conducted to establish the sensitivity of the cross correlation technique in detected changes in the received waveforms due to the presence of damage. Once the sensitivity had been assessed, an investigation into AE and AU impact damage detection using single MFC transducers was conducted.

3.3.1.2 Methodology

A carbon fibre panel was manufactured from 8 plys of 0-90 woven CFRP manufactured by Cycom with the following material code 950-1a-t650-39%-316-1270. The

panel was cured in the autoclave resulting in a panel with dimensions of 500mm x 500mm and 2mm thick. The panels were prepared on a PTFE covered aluminium plate before vacuum. The panels had full vacuum and moulding pressure applied before the recommended curing cycle by Cycom® for 950-1, shown in Figure 3-13 was used. This consisted of a heat up rate from room temperature of 1-2°C/minute to 125°C and held for 2 hours, the panels were then cooled at 3°C/minute. A full vacuum was applied throughout the cure cycle.

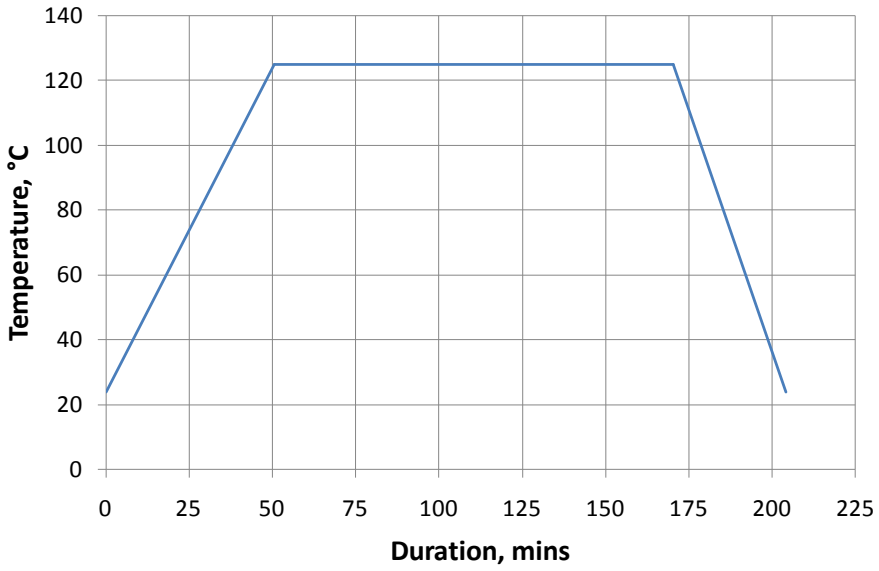

Figure 3-13. Cure cycle for the composite panels

Two Mistras Nano-30s with a working frequency range of 125 to 750kHz were adhered to the panel using a Silicon RTV (Loctite 595) and left to cure for 24 hours. The position of the transducers and damage site can be seen in Figure 3-14. Table 3-1 shows the location of the transducers and the damage site with reference to the bottom left hand corner of the panel. The distance between the transducers was 277mm and the damage was introduced in the middle on a direct path between the two transducers. A Mistras Microdisp with an incorporated wave generation board was used to pulse a 150V square wave through one of the Nano 30s, the other transducer recorded the resulting waveforms in the plate. This was conducted at three different frequencies of 100, 300 and 500kHz. A series of 100 waveforms were recorded when there was no visible damage in the plate and these formed the baseline waveforms which formed the basis of the cross correlation analysis. Damage was then introduced along the centre line between the transducers using a drill, and the drill bit size was increased from 1mm to 13mm. After each damage state was introduced into the panel another series of 100 waveforms were recorded, using

methodology for the baseline waveforms, and this procedure was repeated for each drill bit size. The cross correlation technique was then used to correlate waveforms that were collected at each damage state and to correlate the waveforms at each damage state to that of the baseline waveforms.

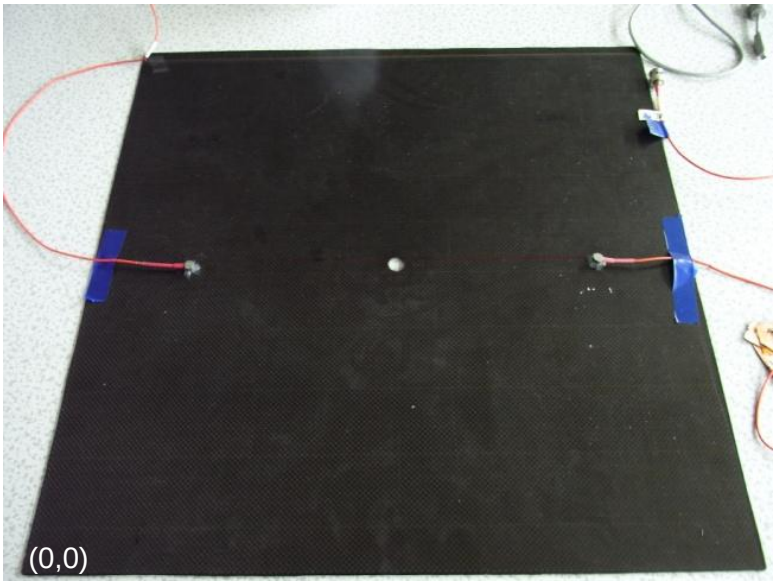

Figure 3-14. Experimental set-up for the preliminary investigations

Table 3-1. Location of the transducers on the panel from the reference corner of (0,0)

	x location, mm	y location, mm
Nano30 #1	135	240
Nano30 #2	412	240
Damage Site	250	240

A further investigation into damage detection using the same transducers both AE and AU techniques for known impact forces was completed. Another carbon fibre panel was manufactured with same dimensions and from the same material and cured under the same process. Two low profile M2807-P2 MFC transducers, which are P2 MFCs with an active area of 28x7mm and a Mistras Pico were adhered to the panel using cyanoacrycate, this configuration can be seen in Figure 3-15. Table 3-2 shows the location of the transducers and damage site measured from the bottom left hand corner as a reference of (0,0).The panel was scanned using an ultrasonic C-scanner to detect if there were any defects in the material from the manufacturing process. A 10MHz probe with a 5mm diameter collimator was used to focus the beam on the specimen. The spatial resolution was 1mm x 1mm and the timing gate was set large enough to record the peak amplitude from the beam reflected

off the glass panel that was placed underneath the specimen. A test bed was fabricated to place the panel underneath the impact test machine and the panel was clamped around the unsupported area in the middle of the test bed, this is shown in Figure 3-16. An Instron Dynatup 9250HV was used to subject the panel to a number of 4J impacts based on an impactor weight of 5.75kg and a velocity of 1.14m/s. An energy of 4J was used to slowly progress the damage in the plate. During the impact event all three transducers were used to record AE using a Mistras PCI-2 system. After each impact the two MFC transducers were used to collect waveforms for the cross correlation technique A 60V square at 100kHz was pulsed to one of the transducers, the voltage was reduced from the previous investigation due to limitation of the transducer, the other recorded the resulting waveform using the same PCI-2 system After each subsequent impact the plate was C-scanned for damage. As previously described a series of baseline waveforms were recorded when there was no damage in the plate. Firstly the cross correlation technique was used to compare the waveforms recorded after each impact with its own data set and the waveforms at each damage state were then compared with the baseline waveforms.

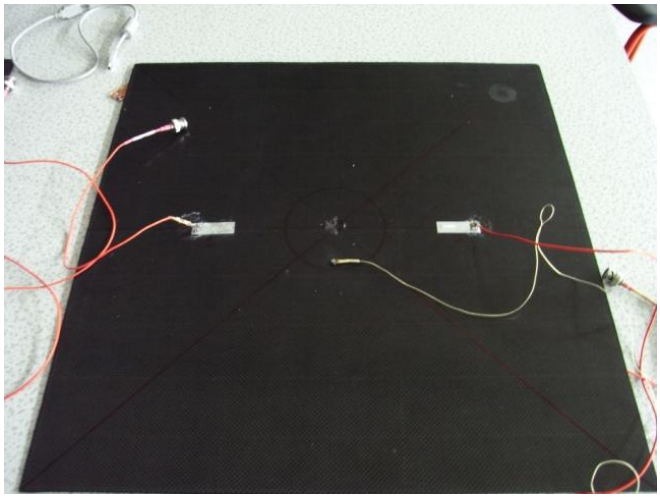

Figure 3-15. Experimental set-up for the impact investigations

Table 3-2. Location of the transducer and damage site for the impact investigation measured from the reference point of (0,0)

	x location, mm	y location, mm
Channel 1 (MFC 1)	135	250
Channel 2 (MFC 2)	365	250
Pico	250	210
Damage Site	250	250

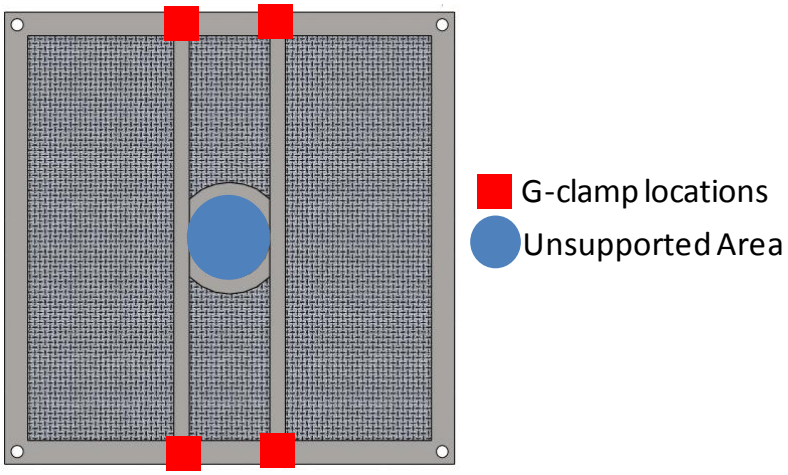

Figure 3-16. Clamping arrangements for the impact investigations

3.3.1.3 Experimental Results and Discussion

Figure 3-17 shows the average cross correlation coefficients calculated from a series of 100 waveforms cross correlated within each data set at each damage level at three different frequencies of 100, 300 and 500 kHz. The cross correlation takes the first waveform within that data set and auto correlates to itself, it then correlates all the other waveforms to the first waveform. This figure shows that the waveforms recorded within each data set are almost identical demonstrated by an average cross correlation coefficient greater than 0.99. The error bars were calculated taking the maximum and minimum coefficients from the average value and shows that the maximum error of 0.0003. This shows that the pulse receive configuration is highly repeatable. This provides confidence that any changes in average cross correlation coefficient when the waveforms are compared with the baseline waveforms is due to the presence of damage and not because of changes in the pulse and receive configuration.

Figure 3-18 shows the average cross correlation coefficients calculated from a series of 100 waveforms when they are correlated with the first baseline waveform for each frequency. This allows any damage in the plate to be detected due to a change in signal propagation as a result of the change in structure. Examining the results of the 100 kHz signal, Figure 3-18 demonstrates that this frequency pulse detects the damage introduced using the 1mm drill bit and shows the greatest potential of detecting the small amount of damage as it has the largest change in cross correlation coefficient. This is due to the size of the defect and the wavelength of the pulsed wave. However the 100 kHz pulse does not detect the changes in signal at larger defect sizes as well as the other two frequencies. The 300 kHz signals detected the greatest change in the received waveforms, overall this is most

likely because the frequency pulse of the wave was close to the resonant frequency of the Nano 30 itself resulting in more energy being inputted into the plate. All the cross correlation coefficients for the three different frequencies show an approximate linear relationship with a decreasing trend from 0 to 10mm drill bit size, however there is a relatively large decrease in cross correlation coefficient using a 13mm drill bit size, this was most probably due to delamination or fibre breakage occurring using the larger drill bit size in the area surrounding the hole. Unfortunately an empirical relationship cannot be drawn between the change in cross correlation coefficient and overall damage due to the drilling process.

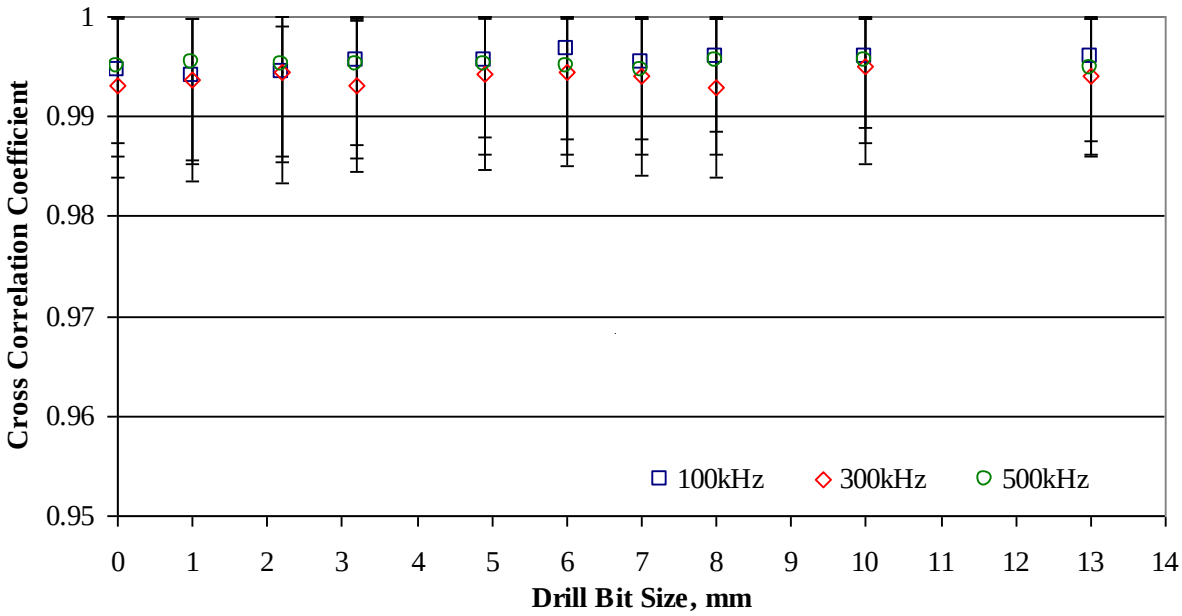

Figure 3-17. Average Cross correlation coefficients of the waveforms collected after each drill bit size and compared within each data set

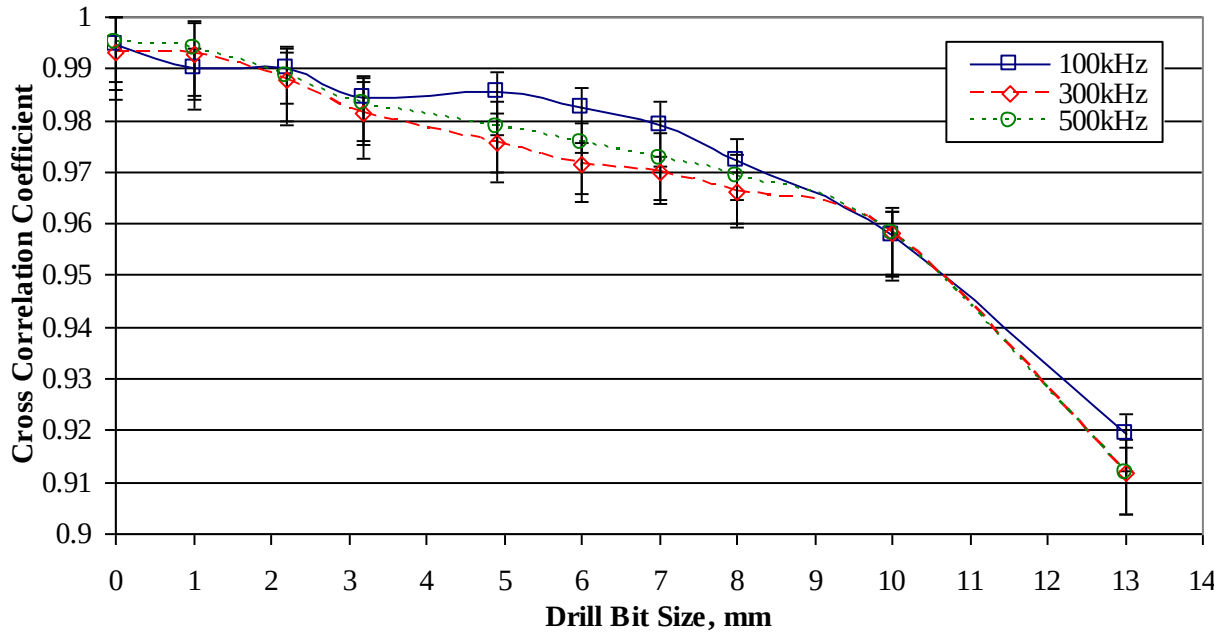

Figure 3-18. Average Cross correlation coefficients of the waveforms collected after each drill bit size and compared with the baseline waveforms.

Figure 3-19 shows the C-scan results after the first impact of 4J based on the drop height and weight of the impactor, the initial impact caused a delamination area of 66mm^2. The C-scan images from the second impact of 4J is shown in Figure 3-20, the figure shows the second impact further increases the delamination area to 320mm^2. The third impact of 4J again further increases the delamination area to an approximate area of 520mm^2, this is shown in the C-scan image in Figure 3-21. The C-scan results shows the progression of damage in the form of delamination from the repeated impacts in the centre of the carbon fibre panel, the C-scan results were used as a method of quantifying the damage in the plate as a function of the delamination area.

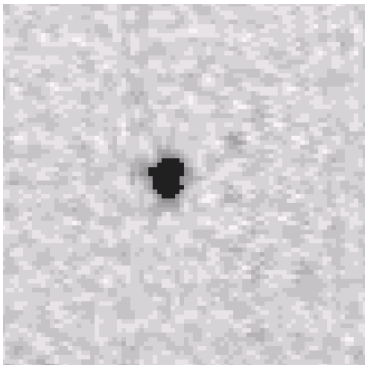

Figure 3-19. C-scan results showing the delamination area after the first impact of 4J.

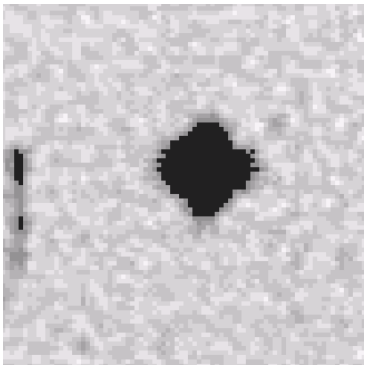

Figure 3-20. C-scan results showing the delamination after the second impact of 4J.

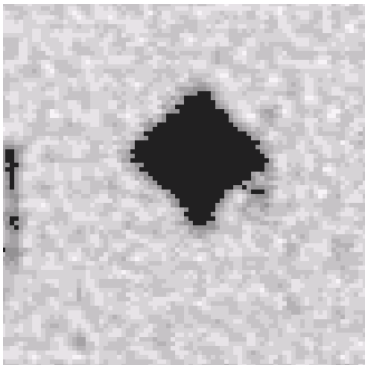

Figure 3-21. C-scan results showing the delamination after the third impact of 4J.

Figure 3-22 shows the AE results while monitoring the impact events, more specifically the acoustic energy of the detected signal attributed to the impact damage in the plate, the acoustic energy is the energy contained within that particular AE waveform. The figure shows the acoustic energy for each of the three channels. Channel 1 and 2 were the MFC transducers and channel 3 was a conventional Mistras Pico transducer. The acoustic energy is correlated against the change in delamination area between the impacts and shows an approximate linear trend for all three channels, showing the energy of the impact AE waveform is closely related to the increase in delamination area. Channel 1 (MFC 1) shows the most linear trend between absolute energy and the change in delamination area demonstrating a relationship between energy released by the impact and the extent of the resulting damage. The energy of the first impact for channel 1 is much lower than the other two channels and for the subsequent impacts channel 1 indicates the highest energy. This could have arisen from uneven clamping force on the unsupported area and the clamping arrangement causing superimposed reflections in the AE waveform. Channel 2 (MFC 2) shows the same trend but it is not as pronounced as channel 1. The absolute energy of the first impact is one of the highest but is considerably lower for the other impacts more likely than is not due to attenuation of the signal in that direction again due to uneven clamping force on the plate. Channel 3 (Pico) was placed in the unsupported area in the centre of the panel and would expect to see the highest energy for all three impacts, however this is not the case, this is due to the reflection for this case having to travel the furthest and therefore not having the same level of superposition on the AE waveforms. Again for channel 3 the relationship is approximately linear and could enable a certain estimate of the delamination area present. It is difficult to further determine the confidence in this relationship as only

three impacts occurred before significant damage was introduced in the plate. A further study would be necessary to progress the damage more slowly. However if the transducer configuration changed the acoustic energy trends would also change due to attenuation and the location of the transducers to the damage. However this could be accounted for if the location of the impact from the channel and the attenuation was known, giving an estimate of damage size.

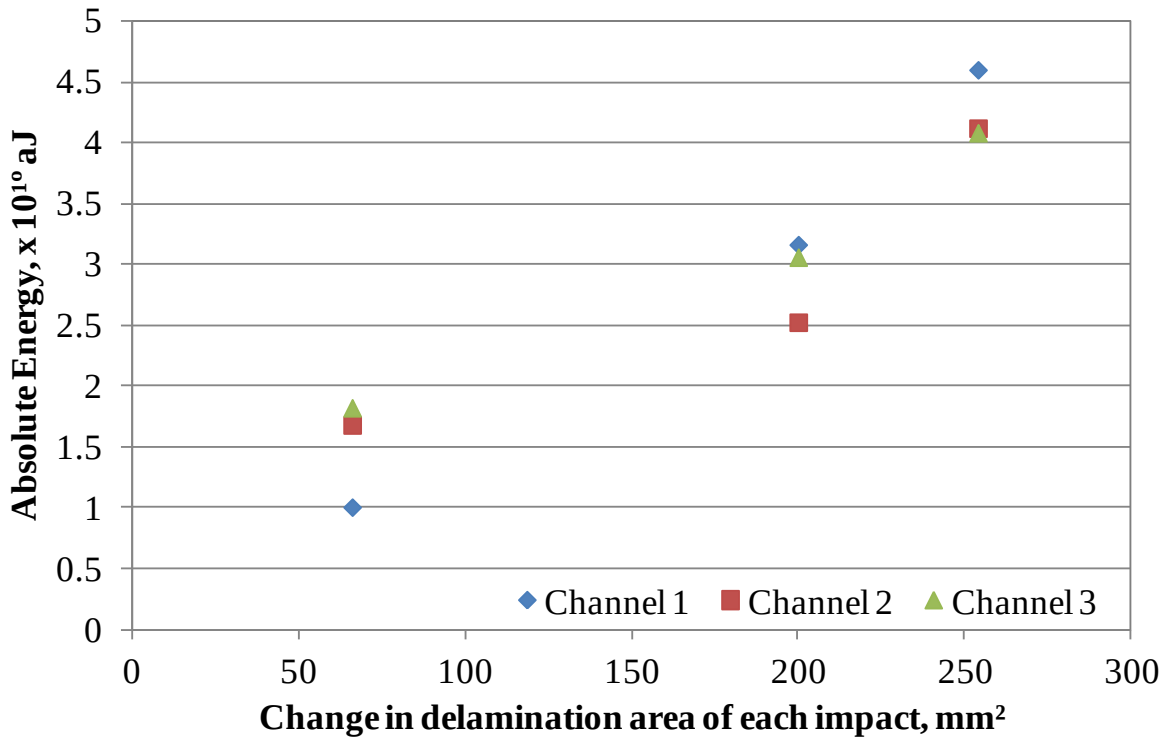

Figure 3-22. Absolute energy trend of the AE data at the impact strike correlated with the change delamination area.

Figure 3-23 shows the average cross correlation coefficients of the waveforms recorded as the baseline and after each impact. These particular waveforms are cross correlated to the first waveforms within their data set. For example the first baseline waveform was used to correlate to all other baseline waveforms. The cross correlation coefficient is now correlated against the delamination area as this was quantified after each impact using a C-scanner. This figure shows that the repeatability of the pulse and receive configuration for each data set is very high, the maximum error from the figure is 0.00065. This gives a large confidence level that the waveforms that are recorded as a new data set are very similar and there is no significant change in these waveforms, therefore suggesting the pulse/receive configuration has not altered.

Figure 3-24 shows the average cross correlation coefficients for 100 waveforms when correlated to the baseline waveforms and shows that as delamination area increases there are changes in the waveforms when compared with the baseline waveforms. The changes in the waveforms after each impact must be due to the presence of damage because the waveforms collected within each data set are almost identical showing the source is repeatable. The cross correlation coefficient becomes less as the impact damage increases, at the largest delamination area of 520mm^2 the average cross correlation falls to 0.8, showing that this technique can detect damage in this configuration. This technique also demonstrates the ability to detect small delamination areas, however after the first impact which caused a delamination area of 66mm^2 the cross correlation coefficient falls from 0.999625 to 0.997448. Although this fall in correlation lies outside the maximum error of 0.00065 found in each data set, careful consideration would be necessary in order to deduce that damage is present. It also depends on the application, in some cases a delamination area of 66mm^2 may be insignificant however in the cases where any level of damage needs to be detected the cross correlation technique may not be best suitable.

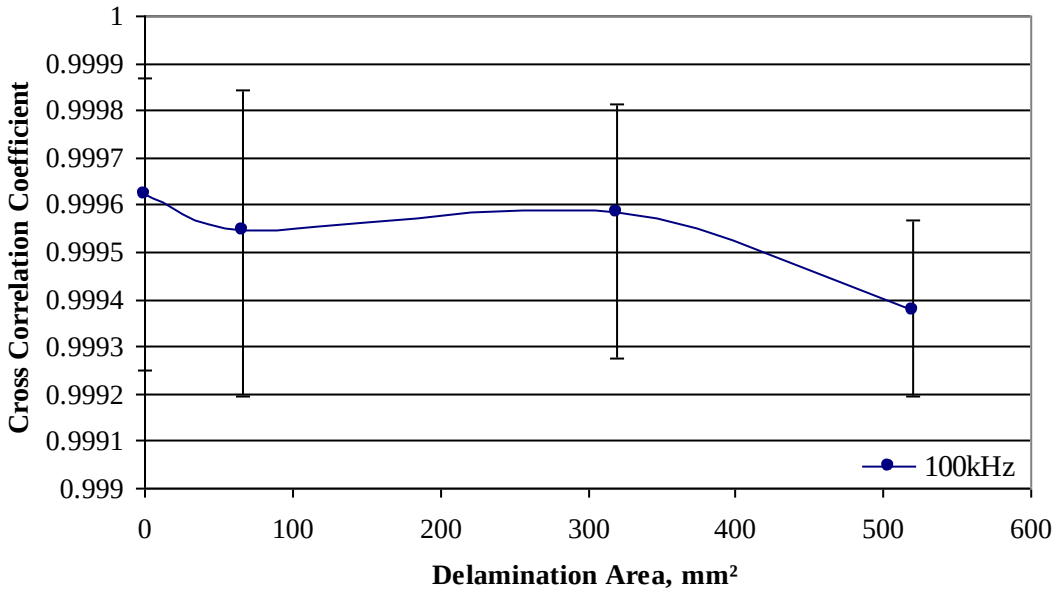

Figure 3-23. Average Cross Correlation the baseline and impact damage waveforms correlated within each data set.

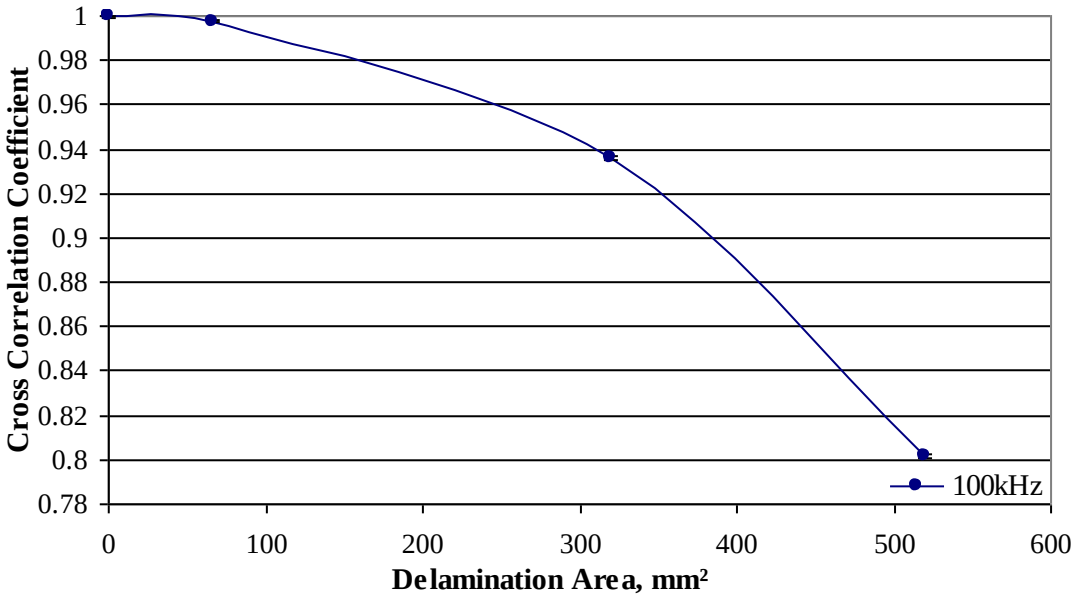

Figure 3-24. Average Cross Correlation the baseline and impact damage waveforms correlated to the baseline waveforms.

3.3.1.4 Conclusions

The AU technique utilising a cross correlation technique for damage detection investigations demonstrated a very simple technique for the detection of damage within a composite plate. The findings show that the cross correlation technique could detect a change in the signal even when a 1mm drill bit was used. Overall the 300kHz signal was the best for detecting damage and this is probably due to the frequency of the pulsed wave being close to the resonant frequency of the transducer. Also the frequency which the energy travels in the plate due to the thickness of the specimen will also have an effect. However no quantification of damage size and fall in cross correlation could be drawn because the amount of damage was not known.

The passive and active health monitoring of carbon fibre panels subjected to impact damage has been demonstrated. Both the AE and AU techniques were able to detect damage in the form of delamination area, quantification of the damage was enabled by utilising a C-scanner. The cross correlation technique was able to detect changes in the received waveforms due to the presence of a delamination, however further work is required to improve the sensitivity of this method, as significant changes in the cross correlation coefficient were only found at the more significant delamination areas. An approximately linear relationship was found between the absolute energy of the impact AE waveforms and the change in the delamination area. This could allow a prediction of the approximate size of

the defect area due to the energy realised. However more data would have to be collected in order to further establish this relationship.

3.3.2 Aluminium 2024 Complex Geometry Fatigue Investigation

3.3.2.1 Introduction

Detecting of fatigue cracks using SHM techniques for the aerospace industry is of paramount importance, therefore an investigation into detecting cracks in complex aerospace aluminium specimens was conducted using the AIC delta T mapping techniques. This was compared with the conventional TOA and delta T mapping technique to assess the improvements of the improved technique over the previous two techniques.

3.3.2.2 Experimental Procedure

Two complex geometry specimens were manufactured from aerospace grade aluminium 2024-T3, the specimens dimensions were 370x200mm with a thickness of 3.18mm. The specimens had a series of differing diameters holes machined around the horizontal and vertical centre lines of the specimens which is shown in Figure 3-25. This created a complex geometry specimen in order to assess performance of the TOA, delta T mapping and AIC delta T mapping techniques. The specimens also had a series of holes machined at either ends of the specimens in order to attach 5mm steel plates either side of the specimen to distribute the load into the specimen from the central 20mm loading pin which can be seen in Figure 3-26. The final experimental set-up of the specimens can be seen in Figure 3-27. M10 bolts were utilised to clamp the two steel mounting plates either side of the specimen, which are not shown in the figure. In order to determine the fatigue loading regimes of the specimen a finite element analysis was conducted using Patran/Nastran. The material properties for the 2024-T3 aluminium can be seen in Table 3-3. A static tensile model was created in Patran/Nastran and showed for a 25kN load resulted in a Von Mises stress calculation of 313MPa in the thin webbed sections and is shown in Figure 3-28. This is above the yield stress of the material and would therefore give a relatively quick test duration. The results of the FEA analysis is shown in Figure 3-28 and after consideration a maximum loading regime of 0.25kN to 25kN was decided upon.

Table 3-3. Material properties of 2024-T3 Aluminium

Young's Modulus	73.1GPa
Poisson's Ratio	0.33
Density	2780 kgm^{-3}
Tensile Yield Strength	290MPa
Ultimate Tensile Strength	440MPa

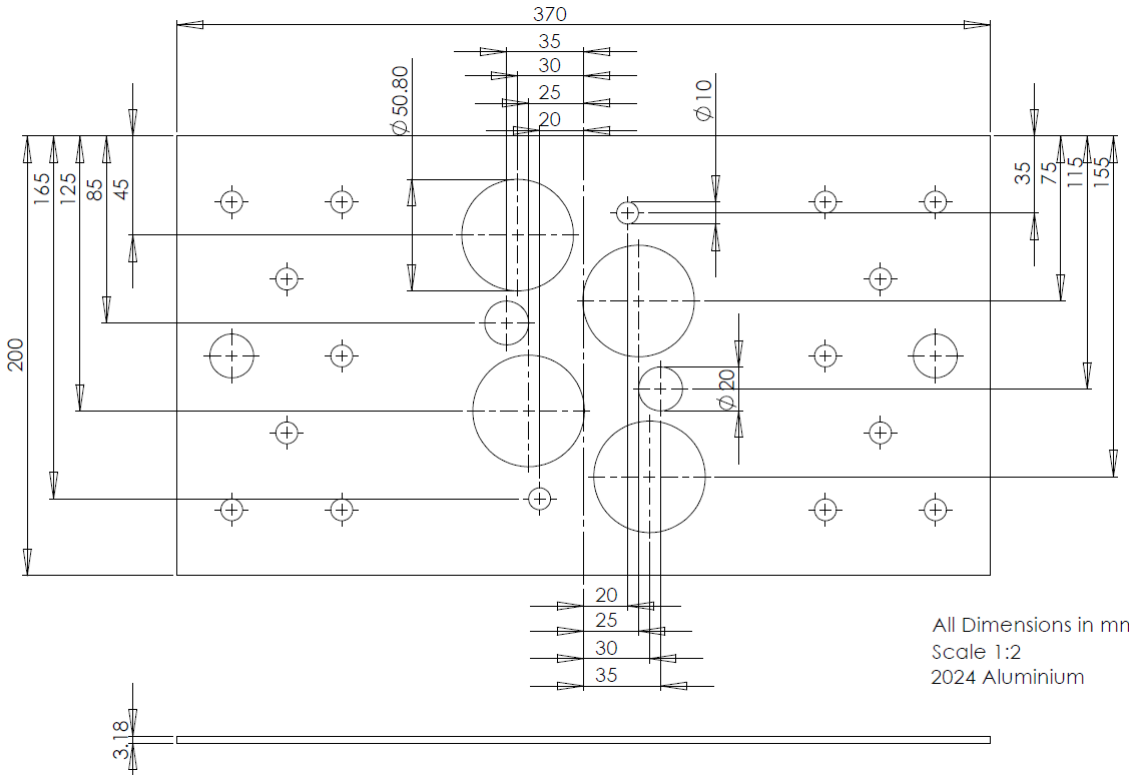

Figure 3-25. Location and dimensions of the central machined holes

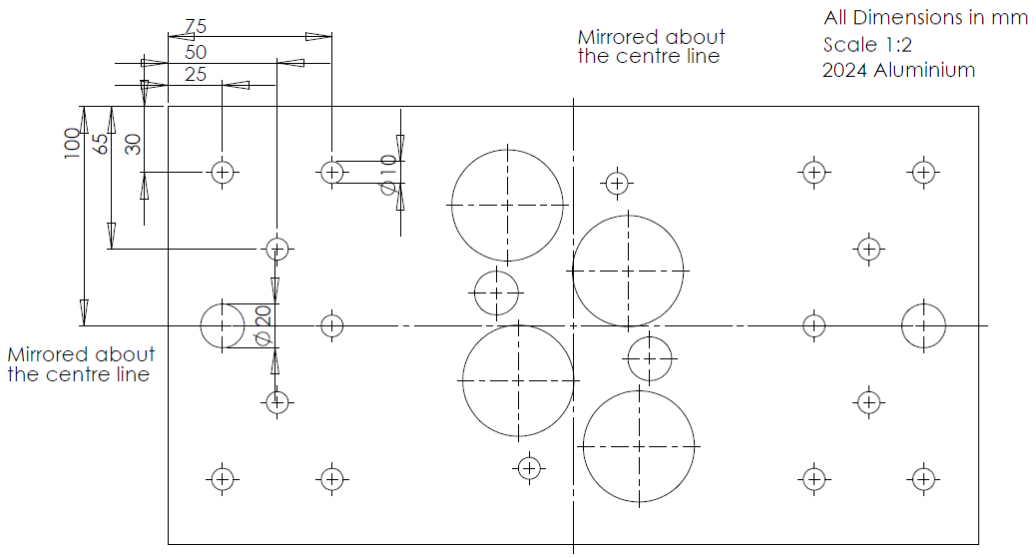

Figure 3-26. Mounting plate dimensions for each specimen

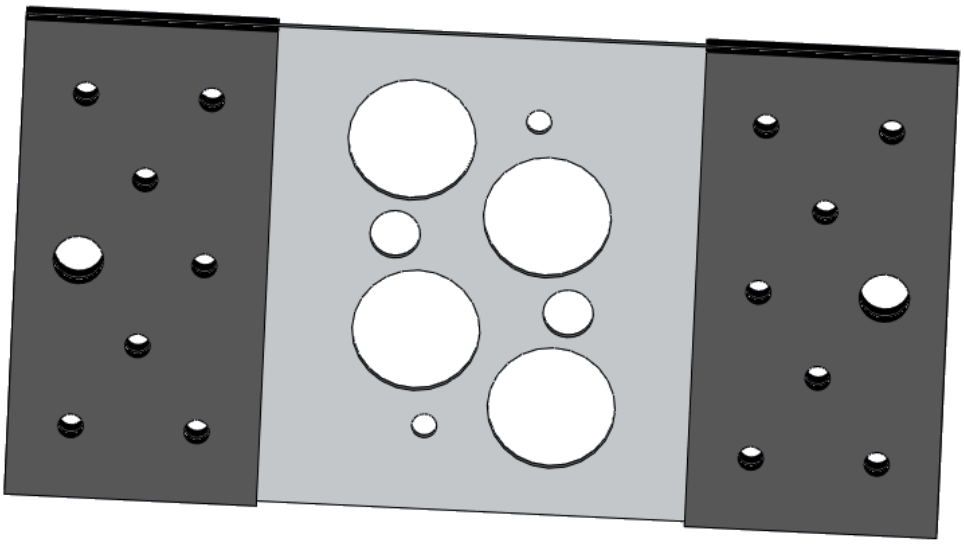

Figure 3-27. Final experimental specimens with load mounted plates attached

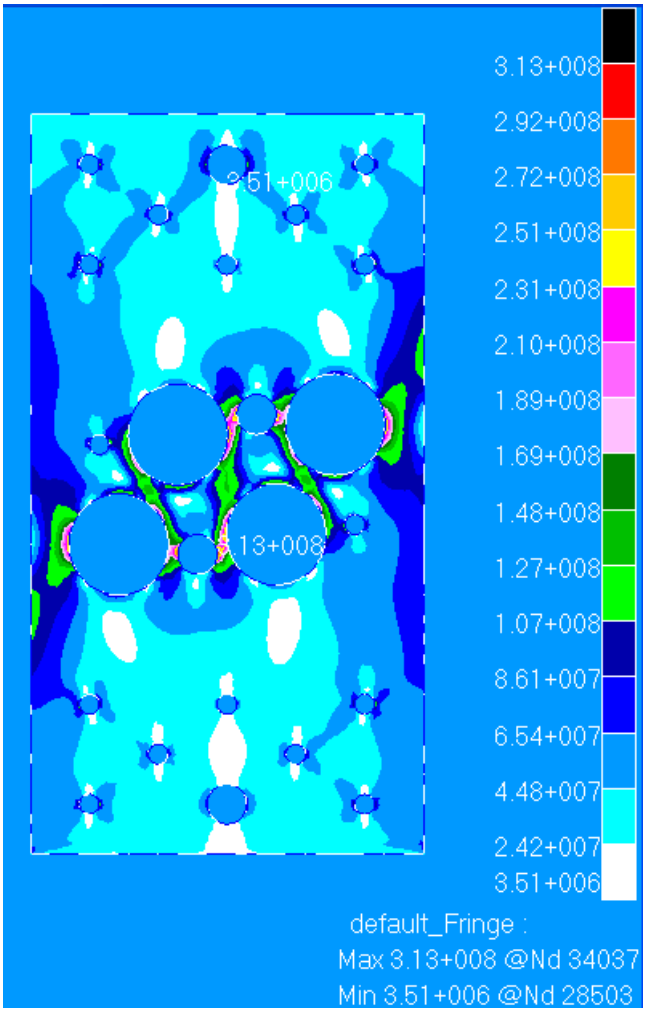

Figure 3-28. FEA analysis of the experimental specimens

Figure 3-29 shows the two specimens used for the fatigue investigations in complex geometry specimens. A variety of commercial AE transducers were used on the two specimens to see which would be most suitable for full scale monitoring of aerospace structures. For specimen one, eight Mistras transducers were utilised; four Nano-30s which were adhered on the front face of the specimen and four WD transducers on the rear face in similar positions to that of the Nano 30s. Nano 30s have physical size of 8 x 8mm (diameter x height) and a working frequency of 125 to 750 kHz. They are a resonant transducer but have a broad band response inside the working range of the transducer. The WD transducers are physical larger with a size of 18 x 17mm (diameter x height) and have a working frequency range 100 to 1000kHz again these transducers are resonant however also have a flat frequency response outside the resonant frequency. All eight transducers were connected to Mistras 0/2/4 pre-amps which had a frequency filter of 20 kHz to 1MHz. The delta T grid on specimen one covered an area of interest of 200mm x160mm and had a

resolution of 10mm. For the second specimen eight transducers manufactured by McWade were utilised, four 150 kHz resonant transducers were mounted on the front face and four 300 kHz transducers were mounted on the rear face. Although no further information is available on the frequency response of these transducers, it was thought that they are true resonant transducers with a sharp fall in response outside of the optimum frequency. These transducers were connected to McWade PA330 pre-amplifiers with the correct frequency rating. For the 150Khz pre-amplifier the nominal frequency response is very narrow at 100-200KHz and the 300KHz pre-amplifier also has a narrow working frequency of 200-400KHz. The delta T grids for specimen 2 covered an area of interest of 200x120mm. Grid resolutions of a maximum of 10mm and minimum resolution between 2 to 5mm were used for the mapping techniques. All transducers were adhered to the panel using a silicon RTV (Loctite 595) and left to cure for at least 24 hours before commencing the testing regime.

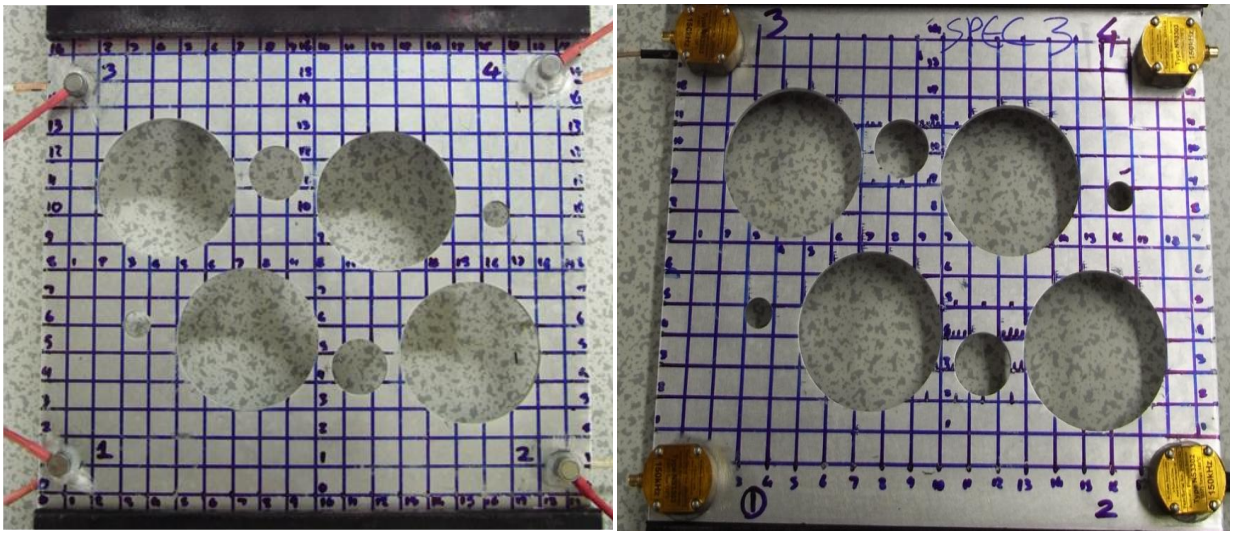

(a) (b)

Figure 3-29. Experimental set-up for (a) specimen 1 and specimen 2

A Mistras PCI-2 system was used to record all AE that were emitted under fatigue loading for both specimens. The same acquisition settings were used for both tests and are outlined in Table 3-4. Before testing commenced 5 H-N sources were used at each node position within the grid to generate arrival times at all of the transducers, this was undertaken in order to create the data required for both the delta T and AIC delta T mapping techniques. After the delta T map data had been collected a series of H-N sources were recorded at random positions on the grid in order assess the performance of both delta T programmes and to make sure the data had been collected correctly. During testing the conventional TOA location algorithm built into the software was utilised and the data was then post processed using both the delta T algorithms. At this stage in the development of the programmes the

process cannot be completed real time. Each specimen was subjected to slightly different testing regimes which are outlined in Table 3-5 and Table 3-6 respectively. Both specimens had bedding in periods up to a peak load of 15kN, this way to make sure that there were no noise issues under loading. The aim of the experiment was to grow a fatigue crack in a relatively short time period due to time constraints of the acquisition system and load machine usage and hence why the peak load was gradually increased during the testing procedure.

Table 3-4. PCI-2 hardware acquisitions settings for fatigue test programme

Threshold	40dB
Pre-amp Gain	40dB
Analogue Filter	100khz - 2MHz
Sample Rate	2MSPS
Pre-trigger length	500µs
Waveform length	3k

Table 3-5. Loading regime for specimen 1

Fatigue loading, kN	Frequency, Hz	Approximate number of total completed cycles
0.25-15	2	7000
0.25-20	2	18000
0.25-22	2	76000
0.25-24	2	96000

Table 3-6. Loading regime for specimen 2

Fatigue loading, kN	Frequency, Hz	Approximate number of total completed cycles
0.25-5	2	7000
0.25-15	2	26000
0.25-20	2	39000
0.25-22	2	51000
0.25-24	2	116000
0.25-24.5	2	148000
0.25-25	2	163000

3.3.2.3 Experimental Results and Discussion

Figure 3-30 shows the resulting fatigue crack for specimen 1 after testing was completed, for specimen one analysis of the failure area suggested a small fatigue crack started at the thin section on the right hand side which propagated a small distance before a

rapid failure, this in turn led to a rapid failure of the other thin section on the left in the figure as no evidence of fatigue crack was seen through visible observation. Visual observation of the specimen was conducted throughout testing, however no damage was observed at the last inspection prior to failure. This suggests the damage propagated and failed within 20,000 cycles. The fatigue crack initiated in the region of higher stress around the thin webbed section between the larger and smaller diameter holes, this was predicted by the FEA analysis seen in Figure 3-28

For ease of representation all further figures regarding AE location results are presented in terms of spatial binning plots. The areas of interest for the two specimens were divided into 5x5mm sub-sections and the location data was interrogated to find the number of locations that occur in any particular sub-section. Once a location was found within a particular section the energy of the waveform event and an event number was recorded. If more than one event occurred in any given sub-section the summation of the total energy contained within the located events and number of events was recorded. The location of the crack is highlighted by the red line. Figure 3-31 shows the spatial binning plot in terms of the number of events located from the TOA technique. The figure shows a significant cluster of events near the top of the specimen in the range of 20-60 events it also shows that there is a saturation of less than 10 events across the majority of the specimens. The main cluster of located events is around 15mm away from the actual crack location, however the cluster itself is not densely populated and would be difficult to determine whether damage had actually occurred

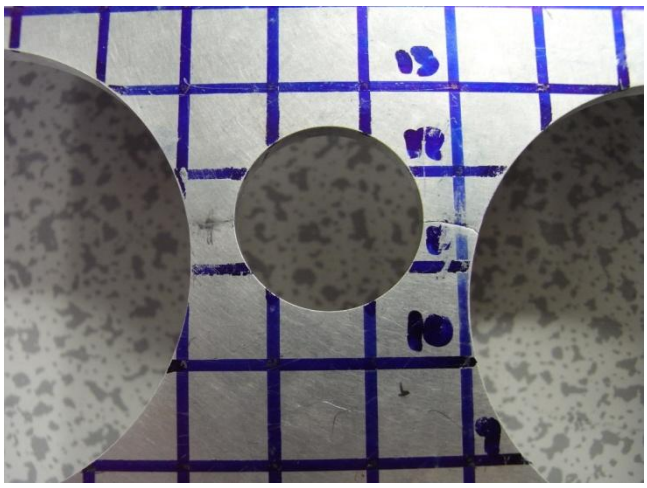

Figure 3-30. Final failure for specimen 1

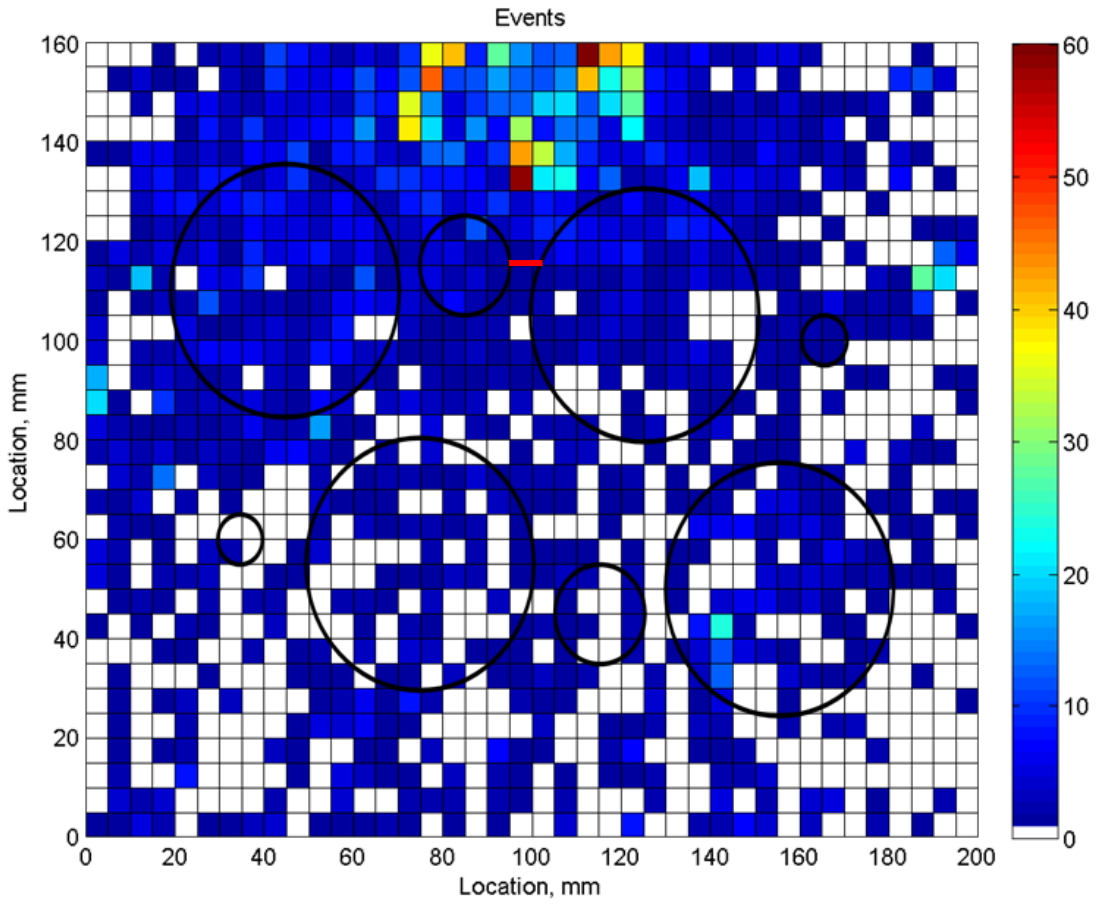

Figure 3-31. TOA binned event locations for the Nano30s

Figure 3-32 shows the a spatial binning plot for the energy contained within a particular bin and shows that the majority of the energy is contained within a cluster at a location of (95,130) and having a size of 5x10mm, the energy contained within this particular bin is in the range 1.8-2.0aJ, this shows for the saturation of the event spatial binning, only one particular cluster is due to these high energy events which are attributed to possible crack growth or initiation. This particular energy cluster is approximately 15mm away from the right hand side thin section fatigue crack. In both figures it should be noted that no significant activity was located at the left hand thin web section which suggests it was a rapid failure of that section. Both figures show the errors in location when assuming a constant wave velocity in such a complex specimen, it suggests that interrogating this specimen with this technique alone would prove difficult to accurately determine the actual location area.

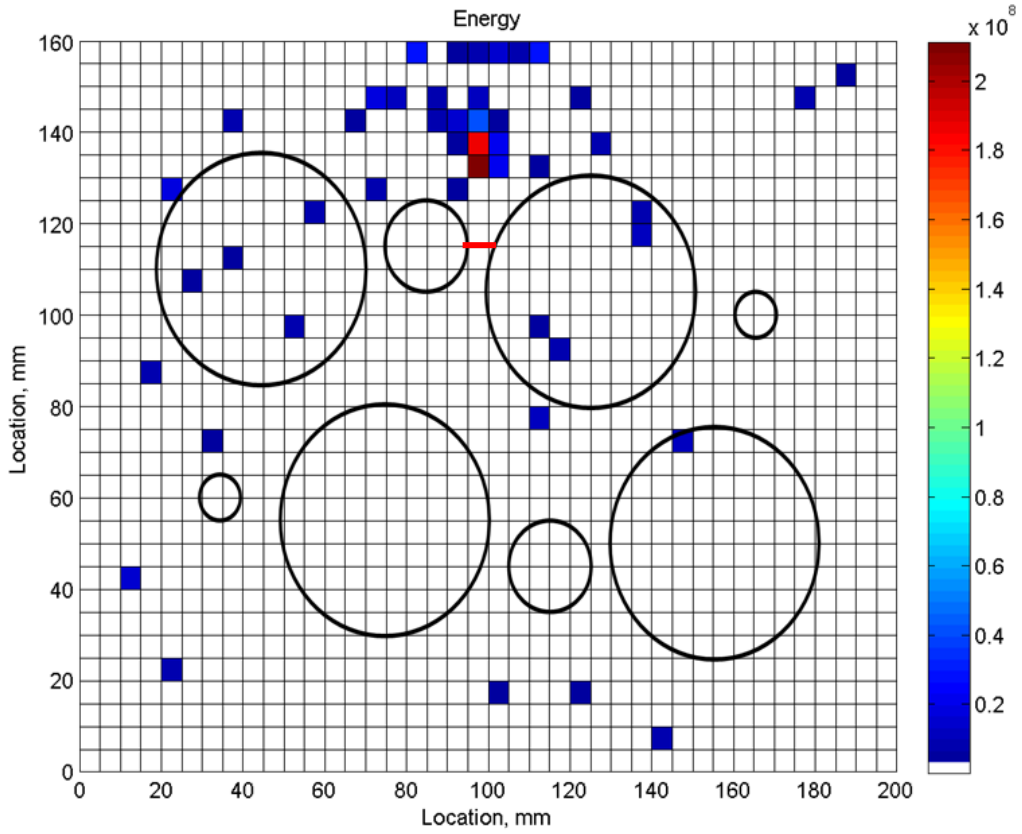

Figure 3-32. TOA binned energy locations for the Nano30s

Figure 3-33 shows the spatial binning of the located events using the delta T mapping technique it shows a significant number of events located at (95,150) with an area of approximately 30mm^2. The Closet distance from this cluster to the actual failure is around 35mm away, showing for this particular specimen and transducers that this technique is worse than the TOA method. It also shows the cluster is similar in size with that of the TOA technique, showing a similar level of accuracy. Due to the way the algorithm was written it is not possible to get an output of the energy attributed to a particular event and hence a spatial binning of the energy of the located events is not presented.

Figure 3-34 shows the spatial binning of the AIC delta T mapping locations and shows a large significant cluster centred around the actual failure location within this large cluster an area of approximately 15x40mm exists where the number of events ranges from 80 to 200. These smaller clusters start from the actual failure location area where an approximately total number of events of 400 events in an area of 100mm^2 are located. Another smaller concentrated number of events totalling around 800 events exist within a similar area at a location of (95,130). The number of located events is much higher within a

particular cluster than the other previous techniques showing higher accuracy in the technique.

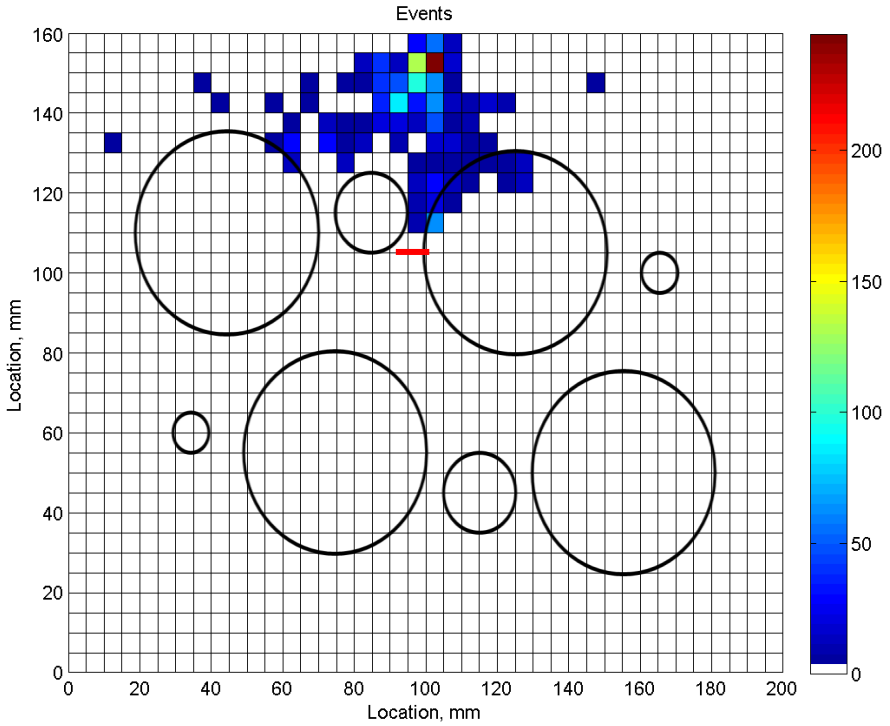

Figure 3-33. delta T mapping binned events locations for the Nano30s

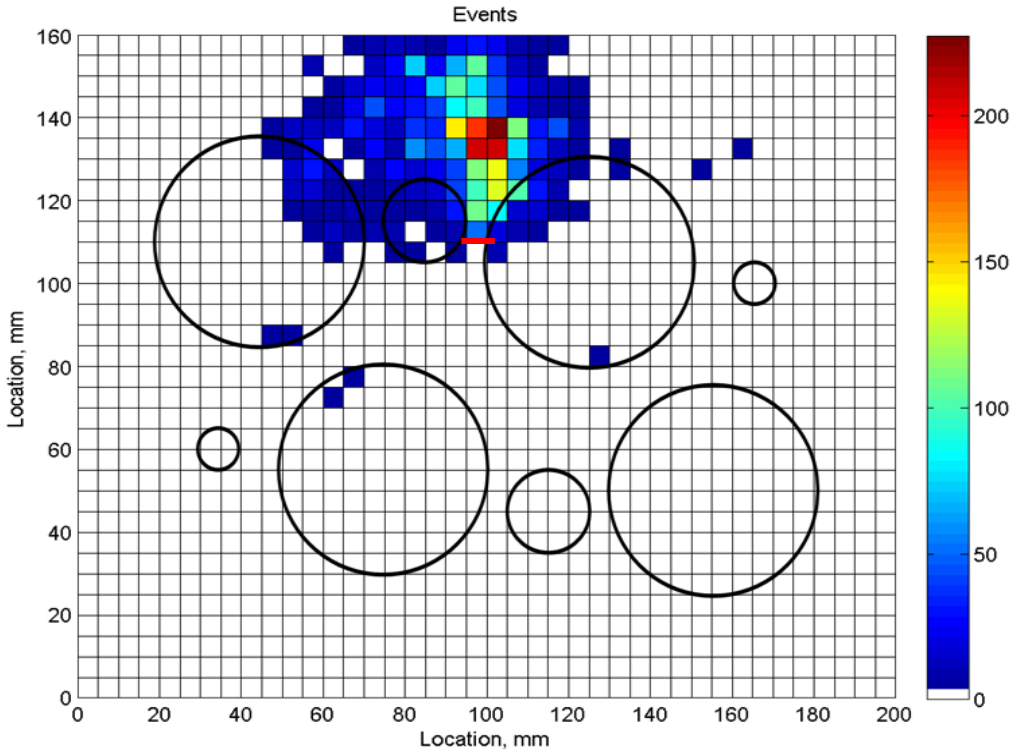

Figure 3-34. AIC delta T mapping binned events locations for the Nano30s

Figure 3-35 shows the AIC delta T mapping technique in terms of the energy contained within a particular spatial bin and from the significant cluster of located events from the previous figure it shows a significant amount of the energy is located at the failure site. The area of this cluster is 100mm^2 and has an energy level of 5 – 8aJ. Therefore this level of energy can be attributed to fatigue crack initiation, growth and crack face closure and shows the cluster with a larger number of events can be attributed to plastic deformation around the thin section of the web. This figure shows the accuracy of the improved delta T mapping technique with the integration of the AIC picker. None of these techniques have located significant activity at the left side failure site further suggesting this was a rapid failure when compared with the fatigue crack growth on the other thin section.

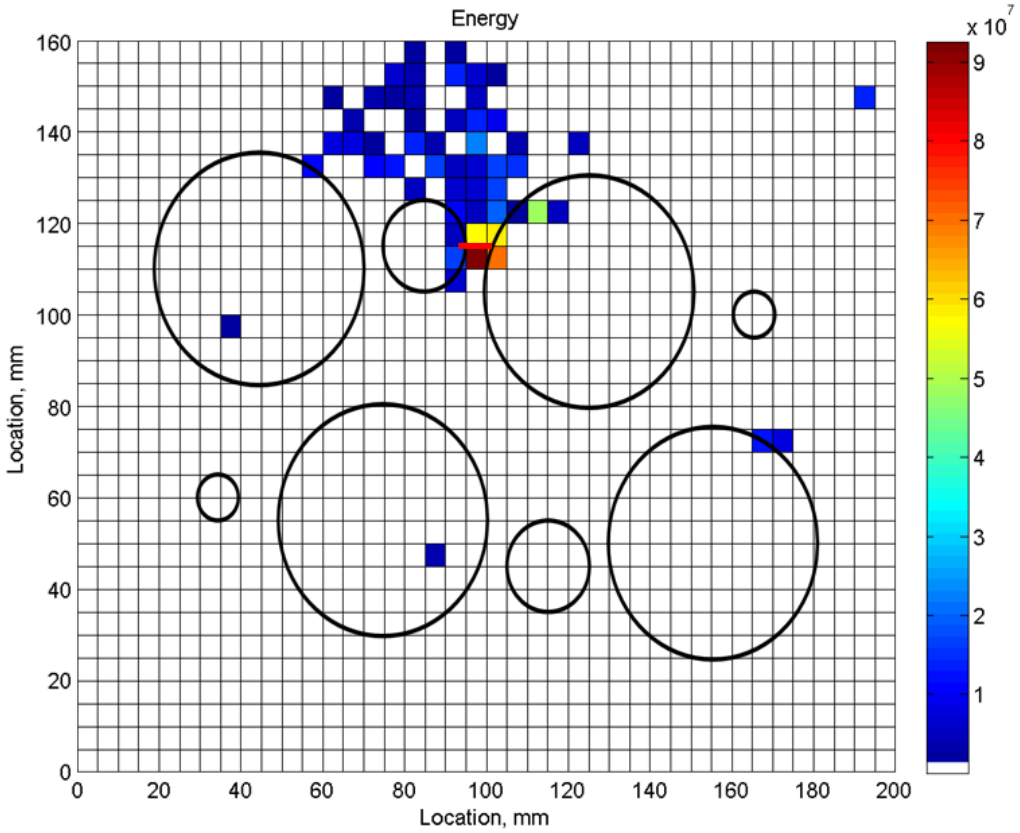

Figure 3-35. AIC delta T mapping binned energy locations for the Nano30s

Figure 3-36 shows the TOA locations in terms of the events contained within a spatial bin for the WDs transducers which were mounted on the rear face of this particular specimen. It shows that there were relatively large amounts of located events across the specimen with a large cluster around the vertical centre line of the specimen near the top edge of the area of interest. It shows that no significant amounts of events were located in the failure region when compared with larger cluster of events already discussed. Figure

3-37 shows the results of the spatial binning of energy contained with the TOA located events it shows that there was a significant amounts of energy located in a strip located at (100,120) with an approximate area of 125mm^2. The closest distance of this area to the failure location is only 5mm. It also shows that the rest of the event locations have relatively lower energy when compared with this certain cluster, suggesting that they have arisen from different source mechanisms. Overall these figures would suggest that for the TOA approach the WDs due to their frequency response are more accurate at determining the location of events with the most energy attributed to the fatigue crack growth.

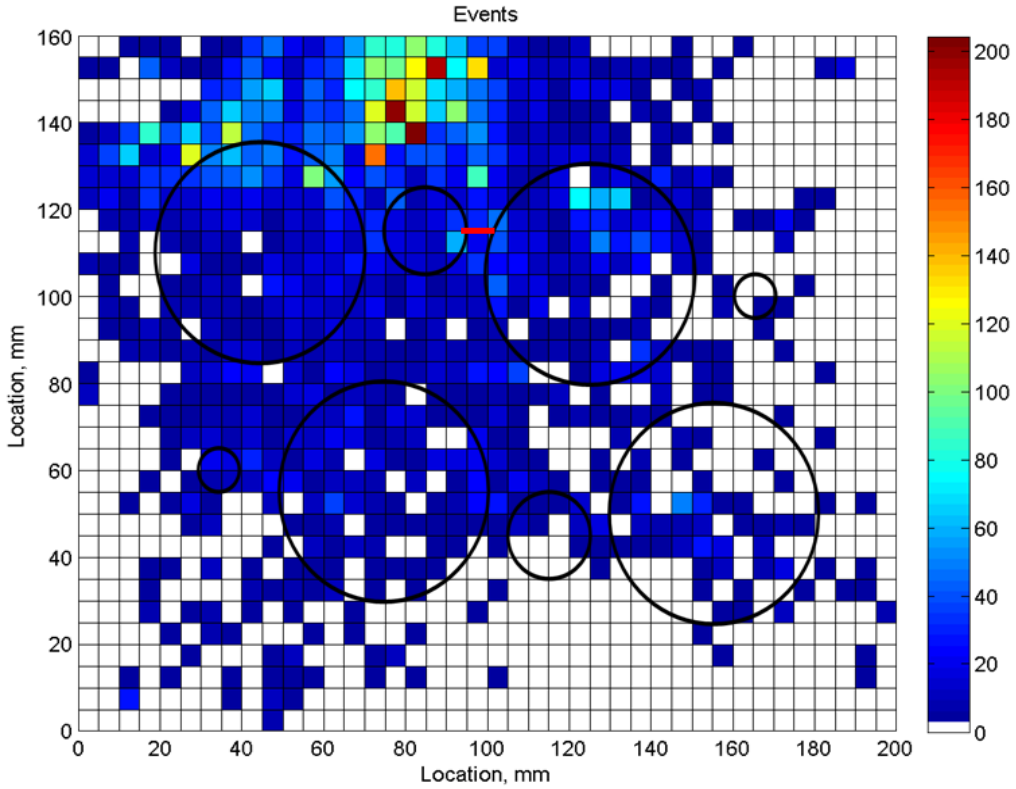

Figure 3-36. TOA binned events locations for the WDs

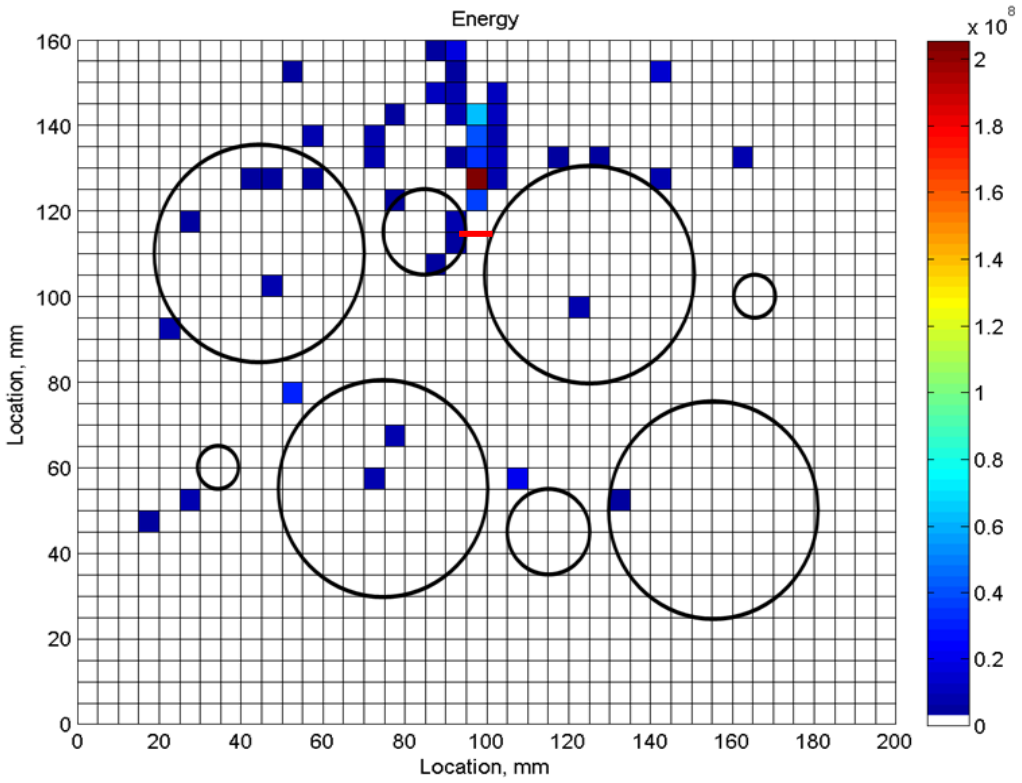

Figure 3-37. TOA binned energy locations for the WDs

Figure 3-38 shows the spatial binning of the located events utilising the delta T mapping technique for the WD transducers and shows the same level of locations when compared with the TOA technique. A significant cluster is located are above the failure site, which contains a large number of events, the approximate centre is (90,130), therefore giving an distance error of 30mm. Unfortunately no comparison of the energy contained within these events can be conducted due to the limitation of the algorithm.

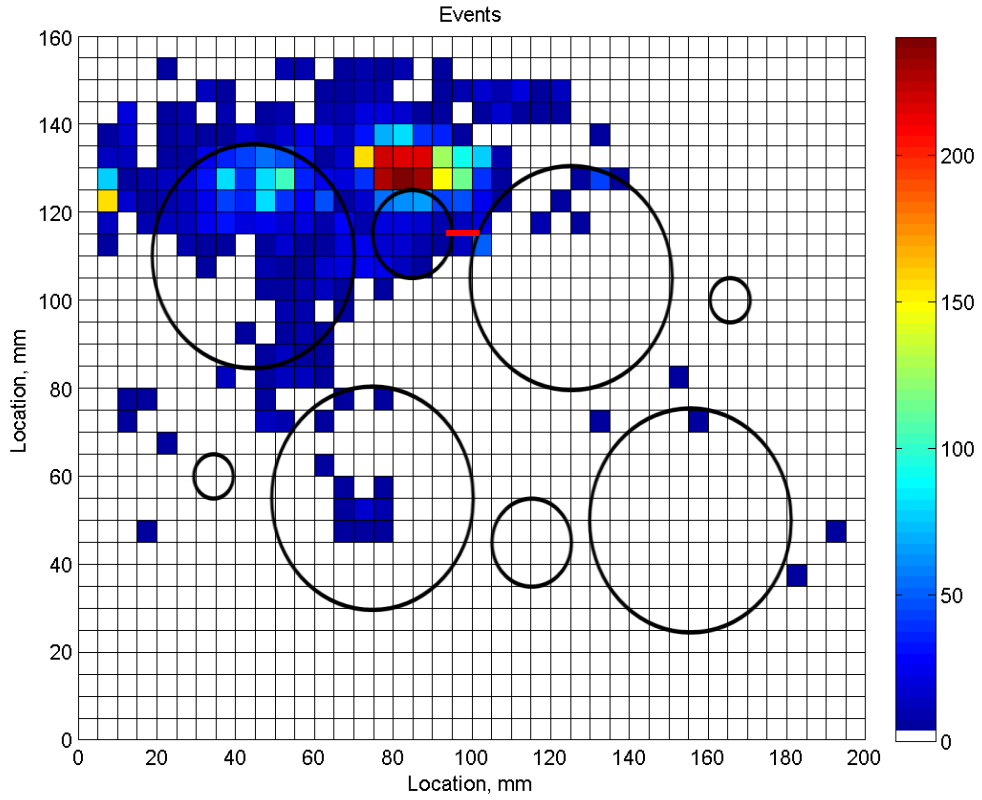

Figure 3-38. delta T mapping location binned energy results for the WDs

Figure 3-39 shows the spatial binning of the events for the AIC delta T mapping technique and shows a large significant cluster with approximately 1000 events being located at (80,125). This cluster of locations is located approximately in the centre of the two thin sections at a vertical distance of 10mm. The techniques show a significant improvement of the clustering of AE events when compared with both the TOA and delta T mapping techniques. Figure 3-40 shows the spatial binning of the energy contained with the located AE events for the AIC delta T mapping technique and although not as clear as the energy spatial binning of the Nano30s it still shows a significant amount of energy contained within locations at the failure site, however there are large energy events located at further distances from the fatigue crack growth area, however these might be necessary due to the fatigue growth but from other sources such as plastic deformation. Overall for all the results of the first specimen the AIC delta T mapping technique consistently located the fatigue crack growth in terms of events and energy on a spatial binning approach. The delta T mapping techniques did not perform as thought when compared with the success this technique had showed in locating damage in steel and composite complex specimens.

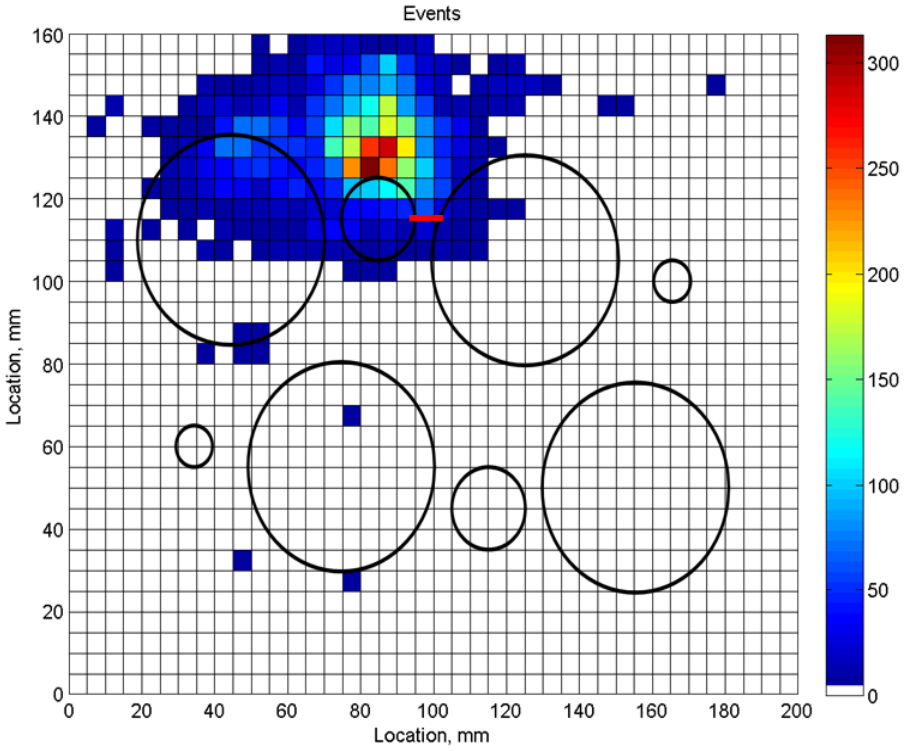

Figure 3-39. AIC delta T mapping binned event locations for the WDs

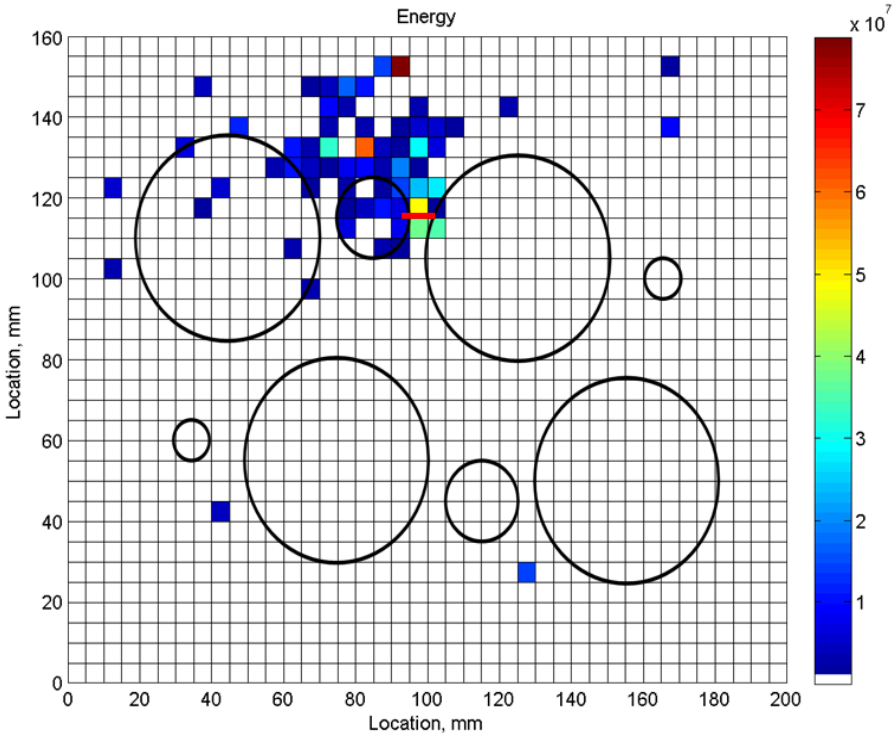

Figure 3-40. AIC delta T mapping binned energy locations for the WDs

Figure 3-41 shows the final failure mechanism for specimen two, a fatigue crack initiated at the right side thin section which propagated across the whole of that section, again there was no damage observed at the last inspection prior to failure, again suggested that the crack initiated and propagated fairly quickly within approximately 16,000 cycles, however testing was halted once the right side thin section had completely failed. Again the failure region agree with the area of higher stress concentration as predicted by the FEA analysis in Figure 3-28.

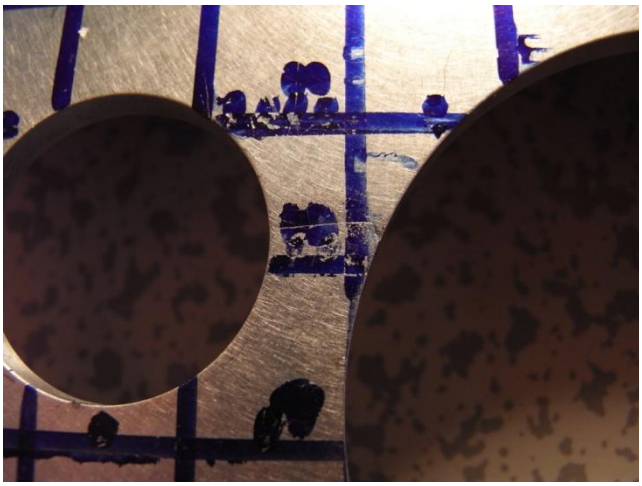

Figure 3-41. Final failure for specimen 2

The following figures show the located AE events for the second specimen which was monitored with 150kHz and 300kHz resonant transducers. The results shown here are for one particular data file where a typical AE analysis determined the final failure occurred, 4343 cycles were recorded within this particular data file. In addition to the previous methodology two AIC delta T maps were generated, the first with a resolution of 10mm and the other where a nominal resolution of 10mm was used for a the majority of the specimen, however a final resolution of 2 and 5mm was used in the predicted failure regions in order to draw a comparison of the resolution of the grids on the located events. Again the same spatial binning approach was used to determine significant activity in the panel. Figure 3-42 shows the TOA location in terms of the number of events contained within a particular spatial bin, the figure shows a sparse scattering of locations with no significant areas of interest indentified. Figure 3-43 shows the energy contained for the spatial binning for the TOA locations and again shows that no significant conclusions can be drawn as to whether there is significant damage has occurred in the panel.

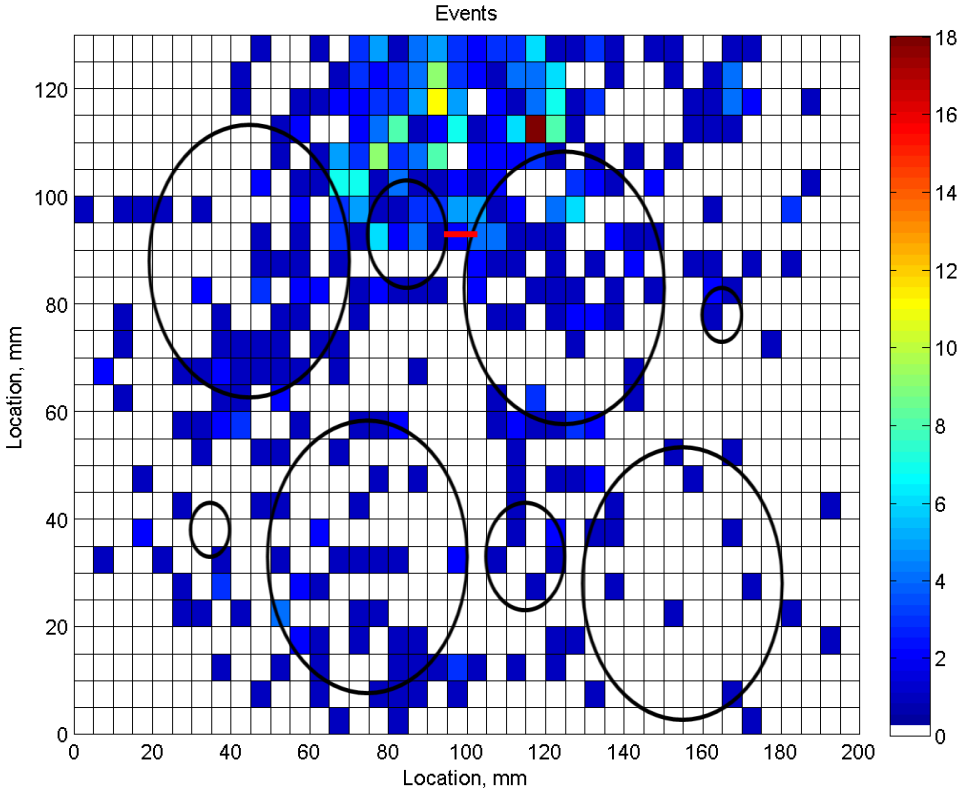

Figure 3-42. TOA binned events location for the 150kHz McWades

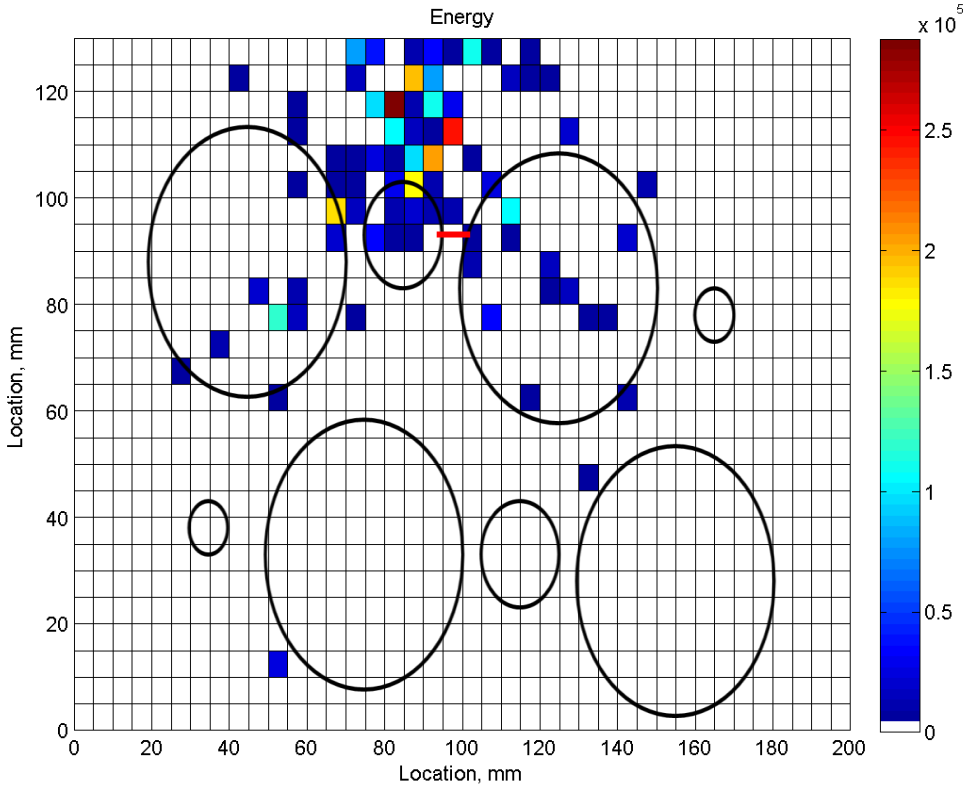

Figure 3-43. TOA binned energy location for the 150 kHz McWades

Figure 3-44 shows the located AE events utilising the delta T mapping technique again the results are presented in terms of a spatial binning of the events within that particular bin with a minimum resolution grid resolution of 10mm, these particular results show an improvement in locations over the conventional TOA technique with approximately 30 events being located in the region of the fatigue crack, however significantly more locations are located around 25mm away from the failure location. The overall clustering of these events is more compact than that of the TOA technique however it would still be difficult to determine any changes in the structure from the figure.

Figure 3-44 shows the results of the spatial binning in terms of the a minimum grid resolution of 10mm, again as for previous results the AIC delta T mapping technique gives a more accurate result with one large cluster of events in and around the actual failure region, with the most concentration of events in close proximity to the failure region. The region of densely populated AE events is located 20mm vertically from the area of the failure. Again this analysis shows a marked improvement over the previous two techniques enabling a more confident interrogation of the results.

Figure 3-46 shows the spatial binning of the energy contained within the located events again for a minimum grid resolution 10mm and shows for the large cluster of events the most energy contained within these located waveforms is excellently correlated to the failure region with a spatial bin of energy of approximately 2.75aJ being located in the exact region of the crack with a larger clustering of energy total approximately 6aJ in an area of 100mm^2 at a distance of 5mm away from the location of the fatigue crack. The energy of the crack growth shows significantly higher energy levels than that of any other noise source and hence could be utilised to determine significant damage within the panel.

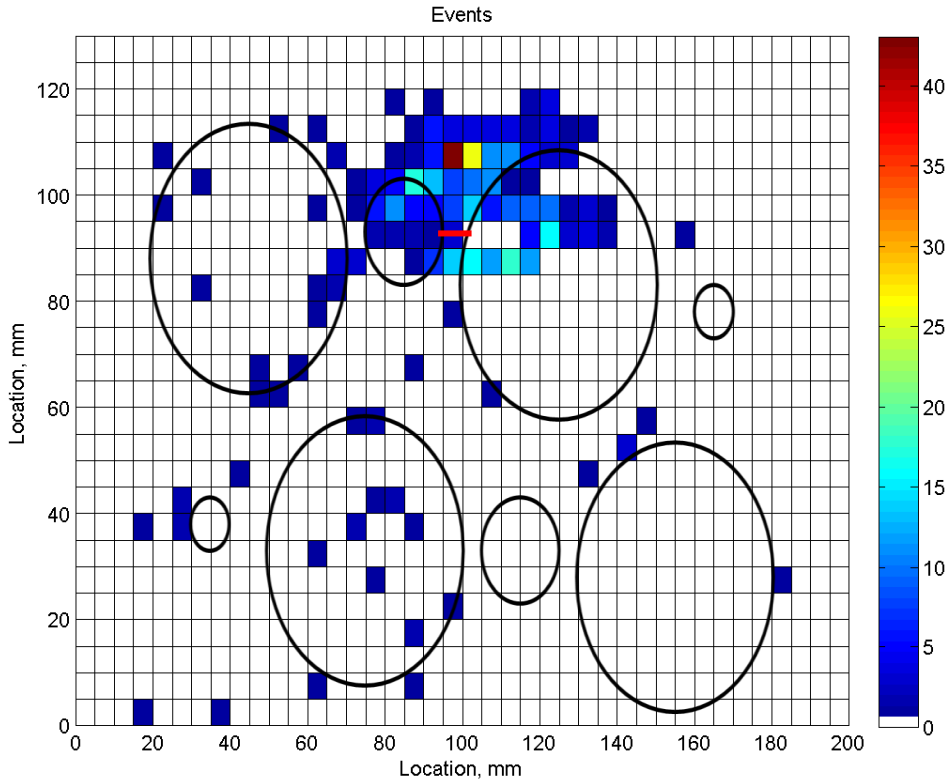

Figure 3-44. delta T mapping binned event location for the 150 kHz McWades

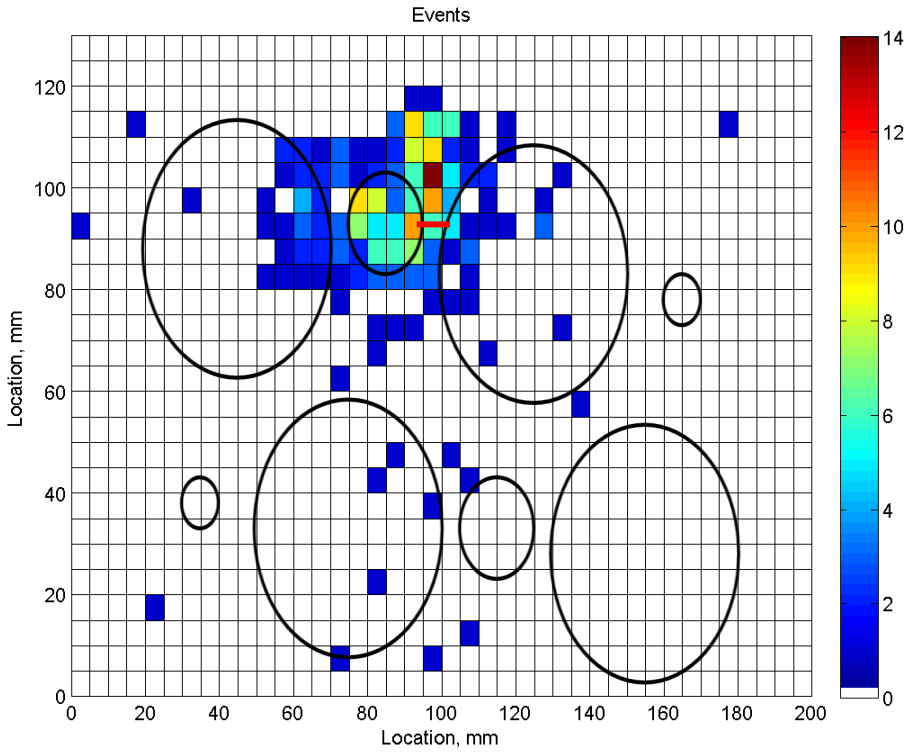

Figure 3-45. AIC delta T mapping binned event locations for 10mm grid resolution for the 150 kHz McWades

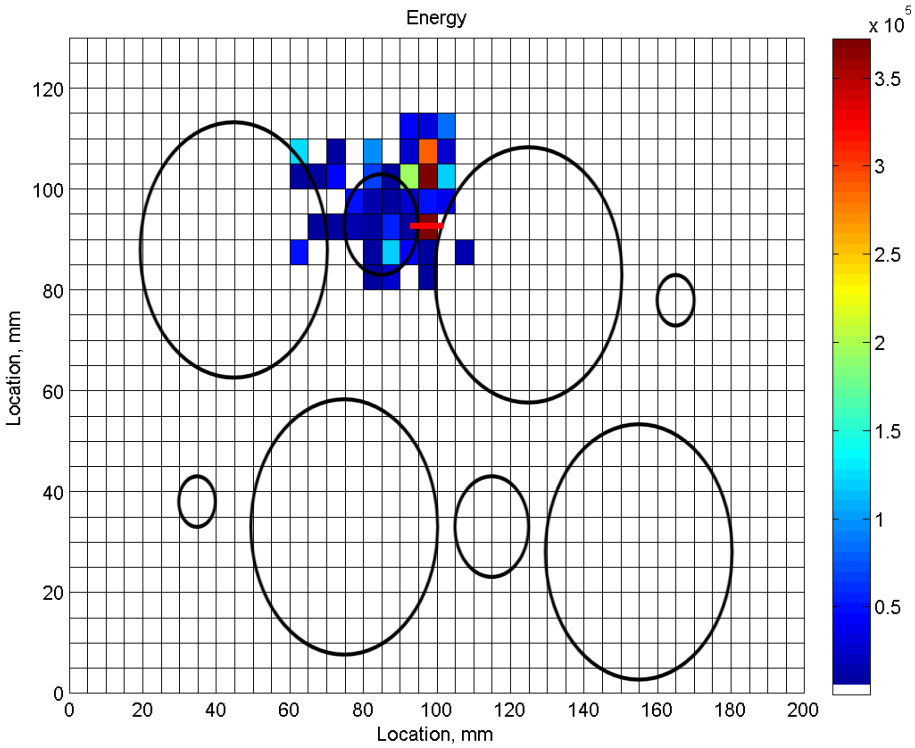

Figure 3-46. AIC delta T mapping binned energy locations for 10mm grid resolution for the 150 kHz McWades

Figure 3-47 shows the results of the spatial binning in terms of the events for a minimum grid resolution of 2 and 5mm respectively in the expected failure regions. Again as expected from previous AIC delta T techniques there is one significant clustering containing a high concentration of events of approximately 40 events being located 5mm away from the fatigue crack location. However it is only when considering the energy contained with these special bins which is shown in Figure 3-48 that excellent correlation between energy contained within the located waveforms and fatigue crack growth correlation. This shows that the energy from initiation crack growth, propagation and crack face closure is significantly higher than other sources.

Figure 3-49 shows the TOA location results for the 300kHz McWade transducers in terms of an event spatial binning and shows no evidence of a cluster with significantly higher levels of activity. There are a larger number of events being located at the top edge of the area of interest, however conclusions cannot be drawn about whether there is damage present in the material. The same can be said for the results of the energy spatial binning which is shown in Figure 3-50 and again shows signs of no significant activity with three spatial bins having significant energy of which the closest is 15mm away from the fatigue crack growth area. The TOA techniques for both specimens and for all transducers has been

undertaken and shows that for this particular complexity of geometry, no significant amounts of damage can be identified from the analysis of the located events.

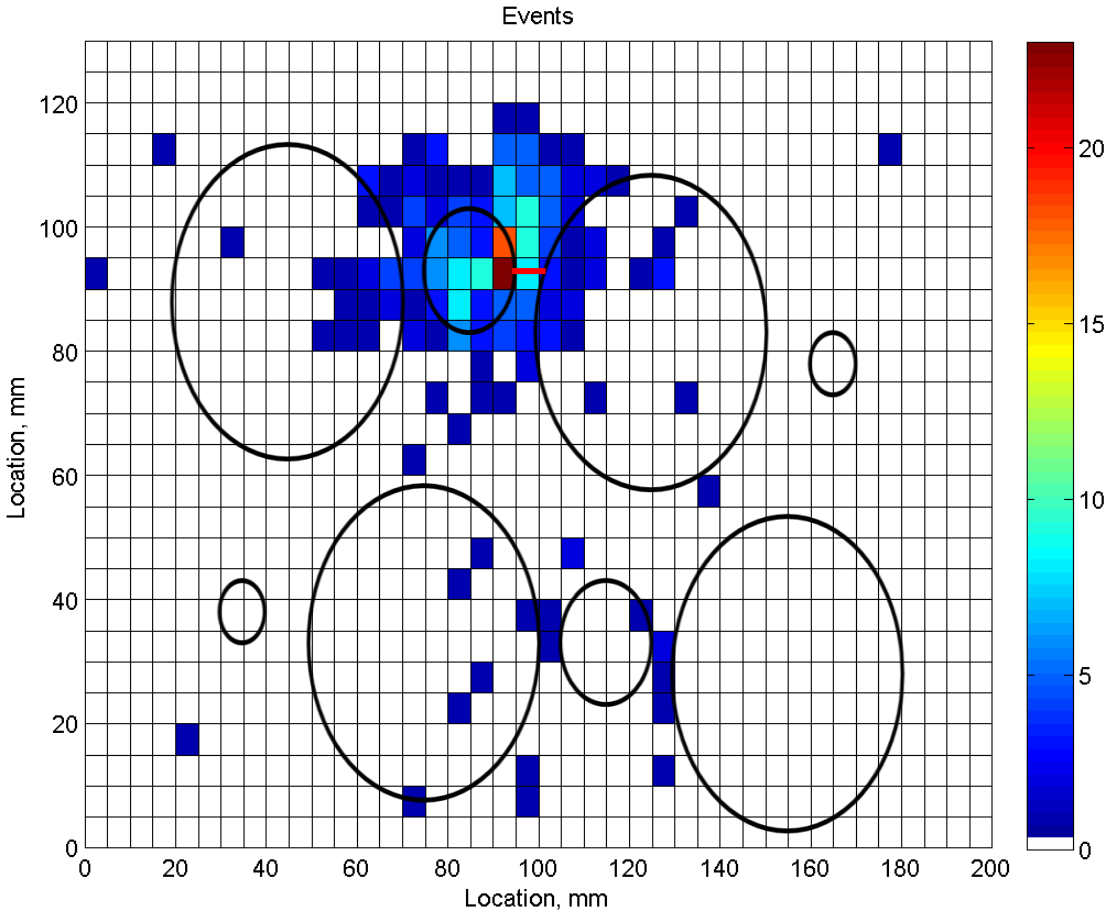

Figure 3-47. AIC delta T mapping binned event locations for a 2-5mm grid resolution in the expected failure regions for the 150 kHz McWades

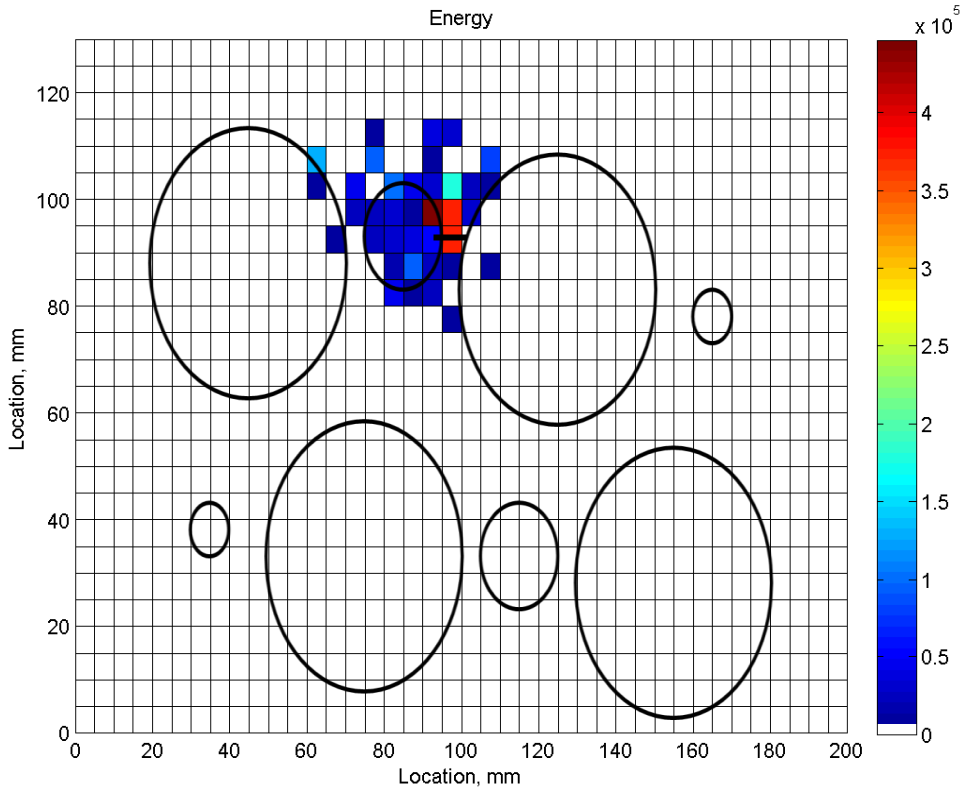

Figure 3-48. AIC delta T mapping binned energy locations for a 2-5mm grid resolution in the expected failure regions for the 150 kHz McWades

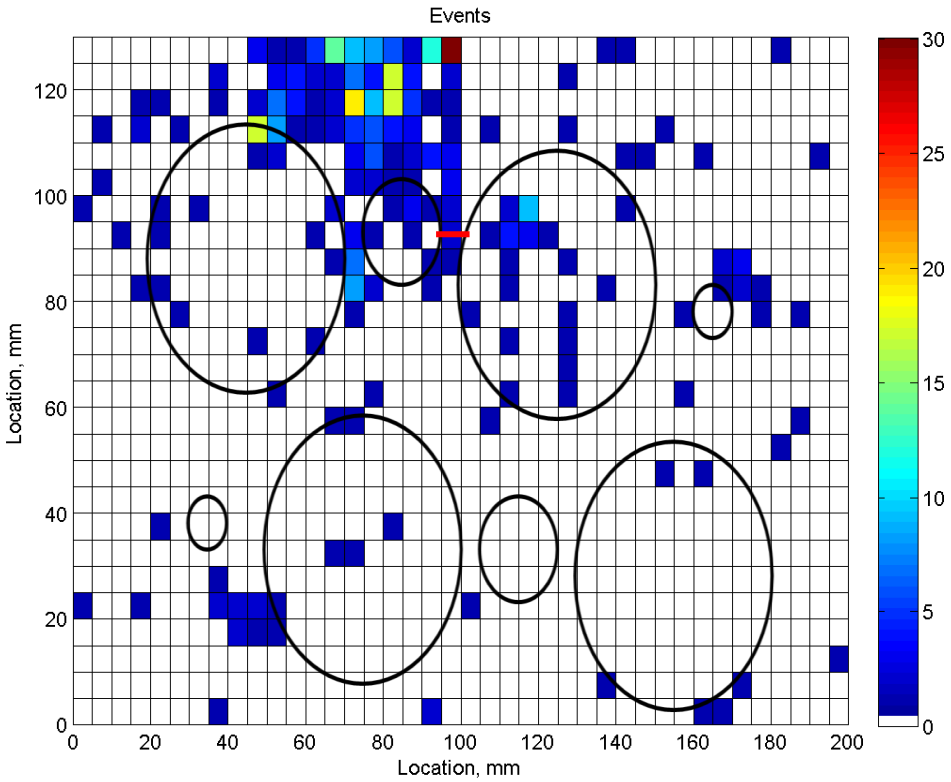

Figure 3-49. TOA binned event locations for the 300kHz McWades

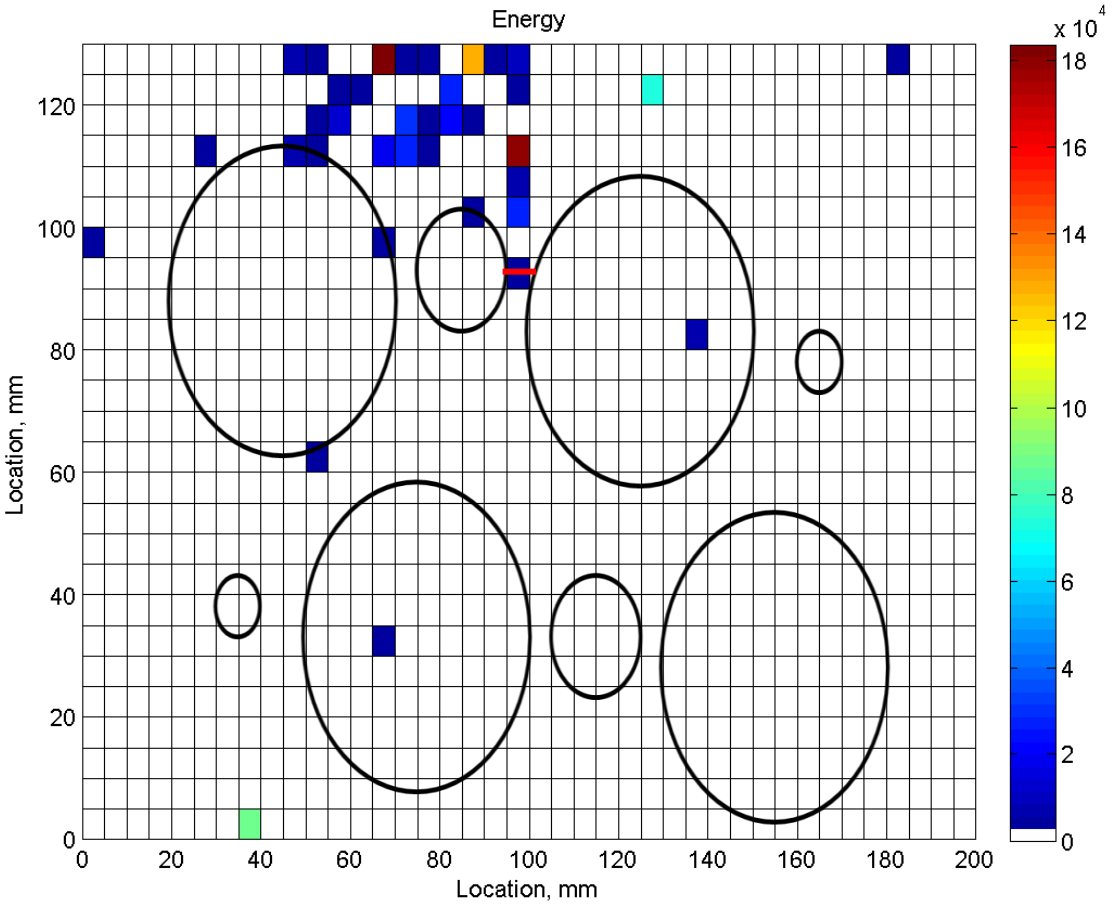

Figure 3-50. TOA binned energy locations for the 300kHz McWades

Figure 3-51 show the results for the delta T mapping techniques for a spatial binning of the located events. The figure shows no significant levels of activity as the maximum number of nine events in a particular bin and overall has located less events that the TOA technique, however this is not surprising as the delta T technique only locates event that have arisen from the area of interest where as the TOA technique can miss locate events close to or outside of the array of the transducers inside the area of interest.

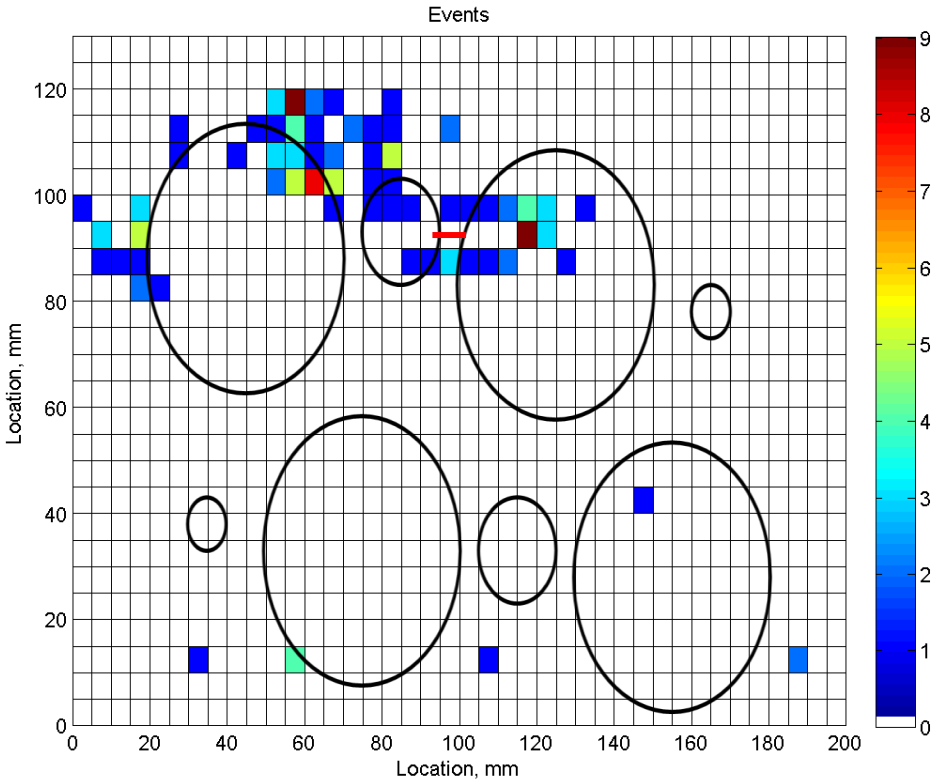

Figure 3-51. delta T mapping binned event locations for the 300kHz McWades for a 10mm grid resolution

Figure 3-52 shows the results of the spatial binning of the events for the 300kHz transducers for a minimum grid resolution of 2 and 5mm respectively in the predicted failure areas and shows an indication that damage may have occurred in the panel as there is a significant cluster of locations at an approximate distance of 5mm from the fatigue crack with a total approximate number of 25 events. Figure 3-53 shows the spatial binning of the energy contained within the located waveforms and shows that the higher levels of energy are being emitted from the crack region which are in the region of 1 to 5 $x10^5$ aJ, the figure shows that no other significant energy levels in the location results and therefore shows the correlation between the energy and the damage mechanisms. Figure 3-54 shows the event spatial binning of the AIC delta T mapping technique for a grid resolution of 2 and 5mm in the region of the expected failure and shows two significant cluster of locations one just to the right of the fatigue crack and second cluster located at a vertical distance of 20mm there are also several events located in the small diameter hole, again this shows the promise of this technique for detecting damage within a complex aluminium specimen. Again analysis of the data as a spatial binning of the energy contained with the located events, as shown in Figure 3-55, shows considerable energy levels of the located events in and around the crack growth region with the majority of this energy cluster is located in the small diameter hole

between the two thin sections on the specimen and shows an approximate location error of 5-10mm.

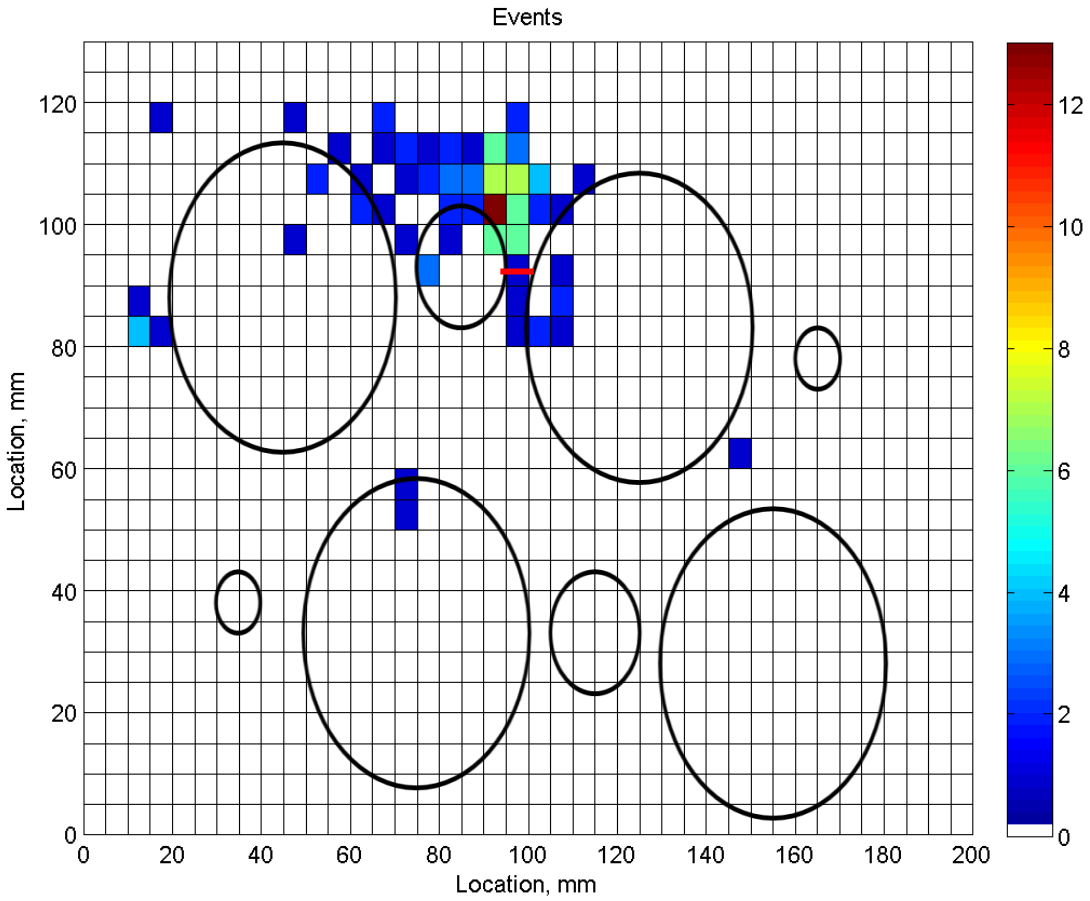

Figure 3-52. AIC delta T mapping binned events locations for the 300kHz McWades for a 10mm grid resolution

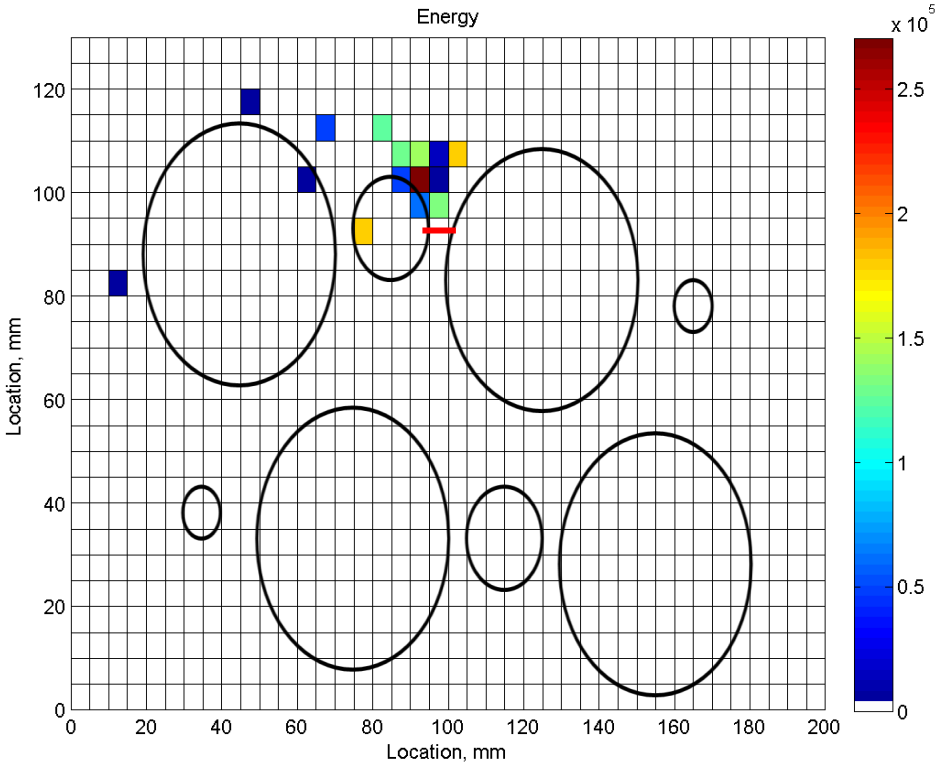

Figure 3-53.AIC delta T mapping binned energy locations for the 300kHz McWades for a 10mm grid resolution

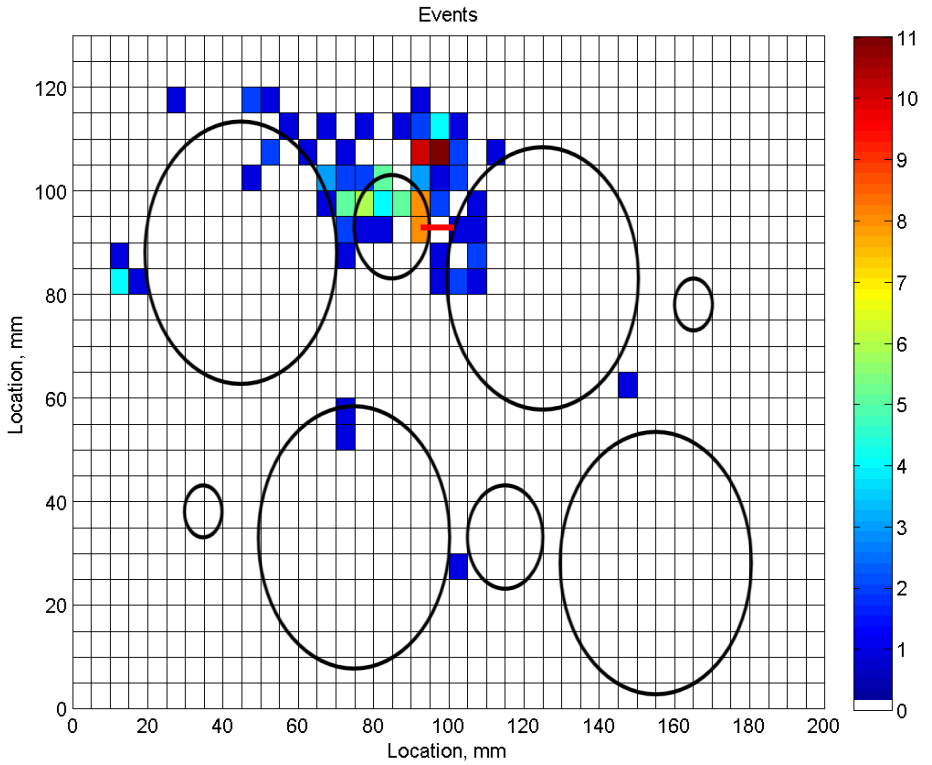

Figure 3-54. AIC delta T mapping binned event locations for the 300kHz McWades for a 2-5mm grid resolution

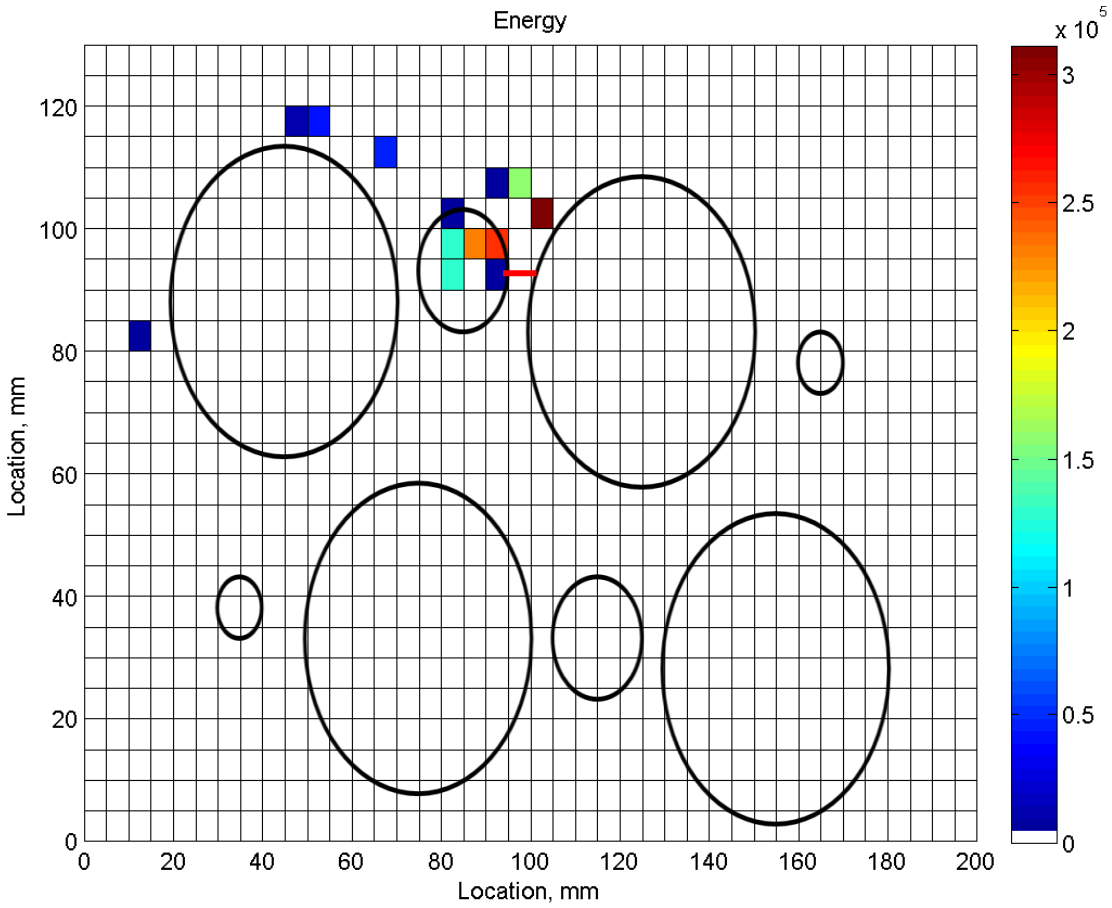

Figure 3-55. AIC delta T mapping binned energy locations for the 300kHz McWades for a 2-5mm grid resolution

The results for two complex tensile fatigue specimens have been presented, these specimens were monitored using a variety of commercial available AE transducers. Results of three different AE locations techniques have been presented for each different group of four transducers. Table 3-7 and Table 3-8 show a summary of the Euclidean distance errors for each specimen and transducer type for the event and energy spatial binning location results respectively. Clusters of high activity located results were selected for each spatial binning plots and the centre estimated. The Euclidean distance error was calculated from the crack location to the estimated cluster centre, if more than one cluster was present the top three were chosen. For all the location errors the first cluster is the most accurate and hence clusters two and three will not be discussed further. Table 3-7 shows for the Nano 30 transducers used on specimen 1, the AIC delta T technique shows no improvement over the TOA technique but a 15mm improvement over the delta T technique. For the WD transducers the AIC delta T technique shows an improvement of 3mm and 21mm over the delta T and TOA techniques respectively. For specimen two the estimated location results

with a 10mm grid resolution for the 150kHz McWade transducers show an improvement of 5mm and 17mm over the TOA and delta T mapping techniques. The finer grid resolution of 2-5mm shows an improvement of 2mm from the 10mm grid resolution, further work should be completed on grid resolution for further specimens to see if the extra time taken to collect training data is worth the overall improvement. For these results, for one specimen and sensor type it does not seem worthwhile. For the 300kHz McWades used on specimen 2 the AIC delta T mapping technique shows an improvement of 13mm and 22mm over the delta T and TOA techniques respectively. The finer resolution results show less accurate locations by 3mm again suggesting further work should be completed on grid resolution.Table 3-8 shows a summary of location results in terms of the energy spatial binning. It was not possible to produce results in terms of energy for the delta T mapping technique as the only input into the algorithm is the arrival time and channel number. For specimen 1 the Nano 30 and WD transducers show an improvement of 17mm and 14mm respectively over the TOA technique. The improvement in location for the 150kHz and 300kHz McWade transducers for specimen 2 is less with an improvement in location of 2mm and 8mm respectively over the TOA technique. The finer grid resolution shows an improvement of 7mm and 1mm respectively and again further work would be required to see if it is worth the extra time to acquire the training data.

Table 3-7. Euclidean distance errors for the events spatial binning location results

		Euclidean Distance Error, mm						
		TOA Clusters			Delta T clusters		AIC Delta T clusters	
		#1	#2	#3	#1	#2	#1	#2
Specimen 1	Nano 30	20	42	40	35	-	20	-
	WD	35	31	-	17	-	14	-
Specimen 2	150khz McWades - 10mm grids	24	25	-	12	11	7	-
	150khz McWades - 2-5mm grids	-	-	-	-	-	5	-
	300khz McWades - 10mm grids	32	35	52	23	42	10	-
	300khz McWades - 2-5mm grids	-	-	-	-	-	13	15

Table 3-8. Euclidean distance errors for the energy spatial binning location results

		Euclidean Distance Error, mm				
		TOA Clusters			AIC Delta T Clusters	
		#1	#2	#3	#1	#2
Specimen 1	Nano 30	20	-	-	3	-
	WD	18	-	-	4	36
Specimen 2	150khz McWades - 10mm grids	14	22	28	12	1
	150khz McWades - 2-5mm grids	-	-	-	5	-
	300khz McWades - 10mm grids	20	36	46	11	19
	300khz McWades - 2-5mm grids	-	-	-	10	12

3.3.2.4 Conclusions

In conclusion the AIC delta T technique shows an improvement in locating AE events due to fatigue crack growth. This is increasingly important when considering the complex geometric features of these specimens and inadequacy of the other techniques to be able to accurately and confidently determine damage in a structure. This is increasingly important when considering the increase of complexity again when considering structural health monitoring of actual aerospace structures. The improvements in the AIC delta T technique also when considering SHM applications means to achieve the same level of accuracy to that of the TOA technique transducers could be placed further apart to give the same level of accuracy, this would mean that the same amount of transducers could be utilised to monitor a larger area and hence reduce the cost of the transducers for full scale monitoring. Also reducing the weight of the system by reducing the number of transducer and amount of cabling

3.3.3 AE source location utilising delta T mapping in composite structures

3.3.3.1 Introduction

Having the ability to detect the early signs of damage is a important objective for SHM systems. Therefore an investigation using the delta T mapping technique to locate small amounts of damage in composite specimens was conducted. Also the robustness of

the technique was assessed which is important when considering the possible lifetime installation of these systems.

3.3.3.2 Experimental Procedure

The tests were conducted on a carbon fibre composite specimens, manufactured from Advanced Composite Group (ACG) MTM28-1/HS-135-34%RW uni-directional pre-preg using a $((0,90)4)_s$ layup with a nominal thickness of 2.15 mm. The specimen was a wide tensile specimen (200 x 370 mm) with a circular cut out which can be seen in Figure 3-56. The specimen used to assess the sensitivity of AE techniques and the performance of the standard “delta T Mapping’’ technique using both artificial H–N sources and real fatigue test data. Fatigue testing was undertaken on the specimen shown in Figure 3-56, the specimen has a 77 mm diameter circular cut out with notches at either side to increase stress and promote damage growth. To transfer load to the specimen, 5 mm thick steel plates were bolted either side of the top and bottom ends and the load was applied via 20 mm pins, reducing the unsupported area to 200 x 170 mm.

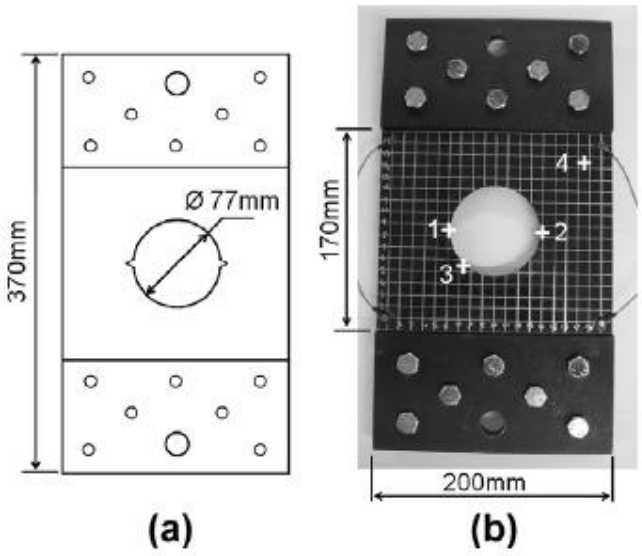

Figure 3-56. Composite fatigue specimen

Four Pancom Pico Z transducers (125–750 kHz) were mounted at the corners of the unsupported area using a rubber toughened cyanoacrylate adhesive. Training data for ‘‘Delta T Mapping’’ was collected at a resolution of 10 mm by utilising H-N sources to generate artificial AE at each node positions within the grid. The corresponding Delta T maps were generated utilising the algorithm. Data were then collected for five H–N sources conducted at both notches and at two arbitrary locations shown in Figure 3-56. The

transducers were removed and remounted in the same positions before repeating the collection of data from the same four locations. This facilitates not only an assessment of the ‘‘Delta T Mapping’’ location accuracy in a complex component but also its sensitivity to the remounting of transducers, which is a likely occurrence during long-term testing in a commercial environment. The AIC delta T mapping technique was not utilised in this experiment due to a short pre-trigger being used to record the waveforms, Sedlak et al (2009) states that there should be a period of a several hundred sample points before and after the threshold crossing and there should be a period of noise in the start of the waveform to gain the best result from the AIC picker. On this basis the AIC picker was not used as it would not have given significant benefits. Finally the tensile specimen was subjected to a fatigue loading regime with peak loads of 30, 35, 40, 45, 50 and 55 kN, full details of the loading regime are given in Table 3-9. The specimen was monitored using the four AE transducers throughout loading. In order to validate the AE results, loading was stopped every 5000 cycles and a Deltatherm 1410 thermoelastic stress analysis (TSA) system was used to assess any changes in the stress field of the specimen. The TSA system detects the small temperature changes occurring in a material subject to cyclic transient loading and the change in temperature observed is directly related to the stress experienced by the material. The system provides a full-field measurement; hence any redistribution of the stress field resulting from damage onset can be detected. The TSA images represent the output of the cameras analogue to digital converter, which is proportional to the thermal radiation from the specimen which is in turn proportional to the stress within the material. It is possible to calibrate the system such that stress measurements can be made, looking instead for changes within the stress pattern that will indicate damage. Several authors have demonstrated damage detection in composite structures using TSA , Emery and Dulieu-Barton (2010) used the TSA technique to evaluate fibre breakage, matrix cracking and delaminations in glass fibre specimens subjected to tensile fatigue loading. Fruehmann et al (2010) used a baseline subtraction of the thermoelastic stress field to detect damage in carbon composites specimens under tensile fatigue. Fruehmann et al (2012) detected damage in carbon fibre aerospace structures using TSA under modal excitation. The TSA measurements were made under cyclic loading conditions of 1–10 kN at a rate of 2 Hz and a reference stress field was ascertained prior to the application of fatigue loading. The fatigue loading was subsequently stopped every 5000 cycles to make further TSA measurements and comparison with the reference stress field highlights any changes that have occurred as a result of damage onset. No AE monitoring was conducted during the TSA measurements. In all cases signals were recorded using a

Mistras PCI-2 acquisition system and arrival time estimation was conducted using a reduced threshold level of 30 dB to improve reliability of triggering. Standard composite monitoring would normally use a threshold level of 45–50 dB.

Table 3-9. Details of fatigue loading regime

Load, kN	Cycles	Total Cycles
3-30	10000	10000
3.5-35	30000	40000
4-40	15000	55000
4.5-45	20000	75000
5-50	65000	140000
5.5-55	10000	150000

3.3.3.3 Experimental Results and Discussion

A further exercise, to assess the performance of the ‘‘Delta T Mapping’’ methodology was conducted on a wide tensile specimen, shown in Figure 3-56. The location results from H–N sources conducted at the left and right notches (locations 1 and 2) and two arbitrary positions (locations 3 and 4) are presented in Figure 3-57. It can be seen, that in the case of the two notches, location accuracy is very good for both the TOA and delta T Mapping techniques. The TOA technique is known to provide more reliable location calculations for sources near to the centre of a transducer array, such as the notches. When the source position moves further away from the centre of the array, i.e. locations 3 and 4, the accuracy of the TOA method is seen to reduce. The locations calculated using the ‘‘Delta T Mapping’’ technique, however, remain accurate in all four cases. Average location errors are presented in Figure 3-58 for the locations seen in Figure 3-57 and also for H–N sources performed at the same four positions following the removal and remounting of the transducers. The error bars represent maximum and minimum location errors for that particular data set. The difference in the delta T Mapping location errors found before and after the remounting of the transducers is observed to be small. Hence it can be concluded that the delta T maps generated from the original training data are still valid after remounting of the transducers, demonstrating the robustness of the delta T mapping approach. Following the remounting of the transducers the delta T mapping location accuracy is consistently greater than the TOA technique. It should be noted that the minimum uncertainty in the location measurement is limited by the radius of the transducer and the accuracy of the transducer placement. In this case the transducer radius is 2.5 mm and placement is expected to be accurate to within ±2 mm, giving a total uncertainty of ±4.5 mm. Following the delta T Mapping assessment discussed above the wide tensile specimen was placed under cyclic loading.

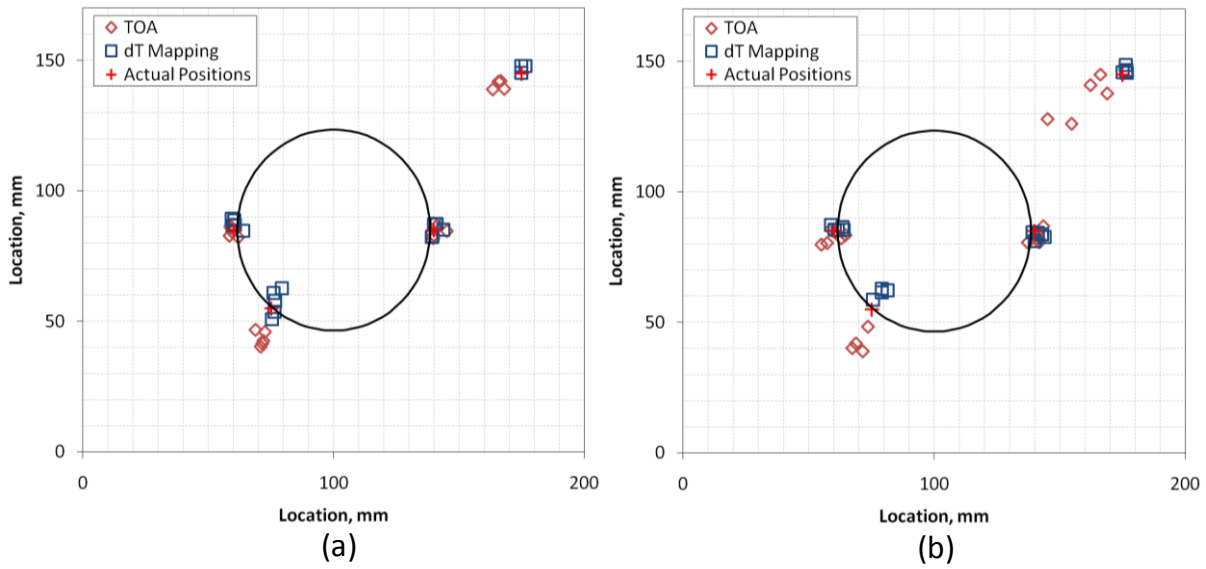

Figure 3-57. Tensile specimen location test results from H-N sources (a) after initial transducer mounting (b) after transducer re-mounting

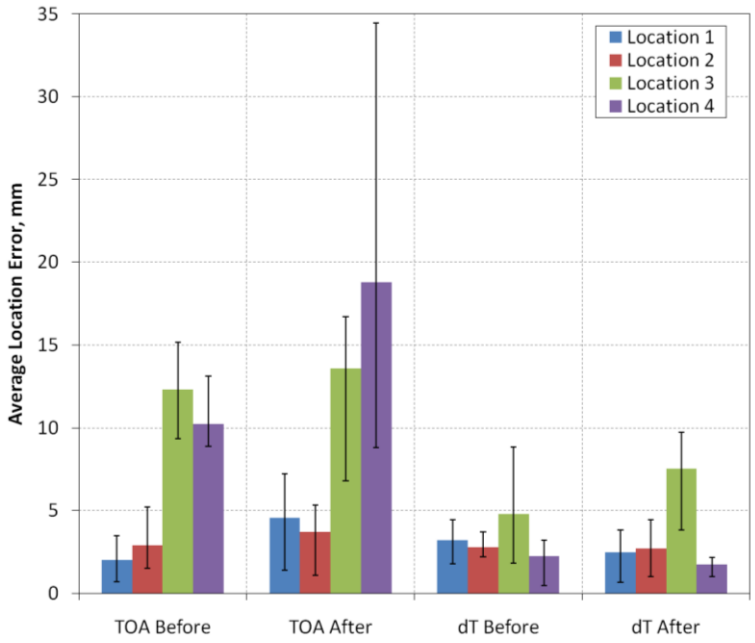

Figure 3-58. Average location error from H-N sources on fatigue specimen

Figure 3-59 shows the difference between the reference stress field, prior to fatigue loading, and the stress fields recorded after 10k, 25k, 75k and 150k load cycles (i.e. the subtraction of the reference stress field from the current stress field); hence any changes in the stress field resulting from the onset of damage will appear as a lighter shade. The first indication of damage onset, albeit a weak indication, could be seen in the images after 25k cycles and is identified by a white arrow. Prior to this no indication of damage is present, as seen in the 10k TSA image, and after 25k cycles the indication of damage continues to

become stronger (75k and 150k TSA images) with clear white areas occurring adjacent to the notches indicating a change in stress field due to damage. The AE locations identified after 10k, 25k, 75k and 150k load cycles are presented in Figure 3-60 and Figure 3-61 from the TOA and delta T Mapping methodologies, respectively, and correspond to the TSA images in Figure 3-60. The plots are presented as two-dimensional binned scatter plots, such that spatial bins with a resolution of 5x5 mm are coloured according to the number of locations they contain. The figures are also overlaid by an outline of the notched circular hole to represent the geometry of the specimen. After 10k cycles and prior to the detection of damage onset using TSA, small numbers of locations are observed in the regions of the two notches, by both location methodologies. The location of signals within these areas indicates the presence of an active damage mechanism at the notches, thus demonstrating the early detection of damage using AE. As discussed above the AE technique is not reliant on defect size and only requires that a source be active for detection. This highlights the potential for the use of AE monitoring as an SHM tool that can provide early detection of damage development in composite structures. Additional locations are observed at the two notches after 25k cycles, clearly identifying the onset of damage, validated by the first indication of damage observed in the TSA images after 25k cycles. It is also clear that more locations are identified at the left hand notch which corresponds to the damage identified in the TSA image. The indication of damage continues to get stronger after 75k and 150k cycles, corresponding to the increasing damage observed in the TSA images. It should be noted that although both the AE and TSA techniques provide a strong indication of damage after 150k cycles, the actual scale of the induced damage is very small. The specimen was still capable of holding the full test load of 55kN and no changes in displacements were observed at peak load. Additionally, very little damage could be identified through visual inspection, with only very minor surface splits running vertically from the notch tips on one side of the specimen was observed. As was the case for artificial sources on the wide tensile specimen, damage signals from the notches are located well by both the TOA and delta T Mapping methodologies. The delta T Mapping location results show a small improvement over the TOA locations, with locations slightly closer to the notches and more tightly clustered. The tighter spatial clustering of signals observed when using delta T Mapping is also beneficial for the early detection of damage, making the presence of signals more apparent to an operator. However the delta T results for the 75 and 150k cycles shows a number of located events not in the notch region this is not the case for the TOA results. Further investigation showed that all the locations outside of the area of the notches have crossing points of 3, this is the smallest number that can be used to determine a location and

therefore the locations are the least confident when considering the maximum number of crossing points that could occur is 21 for four transducers.

3.3.3.4 Conclusion

In conclusion both the TOA and standard delta T mapping technique were able to detect the early onset of damage within a complex composite tensile specimen. The AIC delta T mapping was not implemented in this experiment as the aim of the investigation was to assess the robustness of the delta T algorithm and the ability to detect the early onset of damage. Both location techniques detected damage before it could be validated with the TSA image showing that if AE was employed in a SHM system it would have the ability detect damage before conventional NDT techniques.

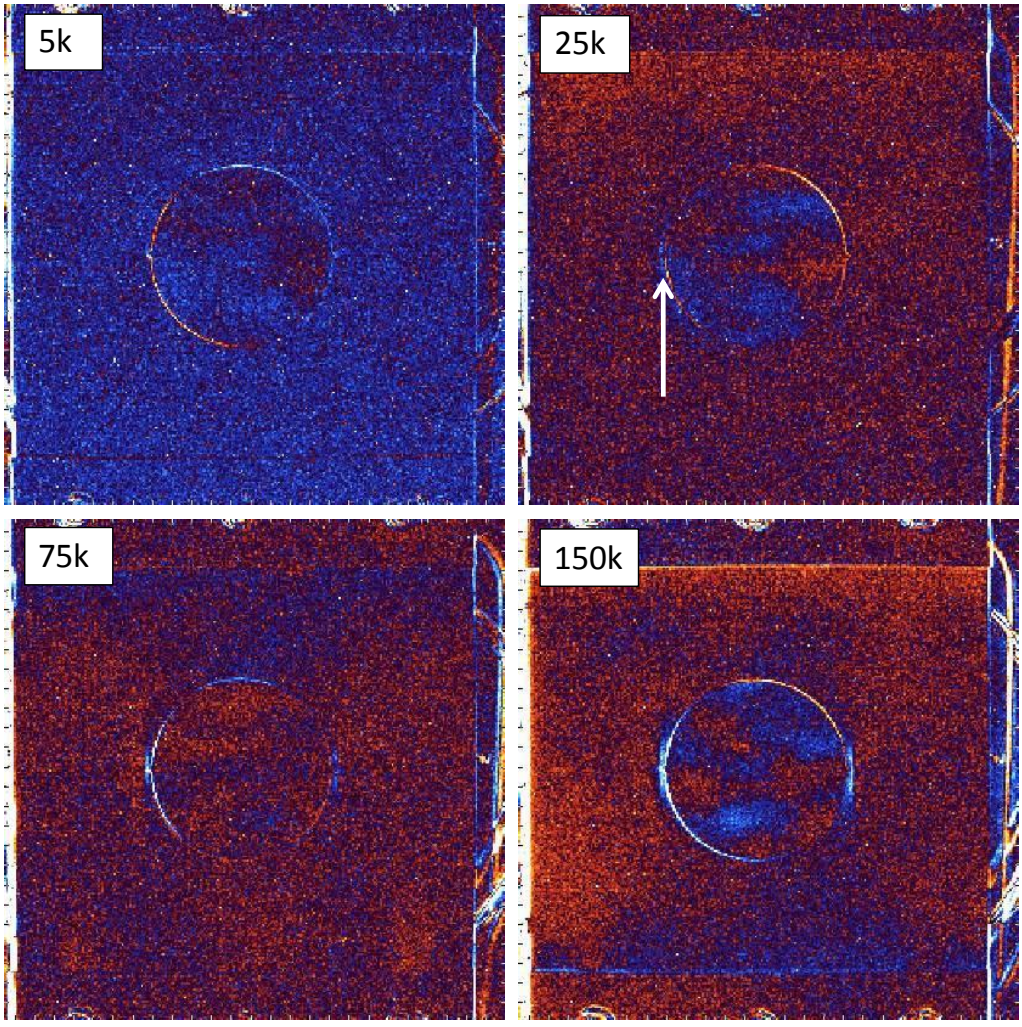

Figure 3-59. TSA images after subtraction from the reference state for 5, 25, 75 and 150k cycles

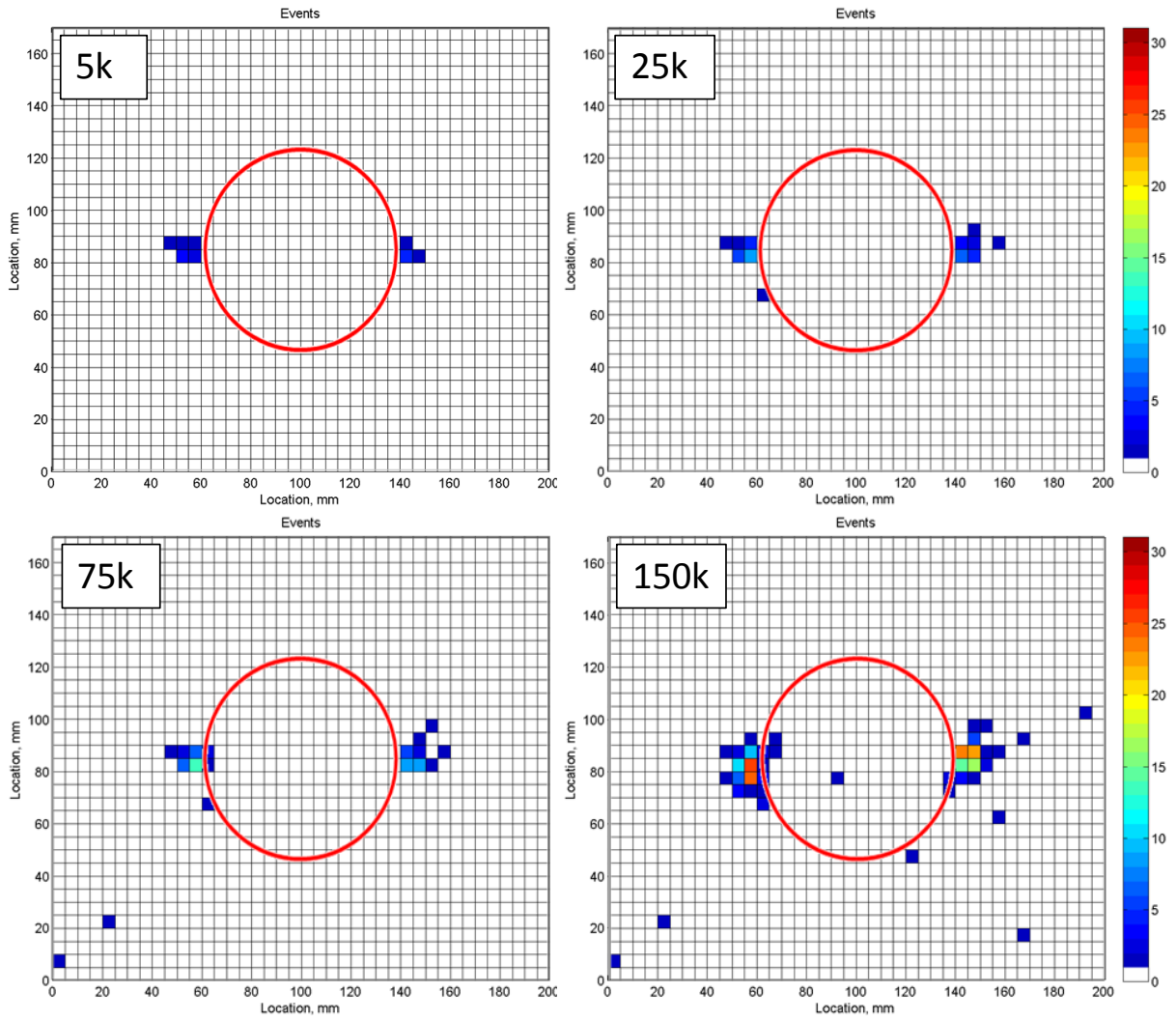

Figure 3-60. Cumulative events spatial binning of the TOA located events for 5, 25, 75 and 150k cycles

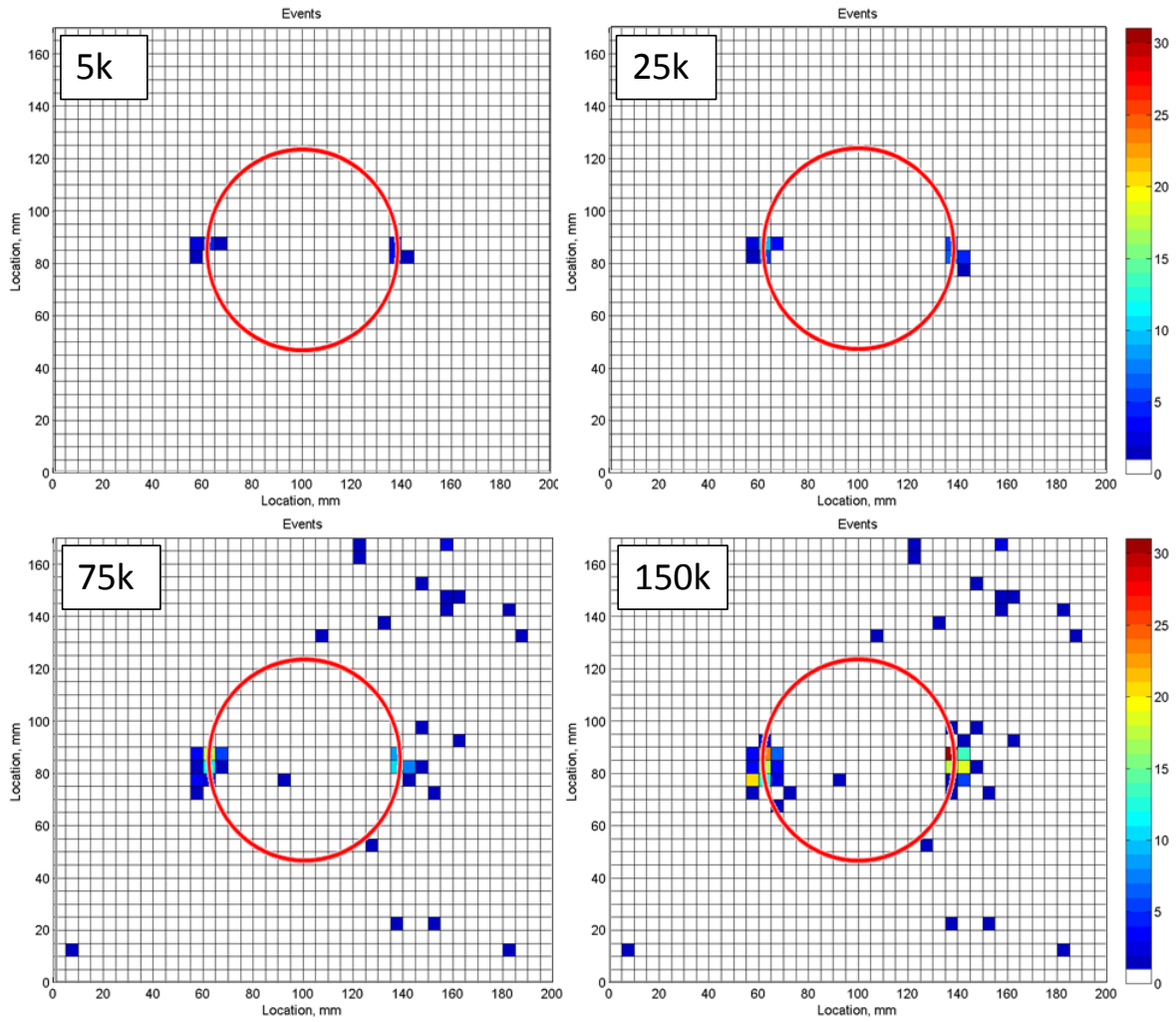

Figure 3-61. Cumulative events spatial binning of the delta T mapping located events for 5, 25, 75 and 150k cycles

3.3.4 Composite Impact Fatigue Investigation

3.3.4.1 Introduction

Composite impact damage can cause large internal damage which may not be detected externally; this can reduce the strength and design life of such components. Therefore the suitability of the AIC delta T mapping technique to detect impact events was conducted. If the impact was not detected could the damage be detected under subsequent fatigue cycles at a tensile load much lower than the failure load. This is important when considering SHM as it could show the ability to detect impact damage during the flight even though the impact was not.

3.3.4.2 Experimental Procedure

A carbon fibre composite panel was manufactured from Advanced Composite Group (ACG) MTM28-1/HS-135-34%RW uni-directional pre-preg using a $((0,90)_4)_s$ layup. The plies of pre-preg were laid onto an aluminium panel with a PTFE adhesive film. Following completion of the lay-up process, the panel was placed in a vacuum bag and cured at 120^{o}C and after trimming the overall dimensions of the specimen were 200mm wide and 370mm long, as shown in Figure 3-62. The specimen was instrumented with 4 Pancom Pico-Z AE transducers, placed at the corners of the area of interest at (10, 150), (190, 150), (10, 10) and (190, 10) respectively and are represented in Figure 3-62 by red circles. The working frequency response of these transducers was 125 to 750 kHz. The transducers were attached using a cyanoacrylate adhesive that also provides an appropriate acoustic couplant, as it provides a good acoustic transmission from the structure to the sensor and assured the sensors would not move under fatigue testing of the specimen . A central area of interest was indentified covering an area of 200mm x 160mm for the purpose of training the delta T maps. For the training data for both AIC and conventional delta T techniques a series of 5 H-N sources were collected at each grid point and the arrival times were recorded at the transducers. The specimen was impacted at position (30, 30) in the area of interest, shown in Figure 3-62 by a red cross. A circular clamp was placed on the specimen in such a way as to leave a 100mm diameter unsupported area centred about the impact location. Five repeated impacts of 5, 7, 8, 8 and 10J were performed at the impact location using an Instrom Dynatup 9250HV impact test machine with a 20mm diameter hemispherical impact tup and an impactor mass of 5.81kg. Following the final impact event an ultrasonic c-scan inspection of the panel was conducted to assess the position and extent of the damage sustained. Once the initial impact investigation had been conducted two sets of steel clamping plates were attached at either end of the specimen in the same configuration as for the aluminium fatigue investigation. The specimen was loaded into a tensile fatigue machine and subsequent fatigue cycles were applied to the specimen. The fatigue cycles ranged from 2-20kN, 3-30kN to 4-40kN and then returned in the same increments but in reverse back to 2-20kN. Throughout both testing regimes AE monitoring was conducted using a Mistras PCI-2 acquisition system. The acquisition settings for the duration of the testing can be seen in Table 3-10. A conventional TOA algorithm was implemented real time as the testing was conducted.

Table 3-10. Acquisition settings for both impact and fatigue testing

Threshold	50dB
Pre-amp Gain	40dB
Analogue Filter	20khz - 2MHz
Sample Rate	5MSPS
Pre-trigger length	500µs
Waveform length	6k

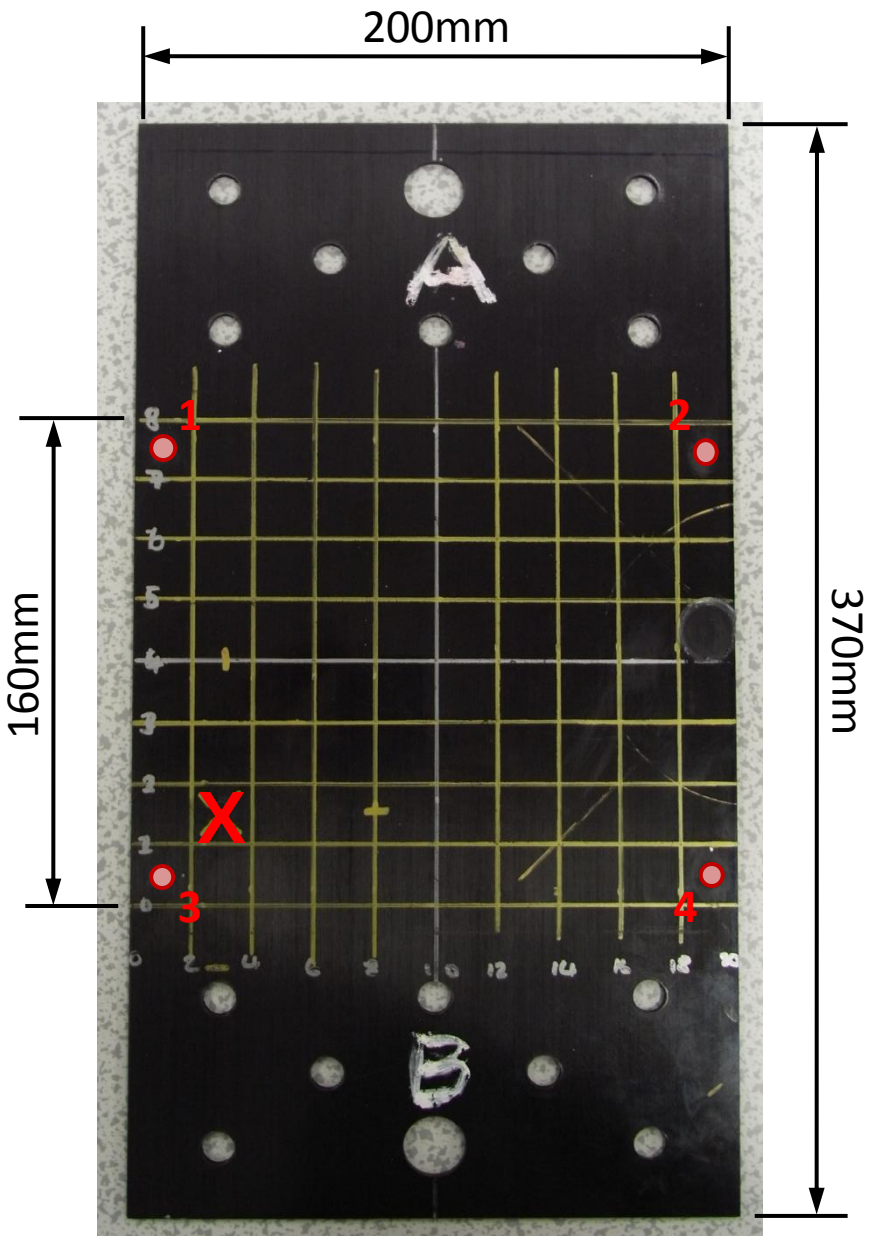

Figure 3-62. Carbon fibre specimen and dimensions – white circles indicate transducer positions and the red cross indicates impact location.

Transducer outputs were pre-amplified by 40dB with a frequency filter of 20 – 1200kHz prior to recording and signal acquisition and arrival time measurement were triggered using a 50dB threshold. A sampled version of all detected signals was also recorded at a sample rate of 5MHz. The sampled waveforms were processed post test using the AIC function to determine the true signal arrival times, which were in turn used in the calculation of source position by the "Delta T Mapping" algorithm. For comparison source positions were also calculated using the threshold based arrival time estimations for both the traditional TOA location and the delta T mapping techniques.

3.3.4.3 Experimental Results and Discussion

Figure 3-63 shows the c-scan results following post impact test inspection of the specimen. A grid representing the monitored area of interest is superimposed over the image and damage resulting from the impact events is highlighted. The specimen bolt holes are visible along the top and bottom edge of the image, outside of the area of interest. Additional areas of signal loss can be seen in the four corners of the area of interest and in the middle of the right hand edge of the specimen, resulting from residue of the adhesive used for transducer coupling and are not caused by damage to the specimen. A 272mm^2 area of delamination was induced by the impact events, however only a barely visible indent was detectable on the impacted surface and only minor splitting was visible on the back face.

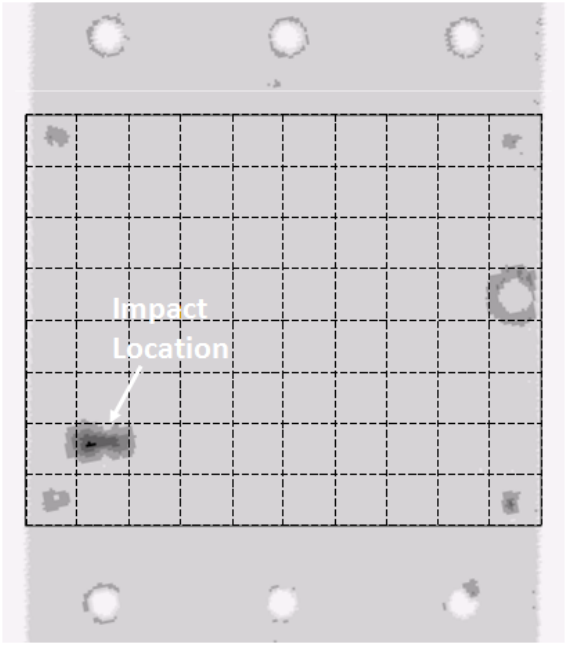

Figure 3-63. C-scan image from post impact testing inspection, overlaid with a grid representing the area of interest.

Figure 3-64 shows the results of the initial impact testing using the TOA (green squares), delta T Mapping (purple circles) and the AIC delta T mapping (blue diamond) algorithms. It is immediately apparent that not only is the TOA location algorithm less accurate but has also located fewer events than Delta T Mapping. In fact, due to the errors arising from a threshold based signal arrival time measurement and the lack of regard for wave speed variation the TOA algorithm was only able to resolve a location for two (impact 1 and 3) out of the five impact events. The Delta T Mapping technique shows an improvement with four impact locations being resolved. However due to reliance of this technique on the arrival time due to a threshold crossing there is no significant improvements in location apart from one location which is located extremely close to the actual impact region. The AIC delta T mapping technique successfully locates all five impact events with considerably higher accuracy than the other techniques and most importantly locates all events within the delamination area itself which is highlighted in the figure.

Table 3-11 presents the Euclidean location errors measured relative to the impact location at (30, 30) for all location techniques. It should be noted however that signals can be assumed to have originated from any position within the observed area of damage. Firstly comparison will be drawn with the commercial TOA techniques. In the two cases where the TOA algorithm was able to resolve a location the Delta T Mapping algorithm offers a 1mm improvement and 9mm deterioration in location accuracy for impacts 1 and 3 respectively. The AIC delta T mapping technique offers a 12mm and 29mm improvement in location accuracy for impact one and three respectively. When comparing the two delta T mapping techniques, the AIC delta T mapping technique shows a considerable improvement of 11mm, 23mm and 38mm in location accuracy for impacts one to three respectively. Impact 5 was not resolved for the delta T mapping technique but the AIC technique locates this impact with an error of 5mm. Impact five is located more accurately by the delta T mapping technique shows an improvement in location error of 2mm. Overall the AIC delta T mapping technique locates the impact events with most accuracy and consistency with an average error of just 7mm This demonstrates how techniques for improving AE source location, such as AIC Delta T Mapping, can provide considerable improvements in location accuracy over traditional methods and in doing so improve detection sensitivity.

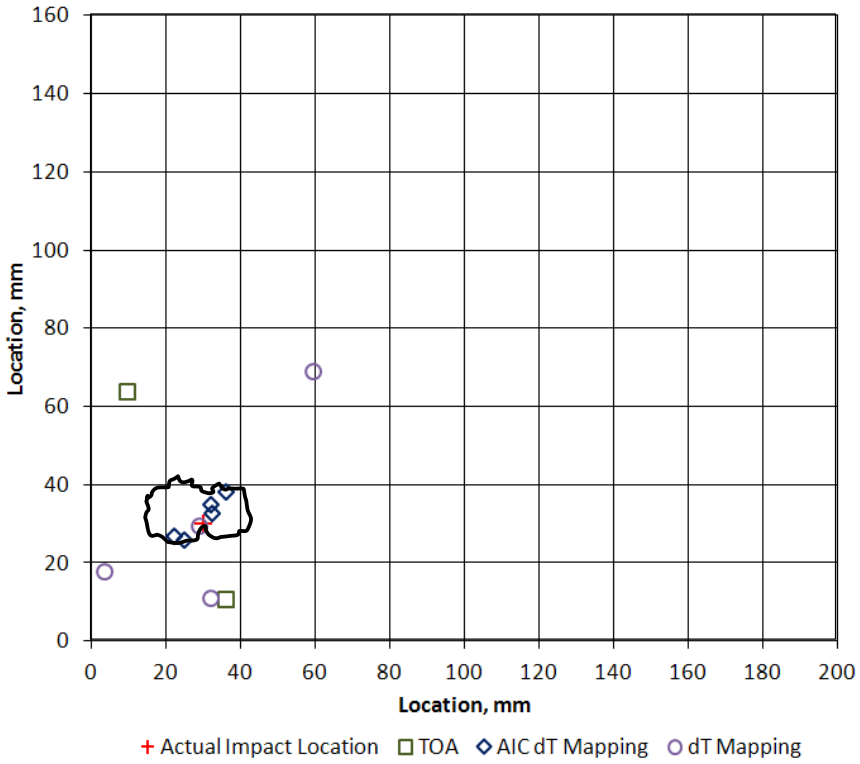

Figure 3-64. Impact testing locations results using all three location techniques.

Table 3-11. The Euclidean location errors for all location techniques

	Euclidean location error, mm		
	TOA Technique	delta T Mapping Technique	AIC delta T Mapping Technique
Impact 1	21	19	9
Impact 2	-	29	6
Impact 3	39	49	10
Impact 4	-	-	5
Impact 5	-	1	4

Figure 3-65, Figure 3-66 and Figure 3-67 show the results of the subsequent fatigue loading of the specimen. No AE activity was recorded at the 2-20kN and 3-30kN cycling loading. Significant activity was recorded at the 4-40kN cycling loading, this increment was conducted for 7000 cycles. The cycling loading was reduced to 3-30kN for a further 2000 cycles where significant activity was again recorded. However at the final increment of 2-20kN no activity was recorded. Suggesting the 4-40kN cyclic loading acoustically activated the damage, it should be noted that this load is far below the ultimate load of the specimen

and suggests in reality impact damage could be detected under fatigue loads substantially lower than the ultimate load of the structure.

Figure 3-65 shows a 5mm by 5mm spatial binning of the energy contained within the located events utilising the TOA algorithm and shows one significant cluster of energy greater than 6aJ. This cluster is located outside the damage area which is also highlighted in the figure and suggests all the acoustic energy from the loading of damage area is contained within a 25mm^2 area which is highly unlikely when considering the total delamination area of 272mm^2. The approximately location error is 15mm from the impact site of (30,30) and is not located within the damage area. Figure 3-66 shows the same spatial binning technique in terms of the number of located events, unfortunately a comparison of the acoustic energy of located events cannot be drawn due to the limitation of the location algorithm. However with the number of located events for all three technique located in the region of approximately 5000-6000 events it is thought the number of events in the one significant bin would also contain a considerable portion of acoustic energy due to the large number of events. With this in mind the delta T mapping technique shows an improvement over the TOA technique with approximately 4500 events being located within one spatial bin at (35,40), however this still lies outside the damage area and locates all the damage within an area of 25mm^2. Figure 3-67 shows the AIC delta T location results in terms of a spatial binning of the acoustic energy contained the located events and shows an improvement over the delta T and TOA techniques due to the technique locating the significant energy within the damage area. The approximate size of this significant cluster is 200mm^2 and considering the actual damage area of 272mm^2, for this particular specimen, set-up and damage type the AIC delta T technique could be used to estimate the area of damage as well as locating it.

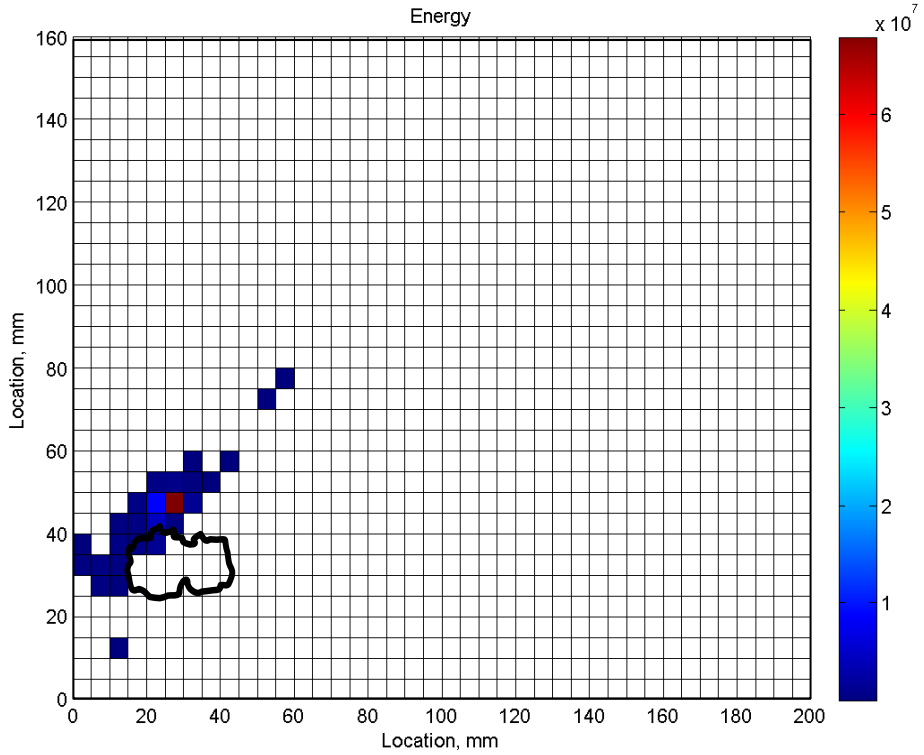

Figure 3-65. Impact fatigue TOA energy binning locations results

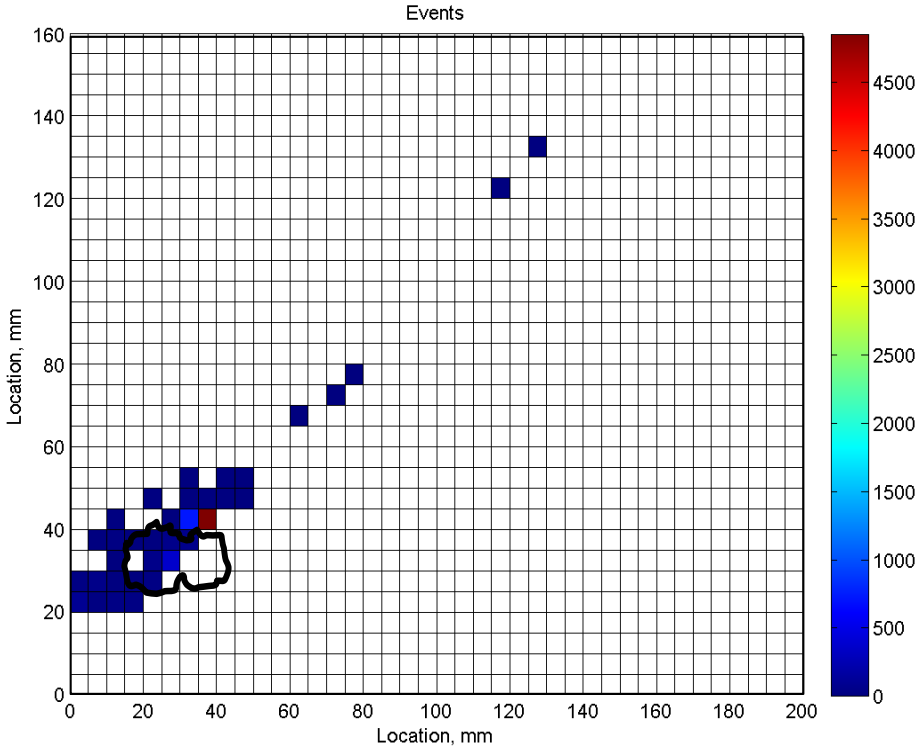

Figure 3-66. Impact fatigue delta T mapping event binning locations results

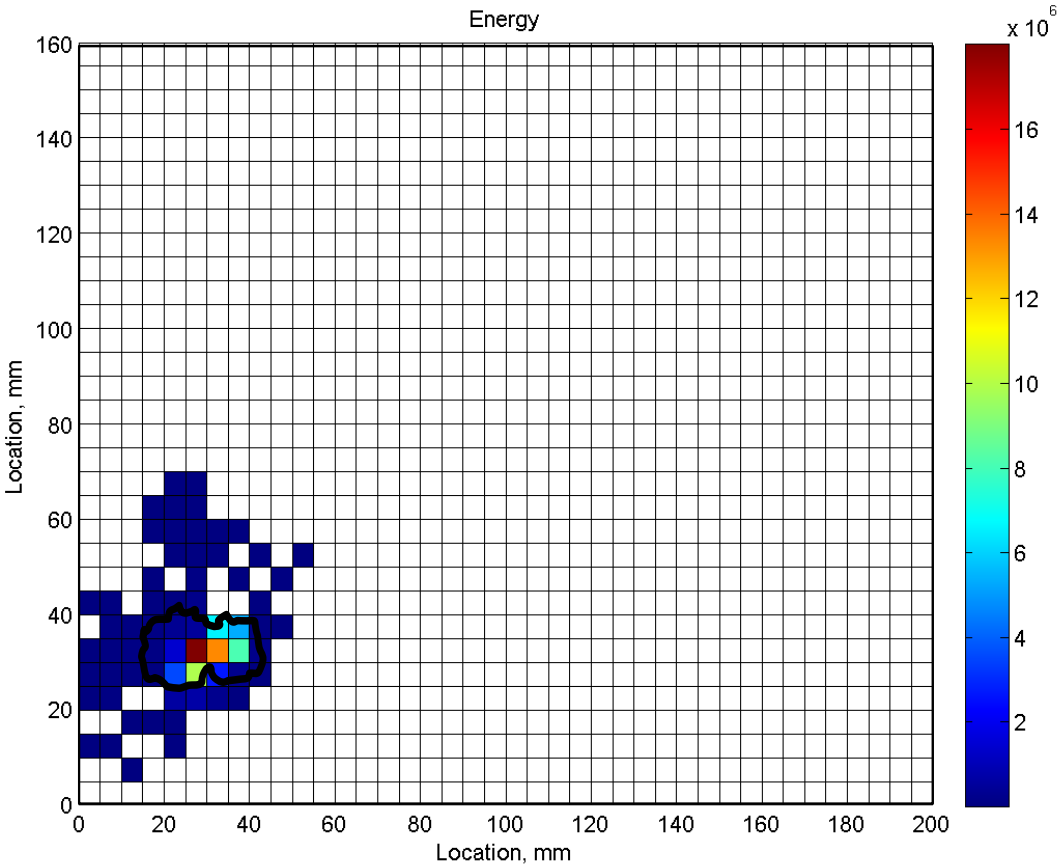

Figure 3-67. Impact fatigue AIC delta T mapping energy binning locations results

3.3.4.4 Conclusions

A series of five impact tests and subsequent fatigue loading test was conducted on a wide carbon fibre composite tensile specimen and monitored using AE. Subsequent visual inspection of the specimen revealed only a barely visible indent at the impact site; however C-scan inspection revealed a significant delamination area of 272mm^2. AE source location for each impact event was calculated using the traditional time of arrival technique and two other novel “Delta T Mapping” approaches, one combined with AIC based arrival time estimation. A significant improvement in detection sensitivity was observed, with the “Delta T Mapping” methodologies detecting and locating all five impact events, compared with only two detected using the TOA algorithm and four with the delta T mapping algorithm. Furthermore the combined approach of “Delta T Mapping” and AIC arrival time estimation demonstrated a significant improvement in location accuracy; offering a 58% and 73% improvement in accuracy when compared with the only two events located by the TOA approach. These results highlight the limitations of using traditional location algorithms in complex materials; limitations that are only likely to increase with application to composite

parts with complex geometry, such as holes, curvature and ply drops. The results also demonstrate how such limitations can be overcome through accurate arrival time determination and the use of advanced location techniques such as “Delta T Mapping”

3.4 Overall Conclusions

The results of several investigations into damage detection and location experiments utilising acoustic emission and acousto-ultrasonics has been presented. Both techniques have shown the ability to determine and locate damage within a structure which is essential for SHM. The cross correlation acousto-ultrasonic technique demonstrates the ability to detect changes in the structure due to different damage mechanisms. However this method relies on a baseline method which compares the state of the structure to that of a healthy state and therefore any changes in the environmental conditions between each state could give rise to a false alarm and further work would be required to determine a change in the structure for varying conditions as well as damage levels. The MFC transducers have shown the ability to be used for both AE and AU monitoring of impact events which means in reality the same transducer could be used for both techniques to be applied to SHM of aircraft components, which would reduce the number of transducers that would be required and hence reduce the cost of the system. The improvements to the delta T mapping technique by using the AIC onset picker for arrival time estimation has shown significant improvements over the standard delta T mapping technique and the conventional TOA method. This has been validated by AE monitoring of complex aerospace grade 2034-T3 aluminium specimens. The improvements have been made not only in terms of locations but also in the confidence of determining damage from the spatial binning plots showing only one significant cluster. The reasons for these improvements is attributed to the exact determination of the arrival time measurement which corresponds to the same part of the wave triggering the arrival time for both the training and test data. This cannot be said for the TOA and delta T mapping technique where miss-triggering can occur due to the attenuation and acoustic amplitude and energy of the damage source signals which means different parts of the signal are causing erroneous difference in arrival times for the two techniques. Investigations into the early detection of damage in composite specimens using TOA and delta T algorithms has been presented. The damage in the specimen was validated using a TSA imaging detect which detected changes in the structure as a function of the emissivity. The delta T technique detected and located damage significantly before the TSA images did, showing the sensitivity of the technique. Further investigations into the impact damage detection and location of damage under subsequent fatigue loading in a composite panel

has been presented which showed the AIC delta T mapping technique was able to detect and locate all impact events well within the damage area itself with a maximum Euclidean error of 10mm when compared with TOA and delta T mapping which were only able to locate two and four of the impact events respectively and to a much higher maximum location error. The subsequent fatigue cycles were detected and located utilising all three techniques, however the TOA and delta T mapping techniques were only able to locate the majority of the damage to a particular spatial binning, whilst AIC delta T located events within the damage area over several spatial bins which in theory could be used to estimate the size of the delamination. The improvements of the AIC delta T mapping when compared with TOA and standard delta T techniques was not as significant for the previous investigations due to the geometrically simplicity of the specimen and due to the source mechanism of the damage type. The AIC delta T mapping technique shows a novel approach to located damage within a structure accurately. The results for the AIC delta T mapping technique when compared with literature show maximum errors of 10mm when compared with 30mm in the literature. Errors as low as a couple of millimetres have been quoted in the literature however, this is for one particular specimen with a certain geometry and material. The AIC delta T mapping technique has shown consistent results of a variety of geometries and material types further demonstrating the robustness of the technique. With higher levels of accuracy over a variety of structures and materials the technique is well suited for location damage for SHM systems on aircraft. Especially considering the improvement over the conventional TOA technique and the delta T mapping techniques. Therefore for the AIC delta T mapping to achieve a similar accuracy to the TOA technique, the transducers could be placed further apart meaning less transducers would be required to monitor the structure, this would reduce the cost and weight of such a system.

4 Energy Harvesting

4.1 Literature Review

Autonomous structural health monitoring systems are becoming a real possibility for monitoring aircraft structures. As discussed in this thesis such a system could detect the early deterioration of a structure and if appropriately applied could make an assessment of the damage severity and therefore remaining life. However for these systems to become viable they would require an architecture consisting of wireless transducer nodes (WSN). This has the effect of reducing the vast amount of wiring and hence the weight of the system. These nodes would require processing and data storage capabilities, wireless communication to send and receive data and a power source to become truly autonomous. It is these autonomous wireless transducer nodes and their operational strategy such as sampling rate, processing capabilities and data transmission that define the power requirements for such systems. Various wireless transducer nodes have been developed in the literature and differ in complexity from simple temperature monitoring to SHM monitoring. Hence the power requirement of the system varies considerably.

Many examples of WSNs are based on a modular approach (Wu et al. 2007). These modules consist of a transducer input unit, a data processing core and wireless communications. The author developed a node that could be used with piezoelectric transducers or strain gauges. By directly connecting the transducer element to the transducer node, processing of the data can be done locally which does not overburden the central data server and reduces the power consumption for transmission of data. The input module comprises transducer inputs and conditioning circuitry as well as a low power op-amp which also acted as a filter for unwanted noise, an ADC chip and a low power micro controller. The processing core utilises the micro controller with additional memory chips for storing long term data. The transducer node used an RF transceiver for its wireless communications. Estimated power based on 3V supply and a 10mA current draw was 30mW however in sleep mode the current draw was 200µA. Two 1.5 V batteries could power the node for a year based on sending data every 4 seconds. A Wireless impedance based wireless SHM node was developed by Mascarenas et al (2007) on an impedance chip coupled with a micro controller and an Xbee radio for wireless communications. The principle of this technique is that the mechanical impedance of a structure is directly coupled with the electrical impedance of the transducers, therefore changes in the structural state altering the mechanical impedance can be detected by monitoring the electrical impedance.

Most of the power required for these nodes is consumed in the wireless communication which can account for 70% of the power requirements. In sleep mode the power requirement was 51μW and it is noted that during typical operation a node would consume 64.35mW, however the maximum power consumption could be as large as 212.85mW. Zhou et al (2009) was able to reduce power consumption of a wireless transducer node by removing the need for digital to analogue converters (DAC) and analogue to digital converters (ADC). This was achieved by using a carefully chosen excitation signal and detecting the phase difference of the impedance analysis. The node consumed 0.15mW in sleep mode, the power increases to 18mW in active mode with the radio off, this stage lasts approximately 13 seconds, which define the acquisition and processing time. The last stage of the process is the transmission of the data and this consumes 70mW, however it only lasts for 0.03 seconds transferring 3 bytes of data at a transmission rate of 250kbps. With this power profile and operating the node every 4 hours the node can be run for 2.5 years using 2 AAA batteries. Wireless transducer nodes have been developed that can detect the deterioration of a structure using impedance and Lamb wave approaches (Kim et al. 2009). This increased complexity of the node raised the power requirements due to use of additional circuitry. Often the need of a wireless transducer node is determined by the structure that requires monitoring. Wireless transducer nodes have been developed for the monitoring of the wear rate within in the pitch link end bearings fitted on a lynx helicopter (Lievan et al. 2009).

For these transducer nodes to be truly autonomous they require a power source, the literature discussed so far has relied on batteries to provide the required power. Batteries have a finite lifetime and even though they can last for a number of years they will require replacing. This will incur a large amount of maintenance and hence cost. Also the areas where batteries are placed may not be accessible. They may also be unsuitable for the environment conditions experienced in an aircraft. One possible solution is the use of energy harvesting techniques, these devices harvest energy that is found in abundance in the environment. In the case of an aircraft environment such sources include vibration and thermal gradients. These energy sources can be harvested using piezoelectric and thermoelectric generators (TEG). Vullers et al (2009) discussed energy harvesting techniques which include resonant vibration harvesters which produce power in the μW range, electromagnetic energy harvesters which are large in size compared to other technologies and thermal energy harvesters which produce power in the μW to mW range depending on the temperature gradient, (noting that thermal resistance is an important factor

in the design). Photovoltaic and ambient RF energy devices have been explored but they are unlikely to produce enough power. Therefore for the remaining part of this literature review will be concentrated on research into piezoelectric and TEGs.

The piezoelectric effect was discovered by J and P Curie in 1880. Where they discovered that certain crystals became electrically polarised when they were subjected to a mechanical strain, the amount of this polarisation is proportional to the mechanical strain, this is known as the direct piezoelectric effect. On the contrary if these materials are exposed to an electric charge they will mechanically deform, this is known as the converse piezoelectric effect. The direct and converse piezoelectric effect can be described by two linear constitutive equations given by equations 4.1 and 4.2 respectively (Zhu and Beeby 2010):

$$\delta = \frac{\sigma}{Y} + d.E \tag{4.1}$$

$$D = \varepsilon.E + d.\sigma \tag{4.2}$$

Where δ is the mechanical strain, σ is the mechanical stress, Y is the Young's modulus of the material ,d is the piezoelectric charge coefficient, E is the electric field, D is the electric displacement or the charge density and ε is the dielectric constant of the piezoelectric material. Piezoceramic materials have greater electro mechanical coupling constant and have higher energy conversion rates, however are brittle and can be damaged easily (Kim et al. 2011). Piezoelectric materials are anisotropic and have different piezoelectric properties in different orientations. This is based on the orientation of the ceramic, direction of measurements and applied stresses, the basis of this is shown in Figure 4-1. Typically piezoelectric generators work in two modes either d_{33} or d_{31}. In d_{33} mode the applied force and poling direction are parallel while in d_{31} the lateral force is perpendicular to the poling direction. The d_{33} mode of operation has much higher electromechanical coupling factors (2 – 2.5 times greater) than d_{31} and can generate much larger open circuit voltages (20 times greater) (Jeon et al. 2005). Despite this d_{31} mode is preferred for energy harvesting due to ease of coupling to a lateral stress whereas the coupling for a required compressive load of d_{33} mode is not practical for energy harvesting application (Beeby et al. 2006; Zhu and Beeby 2010).

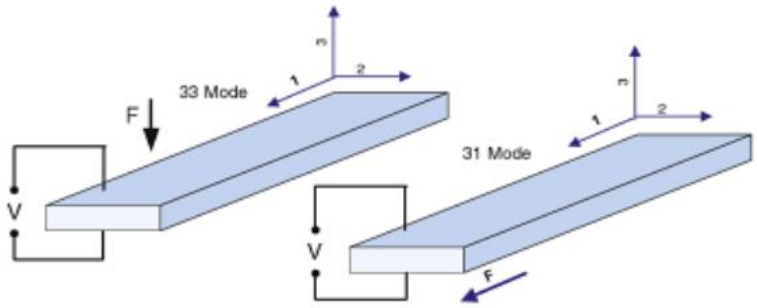

Figure 4-1. Two modes of operation of piezoelectric materials (Priya and Inman 2009)

Figure 4-2 shows the two modes of operation for piezoelectric cantilever beam generators and shows the relationship between the geometry of the device and the generated voltage. For the d_{31} mode the voltage is dependent on the applied stress, σ, piezoelectric voltage constant, g_{31} and the thickness of the material. Whilst for the d_{33} mode the generated voltage is again dependent on the applied stress and piezoelectric voltage constant in this mode, however the geometric feature for this mode is now the length between the interdigitated electrodes (Jeon et al. 2005).

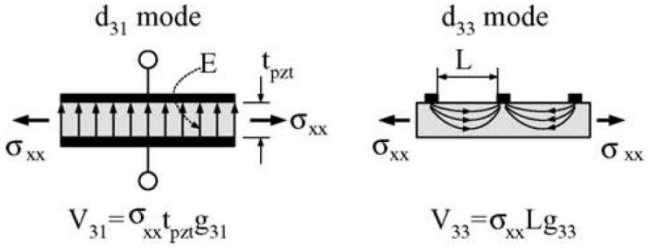

Figure 4-2. modes of operation of piezoelectric cantilever beam generators (Jeon et al. 2005)

Recently, piezoelectric cantilever beams have received a vast amount of attention for their ability to convert vibration to electric energy. Generally, researchers have investigated a classical piezoelectric cantilever beam with or without a tip mass in a unimorph or bi-morph configuration. A unimorph cantilever consists of one piezoelectric layer on a substrate, while bi-morph has two piezoelectric layers either side of the substrate material. The advantages of these device is that they can be tuned to a particular vibration frequency. Zhu and Edkins (2011) developed a simple model for the evaluation of piezoelectric energy harvesting devices. A dynamic model was used to evaluate electromechanical performance based on a cantilever with tip mass. The model included piezoelectric backwards coupling which has a large effect on the power output, generated voltage and tip displacement. Due to high

electromechanical coupling of piezoelectric energy harvesters the backwards coupling states that the electric energy generated will affect the vibration displacement. Ng and Liao (2005) developed three types of cantilever, a triple layer consisting of two piezoelectric layers either side of a metal substrate in a bi-morph configuration with the piezoelectric layers connected in parallel, the same configuration but with the active layers connected in series and finally a unimorph cantilever and can be seen in Figure 4-3. Constitutive piezoelectric equations for each device were derived based the active layers being in thermodynamic equilibrium and therefore have the same internal energy. These equations were used to assess voltage and charge sensitivity and found that the triple parallel device had the lowest voltage and highest charge sensitivity, the series device had the highest voltage and lowest charge sensitivity and for the unimorph had medium voltage and charge sensitivity. The proposed model coupled with an electrical circuit model assessed power output and found the series cantilever generated the greatest power for higher frequencies and load and therefore had the largest operating bandwidth. Ly et al (2011) developed a model for piezoelectric cantilevers based on Euler-Bernoulli beam theory for mode 3-1 bending. Hamilton's principle was used to determine global system equations of motion with model decomposition. The model developed could be used for multiple resonant frequencies, an advantage over conventional single mass spring models which can only deal with the first resonant frequency. The model was validated with experimental investigations on a tape cast piezoelectric cantilever and good agreement was observed between the two. The model enabled the Eigenvalues to be determined in order to match these to the bandwidth of the environmental vibrations. Both the experiments and model found the 2nd resonant model had the largest voltage output of 168mV at 659Hz when compared with the first mode. Again this highlights the necessity to investigate a range of resonant frequencies, however in real world applications it is less likely that vibrations at this frequency will occur.

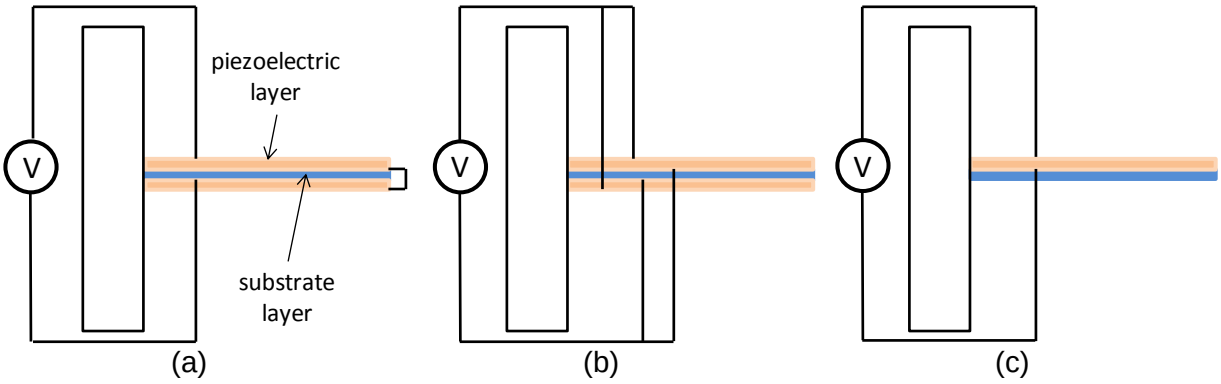

Figure 4-3. Piezoelectric energy harvesting cantilevers (a) triples layer (a) series connection, (b) parallel connection and (c) unimorph series connection

Microelectromechanical systems (MEMS) are being developed which include piezoelectric energy harvesting devices on a miniature scale. Fang et al (2006) developed a MEMS cantilever device with a tip mass to reduce the resonant frequency for low frequency vibrations. The peak power was found to be 2.16μW corresponding to a voltage of 898mV and this was observed at the resonant frequency of the device of 609Hz. Liu et al (2011) fabricated a MEMS based piezoelectric cantilever energy harvester with a low resonant frequency. This is a challenge as most MEMs devices operate at much higher resonant frequencies. This MEMs device consisted of 10 piezoelectric rectangular films on a supporting beam with a silicon proof mass. The MEMs device was subjected to 0.1g acceleration at the resonant frequency of one PZT beam of 35.8Hz. The results showed when 6 PZT patterns were connected in series peak power of 11.4nW at a match load of 12.5MΩ while for six PZT patterns connected in parallel gave a power output of 11.6nW for a matched load of 333kΩ. Although the power outputs are similar the lower load resistance is much more desirable when considering further circuitry. As the circuitry would require a similar resistance in order to achieve maximum power transfer, a lower resistance would be beneficial

All of the devices discussed so far have been resonant devices and therefore only achieve maximum power output at one particular frequency, which in some circumstance maybe ideal. However for aircraft specification applications the vibrations are often broadband in nature. Therefore resonant devices do not offer the most efficient energy transfer across the whole bandwidth. Ferrari et al (2010) showed numerical and experimental investigations of a non-linear piezoelectric cantilever. PZT substrate was applied to steel cantilevers using a screen printing technique. A permanent magnet was placed at the tip of the beam with an opposing polarity magnet placed at various different distances from the tip of the beam. Using a band limited white noise excitation and a close distance between the magnets, a bi-stable state was reached giving a marked improvement in open circuit voltage over a much wider bandwidth with respect to a linear system. Karami et al (2013) developed a small scale non linear wind turbine using bi-morph piezoelectric cantilevers. The device consisted of turbine blades with magnets placed on the base of the turbine blades. These magnets applied a repulsive force to the 4 bi-morph cantilevers with magnets placed at the tip of the cantilever. This repelling force makes the bi-morph bi-stable and increases the power output over a wider bandwidth. Experiment showed tests on a non linear single bi-morph wind harvesting generated 4mW at $10ms^{-1}$.

The research mentioned thus far has focussed on specifically developed piezoelectric cantilevers. Another area that is seeing increasing attention is the use of commercially available piezoelectric actuators or transducers for energy harvesting applications. Sodano et al (2005) assessed three types of piezoelectric cantilevers for the specific application of charging Nickel metal hydride batteries with different capacities from typical machinery vibrations. Three different devices were manufactured, a monolithic PZT patch aluminium substrate cantilever, a MFC aluminium substrate cantilever and a Quickpack bimorph cantilever made up of four piezoelectric rectangular monolithic sheets. At an excitation frequency matching the resonance frequency of each device the power generated was greatest with the PZT cantilever. The Quickpack bimorph cantilever produced less power and does not perform well at resonance due to there being an area with no piezoelectric material and hence causes a strain concentration due to the lack of stiffness at that particular location, this can be seen in Figure 4-4 . The MFC produced large voltages and very little current and hence little power. The efficiency of each device was calculated by measuring input and output power. The PZT cantilever was most efficient at 6%, the Quickpack had an efficiency of 3% and MFC was 1% efficient. Due to the lower power levels of the MFC much of this power could potentially be dissipated by the attached electronics and it was therefore decided it was not feasible to charge batteries using realistic vibrations. The AC voltage was full wave rectified and charged a buffer capacitor and a series of batteries connected in parallel. For a random range of vibration frequencies between 0 – 500Hz the PZT was able to charge different capacity batteries over the range of 1.6 to 32h. The Quickpack device charged the batteries from 7 to 50hrs. Sodano et al (2006) further investigated different piezoelectric actuators for power harvesting applications. The paper presented an experimental comparison of various different interdigitated electrode (IDE) and piezo-composite designs with regard to generating a voltage from a mechanical vibration. Three different piezoceramic composites were tested. These were an MFC and two MIDE Quickpack devices, an IDE and a non IDE model of the QP10n device. The patches were attached to an identical aluminium beam which was resonated at various different frequencies which corresponded to the first 12 bending modes. The maximum power generated by the MFC was lower than the Quickpack apart from at higher frequencies and there were similar results for the MFC and the IDE Quickpack which implies that the power generation has to do with the IDE structure rather than the piezoeceramic fibres. The reason for the lower power figures for the IDE devices was due to the low capacitance which results in higher impedance at all excitation frequencies. The IDE's structures result in a series of capacitor cells that are connected in parallel, which limits the capacitance of the MFC.

Although the power generated is less for an IDE device when compared with a non IDE device, IDE devices are able to generate higher voltage and the application of the electric field leads to a compressive stress state unlike parallel plate capacitor type electrodes where the stress is mainly tensile. Ceramics are prone to cracking in tensile conditions, so therefore IDE devices are envisaged to have a longer life (Chidambaram et al. 2012). Research conducted so far has only assessed the P1 type of MFC. Experimental and mathematical modelling conducted by Song et al (2010) investigated the use of P1 and P2 bi-morph piezoelectric cantilevers with a tip mass for power generation. The bi-morph configurations in parallel connection were subjected to a ±0.05g input at a resonant frequency of 30Hz with full wave rectification and a storage capacitor. It was found that the P1 cantilever produced 2.7mW at a matched load of 500kΩ, the P2 MFC generated 1.7mW at a matched load of 50kΩ. The P1 MFC generated 45.6V while the P2 type generated 15V at a resistance of 1MΩ. However the P2 type was able to generate higher current 0.5mA when compared with 0.2mA for the P1 type at a load of 5kΩ. This agrees with the research presented so far and explains why the P1 MFC is not suitable for charging batteries. It is important to tailor the type of MFC to the load impedance expected for efficient energy transfer. A further parametric analysis using the defined model showed increasing the beam length decreased the power output but increasing the beam thickness also increased the power output. Also reducing the natural frequency for the same input excitation increased the power output. Comparison of series and parallel connection of the active load found that series connection generated higher power at higher loads. The parallel connection generated higher current at lower load resistances. This research was further developed into MFC multi-tier bi-morph harvesters (MTEH) which were compared with a single tier P2 MFC bi-morph cantilever (STEH) (Song et al. 2009).The device consisted of three bi-morph P2 MFC cantilevers stacked on top of one another. Again a mathematical model which included full wave rectification and a storage capacitor was developed and gave good agreement with the experimental results. For a ±0.05g input at 30Hz, similar levels of power output were observed for parallel and series connection resulting in 2.76mW generated at 500kΩ and 2.48mW at 10kΩ respectively. This compared with a STEH which generated at 1.80mW at 100kΩ and 1.7mW at 50kΩ for series and parallel connections respectively. The MTEH shows a 53% improvement in power generation over the STEH. However increasing the number of tiers saturates the power generated due to shunt damping reducing the cantilever tip displacement. Another factor in the design of the piezoelectric device is the shape of the device itself which can affect resonant frequency (Chen et al. 2012). MFCs have been demonstrated to be suitable as SHM transducers for the use the AE and AU techniques.

Likewise piezoceramic discs designed for guided Lamb wave and AE techniques have been assessed for energy harvesting potential (Delebarre et al. 2012). 20mm diameter piezoceramic discs with a thickness of 1 and 2mm polarised through the thickness were mounted on an aluminium plate (0.5 x 0.3m x 3mm). The plated was clamped in a cantilever configuration. The plate was excited at the free end using an electromagnetic shaker. The panel was vibrated from 100- 600Hz and the piezoceramic discs were able to harvest power across the entire frequency with several peaks observed. An FEA model allowed the deduction that the active disc mimicked the natural frequencies of the plate. Careful placement of the harvesters is necessary to ensure the harvesters are placed at nodes of the vibration modes and not anti nodes. Power estimates found at a frequency of 387Hz 27V was generated resulting in 589μW at a load of 22kΩ.

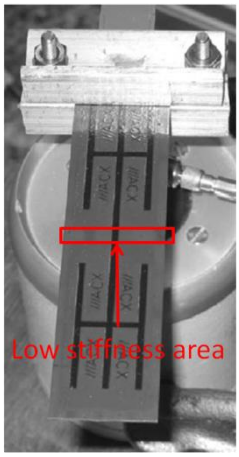

Figure 4-4. Strain concentration area of the Quickpack bi-morph cantiliver

With the use of piezoelectric energy harvesters placed on a structure for energy harvesting applications, determination of the optimal placement in order to achieve maximum power generation is necessary. Bachmann et al (2012)focused on the placement of piezoelectric patches in complex real world structures for maximising the harvested strain energy, determining the electric charge and generalised electromechanical coupling coefficient based on the available strain energy. This was achieved using a finite element model to predict the strain in complex composite materials followed by an exhaustive placement search which covers the whole design space of the structure. Hence a reliable prediction of harvested charge and strain energy of a piezoelectric patch is possible. The model assumes that the introduction of the patch does not alter the modal behaviour and the planar piezoelectric coupling coefficient. Wood et al (2012) developed an optimisation programme which assessed the mode shapes at natural frequencies and hence strain for typical aircraft vibrations ranging from 0 – 400Hz. The programme determined the optimal

location and orientation of MIDE Quickpack devices over the entire specified bandwidth. Liao and Sodano (2012) developed an electromechanical model and loss analysis to determine optimum placement of piezoelectric patches on cantilever beams. For vibrations near the fundamental frequency and for small patch sizes the optimal position is at the root of the cantilever. At higher modes the optimal location can shift. There also exists a maximum patch size where increases above this size do not result in improved performance. This analysis is important so that optimal damping and energy harvesting can occur.

There are many practical applications or scenarios where piezoelectric materials could be used to provide a power source for wireless transducer nodes. Pasquale et al (2011) developed a piezoceramic cantilever which consisted of a 200µm piezoceraminc layer on a PVC substrate. This device was developed for harvesting vibration energy for railway vehicles. The piezoelectric cantilever was applied to a scale model of a railway carriage. The lateral acceleration spectrum measured for an actual railway bogey showed a resonance peak at 5Hz. The cantilever beam was tuned to this frequency by altering the tip mass and beam stiffness. The scale railway carriage was subject to accelerations of 1.53g prior to rectification and peak powers at matched load of 4mW were generated. This was stored in a battery and was able to power two axis accelerometers and an RF transmitter. The device was able to re-charge the battery after use for 0.3 and 16 seconds respectively. Zhu at al (2011) developed a credit card size wireless transducer node that incorporated a T-shaped piezoelectric bimorph cantilever with temperature and pressure transducers and a 3-axis accelerometer, a micro-controller and an RF transmitter with energy storage within a single unit. The energy harvesting device generated 240µW of power at a resonant frequency of 66Hz for a 0.4g vibration when the bi-morph layers were connected in parallel. Ertuk et al (2009) developed an electromechanical model for a load bearing multifunctional wing spar for unmanned aerial vehicles. Model results were evaluated for a 3 layer wing spar (piezoelectric aluminium piezoelectric layer) with dimensions of 500x30x12mm. Modelling found the resonance frequency at open and short circuit states to be 37.86 and 37.27Hz respectively. This was compared with an original wing spar resonant frequency of 39.26Hz. Maximum power output based on open circuit voltage and short circuit current found 458mW/g^2 could be generated at matched load of 13kΩ. A theoretical analysis found the multifunctional wing spar had much lower strength than the original wing spar with the same dimensions. In theory the device would fail at a 0.97g base acceleration when compared with 6.8g of original. This was based on the strength of the piezoelectric material. Experimental verification on a 9 layer wing spar found close agreement between resonant

frequencies at open circuit and short circuit states. The 9 layer device was able to generate 4.1mW/g^2 for a match load of 32kΩ. Further development of the multifunctional wing spar incorporated solid state batteries and a transducer node into one structure (Anton et al. 2012). The wing spar consisted of a metal substrate with MIDE Quickpack device (QP10n) bonded close to the clamped end the followed by two thin film battery layers (Thinergy MEC 101-7SES). A Kapton layer was placed between the substrate and the batteries to prevent electrical shorting. A transducer node was modelled as a lumped mass at an arbitrary position towards the tip of the cantilever. The proposed wing spar was mounted to a shaker and it was found that the model accurately predicts the response of the wing spar. The wing had a maximum peak voltage output of 968.1V/g for series and 674.1V/g for parallel connection. Peak power at the short circuit resonance frequency was 884.9mW/g^2 for load resistances of 64.04 and 16.09kΩ for series and parallel connections respectively. For the open circuit resonant frequency the generated power was 919.9mW/g^2 for load resistances of 503.3 and 126.1kΩ for series and parallel connection respectively. For a ±0.25g vibration for a period of one hour at resonant frequency the piezoelectric layers provide 0.37mA of current to the battery. The discharge test showed the batteries could be discharge at a rate of 1.4mA. The average regulated power during testing was 1.5mW. The additional circuitry consisted of a full wave rectifier and a voltage regulator to charge the batteries. A mathematical model was produced to determine the effects of adding solar and piezoelectric energy harvesting to a UAVs flight endurance (i.e. the length of time the UAV could fly for) (Anton and Inman 2011). The model was coupled with experimental results for power harvested during typical UAV manoeuvres conducted on a sunny day. The results showed that for the flexible solar panel increased the flight endurance by 0.7% if the weight of the additional solar panels was removed from the structural weight. Adding the weight of the piezoelectric panels only decreased flight endurance no matter how much structural mass was removed. This shows the necessity of considering the possible adverse effects of adding energy harvester devices to certain structures.

TEG devices operate on the principle of the Seebeck effect which promotes a thermoelectric electromagnetic field across two different semi-conductors when their junctions are placed across a temperature gradient. TEG devices use n and p type semi-conductors connected in series and thermally in parallel. The device consists of a hot and cold side, when one side is exposed to a heat source and the other a colder source as seen in Figure 4-5. This temperature differential results in a flow of heat which causes a diffusion of charge carriers from hot to cold. N type charge carriers have a negative charge producing

a current from the cold to hot side while the p-type materials have positive charge carriers and generates a current from hot to cold side. This results in an electron current flowing clockwise around the circuit. Voltage produced is proportional to the temperature differential and the difference in Seebeck coefficients of the two materials. This voltage is generally small for thermocouples, therefore many thermocouples are connected in series to form a thermopile which can generate more useable voltages.

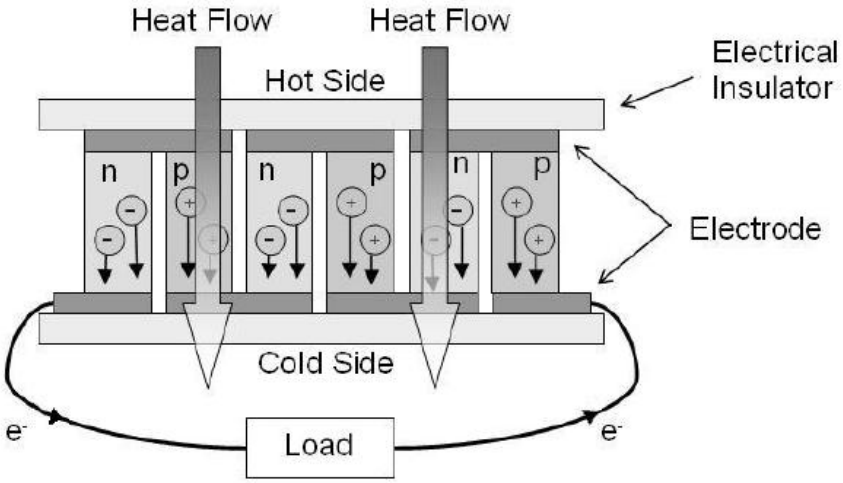

Figure 4-5. Principle of TEG devices

TEG devices have been implemented to harvest power from temperature gradients that exist in a number of different applications. TEG energy harvesting devices have been developed to exploit temperature gradients from large thermal masses, solar irradiation, the human body and aircraft flights. The power generated from a TEG is generally higher than that of a piezoelectric device often in the milli-Watt range. Sodano et al (2007) developed two devices for harvesting thermal gradients from sunlight and from elevated temperatures. The solar energy harvester compromised a solar concentrator with a transparent window and a black body heat sink. The second device consisted of a TEG with a heat sink. Experimental investigation of different stacking configurations of TEG such as 2 x 4 TEGS and 4 x 2 TEGS showed the Seebeck coefficient differed. The stacking caused variation in the temperature gradient across each TEG and the heat sinks ability to remove heat from the cold side due to different contact surface areas. Further testing of the configuration without any passive heat sink showed a maximum power of 40mW for a hot side temperature of 200°C. The two described devices with eight TEGs connected in series were used to charge a 300mAh battery and showed charge times of 17.3 and 3.5 minutes for the solar and waste heat harvesters respectively. This was compared with a charge time for a

piezoelectric device which took 5.8 hours. Lu and Yang (2010) designed a prototype energy harvesting device to exploit temperate gradients between room temperate and a radiator to power a Zigbee automatic valve control system. Careful consideration of the distance between the hot side and the heat sink and insulation of the hot to cold side is necessary in order to maximise the potential temperature gradient. In order to increases the distance between the hot side and the heat sink TEGs were stacked on top of one another. However if too many are stacked this reduces temperature gradient across each module and diminishes power output. Lu and Yang's (2010)device consisted of two pairs of heat sinks and four TEGs in a stack configuration, generated a 150mW for a temperature gradient of 55ºC which can be seen in Figure 4-6. Knight and Davidson (2010a) presented a case study of an energy harvesting devices to generate power from the temperature differential between a black disc illuminated by the sun and a body of water. The device consisted of an aluminium heat sink which was placed in water and on the hot side a black disc was illuminated by the sun. The device was fastened to a foam disc with an acrylic dome placed over it. The dome raised the temperature of the black disc by exploiting the greenhouse effect. Peak power output on a clear winters day was 47mW, however it was noted that at least four TEGs would be required to generate a useable voltage of 3.3V for a wireless transducer node. Wang et al (2011) developed a prototype energy harvesting device using nine TEG modules placed in series in a 3 x 3 array and an aluminium high thermal conductivity heat sink. This was used to generate power from temperature differences in a mechanical plant room. For a mechanical plant room temperature of 70°C, typical temperature differential of 5.5°C can be expected, where the power at matched load was approximately 6mW. This prototype with a power management system was used to power a wireless transducer node. Moser et al (2012) assessed an energy harvesting device to generate energy from temperature gradients between the air and large thermal masses such as buildings and tunnels. In order to realise maximum energy harvested careful consideration of thermal and electrical interfaces with source and load matching is necessary. This would allow a prototype to be developed with maximum power transfer. Trials on a tunnel wall harvesting 70mJ energy per day using a power management system enabled 415 radio frequency signals per day to be sent containing 15bytes of information from temperature gradients of 1.2K. Mousoulis et al (2012) developed an energy harvesting device using TEGs to harvest energy from the body where typically temperature gradients of less than 10°C exist. The TEG was housed on a silicon substrate with a perfluoro carbon liquid pool which formed the cold side. The liquid pool had a boiling point of less than 37°C, this providing additional cooling to remove heat from the cold side. Comparison of the device

with air and HFE 700 showed significant improvements increasing the power output from 0.09mW to 0.194mW. Novel ways of integrating TEG devices are being researched. Ibragimov et al (2012) developed a TEG that could be directly embedded in aluminium during the casting phase. The TEG was made up of 32 thermopiles and was specifically designed to withstand the temperatures and thermo mechanical stresses generated during the casting and cooling down phases of manufacture. This was achieved by them being manufactured on a borosilicate glass substrate and the use of waxy interconnectors to allow stress compensation. Two embedded devices were able to generate 52.8 and 103μW from temperature differentials of 138 and 221ºC respectively. A third device which was not embedded developed 514.5μW for a temperature differential of 596ºC.

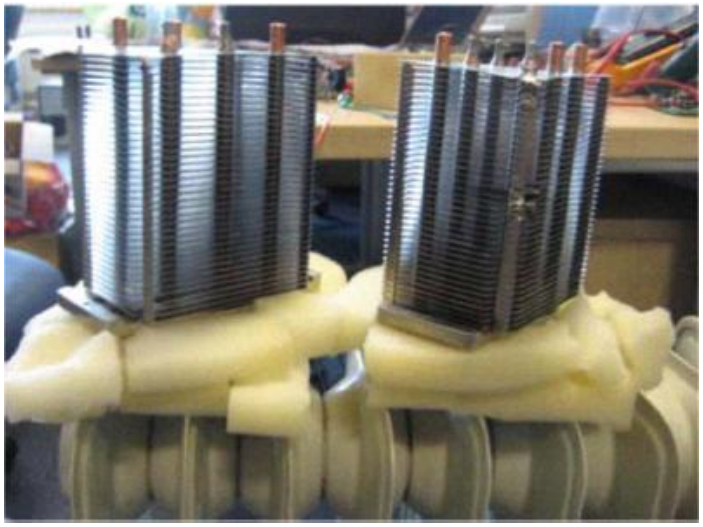

Figure 4-6. TEG energy harvesting device for a automatic valve controller (Lu and Yang 2010)

Prototype energy harvesting devices incorporating TEGs have been developed for specific aircraft environment temperature gradients. Featherston et al (2009) assessed the feasibility of generating power for wireless transducer nodes using a TEG to exploit the temperature difference between the fuel tank and outer wing skin temperatures. A realistic TEG model developed by Min and Rowe (Rowe 1995) was applied to temperatures recorded during flight at the specified location. The results for four flights showed average power levels of 6.6-22mW could be generated at matched load. The model was validated with experimental results for a temperature gradient generated between cold water and air cooled by a vortex tube which resulted in a temperature gradient of up to 30°C. Excellent agreement was observed between the results with average powers of 50mW and 48mW being generated for experiment and theoretical results respectively. Samson et al (2010a) looked at the feasibility of smart seats on aircraft to allow for more efficient pre flight checks

relaying information such as occupancy, seat back, arm and table tray position to a central control panel. This system would require wireless node with energy harvesting supply. A low power transducer was developed which consumed an average 131µW at 3.3V. The EH device consisted of a heat collector, heat sink and a TEG incorporated into the seat itself. Theoretical and experimental validation required six devices in a seat to create 1mW at 0.25V due to the efficiency and storage capacity of the power management system. Bartholome et al (2010) designed an energy harvesting device to exploit the temperature gradients that exist between the fuselage frame and the internal cabin of an aircraft where maximum temperature gradients of up to 37°C can occur. A Perspex casing housed the TEG and an aluminium rod acted as a heat sink between the hot side of the TEG and the heat collector placed on the cabin wall. The Perspex housing was used to protect and insulate the TEG. An experimental investigation of the prototype was conducted where the cold side of the TEG was held at -40°C and the heat collector was kept at room temperature, this resulted in 10mW of power being generated for a device that weighed 17g. Samson et al (2010b) discusses the early development of an aircraft specific energy harvesting device using thermoelectric generators. The device exploits temperature gradients that exist between the fuselage skin and a heat storage device where a material undergoes a phase change during takeoff and landing. This generates an artificial temperature gradient across the TEG. Results from a test flight showed hot and cold temperatures of 20.4 and -21.8°C respectively which resulted in water being shown to be the most promising material due to its high heat capacity and phase change at 0°C. Experimental investigation for various configurations of the device was undertaken and the power to weight ratio was used to determine optimal configuration. This resulted in a device with a single wall container with an internal heat pipe, 2 mounting bolts and 10mm of PU for insulation. A finite element model was generated to determine the temperature differential across the module and showed a theoretical 31.2J could be harvested during a typical takeoff profile(Samson et al. 2010c). Due to different thermal conductivities of water and ice the potential for hot or cold heat storage is not equal during the takeoff and landing profiles. A further investigation into the optimum PCM concluded a material with a phase change of -4.3°C harvested the most energy. The simulations were verified and adapted using experimental results. The experiments estimated a total of 19.9J, the reduction arising due to thermal leakage not being considered in the model. Further simulation and experimental investigation were undertaken to determine the thermal conductivity of the TEG so that the complete stored heat is transferred to the TEG(Samson et al. 2011). Simulated and experimental energy harvested during a typical takeoff generated energy levels of 21.8 and 23.3J respectively.

The difference between experimental and simulated results of 7% occurred due to the lack of convection analysis of the phase change material in the model and losses to the environment. Increased conversion efficiency could be realised using a TEG especially designed for the temperature gradients considered. Experimental and simulated results showed a 13% improvement. The device underwent temperature and vibration cycling testing to certify it for flight and two devices were subsequently installed on an aircraft(Samson et al. 2012). Three test flights were conducted and the devices were able to harvest on average 20.95J for flights one and two and 15.35J for flight three. To exclude damage to the device for the lower energy output of flight three conversions factors were calculated for each device and were found to be constant. Therefore the reduced power outputs were due to a lower ground temperature and lower altitude during flight. The proposed device was implemented with 4 Eureca TEGs connected in series with a load resistance of 39Ω and installed on an aircraft for 28 flight tests. Similar energy outputs of approximately 20J were observed for flights profiles which reach maximum altitude and maintained it for the flight duration and for small fluctuation in altitude around the maximum altitude. Increased energy output of 38J was observed when the flight consisted of multiple take off and landing. The untypical flight profiles gave energies of around 1J this is due to the minimum fuselage temperature being greater than 0ºC and therefore failing to exploit the phase change of distilled water.

Although piezoelectric devices generate lower power levels than TEG, when considering the aircraft application there will be a minimum temperature gradient below which the TEG will not be able to provide enough voltage to power a node through a power management system. This poses a problem, since depending on the temperature gradients required this may not be until a significant time into the flight and hence the system will potentially not generate power for the majority of the flight. In real world applications the solution is implement a piezoelectric device on the aircraft structure to harvest vibration energy as soon as the engines are operational. In this way the piezoelectric devices could provide power when the TEGs power is not available. Such a dual energy harvesting solution would be advantageous. Farinholt et al (2009) used a hybrid energy harvesting solution to provide power for a wireless impedance based structural health monitoring node. A bi-morph piezoelectric beam and a TEG with a passive heat sink were used to harvest energy from a bridge. The hybrid system with two Advance Linear Devices energy harvester modules was used to condition the voltage output from each device. The hybrid system and module were used to charge a 0.1F supercapacitor to 3.5V which was required to power the

wireless impedance node. The TEG charged the capacitor to 1.18V this being the maximum voltage achievable due to the temperature gradients. The piezoelectric cantilever was then used to further charge the battery to 3.5V, resulting in a charge time of 912 seconds to power the system and take measurements. The system had a maximum power consumption of 72.8mW. Gambier et al (Gambier et al. 2012) developed hybrid energy harvesting cantilever incorporating piezoelectric patches, flexible solar cells and thin film batteries. Thermoelectric energy harvesting was also researched with a view to incorporate flexible TEG design into the device. The hybrid cantilevers consisted of an aluminium substrate, followed by the piezoelectric patches and a thin film battery layer, with a flexible solar cell forming the outer layer. This configuration was symmetric about the aluminium substrate layer. Overall dimensions were 93 x 25x 1.5mm. Raw power levels for each type of devices was assessed a TEG with thermally matched heat sink generated 40mW for a temperature differential of 41°C. The solar cells generated 30mW for an irradiance of 437W/m^2 and the piezoelectric patches generated 0.4mW for a 0.1g input excitation. The cantilever and TEG were connected to an associated power management circuit to charge a single battery cell. A temperature gradient of 31°C resulting 6.6mW of battery power, generated with a charge current of 0.4mAh over 15 minutes. The solar cell was subjected 220W/m^2 of irradiance generated 12.5mW of battery power and a charging current 1.3mAh in 26 minutes. Due to the lower power of the piezoelectric layers a smaller capacity battery was used (0.7mAh) and for a 0.5g input at a resonant frequency of 56.4Hz generated resulting in 0.49mW a charge current of 0.38mAh in 3 hours.

4.2 Prototype Wireless SHM system

A prototype wireless system has been indentified for SHM applications in the aerospace sector and can be seen in Figure 4-7. This board is manufactured by the Mistra Group and is a four channel AE and AU system with a Zigbee wireless communication module. The board has dimensions of 100mm x 138mm. In terms of the AE and AU monitoring the board has a maximum sampling rate of 1MHz with a bandwidth of 1 – 250 kHz. AU pulse can generate tone burst or chirp waveforms with a voltage between 5 -40V. The board has two power inlets and requires 5-18V to operate with the inlet with the greatest voltage is used to power the board. The board consumes differing levels of power dependent which mode of operation is used. The lowest power mode is sleep mode with a timer wakeup which consumes 10mW. Another sleep mode is possible, this time with an AE hit or parametric wakeup which consumes 50mW. In full AE mode the board consumes 170mW. This defines the power requirements that the energy harvesting techniques needs to meet.

To assess the feasibility of powering the board using energy harvesting techniques two investigations were conducted. One investigation involved numerical modelling of current thin film TEGs to find the likely power output for various different temperature gradients that exist on an aircraft. The other, involved experimental investigations into the power generation using piezoelectric patches for typical aircraft vibrations.

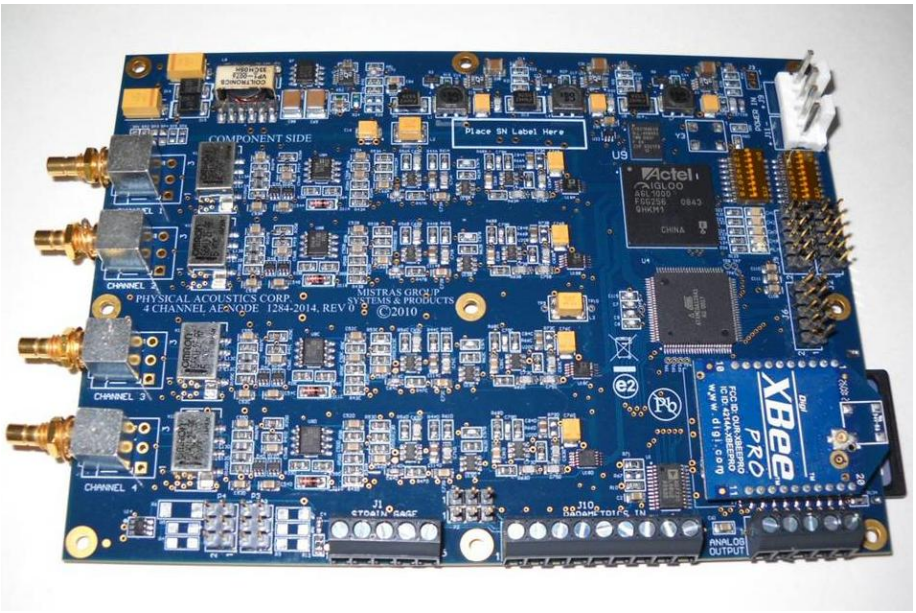

Figure 4-7. Prototype wireless structural health monitoring system

4.3 Thermoelectric Energy Harvesting

4.3.1 Introduction

Certain technological advances have been made in TEG development since previous work conducted at Cardiff University (Featherston et al. 2009). Micropelt have developed a series of thin film TEGs, including the MPG-D751, which was selected for the investigation into the feasibility of powering an SHM system from temperature gradients that exist on an aircraft. These TEGs are manufactured on a silicon substrate using MEMs technology which results in a density of 100 thermoelectric legs pairs per mm^2, which in turn is directly proportional to the voltage output (Bogue 2009). The device uses compounds of Bismuth, Antimony, Telluruim and Selenium to manufacture the leg pairs. The device and a schematic drawing can be seen in Figure 4-8 and Figure 4-9 respectively. To assess the feasibility of these devices temperature data recorded from thermocouples placed on an aircraft was used to generate temperature differentials. These differentials alongside a numerical model were used to generate predicted power levels for different locations on the aircraft.

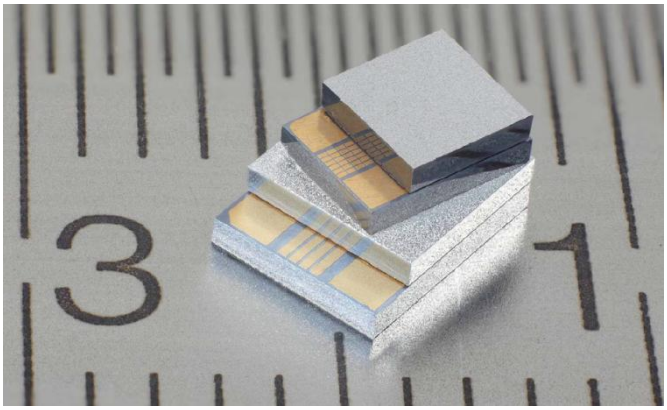

Figure 4-8. Micropelt's thin film range of TEGs (Micropelt 2012a)

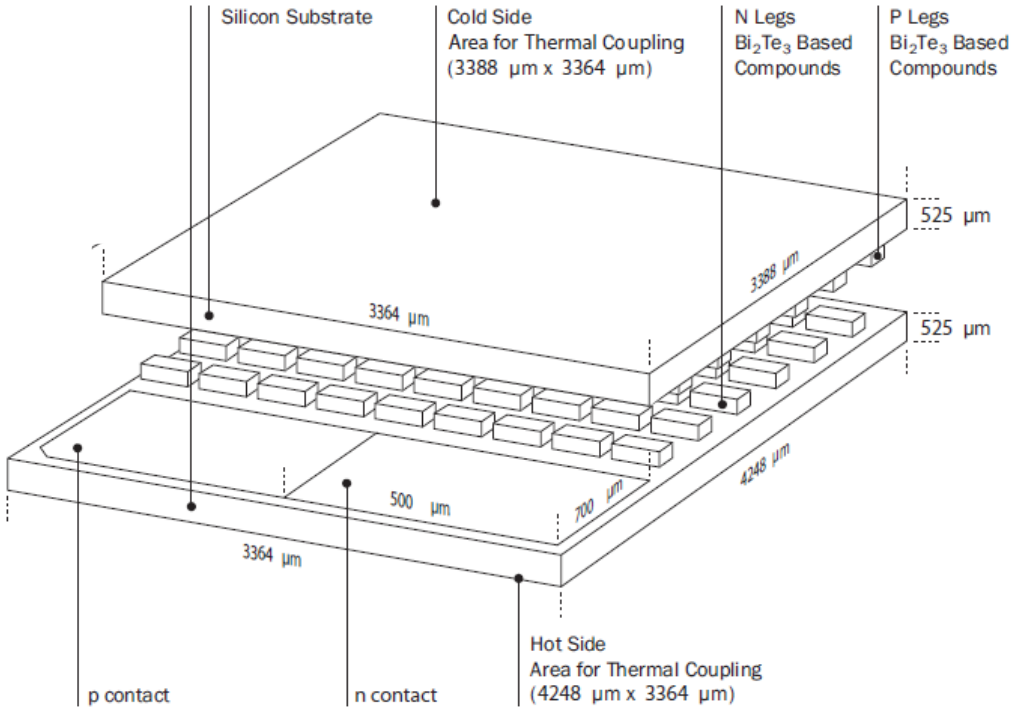

Figure 4-9. Dimensions of the Micropelt MPG-D751 (Micropelt 2012b)

4.3.2 Numerical Modelling Investigation

Using the MPG-D751 as the reference generator, a three dimensional function was derived which defined the output voltage from the TEG in terms of the temperature differential and the mean temperature. In order to derive this function aircraft thermocouple data was analysed to gain the maximum and minimum temperatures and the likely temperature gradients. This effectively defined the boundary limits for the function. These limits were found to be minimum and maximum temperatures of 249 and 318K with a maximum temperature difference of 45K. Due to the voltage of the TEG being proportional to

the temperature differential, the limits for the temperature differential were defined as being from 0 to 68K and maximum and minimum temperatures were used as the mean temperature limits. Micropelt have developed a simulation tool “mypelt” which can be used to assess their TEGs for different temperature applications. This tool can be used to determine the output power and voltage at matched load for certain hot and cold side temperatures. The module has an internal resistance of 396.6Ω and this was used as the load resistance in order to obtain maximum power transfer. The thermal contact resistances of the hot and cold sides were defined as $50x10^{-3}$ cm^2K/W as this is seen as a realistic value by Micropelt. A variety of hot and cold side temperatures were input into the simulation tool within the ranges defined. A number of data points were input to the simulation tool as it was unclear how simulation tool modelled the TEG. The simulation tool was used to define the output voltage for certain hot and cold side temperatures, this was then used to defined the voltage in terms of the temperature differential and the mean temperature. These data points were used to form a surface in a three dimensional plane and MATLAB was then used to fit a surface to the data points using the surface fitting toolbox. Figure 4-10 shows the data points and resulting surface. The surface was defined as f(x,y)=ax+by+c. Excellent correlation was observed between the fitted surface and the data points. This resulted in a three dimension function equation (4.3) which defines the output voltage of a TEG, V, in terms of the temperature differential, ΔT, and mean temperature, T_m

$$V = 0.07802\Delta T - 0.0002928T_m + 0.08471 \quad (4.3)$$

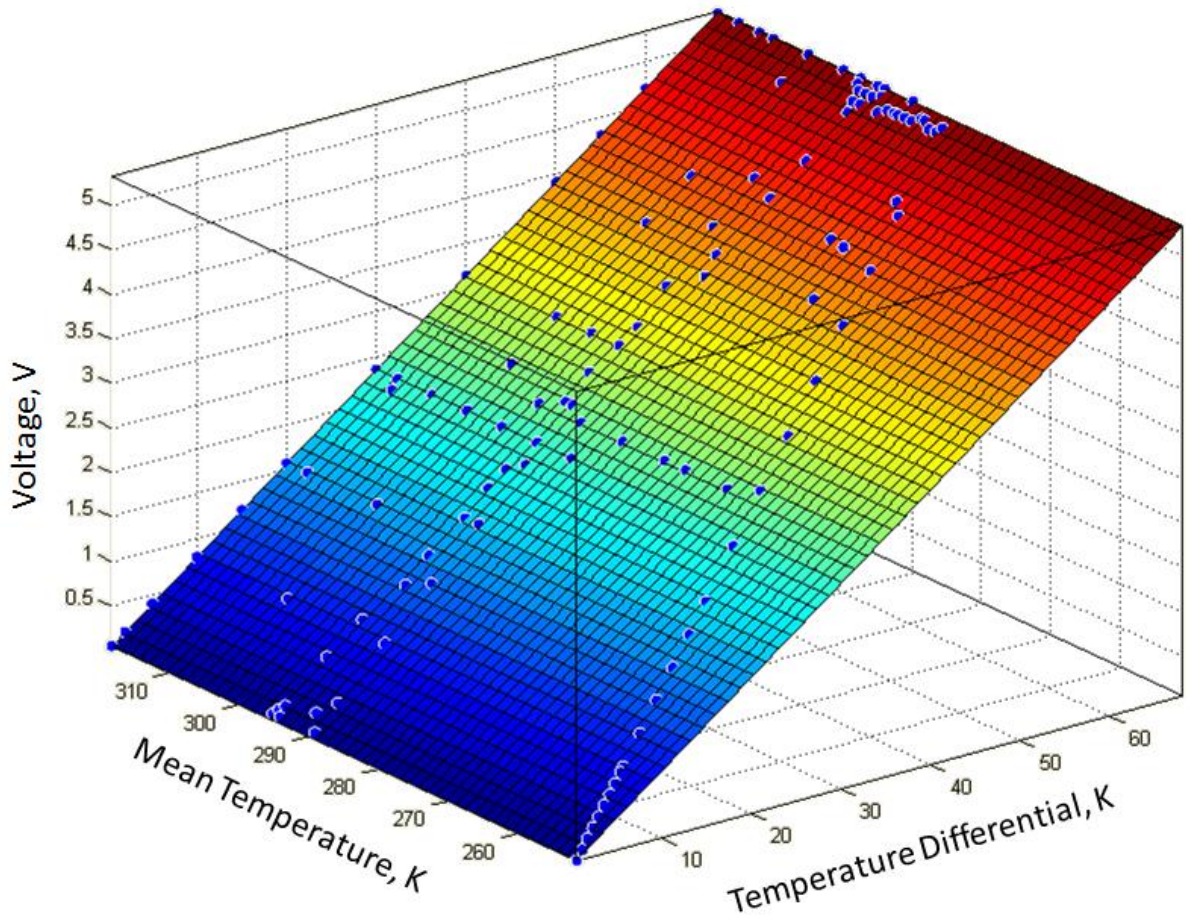

Figure 4-10. Function representing the output voltage of the TEG

The locations for the thermocouples on the aircraft can be seen in Figure 4-11. The areas which were identified for the analysis were the crown, e-bay, cabin, hydraulics, and waste water areas. The ventilation systems were not used as they did not generate significant temperature differences. Thermocouples were placed on the fuselage skin and on any insulation in these areas, there were also thermocouples which represented the ambient temperatures in those areas. The flight data was taken from two separate flights with the first flight resulting in temperature data for the waste water system and the hydraulic systems and the second flight resulting in temperature data for the crown, e-bay and cabin areas. The cargo/bilge area was not used in the analysis as the minimum temperature recorded was outside the temperature range of the simulation tool and presumably the TEG as well.

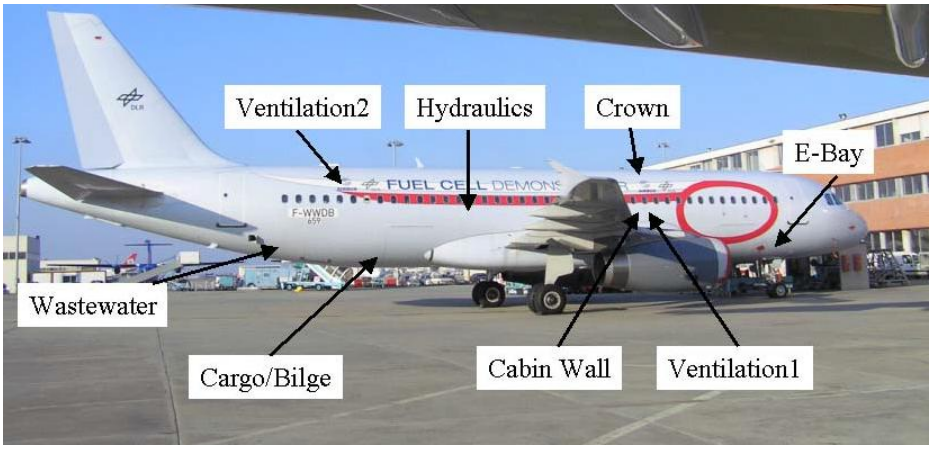

Figure 4-11. Aircraft and location of thermocouples used to simulation TEG power output

4.3.3 Simulated Results and Discussion

Figure 4-12 shows the temperature profiles recorded over a 4 hour period for thermocouples placed on a hydraulic pipeline and in ambient conditions. The figure shows that after an initial 30 minute period the temperature of the pipeline is fairly constant at approximately 35°C. The ambient temperature in this area fluctuates by about 8°C but is fairly constant at approximately 20°C. The subsequent temperature difference is shown in the figure and after the initial 30 minute period is relatively constant with the bounds of 10 and 20°C. Although this data is taken from one particular flight it shows fairly constant temperatures during the flight and therefore could be used as a stable power source if flights are at the same altitude. Figure 4-13 shows the predicted voltage and power output of the TEG using the three dimensional function and the temperature gradients from the hydraulic pipeline to ambient temperatures. The figure shows peak power of 6mW over the four hour period with levels above 1mW being observed across the majority of the flight. The voltage ranges with a maximum of approximately 1.5V but is fairly constant level at around 1V. Although this temperature gradient is fairly constant, it is not sufficient to provide enough power and voltage to directly power the prototype monitoring system with 1 TEG from this particular temperature gradient, however if more TEGs are used the power requirements could be met.

Figure 4-14 shows the recorded temperature using thermocouples placed on two adjacent hydraulic pipelines. The temperature profile for the first pipeline which is referred to as “hydraulic skin 1” has been discussed in the previous paragraph. The second hydraulic pipeline has a similar temperature profile to that of the ambient conditions, however the temperature over the latter half of the flight is lower than that of the ambient temperature.

Both pipelines reach a fairly constant temperature in the first 30 minutes of the flight. A maximum temperature gradient of approximately 23°C is reached around 2 hours into the flight and apart from the first 30 minute period the temperature differential does not drop below 10°C. The resulting power and voltage output from a TEG calculated using the numerical analysis is shown in Figure 4-14. The figure shows the voltage profile reaches a level of 1V after 20 minutes and maintains this level for almost the rest of the monitoring period. Although peak voltage is observed at 2 hours which corresponds to the peak temperature differential. A peak power output of 8.5mW is observed at 2 hrs and for the majority of the flight the power is greater than 2mW. This shows that although the power levels are relatively small they are relatively constant throughout this particular period. Although from these two example cases the power output is not great enough to power the wireless system with one TEG it at least is in the correct magnitude range.

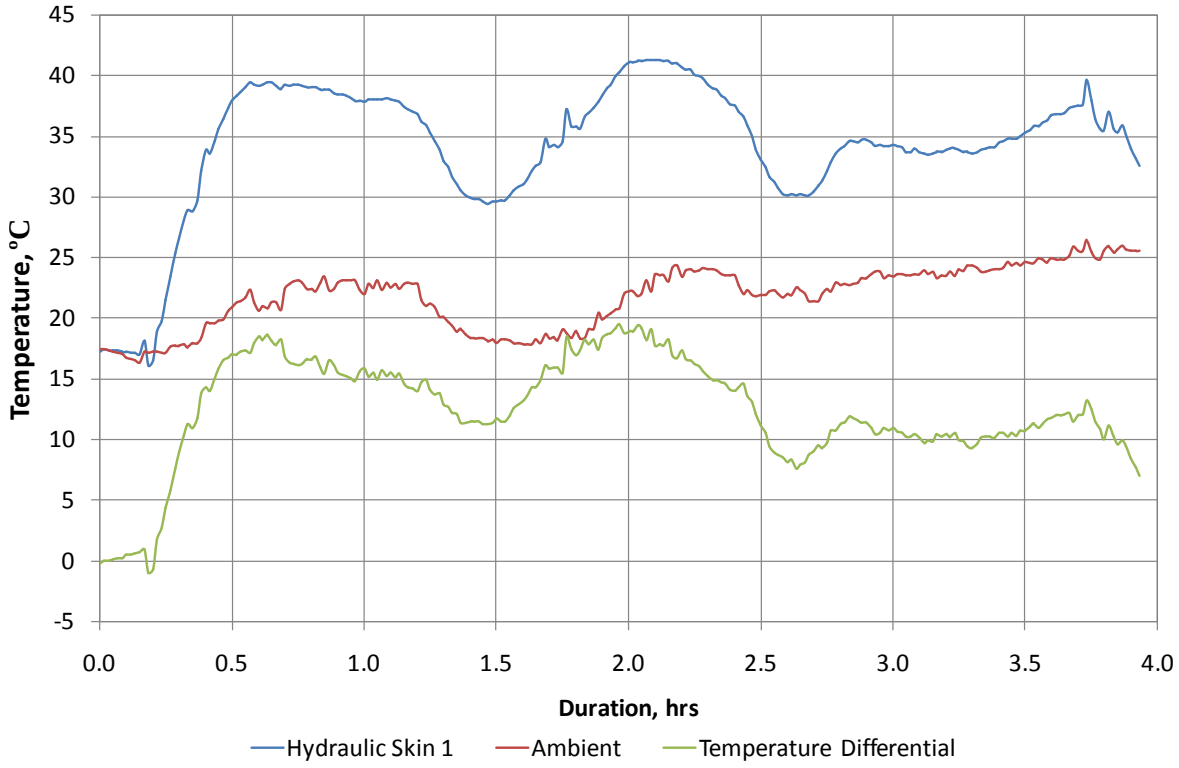

Figure 4-12. Temperature profile for the hydraulic skin 1 and ambient thermocouples

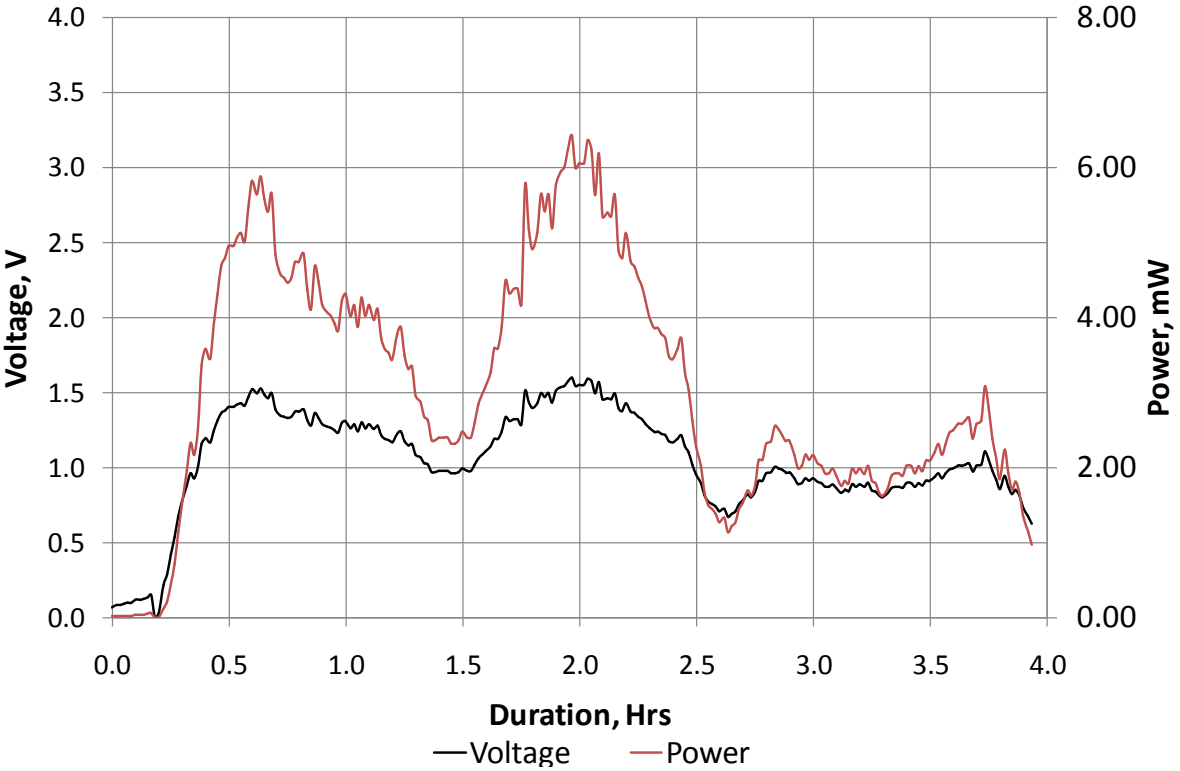

Figure 4-13. Voltage and power output from hydraulic skin 1 to ambient temperature differential

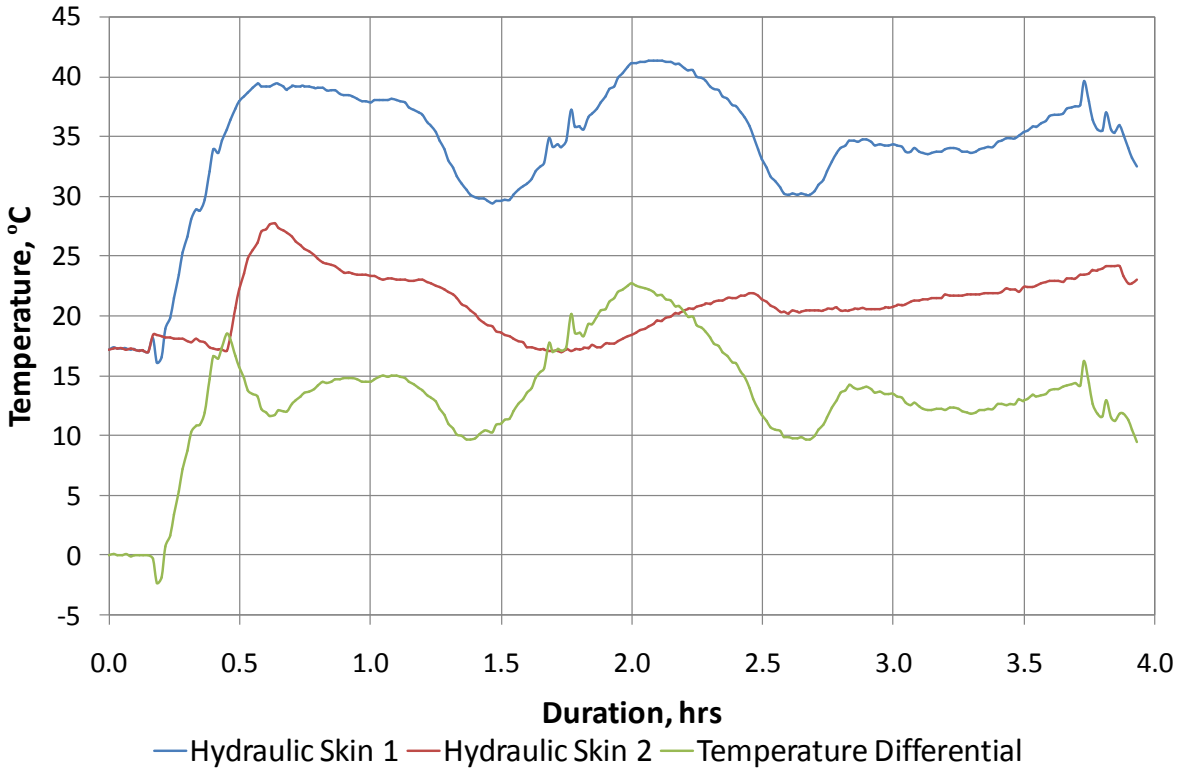

Figure 4-14. Temperature profile hydraulic skin 1 and hydraulic skin 2 thermocouples

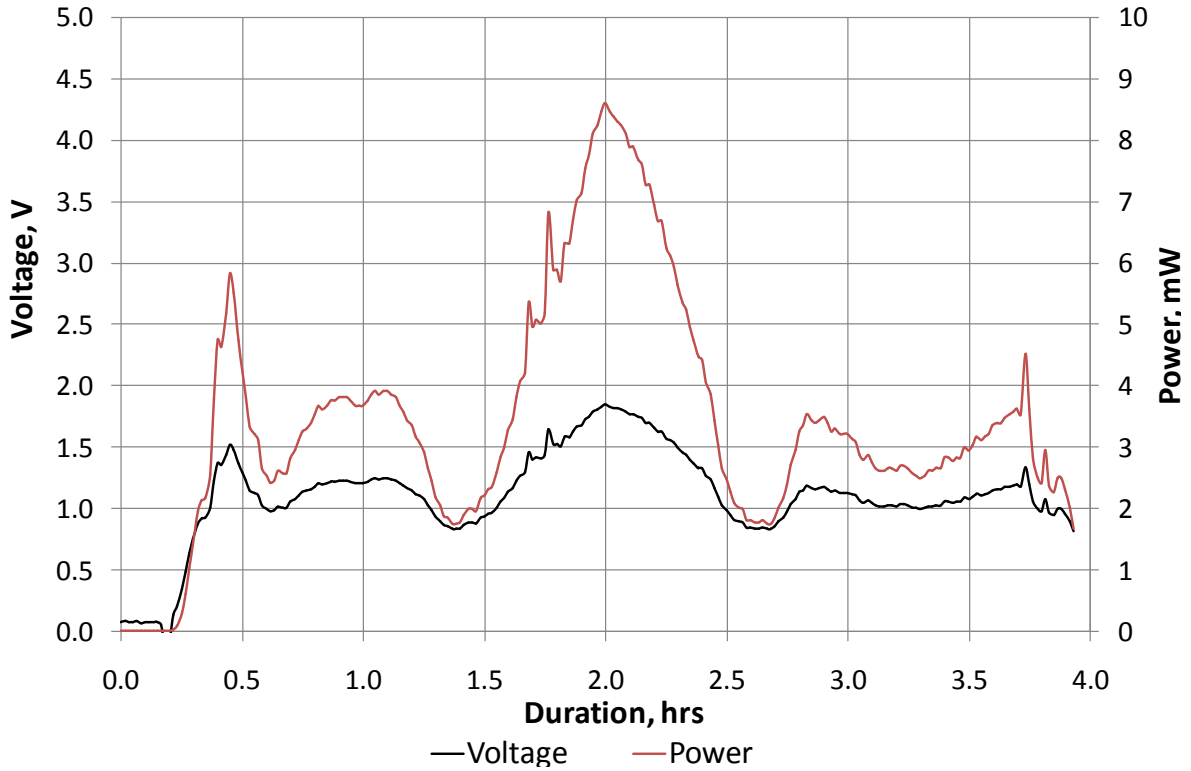

Figure 4-15. Voltage and power output from hydraulic skin 1 to hydraulic skin 2 temperature differential

Figure 4-16 shows the surface temperature of a waste water tank and the ambient temperature from thermocouples placed in this particular location on an aircraft. The temperature data is from a different flight to the results already presented. This data was recorded over a 7 hour period, the ambient recorded temperature starts at 20°C and drops to around -5°C for the first hour after which it continues to decrease to a minimum of -22°C at approximately 5.5 hours. The ambient then starts to increase with a further sudden increase at the end of the flight. Due to the thermal mass of the contents of the water tank and the insulation around the tank the temperature of the water tanks is offset from the ambient temperature. The same decreases in temperature are observed for the ambient temperature however there is an offset in temperature which results in a roughly constant temperature differential of 15°C. The resulting power and voltage of a TEG placed to exploit this particular temperature gradients is shown in Figure 4-17. The figure shows the voltage generated and demonstrates a voltage of 1V can be generated for the majority of the flight. There is an initial start-up period where this 1V level is not reached which extends 40 minutes into the flight, after which the base level is maintained up to 6.5 hrs into the flight. The voltage peaks at a level of 1.5V. This shows the relative steadiness of the voltage that can be generated from this particular temperature gradient. A similar trend is observed for

the power output from 1 TEG where a base level of 2mW is achieved for a large portion of the flight, with peak power of 6mW for the latter half of the flight. Again this temperature differential is not great enough to power the board itself, however several TEGs could be arranged in series or parallel to provide enough voltage and hence power to achieve the desired level.

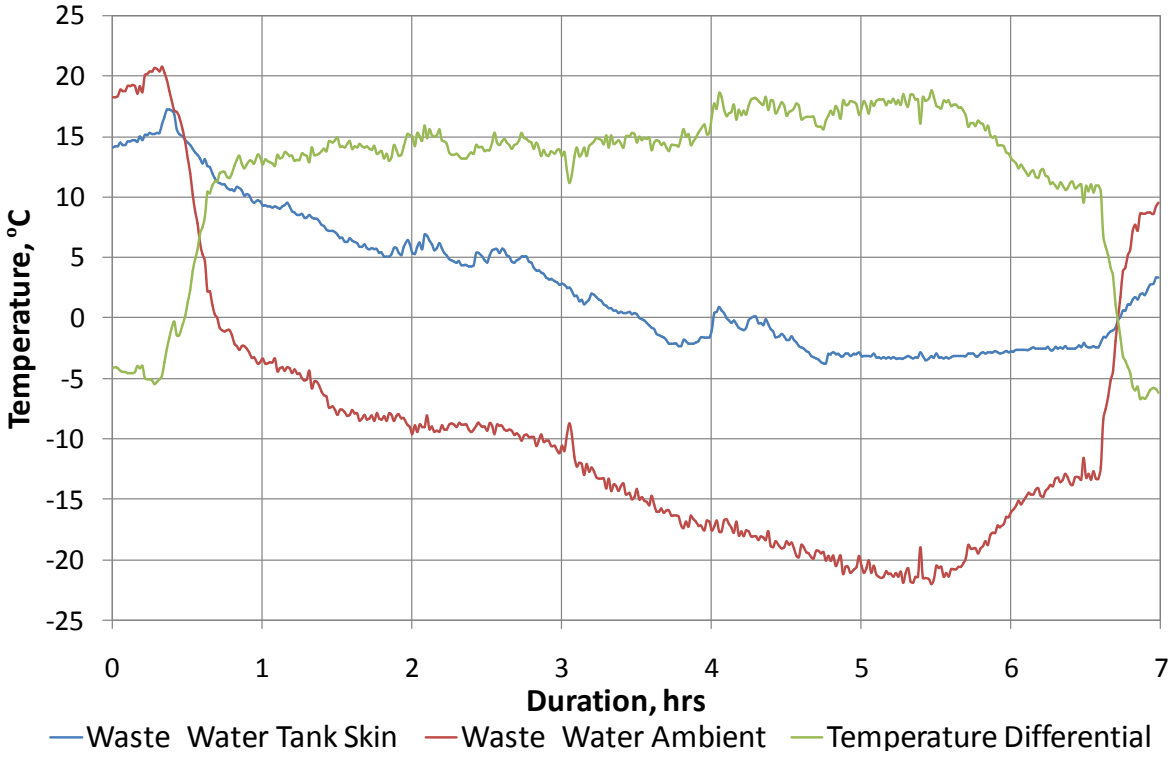

Figure 4-16. Temperature profile for Waste Water Tank skin and ambient thermocouples

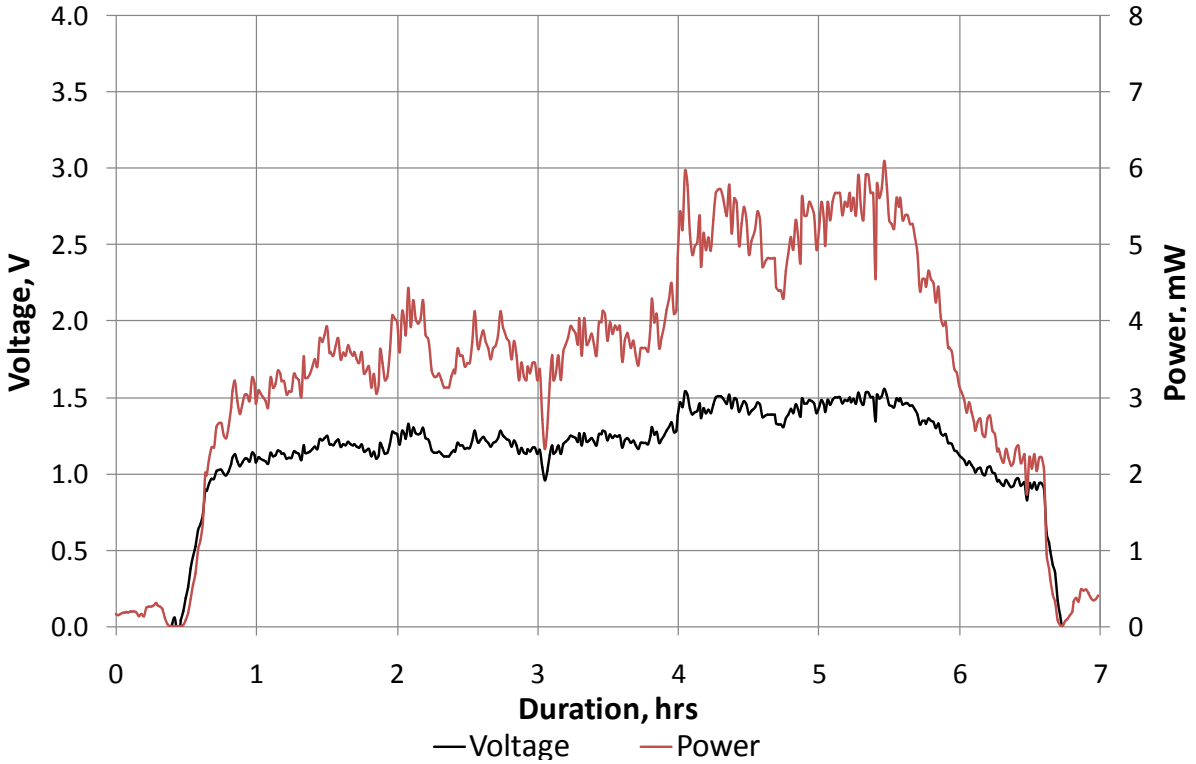

Figure 4-17. Voltage and power output from waste water tank skin to ambient temperature differential

Figure 4-18 shows the temperature of thermocouples placed on the fuselage skin and on the primary insulation in the crown area of the aircraft. The resulting temperature differential can also be seen in the figure. The fuselage temperature shows two distinct periods where the temperature falls to -20ºC for periods of up to 1 hour. This particular flight profile is most likely to correspond to two periods at a relatively higher altitude followed by a period on a runway in between. The temperature for the thermocouple placed on the primary layer of insulation shows a fall in temperature from 30ºC to 20ºC over the first 30 minutes of the flight. This approximate level is maintained for the rest of the flight. This results in a large temperature differential from these locations of 40ºC. This corresponds to a relatively large potential power and voltage output using a TEG which can be seen in Figure 4-19. The voltage profile shows a maximum voltage of above 3V which is maintained for two periods of up to an hour. However at the start of the flight the fuselage temperature is greater than the insulation and hence a negative voltage occurs. This is not a problem however a DC/DC boost converter with a polarity switch would be necessary however additional losses would occur. The power output corresponds to peak power just below 30mW. This particular location shows great promise in powering the system as it would only require 2 TEGs connected in series to provide enough power for the board in sleep mode with parametric or

hit wake up. It still should be noted that this is the power generated at matched load and in reality the external circuitry connected to the TEG is unlikely to have the same internal resistance. The resistance also changes with temperature.

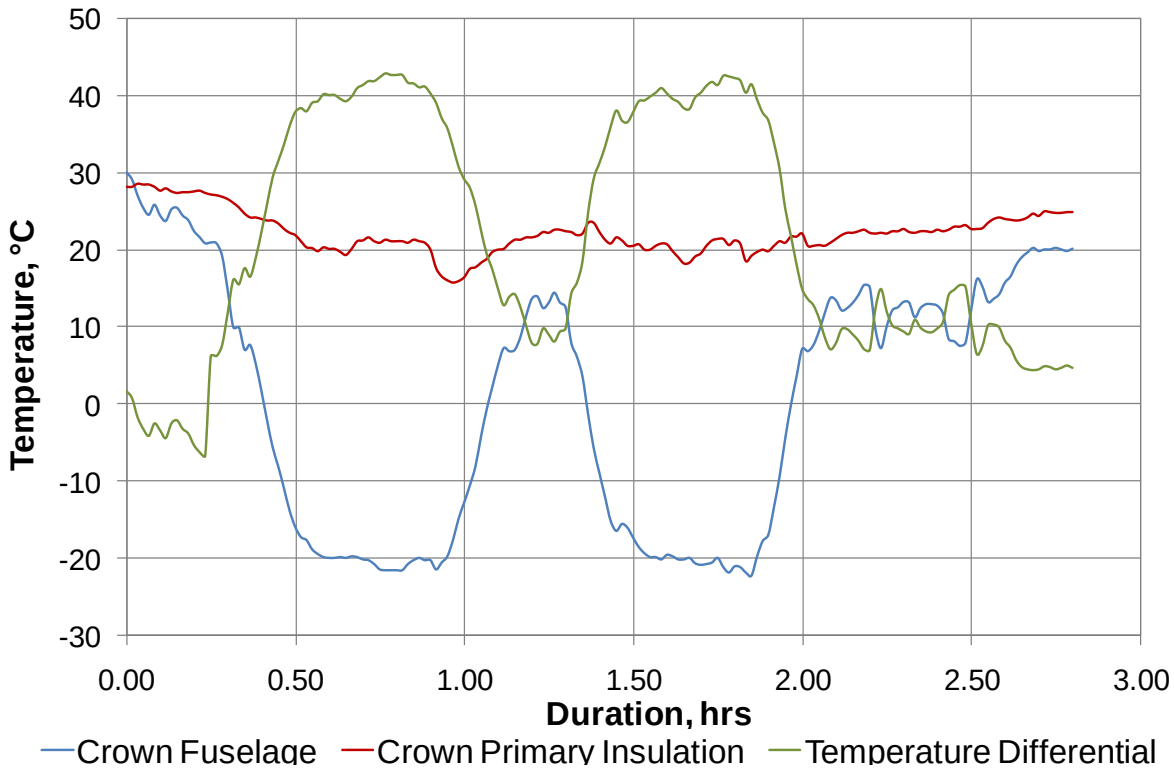

Figure 4-18. Temperature profile for crown fuselage and primary insulation thermocouples

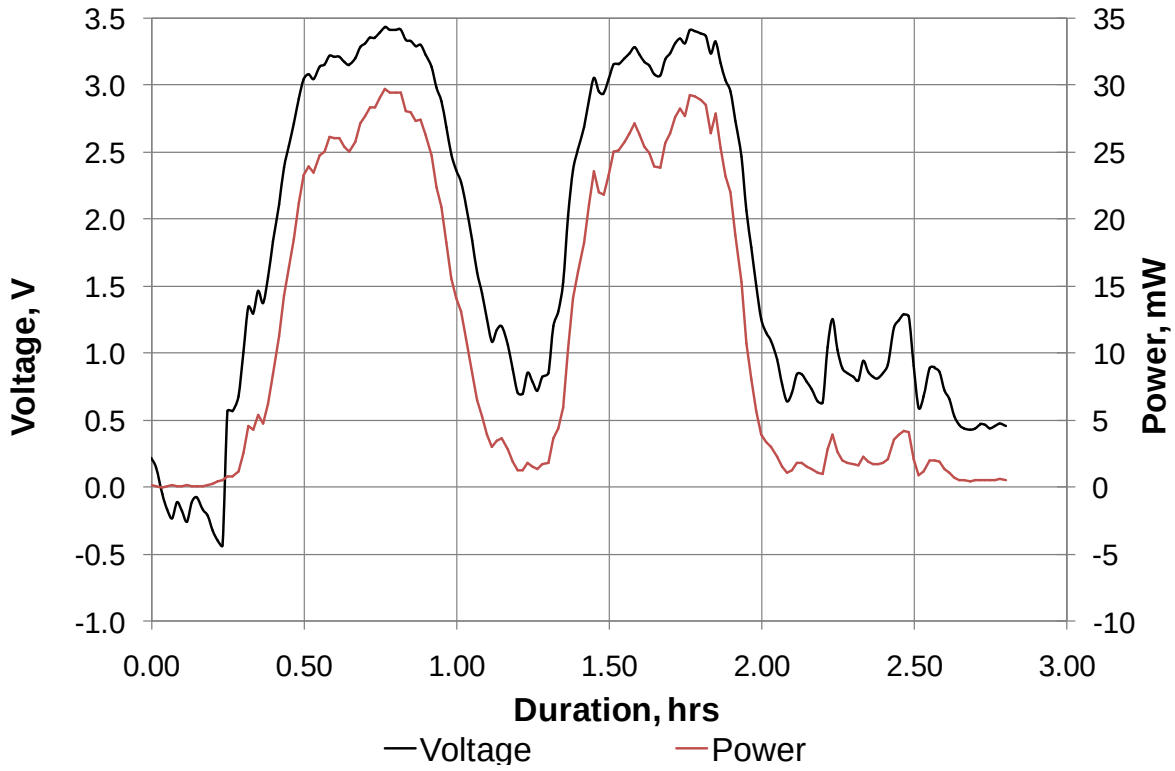

Figure 4-19. Voltage and power output from crown fuselage to primary insulation temperature differential

Figure 4-20 shows the temperature recorded using a thermocouple placed on the fuselage skin and to represent ambient conditions, in the crown area of the aircraft. The temperature profile is very similar to the previous two figures and therefore will not be discussed in detail. A very similar peak temperature differential occurs at a level of 40ºC for two periods of up to an hour. The resulting voltage and power output is shown in Figure 4-21. The figure shows a peak voltage of above 3V and an approximate level of 0.5V is achieved for the majority of the flight. The corresponding power has peak values above 25mW for two periods of up to an hour. Again 2 TEGs connected in series could be used to power the board in the sleep mode from the two peaks in the power observed.

Figure 4-22 shows the temperature profiles over a flight for thermocouples placed on the fuselage skin and on the primary insulation in the e-bay area of the aircraft. A similar fuselage skin temperature is observed as with the crown area of the aircraft, which is to be expected because the data was recorded on the same journey. Minimum temperatures of -20ºC are again observed for periods of up to an hour. Over the same period the temperature of the primary insulations drops from 20ºC to a minimum of 10ºC. This generates peak temperature differentials of over 30ºC for these two periods. The resulting voltage and power outputs which were calculated from the numerical function for this particular temperature

gradient is shown in Figure 4-23. The voltage generated has peak values in these same two periods which results in a voltage of over 2.5V. A minimum voltage of 0.3V is generated for the majority of the flight. The generated power has maximum values of approximately 20mW and 15mW respectively which are generated for periods of up to an hour. Again several TEGs joined in series could provide sufficient peak power to power the board.

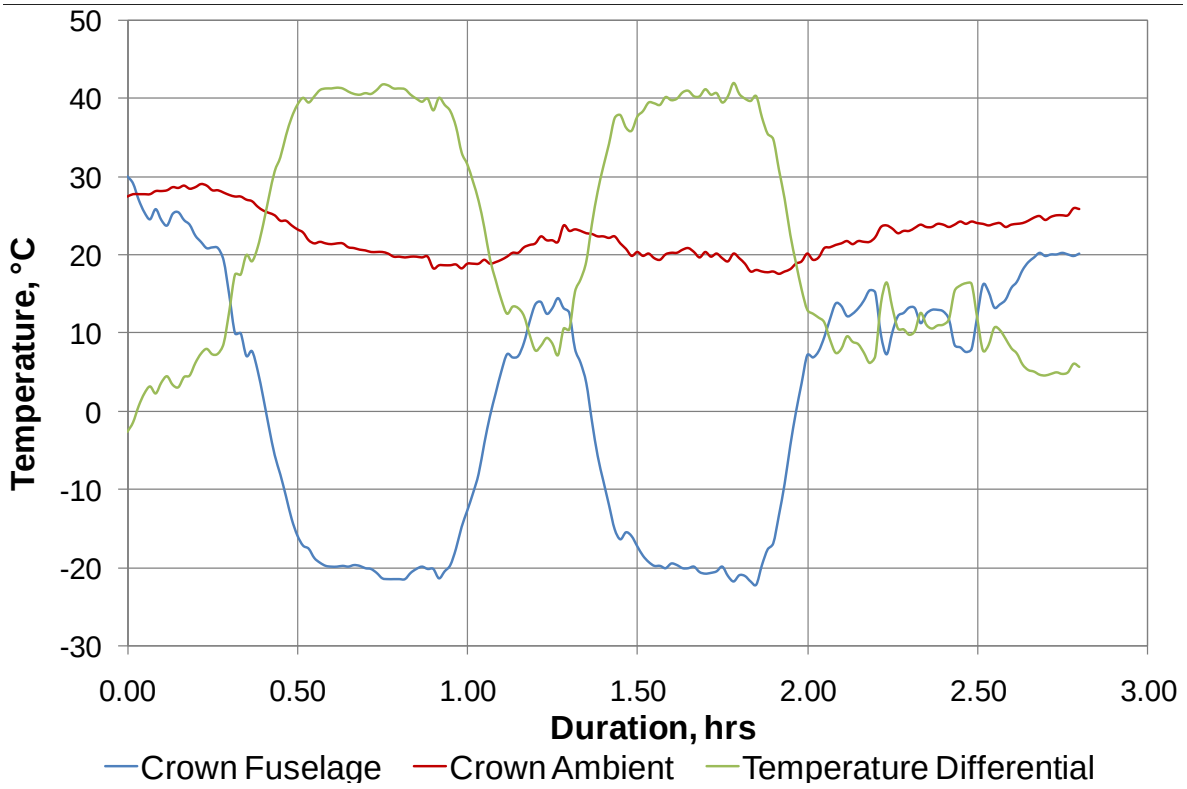

Figure 4-20. Temperature profile for crown fuselage and ambient thermocouples

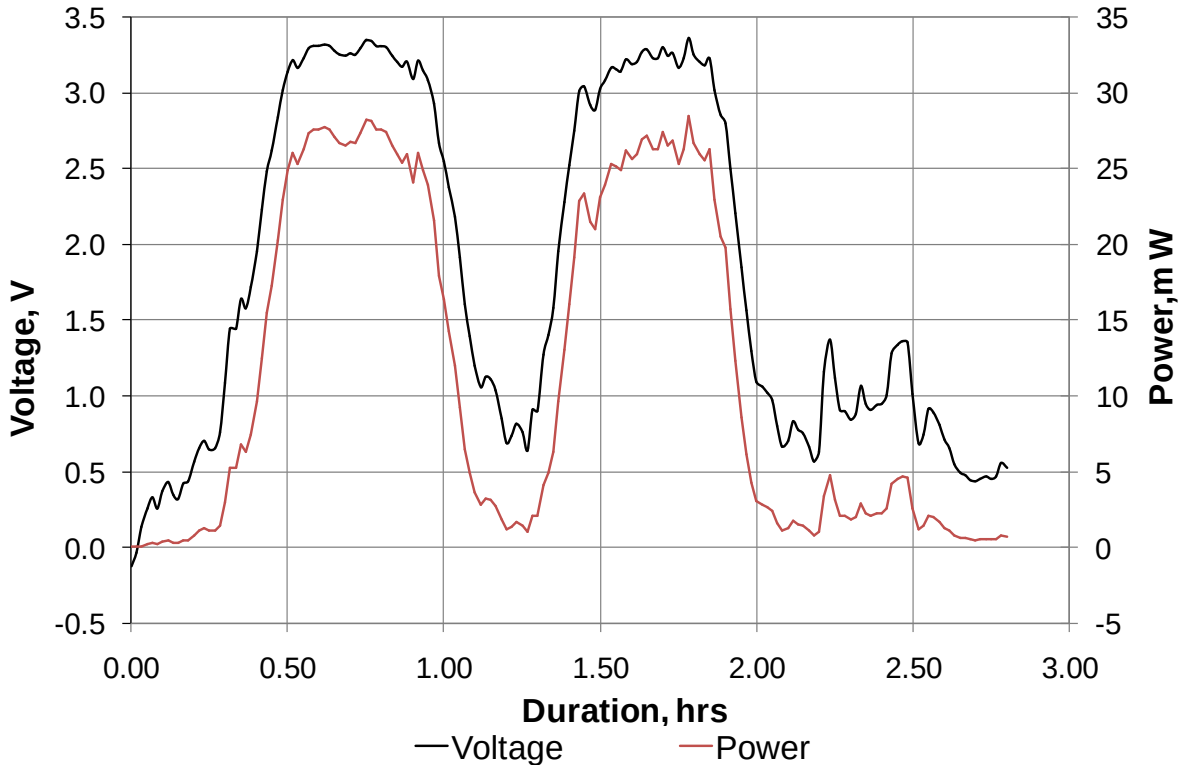

Figure 4-21. Voltage and power output from crown fuselage and ambient temperature differential

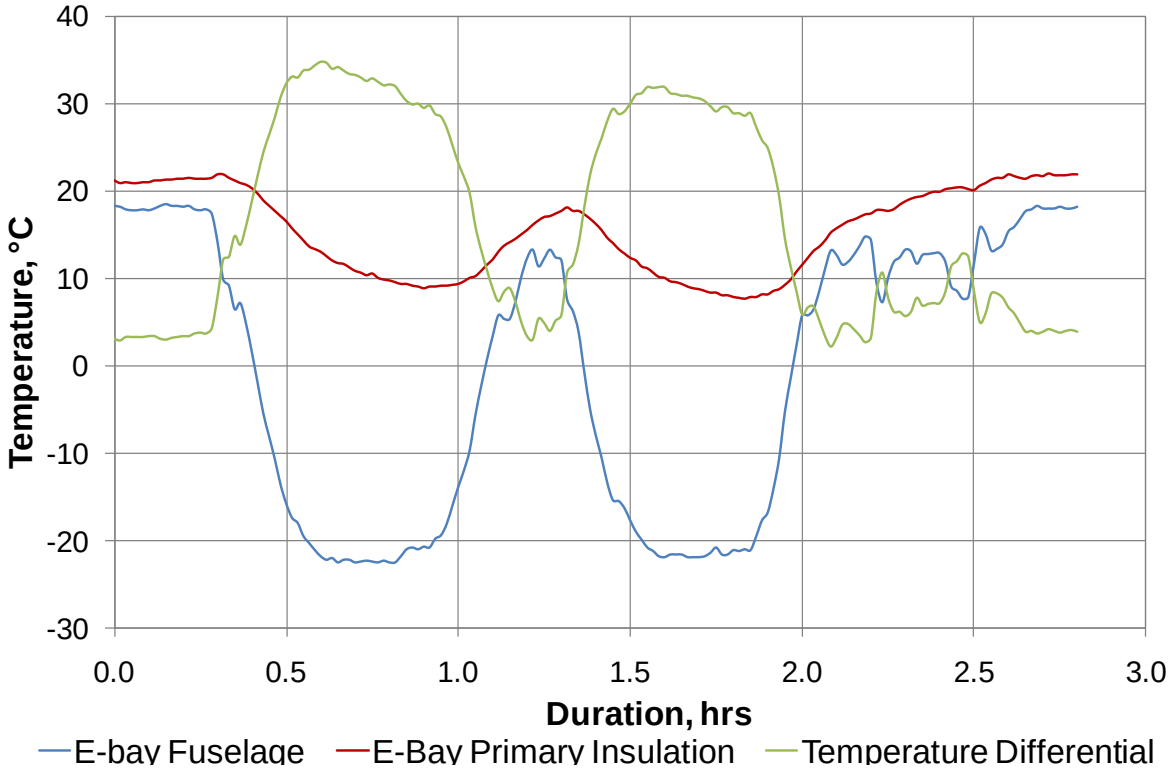

Figure 4-22. Temperature profile for E-bay fuselage and primary insulation thermocouples

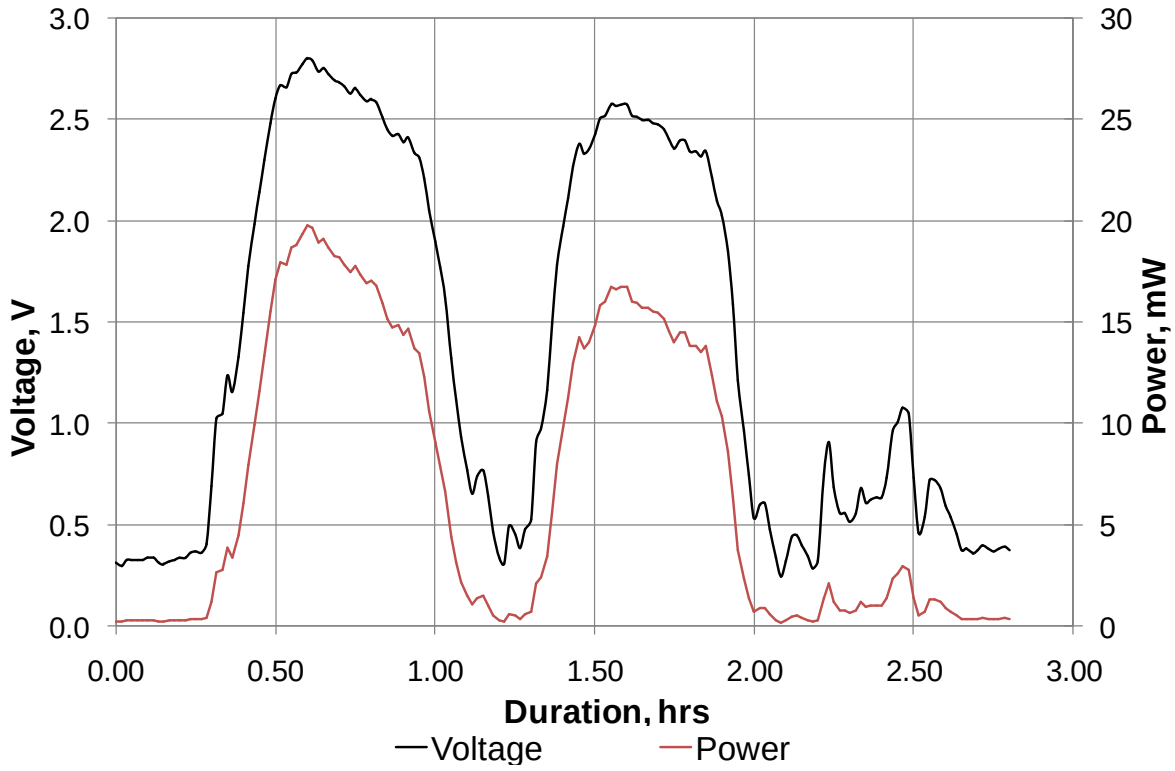

Figure 4-23. Voltage and power output from e-bay fuselage and primary insulation temperature differential

Figure 4-24 shows the temperatures recorded using a thermocouple monitoring the fuselage skin and a thermocouple that represents ambient conditions in the e-bay area of the aircraft. The profile for the fuselage temperature is the same as for the previous e-bay analysis and the ambient temperature differs from the primary insulation temperature only slightly. This is due to the close proximity of these two thermocouples and there not being any other insulation layers in this part of the aircraft. This generates a temperature differential of up to 40°C for the first defined peak and 35°C for the second defined peak. The resulting simulated power and voltage outputs from a TEG placed to exploits this temperature can be seen in Figure 4-25. The voltage generated reaches peak voltages of approximately 3V and a constant voltage level in the order of 0.5V. This relates to peak power levels of 25 and 20mW which is maintained for periods of around an hour. Again this potential temperature differential could be used with several TEGs to provide enough power for the wireless prototype SHM system.

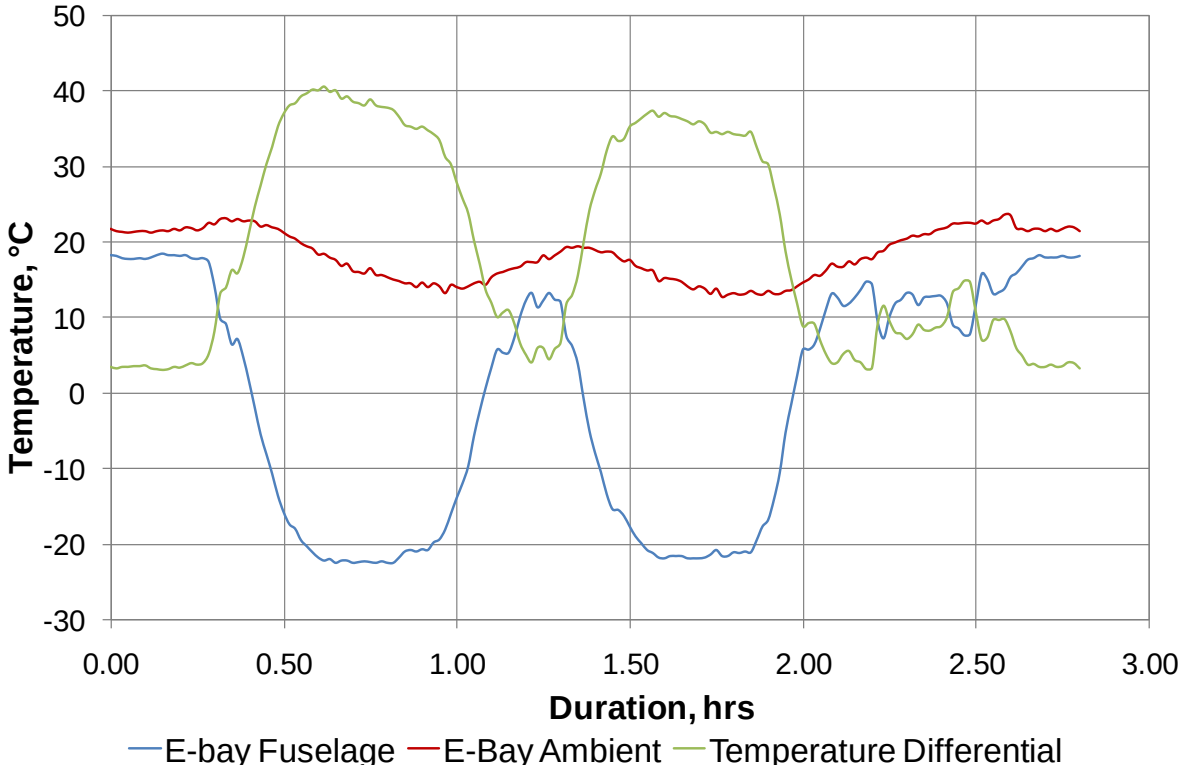

Figure 4-24. Temperature profile for E-bay fuselage and ambient thermocouples

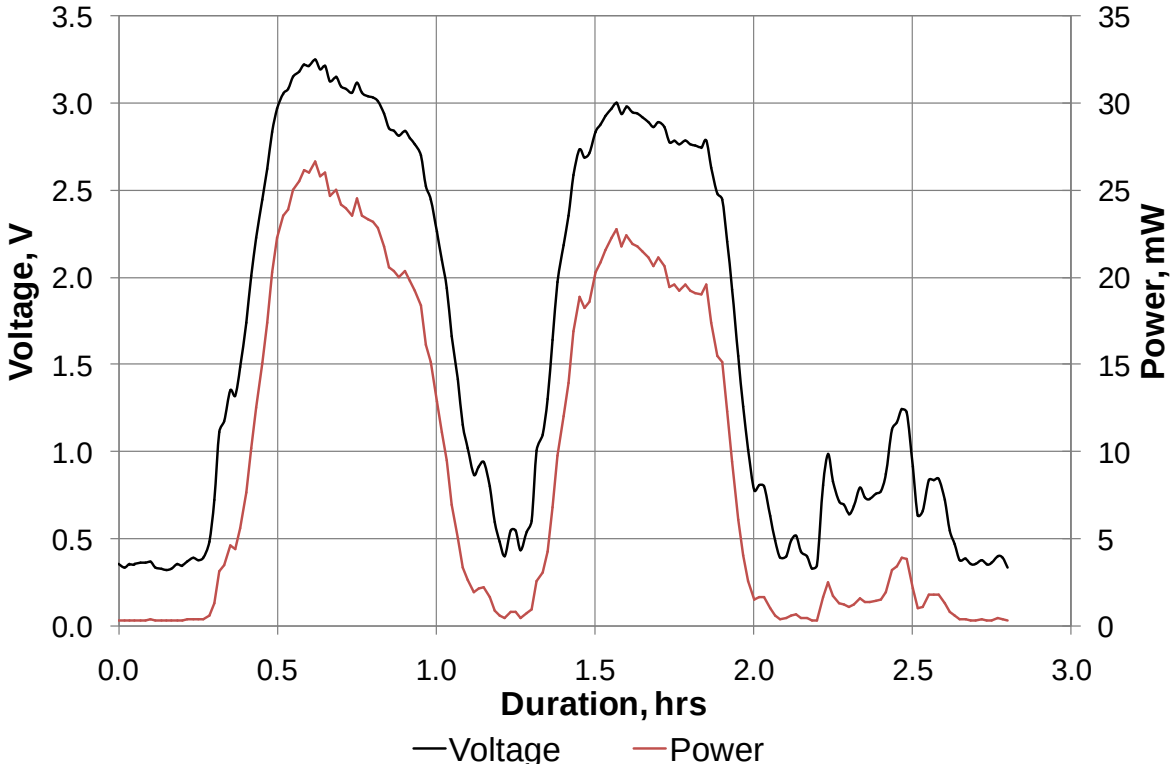

Figure 4-25. Voltage and power output from e-bay fuselage and ambient temperature differential

Figure 4-26 shows the temperature profiles of the fuselage and primary insulation in the cabin walls of the aircraft measured using thermocouples in this particular area. The fuselage temperature profile is similar to that observed in previous scenarios and shows minimum temperatures of -20°C for two periods of approximately an hour. A thermocouple placed on the outside of the primary insulation towards the cabin itself shows the temperature falls from an ambient temperature of 20°C to a minimum temperature of 0°C mimicking a similar cyclic nature. This results in two distinct periods of peak temperature differentials of approximately 30°C. The simulated voltage and power output from a TEG for the temperature gradients shown in Figure 4-26 can be seen in Figure 4-27. The figure shows two distinct peaks in terms of power and voltage, these peak levels are maintained for approximately an hour and 45 minutes respectively. The peak voltages are greater than 2V respectively with corresponding peak values of approximately 12mW. A number of TEGs greater than two would be required to provide enough power for the wireless system.

Figure 4-28 shows temperature data recorded using thermocouples placed on the cabin wall fuselage and on the secondary insulation layer. The next interface in this region is the interior cabin wall itself. The fuselage profile is the same as previously discussed, the temperature of the secondary layer of insulation is constant throughout the whole flight at around 20°C, with only very small reductions in temperature which are observed when the fuselage skin reaches -20°C. This results in a maximum temperature gradient of 40°C, the first peak is observed in the flight from 0.5 to 1 hour and the second from 1.5 to 2 hours. This peak temperature differential is maintained at a peak temperature differential for the periods defined. Figure 4-29 shows the simulated power and voltage which could be achieved if this particular temperature gradient was exploited. The simulated voltage from the TEG reaches peak values of 3.5V and is maintained for two periods of up to 30 minutes, the resulting power output at a matched load of 396.6Ω results in a peak value of 30mW. Again a minimum of 2 TEGs could be used to generate sufficient peak power that would match the power requirements of the prototype wireless system. In reality it may be difficult to produce an energy harvesting device to exploit this temperature as the required heat sink and the distances involved are the largest when compared with other temperature scenarios. Therefore it may be difficult to achieve these temperatures at the hot and cold side of a TEG and if heat sinks are required further analysis would be required to calculate the power to weight ratio of the device.

Figure 4-30 shows the temperature profile for thermocouples placed on the primary and secondary insulation. The profiles have been discussed individually in previous figures.

The simulated results for this scenario have been conducted as it may be easier to fabricate a device to exploit this differential. With this in mind peak temperature gradients of 20°C was achieved. Figure 4-31 shows the simulated voltage and power output for the specified temperature gradient which has a peak voltage of 1.6V which generated approximate peaks of 7mW at matched load.

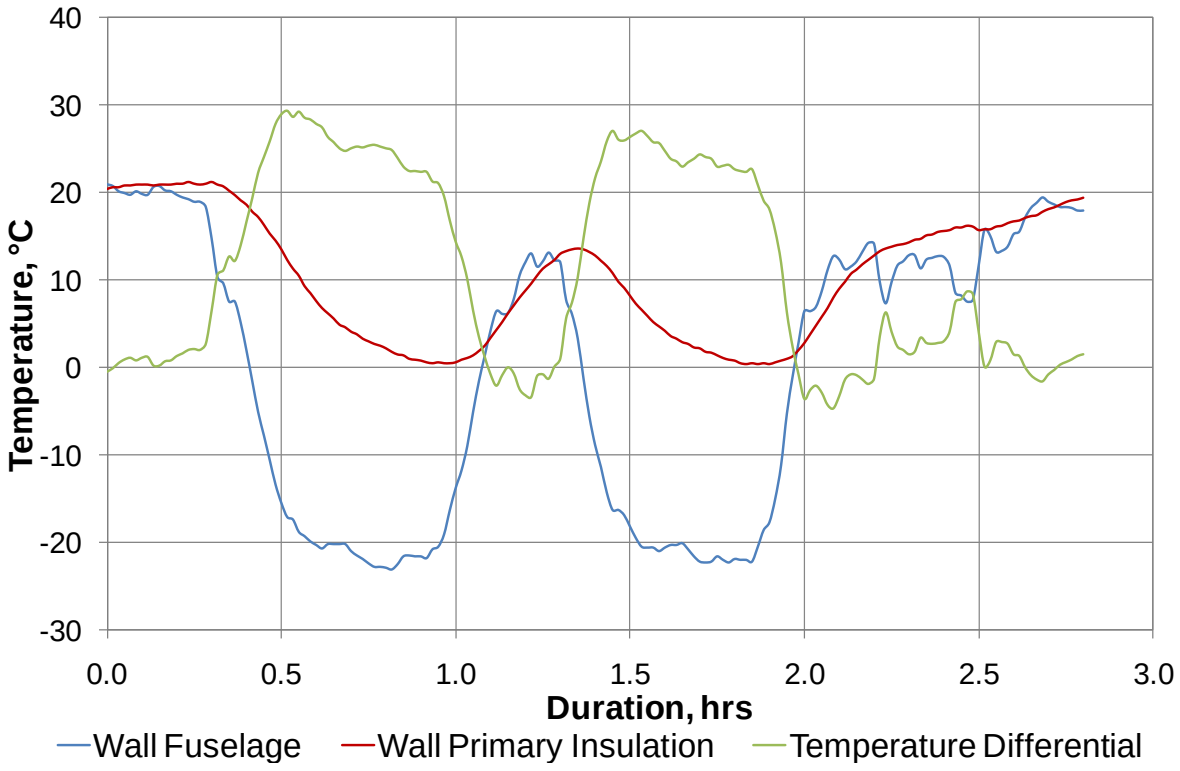

Figure 4-26. Temperature profile for cabin wall fuselage and primary insulation thermocouples

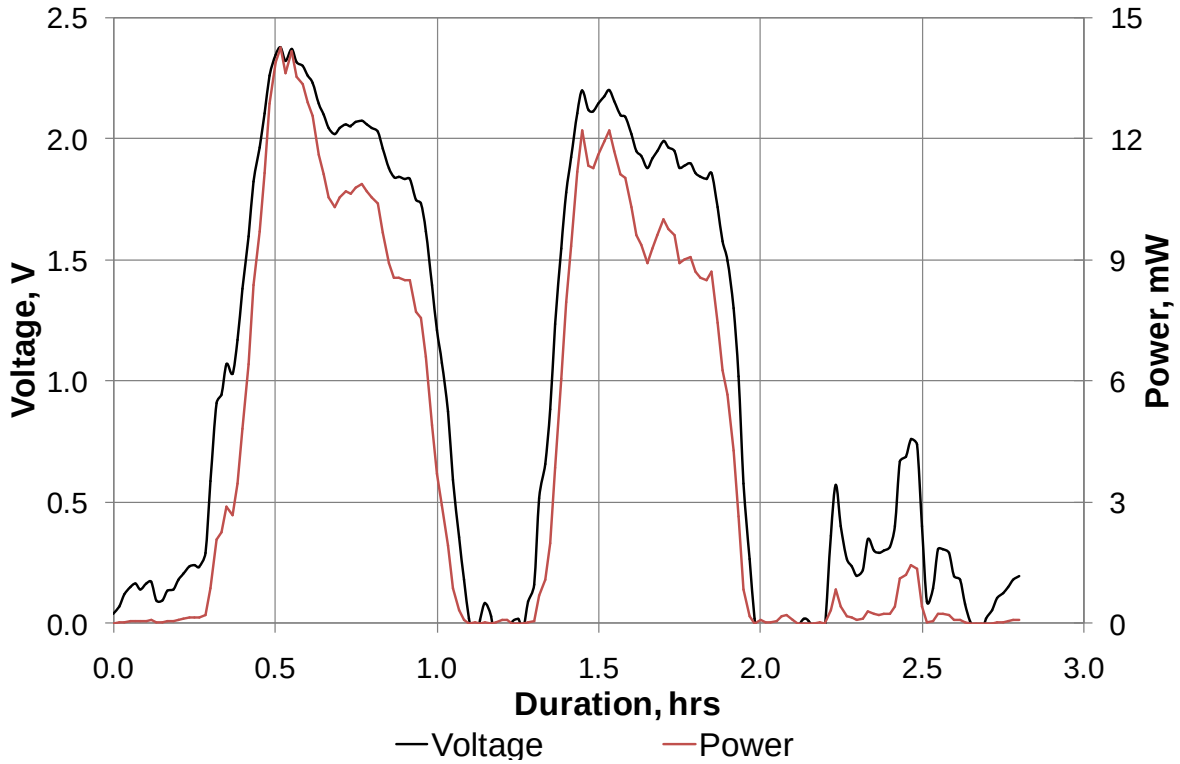

Figure 4-27. Voltage and power output from cabin wall fuselage and primary insulation temperature differential

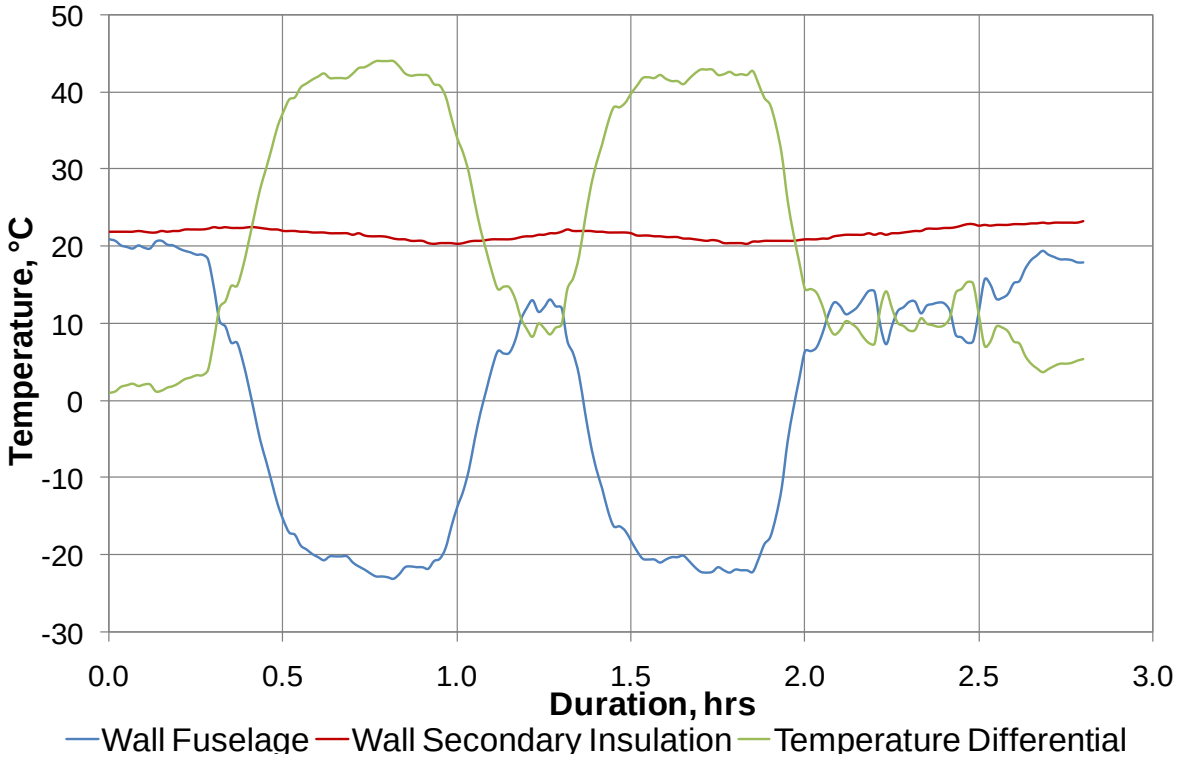

Figure 4-28. Temperature profile for cabin wall fuselage and secondary insulation thermocouples

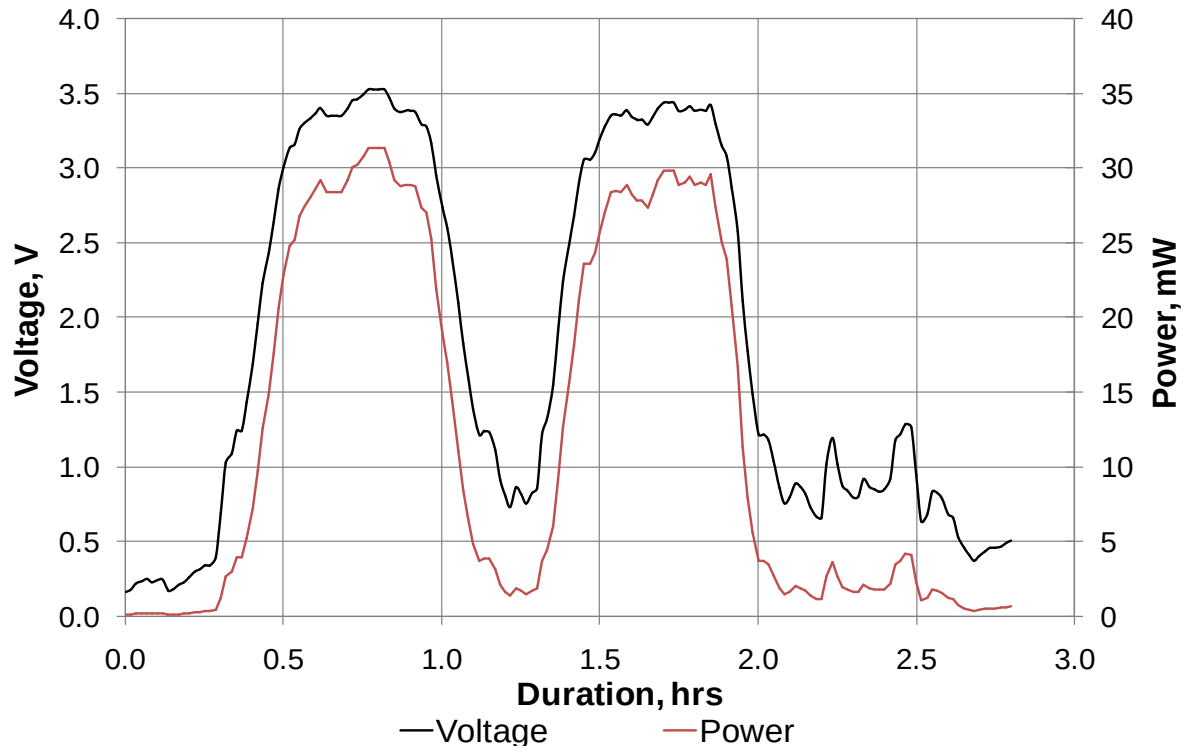

Figure 4-29. Voltage and power output from cabin wall fuselage and secondary insulation temperature differential

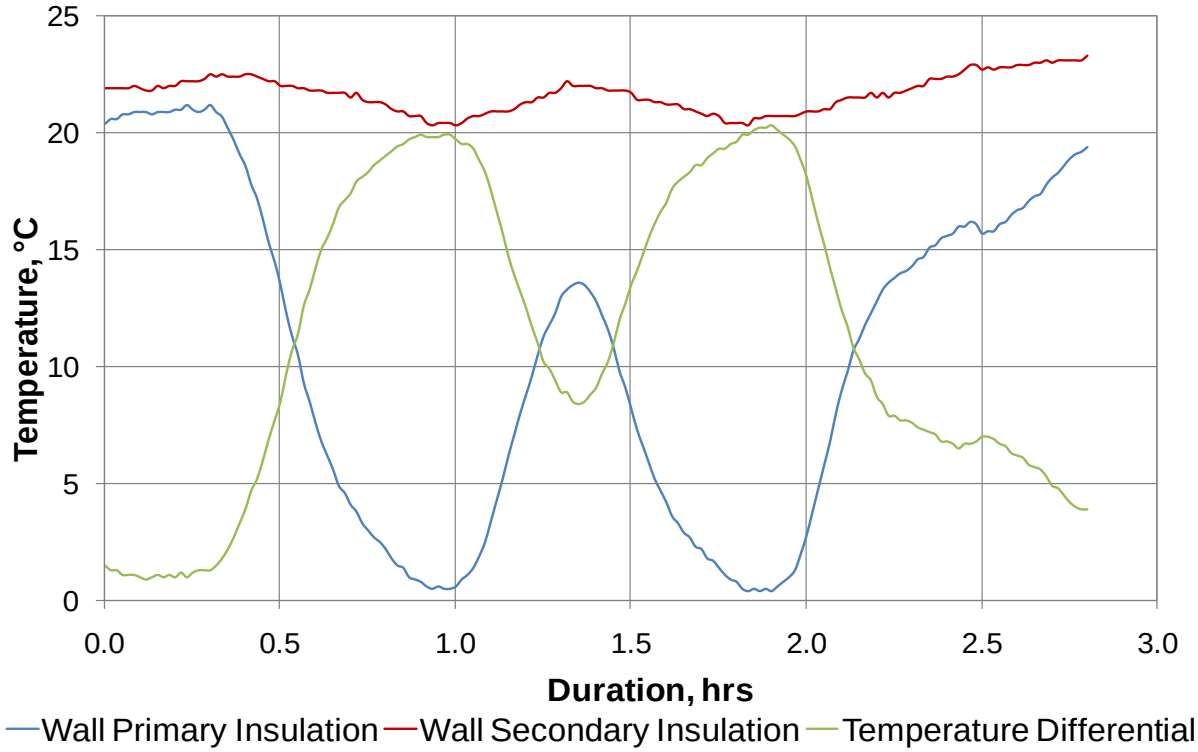

Figure 4-30. Temperature profile for cabin wall primary and secondary insulation thermocouples

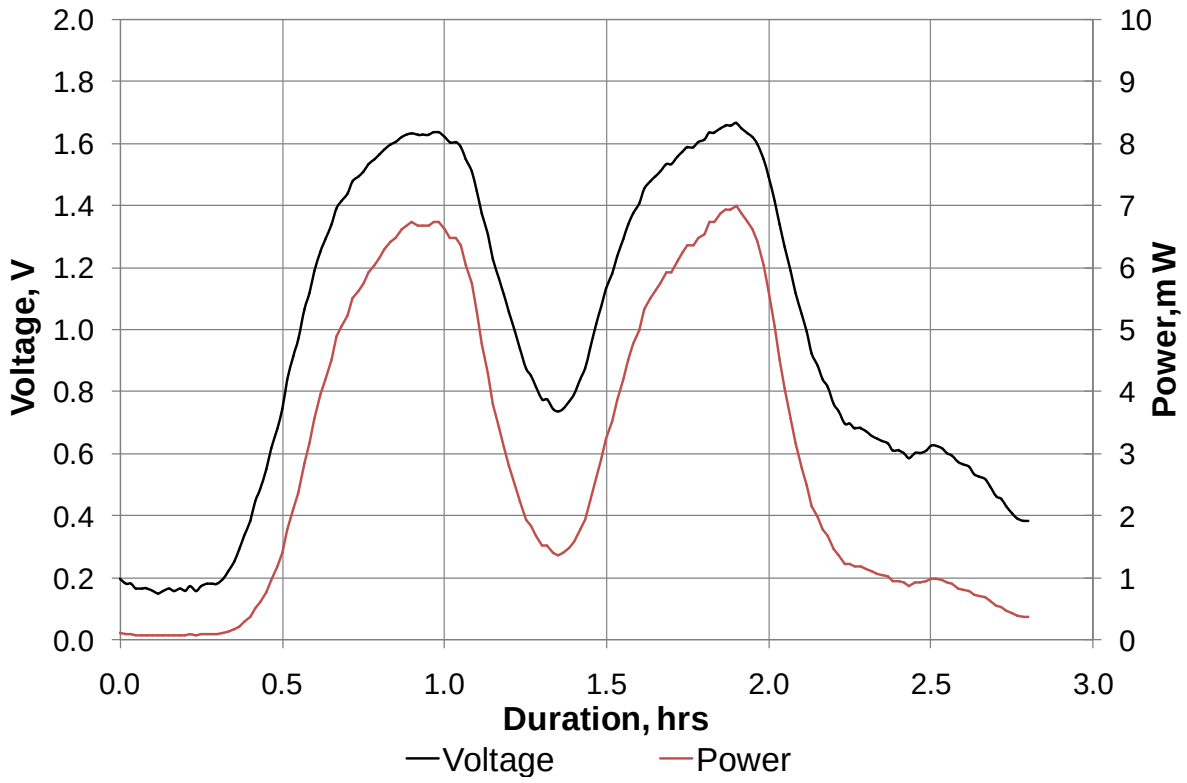

Figure 4-31. Voltage and power output from cabin wall primary and secondary insulation temperature differential

Table 4-1 shows a summary of the results for all the different temperature differentials already discussed. The table shows the peak temperature differential and peak power for each location. In addition the average power was calculated by integrating the peak power profiles and divided by the length of the flight. The average power gives a better indication of whether that a system of TEGs could power the wireless platform. For peak temperature differentials of 18 to 43°C, peak powers from 6 to 30mW can be generated, this results in average power levels of 2 to 10mW. This shows the potential of this device to provide the main power source for the system as the simulated power is in the correct order of magnitude. Taking the examples of the hydraulic pipeline and crown fuselage to ambient differentials an analysis of resulting number of TEGs was conducted to find the number of TEGs that would be required in series to provide 5V and an average power of 50mW. In the case of the hydraulic pipeline 3 TEGs in series provides a peak voltage of 5.54V. Five parallel groups of the 3 TEGs would be required to provide an average of 50mW.This results in a total number of 15 TEGs. However if for example the load resistance was unmatched at 50Ω, utilising the “mypelt” simulation tool this resulted in a TEG voltage reduction of 78%. Assuming the 3D function is still valid and applying a 78% drop in voltage, this would require 10 TEGs in series to provide the 5V and 20 parallel groups to provide an average power of

50mW over this profile. Therefore a total of 325 TEG units would be required, however this creates a large series resistance and it would be more practical to use a voltage booster to reduce the number of TEGs in series. For the crown fuselage skin to the primary insulation differential three parallel groups of two TEGs connected in series would provide a peak voltage of 6.86V generating an average power of 69.38mW, resulting in a total number of 6 TEGs. It is therefore feasible using this type of TEG to provide sufficient power levels for the prototype board. Using the same approach and same assumptions for an unmatched load of 50Ω this would require 7 TEGs in series to provide a 5V the system requires and 13 parallel groups to provide an average power of 50mW. Therefore the number of TEG units required for unmatched load significantly increases by 310 and 85 units respectively for the two examples presented. Therefore in reality solutions would be required to overcome the problem.

Table 4-1. Summary of results from various locations on an aircraft

Temperature Differential Between:	Peak Temperature Differential, K	Peak Power, mW	Average Power, mW
Hydraulic Skin 1	19.50	6.43	3.09
Ambient			
Hydraulic Skin 1	22.70	8.60	3.46
Hydraulic Skin 2			
Waste Water Skin	18.80	6.10	3.41
Waste Water Ambient			
Crown Fuselage	42.90	29.70	10.13
Crown Primary Insulation			
Crown Fuselage	42.00	28.50	10.20
Crown Ambient			
E-Bay Fuselage	34.80	19.78	5.84
E-Bay Primary Insulation			
E-Bay Fuselage	40.60	26.68	8.12
E-Bay Ambient			
Cabin Fuselage	29.40	14.27	3.58
Cabin Primary Insulation			
Cabin Fuselage	44.10	31.34	10.89
Cabin Secondary Insulation			
Cabin Primary Insulation	20.30	6.99	2.27
Cabin Secondary Insulation			

4.3.4 Conclusions

Simulations have been shown that a TEG placed in different locations on an aircraft for a particular flight can produce power in the correct order of magnitude for the requirements of the prototype SHM board. Further analysis of the average power levels showed that 6 – 15 TEGs could be connected in series and parallel to provide sufficient peak voltage and average power levels for the system. However there are some assumptions and limitations in the numerical analysis. Firstly the output power assumes maximum power transfer at matched load, secondly there is no consideration of the design of the subsequent heat sinks or thermal storage devices required to provide the hot and cold temperatures to the TEG. Also it is unknown if in reality these temperature gradients could be maintained at the TEG interface. Further consideration of the structures to be monitored and their proximity to the defined temperature differentials would be necessary in order to reduce the amount of required wiring. Further analysis would be required from further flight data to determine the repeatability of these temperature differentials.

4.4 Vibration Energy Harvesting

4.4.1 Introduction

The piezoelectric effect is observed in certain materials where subject to a mechanical strain, the material becomes electrically polarised. The extent to which this polarisation occurs is directly proportional to the applied strain. The piezoelectric effect exists in two modes, the first is the ability of a material to convert a mechanical strain into an electrical charge, and the other is to transform electrical potential into mechanical strain. The first mode is known as the direct piezoelectric effect and will be used in this investigation to generate power from typical aircraft vibrations. This section of the chapter aims to assess the feasibility of using piezoelectric devices for powering the prototype wireless board.

4.4.2 Experimental Procedure

To investigation the feasibility of providing sufficient power for the requirements of the prototype system a be-spoke test rig was developed to promote deflection and hence curvature and strain in one dimension. The test rig can be seen Figure 4-32 and consisted of a 20mm thick steel base plate with two vertical 15mm thick supports that run the length of the base plate positioned 200mm apart. Two further 15 x 15mm square steel bars were used to clamp the plate to these two vertical supports using four bolts per bar. An LDS V201 electromagnetic shaker driven by a PA25E amplifier was placed underneath the centre of

the panel. An Agilent 33220A waveform generator was used to drive the amplifier with a 100mVpp sinusoidal signal at a variety of signals. In order to promote deflection in one dimension the electromagnetic shaker was connected to a 10 x 10mm aluminium bar via a brass connecting rod which ran along the centre line of the specimen. Two further bars were placed on the top of the specimen in order to clamp the plate.

The specimen and the energy harvesting device can be seen in Figure 4-33, the specimen was manufactured from an aerospace grade BS1470 6082-T6 0.7mm thick aluminium plate which was then cut into a circular diameter of 300mm. A circular panel was used to enable the harvester to be tested at a range of different orientations. A MIDE Quickpack QP10n piezoelectric actuator was adhered to the centre of the panel using M-Bond AE-10 strain gauge adhesive manufacture by Vishay Precision group. The MIDE Quickpack device consists of a monolithic sheet of piezoelectric material housed in a flexible copper clad polyimide laminate. The device itself has dimensions of 50.8 x 25.4 x 0.38mm. The monolithic sheet of piezoelectric material has an active area of 45.97 x 20.57 mm and a thickness of 0.254mm. These devices were primarily developed for sensing and actuation purposes but have found uses as piezoelectric energy harvesters.

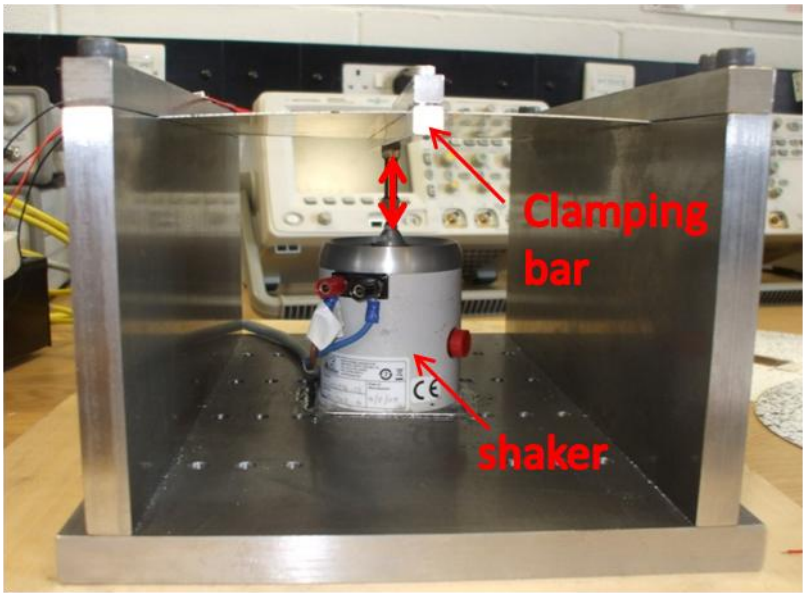

Figure 4-32. Vibration energy harvesting test apparatus

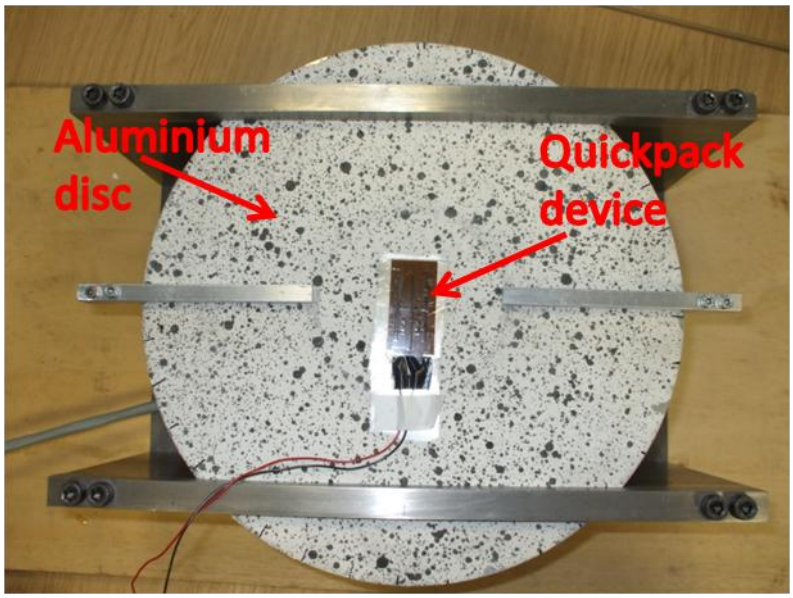

Figure 4-33. Vibration energy harvesting specimen

An initial investigation was conducted in order to assess the potential of this device. The panel was vibrated at typical frequencies ranging from 20 to 300Hz which had been observed from frequency spectrums calculated from accelerometers placed on the wing. An example can be seen in Figure 4-34. This figure clearly shows a frequency bandwidth of a couple of hertz to a maximum frequency of 300Hz. Therefore the panel was vibrated at frequencies from 20Hz to 400Hz. For each incremental frequency an Agilent oscilloscope was used to record the peak and rms AC voltage from the device. A variable resistance junction box was used to change the load resistance on the device from 500kΩ to 1kΩ in order to find the load resistance for maximum power transfer. This preliminary investigation indentified the frequencies at which maximum power generation occurred. A second investigation was conducted using the same energy harvesting device and experimental apparatus. For this investigation a paint speckle pattern was applied to the specimen using spray paint. Firstly a matt white base layer was applied to the specimen, once this had dried a matt black pattern of random speckles of paint was applied by throttling the spray paint valve so it sputtered onto the specimen. This created a random pattern on the specimen so the individual pixels could be tracked in order to determine displacement and strains. The applied pattern can be seen Figure 4-35. This pattern was applied in order to use a digital image correlation (DIC) system to record the displacement of the panel. Two high speed Photron SA-1 cameras were used to capture images at 5000fps, a reference image was calculated before testing at each individual frequency. This was then used in the calculation to determine the displacement of the panel. Once the displacement of the centre line of the

panel was determined for maximum positive and negative profiles, the change in curvature was calculated in order to define relationships between the curvature of the panel and the expected power output.

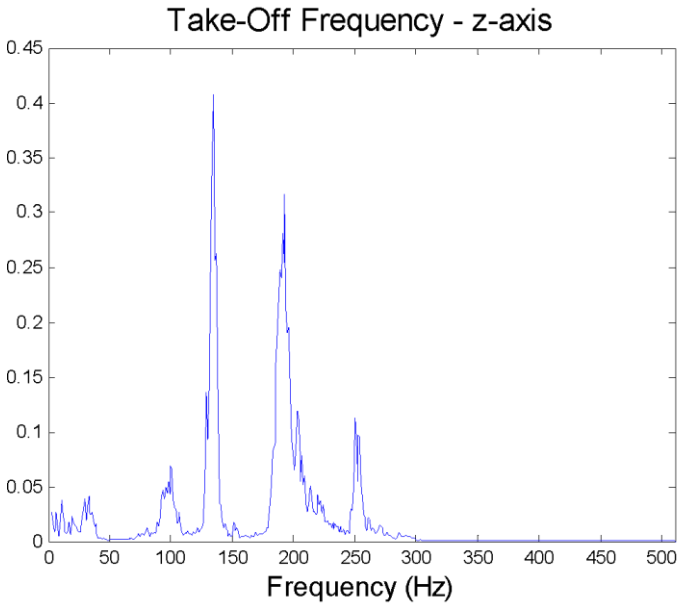

Figure 4-34. FFT of accelerometer data recorded during take off

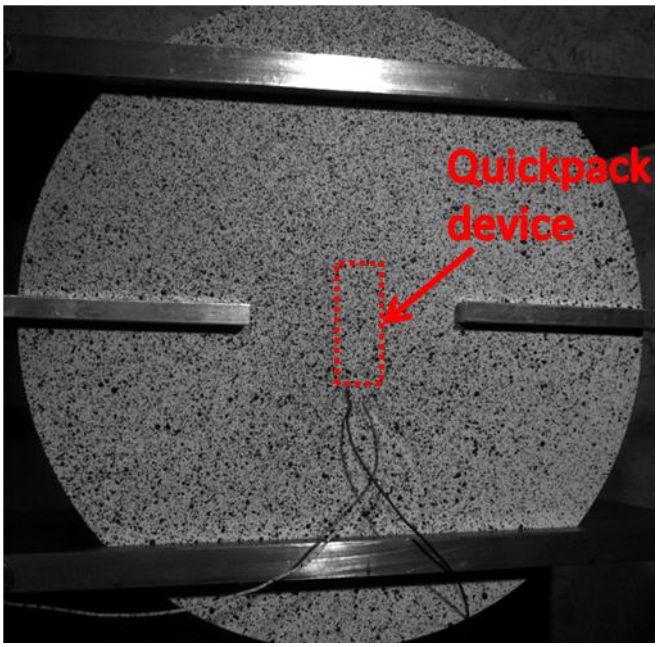

Figure 4-35. High speed image showing the secondary investigation experimental set-up

4.4.3 Experimental Results and Discussion

Figure 4-36 shows the peak AC power for a variety of load resistances for example frequencies from the preliminary investigation. This demonstrates the principle of load

matching where for each frequency of vibration there is a load resistance which corresponds to a peak power output and therefore maximum power transfer. It can also be seen that this particular matched load resistance changes for different frequency vibrations. This is a potential problem in situations where broadband vibrations occur and will lead to inefficient power transfer if resulting electronic circuitry has a constant resistance. Figure 4-37 shows resulting peak AC power at matched load for the range of frequency of vibrations that are typically found during an aircraft flight. For each corresponding frequency the resistance at which maximum power transfer occurs is also shown. The peak power AC power profile shows two frequencies at which considerable amounts of power are generated. The first peak is at 40Hz and corresponds to a peak power of 422μW, the second peak is at 300Hz and corresponding to 1095 μW of peak AC power. The resistances at which maximum power transfer occurs for these peaks are 100 and 10kΩ respectively. Outside these two described peaks very little power is harvested. When comparing these two peaks with the frequency spectrum from typical aircraft vibrations shown in Figure 4-34, these two peaks occur at the lower and higher end of the typical frequency bandwidth, therefore suggesting the device may not the most efficient solution for harvesting power across the whole bandwidth. It is though that these two peak are the device mimicking the natural frequency of the plate as suggested by Delebarre (2012) The load resistance at which maximum power transfer occurs drastically changes from 200kΩ at 20Hz to 5kΩ at 400Hz. A piezoelectric device has a capacitive rather than an inductive internal impedance of a typical power source (Ottman et al. 2002). This therefore means that the reactance of the device changes with frequency of vibration, generally for a capacitive reactance is large at low frequencies and small at high frequencies, this agrees with the change in load resistance for maximum power transfer. However further modelling and experimentation to measure the device impedance would be required for progressing this work further. If a higher resolution of data points in terms of the resistance values was used a smoother trend may occur. This would have to be accounted for when designing a power management system and would probably require further adaptive electronics in order to impedance match the device for the load resistance of the management system. Figure 4-38 shows the RMS power calculated using the RMS voltage recorded on an oscilloscope. As expected the same trend is observed with peaks in the RMS power at 40 and 300Hz respectively, which corresponds to peak rms power of 219 and 443μW respectively. The RMS power can be thought of as the average or continuous power that can be generated. The reasons for the peak at these two vibration frequencies will be discussed when analysing the secondary investigation where DIC measurements were used to record the displacements of the panel.

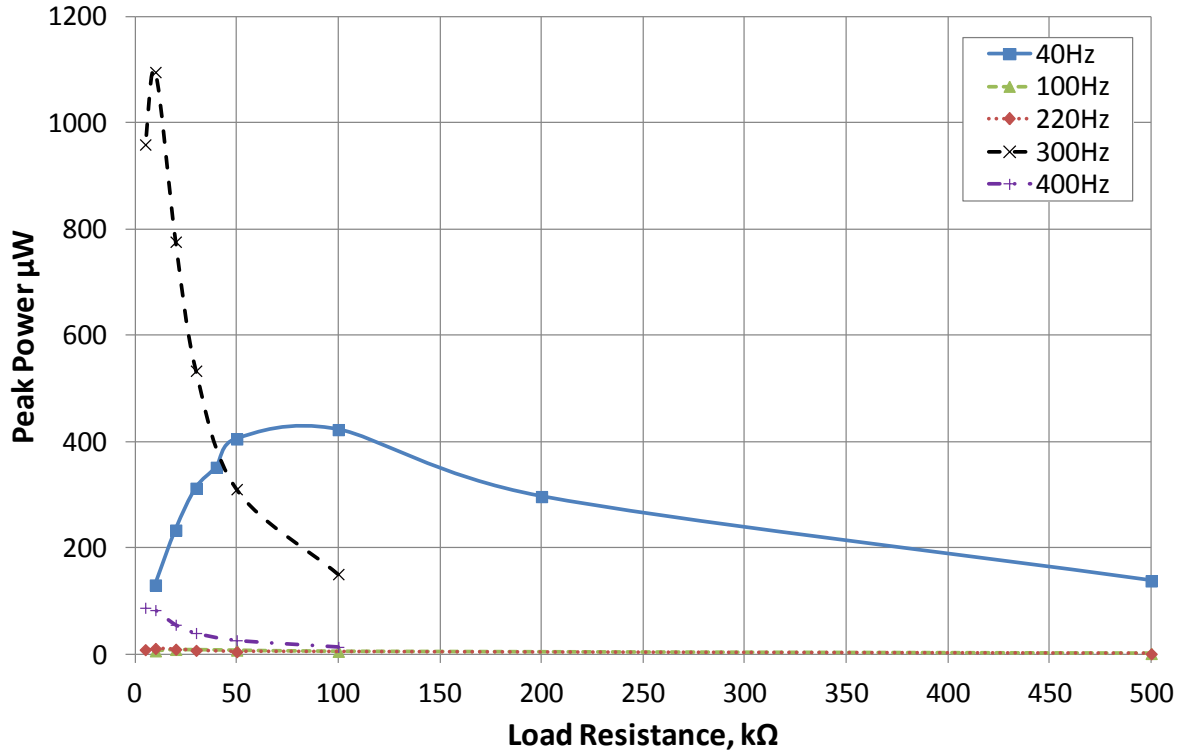

Figure 4-36. Peak power output for a variety of frequencies and load resistance

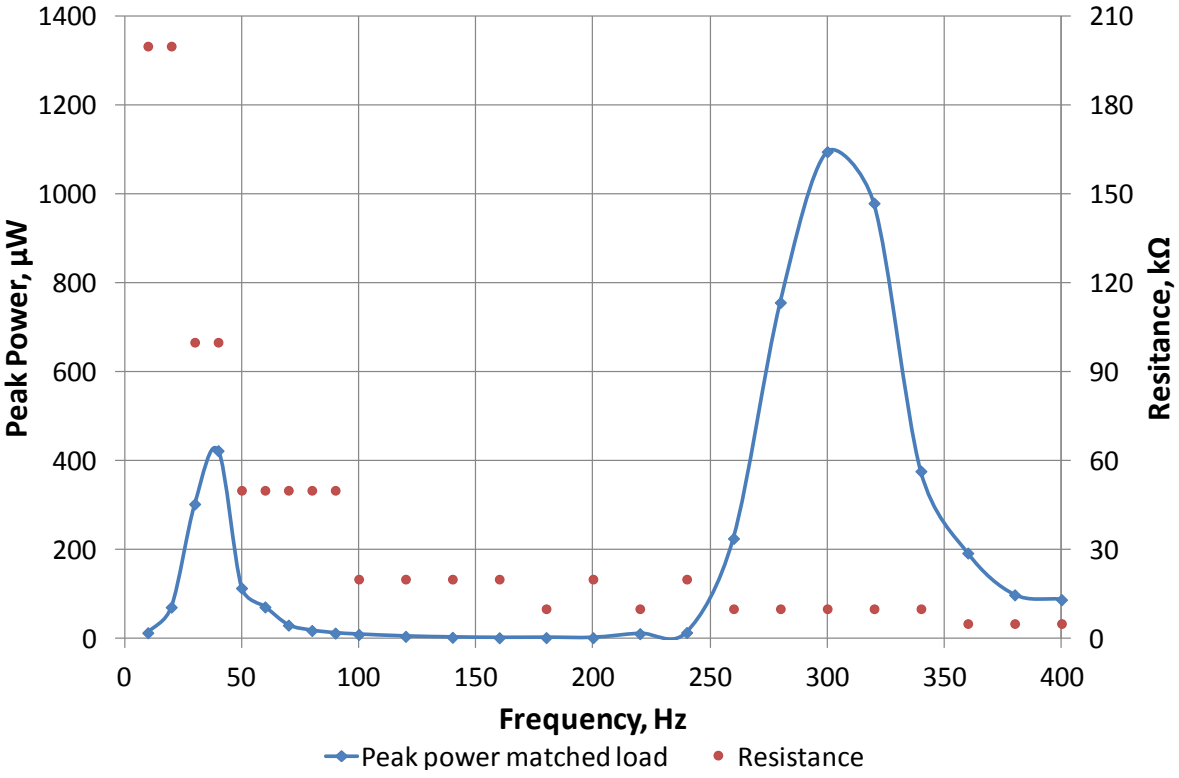

Figure 4-37. Peak power of the QP10n device matched load

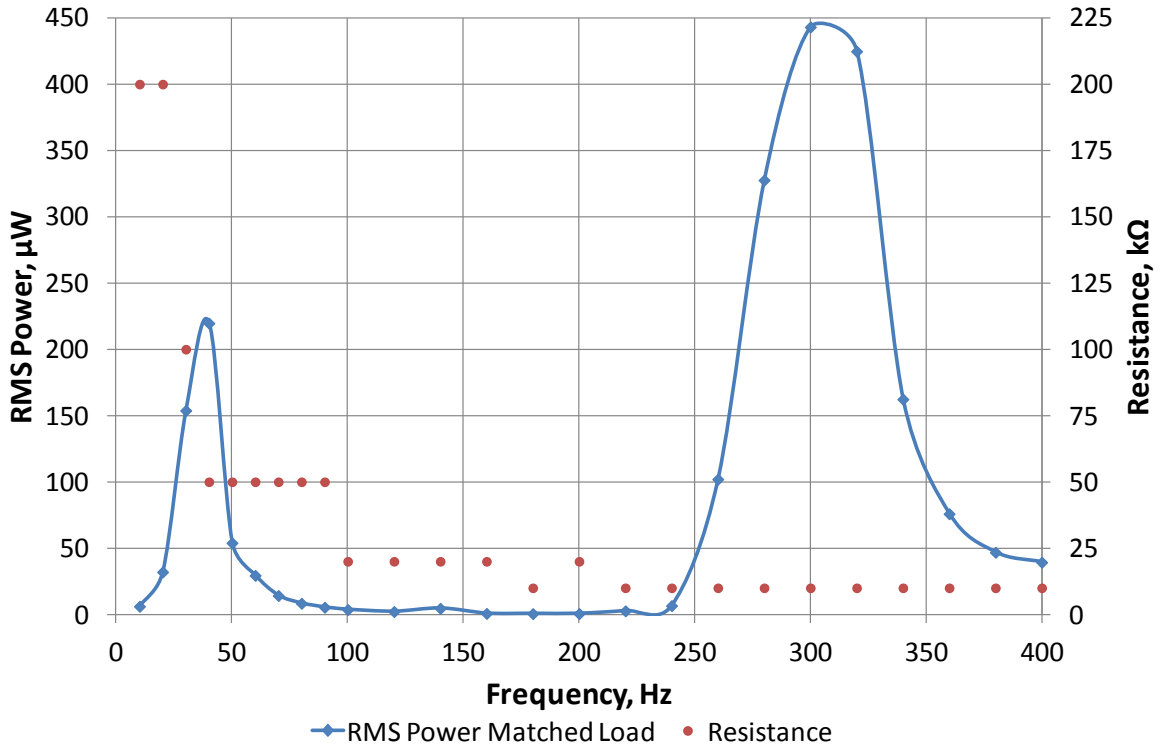

Figure 4-38. RMS power output of the QP10n device at matched load

During removal of the specimen from the apparatus for applying the speckle pattern for the DIC measurements, it was noticed that the threaded bar which connects the brass connecting rod to the electromagnetic shaker showed signs of wear. The connecting rod was clamped to the threaded bar using a grub screw and the results had shown that this was potentially slipping under load. Therefore the threaded bar was bonded to the connecting rod using Araldite rapid to prevent slipping. Since a detailed preliminary investigation had been conducted to determine the frequencies of interest, the secondary investigation used greater frequency increments which resulted in measurements recorded at 20, 40, 60 ,100, 150, 200, 250, 300, 350 and 400Hz. Before testing at each incremental frequency a reference image was recorded using the high speed cameras which formed the baseline condition for the DIC software. Again a variable resistance junction was used to enable the load resistance to be varied for each vibration frequency. Figure 4-39 shows the results for the peak AC power at matched load resistance for each vibration frequency. The same trend is observed with peak in the power at 40 and 300Hz, however the peak power is considerably higher than the previous case, with peak powers of 435 and 2704µW respectively. This further suggests that slipping was occurring between the threaded bar and the brass connecting rod in the previous investigation. Figure 4-40 shows the results of the RMS power for the variety of vibration frequencies. Again the same trend is observed with the

same frequency and higher peak RMS power levels of 218 and 618µW for 40 and 300Hz respectively.

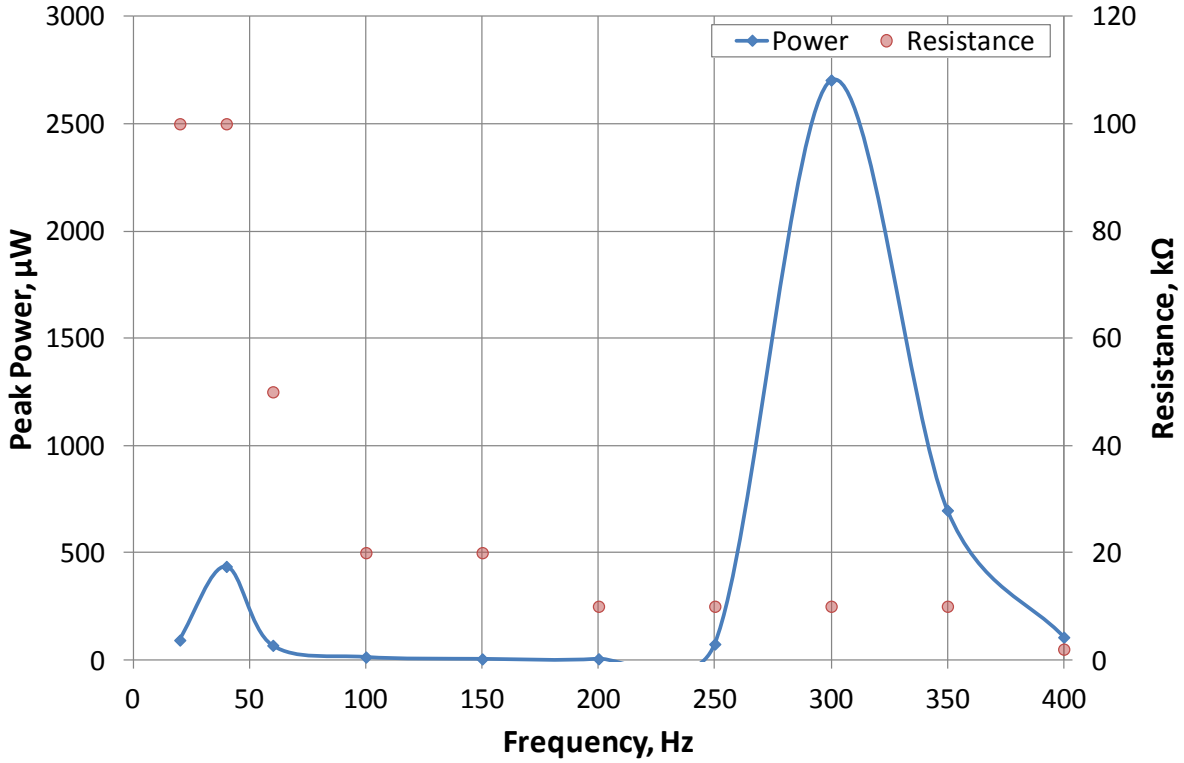

Figure 4-39. Peak power of the QP10n device matched load for the curvature investigation

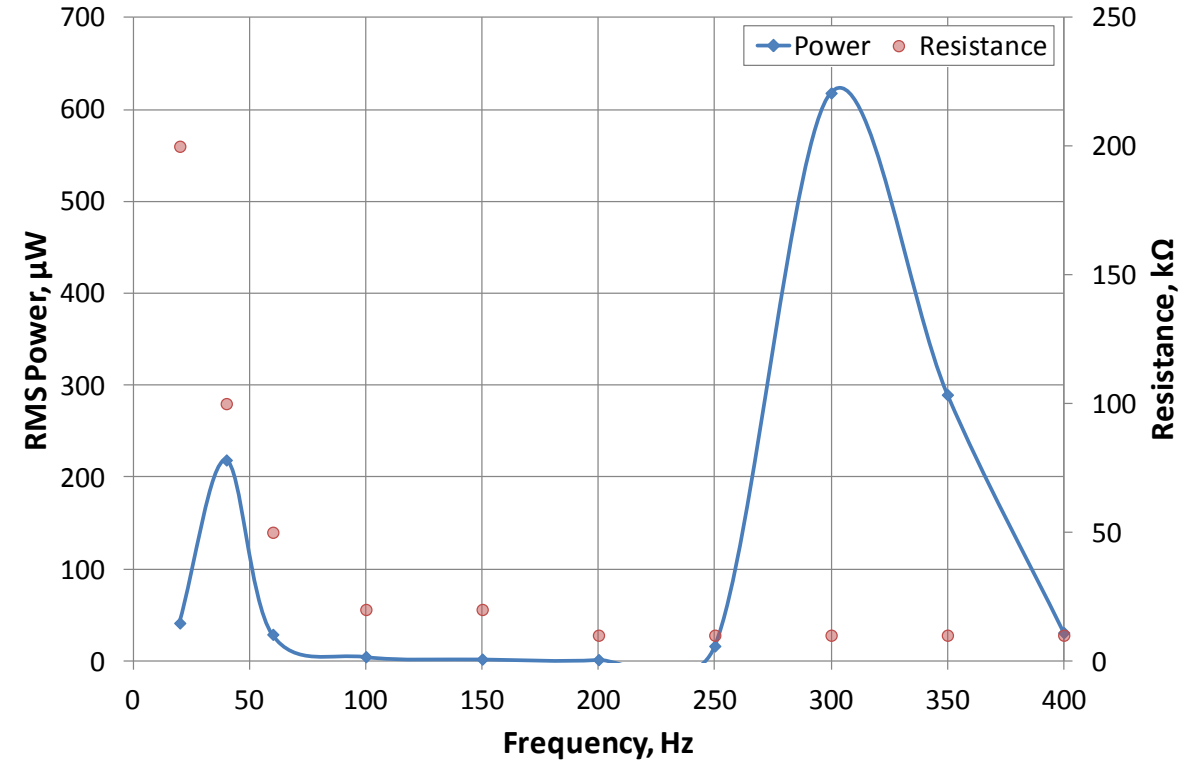

Figure 4-40. RMS power of the QP10n device matched load for the curvature investigation

Figure 4-41 shows the maximum positive and negative displacement profiles for a vibration frequency of 20Hz. The displacement images were created using the DIC software VIC-3D 2010. The images show a peak to peak displacement at the centre of the panel of 0.525mm with peak displacement of 0.306mm and a minimum displacement of -0.219mm. The figure also shows that the test apparatus is generating the most displacement along the horizontal centre line only and therefore is functioning as desired. Figure 4-42 shows the maximum and minimum vertical centre line displacements for a vibration frequency of 40Hz. The peak to peak displacement is 0.673mm and is the largest deflection observed which corresponds to the lower peak in terms of the peak AC and RMS power. The maximum and minimum displacements at the centre of the panel are 0.190 and -0.483mm respectively. Again the apparatus promotes displacement and hence curvature along the vertical centre line only. For a 150Hz vibration frequency the peak to peak displacement is 0.022mm which considerable less than the other two frequencies discussed. This corresponds to a peak displacement of 0.029mm and a minimum displacement of -0.0007mm. It is now evident there is no significant displacement at the centre of the panel and hence curvature which corresponds to a generated peak power of 4.38μW. However if a harvesters was placed on the area highlight by the maximum and minimum displacements, greater power levels would be generated. Hence consideration of the mode shapes and the placement of the harvesters are important to harvest the greatest amount of power. Figure 4-44 shows the maximum and minimum displacements profiles for a vibration frequency of 300Hz, a peak to peak displacement of 0.051mm with maximum and minimum displacements of 0.045 and-0.006mm respectively. Although the order of magnitude of the peak to peak displacement is less than that at 40Hz, the peak power levels are observed at this frequency therefore the displacement alone cannot be used to draw a relationship for the power output because it is proportional to the curvature and rate at which this curvature is generated.

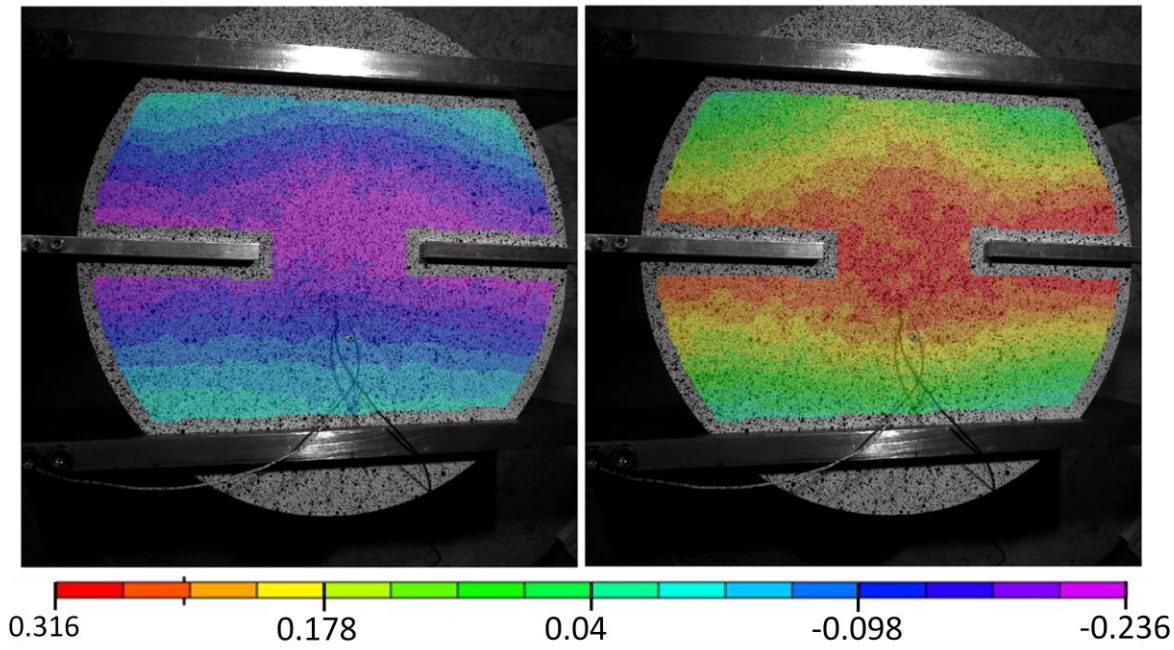

Figure 4-41. Maximum and minimum displacements profiles for 20Hz vibration

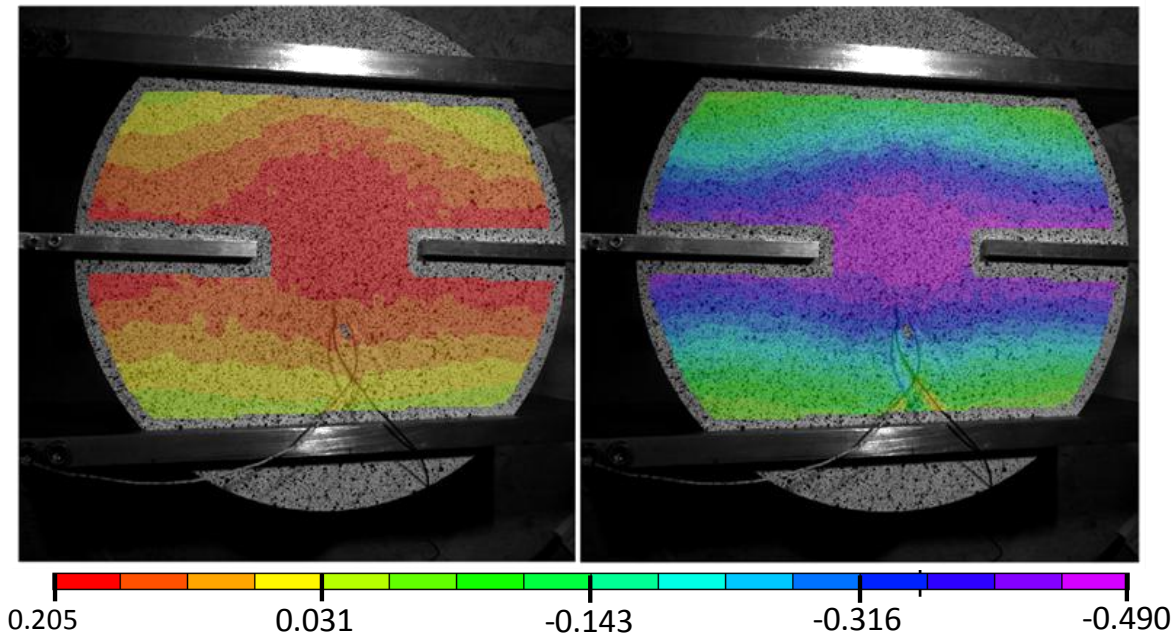

Figure 4-42. Maximum and minimum displacements profiles for 40Hz vibration

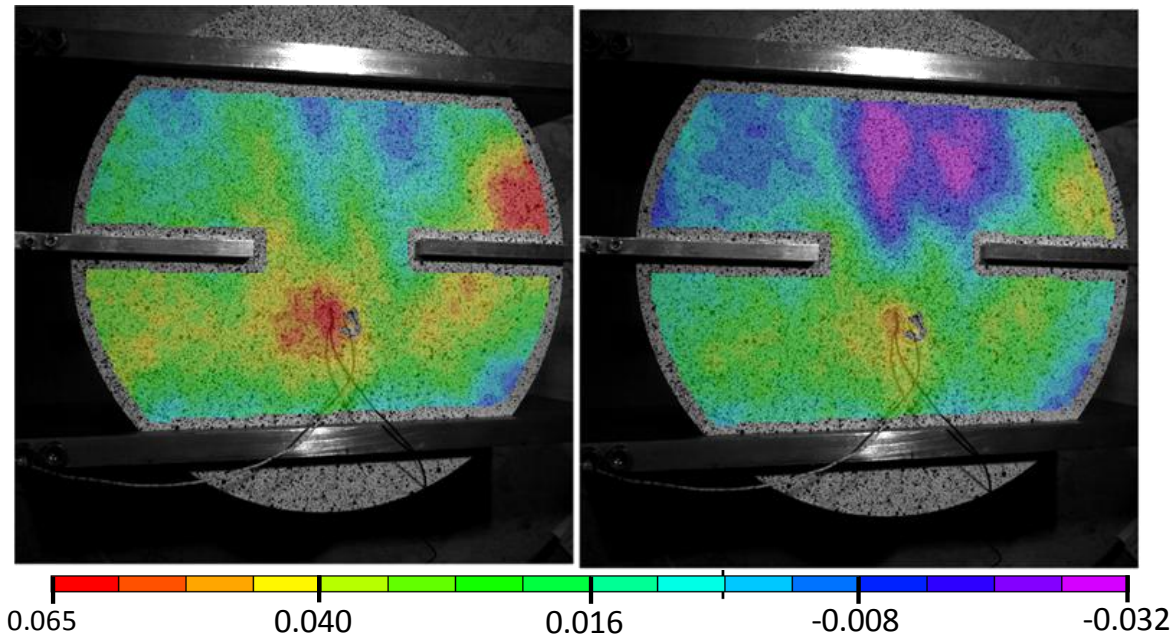

Figure 4-43. Maximum and minimum displacements profiles for 150Hz vibration

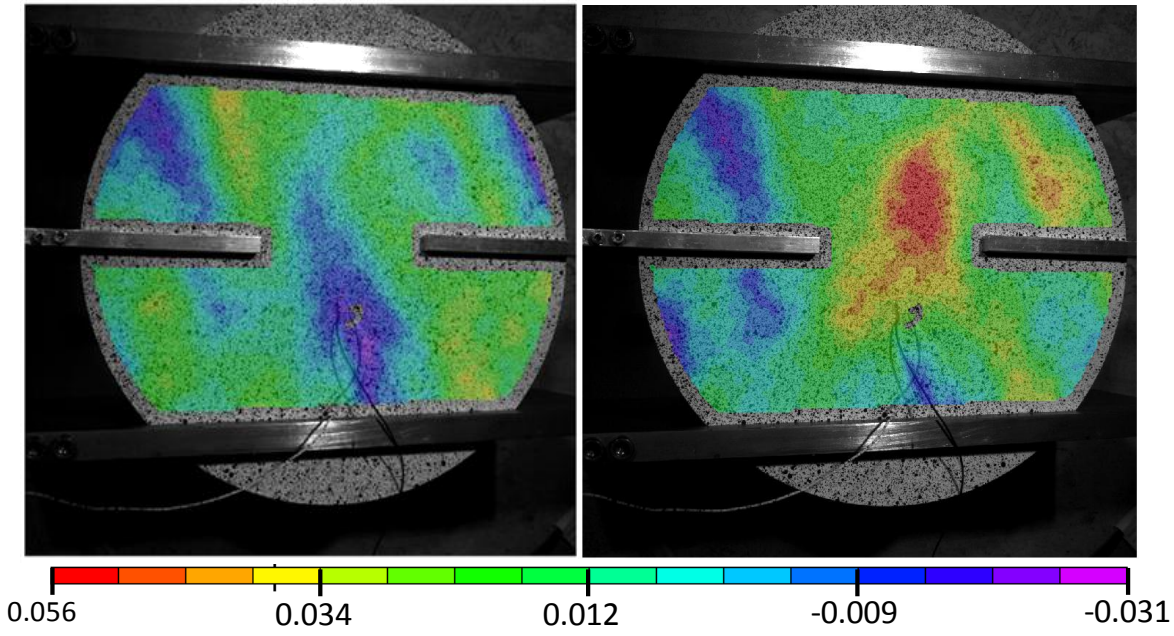

Figure 4-44. Maximum and minimum displacements profiles for 300Hz vibration

In order to derive relationships between curvature and RMS power the displacements profiles for maximum and minimum centre displacements were extracted. The curvature was calculated from the displacement profiles. However there were considerable noise spikes in the data this was due to the small amounts of curvature experienced and due to the edges of the device. Therefore the displacement profiles were smoothed and the curvature was calculated from the smoothed profiles. The resulting curvature profiles were smoothed to

eliminate the spikes due to the edges of the patch. The peak to peak curvature was calculated for the centre of the specimen which corresponded to the centre of the energy harvesting device. Figure 4-45 shows the curvature and the RMS power generated for each vibration frequency and shows peaks in the curvature which correspond to the peaks in the power output, however the peak curvature observed at 40Hz is greater than that at 300Hz whereas the RMS power has the opposite relationship. It should also be noted that the curvatures for 100, 200 and 350Hz are similar, however the power output at 100 and 200Hz is relatively small but at 350Hz the power output is considerable greater. This is possibly due to there being significant curvature across the horizontal centre line which could increase the power generated. Also the sensitivity of the device across the frequency bandwidth is unknown and this will also have an effect on the generated power levels. It is therefore necessary to consider the rate of change of the curvature therefore relationship between the frequency curvature product against frequency were investigated. Figure 4-46 shows the frequency curvature product and the power output for the test frequencies and shows that now the greater frequency curvature product is observed at 300Hz. However the difference between the curvature frequency between 40 and 300Hz is 1.28 times greater at 300Hz whilst power levels at 300Hz are 2.83 greater than those at 40Hz. This suggests that other factor also contribute to the received power levels, however these have not been considered. These relationships with further work will be used in an optimisation programme developed at Cardiff University.

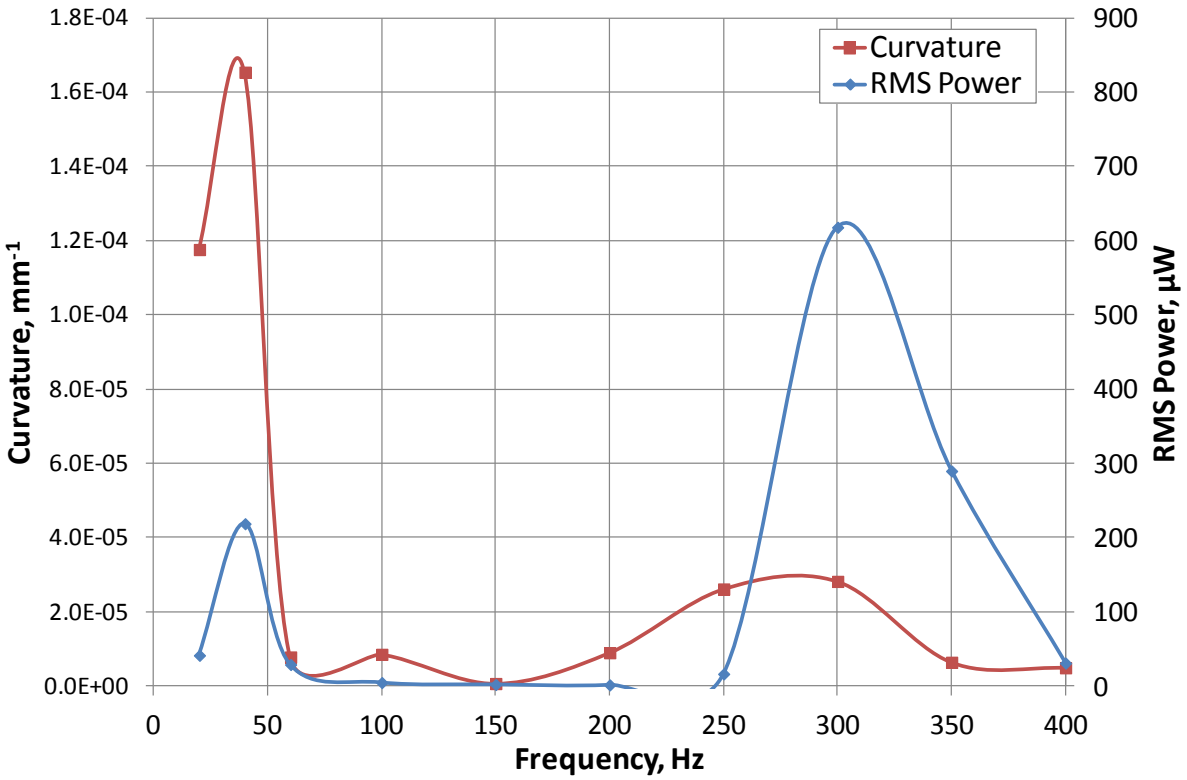

Figure 4-45. Curvature and power for a variety of vibration frequencies

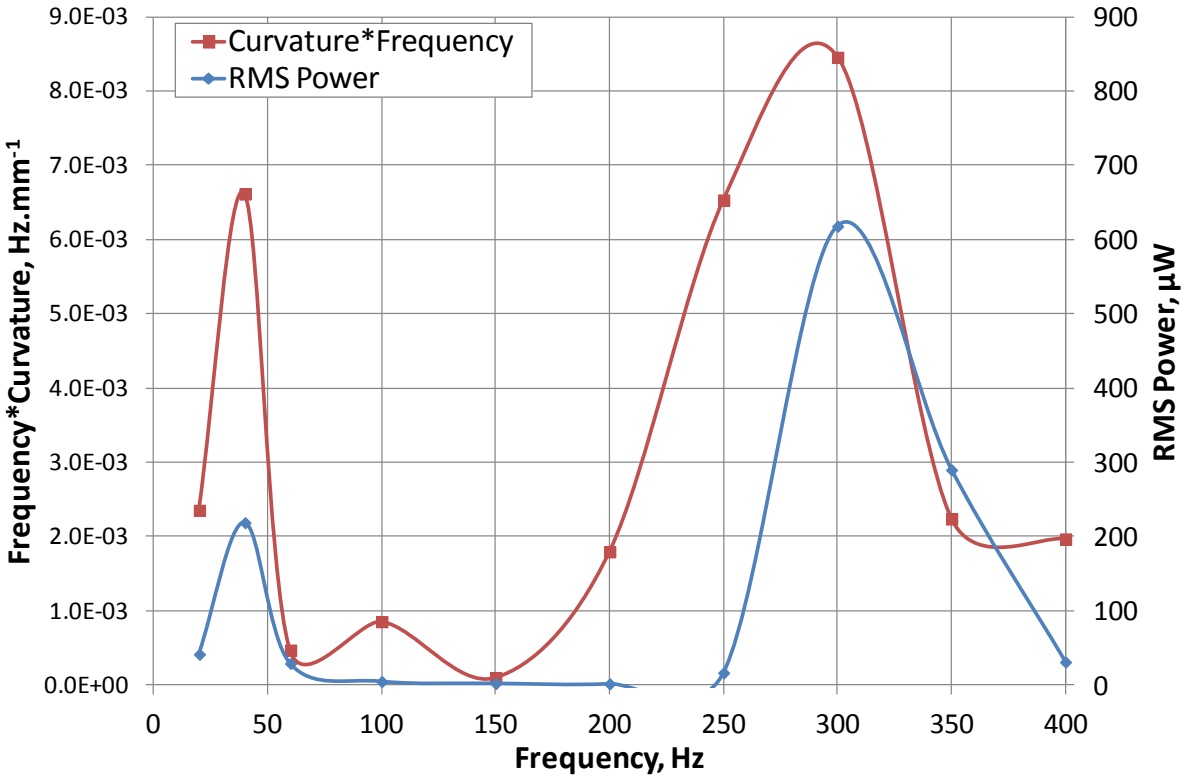

Figure 4-46. Curvature frequency product and power for a variety of vibration frequencies

Overall for typical vibration frequencies power levels of a MIDE Quickpack QP10N were in the range of 4 - 2700μW in terms of peak AC power and the range of 1.5 - 620 μW in terms of the RMS power. This shows that the power output is highly dependent on the frequency and curvature of the specimen and the position of the device with relation to the mode shapes.

4.4.4 Conclusion

Experimental investigations into the feasibility of powering a wireless prototype SHM system using vibration energy harvesters has shown that the maximum power levels generated are considerably lower than the sleep mode with parametric wake up. Also the AC voltage produced from the device would have to be rectified to a DC voltage for the system, this would mean a voltage drop would occur across the diodes of the rectifying circuit reducing the power output further. It would require considerable numbers of these devices to provide enough power for the system. Therefore it is suggested that vibration energy harvesting would be an additional power source.

4.5 Discussion

The power level generated by the vibration harvester is considerably lower than the minimum power levels simulated for the TEG. However it is envisaged on an aircraft that the vibration harvesters would be easier to deploy as they do not rely on specific temperature gradients which may not occur straight away. It would be necessary to have a power management system to transform the dynamic power profiles into a stable source for the SHM system. This management system would require power which the vibration could provide, with the power output from the TEG would be the main source of power for the prototype monitoring system. Furthermore there will be vibration occurring on the aircraft as soon as the engines started running the piezoelectric devices could generate power when the temperature gradients have not developed sufficiently yet. A dual energy harvesting device would reduce the amount of redundancy in the system as power could be generated even if there no significant thermal gradients.

4.6 Conclusion

Energy harvesting techniques through experimental and simulated investigations have been shown to generate power in the correct order of magnitude to provide a power source for a prototype wireless AE/AU system. The input variables to both the experimental and numerical modelling were the frequency of vibration from an aircraft wing and various temperatures measured on a flight from different positions on the aircraft. Although the TEG

harvester showed the potential to generate higher power levels, there may not be a suitable gradient in particular locations where a SHM system is required. Likewise the power output from vibration harvesters were based on data from the wing, the frequency and amplitude of the vibration will vary immensely depending on the location and type of structure. This requires knowledge of the key areas to be monitored on an aircraft to determine the most suitable power source, as the energy harvesting will be required in close proximity to the SHM system itself. A discussion with aircraft operators and manufacturers would be required to determine the most likely areas that require monitoring, so that further likely temperatures and vibrations could be quantified, this would then allow the most suitable power source to be used.

5 Power Management

5.1 Literature Review

Energy harvesting enables the capture of ambient energy and converts it to electricity, however it is often dynamic and erratic in nature and is not suitable as a constant electrical source for many devices. A power management system is therefore required to regulate the dynamic input power and provide a stable output power for a load device. Spies et al (2007) defined the objective of a power management system. This is to match the voltage level of the harvester to the voltage of the load. This must be enabled independently of source or load variations. It is the load power requirement which defines the requirements of such a system (Becker et al. 2009). In the example of a wireless transducer the sleep mode power consumption defines the minimum power requirements. Alongside this the maximum power levels are normally defined by the sending and receiving of data. This defines the energy harvesting strategy and the power management solution. The duty cycle of the wireless transducer node defines the average power consumption and is effectively the length of time the system is fully powered to that of sleep mode and can be used to reduce the average power consumption of the device. There are two main architectures for power management systems these are presented in Figure 5-1 and Figure 5-2 and are described by Bandyopadhyay and Chandrakasan (2012). Figure 5-1 shows the traditional architecture which consists of two conversion stages with an energy storage buffer to supply power when the energy harvester cannot. Dependent on the type of energy harvester the input will either be DC or AC. DC from sources such as TEGs and solar cells does not require modification before the power management system. AC from sources such as piezoelectric, electromagnetic and electrostatic harvesters requires rectification of the AC source to a DC nature. The second type of management system seen in Figure 5-2 is dual path architecture with a control element. This architecture generally has a higher efficiency than the traditional type. In this type there are two parallel conversion paths. The energy harvesting device can directly power the load using the primary converter if enough energy is being harvested. If excess energy is harvested the secondary converter is used to store the excess energy. If the harvesters cannot power the load the back-up converter from the energy storage device can directly power the load. The control element in this system switches between the two parallel paths to determine which powers the load and when energy is stored in the buffer. This is achieved by monitoring various voltage levels in the system. Although the efficiency of this type of system is greater than the traditional type careful consideration of the control

system is necessary so that the system itself does not consume a large amount of the harvested power especially when considering low levels generated by energy harvesters.

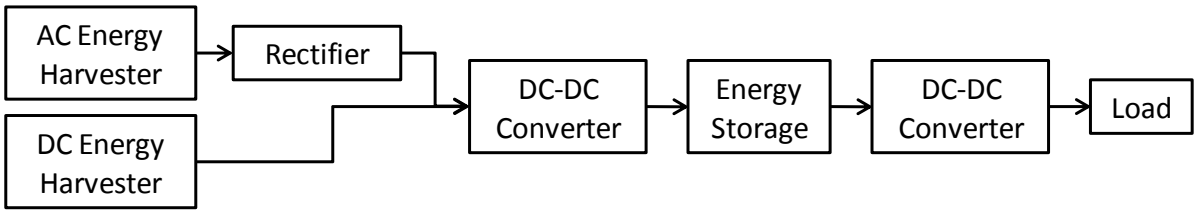

Figure 5-1. Traditional power management architecture(Bandyopadhyay and Chandrakasan 2012)

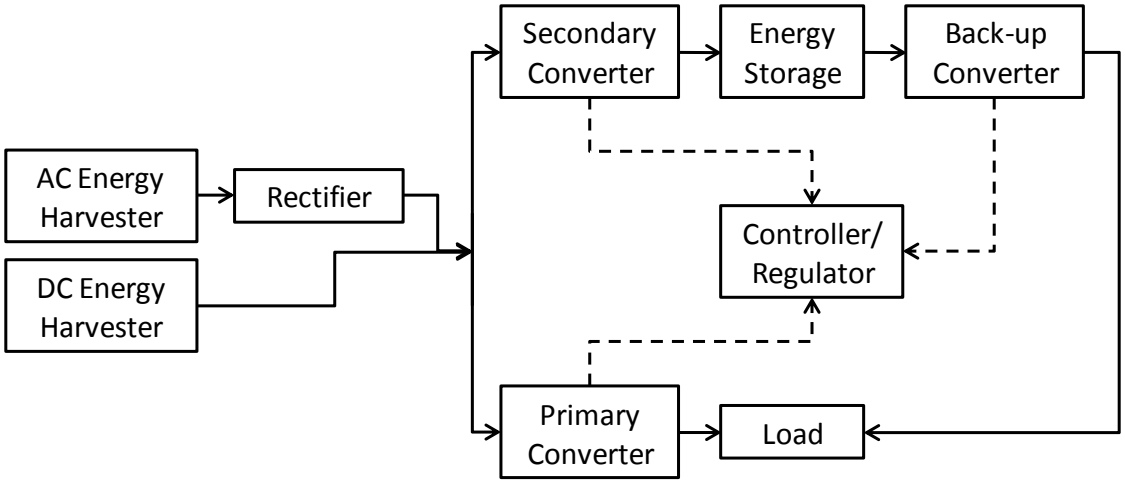

Figure 5-2. Dual path power management architecture with control (Bandyopadhyay and Chandrakasan 2012)

As can be seen from Figure 5-1 and Figure 5-2 there are common elements between the architectures which are crucial for the realisation of a power management system. These are the rectifiers, the DC-DC converters and the energy storage devices. Rectifiers convert an AC output from the energy harvester to a DC source. This is normally achieved by a diode system which results in either half wave or full wave rectification. For a half wave rectifier either the positive or negative current is passed and the other is blocked. This results in a lower average DC voltage because only half the wave is rectified. For full wave rectification both the positive and negatives parts of the waveform are converted to a constant polarity wave. Due to this higher mean voltages are gained. The potential problem with rectification is the voltage drop across the diodes and careful design of the system is necessary to avoid excessive power dissipation. Other forms of rectification with lower voltage drops are being researched and will be discussed later in this chapter.

Often energy harvesting devices do not provide adequate voltage to either charge a storage device or power a system itself. DC-DC converters can then be used to boost the voltage from the device to the required levels for the power management system. Typical systems for boosting voltages are switched capacitor devices such as charge pumps or inductor converters. Switch capacitor converters are often referred to as charge pumps and consist of capacitors and switches or diodes. These take a charge from a source via a capacitor and pump it into an output capacitor where an increase in voltage is observed. The switching of the circuit is often controlled by a clock signal. This can increase the output voltage over successive switching cycles. Palumbo and Pappalardo (2010) presented further details on the overview of charge pumps . Inductive converters are often referred to as DC-DC boost converters and operate in a similar way to a charge pump, however the power is stored and transferred to the output using an inductor. DC-DC converters generally have higher start up voltages when compared with a charge pumps. To reduce the start up voltage a charge pump can be connected in parallel to provide the voltage for the converter. This methodology has been used by Becker et al (2009), Wang et al (2011) and Spies et al (2007). Once the DC-DC converter is operational the charge pump can be switched off to improve the efficiency of the system.

The final aspect of a power management system is the energy storage element where either rechargeable batteries or supercapacitors can be used. Batteries have a higher energy density and low discharge rate but a lower temperature operating range and lifetime. Voltage depression also occurs when the battery is continuously charged and discharged. Overall supercapacitors have a lower energy density and capability but do not suffer from voltage depression and have wider operating temperature ranges and life. The main drawback of these however is the relatively high discharge rates and therefore supercapacitors should be viewed as mainly suitable for short term energy storage.

Many examples of power management systems for energy harvesting using TEGs are present in the literature. Although most systems used the same fundamental components their specification and end load device differ enormously. Spies et al (2007) developed a system for TEG devices using a charge pump and DC-DC converter in parallel. This configuration enables the charge pump to provide the start up voltage required for the DC-DC converter which lowers the overall start up voltage. Once it is operational the charge pump is switched off to improve efficiency. However a key factor is highlighted for such systems where the efficiency can vary dramatically from 31% to 70% dependent on the input voltage (0.13 to 0.3V). For a temperature differential of 5K, 1mW of output power was

generated with an efficiency of 60%. Becker et al (2009) used the traditional architecture with two Maxwell super capacitors in series to store 17.4mWhr. The system had a large start up time and therefore a smaller capacitor was used as a buffer to reduce the charge time. A further DC-DC converter was required at the output to boost the voltage of the capacitor to that required by the transducer node. The system was tested with 2 TEGs connected in series giving an output voltage of 3.3V and resulted in a maximum efficiency of 65%. The same system was used with used with a Micropelt TEG and the efficiency increased to over 70%. A similar power management system based around the use of thermoelectric devices to power an autonomous strain gauge transducer node with an RF transmitter has been developed (Becker et al. 2009). Knight and Davidson (2010b) developed a system to power a Fleck wireless node. The node consumed 132mW when transmitting data, 66mW when receiving and less than 3.3mW when idle. An energy harvesting floatation device was used to exploit the temperate gradient between an expanse of water and the sun's illumination of a black disc in an acrylic dome. A MAX756 boost converter was used which had a start up voltage of 0.9V and boosted the voltage to 3.3V. The device and management system were deployed on a winters day and left to run for two days. 280 samples were received when a temperature difference of 10K occurred. No energy storage was used in the experiment therefore excess energy generated during the day could not be stored. An example of a use of dual path architecture was presented by Lu and Yang (2010) to power a Zigbee automatic valve controller for a radiator. The system consisted of a charge pump and a DC-DC converter in series which operated from 0.3V and stepped the voltage to charge two 2.3V 10F supercapacitors. The system itself consisted of two storage buffers, the primary was the supercapacitors which were directly charge by a TEG, this can be seen in Figure 5-3. When enough energy was stored on the supercapacitor any additional energy was used to directly charge the second buffer and the system itself. When the voltages dropped across the capacitors, the batteries were used to power the system and charge the supercapacitors.

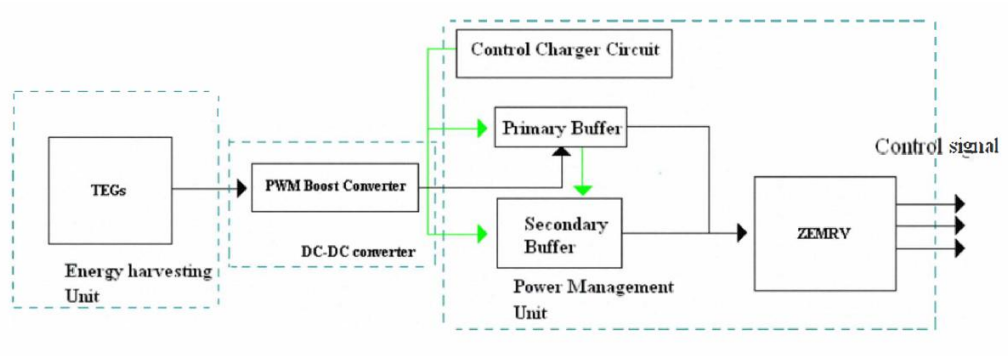

Figure 5-3. Functional diagram for power management system for a TEG device (Lu and Yang 2010)

A charge pump and DC-DC boost converter in series were again used to power a wireless transducer node from low temperature gradients (Wang et al. 2011). The charge pump operated from 300mV and was fed into a capacitor. Once the capacitor reached 700mV the boost converter stepped up the voltage to 3.3V. This system was used to provide power to a wireless transducer node with temperature and humidity transducers. A supercapacitor was used to buffer energy due to the duty cycle of the transducer, this required a further voltage comparator to avoid a low voltage condition. A temperature gradient of 55°C resulted in a 3V output when the TEG voltage output was 0.5V and was able to charge the capacitor from 2.7 to 3.18V in 11.5 minutes. Samson et al (Samson et al. 2011) used the PCM heat storage TEG device and a specific power management system to provide a constant 3.3V output for a wireless transducer node. A super capacitor and a DC/DC boost converter were used to provide adequate voltage for the wireless transducer node. Over a flight period 3.3V was reached 500s into flight. Power management systems have been developed for TEG applications where the maximum temperature gradients was as little as 2.2°C for harvesting energy in a tunnel (Moser et al. 2012). For temperature gradients this low the start up voltage of the DC-DC converter is critical. An En Ocean ECT310 was used to step up the voltage from a 15mV input, however this module is only able to manage positive voltages and therefore will not work if the temperature gradient reverses. A 470µF storage capacitor with an EnOcean transceiver and developed management system was able to collect 70mJ of energy a day which corresponded to 415 radio frequency transmissions of 15 bytes of data. Another application of the use of low temperature gradients is harvesting energy from the human body using TEGs (Mousoulis et al. 2012). The Linear Technologies boost converter used as its start up voltage was between 20 – 500mV. This successfully boosted the voltage from the device to 3V and continued to

work for 20 seconds after the device had been removed from the temperature gradient. Arnold et al (2012) developed a system based on commercially available components. The system was based around a TEG harvesting energy from the temperature gradients that exist between the fuel tank base and outer wing skin of an aircraft. Each component of the system was quantified using a programmable power supply. The system was based on an input rectifier, an input DC-DC converter to provide adequate voltage for the battery and charger and finally a DC-DC output converter to step-up the voltage to the level required for a four channel wireless AE system. Using a system of 51 TEGs (17 parallel groups of 3 TEGs connected in series) and a load resistor to replicate the AE board, the system was able to provide a constant average power of 50mW over a typical flight. This is enough to power the wireless system in sleep mode.

Several power management systems for harvesting energy from piezoelectric harvesters have been developed and reported in the literature. The main difference between these systems and those designed for TEGs is the use of rectifiers to convert the AC input to a DC output. Ng and Laio (2005) utilised diodes, a capacitor and a voltage detector for a piezoelectric management system. The energy harvesting device charged the capacitor until a voltage release threshold was reached. The voltage was then connected to the load, this discharged the capacitor until the minimum voltage was reached. The voltage detector switched the system to charge the capacitor again. The voltage detector was coupled with logic gates and transistors to facilitate the charging and discharging of the capacitor. This prevents over charging and discharging. Input and output powers were measured and the power management device was found to have an efficiency of 46%. Zhu et al (2011) developed a self contained self powered smart transducer node which incorporated a T-shaped piezoelectric bi-morph as the harvester. A rectifier, super capacitor and a step-up voltage regulator were used to generate the 3.3V required for the transducer node. A bridge rectifier was used to charge a supercapacitor. A TPS60197 step up converter was used to boost the voltage from the supercapacitor, this particular device had a start up voltage of 0.9V. However when the regulator was directly connected to the super capacitor, the regulator would drain current before the start-up voltage limit was reached and the system would never switch on. Therefore a Torez low power XC61C voltage detector was used to start the voltage regulator at 1.7V, as this represented the cut off point for the shortest time between transmissions. With a super capacitor of 2V the system charge time was 13 minutes and the system could be operated for 300ms transmitting 90 bits of data using the step up converter.

Various researchers are developing high efficiency systems that could replace the rectification part of a piezoelectric management system. Sun et al (2012) developed a high performance active rectifier by replacing passive diodes with an operational amplifier controlled active counterpart with a switch in parallel with the transducer. This drastically reduces the DC voltage drop that occurs with conventional diode system. The system was implemented using complementary metal–oxide–semiconductor (CMOS) technology and showed 90% power conversion efficiency with 1.5 to 3 times more power extracted when compared with conventional rectifiers and switch rectifiers respectively. Hehn et al (2012) developed a fully autonomous adaptive pulsed synchronous extractor circuit optimised for piezoelectric energy harvesters using CMOS technology. The system is operational from 5.8μW, a buffer capacity is used to store energy and when a voltage level of 1.4V to 5V is reached the system becomes fully active. Increased power extraction was observed for on and off resonant states with increases of 123 and 206% respectively with a chip efficiency of 85% when compared with conventional passive full wave rectification and pulsed synchronous charge extraction respectively. Since a piezoelectric cantilever can be represented as a spring mass damper model, one important factor for power conversion is the damping of the system (Dicken et al. 2012). Increasing the damping of the piezoelectric device can increase the power output. The authors developed a simple single supply pre-biasing circuit which worked on the principle of modifying the voltage on the piezoelectric capacitance resulting in the charge from the current source being forced into a higher voltage resulting in increased work done, higher electric damping and hence higher power output. This simple circuit was shown to have increased energy density when compared with other techniques. Results showed depending on the Q factor of the inductor a power gain of 0-25 times is attainable. The Q factor is the ratio of the energy stored to the energy lost over each cycle.

One part of a power management system that has not been discussed is maximum power point tracking (MPPT). There are two main forms of MPPT, resistive and impedance matching. These systems are often algorithms used in a control manner in the power management system. In essence the MPPT tries to match the resistance or impedance of the harvester to that of the load in order to generate maximum power transfer. Kong and Ha (2012) developed a low power self powered system with maximum power point tracking (MPPT) for piezoelectric cantilever energy harvesters. A discontinuous conduction mode fly back converter, is implemented with MPPT using a micro-controller with a single current transducer. The MPPT is achieved through resistive matching as a piezoelectric cantilever

operating at its resonance frequency is mainly resistive. Impedance matching is not thought to be the best approach for piezoelectric cantilevers as the patch itself has a large capacitance which would require an impractical sized inductor and the source impedance changes as the environmental condition changes. A linear regulator and oscillator are used to enable cold start up, a second regulator operates the supercapacitor to 3V for micro controller operation. The system was testing with 4 bi-morph cantilevers connected in series and generated 8.4mW of output power at a resonance of 47Hz at 0.05g. The power consumption of the controller was 408µW which was quoted to be far less than other devices. A multiple harvester architecture power management system with MPPT and sharing a single inductor have been developed to maximise the energy harvested (Bandyopadhyay and Chandrakasan 2012).

Hybrid energy storage management systems are also being developed to exploit the advantages of batteries and supercapacitors. Saggini et al (2010) developed a hybrid energy storage power management system consisting of a lithium ion battery and a supercapacitor. The hybrid system was chosen for the instantaneous voltage output and charge speed of the supercapacitor coupled with the increased energy density of the battery. The system consisted of a DC bus with a PV cell, super capacitor and lithium ion battery. Each device had a corresponding DC-DC converter. These devices fed into the bus which was managed using algorithms. When the system had enough power to switch, the PV cell was used to charge the capacitor and the controller. When excess energy was available the system switched to charging the battery. When the supercapacitor voltage fell below a reference level, the system switched to the battery powering the bus. This system is thought to be more efficient than a standard two stage conversion system as the each device is operated in parallel rather than having input DC-DC converter, energy storage and output DC-DC converter.

The final aspect of power management systems is the use of multiple energy harvesters at the same time. This reduces the amount of redundancy in the system when one type of harvester cannot provide enough energy. Wickenheiser and Garcia (2009) discussed combined power harvesting from piezoelectric and TEG devices. A typical architecture is presented which requires rectification and TEG and solar cells requiring DC/DC boosters. An impedance matching step is required to regulate the voltage between the transducers at the storage device. Finally a power distribution circuit manages the discharge rate. However in a multiple device power management system careful consideration of interaction between the circuitry and devices is needed since this can affect

the dynamics of the devices which can lead to inefficient power transfer. Bandyyopadhyay and Chandrakasan (2012) developed a multiple harvester architecture power management system with MPPT sharing a single inductor. Each harvester utilised dual path architecture. A reconfigurable switch matrix was used to harvest energy from the three sources. The system can handle input voltages from 20mV to 5V, extracting maximum power whilst sharing the same inductor. The system was able to harvest 2.5mW, 1.3mW and 200µW from photovoltaic, TEG and piezoelectric devices with efficiencies of 83, 58 and 79% respectively. Farinholt et al (2009) developed a management system for a dual piezoelectric and TEG harvesting device for a wireless impedance based SHM node. This was based on Advanced Linear Devices Inc EH300A modules which are specifically designed for a multiple types of energy harvesters and can accept input voltages of ±500V and an output voltage of 1.8 to 3.6V which also has 30mJ of energy storage. Two of these EH managements system were used for piezoelectric and TEG inputs and were arranged in series to increase the voltage and charge a 0.1F super capacitor. A charge time of 912 seconds allowed the impedance at three transducers to be measured and required 2 seconds to perform the task. The super capacitor voltage was further depleted to 2.7V via onboard calculations. This voltage was then disconnected as this was below the stable operation of the micro-controller which could cause damage to the chip.

5.2 Commercial Power Management System

A commercial power management system was chosen as a representative system in order to demonstrate the ability of such a system to store and regulate the dynamic energy harvested by a device to a stable power source for a wireless transducer system. For this demonstration a Cymbet universal energy harvester evaluation kit was used. The board itself can be seen in Figure 5-4. The board is designed to be used with a variety of energy harvesting devices including solar cells, TEGs, and electromagnetic, RF and piezoelectric energy harvesters. The board can handle voltages up to 4V on the low voltage inputs and 20V on the high voltage side, however these inputs are either stepped up or down to 4V for the input to an Enerchip energy processor chip. It should be noted that although the board has multiple connections for energy harvesters devices, it can only be configured to use one at a time. The resulting circuit block diagram for the board can be seen in Figure 5-5 and shows the components used from the evaluation kit. For the DC inputs depending on the voltage level, either step up or down boost converters are used to regulate the voltage and the charge pump is used in parallel with the boost converter to start the energy processor chip. For the AC inputs an additional rectifier is used to take the AC input and regulate to a

DC source, the resulting boost converters and charge pump are used in the same configuration as for the DC inputs. The Enerchip energy processor can be used for any energy harvesting device and contains advanced maximum peak power tracking algorithms for high efficiency energy conversion. This chip essentially matches the energy harvester impedance to the system load impedance as described previously. The final stage in the board is two solid state batteries with an integrated management system. Each battery is rated at an output voltage of 3.8V with a capacity of 50µAh and requires a charging source of 4V. These two batteries are connected in parallel, with the charging process being controlled by the management system to prolong the life of the batteries.

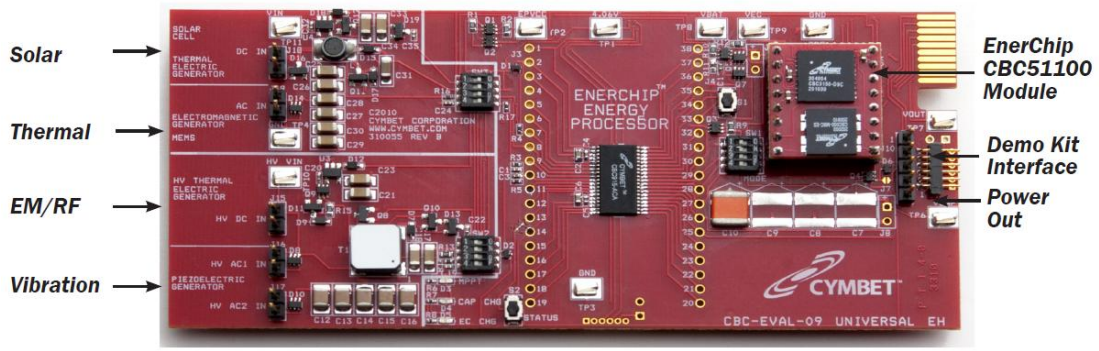

Figure 5-4. Enerchip universal energy harvester evaluation board

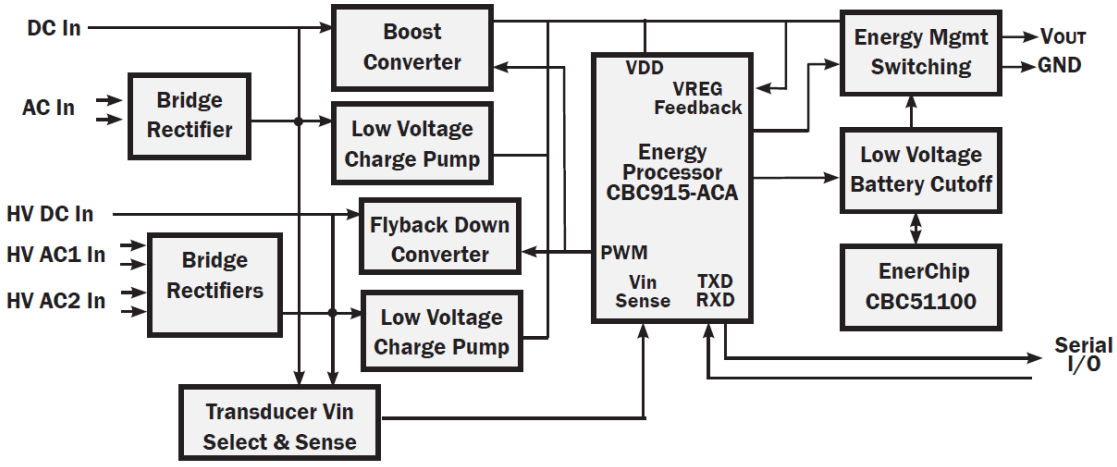

Figure 5-5. Circuit block diagram for the energy harvester evaluation board

5.3 Experimental Procedure

In order to assess the performance of the evaluation board a TEG was used to generate an input voltage from a specified temperature gradient. In order to achieve this, the TEG test apparatus developed by Waring et al (2009), seen in Figure 5-6, was used to generate a voltage for temperature gradients of up to 30°C. This was representative of those

which would be seen by a TEG sandwiched between the fuel tank and the skin of an aircraft wing during flight. The apparatus has two chambers which represent the ‘hot’ and ‘cold’ sides with the TEG sandwiched between the two. For the hot side chamber cold water was used to provide the hot side temperature. For the cold side a vortex tube was used to decrease the temperature of compressed air to around -40°C. The vortex tube and the actual test apparatus can be seen in Figure 5-7. Figure 5-8 shows the principles of the operation of the vortex tube. Compressed air enters tangentially into the tube, developing a vortex which travels down the tube. At the end of the tube a needle valve allows a fraction of the air to escape. The remaining air flow is forced back along the centre of the tube. As the two vortices travel past each other with opposing rotational directions, the air in the inner vortex looses a large portion of its kinetic energy to the outer vortex. This loss of kinetic energy results in a drop in temperature of the inner air stream. By adjusting the needle valve, the temperatures of the hot and cold flows can be easily adjusted.

The following test procedure was followed to assess the performance of the power management evaluation kit. Firstly a thermal compound was applied to the hot and cold sides of the TEG, in order to achieve good thermal contact with the two chambers. A layer of insulation was placed around the TEG to ensure the heat flowed through the TEG only. The whole test rig was placed in a foam surrounding to add further insulation. The hot side of the chamber was attached to a conventional cold water tap and was left to circulate through the apparatus for 15 minutes before testing commenced. This ensured a stable water temperature. Compressed air at a pressure of 100psi was supplied to the vortex tube for a period of approximately 15 minutes, after which the supply was switched off and the apparatus was allowed to warm up to ambient conditions over a period of 80 minutes. The TEG was connected directly to the DC input of the evaluation board, throughout the 100 minute testing duration. A data logger recording thermocouple measurements every 5 seconds was used to record the hot and cold side temperatures and the compressed air inlet and outlet temperature of the cold side chamber. The output voltage of the TEG and the open circuit board voltage were monitored throughout using the same data logger.

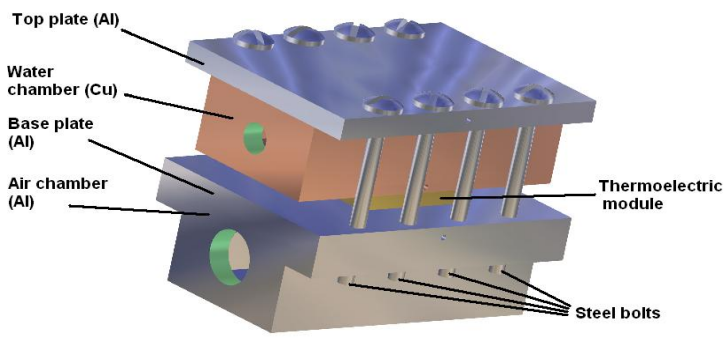

Figure 5-6. TEG harvesting test apparatus (Featherston et al. 2009)

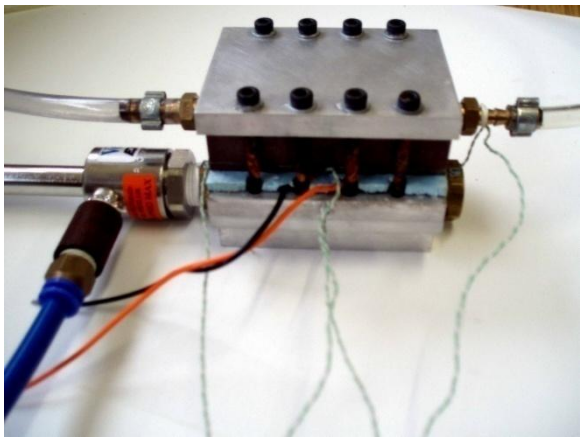

Figure 5-7. Actual test apparatus and vortex tube(Featherston et al. 2009)

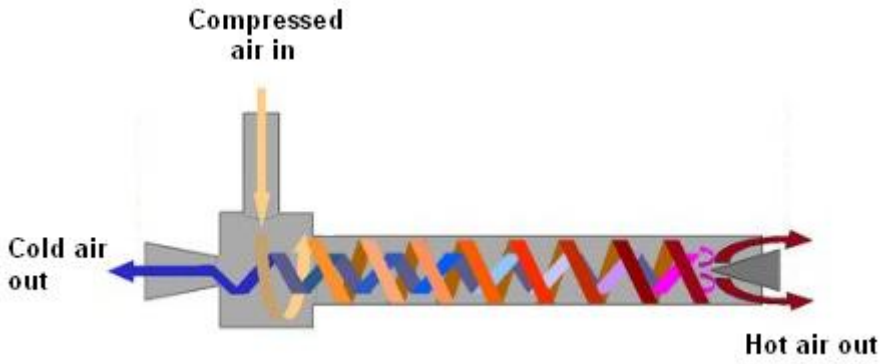

Figure 5-8.Vortex tube operation (Cybernetics 2013)

5.4 Experimental Results and Discussion

The resulting temperature profiles of various thermocouples placed at the described positions in the TEG harvesting apparatus can be seen in Figure 5-10. The hot side temperature remains fairly constant throughout the testing duration apart from the period when the vortex tube is switched on where the temperature falls by 2.5°C. This is thought to have arisen due heat transfer from the hot to the cold side or because the compressed air outlet is causing cooling of the hot side due to space confinements in the laboratory set-up.

The simplicity but effectiveness of the vortex tube can also be seen in the figure. As soon as the vortex tube is switched on the air inlet temperature instantly decreases to -43°C. The corresponding air outlet falls to -33°C. This cooled air results in a cold side temperature of the TEG of -20°C after a period of 10 minutes which is maintained until the supply to the vortex tube is switched off. For the remainder of the test the apparatus is allowed to warm to ambient conditions with the cold side temperature reaching the hot side temperature after a period of 60 minutes.

The resulting temperature gradient and the TEG and board voltages can be seen in Figure 5-10 for the entire duration of the investigation. As can be seen from the figure the temperature gradient shows a fairly rapid increase over the first 10 minutes of testing where the temperature gradient increases to approximately 26°C across the TEG module. Over the following 10 minute period the temperature gradient increases to a maximum of 28°C. After 20 minutes the vortex tube supply is switched off and the temperature gradient gradually decreases to zero after 60 minutes of the test duration. The TEG voltage increases with the temperature gradient for the initial 10 minutes, the voltage after this period remains constant at 700mV. This is most probably due to the load the evaluation board exerts on the TEG which is drawing current from the device. After 20 minutes the voltage falls with the temperature gradient until no voltage is generated after 60 minutes. The voltage output from the board for the entire investigation can also be seen in the figure. The voltage output from the board at the beginning is 700mV suggesting there is some residual voltage in the system. Before the initial power up of the system the voltage drops suddenly. This is not thought to be a characteristic of the board, but may be due to internal switching of the system as it powers up in order to dump the energy to the management chip using the charge pump. The board voltage output reaches a constant level of 3.3V after the TEG reaches a voltage of 500mV at a temperature gradient of 20°C. This suggests that the start-up voltage for this particular TEG is 0.5V, in reality, a power management system with a much lower start-up voltage would be necessary. The voltage output of the board is stated as being 3.5V with fully charged batteries. This suggests that the batteries during this test are not fully charged and the boosted voltage from the TEG is not high enough to enable the batteries to be fully charged. After 30 minutes the board voltage falls to 3.05V. After approximately 48 minutes, the voltage increases to 3.2V. This is thought to be again due to the battery management system. The board voltage remains at around 3.2V till approximately 105 minutes when the system shuts down most probably due to the voltage levels of the batteries being lower than 3.0V. Although not optimised for this particular

application and TEG the system shows the ability to regulate and store harvested energy from a TEG device. It is not thought that the energy harvesting chip would have been working efficiently however due to the lack of external load and hence absence of impedance matching between the source and the output. Although this system does function, it would require further optimisation to operate at lower start-up voltages and be able to handle multiple energy harvesting devices at once. This would reduce the redundancy in the system if the environmental conditions altered during use. It should be noted that the solid state batteries used on the board must be accompanied with a management system as their life is drastically reduced if their voltage is allowed to drop below 3V.

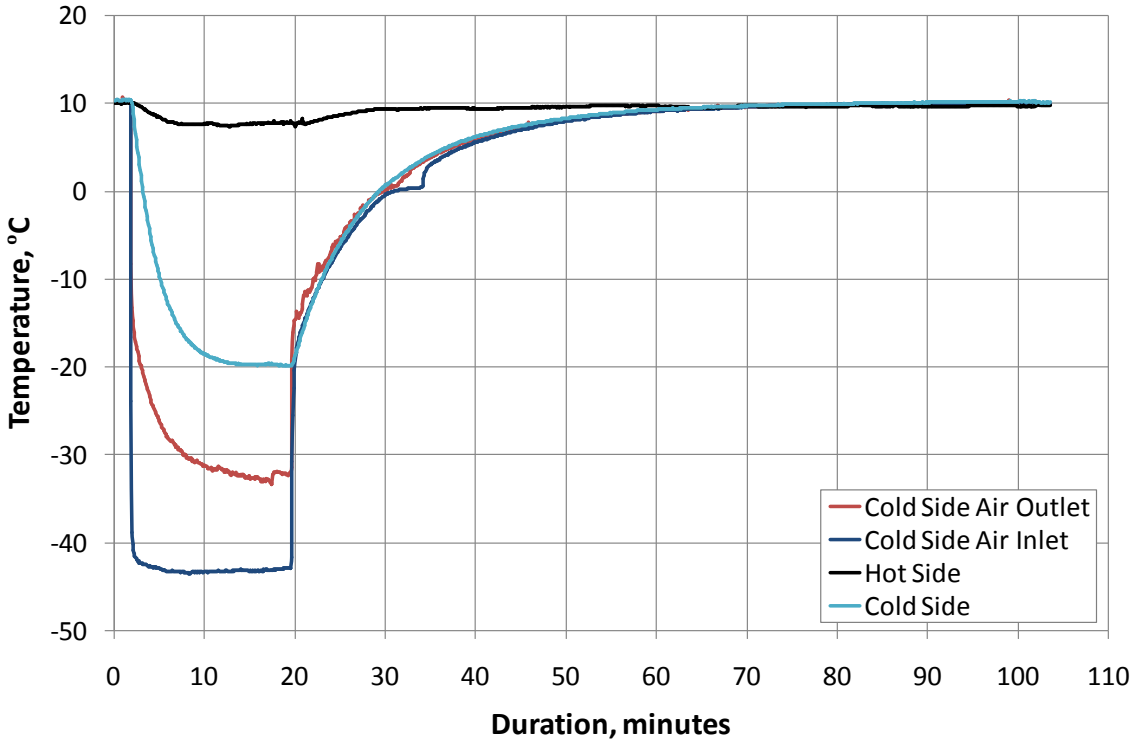

Figure 5-9. Temperature profiles during the test

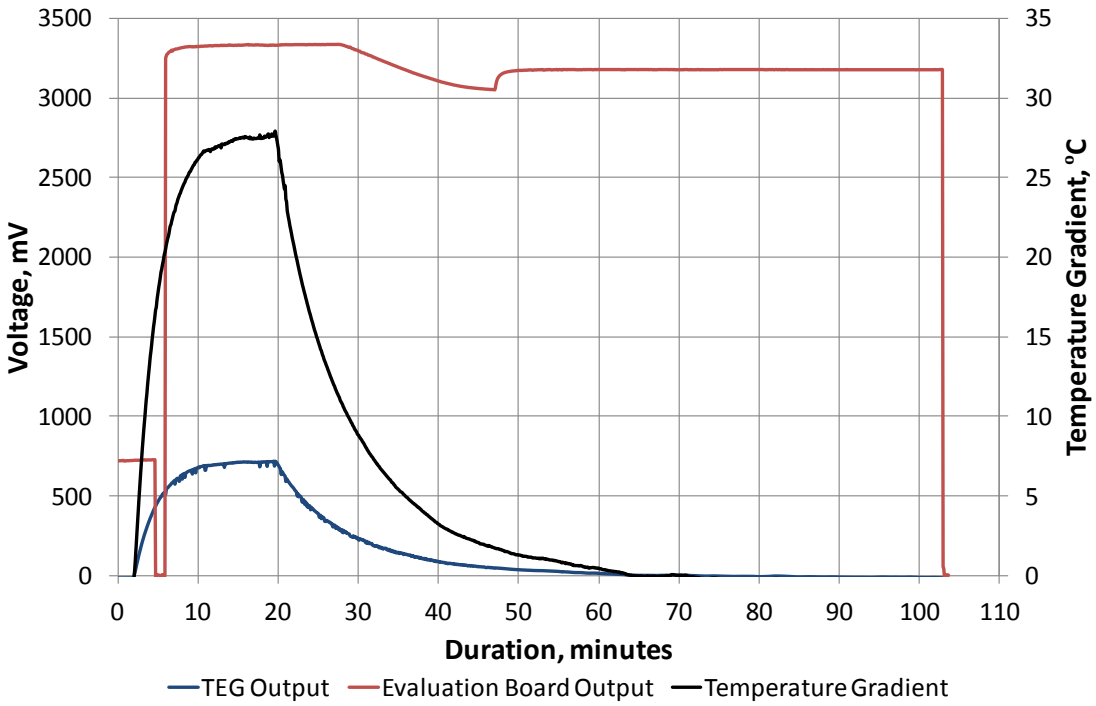

Figure 5-10. Resulting temperature gradient and TEG and board voltage

5.5 Conclusions

A commercial, off the shelf, power management system has been demonstrated to show that the dynamic power generated by thermoelectric energy harvesting can be regulated and stored to provide the stable voltage output necessary for powering a wireless SHM system. This was achieved by connecting the system to a TEG device and subjecting it to a maximum temperature gradient of 27°C for a period of 20 minutes. The voltage level remained constant for a further 85 minutes until the system powered down. If this particular system was required to power the wireless AE/AU system, further modifications would be required. For instance the storage capacity would need to be increased by using further solid state batteries to enabled powering of the system in sleep mode. A further output DC-DC converter would be required to boost the voltage of the batteries to 5V the wireless system requires. Reduction of the start-up voltage although not necessary would be beneficial. Taking the example of the Cymbet CBC3150 solid state battery with incorporated power management, which is used on the evaluation board, to calculate how many units would be required to power the Mistras system. This battery is rated at 3.3V and a 100µA discharge rate, therefore assuming a perfect boost converter up to 5V the Mistras system would require approximately 152 units to power it. The power management system contains a maximum peak power point tracking algorithms, this enables the matching of the energy

harvester's resistance and the load resistance. Therefore the affect of unmatched load to the power management system would not have an adverse effect on the energy transfer.

6 System Integration

6.1 Introduction

This thesis has presented a number of advances made in the areas of acoustic emission, acousto-ultrasonics, energy harvesting and power management for the application of SHM systems for aircraft. These technology areas are of key importance in realising autonomous wireless SHM systems that can be deployed on aircraft structures. The key drivers for these systems are the development of more optimised structures reducing the weight of the aircraft and hence fuel consumption and emissions. The implementation of SHM also facilitates a more efficient maintenance regime, with reduced downtime and hence increased use of assets and reduced operating costs. The increasing use of composite components in an aircraft structure increases the importance of monitoring to detect the onset and growth of barely visible damage that can drastically reduce the service strength and life. The use of such materials however enables sensing elements to be embedded within the structure to enable “smart” structures.

In this chapter the development of a smart carbon fibre wing for detecting and locating impact damage utilising embedded P2 MFC transducers is described. These transducers are used for AE, AU damage detection and for harvesting energy for typical ambient aircraft frequencies. By using the same transducers for all three techniques the number required is vastly reduced. Whilst for the integration of these techniques into the smart wing a wireless acquisition system has not been implemented, this could also be achieved at a later stage bringing together all the enabling technologies and research advances developed earlier to create a smart wing.

A scaled model of an Airbus A320 wing was chosen as the representative structure and this can be seen in Figure 6-1. The normal construction of the wing consists of rib, spars and skins and is mainly aluminium, however composite materials are used for the wing control surfaces and the wing to fuselage fairing. The final 3D CAD model of the wing which was generated using Solidworks^{TM} and can be seen in Figure 6-2. Figure 6-3 shows the overall dimensions in millimetres of the described wing. This chapter discusses the manufacture of the wing alongside the locating and determining impact damage. Finally the feasibility of using embedded MFC transducers for vibration energy harvesting, an alternative to the thermoelectric harvesting presented in Chapter 5 is discussed.

Figure 6-1. Computer generated image of the Airbus A320 taken from airbus.com

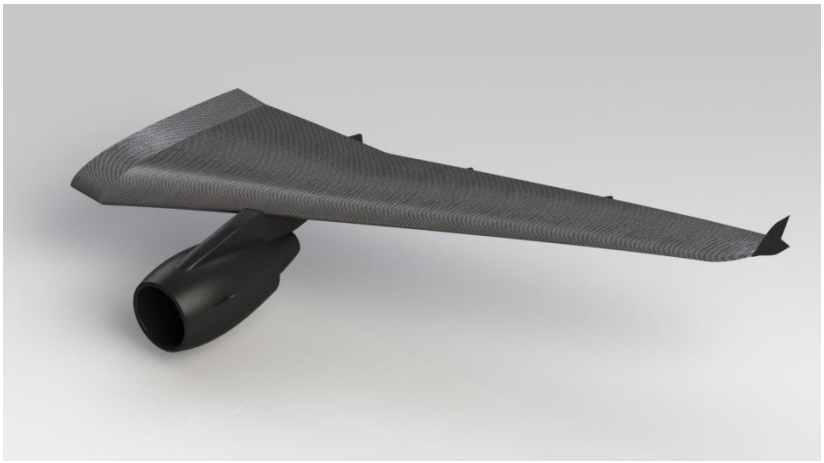

Figure 6-2. Solidworks render of the Airbus A320 scaled wing model

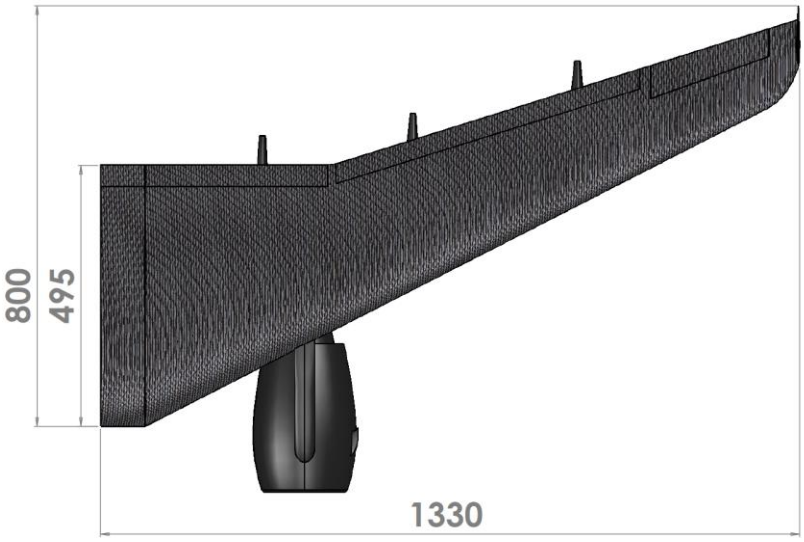

Figure 6-3. Overall dimension in mm of the A320 scaled wing model

6.2 Manufacture

The composite wing used, was manufactured in two halves with a corresponding mould for each half. Each mould was manufactured from three machined tooling blocks which were created from the Solidworks model of the wing. Two tooling blocks of dimensions 500 x 600 x 100mm and a further block of dimensions 550 x 450 x 100mm were used to create each half of the wing in three sections. The tooling blocks were machined from solid on a three axis CNC machine and pegged and bolting together. In order to CNC machine the mould a Solidworks CAD model was converted to a useable format for the machining software, this was achieved using Delcam PX-exchange. This was then imported into Delcam Powermill, where depending on the defined machining operations the software automatically defined the tool path, this was uploaded to the CNC machine to manufacture the part. The mould tool was prepared for use in the autoclave and a PTFE layer was applied to the mould surface which aided in the release of the wing for the mould. The final mould tool can be seen in Figure 6-4 which also shows the preliminary lay up of the composite material.

Figure 6-4. Mould tool and initial layup for the wing

Each half of the wing was manufactured from four plies of composite, two plies of 0-90º woven carbon fibre epoxy pre-preg and two plies 0-90º woven glass fibre epoxy pre-preg. Further details of the materials used are given in

Table 6-1. The lay-up consisted of two outer layers of carbon fibre re-enforced plastic (CFRP), with two central layers of glass fibre reinforced plastic (GFRP). Ten M2814-P2

MFCs were embedded between the two layers of glass fibre at the centre of the wing which can be seen Figure 6-4. Placing the transducers within the glass layers prevented grounding issues between the contacts of the transducers and the carbon fibres. In reality a more suitable arrangement for the embedded transducers might be necessary. A short length of cable was attached to the electrodes of the MFC transducer and a window was cut into the inner carbon fibre layer in order to attach co-axial cables to the MFC transducer, as can be seen in Figure 6-5. The wing was laid into the mould in the previously described layup configuration. The mould and the wing were vacuum bagged and placed in the autoclave for the specified cure cycle. This cycle included heating the specimen to 70 ºC at a rate of 0.5ºC/min holding for 3.5 hours, and cooling at the same rate returning to ambient temperature. The complete cure cycle lasted 6 hours and 50 minutes. A large carbon fibre sandwich panel was manufactured from two layers of 0-90 carbon fibre pre-peg either side of a Nomex honeycomb material (ANA-3.2-48, 10mm thickness and 3.2mm cell size). This was also vacuum bagged and cured in the autoclave using a separate cure cycle. The cycle included heating the specimen to 50ºC at a rate of 0.5ºC/min holding for 18 hours, and cooling at the same rate returning to ambient temperature. Once the wing had been manufactured a layer of Rapid araldite was applied over the connection joints to prevent any damage occurring to the contacts and the cables. In order to stiffen the wing structure, ribs were manufactured from the sandwich panel which matched the profile of the wing which can be seen in Figure 6-4. The final experimental test wing can be seen in Figure 6-6, with attached stiffening ribs and co-axial cables. The figure shows the specified area of interest which was used to collect training data for the AIC delta T mapping technique. Although ten MFCs were embedded only five were used in the AE and AU analysis due to acquisition channel limitations. A commercial Mistras Pico transducer was attached to the underside surface of the wing to draw comparison with the MFC transducers.

Table 6-1. Material specification for the composites wing

	Amber Composites E644 Carbon/Epoxy Prepreg	Amber Composites E644 Glass/Epoxy Prepreg
Prepreg Areal Weight, gsm	205	300
Weave	2*2 Twill	8H Satin
Resin Content	45%	43%
Fibre Type	HS0800 (3K)	E (7581)

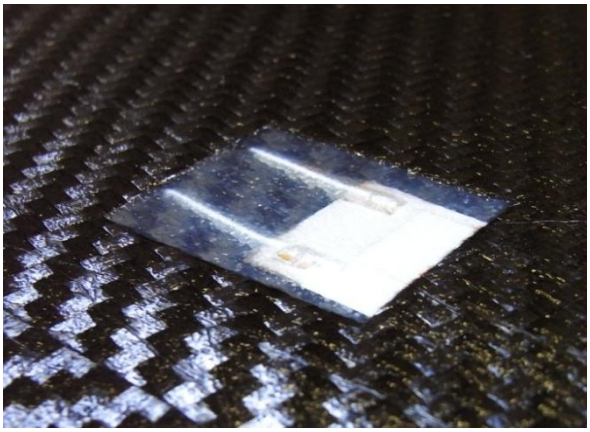

Figure 6-5. Close up image of an embedded MFC transducer

Figure 6-6. One half of the smart wing which was used for the experimental investigation

6.3 Experimental Procedure

To assess the ability of the smart wing to detect damage an impact investigation was conducted. The wing was subjected to a number of impacts, AE was used to locate the damage and a cross correlation AU technique was used to detect the damage. Only the top half of the wing seen in Figure 6-6 was used in this investigation. The grid that can be seen in the figure represents the area of interest that was chosen for the AIC delta T mapping technique. The experimental set up for the investigation can be seen in Figure 6-7. The numbered channels show the transducers that were used in the investigation. Channels one to five were the embedded M2814-P2 MFCs, channel 6 which is presented as a red circle was a Mistras Pico transducer. This was used to draw a comparison with the MFC transducers. The actual impact location is represented by the blue circle. Before any testing was conducted training data was calculated for the grid shown in Figure 6-6. Five H-N

sources was used to generate artificial AE at each node positions in the grid. The grid spacing density between each node position was 20 x 20mm. the H-N sources generated artificial AE in the wing in order to record the arrival times at the transducers. After completion of the training data a series of baseline waveforms were recorded for the AU technique. A round robin configuration was used with each transducer acted as a transmitter in turn and the resulting waves were recorded on all the other channels. For pulsing the MFC transducers a 100kHz 60V peak to peak single cycle square actuation signal was used, generated using a Mistras Wavegen board. When channel six was a transmitter the same type and frequency of square wave was used however a peak to peak voltage of 300V was used. A lower peak to peak voltage was used for the MFC channels due to the operational limits of this type of transducer. There was no damage present in the wing when the baseline measurements were recorded which was confirmed by an ultrasonic C-scan. A 10MHz probe with a 5mm diameter collimator was used to focus the beam. The spatial resolution was 1mm x 1mm and the timing gating was set large enough to record the peak amplitude from the beam reflected of the glass panel that was placed underneath the specimen. H-N sources were used to generate artificial AE in the wing at five arbitrary positions on the wing in order to assess the performance of the delta T mapping technique. An Instron Dynatup 9250HV impact test machine with a hemispherical 20mm diameter impact tup with a mass of 7.9694kg was used to impact panel at the same position (represented by the blue circle in Figure 6-7) with increasing drop heights and energy. The details for the impacts on the wing can be seen in Table 6-2. During the seven impacts AE monitoring was conducted using channels one to six, the acquisition settings for AE and AU monitoring can be seen in Table 6-3. After the last impact further waveforms were recorded for the AU technique using the same configuration as previously described.

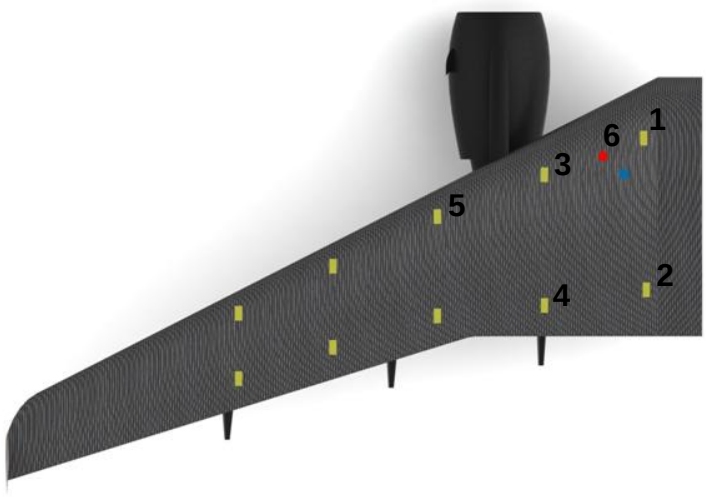

Figure 6-7. Experimental set up for the impact investigation

Table 6-2. Details for the impact investigation

Impact Number	Drop Height, mm	Impact Energy, J
1	30	2.35
2	30	2.35
3	40	3.13
4	50	3.91
5	60	4.69
6	70	5.47
7	80	6.26

Table 6-3. Acquisitions settings for the AE and AU monitoring

Threshold	40dB
Pre-amp Gain	40dB
Analogue Filter	20khz - 2MHz
Sample Rate	2MSPS
Pre-trigger length	500µs
Waveform length	3k

After conclusion of the impact investigation, a study into the feasibility of using the embedded MFC transducers for harvesting energy from ambient vibrations was conducted. The experimental set up can be seen in Figure 6-8 where the wing was clamped in a test rig at one end. An aluminium bracket was bonded to the stiffener rib highlighted in the figure, this bracket was bonded to the connecting rod of the electromagnetic shaker which was rigidly attached to the base of the test rig. An LDS V201 electromagnetic shaker with a

PA25E amplifier was driven by an Agilent 33220A waveform generator with a 100mVpp sinusoidal signal at a variety of frequencies. An Agilent oscilloscope was used to record the voltage trace of the MFC used in the investigation which is highlighted in the figure. A variable resistance junction box was used to alter the load resistance for each frequency of vibration from 1MΩ to 5kΩ. For each load resistance the voltage drop was calculated so that the power of the device could be calculated. The investigation was conducted for frequencies in the range of 10 to 400Hz, This range was chosen as it represents the frequencies that exist during an aircraft flight. The oscilloscope recorded the AC voltage trace and the RMS voltage this enabled the peak and RMS power to be calculated.

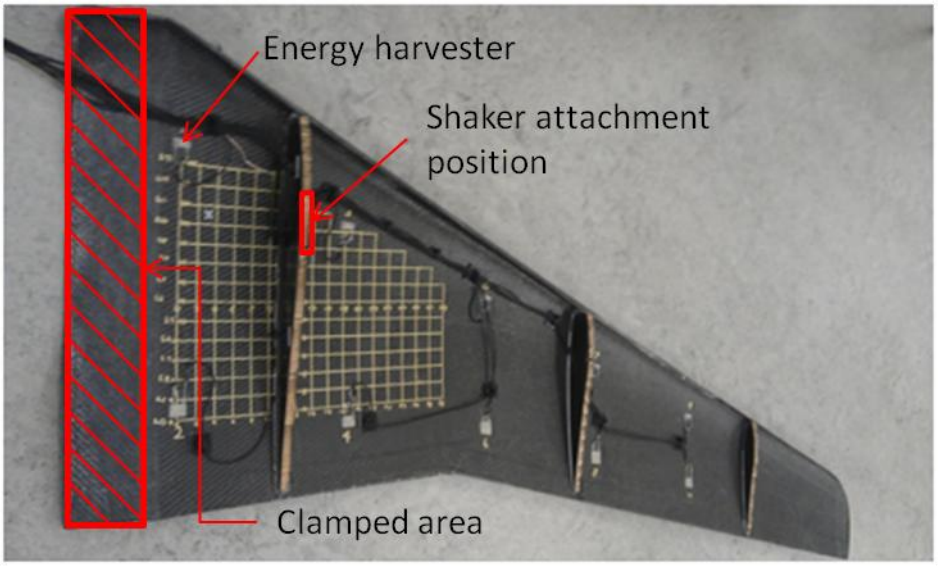

Figure 6-8. Experimental set-up for vibration energy harvesting investigation

6.4 Experimental Results and Discussion

An initial ultrasonic c-scan of the wing used for the experimental investigation showed no significant damage present from the manufacturing phase as can be seen in Figure 6-9. The darker areas in the image show the embedded transducers and the attached cabling. The stiffening ribs had not been attached to the wing and therefore are not present in the c-scan. The c-scan image shows that there was no damage present in the wing when the baseline AU measurements were recorded and therefore any changes in waveforms that may occur after the impact investigation were due to possible damage in the wing.

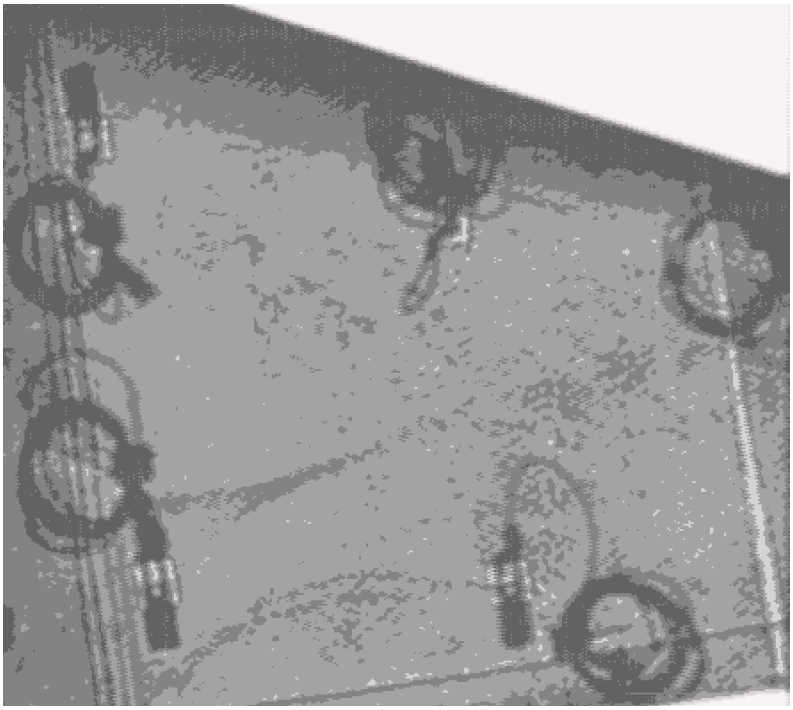

Figure 6-9. Preliminary C-scan of the smart wing

To assess the performance of the training recorded for the delta-T mapping technique a series of five H-N sources were used to generate artificial AE for five arbitrary positions as labelled in Figure 6-10. The resulting locations calculated using the conventional time of arrival and the AIC delta T mapping are also shown in the figure. The figure highlights the transducer positions as well. It can be seen from the figure that for locations 1,3,4 and 5 the AIC delta T mapping is consistently more accurate and precise than the TOA method. The only position where the results from the TOA analysis are comparable to the delta T mapping technique is at location 1 which was the impact location for the subsequent impact investigations. For this location position accuracy of both techniques is very similar. This is most likely due to the wave velocity used for the algorithm being the most accurate for the propagation angles from source to transducer. Position 2 is the least accurate for both techniques, this can be explained for the TOA as being due to the influence of the stiffening rib increasing the complexity of the structure in this area. For the AIC delta mapping the stiffening rib was present for the training data so its affect on the wave propagation should be accounted for in the training data. The most probable cause for the location error at this position could be due to the iteration of the grid data that is missing due to the placement of the stiffener which may cause slight discrepancies in the grid data. To quantify the location error the Euclidean distance error was calculated between the actual and calculated locations and averaged for each individual location, this is shown in Figure 6-11. Different

cluster diameters were used for the AIC delta-T mapping, this specified diameter was used to calculate the actual locations from all the crossing points, where an analysis of how close the points are to one another is carried out. The error bars represent the maximum and minimum distance errors for each technique at each location. Overall the AIC delta T mapping technique with different cluster diameters is more accurate than the TOA technique, the reasons for the greater error in the TOA technique is due the assumption of a homogenous wave speed in the material which is not the case for composite material. For the delta T technique a cluster diameter of 10mm gives the best location, followed by the 20mm diameter. The 30mm diameter depending on the location is equivalent to the other technique (locations 1, 4 and 5), considerably worse (location 3) or more accurate (location 2). This highlights the importance of trying to select the best cluster diameter for located actual test data. With the results from this Euclidean distance error a cluster diameter of 10mm was chosen to locate the actual impact events. The AIC delta T mapping technique has overall shown an improvement over the conventional technique.

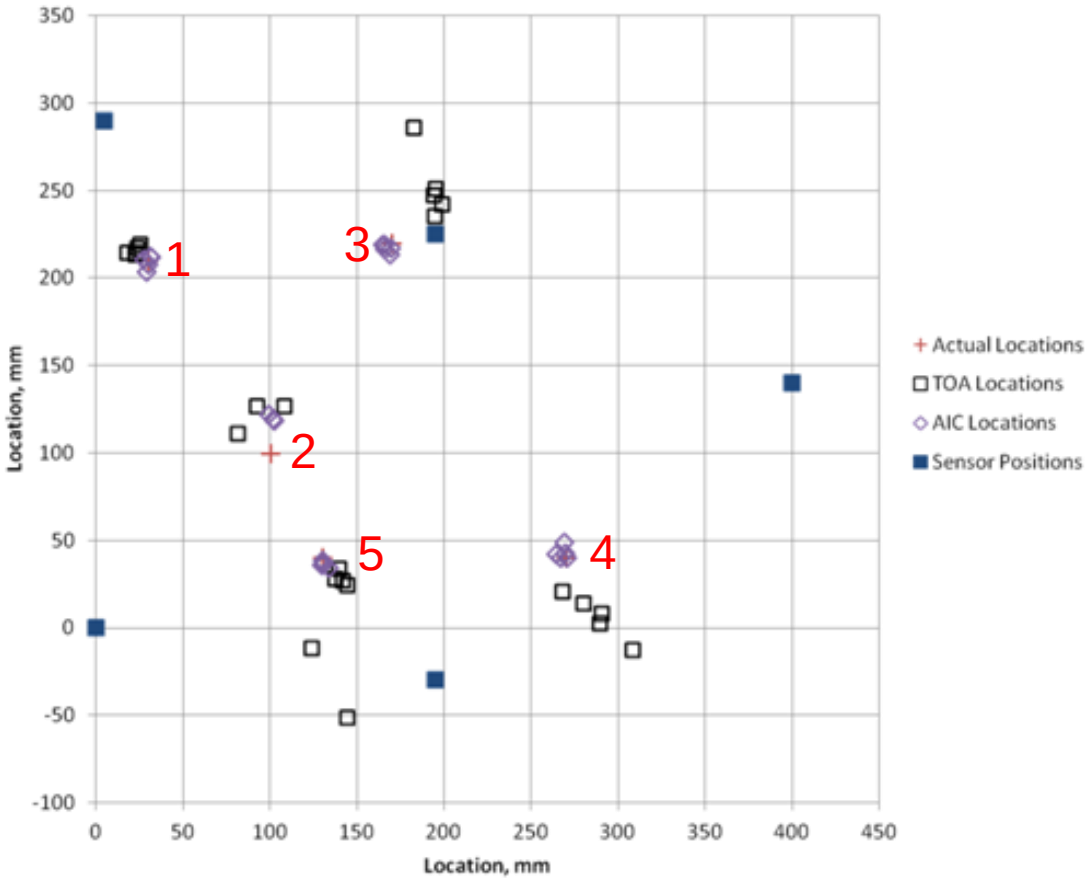

Figure 6-10. TOA and AIC delta-T mapping locations for five arbitrary positions

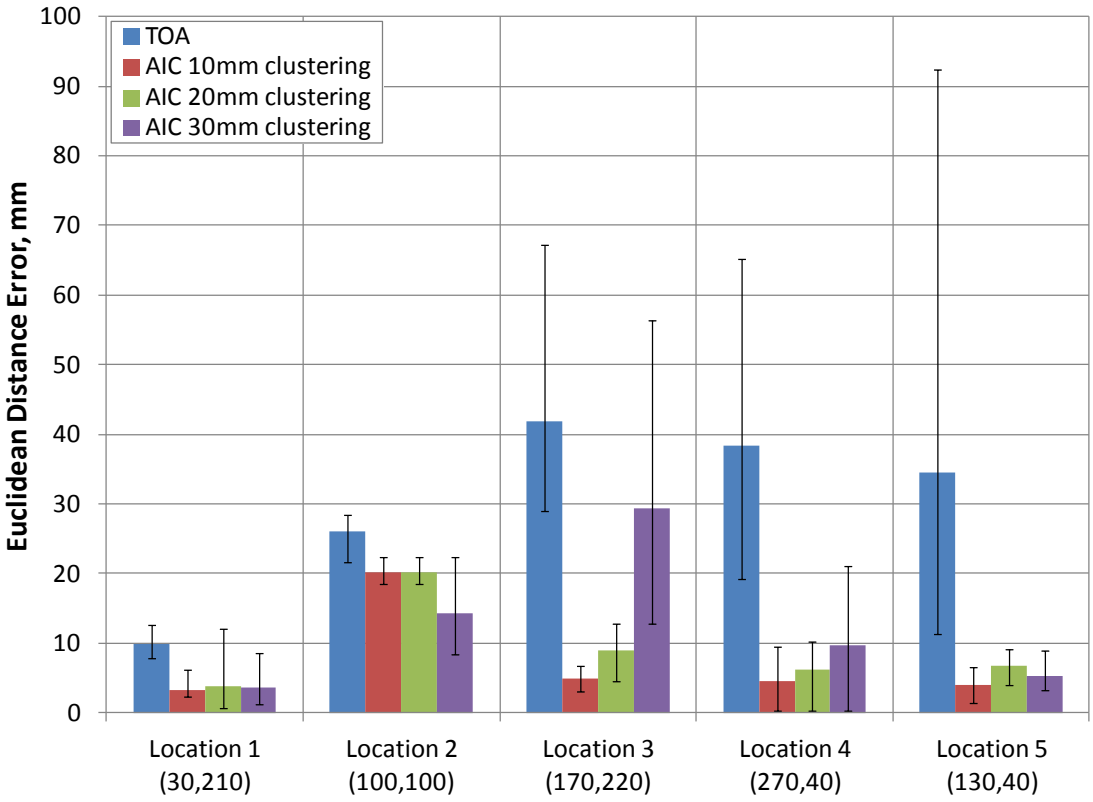

Figure 6-11. Average Euclidean distance error for five arbitrary positions

Figure 6-12 shows an ultrasonic C-scan of the wing conducted after the impact investigation. As for the previous C-scan image the embedded MFC transducers and the cabling can be seen. Also the stiffener which had been bonded to the wing for the impact investigation is now present on the image. There is now a delamination area highlighted by the red circle which was not present in Figure 6-9. This area of signal loss can therefore be attributed to damage from the impacts events. Figure 6-13 shows a close up of the damage area, using the "-6dB drop method" where a signal drop of 6dB is used to determine the defect edge. The supporting research for the technique is discussed by Smith (1998) and Broughton (1998). Using this technique an estimated damage area of 100mm^2 area was indentified which corresponds to delamination damage. The location results for each individual impact can be seen in Figure 6-14, the C-scan image shown in Figure 6-12 is overlaid on the location results. The TOA and AIC delta T mapping technique are all located in close proximity to the actual impact locations and the delamination area respectively. A visual observation of the results would suggest the AIC mapping technique has located six out of the seven impact events more accurately than the TOA method. However as was evident in Figure 6-10 the impact location was in the same position as location 1 in the H-N source investigation and this gave good results for both the techniques for the reasons

previously discussed. The Euclidean distance error for each individual impact is shown in Figure 6-15, the dashed lines in the figure represent the average errors calculated from all the impact events. On average the AIC delta T mapping technique shows an approximated 4mm improvement over the TOA technique. The locations were calculated from the highest amplitude and energy AE hits which correspond to the damage mechanism rather than the impact with the wing itself. For impacts 1 and 2 there are significant improvements of approximately 12 and 15mm respectively when comparing with the TOA method. Impacts 4, 6 and 7 show an approximate improvement of 1, 2 and 4mm respectively over the TOA technique. Impact 3 shows a decrease in accuracy when compared with the TOA method which shows a 2mm improvement over the delta-T mapping technique. The located impact event for impact 5 for the delta-T technique is of some concern as the technique shows a decrease in accuracy of approximately 10mm when compared against the TOA technique. The reasons for this decrease in accuracy were investigated further, the AIC picker was able to determine accurately the arrival time of the transducer so the decrease could not be attributed to that. It should be noted that location accuracy is general defined by the size of your sensing area. These particular MFCs were 28x14mm when considering this location 5 is still within the transducer spacing

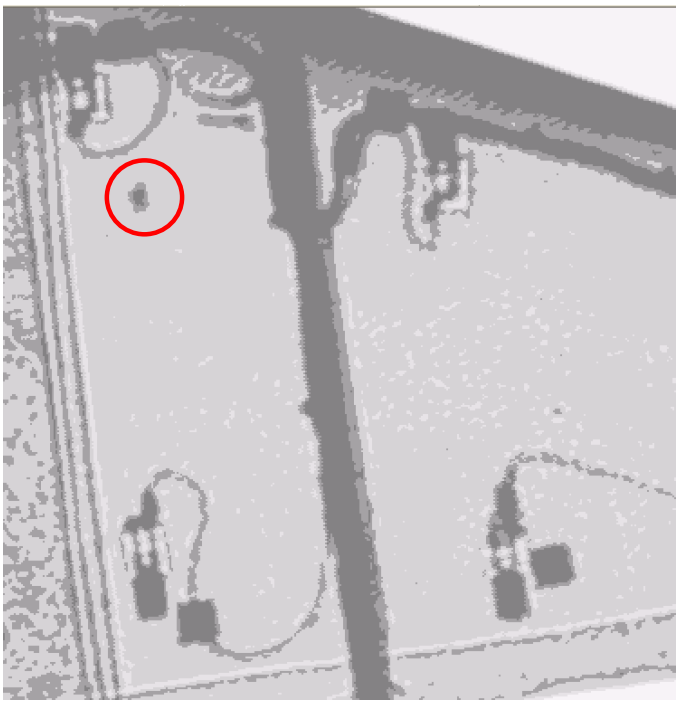

Figure 6-12. Ultrasonic C-scan of the wing after the impact investigation

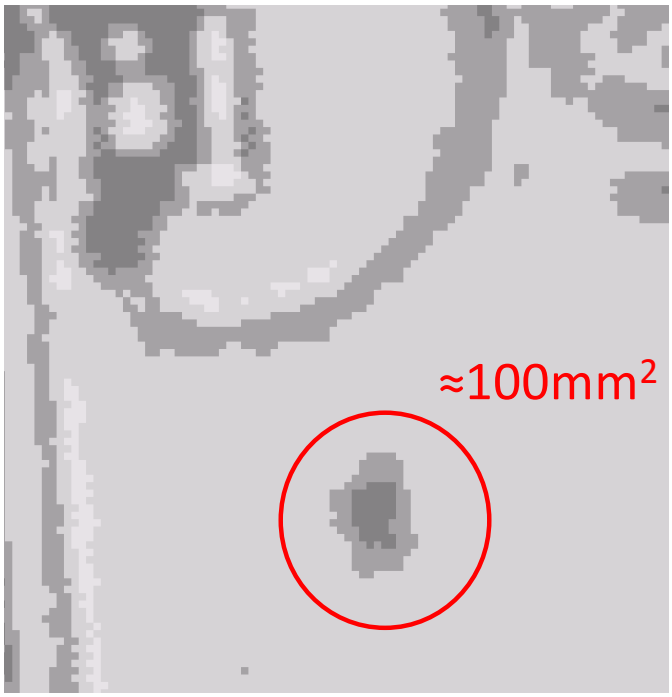

Figure 6-13. Close up of the delamination area and the estimation of the damage area

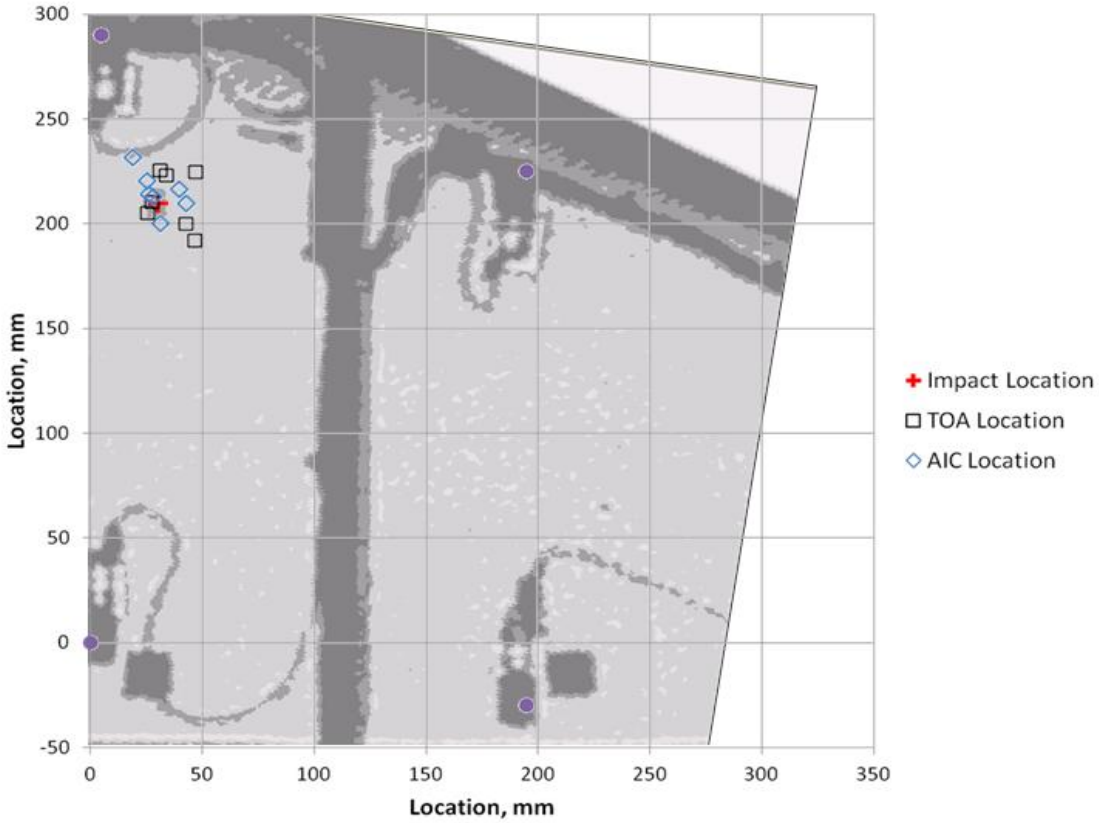

Figure 6-14. TOA and Delta T mapping locations for the impact events

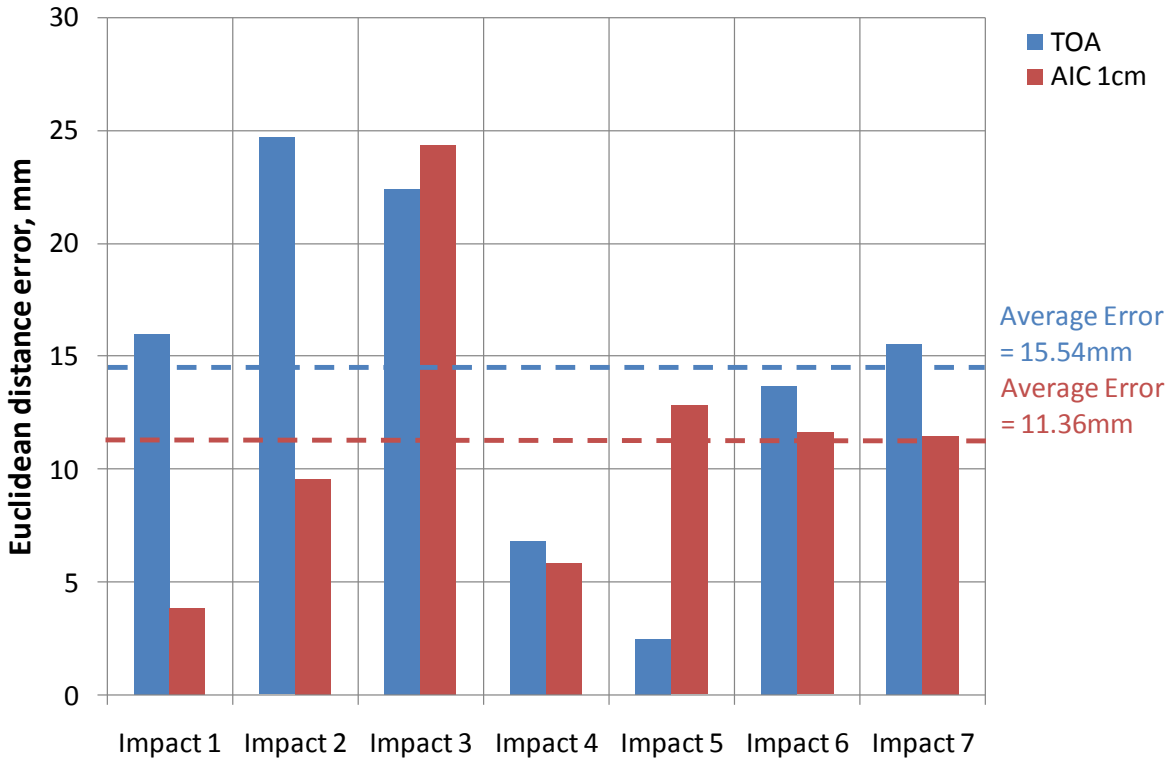

Figure 6-15. Euclidean distance errors for each impact event

Figure 6-16 and Figure 6-17 show the AE wave streams for the impact event and the resulting load trace from the load cell on the impact test machine for impacts 2 and 7 respectively. Impact 1 was not used in this analysis as the air brakes on the test rig failed to actuate which resulted in multiple impacts on the wing. These wave streams overlaid with the impact load trace can be used to determine between impacts that cause damage and those that do not. The load trace for impact 2 shown in Figure 6-16 shows a peak load of 600N and apart from higher frequency components of the load trace shows a smooth curve with no specific drops. This means that there is very little or no significant damage introduced into the wing after the second impact. When comparing this with the AE wave stream recorded from channel 1, which was in close proximity to the damage itself as shown in Figure 6-7, it shows the initial impact on the panel which corresponds to the first increase in load from background noise. There is no further significant AE activity till around 15ms, this activity is thought to have arisen due to the damage mechanism, however there is no significant activity here which corresponds with the load trace. When comparing the information for impact 2 with impact 7, the load trace and AE wave stream recorded are significantly different. A C-scan of the wing after impact 7 showed an estimated delamination area of 100mm^2. Therefore the subsequent impacts from 2 through to 7 did introduce

damage into the panel. No comparison of the damage progression can be made as the wing was not C-scanned after each individual impact. From the load trace recorded from the impact load cell for impact 7 which is shown Figure 6-17, it can be seen that a peak load close to 800N was observed, however there is little symmetry in the load trace when compared with impact 2. The load trace also shows specific drops in load. Therefore it is deduced that significant damage has been introduced which is confirmed with the ultrasonic C-scan. Further analysis of the AE wave stream recorded for impact 7 shows significant activity occurring after 10ms. This increase in AE activity corresponds to the loss of symmetry of the load trace and the specific drops in load observed. Therefore it is most likely that this increased activity is from the damage mechanisms in form of the delamination growth in the panel. Unfortunately a constant gain was used during the investigation which saturated the ±10V AE channels after the second impact so no comparison of the wave streams throughout testing can be drawn.

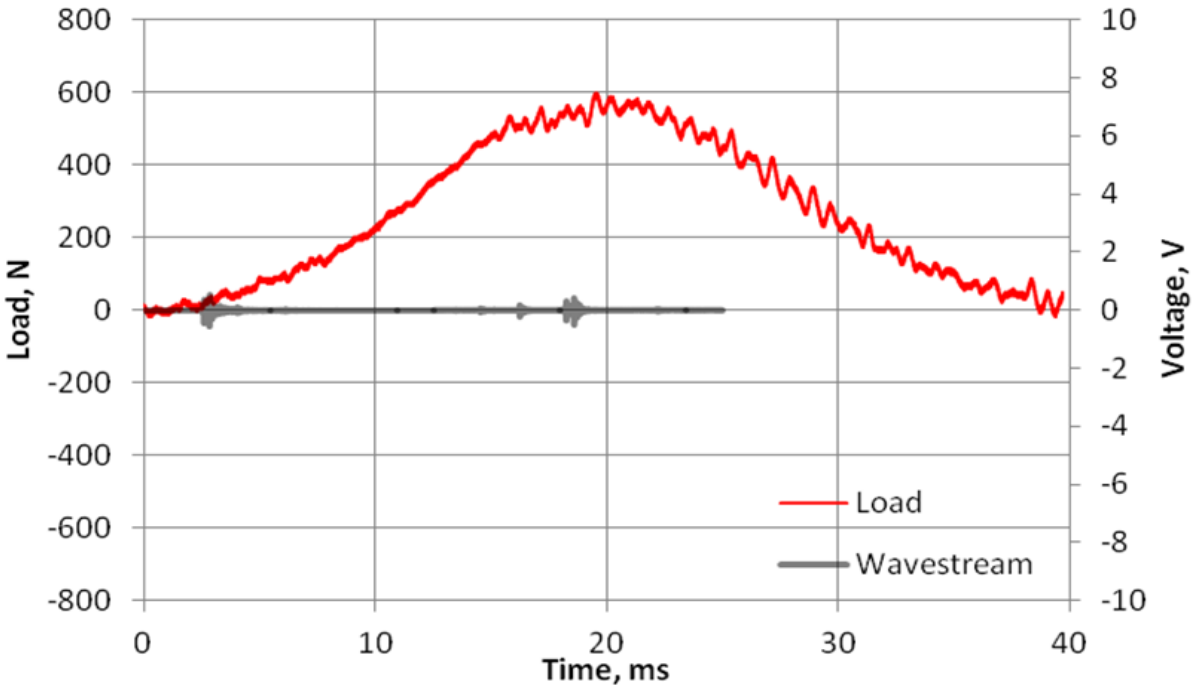

Figure 6-16. AE wave stream and the load trace from the impact test machine for impact 2

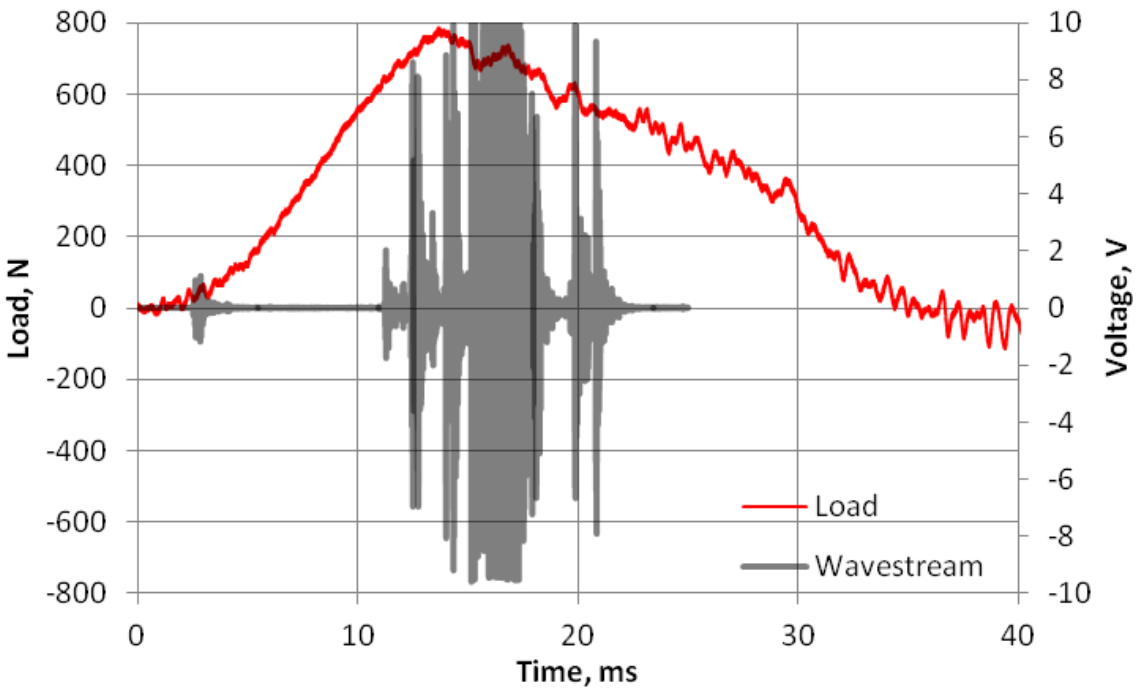

Figure 6-17. AE wave stream and the load trace from the impact test machine for impact 7

Figure 6-18 shows the average cross correlation coefficients calculated for a hundred recorded waveforms when channel 1 was used as a transmitter pulsing a 100kHz 60V peak to peak square wave. The figure shows cross correlation coefficients for three sets of data. The first is when the first waveform is compared with all other waveforms recorded in that data prior to the impact investigation. The second is for the first waveform recorded after the impact investigation and compared with all other waveforms within that data. Finally the third compares the first waveform recorded prior to the impact investigation to those recorded after the impact investigation and should indicate whether any damage has occurred within the panel. The following AU cross correlation results shown in Figure 6-23, Figure 6-24, Figure 6-25, Figure 6-26 and Figure 6-27 follow the same methodology as described above. Figure 6-18 shows the average cross correlation coefficients for each receiving channel. When compared waveforms in each data set for pre and post impact have a correlation coefficient greater than 0.99, there is a high level of repeatability between the pulse and receive configuration. Therefore when comparing the waveforms recorded before and after the investigation the reduction in the cross correlation observed is due to the presence of damage within the wing. This technique shows the ability to detect very small amounts of damage within a structure. For channels 2 to 5 there is a reduction in the similarity of the waveforms prior to impact dependent on the propagation direction. Channels 2 and 3 are closest to the damage location and yet show less of a reduction in correlation when

compared with channels 5 and 6. This would suggest that the further the propagation direction the greater the reduction in cross correlation coefficient. To further investigate this, the wavelet transforms for each channel for the pre and post impact states were calculated and then subtracted from each other as outlined in chapter 2. Figure 6-19 illustrates the wavelet subtraction with channel 1 as the transmitter and channel 2 the receiver, which shows the greatest change in the wavelet transform for the first arrival of the waveform at approximately 550µs. Figure 6-20 shows the wavelet transform subtraction between channels 1 and 3 where the maximum changes in wavelet coefficient can be observed around 600, 650 and 750µs. When comparing Figure 6-19 and Figure 6-20 similar areas of change in the wavelet transform are seen at 500-600µs and 750µs, however a difference in wavelet coefficient is observed at 650µs. This suggests that the first arrival of the waveform is least sensitive to the damage area. This is probably due to the in-plane nature of the embedded transducers and the wavelength of the propagating wave in relation to the damage size. It further suggests that reflected propagation paths show the greatest change in correlation coefficient due to possible mode changes occurring at the interaction with the boundary of the wing. Figure 6-21 shows the wavelet subtraction for channels 1 to 4 and shows significant changes in the wavelet subtraction at 600, 700 and 900µs. The magnitude of these changes is greater than observed previously and provides further evidence to the already stated theory. A similar pattern is observed for the wavelet substation between channels 1 and 5 as shown in Figure 6-22, however there are more areas where the magnitude of the changes in the wavelet coefficient are greater for the majority of the waveform length. This suggests that the various reflection propagation paths show the greatest interaction with the damage. Channel 6 shows the greatest reduction in the average cross correlation coefficient. This is due to this transducer being a commercial transducer mounted to the underside of the wing. Its close proximity to the damage location, increased sensitivity when compared with the MFC transducer and wider bandwidth mean it is more sensitive to the changes in the waveform due to the presence of damage. These transducers are also predominantly out of plane transducers and considering that a delamination is an out of plane mechanism suggests the waveform will be most sensitive to the damage itself. Another consideration is the directional nature of the MFC transducer for which the greatest sensitivity will be observed parallel to the piezoceramic fibre direction and least sensitivity will be perpendicular to the piezoceramic fibre. This is further exaggerated by the fibre nature of the wing with fibre directions in the 0 and 90° directions.

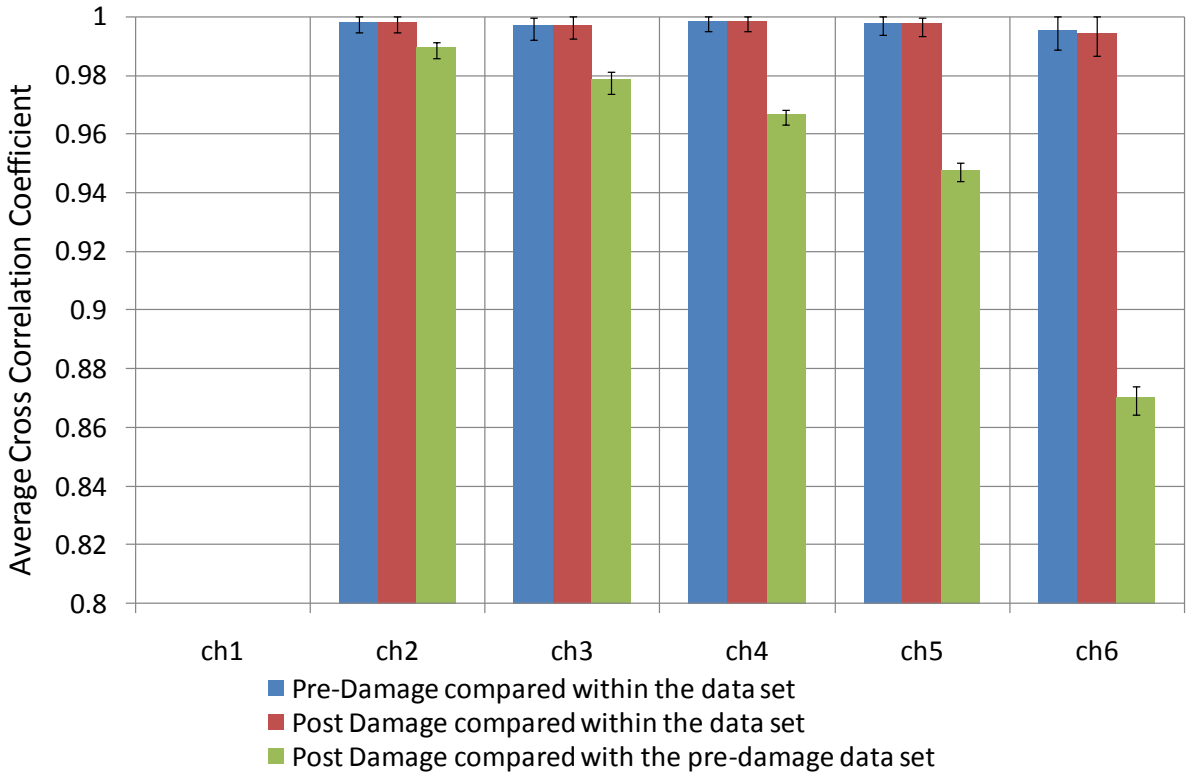

Figure 6-18. Average cross correlation coefficients for channel 1 as a transmitter

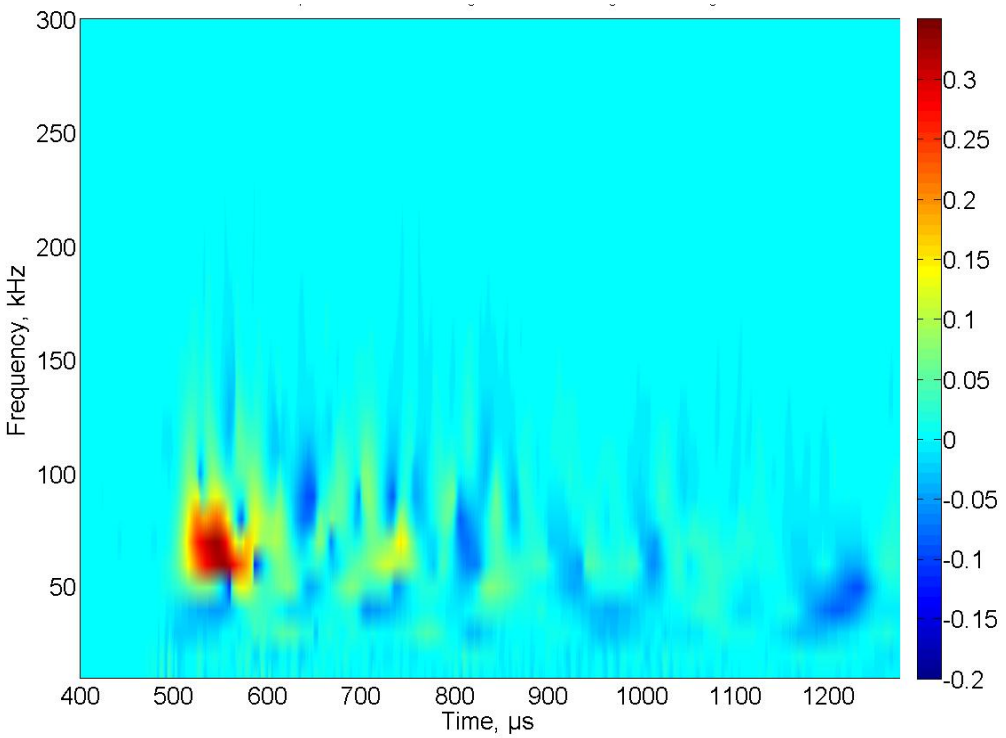

Figure 6-19. Wavelet subtraction for pre and post impact wavelet transforms for path 1 to 2

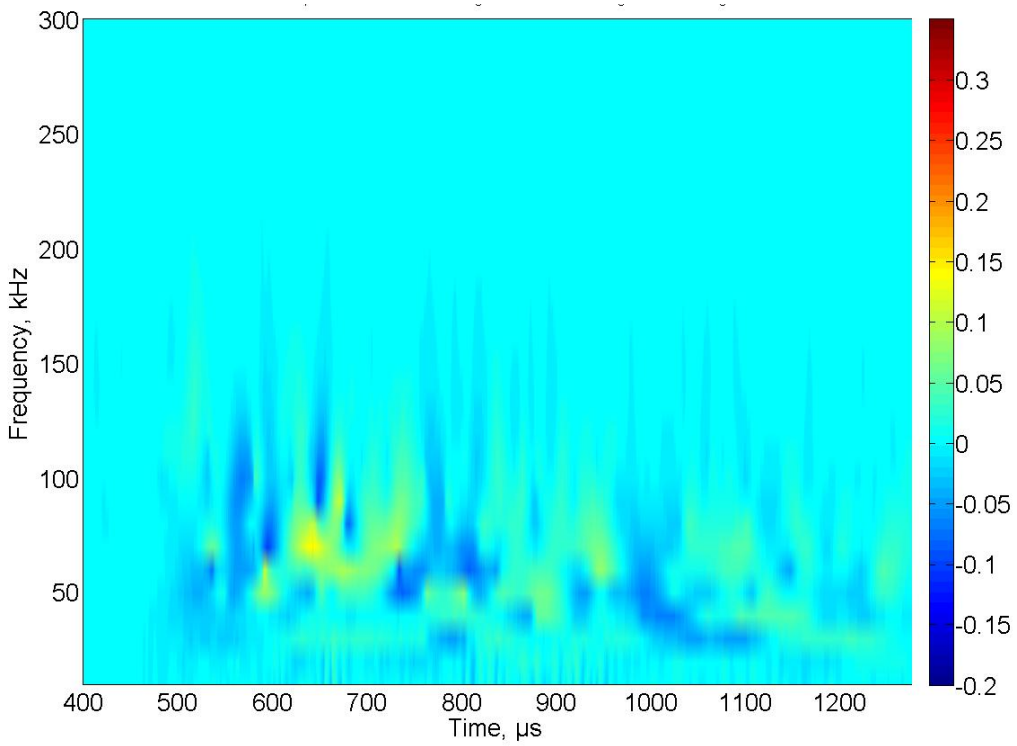

Figure 6-20. Wavelet subtraction for pre and post impact wavelet transforms for path 1 to 3

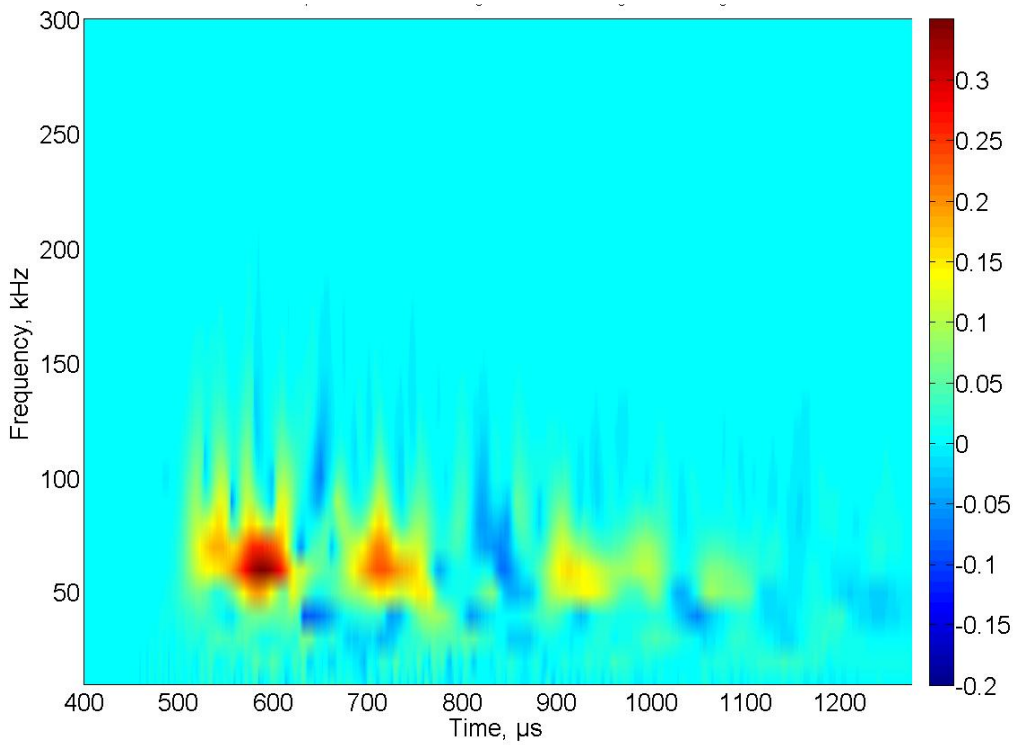

Figure 6-21. Wavelet subtraction for pre and post impact wavelet transforms for path 1 to 4

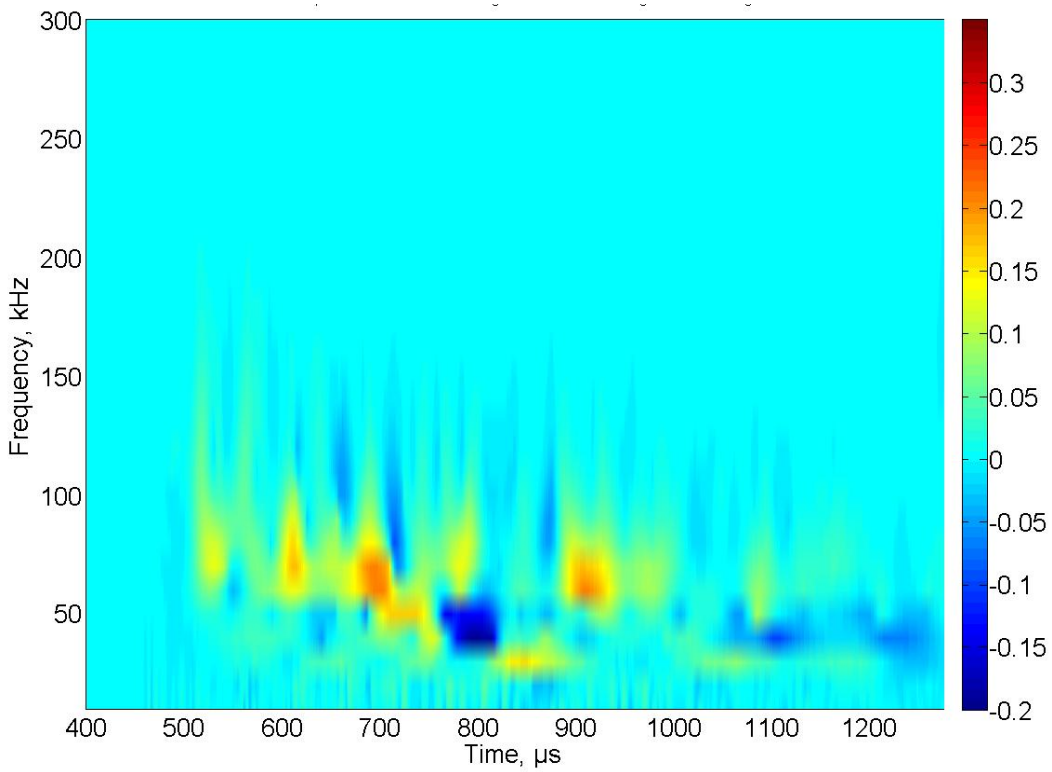

Figure 6-22. Wavelet subtraction for pre and post impact wavelet transforms for path 1 to 5

Figure 6-23 shows the average wavelet coefficient when channel 2 was a transmitter and all other channels were receivers. High levels of repeatability are observed for the pre and post impact investigation with average correlation coefficients greater than 0.99 for all channels. This means that there is a high level of similarity between the waveforms recorded within each data set. Any reductions in correlation that are observed when comparing waveforms recorded before and after the impact events therefore are due to the damage and not changes in the pulse and receive configuration. Again damage is detected by a reduction in the average cross correlation coefficient. Propagation paths 1 and 2 show the least reduction in similarity along with channel 4 even though the damage is located on a direct or very close to direct path. Channels 3 and 5 show the greatest reduction in correlation to an approximate level of 0.93, this is thought to be because of the interaction of the reflected propagation paths with the damage. Again the commercial transducer shows the greatest drop in correlation as previously discussed.

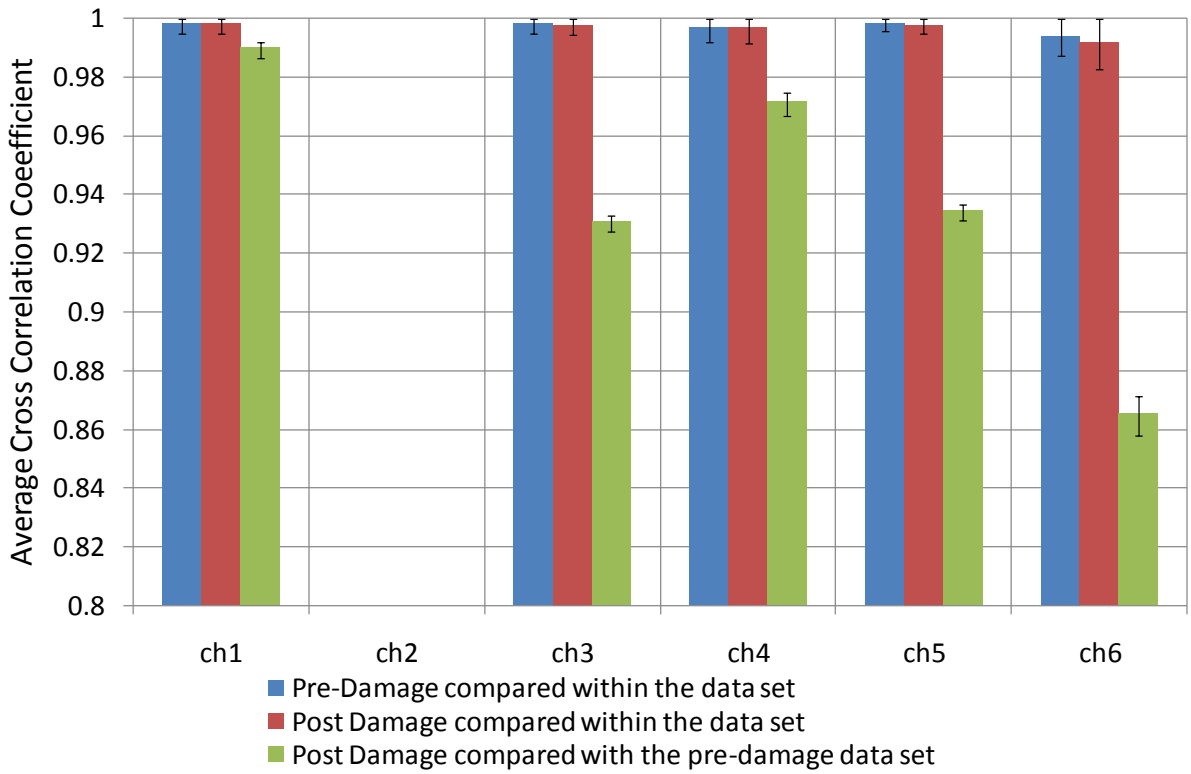

Figure 6-23. Average cross correlation coefficients for channel 2 as a transmitter

Figure 6-24 shows the average cross correlation coefficient when channel 3 was transmitting and all other channels were receiving. Again a high level of similarity of the waveforms recorded within each data set is observed, meaning a high level of repeatability is observed for the pulse receive configuration and therefore any reduction in correlation must be due to the presence of damage. When the signals are compared between the healthy and damaged states a fall in correlation is observed demonstrating the ability to detect damage. Propagation paths from 3 to 4, 1 and 5 show the least decline in the similarity of the waveforms between undamaged and with damage introduced. Channel 2 shows the greatest drop in correlation for the MFC transducers and overall the commercial transducer shows the greatest fall in similarity.

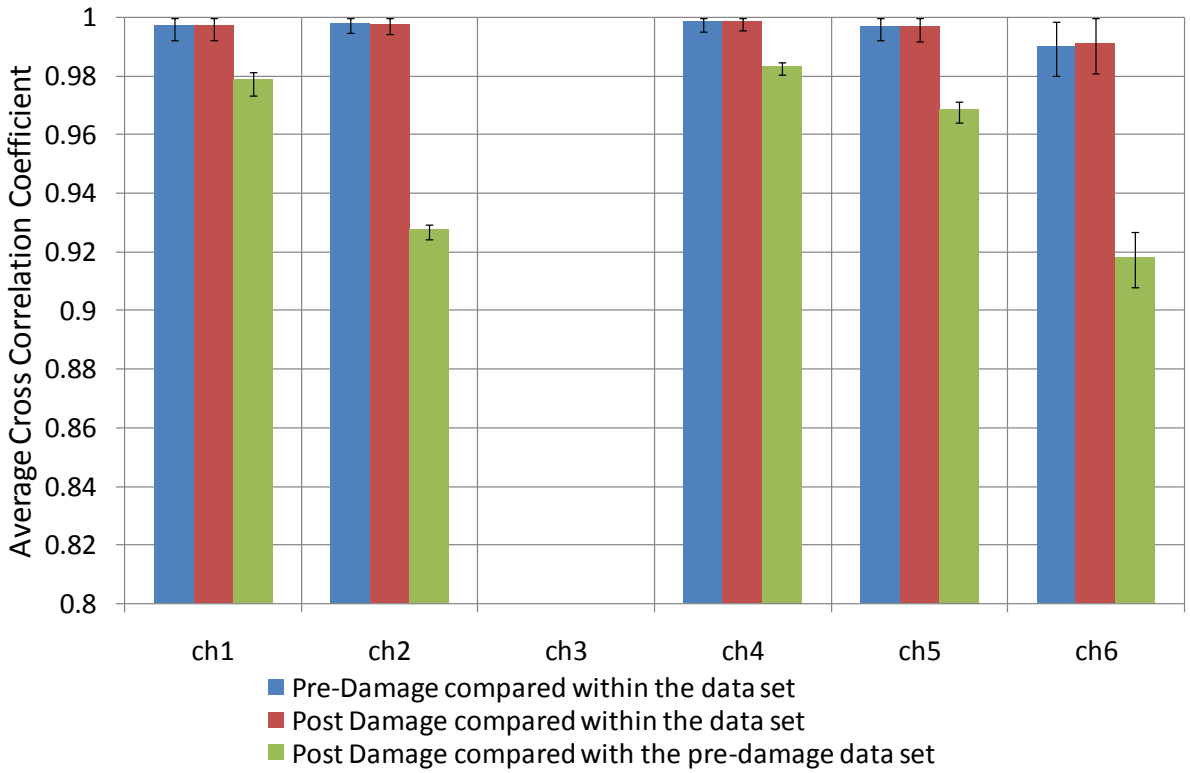

Figure 6-24. Average cross correlation coefficients for channel 3 as a transmitter

Figure 6-25 shows the average cross correlation coefficient when channel 4 was used to transmit the actuation signal and all other transducers were set to receive. For channels 1,2 and 3 a reduction in correlation from healthy to a reduction to 0.96 in the damaged state, however channel 5 shows the largest drop in correlation to 0.89. This further suggests that it is the reflected waveform propagation paths that show the greatest interaction with the damage rather than the first arrival of the waveform. It is not thought that attenuation of the signal is causing the signal to noise ratio to increase for increasing propagation distances and therefore causing the correlation to drop, as the propagation distances between channel 5 and 1 are similar yet a large difference in correlation is observed. This, coupled with the damage being on a direct path between channel 4 and 1, provides further evidence to the proposed theory.

Figure 6-26 shows the average cross correlation coefficient when channel 5 was used as a transmitter and all other channels were receivers. Again a high level of similarity of the waveforms observed and correlation within each data set pre and post impact investigation can be seen. All channels successfully detect the delamination area within the wing as all channels observed a fall in the similarity of the waveforms when comparing the waveform recorded from the healthy state to that after the impact investigation. Again a non

typical pattern is observed where damage on or near a direct path does not result in as large a fall in correlation when compared with those on an indirect path with regards to the damage location. This suggests that it is the reflected parts of the waveform which show the greatest sensitivity to the damage. Overall again the commercial transducer is able to detect the greatest decline in the cross correlation coefficient.

Figure 6-27 shows the average cross correlation coefficient when the commercial transducer was used as a transmitter and the resulting waveforms in the wing were recorded on all the remaining MFC channels. For all channels there is a greater reduction in cross correlation coefficient with respect to any of the MFC transmitter cases. This is due to the out of plane nature of the commercial transducer and an out of place wave being most sensitive to delamination damage. Even though the MFC transducers are mainly thought to be in-plane some of the out-of plane waves will be detected due to the Poisson effect.

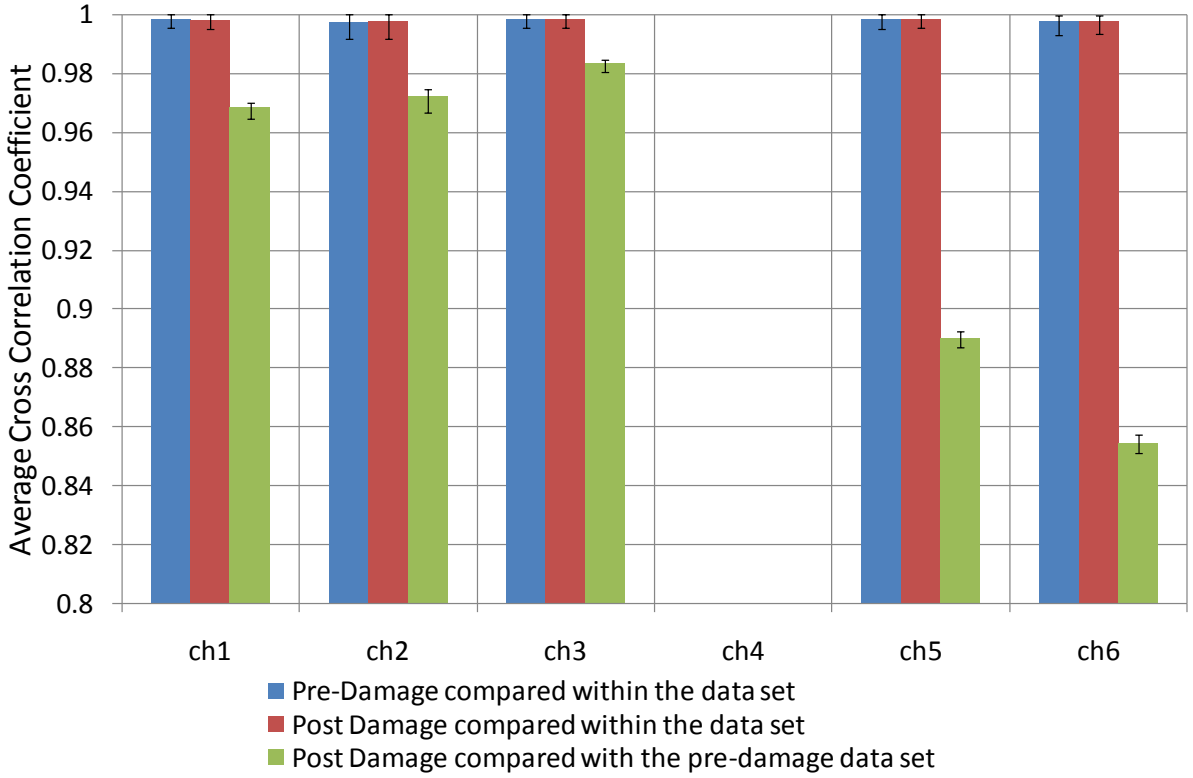

Figure 6-25. Average cross correlation coefficients for channel 4 as a transmitter

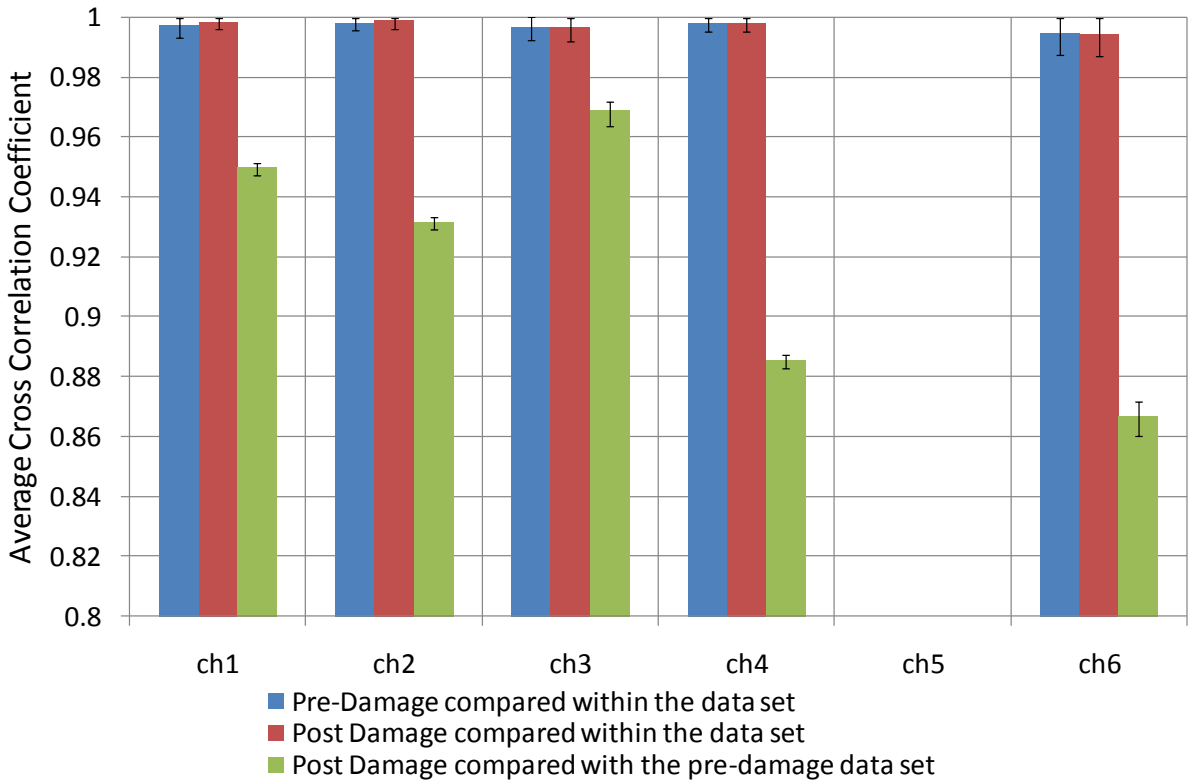

Figure 6-26. Average cross correlation coefficients for channel 5 as a transmitter

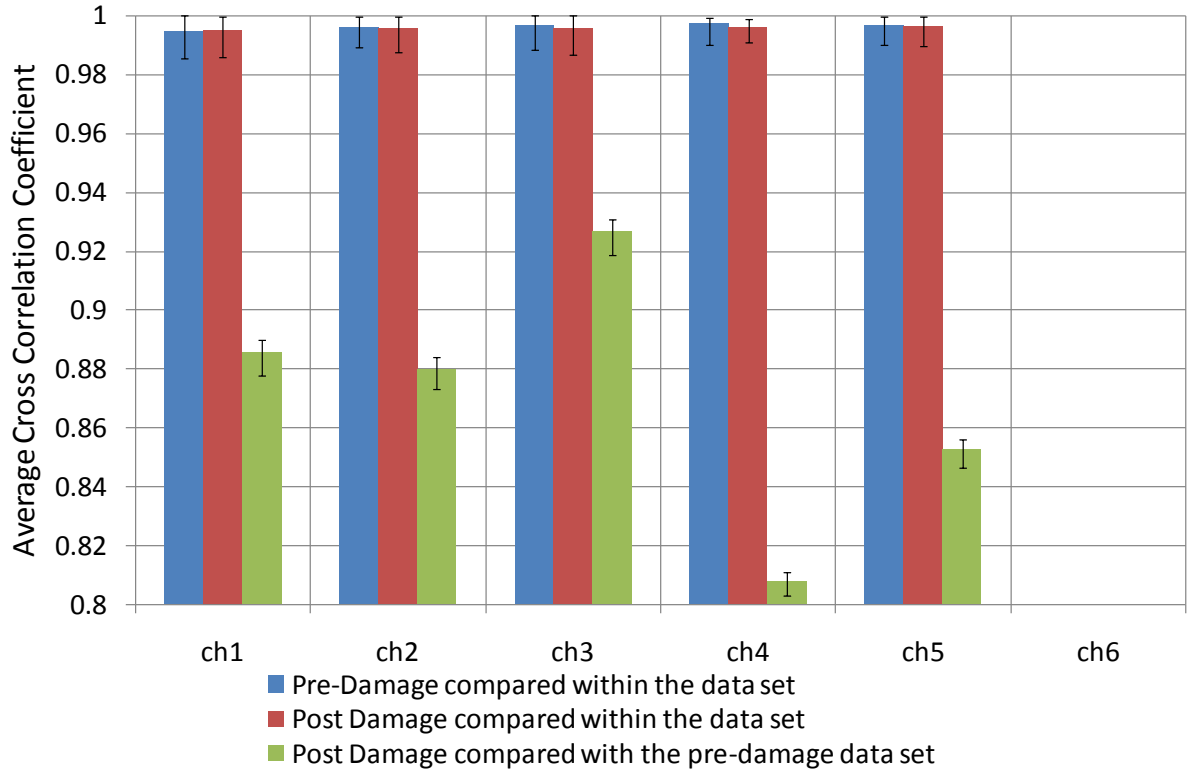

Figure 6-27. Average cross correlation coefficients for channel 6 as a transmitter

Overall the damage detection methodologies employed on the smart wing have been able to successfully detect and accurately locate impact damage with MFC transducers used in both AE and AU monitoring techniques.

In terms of energy harvesting through active vibration, Figure 6-28 shows the peak power harvested when the MFC denoted as channel 1 was used to harvest ambient vibration produced using an electromagnetic shaker. The power levels correspond to the load resistance where maximum power transfer occurs due to load matching. The corresponding load resistance that the power was harvested at is also shown in the figure. The power generated is highly dependent on the frequency and therefore the vibration mode shape, curvature and displacement of the wing in relation to the location of the MFC. Power is harvested in the range of 0.05 to 12.2 μW. This is relatively low however this is due to the MFC being embedded within the structure in the central layer and therefore experiencing the least amount of strain and also the location of the harvesting with relation to the expected mode shapes has not been optimised. However it should be noted that this is the output of one harvester only. There is a considerable fall in the load resistance from 500kΩ at 10Hz to 10kΩ at 400Hz. A carefully designed power management system would be required in order to ensure maximum power transfer across the frequency bandwidth. Peaks are observed in the harvesting power at 50, 275 and 350Hz which correspond to peak powers of 9, 10 and 12μW respectively. Two smaller peaks are observed at 125 and 200Hz which corresponds to power of 1 and 2.63μW, again showing the dependence of the attainable power levels on the frequency. The peaks in power are most likely to be observed when there is an increase in curvature at the harvester, which is linked to the mode shape and location of the harvester with respect to the peaks in the mode shape. Figure 6-29 shows the RMS power generated for the same harvesting MFC. This gives an idea of the average power levels generated where the range of power harvesting is between 0.02 to 5.5μW. The same drop in load resistance is observed and the same peaks in the power in terms of the frequency. It is thought that with further optimisation of the placement of the harvesters increased levels of power could be harvested. However the investigation stands as a benchmark where further improvements could be made.

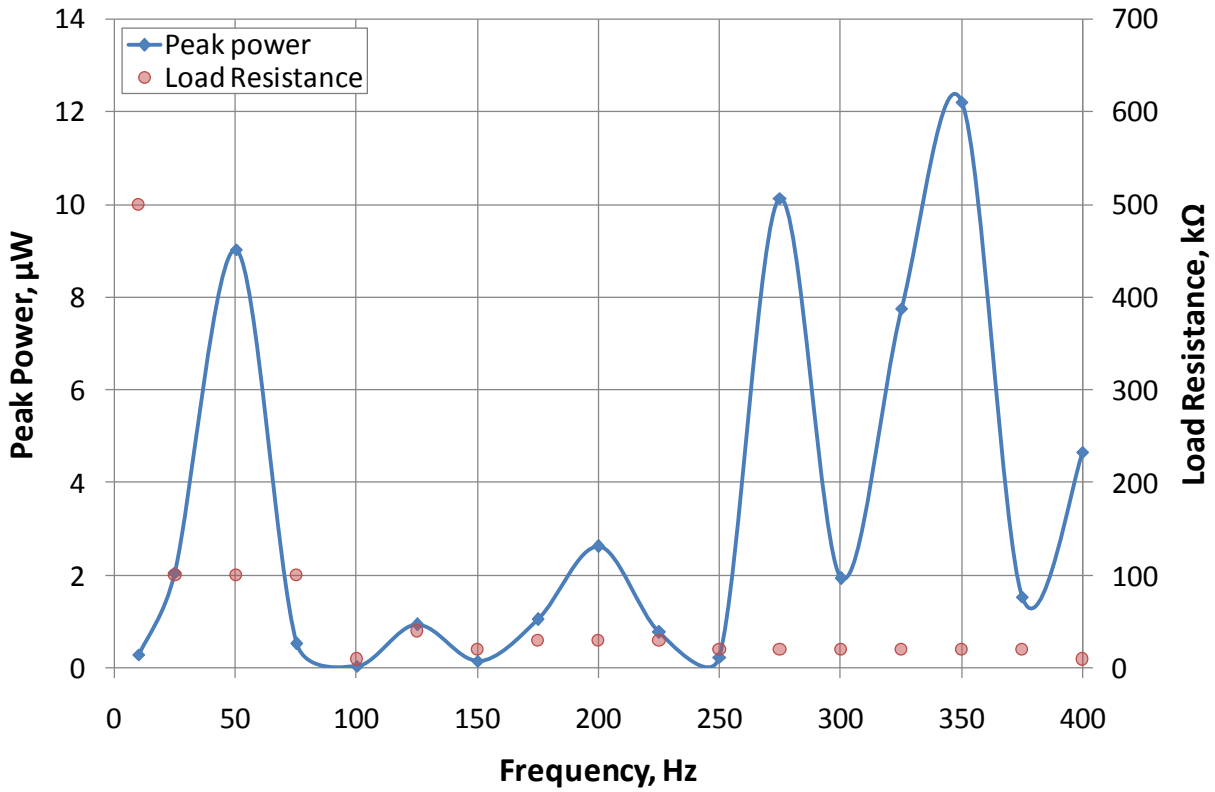

Figure 6-28. Peak power harvested from various frequency of vibrations

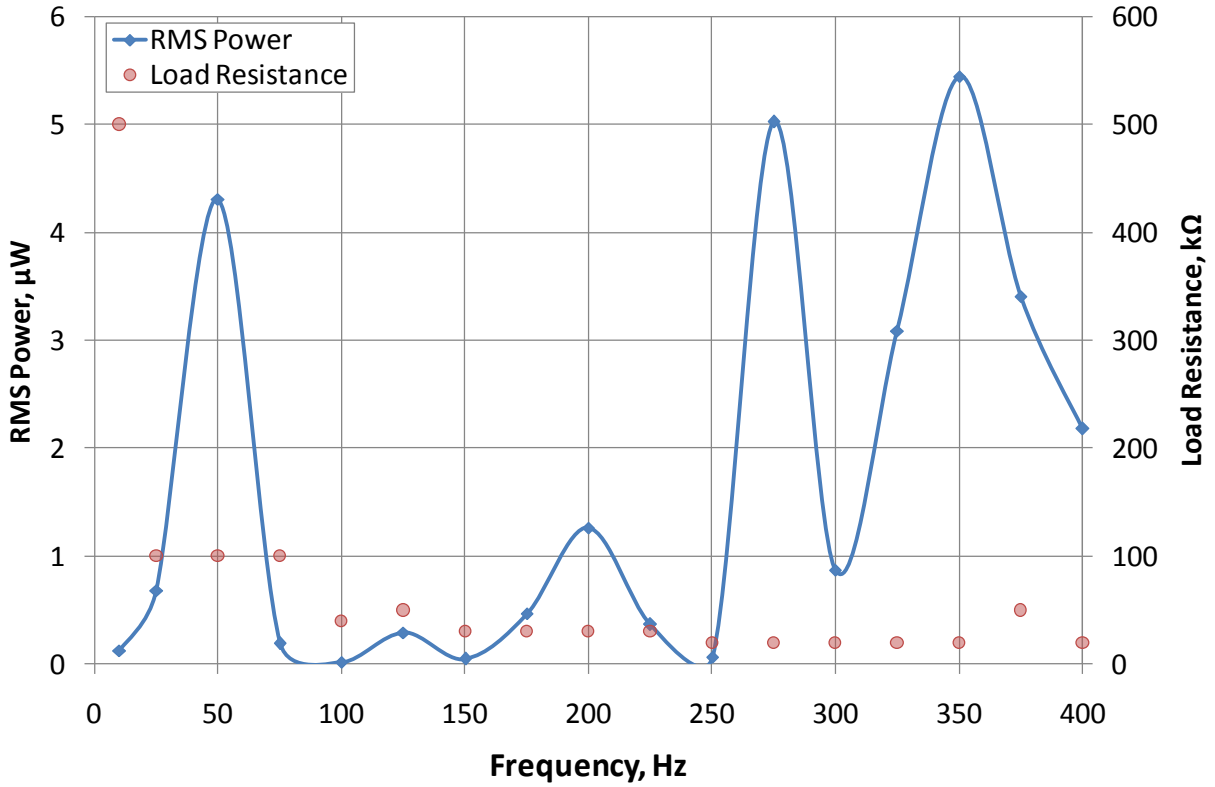

Figure 6-29. RMS power harvested from a variety of vibration frequencies

6.5 Conclusions

In conclusion the smart wing has been able to accurately locate and detect impact damage within the structure after subsequent impacts at the same position. The same embedded transducers have been used to conduct both passive and active monitoring as well as harvesting energy from ambient vibrations. This in real world applications could mean that the amount of transducers required would be substantially less if one transducer could be used for the three proposed techniques (detection, location and energy harvesting). It also demonstrates the feasibility of developing an autonomous system with individual nodes having their power supplied through energy harvesting and transmitting data wirelessly.

7 Overarching discussion, conclusions and further work

7.1 Discussion

Research investigations were conducted into the key technologies which form wireless SHM systems. These crucial elements include transducer technology, damage detection, energy harvesting and power management. This thesis has provided significant advances in damage detection and multi-functional transducers and has identified key enabling technologies in energy harvesting and power management.

In terms of transducer technology for SHM AE and AU techniques, both commercial off the shelf piezoelectric transducers and the proposed novel MFC transducers have been systematically tested within the harsh environment experienced during flight. It was revealed that, despite the transducers retaining functionality after exposure to these environments, significant changes in the frequency and amplitude response of the transducers was demonstrated at the elevated temperature using cross correlation techniques. In the context of baseline AU analysis, this could result in a “false positive” for damage due to changes in the environment and not of the structure itself. With this in mind, whilst commercial transducers could be permanently mounted on aircraft structures, compensation methods would be required to remove environmental effects in order to avoid false alarms. Testing of appropriate bonding materials and sealants would also be required prior to approval at the highest technology readiness level.

The improved AE damage location technique developed in this work has consistently shown improved results across material types, damage mechanisms and transducer types, compared with both the conventional TOA technique and the threshold triggered Delta T mapping. The studies conducted have shown that, irrespective of specimen geometry and damage mechanism, the AIC delta T mapping technique can accurately locate flaws within a material.

Dual AE and AU monitoring of structures using a single novel MFC transducer has been used successfully to locate and detect damage. This important new application enables a larger transducer array to be utilised whilst maintaining the same location accuracy as that achieved with the TOA technique. Alternatively this would enable less transducer to monitor the same area and would reduce the cost of the system. Furthermore, the ability for transducers to have multiple functionality would vastly reduce the required quantity of transducers. These dual functionality techniques have also been demonstrated

successfully using embedded MFC composite specimens, which, when considering the increased uptake of composite structures could lead to smart structures being developed. This could be achieved by embedded these transducers during the manufacturing stage, further protecting the transducer. Although a number of the specimens studied have a level of complexity, an actual aerospace component increases the complexity further. The techniques developed here should therefore be implemented on actual aircraft structures in the next stage of development.

Energy harvesting techniques which utilise piezoelectric and TEGs to harvest ambient energy have been shown to produce raw power levels at the right order of magnitude to power a prototype wireless SHM system. However there is still a gap between the harvested power and that consumed by such a system and this needs to be addressed in order to realise a truly autonomous SHM system. Experimental investigation of piezoelectric patches for typical aircraft frequency vibrations showed that peak power levels ranging from 4μW to 2.7mW's could be generated however this is dependent on a very complex relationship which includes the positions of the device, vibration frequency, acceleration and curvature. Piezoelectric patches which conform to the structure have been chosen rather than cantilever devices due to their low profile and ability to be embedded within the structure, as well as the possibility of using the same devices as transducers. This would not be possible with cantilever devices. Piezoelectric energy harvesting is envisaged to be easier to integrate into aircraft structures and do not rely on specific areas where certain environmental effects occur, but it does rely on selecting regions of high vibration. Numerical analysis of possible power levels generated from a single thin film TEG have shown peak powers ranging from 6 up to 30mW and average power levels of 3 to 10mW. Further validation of these power levels is required however it is thought that in reality power levels would be less due to maintaining the temperature gradients at the TEG and thermal resistance of the connecting surfaces. However from the research conducted it is envisaged that TEG power levels would be better considered for the main power source for a SHM system, with complimentary power levels from vibration energy harvesters.

Commercial power management components and systems are available that can manage and regulate the dynamic power levels generated from the TEG and provide a stable output for a SHM system. There exist in the literature specific power management systems for aircraft environments however these systems are developed for specific wireless transducer nodes. Further work could enable the development and application-specific optimisation of power management systems for the wireless AE and AU system proposed in

this work. Testing of a commercial power management system showed that a stable 3.3V output voltage could be achieved from the varying input voltage from a TEG. The system continued to operate for a period of 40 minutes when no voltage was produced by the TEG. This particular system does require further optimisation with regards to storage capacity and start up voltage levels.

The developed of a smart structure demonstrator was used to show that these methodologies and technique could be implemented using the same transducers for damage detection and location and energy harvesting. A fully integrated solution however has not been implemented, which of course is another important factor before such systems can be introduced onto an aircraft.

7.2 Conclusions

- Conventional transducer technologies exist that could be deployed and used to measure the deterioration of a structure.
- Novel flexible low profile transducers exist which have the advantage of being easy to embed enabling the development of smart structures.
- These novel transducers have also been shown to detect, locate damage and harvest energy, although a deeper understanding of the operation mechanisms is required.
- Using single transducer types for both AE and AU analysis vastly reduces the number of transducers required thus reducing the cost of the system.
- A series of investigations showed the use of the AIC delta T mapping when compared with the conventional Delta T mapping and TOA algorithms has demonstrated robust and accurate damage location. For complex aluminium specimens the AIC delta T mapping technique shows an average improvement of 11mm and 19mm for specimen 1 and 2 respectively over the TOA technique in terms of event spatially binning. For locating H-N sources on a composite specimen the average improvement of the AIC delta T over the TOA technique was 6mm. For located impacts on a composite panel the average improvement of the AIC delta T over the TOA technique was 23mm.
- Allowing for the easier interpretation of damage location results on complex specimens found in actual aircraft components. The merits of the improved technique have been demonstrated for metallic and composite components

which are important when considering the hybrid nature of materials in modern and future aircraft structures.

- Energy harvesting is seen as a viable option for the powering of self powered autonomous wireless systems with individual power supplies. Numerical simulation of the TEG power output showed average power levels of 2.3mW to 10mW could be generated. For experimental testing of a piezoelectric vibration energy harvester generated RMS power between 2 to 620µW. However further development is required in order to fully match the consumption of the prototype wireless system.
- Energy harvester would eliminate the problems with the use of batteries such as access and replacement.
- Power management systems can be designed using commercial available components to provide the stable power source required for a wireless SHM system although careful consideration of the efficiency of the components is required in order to maximise the already small power levels harvested. Testing of a commercial power management system generated a 3.3V battery output from a dynamic input power from a TEG.

Significant advances in the individual elements that contribute to an SHM system have been made, now effort needs to be focussed on the connecting interfaces between these individual elements.

7.3 Future work

Although this thesis has advanced the state of the art in the modular components of SHM systems, further work is required in order for these systems to be incorporated into aircraft, these include:

- Robustness testing of the AIC picker with regards to the reduced sampling rates and frequencies that could be achieved with actual wireless AE and AU systems
- Further reduction in the power requirements of wireless transducer systems for AE and AU techniques to achieved truly low powered devices
- Damage detection investigation on full sized aircraft structures using AE and AU techniques
- Development of MFC transducers for the specific application of sensing rather than actuation purpose incorporating optimisation for multi-functionality

- Advanced wireless timing strategies to realise individual wireless transducer systems which can effectively communicate between nodes with sufficient timing accuracy to enable damage detection and location
- Improved efficiencies of energy harvesting devices through advanced material and implementation techniques
- Advanced signal processing techniques for AE location and characterisation of damage type
- Improved efficiency of power management systems
- Optimisation of the location of embedded transducers within the ply-lay up for improved damage detection using AE and AU techniques
- Realisation of improved processing capability with reduced power consumption to enable advanced AE and AU sub-routines to be conducted at the transducer node and to reduce power consumption of the wireless communication

References

Akaike, H. 1974. Markovian Representation of Stochastic Processess and its Application to the Analysis of Autoregressive Moving Average Processes. *Annals of the Institute of Statistical Mathematics* 26(1), pp. 363-387.

Aljets, D. et al. 2010. Acoustic Emission Source Location in Plate-Like Structures using a Closely Arranged Triangular Sensor Array. *Journal of Acoustic emission* 28, pp. 85-98.

Anton, S. R. et al. 2012. Multifunctional Unmanned Aerial Vehicle Wing Spar for Low-Power Generation and Storage. *Journal of Aircraft* 49(1), pp. 292-301.

Anton, S. R. and Inman, D. J. 2011. Performance Modelling of Unmanned Aerial Vehicles with On-board Energy Harvesting. *Proceedings of the SPIE* 7977(79771H).

Arnold, M. et al. 2012. Energy Management Systems for Energy Harvesting in Structural Health Monitoring Applicationa. *Key Engineering Materials* 518, pp. 137-153.

ASTM. 1982. Definitions of Terms Relating to Acoustic Emission. *American Society for Testing and Materials,* E610-82.

Bachmann, F. et al. 2012. Optimum Piezoelectric patch positioning: A Strain Energy Based Finite Element Approach. *Journal of Intelligent Material Systems and Structures* 23(14), pp. 1575-1591.

Bandyopadhyay, S. and Chandrakasan, A. P. 2012. Platform Achitecture for Solar, Thermal and Vibration Energy Combining with MPPT and Single Inductor. *IEEE Journal of Solid-State Circuits* 47(9), pp. 2199-2215.

Baram, J. and Rosen, M. 1979. Acoustic emission generated during the tensile testing of aluminium alloys. *Materials Science and Engineering* 40(1), pp. 21-29.

Baram, J. and Rosen, M. 1981. Prediction of low-cycle fatigue life by acoustic emission -1: 2024-T3 aluminium alloy. *Engineering Facture Mechanics* 15(3-4), pp. 477-486.

Barbezat, M. et al. 2004. Acoustic Emission Sensor Properties of Active Fibre Composite Elements Compared with Commercial Acoustic Emission Sensors. *Sensors and Actuators A: Physical* 114(1), pp. 13 - 20.

Barbezat, M. et al. 2007. Integrated Active Fiber Composite Elements: Characterisation for Acoustic Emission and Acousto-Ultrasonics. *Journal of the Acoustical Society of America* 18(5), pp. 515-524.

Bartholome, K. et al. eds. 2010. *Energy-Autarkic Sensor Technology in Aircraft*. 8th European Conference on Thermoelectrics. Italy.

Baxter, M. G. 2007. *Damage Assessment by Acoustic Emission (AE) During Landing Gear Fatigue Testing.* Cardiff University.

Baxter, M. G. et al. 2007. Delta T Source Location for Acoustic Emission. *Mechanical Systems and Signal Processing* 21(3), pp. 1512 - 1520.

Becker, T. et al. 2009. Autonomous Sensor Nodes for Aircraft Structural Health Monitoring. *IEEE Sensors Journal* 9(11), pp. 1589-1595.

Beeby, S. P. et al. 2006. Energy Harvesting Vibration sources for Microsystems Applications. *Measurement Science and Technology* 17(12), pp. R175-R195.

Beral, B. and Speckmann, H. eds. 2003. *Structural Health Monitoring (SHM) for Aircraft Structures: A Challenge for System Developers and Aircraft Manufacturers*. Structural Health Monitoring 2003: From Diagnostics & Prognostics to Structural Health Management: Proceedings of the 4th International Workshop on Structural Health Monitoring. California.

Bockenheimer, C. et al. eds. 2009. *Guided Technology Development and Maturity Assessment of SHM Airbus*. Structural Health Monitoring 2009: From System Integration to Autonomous Systems, Proceedings of 7th International Workshop on Structural Health Monitoring. California.

Boczar, T. and Lorenc, M. 2004. Determining the Repeatability of Acousticd Emission Generated by the Hsu-Nielsen Calibrating Source. *Molecular and Quantum Acoustics* 25, pp. 177-187.

Bogue, R. 2009. Energy Harveting and Wireless Sensors: A Reveiw of Recent Developments. *Sensors Review* 29(3), pp. 194-199.

Bowen, C. R. et al. 2006. Optimisation of Interdigitated Electrodes for Piezoelectric Actuators and Active Fibre Composites. *Journal of Electroceramics* 16(4), pp. 263-269.

Broughton, W. R. et al. 1998. Overiew of DTI-funded Programme on 'Standardised Procedures for Ultrasonic Inspection of Polymer Matrix Composites. *Insight – Non-Destructive Testing and Condition Monitoring* 40(1), pp. 8-11.

Chang, F. K. and Markmiller, J. F. C. 2006. A New Look in Design of Intelligent Structures with SHM. *Structural Health Monitoring 2006: Proceedings of the Third European Workshop on Structural Health Monitoring*, pp. 5 - 20.

Chen, W. et al. 2012. Research on Energy Harvesting Behaviours of Different Shapes of Piezoelectric Vibrator. *Applied Mechanincs and Materials* 164, pp. 441-445.

Chidambaram, N. et al. 2012. Measurement of Effective Piezoelectric Coefficients of PZT Thin Films for Energy Harvesting Application with Interdigitated Electrodes. *IEEE Transactions on Ultrasonics, Ferroelectrics and Frequency Control* 59(8), pp. 1624-1631.

Chlada, M. et al. 2010. Neural Network AE Source Location Apart From Structure Size and Material. *Journal of Acoustic Emission* 28, pp. 99-108.

Ciampa, F. and Meo, M. 2010. A New Algorithm for Acoustic Emission Localization and Flexural Group Velocity Determination in Anisotropic Structures. *Composites: Part A* 41(12), pp. 1777-1786.

Clarke, T. et al. 2009. Evaluation of the Damage Detection Capability of a Sparse-Array Guided-Wave SHM System Applied to a Complex Structure Under Varying Thermal Conditions. *IEEE Transactions on Ultrasonics, Ferroelectrics and Frequency Control* 56(12), pp. 2666-2678.

Clarke, T. et al. 2010. Guided Wave Health Monitoring of Complex Structures by Sparse Array Systems: Influence of Temperature Changes on Performance. *Journal of Sound and Vibration* 329(12), pp. 2306 - 2332.

Cousland, S. M. and Scala, C. M. 1983. Acoustic emission during the plastic deformation of aluminium alloys 2024 and 2124. *Materials Science and Engineering* 57(1), pp. 23-29.

Croxford, A. J. et al. 2010. Efficient Temperature Compensation Strategies for Guided Wave Structural Health Monitoring. *Ultrasonics* 50(4-5), pp. 517-528.

Cybernetics, R. 2013. [Online]. Available at: http://www.rmcybernetics.com/projects/experiments/experiments_vortex.htm [Accessed: 27/01/2013].

Delebarre, C. et al. 2012. Power Harvesting Capabilities of SHM Ultrasonic Sensors. *Smart Materials Research* 2012(387638).

Dicken, J. et al. 2012. Power-Extraction Circuits for Piezoelectric Energy Harvesters in Miniature and Low-Power Applications. *IEEE Transactions on Power Electronics* 27(11), pp. 4514-4529.

Ding, Y. et al. 2004. A New Method for Waveform Analysis for Estimating AE Wave Arrival Times Using Wavelet Decomposition. *NDT & E International* 37(4), pp. 279-290.

Eaton, M. 2007. *Acoustic Emission (AE) Monitoring of Buckling and Failure in Carbon Fibre Composite Structures.* Cardiff University.

Eaton, M. et al. 2011. Characterisation of Damage in Composite Structures using Acoustic Emission. *Journal of Physics: Conference Series* 305(012086), pp. 1-9.

Eaton, M. et al. 2009. Use of Macro Fibre Composite Transducers as Acoustic Emission Sensors. *Remote Sensing* 1(2), pp. 68 - 79.

Eaton, M. J. et al. 2012a. Detection and Location of Impact Damage using Acoustic Emission. In: *Second International Conference on Advanced Composite Materials and Technologies for Aerospace Applications (ACMTAA-2012).* Wrexham.

Eaton, M. J. et al. 2012b. Acoustic Emission Source Location in Composite Materials using Delta T Mapping. *Composite: Part A* 43(6), pp. 856-863.

Eaton, M. J. et al. 2012c. Structural Health Monitoring of Composite Structures Using Embedded Sensors. In: *ECCM15 - 15th European Conference on Composite Materials.* Venice.

Emery, T. R. and Dulieu-Barton, J. M. 2010. Thermoelastic Stress Anaylsis of Damage Mechanisms in Composite Materials. *Composites: Part A* 41(12), pp. 1729-1742.

Ertuk, A. et al. 2009. Piezoelectric Energy Harvesting from Multifunctional Wing Spars for UAVs - Part 1: Coupled Modelling and Preliminary Analysis. *Proceedings of the SPIE* 7288(72880C).

Fang, H. B. et al. 2006. Fabrication and Performance of MEMS-based Piezoelectric Power Generator for Vibration Energy Harvesting. *Microelectronics Journal* 37(11), pp. 1280 - 1284.

Farinholt, K. et al. 2009. Energy Harvesting and Wireless Energy Transmission for Embedded Sensor Nodes. *Proceedings of the SPIE* 7288(728810).

Featherston, C. A. et al. 2009. Thermoelectric Energy Harvesting for Wireless Sensors Systems in Aircraft. *Key Engineering Materials* 413-414, pp. 487-494.

Ferrari, M. et al. 2010. Improved Energy Harvesting from Wideband Vibrationsby Nonlinear Piezoelectric Converters. *Sensors and Actuators A: Physical* 162(2), pp. 425-431.

Fromme, P. and Sayir, M. B. 2002. Detection of Cracks at Rivet Holes using Guided Waves. *Ultrasonics* 40(1-8), pp. 199 - 203.

Fruehmann, R. K. et al. 2010. Assessment of Fatigue Damage Evolution in Woven Composite Materials using Infra-Red Techniques. *Composite Science and Technology* 70(6), pp. 937-946.

Fruehmann, R. K. et al. 2012. The Application of Thermoelastic Stress Analysis to Full Scale Aerospace Structures. *Journal of Physics: Conference Series* 382(012058).

Gambier, P. et al. 2012. Piezoelectric, Solar and Thermal Energy Harvesting for Hybrid Low-Power Generator Systems with Thin-Film Batteries. *Measurement Science and Technology* 23(1), pp. 1-11.

Giurgiutiu, V. 2003. Embedded Ultrasonics with Piezoelectric Wafer Active Sensors for Structural Health Monitoring of Thin Wall Structures. *Proceedings of IMECE 2003: 2003 ASME International Mechanical engineering Congress* 43552, pp. 1 - 9.

Grondel, S. et al. 2004. Health Monitoring of a Composite Wing Box Structure. *Ultrasonics* 42(1-9), pp. 819 - 824.

Grosse, C. 2000. *Winpecker version 1.2. Instruction Manual Stuttgart: University of Stuttgart*.

Gu, H. and Wang, L. 2009. A Monolithic Interdigitated PVDF Transducer for Lamb Wave Inspection. *Structural Health Monitoring* 8(2), pp. 137-148.

Hamstad, M. A. et al. 2002. A Wavelet Transform Applied to Acoustic Emission Signals: Part 2: Source Location. *Journal of Acoustic Emission* 20, pp. 62-82.

Han, J. et al. 2006. The Propagation of Lamb Waves in a Laminated Composite Plate with a Variable Stepped Thickness. *Composite Structures* 76(4), pp. 388 - 396.

He, T. et al. 2012. Near-Field Beamforming Analysis for Acoustic Emission Source Localization. *Ultrasonics* 52(5), pp. 587-592.

Hehn, T. et al. 2012. A fully Autonomous Integrated Interface Circuit for Piezoelectric Harvesters. *IEEE Journal of Solid-State Circuits* 47(9), pp. 2185-2198.

Hensman, J. et al. 2010. Locating Acoustic Emission Sources in Complex Structures using Gaussian Processes. *Mechanical Systems and Signal Processing* 24(1), pp. 211-223.

Hinkley, D. V. 1971. Inference About the Change-Point for Cumulative Sum Tests. *Biometrika* 58(3), pp. 509-523.

Hita-Romero, M. ed. 2006. *New Technology Frontiers on Commercial Aircrafts*. Structural Health Monitoring 2006: Proceedings of the 3rd European Workshop on Structural Health Monitoring. Spain.

Hsu, N. N. and Breckenbridge, F. R. 1981. Characterisation and Calibration of Acoustic Emission Sensors. *Materials Evaluation* 39(1), pp. 60 - 68.

Ibragimov, A. et al. 2012. A Thermoelectric Energy Harvester Directly Embedded into Casted Aluminium. *Electron Devices Letters, IEEE* 33(2), pp. 233-235.

Ihn, J. B. and Chang, F. K. 2008. Pitch-catch active sensing methods in structural health monitoring for aircraft structures. *Structural Health Monitoring 2008* 7(1), pp. 5-19.

Jeon, Y. B. et al. 2005. MEMS Power Generator with Transverse Mode Thin Film PZT. *Sensors and Actuators A: Physical* 122(1), pp. 16-22.

Jeong, H. 2001. Analysis of Plate Wave Propagation in Anisotropic Laminates using Wavelet Transform. *NDT & E International* 34(3), pp. 185-190.

Jeong, H. and Jang, Y.-S. 2000. Wavelet Analysis of Plate Wave Propagation in Composites Laminates. *Composites Structures* 49(4), pp. 443-450.

Jiao, J. et al. 2004. Application of Wavelet Transform on Modal Acoustic Emission Source Location in Thin Plates with One Sensor. *International Journal of Pressure Vessels and Piping* 81(5), pp. 427-431.

Jingpin, J. et al. 2008. Acoustic Emission Source Location Methods using Mode and Frequency Analysis. *Structural Control and Health Monitoring* 15(4), pp. 642-651.

Kapoor, H. et al. eds. 2009. *Prospective Applications for SHM on Commercial Aircraft*. Structural Health Monitoring 2009: From System Integration to Autonomous Systems. Proceedings of the 7th International Workshop on Structural Health Monitoring. California.

Karami, M. A. et al. 2013. Parametrically Excited Nonlinear Piezoelectric Compact Wind Turbine. *Renewable Energy* 50, pp. 977-987.

Katerelos, D. T. G. et al. 2009. In-situ Damage Monitoring of Cross-ply Laminates using Acoustic Emission. *Plastics, Rubber and Composites* 38(6), pp. 229 - 234.

Kim, H. S. et al. 2011. A Review of Piezoelectric Energy Harvesting Based on Vibration. *Internatioal Journal of Precision Engineering and Manufacturing* 12(6), pp. 1129-1141.

Kim, J. K. et al. 2009. A Practical System Approach for Fully Autonomous Multi-dimensional Structural Health Monitoring. *Proceedings of the SPIE: Sensors and Smart Structures Technologies for Civil, Mechanical, and Aerospace Systems 2009* 7292(72921L).

Kim, Y. H. et al. 2007. Damage Assessment in Layered Composites using Spectral Analysis and Lamb Wave. *Composites Part B: Engineering* 38(7-8), pp. 800 - 809.

Kitagawa, G. and Akaike, H. 1978. A Procedure for the Modeling of Non-Stationary Time Series. *Annals of the Institute of Statistical Mathematics* 30(1), pp. 351-363.

Knight, C. and Davidson, J. 2010a. *Advances in Wireless Sensors and Sensor Networks*. Springer.

Knight, C. and Davidson, J. 2010b. Thermoelectric Energy Harvesting as a Wireless Sensor Node. *Proceedings of the SPIE* 7643(76431E).

Kong, N. and Ha, D. S. 2012. Low-Power Design of a Self-Powered Piezoelectric Energy Harvesting System with Maximum Power Point Tracking. *IEEE Transactions on Power Electronics* 27(5), pp. 2298-2308.

Konstantinidis, G. et al. 2007. An Investigation into the Temperature Stability of a Guided Wave Structural Health Monitoring System using Permanently Attached Sensors. *IEEE Sensors Journal* 7(5), pp. 905-912.

Kurz, J. H. et al. 2005. Strategies for Relaible Automatic Onset Time Picking of Acoustic Emissions and of Ultrasound Signals in Concrete. *Ultrasonics* 2005(7), pp. 538-546.

Liao, Y. and Sodano, H. A. 2012. Optimal Placement of Piezoelectric Material on a Cantilever Beam for Maximum Piezoelectric Damping and Power Harvesting Efficiency. *Smart Materials and Structures* 21(10), pp. 1-9.

Lievan, N. A. J. et al. 2009. Towards Wireless Sensor Usage and Health Monitoring of Helicopter Rotor Components. *AIAC-13 Thirteenth Australian International Aerospace Congress/ Sixth DSTO International Conference on Health and Usage Monitoring*.

Lin, B. and Giurgiutiu, V. 2006. Modelling and testing of PZT and PVDF Piezoelectric Wafer Active Sensors. *Smart Materials and Structures* 15(4), pp. 1085-1093.

Liu, H. et al. 2011. A MEMS-based Piezoelectric Cantilever Patterned with PZT Thin Film Array for Harvesting Energy from Low Frequency Vibrations. *Physics Procedia: 2011 International Conference on Opticsin Precision Engineering and Nanotechnology* 19, pp. 129 - 133.

Liu, T. et al. 2002. Single Mode Lamb Waves in Composite Laminated Plates Generated by Piezoelectric Transducers. *Composite Structures* 58(3), pp. 381 - 396.

Lokajicek, T. and Kilma, K. 2006. A First Arrival Identification system of Acoustic Emission Signals by Means of a High-Order Statistics Approach. *Measurement Science and Technology* 17(9), pp. 2461-2466.

Loutas, T. H. and Kostopoulos, V. 2009a. Health monitoring of carbon/carbon, woven reinforced composites: Damage assessment by using advanced signal processing techniques. Part I: Acoustic emission monitoring and damage mechanisms evolution. *Composite Science and Technology* 69(2), pp. 265 - 272.

Loutas, T. H. and Kostopoulos, V. 2009b. Health monitoring of carbon/carbon, woven reinforced composites: Damage assessment by using advanced signal processing techniques. Part II: Acousto–ultrasonics monitoring of damage development. *Composite Science and Technology* 69(2), pp. 273 - 283.

Lu, X. and Yang, S.-H. eds. 2010. *Thermal Energy Harvseting for WSNs*. IEEE International Conference on Systems, Man and Cybernetics. Istanbul.

Ly, R. et al. 2011. Modelling and Characterization of Piezoelectric Cantilever Bending Sensor for Energy Harvesting. *Sensors and Actuators A: Physical* 168(1), pp. 95-100.

Lympertos, E. M. and Dermatas, E. S. 2007. Acoustic Emission Source Location in Dispersive Media. *Signal Processing* 87(1), pp. 3218 - 3225.

Maeda, N. 1985. A Method for Reading and Checking Phase Times in Auto-Processing System of Seismic Wave Data. *Zisin = Jishin* 38(3), pp. 365-379.

Maria De Rosa, I. and Sarasini, F. 2010. Use of PVDF as Acoustic Emission Sensor for In Situ Monitoring of Mechanical Behaviour of Glass/Epoxy Laminates. *Polymer Testing* 29(6), pp. 749-758.

Markmiller, J. F. C. and Chang, F. K. 2010. Sensor Network Optimization for a Passive Sensing Impact Detectiom Technique. *Structural Health Monitoring* 9(1), pp. 25-39.

Mascarenas, D. L. et al. 2007. Development of an Impedance-based Wireless Sensor Node for Structural Health Monitoring. *Smart Materials and Structures* 16(1), pp. 2137 - 2145.

Matt, H. M. 2007. *Structural Diagnostics of CFRP Composite Aircraft Components by Ultrasonic Guided Waves and Built-in Piezoelectric Transducers.* University of California San Diego.

Matt, H. M. and Lanza di Scalea, F. 2007. Macro-Fiber Composite Piezoelectric Rosettes for Acoustic Source Location in Complex Structures. *Smart Materials and Structures* 16(4), pp. 1489 - 1499.

Michaels, J. E. and Michaels, T. E. 2007. Guided Wave Signal Processing and Image Fusion for In Situ Damage Localization in Plates. *Wave Motion* 44(6), pp. 482 - 492.

Micropelt. 2012a. *http://micropelt.com/products/products.php* [Online]. Available at: [Accessed.

Micropelt. 2012b. *MPF-D651 MPG-D751 Thin Film Thermogenerators and Sensing Devices* [Online]. Available at: [Accessed.

Miller, R. K. et al. 2005. *Nondestructive Testing Handbook, Third Edition: Volume 6, Acoustic Emission Testing*. ASNT.

Morton, T. M. et al. 1973. Acoustic emissions of fatigue crack growth. *Engineering Facture Mechanics* 5(3), pp. 691-697.

Moser, A. et al. 2012. Thermoelectric Energy Harvesting from Transient Ambient Temperature Gradients. *Journal of Electronic Materials* 41(6), pp. 1653-1661.

Moulin, E. et al. 1997. Piezoelectric Transducer Embedded in a Composite Plate: Application to Lamb Wave Generation. *Journal of Applied Physics* 82(5), pp. 2049-2055.

Mousoulis, C. et al. eds. 2012. *Thermoelectric Energy Scavenging with Temperature Gradient Amplification*. IEEE International Conference on Micro Electro Mechanical Systems (MEMS). Paris.

Ng, T. H. and Liao, W. H. 2005. Sensitivity Analysis and Energy harvesting for a Self Powered Piezoelectric Sensor. *Journal of Intelligent Material Systems and Structures* 16(10), pp. 785-797.

Ottman, G. K. et al. 2002. Adaptive Piezoelectric Energy Harvesting Circuit for Wireless Remote Power Supply. *IEEE Transactions on Power Electronics* 17(5), pp. 669-676.

Paget, C. A. 2001. *Active Health Monitoring of Aerospace Composite Structures by Embedded Piezoceramic.* KTH Royal Institute of Technology.

Paget, C. A. et al. 2003. Triangulation Algorithm for Damage Location in Aeronautical Composites Structures. In: Chang, F.K. ed. *Structural Health Monitoring 2003: From Diagnostics & Prognostics to Structural Health Management: Proceedings of the 4th International Workshop on Structural Health Monitoring.* California. pp. 363-370.

Paget, C. A. et al. 2000. Behaviour of an Embedded Piezoceramic Transducer for Lamb Wave Generation in Mechanical Loading. *Proceedings of the SPIE, Smart Structures and Materials 2000: Smart Structures and Integrated Systems* 3985, pp. 510-520.

Palumbo, G. and Pappalardo, D. 2010. Charge Pump Circuits: An Overview on Design Strategies and Topologies *IEEE Circuits and Systems Magazine* 10(1), pp. 31-45.

Park, S. et al. 2009. Instantaneous Baseline Damage Detection Using a Low Power Guided Waves System. *Structural Health Monitoring 2009: Proceedings of the Seventh International Workshop on Structural Health Monitoring* 1, pp. 505 - 512.

Pasquale, G. D. et al. 2011. Piezoelectric Energy Harvesting for Autonomous Sensors Netwrok on Safety-Improved Railway Vehicles. *Proceedings of the Instrituion of Mechanical Engineers, Part C: Journal of Mechanical Engineering Science* 226(4), pp. 1107 - 1117.

Pearson, M. R. et al. 2011. Impact Damage Detection and Assessment in Composite Panels using Macro Fibre Composites Transducers. *Journal of Physics: Conference Series* 305(12049).

Pearson, M. R. et al. 2012. Energy Harvesting for Aerospace Structural Health Monitoring Systems. *Journal of Physics: Conference Series* 382(12025).

Petitjean, B. et al. eds. 2006. *Damage Dectection on Aerospace Structures: Last Developments at EADS*. Structural Health Monitoring 2006: Proceedings of the 3rd European Workshop on Structural Health Monitoring. Spain.

Pollock, A. 1986. Classical Wave Theory in Practical AE Testing. *Progress in Acoustic Emission III, Proceedings of the Eighth International Acoustic Emission Symposium, The Japanese Society for Nondestructive Testing*, pp. 708 - 721.

Priya, S. and Inman, D. J. 2009. *Energy Harvesting Technologies*. Springer.

Pullin, R. et al. 2012a. Identification of the Onset of Cracking in Gear Teeth Using Acoustic Emission. *Journal of Physics: Conference Series* 382(12050).

Pullin, R. et al. 2012b. On the Development of a Damage Detection System using Macro-fibre Composite Sensors. *Journal of Physics: Conference Series* 382(12049).

Pullin, R. et al. 2011. Assessment of bonded patch bridge repairs using acoustic emission and Acousto-Ultrasonics. *Key Engineering Materials: Structural Health Monitoring II* 518.

Pullin, R. et al. 2005. Modal Analysis of Acoustic Emission Signals from Artificial and Fatigue Crack Sources in Aerospace Grade Steel. *Key Engineering Materials: Damage Assessment of Structures VI: DAMAS 2005: Proceedings of the 6th International Conference on Damage Assessment of Structures* 293 - 294, pp. 217 - 226.

Raghavan, A. 2007. *Guided-Wave Structural Health Monitoring.* The University of Michigan.

Rajagipalan, J. et al. 2006. A Single Transmitter Multi-Receiver (STMR) PZT Array for Guided Ultrasonic Wave Based Structural Health Monitoring of Large Isotropic Plate Structures. *Smart Materials and Structures* 15(5), pp. 1085 - 1093.

Ramberg, W. and Osgood, W. R. 1943. Description of Stress-Strain Curves by Three Parameters. *Techical Note No. 902* National Advisory Comittee for Aeronautics.

Rindorf, H. J. 1981. Acoustic Emission Source Location in Theory and in Practice. *Bruel and Kjaer Technical Review* No 2, pp. 3 - 44.

Rippengill, R. et al. 2003. Automatic Classification of Acoustic Emission Patterns. *Strain* 39(1), pp. 31-41.

Rowe, D. M. ed. 1995. *CRC Handbook of Thermoelectrics.* CRC Press.

RTCA. 2004. *D0-160E Environmental Conditions and Test Procedures for Airborne Equipment*.

Ruggier, E. et al. 2002. *Smart Materials in Inflatable Structure Applications*.

Saggini, S. et al. eds. 2010. *Supercapacitor-based Hybrid Storage Systems for Energy Harvesting in Wireless Sensor Networks*. 25th Annual IEEE Applied Power Electronics Conference and Exposition California.

Samson, D. et al. 2010a. Energy Harvesting for Remote Monitoring of Aircraft Seats. *Sensor Letters* 8(2), pp. 328-335.

Samson, D. et al. 2010b. Optimisation of a Heat Storage Device for an Aircraft Specific Thermoelectric Power Generator. In: *8th European Conference on Thermoelectrics.* Italy.

Samson, D. et al. 2011. Wireless Sensor Node Powered by Aircraft Specific Thermoelectric Energy Harvesting. *Sensors and Actuators A: Physical* 172(1), pp. 240-244.

Samson, D. et al. 2012. Flight Test Results of a Thermoelectric Energy Harvester for Aircraft. *Journal of Electronic Materials* 41(6), pp. 1134-1137.

Samson, D. et al. 2010c. Aircraft-Specific Thermoelectric Generator Module. *Journal of Electronic Materials* 39(9), pp. 2092-2095.

Scala, C. M. and Cousland, S. M. 1983. Acoustic Emission during fatigue crack propagation in the aluminium alloys 2024 and 2124. *Materials Science and Engineering* 61(3), pp. 211-218.

Scala, C. M. and Cousland, S. M. 1985. Acoustic emission during fatigue of aluminium alloy 2024: the effect of an overload. *Materials Science and Engineering* 76, pp. 83-88.

Scholey, J. J. et al. 2009. A Generic Technique for Acoustic Emission Source Location. *Journal of Acoustic Emission* 27.

Schubert, L. et al. 2009. Interaction of Lamb Waves with Impact Damaged CFRP's - Effects and Conclusions for Actouso-Ultrasonic Applications. *Structural Health Monitoring 2009 - Proceedings of the 7th International Workshop on Stuctural Health Monitoring* 1, pp. 151-158.

Schumacher, T. et al. 2012. Towards a Probabilistic Acoustic Emission Source Location Algorithm: A Bayesian Approach. *Journal of Sound and Vibration* 331(19), pp. 4233-4245.

Sedlak, P. et al. 2009. New Automatic Localization Technique of Acoustic Emission Signals in Thin Metal Plates. *Ultrasonics* 49(2), pp. 254-462.

Shehadeh, M. et al. 2006. Acoustic Emission Source Location for Steel Pipe and Pipeline Applications: The Role of Arrival Time Estimation. *Proceedings of the Institue of Mechanical Engineers, Part E: Journal of Process* 220(2), pp. 121-133.

Smith, R. A. et al. 1998. Diffraction and Shadowing Errors in -6dB Defect Sizing of Delaminations in Composites. *Insight – Non-Destructive Testing and Condition Monitoring* 40(1), pp. 44-49.

Sodano, H. A. et al. 2005. Comparison of Piezoelectric Energy Harvesting Devices for Recharging Batteries. *Journal of Intelligent Material Systems and Structures* 16(10), pp. 799-807.

Sodano, H. A. et al. 2006. An experimental comparison between several active composite actuators for power generation. *Smart Materials and Structures* 15(5), pp. 1211 - 1216.

Sodano, H. A. et al. 2004. An Investigation into the Performance of Macro-Fiber Composites for Sensing and Structural Vibration Applications. *Mechanical Systems and Signal Processing* 18(3), pp. 686-697.

Sodano, H. A. et al. 2007. Recharging Batteries using Energy Harvested from Thermal Gradients. *Journal of Intelligent Material Systems and Structures* 18(1), pp. 3-10.

Song, H. J. et al. 2009. Performance Evaluation of Multi-Tier Energy Harvesters Using Macro-fiber Composite Patches. *Journal of Intelligent Material Systems and Structures* 20(17), pp. 2077-2088.

Song, H. J. et al. 2010. Energy Harvesting Devices Using Macro-fiber Composite Materials. *Journal of Intelligent Material Systems and Structures* 21(6), pp. 647-658.

Spies, P. et al. eds. 2007. *Energy Harvesting for Mobile Communication Devices*. International Telecommunications Energy Conference. Italy.

Stiffler, R. and Henneke, E. G. 1983. The Application of Polyvinylidene Flouride as an Acoustic Emission Transducer for Fibrous Composite Materials. *American Society for Nondestructive Testing - Materials Evaluation* 41(8), pp. 956-960.

Sun, Y. et al. 2012. An Integrated High Performance Active Rectifier for Piezoelectric Vibration Energy Harvesting Systems. *IEEE Transactions on Power Electronics* 27(2), pp. 623-627.

Surgeon, M. and Wevers, M. 1999a. Modal Analysis of Acoustic Emission Signals from CFRP Laminates. *NDT & E International* 32(6), pp. 311-322.

Surgeon, M. and Wevers, M. 1999b. One Sensor Linear Location of Acoustic Emission Events using Plate Wave Theories. *Materials Science and Engineering:A* 265(1-2), pp. 254-261.

Suzuki, H. et al. 1996. Wavelet Transform of Acoustic Emission Signals. *Journal of Acoustic Emission* 14, pp. 69-84.

Theobald, P. and Thompson, A. 2005. *Towards a Calibrated Reference Source for In-Situ Calibration of Acoustic Emission Measurement Systems*. National Physical Laboratory: National Physical Laboratory.

Tracy, M. and Chang, F. K. 1996. Identifying Impact Laod in Composite Plates Based on Distributed Piezolectric Sensor Measurements. *Proceedings of SPIE - The Society of Photo-Optical Instrumentation Engineers* 2717, pp. 231-236.

Vishnuvardhan, J. et al. 2009. Structural Health Monitoring of Anisotropic Pates using Utrasonic Guided Wave STMR Array Patches. *NDT & E International* 42(3), pp. 193 - 198.

Vullers, R. J. M. et al. 2009. Micro Power Energy Harvesting. *Solid-State Electronics* 53(7).

Wang, C. S. and Chang, F. K. 2000. Diagnosis of Impact Damage in Composite Structures with Built-in Piezoelectroc Network. *Proceedings of SPIE - The Society of Photo-Optical Instrumentation Engineers* 3990, pp. 13-19.

Wang, W. et al. 2011. Thermoelectric Powered Autonomous Wireless Sensor Module for Temperature Monitoring. *Applied Mechanincs and Materials* 63-64, pp. 978-982.

Wanga, C. H. et al. 2003. Computerized Time-reversal Method for Structural Health Monitoring. *Proceedings of the SPIE* 5046(48).

Wickenheiser, A. and Garcia, E. 2009. Combined Power Harvesting from AC and DC Sources. *Proceedings of the SPIE* 7288(728816).

Wilkie, W. et al. 2002. *Reliability Testing of NASA Piezo-Composite Actuators*.

Williams, R. B. and Inman, D. J. 2002. An Overview of Composite Actuators with Piezoceramic Fibers. In: *IMAC-XX: Conference & Exposition on Structural Dynamics - Smart Structures and Transducers.*

Williams, R. B. et al. 2003a. *Nonlinear Mechanical Behaviour of Macro Fiber Composites Actuators*.

Williams, R. B. et al. 2003b. *Temperature Dependen Coefficients of Thermal Expansion for Macro Fiber Composite Actuators*.

Wood, O. J. et al. 2012. Optimised Vibration Energy Harvesting for Aerospace Applications. *Key Engineering Materials* 518, pp. 246-260.

Wright, J. A. 2005. *Piezoelectric Fiber Composites for Ultrasound Transduction*.

Wu, J. et al. 2007. A Wireless Sensor Network Node Designed for Exploring a Structural Health Monitoring Application. *Smart Materials and Structures* 16(5), pp. 1898 - 1906.

Yamada, H. et al. 2000. Lamb Wave Source Location of Impact on Anisotropic Plates. *Journal of Acoustic Emission* 18, pp. 51-60.

Yan, T. et al. 2004. A Conical Piezoelectric Transducer with Integral Sensor as a Calibrating Acoustic Emission Energy Source. *Ultrasonics* 42(1-9), pp. 431-438.

Zagrai, A. N. 2002. *Piezoelectric Wafer Active Sensors Eleectro-Mechanical Impedance Structural Health Monitoring.* University of South Carolina.

Zhao, X. et al. 2007. Active health monitoring of an aircraft wing with embedded piezoelectric sensor/actuator network: I. Defect detection, localization and growth monitoring. *Smart Materials and Structures* 16(4), pp. 1208 - 1217.

Zhou, D. et al. 2009. Ultra Low-Power Autonomous Wireless Structural Health Monitoring Node. *Structural Health Monitoring 2009: Proceedings of the Seventh International Workshop on Structural Health Monitoring* 1, pp. 797 - 804.

Zhu, D. and Beeby, S. P. 2010. *Kinetic Energy Harvesting*. Springer.

Zhu, D. et al. 2011. A Credit Card Sized Self Powered Smart Sensor Node. *Sensors and Actuators A: Physical* 169(2).

Zhu, M. and Edkins, S. 2011. Analytical Modelling Results of Piezoelectric Energy Havesting Devices for Self-Power Sensors/Sensor Networks in Structural Health Monitoring. *Procedia Engineering* 25, pp. 195-198.

Ziola, S. M. and Gorman, M. R. 1991. Source Location in Thin Plates using Cross-Correlation. *Journal of the Acoustical Society of America* 901(5), pp. 2551-2556.